George C. Sih

Solid Mechanics and Its Applications

Multiscale Fatigue Crack Initiation and Propagation of Engineering Materials: *Structural Integrity and Microstructural Worthiness*

Fatigue Crack Growth Behaviour of Small and Large Bodies

Springer

Multiscale Fatigue Crack Initiation and Propagation of Engineering Materials: Structural Integrity and Microstructural Worthiness

SOLID MECHANICS AND ITS APPLICATIONS
Volume 152

Series Editor: G.M.L. GLADWELL
Department of Civil Engineering
University of Waterloo
Waterloo, Ontario, Canada N2L 3GI

Aims and Scope of the Series

The fundamental questions arising in mechanics are: *Why?*, *How?*, and *How much?* The aim of this series is to provide lucid accounts written by authoritative researchers giving vision and insight in answering these questions on the subject of mechanics as it relates to solids.

The scope of the series covers the entire spectrum of solid mechanics. Thus it includes the foundation of mechanics; variational formulations; computational mechanics; statics, kinematics and dynamics of rigid and elastic bodies: vibrations of solids and structures; dynamical systems and chaos; the theories of elasticity, plasticity and viscoelasticity; composite materials; rods, beams, shells and membranes; structural control and stability; soils, rocks and geomechanics; fracture; tribology; experimental mechanics; biomechanics and machine design.

The median level of presentation is the first year graduate student. Some texts are monographs defining the current state of the field; others are accessible to final year undergraduates; but essentially the emphasis is on readability and clarity.

For a list of related mechanics titles, see final pages.

G.C. Sih

Editor

Multiscale Fatigue Crack Initiation and Propagation of Engineering Materials: Structural Integrity and Microstructural Worthiness

Fatigue Crack Growth Behaviour of Small and Large Bodies

Springer

G.C. Sih
East China University of Science
Shanghai, China

and

Institute of Fracture and Solid Mechanics
Lehigh University
Bethlehem, Pennsylvania, USA

ISBN-13: 978-1-4020-8519-2 e-ISBN-13: 978-1-4020-8520-8

Library of Congress Control Number: 2008xxxxx

Printed on acid-free paper

9 8 7 6 5 4 3 2 1

springer.com

Table of Contents

Foreword

What can be added to the fracture mechanics of metal fatigue that has not already been said since the 1900s? From the view point of the material and structure engineer, there are many aspects of failure by fatigue that are in need of attention, particularly when the size and time of the working components are changed by orders of magnitude from those considered by traditional means. The 21st century marks an era of technology transition where structures are made larger and devices are made smaller, rendering the method of destructive testing unpractical. While health monitoring entered the field of science and engineering, the practitioners are discovering that the correlation between the signal and the location of interest depends on a priori knowledge of where failure may initiate. This information is not easy to find because the integrity of the physical system will change with time. Required is software that can self-adjust in time according to the monitored data. In this connection, effective application of health monitoring can use a predictive model of fatigue crack growth.

Earlier fatigue crack growth models assumed functional dependence on the maximum stress and the size of the pre-existing crack or defect. Various possibilities were examined in the hope that the data could be grouped such that linear interpolation would apply. The idea of associating fatigue test data with design was made when the data led to a straight line relationship with the range of mode I stress intensity factor on a log-log plot. The y-intercept and slope of this line were found by curve fitting and considered to be material specific even though they also depended on specimen size. Wide acceptance of this approach was soon adopted due to the simplicity of integrating the two-parameter relation for determining the critical crack length for different specimen configuration. Moreover, the stage of slow and stable crack growth was able to be delineated from the onset of unstable and rapid crack propagation. Even at this date efforts are being made to better understood the physical meaning of the crack growth rate data outside the range of the two-parameter straight line zone referred to as region II. Region I and III are associated, respectively, with fatigue crack initiation and fast crack propagation, not to mention the two transitional zones where region II connects to regions I and III. Despite the exhaustive undertakings

to examine microphotographs the phenomenon of multiscale fatigue crack growth remains elusive.

One of the main objectives of this book is to examine size-scale dependent microstructure evolution of fatigue damage affiliated with small specimens ranging from micrometer to nanometer. These details enhance the understanding of small scale fatigue damage mechanisms. The scale of investigation is also expanded by several orders of magnitude to include slip mismatch due to differences in grain size, orientation, micro-texture, etc which arise because of the irregular propagation of short cracks. The fatigue damage map method (FDMM) was used to quantify the results which are compared with multiscale test data. In addition the effects of strain rate, temperature and hold time on the high temperature on the low cycle fatigue of austenitic and ferritic steels and Nimonic PE16 superalloy are also examined to study their microstructural changes and crack initiation and propagation behavior.

Modeling crack growth rate data under simple and complex load spectra differing from the conventional approaches invoking crack closure or constraint effects are attempted. Micro to macro range of crack sizes in a variety of metals are used to correlate data on a straight line referred to a linear scale covering the regions I, II and III with two empirical parameters. A large number of problems are considered. They include the 1969 Lockheed F-111 wing fatigue test; the F/A-18 final test program; the round robin helicopter test program; cracking in composite patched panels; USAF C-141 repair; and NASA centre notch panel tests.

Analytical dual scale model is presented to describe the transitory behavior of micro-/macro-cracking for the fatigue of 7075-T6 and 2024-T3 aluminum pre-cracked panels. Accounted for are small cracks that can close in compression and open in tension as in the case of alternating fatigue loading. Interactive effects of load, geometry and material are considered by using three independent micro/macro parameters to render the fatigue growth rate data form invariant in a log-log plot. The straight line correlation enables the connection of data referred to micro- and macro-cracking in fatigue. The same approach was applied to analyze the fatigue life of cables and steel wires of the Rungyang cable-stayed bridge based on the design data with and without traffic. The wide variations of predicted life for the 52 cables can be problematic for the future maintenance of the bridge as some cables may need early replacement while others can still be used.

Improved fatigue damage tolerance behavior of aerospace high purity 2024 aluminum alloy is discussed in connection with load sequence and spectrum effects. Of equal concern for aerospace application is thermo-mechanical fatigue in the presence of oxidation and creep strain

accumulation. Virtual testing methodology is explored for fatigue crack growth associated with the safe-life assessment of aerospace structural components. Fatigue data of butt welded joints of aluminium alloys for 6061-T6 and 6082-T6 coupon specimens are found and needed to quantify the influence of three different welding techniques. They are the metal inert gas welding, laser beam welding and friction stir welding.

It should be said the consideration of length alone is not enough for distinguishing micro- from macro-defect since the change of defect morphology may take place during scale transition. Creation of macro-fracture free surface is caused predominantly by mechanical load giving rise to symmetric or skew-symmetric geometric pattern whereas asymmetry typifies the creation of micro-fracture that are obstructed by the highly irregular material microstructure. Microcracks tend to wonder by curving and branching because of the inherent different constraint of the adjoining crack surface. Micro-photos of fatigue striations suggest that the very tip of a microcrack always remains open on account of geometric asymmetry. This additional tip distance suggests a micro-stress singularity that can differ from the macro-stress singularity. It so happen that a micro-/macro-crack can possess a double singularity: one weak and one strong. The dual singularity gave allowance to scale transition where a microcrack can turn to a macrocrack or vice versa. This is precisely what occurs in tension/compression alternating fatigue loading. Micro- and macro-cracking correspond, respectively, to crack opening (tension) and closing (compression). Reference can be made to macromechanical and microstructural to accentuate the influence of scale with cause. Nanochemical would refer to imperfection size resulting from chemical reaction.

The cause of fatigue can be traced to the loss of electrons from metal atoms in chemical reaction. Such a process in the presence of repeated mechanical loading even for small amplitude can greatly reduce the life of metals. The destruction can involve oxidation that increases the susceptibility of the local region to nanocrack initiation. The grain boundary is a likely location where the atoms are more loosely packed. A simple approach would be to use a mean characteristic length to describe a nano defect with the corresponding energy density weighed by a scale factor related to inhomogeneity of the atoms or the atomic lattices. The same can be done at the micro and macro scale level. When needed scale divisions can be further refined by introducing meso regions to fill the gaps from one scale range to another. Cause-and-effect studies of material damage in fatigue require a sufficiently long stretch of scaling such that nano data can be brought up to the macroscopic scale. Use can be made of the overwhelming amount of micrograph data presented in this volume. They

demonstrate the different fatigue crack growth details due to strain rate, temperature, loading type, material, processing technique and other factors. In this way the practitioner can benefit. Although the foregoing task is still far from being accomplished, it is essential to start focusing attention in that direction.

No work on fatigue crack growth can possibly claim to be complete. The interpretation of the same data can vary as the physical models will differ. The field of fatigue damage being as important as it is to material and structure application, the entailing course of future development is inextricably linked to the social, political, economic and ideological predilection of the establishment. The limited attempt made here can only represent the views of the contributors to whom gratitude is due. Special thanks go to Ren Huifang who design the book cover and to Shen Shufang who help to format the manuscripts.

Shanghai, China, 2007
G. C. Sih

Contributors

Barter S
Air Vehicles Division, Defence Science and Technology Organisation,
506 Lorimer Street, Fishermans Bend 3207, Australia
Simon.Barter@defence.gov.au

de Castro PMST
Faculdade de Engenharia da Universidade do Porto Rua Dr. Roberto Frias,
200-465 Porto Portugal
ptcastro@fe.up.pt

Dini D
Department of Mechanical Enginineering, Imperial College London South,
Kensington Campus, London SW7 2AZ, UK
d.dini@imperial.ac.uk

Farahmand B
The Boeing Company, IDS, 5301 Bolsa Ave, Huntington Beach,
CA 92647, USA
Bob.Farahmand@Boeing.com

Höppel HW
Department of Materials Science and Engineering, Universität
Erlangen-Nuernberg, Martensstrasse 5, D-91058 Erlangen, Germany
hoeppel@ww.uni-erlangen.de

Jones R
Cooperative Research Centre for Integrated Engineering Asset Management
(CIEAM), Department of Mechanical Engineering, Monash University, P.O.
Box 31, Monash University, Victoria, 3800, Australia
Rhys.Jones@eng.monash.edu.au

Kermanidis AlTh
Department of Mechanical and Industrial Engineering, University of
Thessaly, 38334 Volos, Greece
akermanidis@mie.uth.gr

Korsunsky AK
Department of Engineering Science, University of Oxford, Parks Road, Oxford OX13PJ, UK
Alexander.korsunsky@eng.ox.ac.uk

Mannan SL
National Engineering College, Kovilpatti, TN, India
sardari_mannan@yahoo.com

Molent L
Air Vehicles Division, Defence Science and Technology Organisation, 506 Lorimer Street, Fishermans Bend 3207, Australia
Lorrie.Molent@dsto.defence.gov.au

Moreira PMGP
Faculdade de Engenharia da Universidade do Porto Rua Dr. Roberto Frias, 4200-465 Porto, Portugal
pmgpm@fe.up.pt

Mughrabi H
Department of Materials Science and Engineering, Universität Erlangen-Nuernberg, Martensstrasse 5, D-91058 Erlangen, Germany
Hael.Mughrabi@ww.uni-erlangen.de

Pantelakis SpG
Laboratory of Technology and Strength of Materials, Department of Mechanical Engineering and Aeronautics, University of Patras, Greece
pantelak@mech.upatras.gr

Peng D
DSTO Centre of Expertise for Structural Mechanics, Department of Mechanical Engineering, Monash University, P.O. Box 31, Monash University, Victoria, 3800, Australia
Daren.Peng@eng.monash.edu.au

Pitt S
Air Vehicles Division, Defence Science and Technology Organisation, 506 Lorimer Street, Fishermans Bend, Victoria 3207, Australia
monsafe@bigpond.net.au

Richter-Trummer V
Combustion Systems Engineering, Rolls-Royce plc, P.O. Box 31, Derby DE24 8BJ, UK
valentine@fe.up.pt

Rodopoulos CA
Laboratory of Technology and Strength of Materials, Department of Mechanical Engineering and Aeronautics, University of Patras, Panepistimioupolis, Patras 26500, Greece
Rodopoul@mech.upatras,gr

Sih GC
International Center for Sustainability, Accountability and Eco-Affordability of Large Structures (ICSAELS) Advanced Technology for Large Structural Systems (ATLSS), Lehigh University, Bethlehem, PA 18015, USA; and Department of Mechanical Engineering and Mechanics, Lehigh University, Bethlehem, PA 18015, USA
gcs8866@yahoo.com

Tang XS
School of Bridge and Structural Engineering, Changsha University of Science and Technology, Changsha, Hunan 410076, China
Tang-xuesong231@sohu.com

Valsan M
Indira Gandhi Centre for Atomic Research, Kalpakkam, TN, India

Walsh MJ
Combustion Systems Engineering, Rolls-Royce plc, P.O. Box 31, Derby DE24 8BJ, UK
Michael.Walsh@Rolls-Royce.com

Wang ZG
Shenyang National Laboratory for Materials Science, Institute of Metal Research, Chinese Academy of Sciences, 72 Wenhua Road, Shenyang 110016, China
zhgwang@imr.ac.cn

Zhang GP
Shenyang National Laboratory for Materials Science, Institute of Metal Research, Chinese Academy of Sciences, 72 Wenhua Road, Shenyang 110016, China
gpzhang@imr.ac.cn

Application of Virtual Testing for Obtaining Fracture Allowable of Aerospace and Aircraft Materials

B. Farahmand
The Boeing Company, IDS
5301 Bolsa Ave, Huntington Beach, CA 92647, USA
Email: bob.farahmand@boeing.com

Abstract

Fracture toughness and fatigue crack growth rate data are two key parameters which are necessary for conducting safe life analysis of fracture critical parts used in space and aircraft structures. Currently, these allowables are obtained through the ASTM testing standards which are costly and time consuming. In many occasions, due to budget limitations and deadlines set forth by the customer, it is not possible to conduct fracture related tests in time. A proposed numerical approach has been developed [1-3] that is based on the extended Griffith theory and can predict fracture allowables for a variety of alloys. The simplicity of the concept is based on the use of basic, and in most cases available, uniaxial full stress-strain data to derive material fracture toughness values. Because the fracture toughness is thickness dependent, its value for several thicknesses can be calculated and used in the residual strength capability analysis. More importantly, its value is used to predict the region III of the fatigue crack growth rate curve. Regions I & II of the da/dN versus ΔK curve can be estimated separately and will be connected to region III to establish the total fatigue crack growth rate data. As the result of this work two computer codes, fracture toughness determination (FTD) and fatigue crack growth (FCG), were generated under the NASA contract. Results of fracture toughness and fatigue crack growth rate data calculated by this approach were compared with numerous test data in the NASGRO database [4]. Excellent agreements between analyses and test data were found, which will validate the FTD and FCG methodology. This novel approach is referred to as the virtual testing technique. It enables engineers to generate fracture allowable analytically by eliminating unnecessary tests. Yet, there is another innovative approach in the virtual testing arena that relies on the multiscale modeling and simulation technique. This technique is becoming popular in the field of computational materials, where failure mechanism is defined from the bottom up approach. The methodology is based on the ab-initio concept where it is assumed that the failure of material will initiate from the atomistic level, where nanocracks under the applied load will grow (as the

G.C. Sih (ed.), Multiscale Fatigue Crack Initiation and Propagation of Engineering Materials: Structural Integrity and Microstructural Worthiness, 1–22.

result of poor bonding) and advance toward the micro, meso, and macro level, which thereafter will cause total structural failure. It should be noted that in most cases microscopic cracks already pre-existed in the part during the machining operation, assembling parts, or rough handling. Section 6 will briefly review the application of multiscale modeling and simulation technique and its application on aerospace and aircraft parts.

1. Introduction & Background

The requirements of all fracture control plans for space and aircraft structures dictate that fracture critical components must have adequate life during their service operation. The safe-life assessment of these components requires information on material allowables such as: the plane stress (K_c), plane strain (K_{Ic}), part-through fracture toughness (K_{Ie}), and the fatigue crack growth rate properties. Fracture tests under the ASTM testing standard procedures require detailed specimen preparation, pre-fatiguing the notch, fatigue crack growth rate measurements and interpretation of raw data, which are all costly and time consuming. Furthermore, in order for valid material property data to be produced for each case-specific material batch, a substantial number of tests will typically need to be performed. Therefore, any method that can improve and optimize this process, and reduce the number of experimental tests, will help reduce costs without compromising any safety issues. The proposed analytical technique uses fundamental fracture-mechanics-based reasoning to establish a link between plastic damage development in uniaxial stress-strain data and the material's fracture mechanics allowables. Even though the methodology is working for a variety of aerospace alloys, further validation for a wider range of materials may be required. In this work, the concept uses steel, aluminum and titanium based alloys from a pedigree database. Furthermore, it quantifies material property sensitivity to the predictions for K_{Ic} and K_c and the subsequent estimation of ΔK_{th} threshold and the Paris constants, C and n values. The prediction of K_{Ic} and K_c is based on the energy balance approach. It has been shown previously that material residual strength capability curve (a plot of fracture stress versus half a crack length) can be generated through the Griffith theory for an elastic media. This has been extended to account for the presence of plastic deformation at the crack tip [1, 3]. The energy absorption rate at the crack tip process zone could be assumed to have a similar mode of deformation of uniaxial specimens. Hence the material stress-strain curve of a uniaxial specimen can reflect the local energy dissipation profile within the process zone and can describe the fracture behavior of a cracked specimen as long as the stress and strain distribution and the subsequent energy balance is satisfied. Similar ideas of

a process zone have been previously considered at high temperatures [5] whereby creep cracking within a process zone can be described by the failure behavior of uniaxial creep test. In this proposed model, the failure range in the process zone is due to the elastic/plastic loading in a uniaxial tensile test specimen, whereas in the creep case the criteria for the damage process is a time dependant elastic/plastic/creep phenomenon. However, it has been shown that creep and plasticity can be treated in a self-similar manner using non-linear fracture mechanics concepts.

In a tensile case, the total energy per unit thickness absorbed in plastic straining around the crack tip, U_P, can be written as the sum of two energy terms ($U_P = U_F + U_U$) where U_F and U_U are the energy absorbed per unit thickness in plastic straining of the material beyond the ultimate at the crack tip and below the ultimate stress near the crack tip, respectively. The rate of energy absorbed at the crack tip in terms of available and consumed energy terms, U_E, U_S, U_F and U_U, can be rewritten by $\partial [U_E - U_S - U_F - U_U]/\partial c = 0$. Determining the rate at which energy is absorbed in crack tip plastic deformation ($\partial U_F/\partial c$ and $\partial U_U/\partial c$), the residual strength capability equation for ductile material can be established. The quantity $\partial U_S/\partial c$ is the energy rate for creating two new crack surfaces. Having fracture stress and half critical crack length on hand, the critical value of the stress intensity factor (fracture toughness, K_c) can be calculated. More importantly, the variation of material fracture toughness, K_c, as a function of part thickness, can be established, which is extremely useful when conducting a safe-life assessment of fracture critical components of aircraft and space hardware where parts thickness can vary significantly. Section 2 will include the detail description of the extended Griffith theory.

Fracture toughness values calculated for a variety of aerospace alloys were in excellent agreement with test data which will be discussed in section 3. Moreover, this technique was further extended to predict the fatigue properties of aerospace metallic material under a cyclic loading environment. Fatigue crack growth rate tests under the ASTM E645 testing standard procedures are costly and time consuming. In the proposed technique, each region of the da/dN curve will be established separately and then connected to obtain the total fatigue crack growth rate data. It uses the predicted K_c and K_{Ic} values to derive the Paris constants, C & n. Section 4 includes a detailed explanation related to this topic.

2. Detail Description of the Extended Griffith Theory

This theory assumes the fracture characteristics of a metal, local to the crack tip, are directly related to its ability to deform. Crack tip straining is assumed to be of two kinds: local strainability at the crack tip (the region of

highly plastic deformation) and uniform strainability near the crack tip. Thus, fracture behavior can be characterized by two energy released terms representing the absorbed energy at and near the crack tip. Both terms can be shown to be determinable from the full uniaxial stress-strain curve. The two deformation regions are illustrated in Fig. 1. The total energy per unit thickness absorbed in plastic straining of the material around the crack tip, U_P, can be written as:

$$U_P = U_F + U_U \tag{1}$$

where U_F and U_U are the energy absorbed per unit thickness in plastic straining of the material beyond the ultimate at the crack tip and below the ultimate stress near the crack tip, respectively. Eq. (1) can be rewritten as:

$$\partial[U_E - U_F - U_U]/\partial c = 0 \tag{2}$$

where $\partial U_F/\partial c$ and $\partial U_U/\partial c$ are the rates at which energy is absorbed in plastic straining beyond the ultimate stress at the crack tip and below the ultimate stress near the crack tip, respectively. To obtain a relationship between the applied stress and critical crack length, the energy absorption rates, $\partial U_F/\partial c$ and $\partial U_U/\partial c$, for the two plastic regions formed around the crack tip must be determined. Sections 2.1 and 2.2 will discuss the derivation of $\partial U_F/\partial c$ and $\partial U_U/\partial c$ terms, respectively. Applied stress and crack length relationship will be discussed in section 2.3.

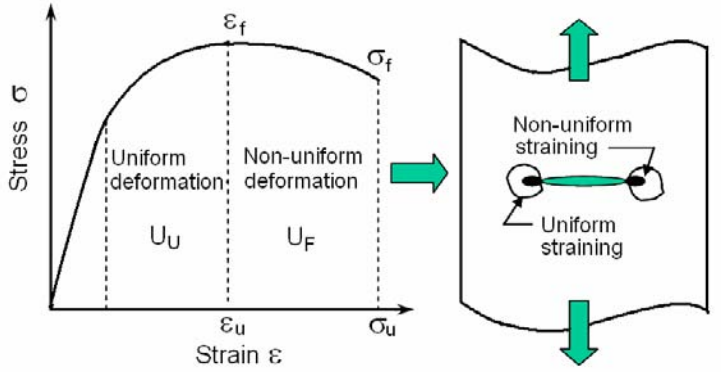

Fig. 1 The crack tip plastic zone and different region of the stress-strain curve.

2.1 Determination of $\partial U_F/\partial c$ term

To obtain the energy absorption rate for the highly strained region at the crack tip, the extended Griffith equation in terms of its components can be rewritten as:

$$\frac{\pi\sigma^2 c}{E} = 2T + \frac{\partial U_F}{\partial c} + \frac{\partial U_U}{\partial c} \tag{3}$$

where $2T=\partial U_S/\partial c = \beta E\alpha$ is the surface tension of the material, that is, the work done in breaking the atomic bonds, α is the atomic spacing in angstroms, E is the material modulus of elasticity, and β is the correction factor ($3.94\text{x}10^{-10}$ inch/angstrom). The quantity $\partial U_F/\partial c$ in Eq. (3), is set equal to $W_F h_F$, where W_F is equal to the unrecoverable energy density (energy per unit volume) represented by the area under the plastic uniaxial engineering stress-strain curve (from the stress at which necking begins to the stress at the fracture point) for an uncracked tensile specimen. For a given alloy, the area under the stress-strain curve from the stress at which necking begins to the stress at the fracture point is a constant for a wide range of thicknesses, and therefore, the value of W_F is a constant. It is assumed that essentially all of the energy represented by W_F is absorbed at the crack tip in a single dominant coarse slip band. The quantity h_F is the size of the highly strained portion of the small region at the crack tip as a result of W_F. Its minimum value is considered to be equal to the effective height of a coarse slip band oriented to make an angle of 45^o with the plane of the crack under monotonic load. At room temperature the quantity h_F = 0.00056 in. (approximately 10 micrometers). An empirical relationship based on test data [1,3] has been developed for tough metals with large necking strains that gives a higher h_F value and better correlation with the test data than the value h_F = 0.00056 in. It is assumed that the quantity h_F is directly related to the energy per unit volume, W_F, for the material in consideration, and was formulated as:

$$h_F = \gamma(E^2/\sigma_U^3)W_F \tag{4}$$

where $\gamma \doteq (8/\pi)\alpha h_{\min}$, σ_U is the material ultimate allowable stress, $h_{\min}$=0.00056 in. and α is material atomic spacing. The atomic spacing, α, for Aluminum, Titanium alloys, and Iron and Nickel are 2.86 and 2.48 Angstrom, respectively. The quantity W_F in Eq. (4) is the area under the

stress strain curve from necking up to fracture (see Fig. 1) and is approximately equal to:

$$W_F = \bar{\sigma}_{UF}\varepsilon_{PN} \tag{5}$$

where $\bar{\sigma}_{UF}$ is the neck stress and its value is taken at the centroid of the plastic energy bounded on the top by the stress-strain curve from the beginning of necking to fracture and on the bottom by a straight line from the beginning of necking to fracture. For material with a negligible amount of necking the neck stress $\bar{\sigma}_{UF} = (\sigma_{Ult} + \sigma_F)/2$. The plastic straining, ε_{PN}, (Eq. 5) at the onset of necking is fully discussed in reference [1]. Eq. (3) in terms of h_F, $\bar{\sigma}_{UF}$, and ε_{PN} can be expressed as:

$$\frac{\pi\sigma c}{E} = 2T + h_F\bar{\sigma}_{UF}\varepsilon_{PN} + \frac{\partial U_U}{\partial c} \tag{6}$$

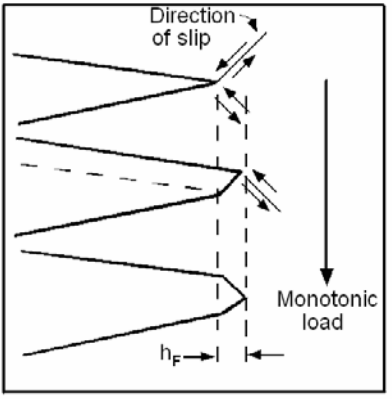

Fig. 2 The quantity h_F is the effective height of the highly strained portion of the small region at the crack tip as a result of W_F.

2.2 Determination of $\partial U_U/\partial c$ term

The quantity $\frac{\partial U_U}{\partial c}$ can be expressed as $W_U h_U$, where W_U is the unrecoverable energy density represented by the area under the plastic uniaxial stress-strain curve from the elastic limit stress, σ_L, to the ultimate allowable stress, σ_U, for an un-cracked specimen. Eq. (6) becomes:

$$\frac{\pi\sigma^2 c}{E} = 2T + h_F\bar{\sigma}_{UF}\varepsilon_{PN} + W_U h_U \tag{7}$$

The effective height of the volume in which W_U is absorbed in the uniform plastic region at the crack tip is h_U. Steps taken to derive the energy rate term, $\frac{\partial U_U}{\partial c}$, for the plane stress condition are as follows:

- Obtain the true crack tip stresses (σ_{Tr}, $\sigma_{T\theta}$, and $\sigma_{Tr\theta}$) in terms of applied stress and crack length in polar coordinates by using the linear elastic fracture mechanics. These stresses are responsible for material deformation at the crack tip region.
- Use the octahedral shear stress theory [1, 3] to correlate the biaxial tension stress with the true uniaxial tension stress, σ_T.
- Apply the crack tip uniaxial tension strain, ε_T, in the energy absorption rate equation, to obtain the $\frac{\partial U_U}{\partial c}$ term (or $W_U h_U$).

The term $\frac{\partial U_U}{\partial c}$ in its final form is given by:

$$\frac{\partial U_U}{\partial c} = h\left(\frac{n+1}{n-1}\right) W_U \left[\frac{\varepsilon_{FT}\varepsilon_{TL}}{\varepsilon_{TU}\varepsilon_T}\right] * \left[\left(\frac{\varepsilon_{TU}}{\varepsilon_{TU}}\right)^{-} - 1\right]\beta \tag{8}$$

where h=0.00056 inch. The unrecoverable energy density W_U is:

$$W_U = \frac{n}{n+1}\varepsilon_{TPU}\sigma_{TU}\left[1 - \left(\frac{\sigma_{TL}}{\sigma_{TU}}\right)^{n+1}\right] \tag{9}$$

2.3 Applied stress and crack length relationship

Eq. (3) describing the extended Griffith theory in terms of crack length, c:

$$c = \frac{E}{\pi\sigma^2}[2T + W_F h_F + W_U h_U] \tag{10}$$

For a thin plate the value of β=1.3 describing the thickness correction for the plane stress conditions. Expressing half a crack length, c, in terms of its components, $W_U h_U$ and $W_F h_F$, for wide plate becomes:

$$c = \frac{E}{\pi\sigma^2\mu}\left\{2T + \bar{\sigma}_{UF}\varepsilon_{PN}h_F k + h * \left(\frac{n}{n-1}\right)\sigma_{TU}\varepsilon_{TU}\left[1 - \left(\frac{\sigma_T}{\sigma_{TU}}\right)^{n+1}\right]\right.$$
$$\left. * \left[\frac{\varepsilon_{TF}\varepsilon_{TL}}{\varepsilon_{TU}\varepsilon_T}\right] * \left[\left(\frac{\varepsilon_{TU}}{\varepsilon_{TL}}\right)^{n-1/n} - 1\right]\beta\right\} \tag{11}$$

where n is the strain hardening coefficient. For a finite width condition the width correction factor Y is included:

$$c = \frac{E}{\pi\sigma^2\mu Y^2}\left\{2T + \bar{\sigma}_{UF}\varepsilon_{PN}h_F k + h * \left(\frac{n}{n-1}\right)\frac{\sigma_{TU}\varepsilon_{TU}}{Y^6}\left[1 - \left(\frac{\sigma_T}{\sigma_{TU}}\right)^{n+1}\right]\right.$$
$$\left. * \left[\frac{\varepsilon_{TF}\varepsilon_{TL}}{\varepsilon_{TU}\varepsilon_T}\right] * \left[\left(\frac{\varepsilon_{TU}}{\varepsilon_{TL}}\right)^{n-1/n} - 1\right]\beta\right\} \tag{12}$$

where $Y = \left(\cos\frac{\pi c}{W}\right)^{-1}$. Other terms in Eq. (12) are related to true stress and strain and are defined as:

$c = Half\ crack\ length$
$n = Strain\ hardening\ coeficient$
$\sigma = Applied\ stress$
$\sigma_T = True\ stress$
$\sigma_{TU} = True\ stress\ at\ ultimate$
$\sigma_{UF} = Stress\ between\ ultimate\ \&\ fracture$
$\varepsilon_T = True\ strain$
$\varepsilon_{PN} = Plastic\ strain\ at\ necking$
$\varepsilon_{TU}, \varepsilon_{TL}, \varepsilon_{TL} = True\ strain\ at\ ultimate, \lim it\ \&\ fracture$
$k, \mu, \beta = Thickness\ corrections$

Parameters μ, k and β are factors that are used to account for the thickness correction and they are applied to both sides of the components of Eq. (12) where energy is available and consumed for plastic deformation. Fig. 3 describes the shear lip formation in the plane-stress fracture, whereas a plane-strain fracture is characterized by a flat fracture surface. It is assumed that the energies released and absorbed in plane-stress and

plane-strain are in proportion to these thicknesses. Let t_0 be the maximum thickness for plane-stress fracture. The thickness corrections k & μ are applied to two strained regions at the crack tip. These quantities, thickness parameters are expressed in terms of maximum thickness for plane stress fracture, t_0 (the amount of shear lip), total thickness, t, (Fig. 3) and Poisson's ratio ν.

$$k = \left[\frac{t_0}{t} + \left(2\frac{t-t_0}{t}\right)\right],\ \mu = \left[\frac{t_0}{t} + (1-\nu^2)\left(\frac{t-t_0}{t}\right)\right],\ \beta = \left[0.13\frac{t_0}{t} + 0.12\left(\frac{t-t_0}{t}\right)\right]$$

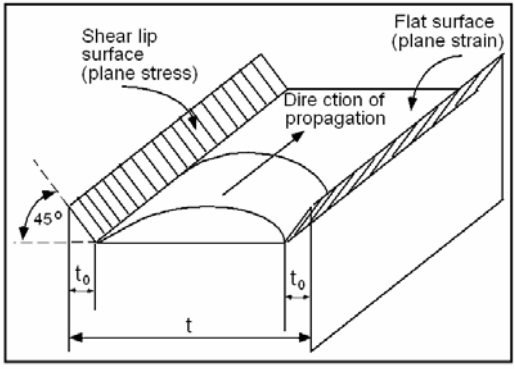

Fig. 3 The shear lip formation in the plane-stress fracture. The plane-strain fracture is characterized by a flat fracture surface.

3. Fracture Toughness Calculation

To obtain the fracture toughness value of aerospace alloys through the virtual testing approach (by applying the proposed technique), the equation of the stress intensity factor of a center crack specimen can be used, $K=Y\sigma\sqrt{\pi c}$, where half crack length, c, can be calculated via Eq. (12). It should be noted that a full stress-strain curve for the material under investigation must be available as shown in Fig. 1. To validate the result of this technique, test data from the NASGRO material database [4] were selected and the variations of K_c versus part thickness were plotted for two aluminum alloys using the FTD software [6], Fig. 4. The effect of plate width and crack length on fracture toughness (narrow and wide plates) was compared with the data from the NASGRO database [4].

It should be noted that the NASGRO curve for a given material is not based on numerous tests at different thicknesses through which a smooth curve passes. Rather, it is based on a relationship between K_c and thickness

observed from multiple materials (Fig 5). This relationship is available via an empirical equation proposed by [7] as a function of K_{Ic} and material yield value, which represent the lower bound of K_c values for a given part thickness. Fig. 5 contains numerous test data which umbrellas the whole range of plate width and crack lengths, a. The estimated empirical NASGRO curve fit represents the lower bound and in some cases the typical values of K_c. The upper bound value of data shown in Fig. 5 must be associated with larger cracks and wider plates. For this reason the FTD has the option of plotting the fracture toughness versus thickness variations for plates of different width. The narrow plate represents the fracture toughness associated with small cracks where the residual strength can be as high as 75% of the material yield value. Good agreement between the physical testing and analysis can be seen when analytical data were compared with typical values of test data.

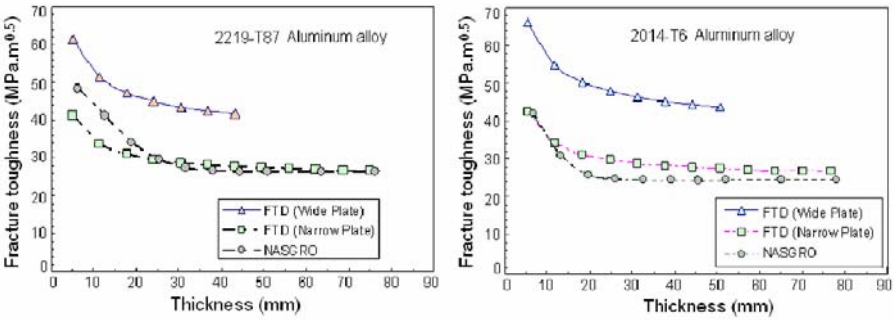

(a) 2219-T87 (b) 2014-T6

Fig. 4 Example of Fracture toughness versus plate thickness for two aluminum alloys compared to NASGRO data [4]).

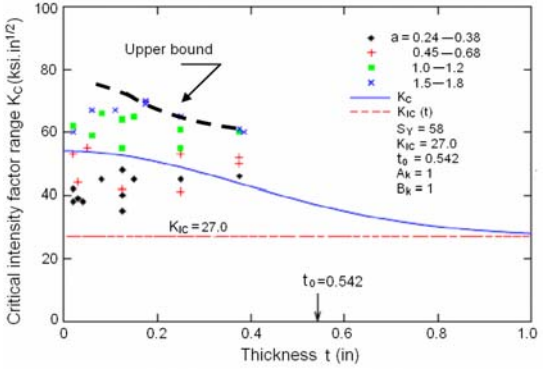

Fig. 5 Measured Fracture Toughness versus thickness for several crack lengths of 2219-T87 aluminum [1]).

4. Generating Fatigue Crack Growth Rate Curve without Testing

4.1 Establishing region I (fracture toughness)

The testing procedure in the ASTM E647 is currently used to obtain fatigue crack growth rate data through physical testing. The proposed technique identifies the relevant parameters affecting the micro-mechanical behavior within a plastic process zone and relates it to plastic damage in uniaxial tensile tests. It then uses the data from the uniaxial stress/strain test to derive the materials' fracture toughness values via the extended Griffith theory. The fracture toughness value is used to establish region III of the da/dN versus ΔK curve (the accelerated region). The total curve will then be plotted by estimating the other two regions of the curve (Fig. 6). Using data derived from the analysis of a wide range of tensile data it has been established [8] that a relationship exists between K_{th} (ΔK_{th} for R=0) and the plane strain fracture toughness for aluminum, K_{Ic}, giving $\alpha = K_{Ic}/\Delta K_{th}$.

4.2 Establishing region II (Paris region)

To estimate the Paris region, the two quantities K_c & K_{th} must be available. These two quantities will be helpful to establish two points in the Paris region. The two points in Fig. 6 (the lower and upper points of the Paris region corresponding to points 1 and 2) have unique properties which are common among many aluminum alloys. The lower point in the steady crack growth rate region, just before getting into the threshold zone of the fatigue curves (point 1 of Fig. 6), has a material independent property. That is, the ratio of the stress intensity factor, K, at the mean lower bound point and the threshold value, K_{th}, ($\Delta K/\Delta K_{th}$ for $R=0$) is ~1.125 for the crack growth rate per cycle, da/dN ~2.54E-6 mm/cycle (~1.0E-7 in./cycle). In the upper region of the da/dN curve (at the end of the steady crack growth Paris region, point 2 of Fig. 6), the ratio of the upper bound stress intensity factor, K, and its critical value, K_c, ($\Delta K/K_c$ for R=0) is found to be ~0.9 for the da/dN ~0.127 mm/cycle (~0.005 in./cycle) from the data. These two unique points in the Paris region were found when plotting numerous fatigue crack growth rate data for aluminum as shown in Fig. 7. Therefore, by having the two quantities K_c and K_{th} available, the two points in the Paris region can be

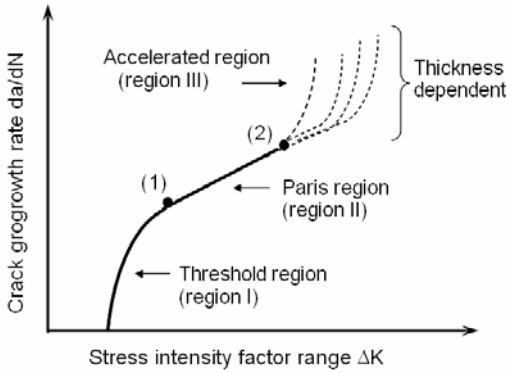

Fig. 6 Three regions of the d*a*/d*N* curve (threshold, Paris and accelerated regions).

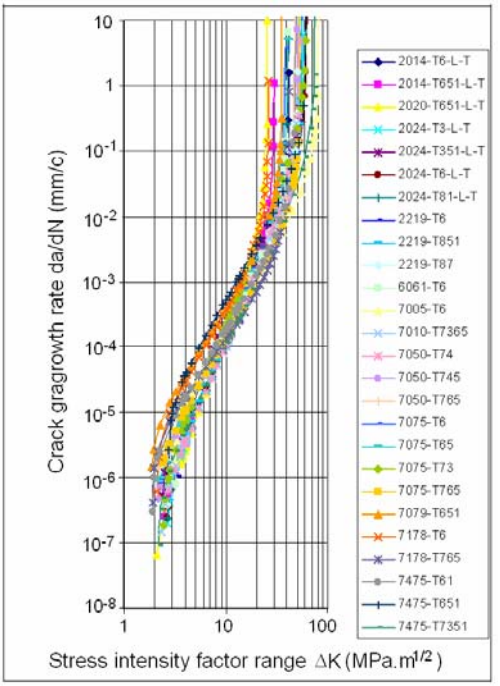

Fig. 7 Fatigue crack growth rate curve for several aluminum alloys where the two points in the Paris region are unique.

$$\frac{da}{dN} = \frac{C(1-f)^n \Delta K^n \left(1 - \frac{\Delta K_{th}}{\Delta K}\right)^p}{(1-R)^n \left(1 - \frac{\Delta K}{(1-R)K_c}\right)^q} \tag{13}$$

generated. Hence, the C and n of fatigue crack growth rate constants shown in Eq. (13) (region II) can be determined [4]. The above assumptions used for establishing the Paris region are also applicable to Titanium and Steel alloys.

4.3 Establishing region III (threshold stress intensity factor, K_{th})

The methodology used to estimate the threshold stress intensity factor analytically is based on studying the threshold values of more than one hundred tests from different metallic alloys and relating it to several key static and fracture allowables. The variation of K_{th} values for $R=0$ for each alloy were compared with the variation of other parameters such as material yield, F_{ty}, final elongation, ε_f, and the plane strain fracture toughness, K_{Ic}. The quantity K_{th} was found to be related to the material plane strain fracture toughness for aluminum alloys, where $K_{Ic} = \alpha K_{th}$. In the latter portion of this section we will also assess the relationship between the K_{th} and final elongation, ε_f, for aluminum, titanium and steel alloys separately. Fig. 8 shows the NASGRO value of K_{th} for several aluminum, titanium and steel alloys. Fig. 9 shows the plot of $\alpha = K_{Ic}/K_{th}$ for the data points shown in Fig. 8. From Figs 8 and 9 it can be seen that the NASGRO value of K_{th} is material dependent and has varying ranges for aluminum, titanium and steel alloys. From the experimental K_{th} values in Fig. 8, mean values of $\Delta K_{th}=2.5$ MPa$\sqrt{m}$ for Aluminum alloys, $\Delta K_{th}=4$ MPa$\sqrt{m}$ for the Titanium alloys and $\Delta K_{th}=5$ MPa$\sqrt{m}$ for steels are found. The scatter for the steels are seen to be highest because of different types of steel with wide range of tensile properties and the scatter for Aluminum is seen to be the lowest.

Looking at the stress-strain curves for several aluminums, the final elongation for most aluminums fall between 8 and 12% with K_{Ic} values range from 20 to 27 MPa$\sqrt{m}$. This is one reason for aluminums alloys having the minimum amount of scatter as indicated in Fig. 8 when compared with the steel. The range of α for aluminums and titanium falls approximately between 7-14 and 9-16, respectively (see Fig. 9). The range of α for variety of steels is also shown in Fig. 9 and their lower and upper values are 5 and 25, respectively.

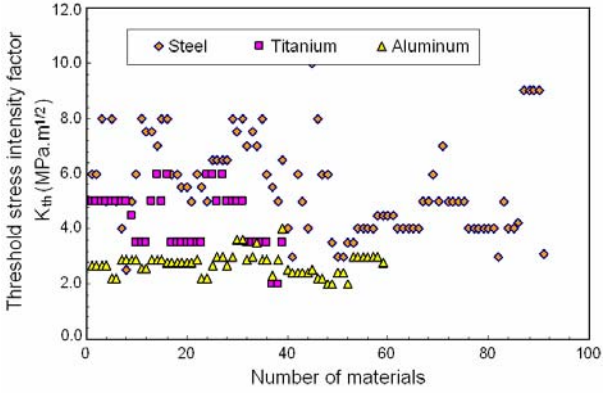

Fig. 8 Threshold stress intensity factor values for more than one hundred alloys.

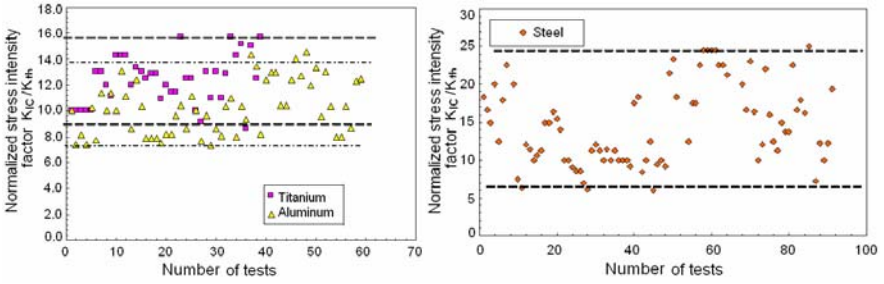

Fig. 9 The plot of $\alpha=K_{Ic}/K_{th}$ for the data points shown in Fig. 8.

To understand the physical relationship that may exist between tensile and fracture behavior, correlations between them has been established for the different alloys. Fig. 10 shows the relationship between tensile final elongation, ε_f, and K_{th} for the data of different alloys. Fig. 10 suggests that the tensile elongation could be an important factor in understanding the fracture properties in these alloys and improving the predictions for fatigue and fracture. Using the best fit equations shown in the Fig. 10, it would possible to get the K_{th} using available tensile ductility for use in the FCG code [6] to calculate da/dN data. The best fit equations for K_{th} give:

$$K_{th} = -0.6337 + 0.3148\varepsilon_f \tag{14}$$

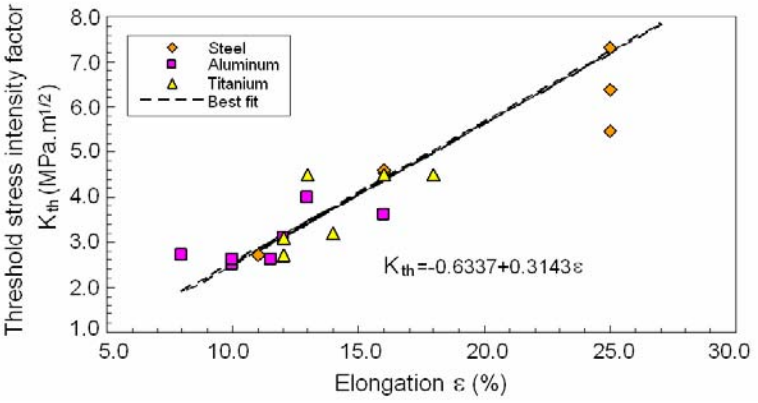

Fig. 10 Best fit curve for the variation of K_{th} versus elongation, ε_f .

Eq. (14) gives a very good indication of a linear relationship between K_{th} and ε_f. This will allow FCG to use the estimated K_{th} from Eq. (14) to generate the total da/dN curve. The total predicted fatigue crack growth data, covering all the regions of the da/dN curve, can then be plotted using Eq. (13), where the fracture parameters and constants are taken from the estimated K_c, K_{th}, and the Paris constants C and n values. For any other range of R-ratios the Newman closure equation, *f*, [4] can be used to establish the full fatigue crack growth rate curve when $R \neq 0$. In all cases the constants p and q of equation 13 were taken as 0.5 and 1, respectively.

5. Comparison of Predicted Bounds with Experimental Fatigue Crack Growth Data

Established and then compared with fatigue crack growth test data in NASGRO database. The computer program, [6] which can run the simulations of the model, and the World Wide Web were made available in order to verify a number of test cases. The input of data can be treated as deterministic data or as probabilistic bounds of the data. Based on the above-mentioned assumptions (construction of accelerated, Paris, and threshold regions), the fatigue crack growth curves for three alloys are e.

The use of the statistical method gives further confidence to the methodology and is therefore crucial to any sensitivity analysis that would be needed in design and life estimation methods. In obtaining material properties data through physical or virtual testing, it is always expected some level of scatter on fracture toughness and fatigue crack growth values. The scatter is due to material variations through heat lots when the material

is processed. A lesser amount of variation can also be observed in test coupons that have been machined from a given plate of a given manufacturer by a specified heat lot. For comparison with test data, the upper and lower bounds for alpha, α, for each of the alloy sets were taken from Fig. 9 and compared with test data available in NASGRO. Figs. 11-13 show the predicted bounds of fatigue crack growth curves for the Al, Ti and the steel family of alloys. In all cases the experimental data fall between the two limits of ε_f value. Numerous data comparisons between analyses and test data are available and are reported in [8].

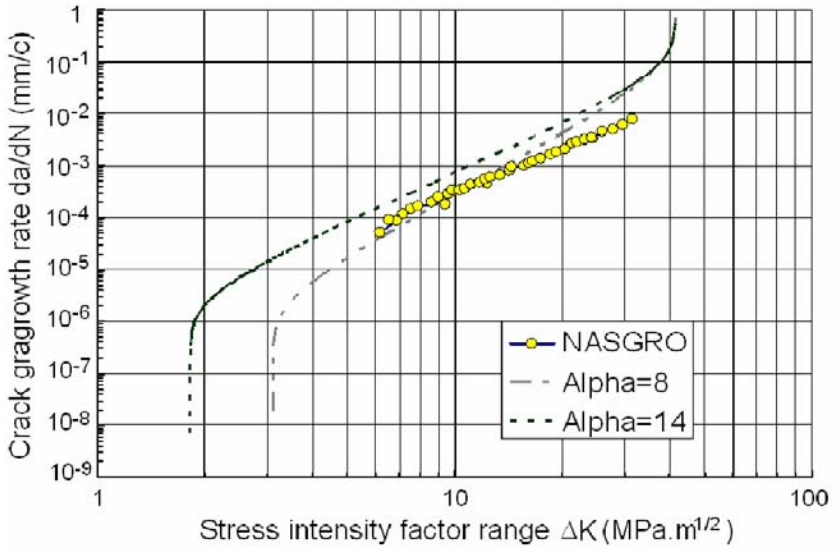

Fig. 11 FCG and NASGRO d*a*/d*N* curves for 6061-T62 aluminum.

For life assessment analysis of structural components it will be appropriate to use the lower bound d*a*/d*N* data corresponding to the upper bound α values. The upper bound values of α (lower K_{th} value) can provide a conservative life assessment. It may be possible to avoid unnecessary conservatism by tuning the threshold value to the material ductility, using the correlations shown by Eq. (10), in order to obtain a better agreement with the test data.

6. Fracture Mechanics & Multiscale Modeling & Simulation

The virtual testing methodology discussed in the previous sections of this chapter was based on the continuum mechanics approach, where the linear

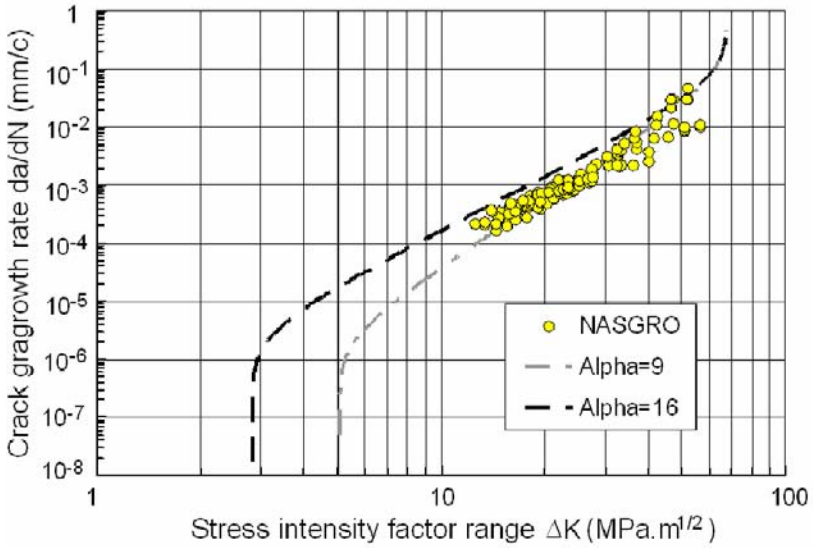

Fig. 12 FCG and NASGRO d*a*/d*N* curves for Ti-2.5 Cu Titanium.

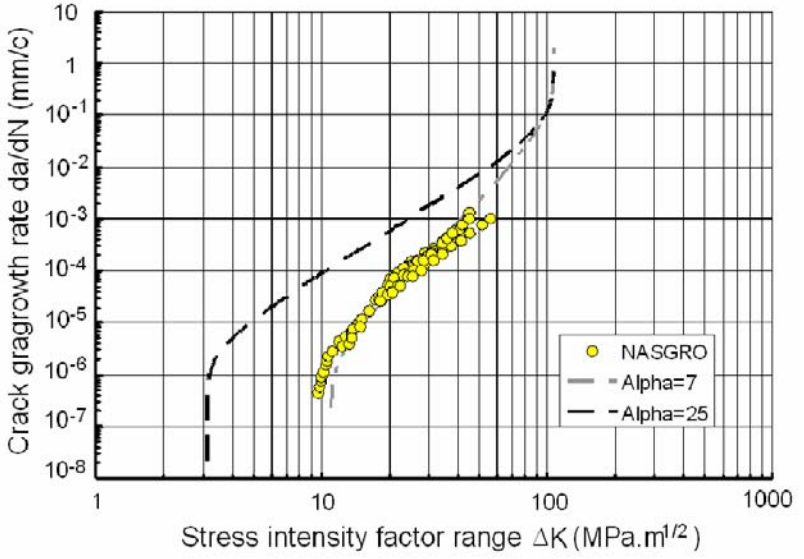

Fig. 13 FCG and NASGRO d*a*/d*N* curves for Inconel 706 Steel.

elastic fracture mechanics were used to describe the crack tip behavior. Furthermore, fracture mechanics allowables were obtained analytically through the extended Griffith theory, which can enable engineers to generate fracture related data without conducting ASTM testing. Both the fracture toughness and fatigue crack growth rate data can be generated via the FTD & FCG computer codes and can be used in life assessments of

fracture critical parts. It should be noted that all the assumptions used in the derivation of K_c and the da/dN data were based on large crack behavior. However, in reality the initial cracks embedded in material prior to their service usage are much smaller in length and the laws of continuum mechanics may not apply in order to assess their behavior. The largest flaw size that escapes inspection after machining parts, prior to their service usage, depends on the capability of NDI technique. If the NDI inspection shows the surface of the part is free from cracks, the analyst will use the standard NDI flaw size as the initial flaw in their damage tolerant analysis [4]. The standard NDI initial flaw size is different for different NDI method and it is related to the capability of the inspection technique. The life assessment analysis results based on this approach are too conservative and in some cases lead to redesigning the part and adding unnecessary weight into the structure. Experimental and analytical work showed that the typical flaw size found on the surface of the part after machining operation and prior to service operation is much smaller than the standard NDI flaw size, typically of the order of a few microns in dimensions. Clearly, the safe-life analysis for this crack will result in a much larger number of cycle-to-failure when fatigue crack growth analysis is performed.

To assess microscopic crack growth when subjected to a load varying environment is challenging, and the conventional linear elastic fracture mechanics based on large crack methodology is not applicable for predicting fracture allowables. The virtual testing methodology for crack growth behavior must be assessed by the multiscale modeling and simulation approach. Recently, industries are transitioning from conventional metallic alloys to super light high strength material such as the next generation of high-performance structural and multifunctional composites reinforced with nanoparticles. Weight has been and always will be the driver for aircraft and aerospace structure designs. Depending on the application, the cost savings associated with the weight reduction of structural parts is estimated to range from $100/lb to $10,000/lb. Aerospace and other industries have made significant investments in nanomaterials in an attempt to modify proven material systems to have superior mechanical-/thermal/electrical properties. Successes with nanocomposite materials have been seen in limited applications across the composites sporting goods industry or with lower-grade polymers. Incorporating nanoparticles into existing material systems is proving to be more difficult that one would anticipate.

Carbon nanotubes have many remarkable stand-alone physical characteristics such as novel electronic properties, exceptionally high axial strengths, and outstanding axial Young's moduli (~an order of magnitude above metallic alloys). However, once incorporated into a

composite-materials system, these benefits, in some cases, are negated if bonding between the resin and nanotubes are weak. Proper dispersion and functionalization (establishing strong bonds between Carbon nanotubes and polymer) of nanotubes in the polymer matrix can enhance the mechanical and fracture toughness of nanocomposites. In most cases the failure initiation in nanocomposites is at the interface area, where a lack of bonds between the polymer matrix and nanotubes are weak. Fig. 14 shows the nanocrack initiation at the interface that will contribute to the material degradation and premature failure of the part when subjected to a service load.

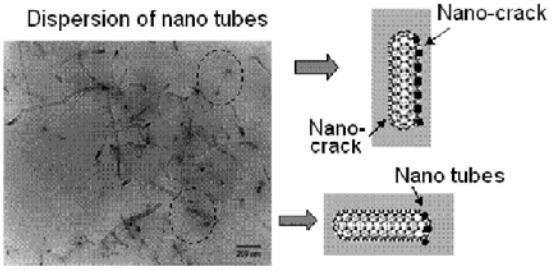

Fig. 14 Weak interface bonds between nanotubes and polymer can be the source of damage initiation.

The multiscale modeling of resin and carbon nanotubes can be conducted through the coarse-graining technique to assess the localized regions of Fig. 14. A beads-and-springs concept will be used to represent the polymer and the nanotubes within the matrix, which can reduce the computational time and scaling considerably vs. the use of explicitly atomistic models [9-21]. As shown in Fig. 15, the ~200+ atoms will be replaced by a few beads-and-springs, where each bead represents several atoms of polymer and nanotubes, including the interface interactions. Nano-cracks are incorporated into the modeling by allowing them to have various sizes, where their length can be as small as a few nanometers and as large as a few microns (mimicking the width and length of nanotubes).

6.1 Brief description of the coarse grain technique

Multiscale modeling simulation technique will be implemented to assess the global properties of the nanocomposites through the coarse grain technique [9-19]. The Materials Studio of Accelrys software [19] is a powerful tool that can be used to bridge the length scale describing the interface bonds

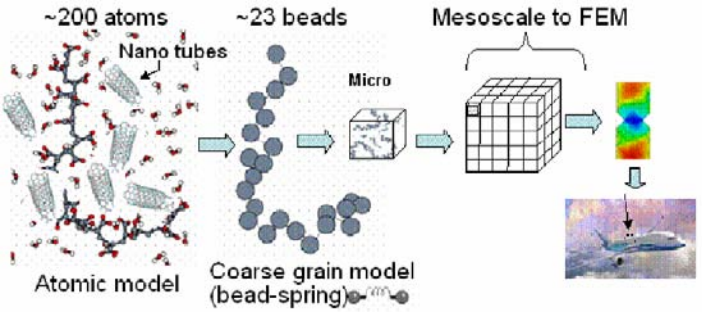

Fig. 15 The coarse grain technique approach linking atomistic model to the airframe parts.

behavior between nanotubes and the resin to micro, meso and the airframe parts. The scale linking is possible via implementation of several powerful modules in the Accelrys as well as the Materials Visualizer tool for modeling the polymer of choice. A few examples of Material Studio modules are Amorphous Cell Construction, Blends, DMole, Dissipative Particle Dynamics (DPD), Discover, and Synthia. For example, the Synthia calculates polymer properties using advanced Quantitative Structure-Property Relationships (QSPRs). It allows researchers to rapidly screen candidate polymers for a wide range of properties, and allows the property prediction of copolymer blends. Or, the DPD module will help analyst to obtain the global properties of nanocomposite through the coarse grain technique by establishing super cells containing several molecules of a given polymer.

7. Conclusion

The proposed analytical approach (also referred to as the virtual testing) can provide a useful tool for engineers to derive fracture toughness and fatigue crack growth data for classical metal alloys used in the aerospace industry when only a few or no test data are available. The methodology is based on continuum mechanics and basic material properties. It was shown that fracture properties can be predicted by the energy under the uniaxial tensile test via the extended Griffith theory. Two computer codes (FTD & FCG) have been developed that can estimate material fracture toughness and fatigue crack growth rate data. Excellent agreements between analytical results and test data were found for variety of alloys used in aerospace. In addition to the deterministic calculations in the program a probabilistic module has been developed to allow the user to reach a better understanding

of the effect of scatter on material reliability, and life prediction. It has been found that material plane strain and stress fracture toughness are sensitive to material variations observed in the full stress-strain curve. Moreover, material fatigue crack growth curve is sensitive to parameters that contribute to the threshold, Paris, and accelerated regions. The proposed method takes into account both these effects in the predictions for fracture toughness and fatigue crack growth rates.

A multi-scale computational modeling approach that will dramatically reduce computational time was also discussed. This approach outlines a methodology to overcome one of the primary challenges associated with hierarchical modeling of materials: namely, the accurate prediction of physical/chemical properties and behavior from the nanoscale to the macroscale without a loss of intrinsic structural information. Due to large computational-power requirement, the computational modeling of large atomistic systems is not possible and the coarse-grain modeling technique for computational material study can be used. This technique will dramatically reduce computational complexity where computation times can be reduced by several orders of magnitude.

The proposed computational method will use the coarse-grain simulation technique to bridge these length scales and to address the mechanical behavior of NanoComposite materials based fully or in part on the fundamental laws of physics (classic and quantum). This will enable the material scientist to alter key variables, via modeling, by varying parameters such as bond capability, NanoTube length, nanotube strength, and single-walled NanoTube versus multiwalled tubes, etc. before attempting to conduct laboratory tests, which can be costly and time consuming. The impact of each the above elements on global properties can be addressed through a reliable software tool that can be applied to fully assess all the regions of the time and length scale.

To remain competitive in the world market, it is imperative that the U.S. aerospace community invest in fundamental technologies and novel applications. The increased reliance on validated simulation methods linked to rapid, interdisciplinary design is a clear indicator that a Computational Materials program is required in order to take advantage of the multifunctional benefits of nano-structured materials in aerospace structures.

References

[1] Farahmand B. The fracture mechanics of ductile metals theory. In: Fatigue & fracture mechanics of high risk parts. Chapman & Hall, New York, (1997) 289-322.

[2] Farahmand B. The fracture mechanics of ductile metals theory. In: Fracture mechanics of metals, composites, welds, and bolted joints. Kluwer Academic Publisher, Boston, (2000)237-277.
[3] Farahmand B. Predicting Fracture and fatigue crack growth properties using tensile properties. J Eng Frac Mech, 2007, Accepted for publication.
[4] JSC, SRI, ESA, FAA. Fatigue crack growth computer program. NASGRO 4.0, 2000.
[5] Nikbin KM, Smith DJ and Webster GA. Prediction of creep crack growth from uniaxial data. Proceedings of the Royal Society of London, 1984.
[6] NASA/LaRC Contract # NAS-01067. Virtual Testing. NASA Langley Research Center, Alpha STAR Corporation and Boeing Aerospace Company, 2000.
[7] Vroman GA. Material thickness effect on critical stress intensity factor. Monograph #16, TRW Space and Technology Group, 1983.
[8] Farahmand B, Xie D and Abdi F. Estimation of fatigue and fracture allowables for metallic materials under cyclic loading. AIAA Conference, 2007.
[9] Baschnagel J, Binder K and Doruker P. Bridging the gap between atomistic and coarse-grained models of polymers. Adv. Polym. Sci., (2000) 41-156.
[10] Carmesin I and Kremer K. Monte Carlo and molecular dynamics simulations of polymers. Macromolecules, 21 (1988) 2819.
[11] Paul W, Binder K, Kremer K, Heermann D. Dynamics of polymer solutions and melts. Reptation predictions and scaling of relaxation times. J of Chemical Phys, (1991) 7726-7740.
[12] Baschnagel J, Binder K, Paul W, Laso, Suter UW and Batoulis I. On the construction of coarse-grained models for linear flexible polymer chains. J. Chem. Phys, (1991) 6014-6025.
[13] Doruker P and Mattice W. A second generation of mapping/reverse mapping of coarse-grained and fully atomistic models of polymer melts Macromolecules. Institute of Polymer Science, 1997.
[14] Groot, R and Warren P. Dissipative particle dynamics: Bridging the gap between atomistic and mesoscopic simulation. J. Chem. Phys., (1997) 4443-4435.
[15] Tartakovsky A M and Meakin P. A smoothed particle hydrodynamics model for miscible flow in three-dimensional fractures and the two-dimensional Rayleigh-Taylor instability. J. Comput. Phys., (2005) 610-624.
[16] Groot RD andRabone KL. Mesoscopic simulation of cell membrane damage, morphology change and rupture by nonionic surfactants. J. of Biophys., (2001) 725-736.
[17] Reith D, Meyer H and Muller F. Deriving effective mesoscale potentials from atomistic simulations. Max-Planck-Institut fur Polymerforschung, Ackermannweg,(2003) 1625-1636 .
[18] Gates TS, Odegard GM, Frankland JV and Clancy TC. Multi-scale modeling and simulation of nanostructured materials. Composites Science and Technology, (2005) 2416-2434.
[19] Accelrys . Materials studio release notes, Release 4.1, Accelrys Software, Inc., San Diego, 2006.

An Equivalent Block Approach to Crack Growth

R. Jones[1,2*], **S. Pitt**[3] **and D. Peng**[2]
[1]Cooperative Research Centre for Integrated Engineering Asset Management (CIEAM), Department of Mechanical Engineering, Monash University, P.O. Box 31, Monash University, Victoria, 3800, Australia
[2]DSTO Centre of Expertise for Structural Mechanics, Department of Mechanical Engineering, Monash University, P.O. Box 31, Monash University, Victoria, 3800, Australia.
[3]Department of Mechanical Engineering, Monash University, P.O. Box 31, Monash University, Victoria, 3800, Australia
**Email: Rhys.Jones@eng.monash.edu.au*

Abstract

This work is concerned with the recent developments in the formulation and application of the generalised Frost-Dugdale crack growth law and illustrates how it can be used to predict crack growth, from near micron size initial flaws, under variable amplitude load spectra.

1. Introduction

The problems of global warming, which led to the Koyoto agreement, and the potential depletion of oil reserves have focused attention on the need for even greater fuel efficiency. This has led Boeing to design their latest civil aircraft the B-787 Dreamliner to achieve a 20% reduction in fuel. In contrast in 2006 the USAF used ~$6 billion worth of jet fuel, and as a result is now actively seeking ways to reduce its carbon footprint. In military and civil aircraft the majority of the heavy primary structural members are dominantly metallic. Thus a means for lightening these life limiting metallic parts is essential. However, all new aircraft design and structural changes made to in-service aircraft require a damage tolerance analysis, as outlined in the US Joint Services Structural Guidelines JSSG-2006. The purpose of this requirement is to ensure that any cracks present in the structure will not cause loss of the structure for some predetermined period of in-service operation. Thus the challenge is to reduce weight without compromising structural integrity. This requires tools that can accurately estimate the entire fatigue crack growth history under complex variable amplitude load spectra. To meet this challenge it is necessary to have the capability to:

G.C. Sih (ed.), Multiscale Fatigue Crack Initiation and Propagation of Engineering Materials: Structural Integrity and Microstructural Worthiness, 23–45.

(1) Rapidly and accurately assess the durability, and therefore the safety, of existing and new designs and structural modifications under both current and future operational environments; and
(2) To allow a reduction in weight without compromising safety or durability.
One possible approach is to use an equivalent block method whereby crack growth data either generated from the measured load spectra, or one mandated by the certifying authority, is used to develop an expression for the average crack growth per load block. The development of one such equivalent block method, which is based on the generalised Frost-Dugdale law [1,6], for predicting fatigue crack growth under variable amplitude loading is a focal point of this Chapter. The ability of this law to model cracks growing under constant amplitude loading was studied in [1-6], and its applicability to predict crack growth in both specimens and in F-111 and F/A-18 aircraft full-scale fatigue tests was illustrated in [1, 6].
A background to the prognosis tools discussed in this Chapter is presented prior to assessing crack growth under variable amplitude loading. At this stage it should be mentioned that most current approaches are based on the concept of similitude. This Chapter reveals that this hypothesis is invalid in Region I.

2. Crack Growth

The recent papers [1-6] have shown that the generalized Frost-Dugdale law can be applied to a wide class of engineering problems and that there is often a near linear relationship between the log of the crack size and the life, i.e. the number of cycles, or blocks. These observations are reinforced by the work presented in [7] which studied the growth of physically small cracks, which ranged in size from 20 microns to several mm's in length, in an austenitic-ferritic 2205 duplex stainless steel and a range of other materials and concluded that over these length scales da/dN was proportional to the crack length and that the crack growth history could be written as per Frost & Dugdale, in the form:

$$a = a_i \, e^{\varpi N} \tag{1}$$

where ϖ is a load and geometry dependent parameter, and a_i is the initial flaw size. A near linear relationship between ln(a) and N has also been reported, for physically small cracks, by a large number of researchers [8-14]. This conclusion, i.e. a near linear relationship between ln(a) and N, was also one of the primary findings reported in an early USAF/General Dy-

namics [15] study into small crack growth undertaken as part of the F-16 research and development program. The observation that da/dN was often proportional to the crack length led to the conjecture [1-6] that in the low to mid range ΔK region, i.e. in Region I and part way into Region II, the increment in the crack length per cycle (da/dN) could be described by the generalised Frost-Dugdale law, viz:

$$\begin{aligned} da/dN &= C' \, (a/a^*)^{(1-\gamma/2)} \, (\Delta\kappa)^{\gamma} - (da/dN)_0 \\ &= C^* \, a^{(1-\gamma/2)} \, (\Delta\kappa)^{\gamma} - (da/dN)_0 \end{aligned} \qquad (2)$$

where $\Delta\kappa$, is the crack driving force, C', a*, and γ are constants, $C^* = C'/a^{*(1-\gamma/2)}$ and $(da/dN)_0$ reflects both the fatigue threshold and the nature of the notch (defect/discontinuity) from which cracking initiates. Note that this law has da/dN dependent on both the crack driving force and the crack length.

For the special case of a small crack in a large centre cracked panel under remote constant amplitude loading with R ~ 0.0 equation (2) implies that da/dN is proportional to the quantity $a\Delta\sigma^{\gamma}$. This relationship agrees with that derived by Tomkins [13] who assumed that crack growth was proportional to the accumulated plastic strain, which was averaged over a characteristic length ahead of the crack length.

Equation (2), which is a generalized form of the Frost-Dugdale law in that γ is not assumed to be 3 as in [6], also resembles the fractal based crack growth law proposed in [16-18], and has da/dN proportional to both $\Delta\sigma^{\gamma}$ and the crack length *a* as per [7].

A similar equation was developed in [19] which also found that the increment in the crack length per cycle (da/dN) was a function of both the stress intensity factor K and the crack length. A similar crack growth law was also proposed in [20]. Here they considered a crack to have a series of dislocations ahead of the crack tip, which they termed a super dislocation, and that crack growth occurred as a result of the formation of micro-cracks ahead of the crack tip. These assumptions led to a crack growth equation of the form:

$$da/dN = \chi \, \Delta\sigma^{(1/\lambda-1)} \, (\Delta K - \Delta K_{th})^2/(K^2_{Ic} - \Delta K^2) \qquad (3)$$

where χ, and λ are material constants and K_{Ic} is the plane strain Mode I fracture toughness. It should be noted that for small cracks ΔK is proportional to $\Delta\sigma\sqrt{\pi a}$ so that when $\Delta K << K_{Ic}$, and $\lambda = 1/(\gamma - 1)$ then equations (2) and (3) have a similar form. However, the question of what to use for

$\Delta\sigma$ when the stress field is complex means that equation (2) has greater generality than equation (3).

In this context it should be noted that [21], which presented an analytical solution for a flaw growing with a non sharp notch, also found that the similitude hypothesis does not hold in Region I. Indeed, for the range of problems considered in [20] their non-similitude growth law had the same form for flaws that ranged from near microns to approximately 10 mm's.

These findings together with the realisation, presented in [22] that "in the threshold regime, there is something missing either in the (crack closure) model" and the statement in [23] that "a small crack may not be closed for as much of the load cycle as a larger crack", i.e. that crack closure effects are less significant for small cracks, led reference [4], to question the validity of the similitude hypothesis, that underpins most current crack growth models, in Region I. (In this chaper the hypothesis of similitude is taken to be as first proposed by [24], viz: that for constant amplitude loading the increment in crack length per cycle (da/dN) takes the form:

$$da/dN = f(K_{max}, R) \tag{4}$$

where $f(K_{max}, R)$ is only a function of K_{max}, the maximum value of the stress intensity factor in the cycle, and R (= K_{min}/K_{max}), where K_{min} is the minimum value of the stress intensity factor in the cycle, and where $\Delta K = K_{max} - K_{min} = K_{max}(1-R)$. This means that: Two different cracks growing in identical materials with the same stress intensity factor range ΔK, and the same K_{max}, will grow at the same rate.

As remarked in [1, 6] a hypothesis, in this case similitude i.e. equation (4), can be disproved by a single counter example. A number of counter examples were presented in [1]. One example presented involved the work of [25] that presented crack growth for a Grade 1 austempered ductile iron obtained using a compact test specimen as per the ASTM guideline[1] (E647-95a). Figure 1 presents a conventional da/dN versus ΔK plot of the data whilst Figure 2 presents an analysis of the data associated with Region I, and also the lower portion of Region II, which reveals a (near) linear relationship between da/dN and $\Delta K^3/a^{1/2}$ as per Equation (1) with $\gamma = 3$. As such the da/dN was a function of both ΔK and the crack length a, and hence similitude does not follow.

[1] Information on the crack length, load da/dN, and K at each point in this test is contained in the spreadsheet associated with Figure 1.

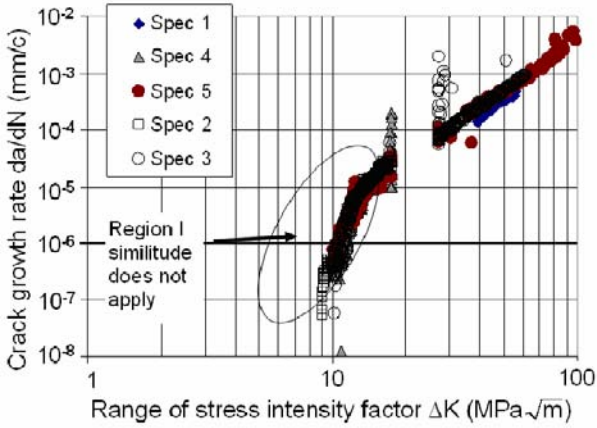

Fig.1 Crack Growth in L6B-2, from [25].

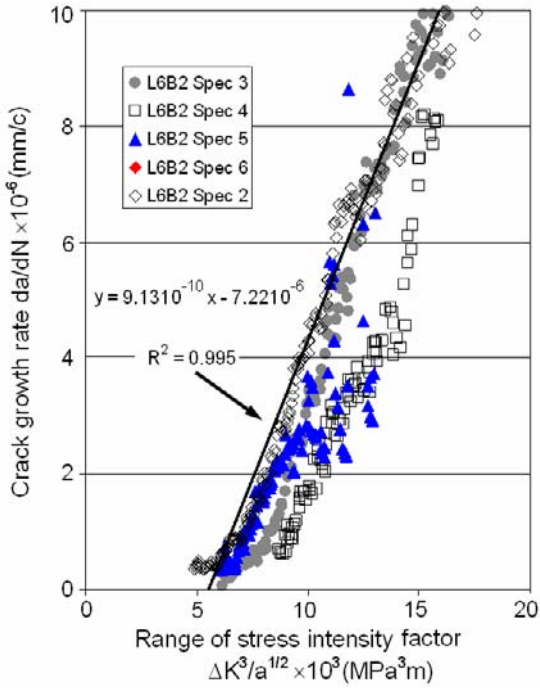

(a) First set data

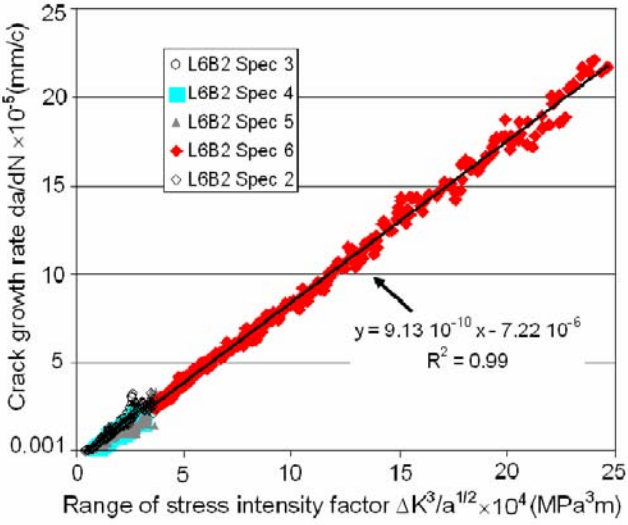

(b) Second set data

Fig. 2 Crack growth in Region I in L6B-2, adapted from [25].

Crack growth data for a Grade 1 austempered ductile iron obtained using a compact test specimen as per the ASTM guidelines (E647-95a) was also analysed in [1], see Figures 3 and 4. (As in the previous example information on the crack length, load da/dN, and K at each point in this test is contained in the spreadsheets associated with Figures 3 and 4.) The test specimens were supplied by ADI Engineering, Process and Heat Treatment Pty. Ltd. and had a chemical composition in %wt of; 2.50C, 0.28Mn, 2.6Si and less than 0.1P. Analysis of the data associated with Region I again reveals a (near) linear relationship between da/dN and $\Delta K^3/a^{1/2}$, see Figure 4a). As such the crack growth rate is a function of both ΔK and the crack length a and similitude does not hold. In this case it was found that $\gamma = 3$, $C^* = 9.42\ 10^{-10}$, and $(da/dN)_0 = -2.76\ 10^{-6}$. It is again interesting to note that, as shown in Figure 4 b), this relationship extends into Region II.

In each of the examples presented the experimental results reveal that in Region I and into Region II the increment in the crack length per cycle da/dN has the form:

$$da/dN = \Delta K^{\gamma}\, a^{1-\gamma/2} - (da/dN)_o \tag{5}$$

As such these counter examples disprove the similitude hypothesis in Region I. A more extensive collection of counter examples is given in [1, 6].

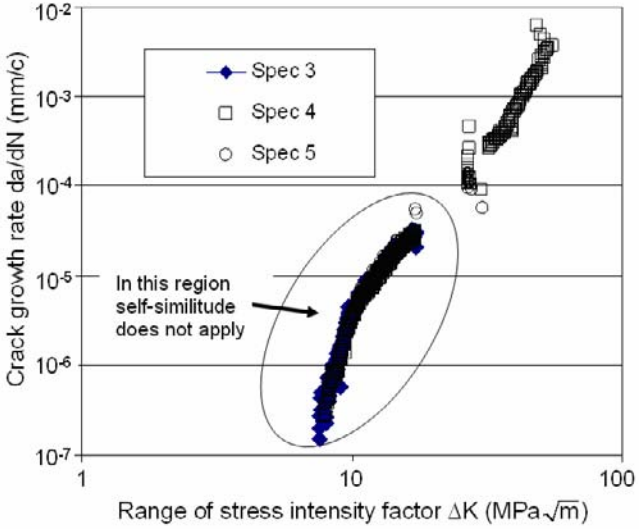

Fig. 3 Crack Growth in an austempered ductile iron, from Khan and Chen [25].

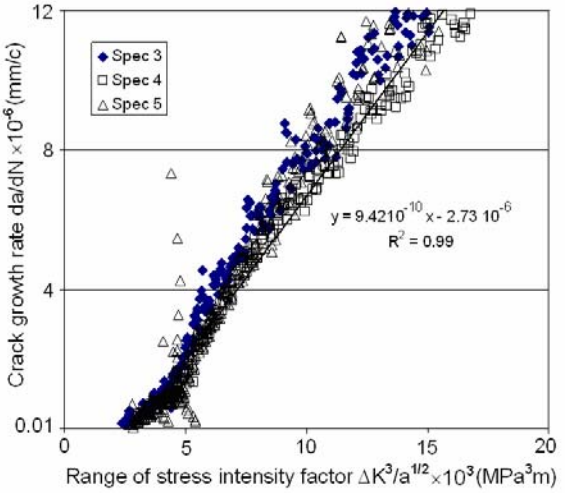

Fig. 4 Crack growth in Region I in an austempered ductile iron, adapted from Khan and Chen [25].

The test data presented in [26], which presented crack growth data obtained using the ASTM standard constant stress ratio test method for middle crack tension, compact tension and eccentrically loaded edge-crack tension specimens, also revealed that similitude does not hold in Region I. In this study it was found that the increment in the crack length per cycle (da/dN)

was not a unique function of ΔK and R, see Figure 5. Thus since for constant R ratio tests $K_{max} = \Delta K/(1-R)$ this means that the similitude hypothesis first proposed in [24] was invalid.

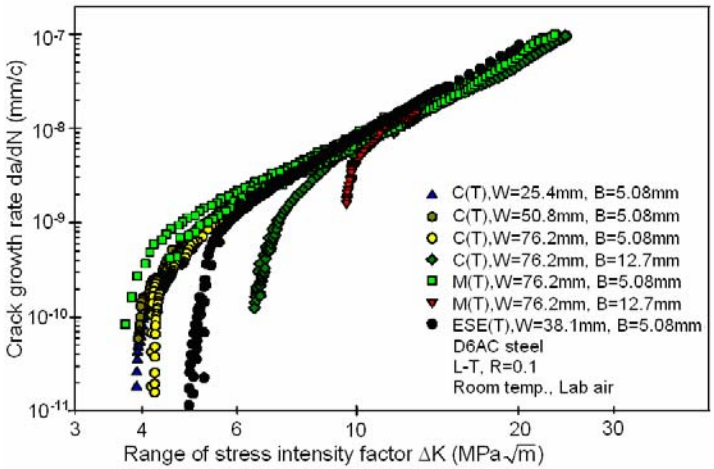

Fig. 5 Non similitude crack growth in D6ac steel, from Forth et al. [26].

The crack growth data presented above, which cover several quite different rail industry steels as well an aircraft industry steel (D6ac), confirm that in Region I, and also in the lower portion of Region II, da/dN is a function of both ΔK, and K_{max} *and the crack length a*. As such these various counter examples reveal that the similitude hypothesis inherent in the the majority of crack growth models is invalid in Region I. In contrast the examples presented above and those presented in [1, 5, 6, 27] show that in Region I, and also in the lower portion of Region II, crack growth follows the generalised Frost-Dugdale crack growth law, which as shown in [1] accurately predicts crack growth from near micron size flaws.

3. An Equivalent Block Method for Predicting Fatigue Crack Growth

Many practical engineering problems, i.e. cracking in rail and aircraft structures, involve complex load spectra that can be approximated by a number of repeating load blocks. In certain circumstances these repeated blocks of loads can be treated as equivalent to load cycles. To this end let us consider the case of block loading, where each block consists of a spectrum with n cycles that have peak stresses of σ_i, i =1… n, with the associated cyclic ranges being $\Delta\sigma_i$, i =1… n. Also assume that:

i) The slope of the a versus block curve has a minimal number of discontinuities.
ii) There are a large number of blocks before failure.

With these assumptions reference [28] built on equation (2) to derive the following expression for the crack growth per block, da/dB, viz:

$$da/dB = \underline{C}^* K_{max}^{\gamma} a^{1-\gamma/2} - da/dB_0 \quad (6)$$

where $\tilde{C}$ is a spectra dependent constant, and K_{max} is the maximum value of the stress intensity factor in the block. However, this formulation can be derived from a number of assumed forms for the crack driving force. To this end let us assume that crack growth per cycle can be expressed as:

$$da/dN = C^* a^{(1-\gamma/2)} (f(R) \Delta K)^{\gamma} \quad (7)$$

where γ is a constant, and f(R) is a function of the R ratio. Setting f(R) = 1 yields a non-similitude variant of the Paris growth law, whilst setting:

$$f(R) = 1/(1-R)^p \quad (8)$$

where p is a constant, yields a non-similitude variant of the Walker crack growth law [29], and setting yields a non-similitude variant of Elber's crack closure law [30].

$$f(R) = (0.5+0.4R) \quad (9)$$

If there are a large number of blocks before failure then, to a first approximation, the crack length *a* can be considered to be a constant in any given block, and hence β can also be assumed to be a constant within that block, and that ΔK_i can be expressed as:

$$\Delta K_i = \beta \, \Delta\sigma_i \sqrt{(\pi a)} \quad (10)$$

With these assumptions the crack growth per block, da/dB, can be written as

$$da/dB = \sum_{i=1}^{n} C^* a^{(1-\gamma/2)} (f(R_i) \Delta K_i)^{\gamma} \quad (11)$$

which on substituting for ΔK_i as given by equation (10) can be expressed as:

$$da/dB= \sum_{i=1}^{n} C^*a^{(1-\gamma/2)} (f(R_i)\ \beta\ \Delta\sigma_i\pi^{1/2}a^{1/2})^{\gamma}$$

$$= (\beta\pi^{1/2})^{\gamma}\ a \sum_{i=1}^{n} C^*\ (f(R_i)\ \Delta\sigma_i)^{\gamma} \qquad (12)$$

where R_i is the R ratio associated with the i'th cycle.Equation (12) can be written in a number of forms. One such form is:

$$da/dB= (\sigma_{max}\ \beta\pi^{1/2})^{\gamma}\ a \sum_{i=1}^{n} C^*\ (f(R_i)\ \Delta\sigma_{i/}\ \sigma_{max})^{\gamma}$$

$$= [\sum_{i=1}^{n} C^*\ (f(R_i)\ \Delta\sigma_{i/}\ \sigma_{max})^{\gamma}]\ \ K_{max}{}^{\gamma}/a^{\gamma/2-1}$$

$$= \tilde{C}\ K_{max}{}^{\gamma}/a^{\gamma/2-1} \qquad (13)$$

where

$$\tilde{C} = [C^*(f(R_i)\ \Delta\sigma_i\ /\sigma_{max})^{\gamma}] \qquad (14)$$

and

$$K_{max} = \sigma_{max}\ \beta\ \sqrt{(\pi\ a)} \qquad (15)$$

where σ_{max} is the maximum stress seen in the block, and K_{max} is the corresponding is the maximum value of the stress intensity factor seen in the block.

This formulation represents a non-similitude variant of that proposed in [31-34]. Researchers at Boeing (Seattle) [35] also developed a related (non-similitude) approach whereby instead of equation (13) da/dB was expressed as:

$$da/dB = C\ (K/g(a/t))^{m} \qquad (16)$$

where the function g(a/t), which is a function of ratio of the crack length (a) to the thickness (t) of the specimen, was experimentally determined. This formulation was necessary to enable the predictions to match the measured

crack length histories, which as shown in [5] followed the generalised Frost-Dugdale crack growth law.

At this stage it is important to note that:

i) As shown in [2] for cracks with very small initial sizes, in some cases the initial flaw sizes were of the order of several microns, growing under variable amplitude loading there was a near linear relationship between the average increment in the crack length per block and the crack length that held up till (near) failure. This implies that any crack growth equation should apply to Regions I, II, and III.
ii) When analysing crack growth in the F/A-18 wing attachment centre barrel fatigue test [1] the best results were obtained when the generalised Frost-Dugdale law was used well into Region II.
iii) The review paper [36] on crack growth and similitude concluded that similitude was lost during fatigue crack growth under variable amplitude loading.
iv) Quantitative fractography [37, 38] has shown that the mechanisms underpinning crack growth under constant and variable amplitude loading differ.

As a result, although under constant amplitude loading the generalised Frost-Dugdale law is only strictly applicable to Region I and to the lower portion of Region II, this "equivalent block" variant, i.e. Equation (13), can be extended to have a form consistent with both Regions I, II and III, viz:

$$da/dB = (a^{1-\gamma/2} K_{max}^{\gamma} - da/dB_o)/(1.0 - K_{max}/K_c) \quad (17)$$

where a is now the average crack length in the block, $\tilde{C}$ is a spectra dependent constant, and K_c is the apparent cyclic fracture toughness. Here, as described in [1, 6], the term da/dB_o reflects the both nature of the discontinuity from which the crack initiates and the apparent fatigue threshold for this particular block loading spectra. However, it should be noted that this variant of the generalized Frost-Dugdale law is only applicable to crack growth data where the slope of the a versus Block curve has minimal discontinuities.

4. Examples

Case 1) Consider the crack growth data presented in [39] for Al7010-T73651 compact tension specimens tested under variants of the Rotarix helicopter load spectrum. These specimens had a thickness of 17.5mm and a width of 70mm. Four different variants of the Rotarix spectrum (termed

Rot 16, 20, 24, 32) were tested, see [39]. The Rotarix spectrum used was representative of that experienced by a typical rotary wing structure. It had a large number of small cycles at high R-values. The baseline Rotarix spectrum represented 140 flights, which corresponded to 190.5 hours of flight, for more details see [39]. In these spectra cycles were progressively removed from the original baseline Rotarix spectrum to produce different spectra, see [39]. The Rot 16 spectrum was the largest spectrum and contained 99.4% of the original spectrum. The Rot 20 and 24 spectra were very similar and only the Rot 16, Rot 20 and the Rot 32 spectra were analysed. The relationship between the maximum stress intensity factor in the block K_{max} and the crack length is given in Figure 7.

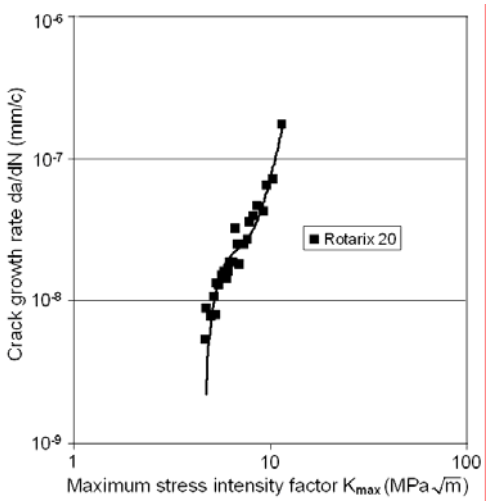

Fig. 6 Crack growth rate for the Rotarix 20 spectra, adapted from [39].

The resultant experimental and the computed crack length histories, obtained using Equation (15) with the value of γ fixed at three and the values of $\tilde{C}$ and K_c as given in Table 1, are shown in Figure 8 where we again see good agreement between the computed and the measured crack length history. (In these problems the left hand side of Equation (15) is da/dCycles.) As in the previous examples information on the crack length, load da/dN, and K at each point in this test is contained in the associated spreadsheet.

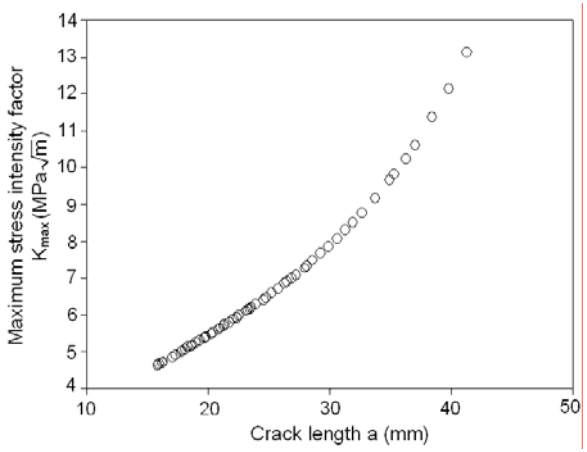

Fig. 7 Stress intensity factor versus crack length from [39].

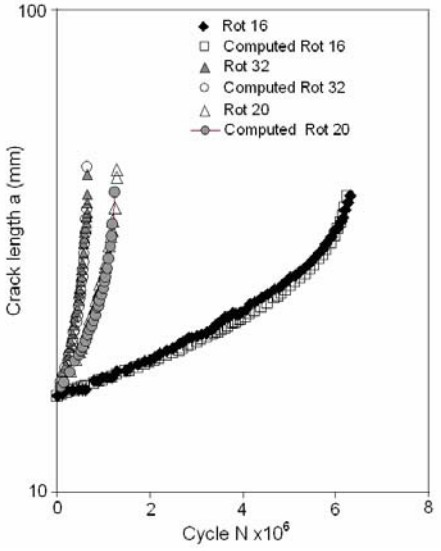

Fig. 8 Experimental and computed crack length history under Rotarix spectra, from [39].

Table 1 Values of $\tilde{C}$ and K_c for specimens tested under a Rotarix spectra.

Spectrum	$\tilde{C}$ x 10^{-8} (fitted)	K_c
Rot 16	.01	30
Rot 20	.50	30
Rot 32	1.0	30

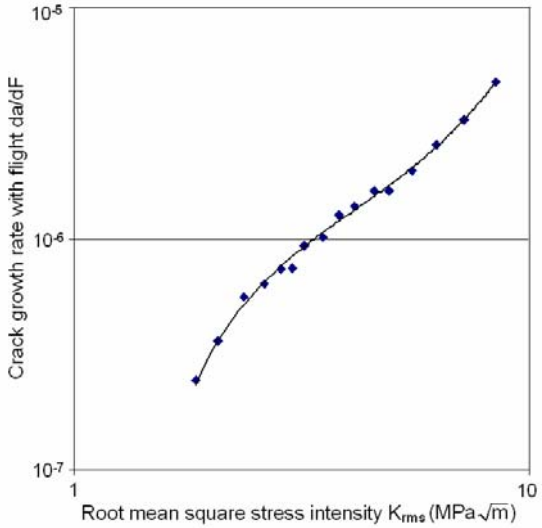

Fig. 9 Crack growth rate under gust load spectra.

Case 2) Crack growth data for growth from a 20 mm diameter hole in a 2mm thick 7075-T6 aluminium alloy sheet tested under a Fokker-F27 gust spectra was presented in [40]. This work presented a plot of the crack growth (m/flight) against K_{rms}, the root mean square value of K seen in a block, which shows a typical sigmoidal shape, see Figure 9. However, as shown in Figure 10 the average increment in the crack length per flight conforms to equation (17). As in the previous examples information on the crack length, load da/dN, and K at each point in this test is contained in the associated spreadsheets.

5. Fatigue Crack Growth Analysis of a High-Frequency Loaded Helicopter Coupon – The AHS Round-Robin Problem

The objective of the Helicopter round-robin study outlined in [41] was to assess the capability of current structural analytical tools to predict fatigue crack growth. The round-robin test specimen was chosen to represent a complex aerospace component, subjected to a typical rotorcraft spectrum (Asterix). The geometry was a flanged plate with a central lightning hole, see Figure 11. The study required the participants to predict crack growth from a 2 mm (radius) corner defect on the inner edge of the large central hole to the failure, where failure was defined as a projected surface crack length of 25 mm. The crack growth path is shown in Figure 12.

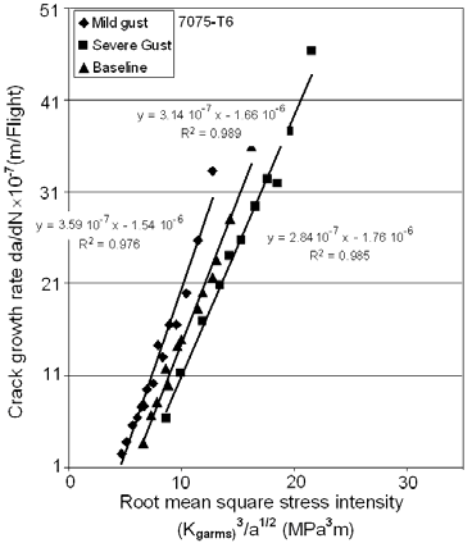

Fig. 10 Crack growth rate correlation to the Frost-Dugdale law.

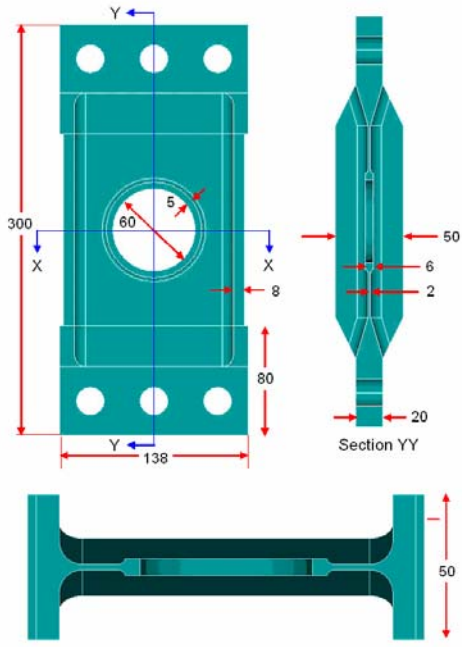

Fig. 11 Round-Robin crack configuration [41].

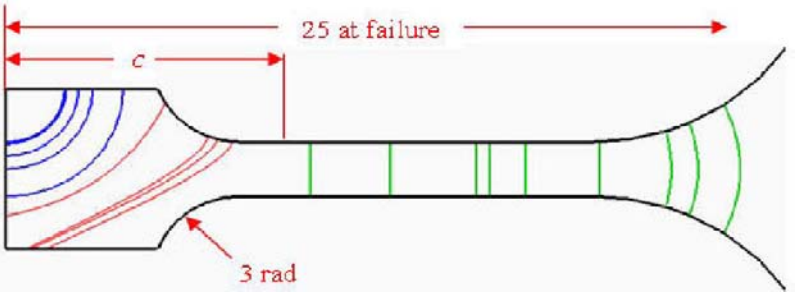

Fig. 12 Schematic diagram of the round-robin crack growth evolution (all dimensions are in mm).

The crack was found to grow for a considerable part of its life as a part through crack. The crack subsequently transitioned from the 6 mm reinforced hole-edge into the 2 mm thick web, and later into the larger thickness as it approached a flange. The component was made from 7010-T73651 aluminum alloy, and as in [41, 42], was assumed to have a Youngs modulus of 70,000 MPa, a Poisson's ratio of 0.3, and a fracture toughness of 34 MPa √m.

The Asterix load sequence used in this study was derived from strain data measured on a helicopter lift frame, see [42]. The maximum and minimum stress points in the spectrum were given as 100 and -4 respectively. The Asterix spectrum represented 190.5 flights, or 140 sorties, and was consisted of 371,610 cycles. The largest stress in the spectrum was to 130MPa. A text file named "Helicopter Round Robin Spectra" containing this spectra is available with this chapter.

5.1 Finite element analysis

A 3D finite element model of the round-robin component was first created. Symmetry considerations mean that it was only necessary to model half of the structure, as shown in Figure 13. The model was hex-meshed, and consisted of 61,962 9-noded CHEXA elements with a total of 268,478 nodes. It was subjected to a peak (remote) load which corresponded to a net section stress at the plane of symmetry of 130 MPa. The model was then imported into the NEi/NASTRAN to compute the resultant stress field. The computational analysis took approximately 1352 seconds CPU time on a PIV personal computer running under a Linux operating system.

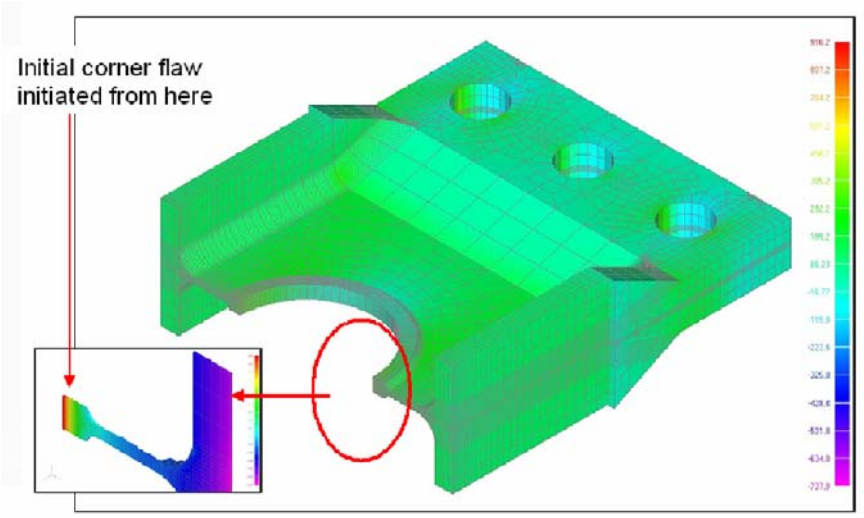

Fig. 13 Nominal stress distribution at the crack face.

The generalised Frost-Dugdale crack growth law was used [27] to predict the crack growth history from an initial 2 mm quadrant flaw to a surface crack length of 25 mm. In the first instance κ was taken to be the stress intensity factor range ΔK. For the purpose of simplicity in the present analysis, the value of $\overline{C}$ was determined by using a simple curve fitting technique, where $\overline{C}$ was manually adjusted to match the time to grow from a 2 mm to a 4 mm corner crack. This approach yielded a value of $\overline{C} = 1.28 \times 10^{-11}$, and $\gamma = 3$.

When predicting crack growth from 2 to 5 mm the weight function technique was used to compute the stress intensity factors from the stress field obtained using the (uncracked) NEi-Nastran finite element model. However, in the thinner section the 2D stress intensity factor solution given in [41, 42] was used, for more details see [27]. The resultant Beta factor solution used in the analysis is shown in Figure 14 along with that given in the original proposal [41, 42] and the Beta factor used in [43].

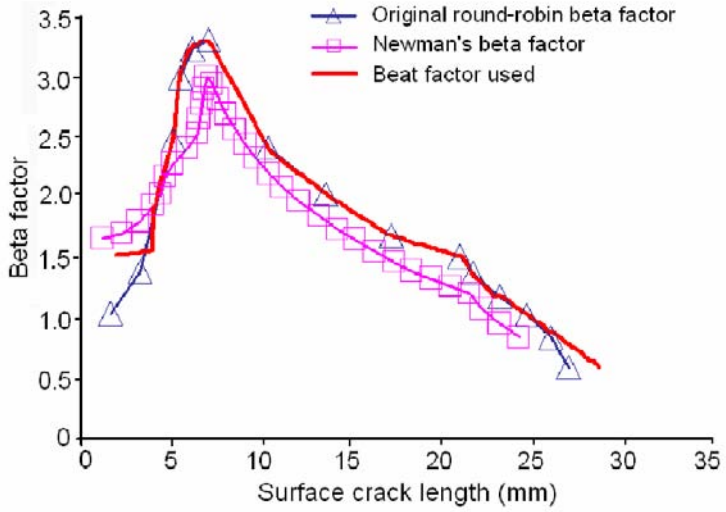

Fig. 14 Beta factors used in the analysis.

5.2 Results and discussion

The crack length histories for two test specimens was presented in [42]. The starting defect in specimen number 1 was a spark machined quarter circular corner crack of 2 mm radius located at the edge of the hole. In test 2, the defect radius was 1.5 mm, and the defect was grown as a fatigue crack under the Asterix spectrum up to 2 mm radius and crack growth data were recorded from this point up until failure. From Figure 15 it can be seen that there was little difference in the crack growth histories. Both started at a moderate growth rate which steadily increased to a fairly rapid rate and was then followed by a much slower rate of crack growth.

In the round-robin study most of the predictions submitted to the organizers did not match the test data particularly well, see [42]. However, as can be seen in Figure 15 the predictions obtained using the generalised Frost-Dugdale law were in good agreement with the measured data.

This problem was also analysed using the average block variant, viz:

$$da/dB = a^{(1-\gamma/2)} K_{max}{}^{\gamma} \tag{18}$$

with $\gamma = 3$ and $\tilde{C} = 0.92\ 10^{-15}$ and the results are also presented in Figure 15 which again shows an excellent agreement between the predicted and the measured crack length history. As in the previous example information

on the crack length, load da/dN, and K at each point in this test is contained in the spreadsheet associated with Figure 15.

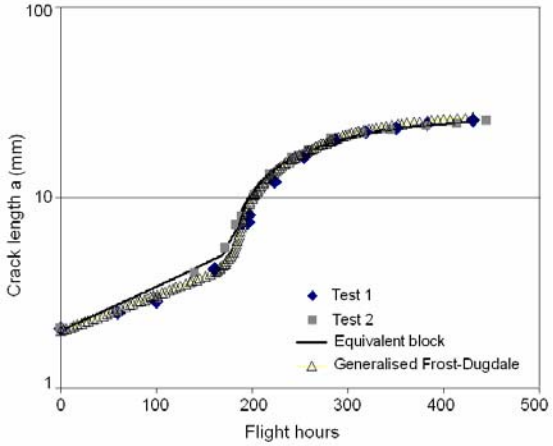

Fig. 15 Computed surface crack length history.

It is informative to contrast this solution with the conclusions reached in [43], who used FASTRAN,viz:

> the early stages of crack growth compared very well with the test data. But, again, the crack-growth rates in the 2-mm thick section were too fast.

This shortcoming is largely removed in the present study, see Figure 15. It should be noted that interest in this problem was kindled due to the conclusions reached by US Army researchers [44], who used AFGROW and NASGRO to predict the crack length history for this problem, who stated:

i) "It is evident that the crack growth was under-predicted for the crack length below 5 mm and is over-predicted when crack length is more than 10 mm."

ii) "More research; especially in the area of modeling crack growth near the crack growth threshold and determining experimentally the crack growth threshold values are needed."

Indeed, the present crack growth law was specifically formulated to address point (ii), and its ability to predict crack growth history for this complex and challenging problem is particularly pleasing. Its ability to predict crack growth for a range of other complex problems is shown in [1, 27, 45, 46].

6. Conclusion

This work has shown that in Region I crack growth data reveals the similitude hypothesis to be invalid. It has summarised recent work on the generalised Frost-Dugdale crack growth law and revealed how it can be used to predict crack growth under both constant and variable amplitude loading. The various examples presented show that this approach:

i. is generally consistent with experimental results,
ii. provides a reasonable representation of macroscopic observations of crack growth in a range of alloys,
iii. can be used to predict crack growth from near micron size initial flaws, and
iv. has the potential to accurately predict crack growth in real aircraft structures under variable amplitude load spectra.

References

[1] Jones R., Molent L. and Pitt S. Crack growth of physically small flaws, International Journal of Fatigue, 29 (2007) 1658-1667.
[2] Molent L. Jones R. Barter S. and Pitt S., Recent Developments In Fatigue Crack Growth Assessment, International Journal of Fatigue, 28(12) (2006) 1759-1768.
[3] Barter S., Molent L. Goldsmith N. and Jones R. An experimental evaluation of fatiguecrack growth, Journal Engineering Failure Analysis, 12(1) (2005) 99-128.
[4] Jones R. Barter S. Molent L. and Pitt S. A multi-scale approach to crack growth, Multiscaling in molecular and continuum mechanics: biology, electronics and material science, Edited by G. C. Sih, Springer, October, 2006.
[5] Jones R. Molent L., Pitt S. and Siores E. Recent developments in fatigue crack growth modelling, Proceedings 16th European Conference on Fracture, Alexandropoulos, Greece,July 2006.
[6] Jones R. Chen B. and Pitt S. Similitude: cracking in steels, Theoretical and Applied Fracture Mechanics, 48(2) (2007) 161-168.
[7] Polak J. and Zezulka P. Short crack growth and fatigue life in austenitic-ferritic duplex stainless steel, Fatigue Fract Engng Mater Struct, 28 (2005) 923–935.
[8] Harkegard G. Denk J. and Stark K. Growth of naturally initiated fatigue cracks in ferritic gas turbine rotor steels, International Journal of Fatigue, (2005) 1–12.
[9] Nisitani H. Goto M. and Kawagoishi N. A small-crack growth law and its related phenomena, Engineering Fracture Mechanics, 41(4) (1992) 499-513.

[10] Kawagoishi N. Chen Q. and Nisitani H. Significance of the small crack growth law and its practical application, Metallurgical and Materials Transactions A, 31A (2000) 2005 2013.
[11] Caton MJ.,Jones JW. Boileau JM. and Allison, JE. The effect of solidification rate on the growth of small fatigue cracks in a cast 319-type aluminum alloy, Metallurgical and Materials Transactions A, 30A (1999) 3055-3068.
[12] Murakamia Y. and Miller K.J. What is fatigue damage? A view point from the observation of low cycle fatigue process, International Journal of Fatigue, (2005) 1–15.
[13] Tomkins B. Fatigue crack propagation-an analysis, Phil. Magazine, 18 (1968) 10411066.
[14] Polák J. Interpretation of the coffin-manson law in terms of short crack growth, Proceedings Fatigue 06, Atlanta, USA, May 2006.
[16] Potter JM. and Yee BGW. Use of small crack data to bring about and quantify improvements to aircraft structural integrity, Proceedings AGARD Specialists Meeting on Behavior of Short Cracks in Airframe Structure, Toronto , Canada , 1982.
[17] Carpinteri A. Scaling laws and renormalization groups for strength and toughness of disordered materials. Int. J. Solids Struct., 31 (1994) 291–302.
[18] Carpinteri A. and Spagnoli An. A fractal analysis of size effect on fatigue crack growth, Int. J. Fatigue, 26 (2004) 125–133.
[19] Spagnoli An. Self-similarity and fractals in the Paris range of fatigue crack growth. Mechanics of Materials, 37 (2005) 519–529.
[20] Dong P. Hong JK. and Cao Z, Stresses and stress intensities at notches: ‘anomalous crack growth’ Revisited, International Journal of Fatigue, 25 (2003) 811–825.
[21] Ding HZ. and Xing XS. A plastic flow-induced fracture theory for fatigue crack growth, Journal Of Materials Science, 31 (1996) 4099–4103.
[22] Sih GC. and Tang XS. Form-invariant representation of fatigue crack growth rate enabling linearization of multiscale data, Theoretical and Applied Fracture Mechanics, 47(2007) 1–14.
[23] Newman JC. Jr. Brot A. and Matias C. Crack-growth calculations in 7075-T7351 aluminum alloy under various load spectra using an improved crack-closure model, Engineering Fracture Mechanics , 71 (2004) 2347–2363.
[24] Newman JC.Jr. Phillips EP. and Swain MH. Fatigue life prediction methodology using small crack theory, International Journal of Fatigue, 21 (1999) 109-119.
[25] Paris PC. Gomez RE. and Anderson WE. A rational analytic theory of fatigue. The Trend in Engineering, 13(1) (1961) 9-14.
[26] Khan AS. and Chen B.K. Evaluation of austempered ductile iron for application to rail cast components, Asia Pacific Industrial Engineering and Management Systems Conference,Gold Coast, Australia, Dec 2004.
[27] Forth SC. Johnston WM. and Seshadri BR. The effect of the laboratory specimen on fatigue crack growth rate, Proceedings 16th European Conference on Fracture, Alexandropoulos, Greece, July, 2006.

[28] Tiong U.H., Jones R. and Molent L., Damage Tolerance Analysis of a Helicopter Component, Proceedings 1st International Conference on Damage Tolerance Assessment of Aircraft Structure, Delft, The Netherlands, September 25th-28th, 2007.
[29] Jones R. and Pitt S., Crack patching: revisited, Composite Structures, 7667(32) (2006) 218-223.
[30] Walker E.K., The effect of stress ratio during crack propagation and fatigue for 2024-T3 and 7076-T6 aluminum. In: Effect of Environment and Complex Load History on Fatigue Life, ASTM STP 462, Philadelphia: American Society for Testing and Materials, 1970, 1-14.
[31] Elber W., The significance of fatigue crack closure, Damage Tolerance of Aircraft Structures, ASTM STP-486 (1971), 230-242.
[32] Schijve J., Fatigue crack growth under variable-amplitude loading, Engineering Fracture Mechanics, Engineering Fracture Mechanics, (1979) 207-221.
[33] Gallagher J.P. and Stalnaker H.D., Developing normalised crack grwth curves for tracking damage in aircraft, American Institute of Aeronautics and Astronautics, Journal of Aircraft, 15(2) (1978) 114-120.
[34] Miedlar P.C., Berens A.P., Gunderson A. and Gallagher J. P., Analysis and support initiative for structural technology (ASIST), AFRL-VA-WP-TR-2003-3002.
[35] Barsom, J.M. and Rolfe, S. T.: Fracture and fatigue control in structures: Applications of fracture Mechanics, Butterworth-Heinemann Press, November 1999.
[36] Miller M., Luthra V.K. and Goranson U.G.: Fatigue crack growth characterization of jet transport structures, Proc. of 14th Symposium of the International Conference on Aeronautical Fatigue (ICAF), Ottawa, Canada, June 10-12, 1987.
[37] Davidson D.L., How Fatigue Cracks Grow, Interact with Microstructure, and Lose Similitude, Fatigue and Fracture Mechanics: 27th Volume, ASTM STP 1296, R. S. Piascik, J. C. Newman, and N. E. Dowling, Eds.: American Society for Testing and Materials, (1997) 287-300.
[38] Molent L., McDonald M., Barter S. and Jones R., Evaluation of spectrum fatigue crack growth using variable amplitude data. International Journal of Fatigue, in press.
[39] White P., Barter S. and Molent L., Observations of crack path changes under simple variable amplitude loading in AA7050-T7451, Int. Journal of Fatigue, (In press).
[40] Zitounis V., Fatigue crack growth rates under variable amplitude load spectra containing tensile underloads, PhD Thesis, Cranfield, 2004.
[41] Wanhill R.J.H., Gust severity effects on fatigue crack propagation in aluminium alloy sheet materials, International Journal of Fatigue, 1(3) (1979) 118-123.
[42] Cansdale R. and Perrett B., The Helicopter Damage Tolerance Round Robin Challenge, Workshop on Fatigue Damage of Helicopters, University of Pisa, September 12-13, 2002.

[43] Irving P.E., Lin J. and Bristow J.W., Damage tolerance in helicopter - Report on the round robin challenge, presented at American Helicopter Society 59th Annual Forum, Phoenix, Arizona, 2003.
[44] Newman J.C., Irving P.E., Lin J. and Le D.D., Crack growth predictions in a complex helicopter component under spectrum loading, Fatigue Fract Engng Mater Struct, 29 (2006) 949-958.
[45] Vaughan R.E. and Chang J.H., Life prediction for high cycle dynamic components using damange tolerance and small threshold cracks, presented at American Helicopter Society 59th Annual Forum, Phoenix, Arizona, 2003.
[46] Jones R., Peng D. and Tiong U.H., An Equivalent Block Approach To Fatigue Crack Growth, 5th Australasian Congress on Applied Mechanics, ACAM 2007, 10-12 December 2007, Brisbane, Australia.
[47] Molent L., Jones R. and Pitt S., Understanding crack growth in fuselage lap joints, Theoretical and Applied Fracture Mechanics, available on line.

Prediction of Fatigue Crack Growth Rates in Ti-6Al-4V Alloy

A. M. Korsunsky[1*], **D. Dini**[2] **and M. J. Walsh**[3]
[1] Department of Engineering Science, University of Oxford, Parks Road, Oxford OX1 3PJ, UK
[2] Department of Mechanical Engineering, Imperial College, Exhibition Road, London SW7 2AZ UK
[3] Combustion Systems Engineering, Rolls-Royce plc, P.O. Box 31, Derby DE24 8BJ, UK
**Email:* *alexander.korsunsky@eng.ox.ac.uk*

Abstract

Crack initiation under thermo-mechanical fatigue is analyzed with consideration given to oxidation and creep strain accumulation. Transitions and interactions between different mechanisms, crack initiation and crack propagation rates display significant scaling and size effects. The objective of this work is to present experimental data for crack initiation and propagation in aerospace alloys, and to offer some means of describing these data so as to develop improved capabilities for life prediction in aerospace materials and assemblies.

1. Introduction

Reliable prediction of fatigue crack growth rates in aerospace materials and components underpins the so-called defect-tolerant approach to lifing. In this methodology the presence or appearance of defects and cracks in components is accepted. However, safe operation is guaranteed by regular inspections and health monitoring, and ensuring (by means of reliable modeling) that no crack may grow far enough to reach the critical size in the interval between inspections.

Under such circumstances it is clear that particular attention has to be paid to the development and validation of predictive modeling capabilities for fatigue crack propagation. The situation is complicated by the fact that it is often a challenge to represent correctly the in-service loading experienced by a cracked component. In practice, on top of the major cycles associated with each flight (LCF component), cycles of higher frequency and lower amplitude are also present (HCF component). Sensitivity to dwell at maximum load is also often observed. Furthermore, it is well established

G.C. Sih (ed.), Multiscale Fatigue Crack Initiation and Propagation of Engineering Materials: Structural Integrity and Microstructural Worthiness, 47–64.

that complex load sequences involving overloads and underloads result in fluctuations of fatigue crack growth rates (retardation and acceleration) that must be accounted for in crack growth calculations.

Damage tolerant design (DTD) has become accepted as a method of fatigue lifing of airframe structures since early 1970's, when military specification MIL-A-83444 was introduced in 1971 [0]. In view of the substantial improvements in safe component lives and the associated cost savings, damage tolerant design soon became the subject of much academic research and industrial development. In 1982 the Advisory Group for Aerospace Research and Development (AGARD) headquartered in France asked its Structures and Materials Panel to form sub-committees devoted to this subject [0]. One of these two sub-committees, SMP/SC.33, was formed in 1983 to organize a cooperative test programme between NATO countries with the purposes of (i) promoting familiarity of laboratories with test techniques for DTD of engine disc materials, (ii) standardizing test specimen geometries and test techniques, and (iii) calibrating the results from participating laboratories through a round robin test programme.

The programme focused on the use of typical engine disc materials, Ti-6Al-4V, IMI 685 and Ti-17, and the use of realistic engine loading sequences. The data were intended to provide a basis for the evaluation of different modeling techniques for the prediction of fatigue crack growth rates (FCGRs) and component lives. The Core Programme focused on Ti-6Al-4V using detailed test procedures [0]. The Ti-6Al-4V material for the round robin test programme was provided by Rolls-Royce from RB211 fan disc forgings. There were in total 216 tests carried out by 12 different laboratories. Good repeatability of crack growth testing was confirmed, with potential drop technique proving extremely accurate in measuring crack sizes. The database of fatigue crack growth data for Ti-6Al-4V material was deemed to be large enough to be used in the Supplemental Programme for life prediction modeling.

The predictive models used in the Supplemental Programme all relied on Elber's plasticity-induced crack closure concept [0] and the effective stress intensity factor range ΔK_{eff}, except for the Rolls-Royce approach. The latter approach used the Walker model [0] in the form

$$\frac{da}{dN} = \left(\Delta K (1-R)^m\right)^n \quad , \tag{1}$$

where R denotes the ratio of minimum to maximum stress (stress intensity factor).

2. Experimental Programme and Results

The specimens used in the programme were made from material in the form of solution treated and aged compressor disc forgings provided by Rolls-Royce. Typical mechanical properties of Ti-6Al-4V material were: 0.2% yield stress 870 MPa, ultimate tensile strength 970 MPa, elongation to failure 11%, reduction in area 27%, fracture toughness 70 $MPa \cdot m^{1/2}$. Typical grain size of this material was 25μm [0].

Specimens designation used in the testing programme was composed using a six letter code, as follows: **LA-GE-##**, where **LA** indicates the laboratory where testing was carried out, **GE** indicates the crack geometry, and ## indicates the specimen test number in a particular series.

Laboratories contributing to the testing programme on Ti-6Al-4V were the following:

AF Air Force Materials Laboratory (AFML), WPAFB, Dayton, Ohio, USA
CE Centre d'Essais Aéronautique de Toulouse (CEAT), France
PI University of Pisa, Pisa, Italy

Two specimen geometries were used for fatigue crack propagation testing. ASTM compact tension specimens, designated **CT**, were used for the consideration of long crack growth regime where typically the assumption of two-dimensional through-thickness crack geometry can be used. The second specimen geometry, designated **CC**, corresponded to the corner crack specimen developed by Rolls-Royce [0] in order to simulate corner crack flaw geometries subjected to three-dimensional stress fields typically found in disc bore locations and at fastener holes [0]. Geometry of both **CT** and **CC** specimens are shown in Figure 1. Crack length data were collected using potential drop technique.

Loading sequences considered in the programme included two constant amplitude sequences characterised by R-ratios (ratio of minimum to maximum applied load) of R = 0.1 and R = 0.7. The waveform shape was trapezoidal with the frequency of 0.25 Hz (cycle duration 4 seconds). In addition to the constant amplitude sequences, further 'simple sequences' were used. Three of these were selected to study the effect of minor cycles on a single major cycle, and designated SS1, SS2 and SS3, respectively. As illustrated in Figure 2(a), these sequences can be considered as constant amplitude trapezoidal cycles with a dwell at peak load that is replaced with 10 minor cycles. Minor cycle amplitudes were 10% unload from peak load for SS1, 30% unload for SS2, and 50% unload for SS3, respectively. For

SS1, 30% unload for SS2, and 50% unload for SS3, respectively. For these three loading sequences the R-ratio of major cycles was set to zero, and all loading and unloading rates in major and minor cycles were constant, resulting in cycle duration of 13 seconds for SS1, SS2 and SS3.

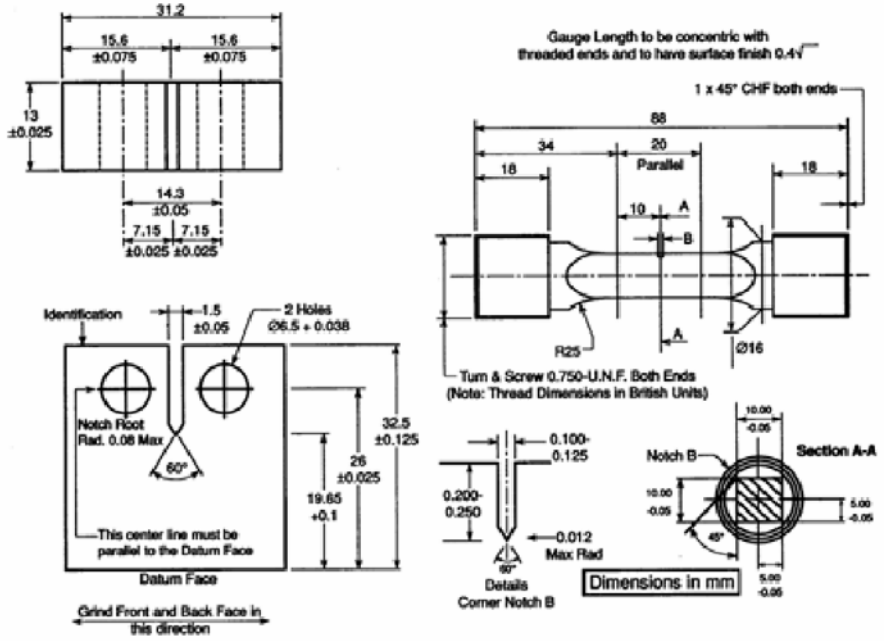

(a) Compact tension specimen (b) Corner crack specimen

Fig. 1 Compact tension (CT) and corner crack (CC) specimen geometries [0].

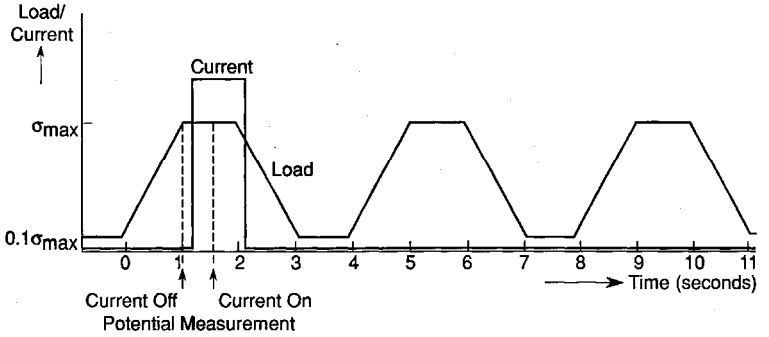

Fig. 2 Illustration of the trapezoidal waveform used for constant amplitude tests (CST) [0].

Loading sequence SS4 (Figure 2b) contained a single overload with the ratio of 1.7 after every 1000 constant amplitude triangular cycles. The purpose of this test was to investigate the retardation effect due to overload.

Alongside the 'simple sequences' outlined above, complex sequences were also utilised, namely, the full Cold TURBISTAN sequence [0] and three modified versions. TURBISTAN loading sequence is a variable amplitude loading standard and comprises 100 individual flights with an average of 154 end points per flight. Four TURBISTAN sequences used contained minor cycle omission levels of 0%, 10%, 30% and 50%, respectively. The loading sequences resulting from various levels of omission are illustrated in Figure 4.

Experimental results from the AGARD report [0] used in this study are illustrated in Figures 3 and 4 as Paris plots of fatigue crack growth rate (FCGR) vs applied stress intensity factor range for compact tension (CT) specimens. Figure 3 shows significant divergence between results obtained using different loading sequences, suggesting that using applied stress intensity factor ΔK_{appl} alone does not allow obtaining adequate correlation for FCGR. Further detailed analysis revels that the data for loading sequences SS1, SS2 and constant amplitude cycling (CST) collapse well. However, significant deviation is observed in the remaining simple loading sequence data, particularly for sequence SS4 (containing periodic overload every 1000 cycles), and, to a lesser extent, for sequence SS3 (containing minor cycles with 50% unloads).

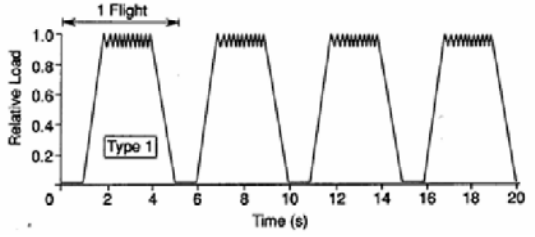

(a-1). Simple loading sequence type 1 (SS1).

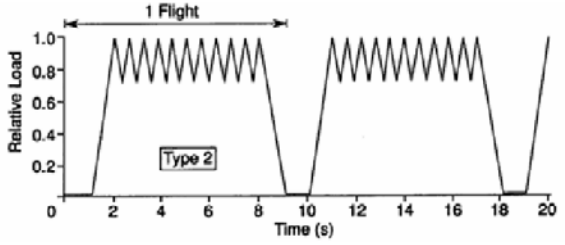

(a-2). Simple loading sequence type 2 (SS2)

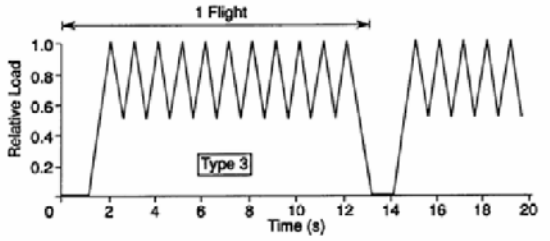

(a-3). Simple loading sequence type 3 (SS3).

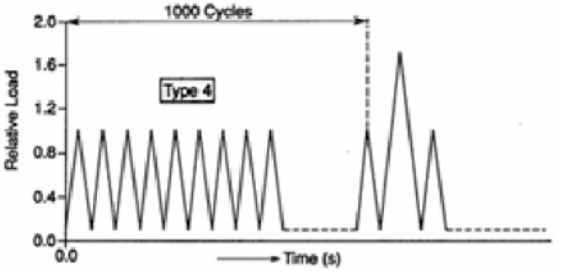

(b) Simple loading sequence type 4 (SS4).

Fig. 3 Simple loading sequence type 1,2,3 and 4 (SS1,SS2,SS3 and SS4) [0]

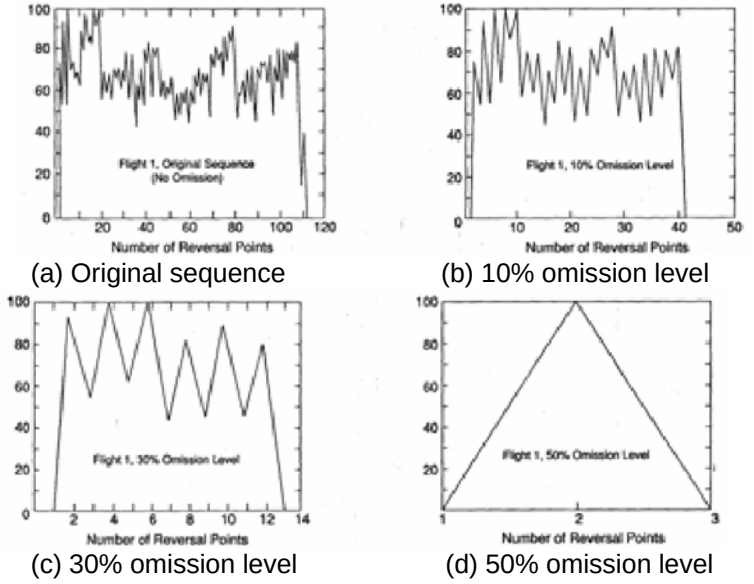

(a) Original sequence (b) 10% omission level

(c) 30% omission level (d) 50% omission level

Fig. 4 Example of TURBISTAN flight number 1 loading sequence with various omission levels [0].

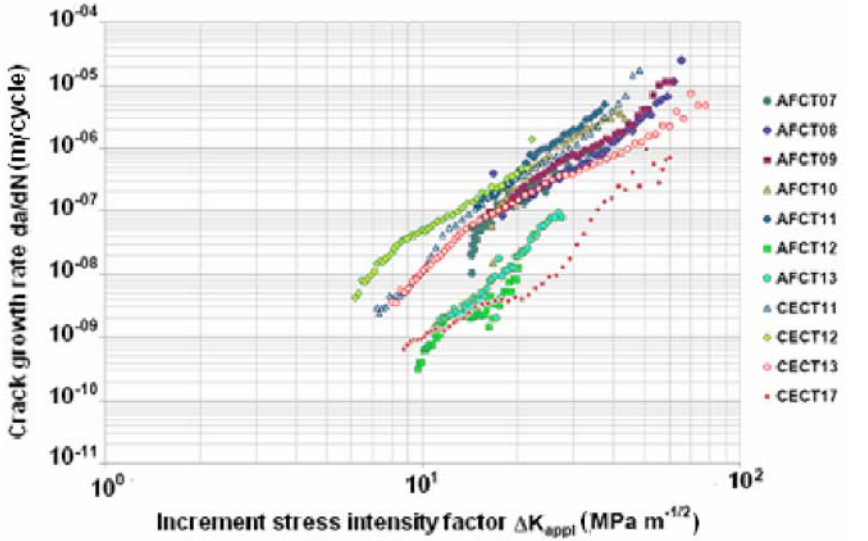

Fig. 5 Experimental results for fatigue crack growth rate (FCGR) vs applied stress intensity factor range for compact tension (CT) specimens used in the AGARD test series [0]. Simple loading sequences (SS1, SS2, SS3 and SS4) were applied.

Analysis of the results presented in Figure 5 for TURBISTAN loading sequences with different percentages of omission shows that acceptably good correlation is achieved, perhaps with the exception of some sensitivity to loading details for conditions approaching the lower threshold.

Review of the results contained in the AGARD addendum report [0] draws, amongst others, the conclusions that (i) for simple loading sequences, using R=0.1 as baseline, the addition of minor cycles *does not* influence fatigue crack growth rate (FCGR) until the magnitude of the minor cycle reaches 50% (as in SS3) of the major cycle; and that (ii) the overload sequence, SS4, compared to the baseline R=0.1 data, retards the fatigue crack growth rate by a factor of eight at ΔK =10 MPa·m$^{1/2}$, and a factor of four at ΔK =30 MPa·m$^{1/2}$.

Consider the suitability of a recently proposed model of. [0,0] for the prediction of fatigue crack growth rates (FCGR's) in Ti-6Al-4V material using a simplified description of plastic deformation in the vicinity of crack tip, in combination with the use of the two-parameter crack driving force. The model is introduced, and its application to the set of AGARD data is illustrated below.

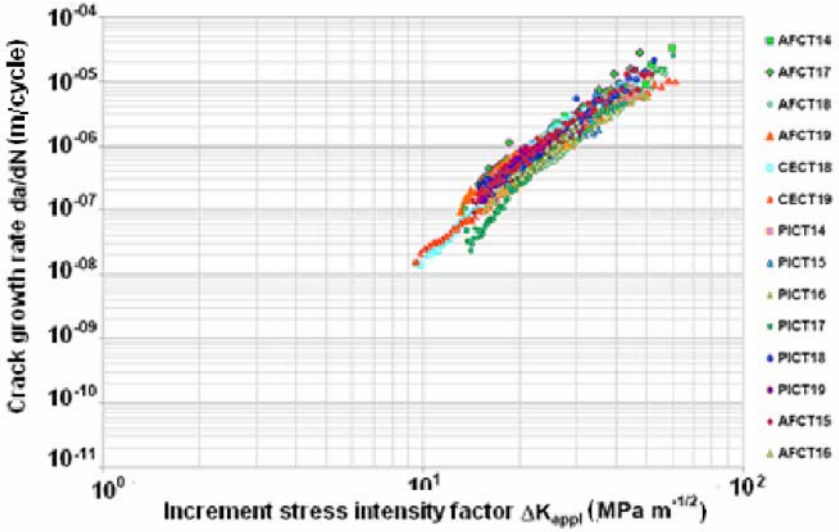

Fig. 6 Experimental results for fatigue crack growth rate (FCGR) vs applied stress intensity factor range for compact tension (CT) specimens used in the AGARD test series [0]. TURBISTAN loading sequences were applied.

3. The Two-Parameter Crack Driving Force

The work in [0, 0] presented a two-parameter approach to fatigue crack growth prediction in steel, aluminium and titanium alloys. The purpose of this approach is to account for the influence of stress ratio on fatigue crack growth through detailed semi-analytical consideration of the development and effect of residual stress around the tip of the growing fatigue crack. In all cases the driving force is expressed as a combination of the maximum stress intensity factor, $K_{\max}$, and the stress intensity range, ΔK, where both parameters are corrected for the presence of residual stress. The purpose of this approach was to correlate fatigue crack growth data obtained under a wide range of load ratios and fatigue crack growth rates from near-threshold to high growth rate regimes. The principal advantage of the approach lies in the fact that no finite element modeling of the near-tip deformation is required, since material response is described in terms of Ramberg-Osgood strain-stress relations, in combination with the Neuber rule. In [0] the model was successfully verified using fatigue crack growth data for Ti–6Al–4V titanium alloy with load ratios ranging from -1 to 0.7.

Use is made of the above approach to correlate the data obtained in the AGARD programme, and discuss the results in view of the suitability of this method for damage tolerant design calculations.

The starting point for the analysis is the introduction of inherent small, but finite crack tip blunting radius, ρ^*. The consequence of this assumption is two-fold. On the one hand, under tensile loading it may now be noted that the crack tip stress-strain field is no longer singular; in fact, instead of the classical stress intensification expressions, the stress distribution can be described using the formulae given in [0], of the form

$$\sigma_y = \frac{K}{\sqrt{2\pi x}}\left(1+\frac{\rho^*}{2x}\right)+... \tag{2}$$

The maximum stress at the crack tip is attained at $x = \rho^*/2$ and is equal to

$$\sigma_y^{\max} = \frac{2K}{\sqrt{\pi\rho^*}}. \tag{3}$$

On the other hand, the presence of finite radius ensures that upon the application of compressive stress to the crack its shores cannot immediately close simultaneously (as might be the case for a crack with an infinitely sharp tip). Instead, close to the tip the crack would remain open, forming a cavity that can be approximated as a circle, with the possibility of some reverse plastic flow due to stress concentration. Interesting aspect of this simplifying assumption is then the fact that the asymmetry of deformation response to tensile and compressive applied stresses is explicitly captured in the micromechanical description. The authors of the Noroozi et al. analysis note that the origin of such view can be traced back to Neuber's concept of 'microsupport', that postulates the existence of the smallest material-specific length scale (notch radius) that is still perceived to be different from a sharp crack. The same material parameter is also used to define the length dimension of elementary material volumes within which failure processes occur. It is interesting to observe that this view can also serve as a basis for developing an explanation for the KT fatigue threshold diagram [0].

Crack propagation is considered to be due to sequential failure of elementary material volumes occupying the segments between $x_i = \rho^*(2i-1)/2$ and $x_{i+1} = \rho^*(2i+1)/2$ with respect to the tip centre position [0]. Average stress in each such volume is computed as follows:

$$\tilde{\sigma}^{e}_{y,i} = \frac{1}{(x_{i+1} - x_i)} \int_{x_i}^{x_{i+1}} \frac{K}{\sqrt{2\pi x}} \left(1 + \frac{\rho^*}{2x}\right) \mathrm{d}x = \frac{K \psi_{y,i}}{\sqrt{2\pi\rho^*}}, \qquad (4)$$

where therefore

$$\psi_{y,i} = \frac{2}{(x_{i+1} - x_i)} \left[\sqrt{\frac{\rho^*}{x}} \left(x - \rho^*/2\right) \right]_{x_i}^{x_{i+1}}, \ \psi_{y,1} = 1.63299, \text{ etc.} \qquad (5)$$

Further development of the micromechanical model of Noroozi et al. [0] proceeds by taking into account the reverse plastic deformation in the vicinity of the crack tip and its effects on residual stress formation, and hence on the stress intensity factor modification. Material deformation is described using a simplified strain energy equivalence procedure, also due to [0], that allows the prediction of inelastic strains and stresses within elementary material volumes ahead of the crack tip. Note that this task can be accomplished without recourse to detailed finite element analysis, although the results obtained in this way show reasonable agreement with such simulations [0]. Cyclic uniaxial material response can be conveniently described by the Ramberg-Osgood additive strain-stress law,

$$\varepsilon = \left(\frac{\sigma}{E}\right) + \left(\frac{\sigma}{K'}\right)^{1/n'} . \qquad (6)$$

The two terms represent elastic and plastic strains, respectively. Parameters *K'* and *n'* can be readily identified by fitting functional relationship in equation (2) to material's uniaxial macroscopic cyclic stress-strain curve.

A further aspect of the Noroozi et al approach is the use of the Coffin-Manson strain-life curve in combination with Smith-Watson-Topper parameter [0], in the form:

$$\sigma_{\max} \frac{\Delta\varepsilon}{2} = \frac{(\sigma'_f)^2}{E} (2N)^{2b} + \sigma'_f \varepsilon'_f (2N)^{b+c} . \qquad (7)$$

Here N is the number of cycles to failure; $\sigma_{\max}$ and $\Delta\varepsilon$ refer to the maximum stress and strain range in the stabilized fatigue cycle, respectively; σ'_f and ε'_f are fatigue stress and strain parameters, respectively; and b and c are strain-life fatigue law exponents.

Analytical predictions for fatigue crack growth rate (FCGR) were expressed in [0] in the following form:

$$\frac{da}{dN} = C\Delta\kappa^{\gamma}$$
$$\Delta\kappa = K_{\max,tot}^{p}\Delta K_{tot}^{1-p} \tag{8}$$

Here for the case of predominantly elastic behaviour (near the lower fatigue crack growth threshold) the following parameters are used:

$$p_{el} = 0.5; \qquad \gamma_{el} = -1/b$$
$$C = 2\rho^{*}\left[\frac{\left(\psi_{y,1}\right)^{2}}{4\pi\rho^{*}\sigma_{f}^{'2}}\right]^{-1/2b} \qquad \textit{in Plane Stress} \tag{9}$$
$$C = \frac{2\rho^{*}}{\left(1-\nu^{2}\right)^{1/2b}}\left[\frac{\left(\psi_{y,1}\right)^{2}}{4\pi\rho^{*}\sigma_{f}^{'2}}\right]^{-1/2b} \qquad \textit{in Plane Strain}$$

For the case of predominantly plastic behaviour (i.e. at higher values of stress intensity factor range) the following parameters are used:

$$p_{pl} = \frac{n'}{n'+1}; \qquad \gamma_{pl} = -\frac{2}{b+c}$$
$$C = 2\rho^{*}\left[\frac{\left(\psi_{y,1}\right)^{2}}{2^{\frac{n'+3}{n'+1}}\pi\rho^{*}\sigma_{f}^{'}\varepsilon_{f}^{'}E}\right]^{-\left(\frac{1}{b+c}\right)} \qquad \textit{in Plane Stress} \tag{10}$$
$$C = \frac{2\rho^{*}}{\left(1-\nu^{2}\right)^{1/2b}}\left[\frac{\left(\psi_{y,1}\right)^{2}}{2^{\frac{n'+3}{n'+1}}\pi\rho^{*}\sigma_{f}^{'}\varepsilon_{f}^{'}E}\right]^{-\left(\frac{1}{b+c}\right)} \qquad \textit{in Plane Strain}$$

In order to be able to plot both the predictions obtained assuming predominantly elastic and predominantly plastic behaviour on the same graph and compare them to the experimental data, we need to write the fatigue crack driving force, $\Delta\kappa$, for the predominantly elastic behaviour as a function of the applied stress ratio and the driving force for the predominantly plastic behaviour. If we neglect the effect of residual stresses on the total stress intensity factors and assume $R_{\text{appl}} \geq 0$, then

$$\Delta\kappa^{el} = \left(1-R_{appl}\right)^{p_{pl}-p_{el}}\Delta\kappa^{pl} \tag{11}$$

It should be noted that all results discussed below are plotted with respect to the fatigue crack force for the predominantly plastic behaviour, *i.e.* $\Delta\kappa = \Delta\kappa^{pl}$.

After calculating the residual stress intensity factor, K_r, as described in [0], it is necessary to modify the applied maximum stress intensity factor, $K_{max,appl}$ and the applied stress intensity factor range, K_{appl}. This modification accounts for the effect of the residual stress on the fatigue crack growth. The interactions of the stress intensity factor, the plastic zone and the residual stress manifest themselves through the change (decrease) of the resultant maximum stress intensity factor, $K_{max,tot}$, without significant changes in the resultant minimum stress intensity factor, $K_{min,tot}$. It is assumed that the residual stress intensity factor, K_r, contributes mainly to the change (decrease) of the resultant maximum stress intensity factor, $K_{max,tot}$, and subsequently to the resultant stress intensity range, ΔK_{tot}. However, the magnitude of the residual stress effect depends on the applied stress ratio and it has to be treated differently for positive and negative applied stress ratios, R_{appl}.

Figure 7 illustrates several consequences of applying the model to AGARD fatigue crack growth rate data for simple loading sequences.

Firstly, comparison with the same data plotted in Figure 5 in a conventional form (da/dN vs K_{appl}) reveals that better collapse of the results towards a master curve is achieved. This is primarily the consequence of taking into account stress intensity factor modification in fatigue cycles with the R ratio less of equal to 0.5 (for minor cycles) that arises from the presence of residual stresses. Secondly, the quality of agreement with the data achieved by the plastic regime prediction is on the whole satisfactory, with the slope and location of the trend line capturing the overall location of the data points. However, the quality of agreement in the predominantly elastic regime leaves room for improvement. Note that the effect of the residual stresses was neglected in deriving the modified stress intensity driving force, $\Delta\kappa$, for predominately elastic behaviour. Furthermore, in the limited version of the model used here the collapsing of the data points is performed making the assumption that the specimens are subjected to uniform loading histories. Therefore, the influence of overload, underload and mixed LCF/HCF cycling (replicating in-service conditions) are not adequately captured. It is important to note, however, that improved, more detailed models have been proposed that capture the history effect by calculating the stress-strain response at the crack tip for each consecutive load reversal. The magnitude and distribution of residual compressive stresses is then continuously monitored and updated during cycling, and serve as the basis for predicting the response during the next load reversal. Furthermore, a memory model has been proposed that postulates the influence of past stress history on the growing fatigue crack.

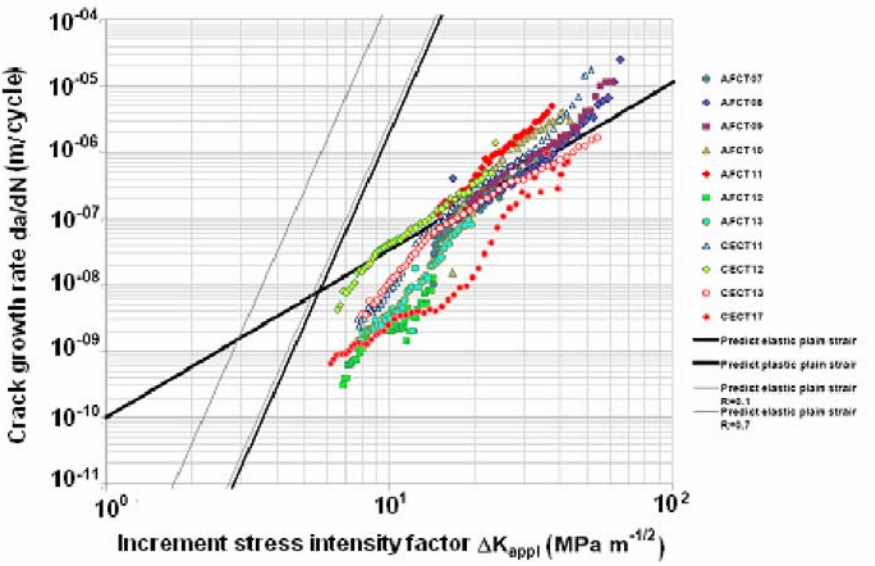

Fig. 7 Correlation obtained for FCGR's using two-parameter fatigue crack driving force for simple loading sequences.

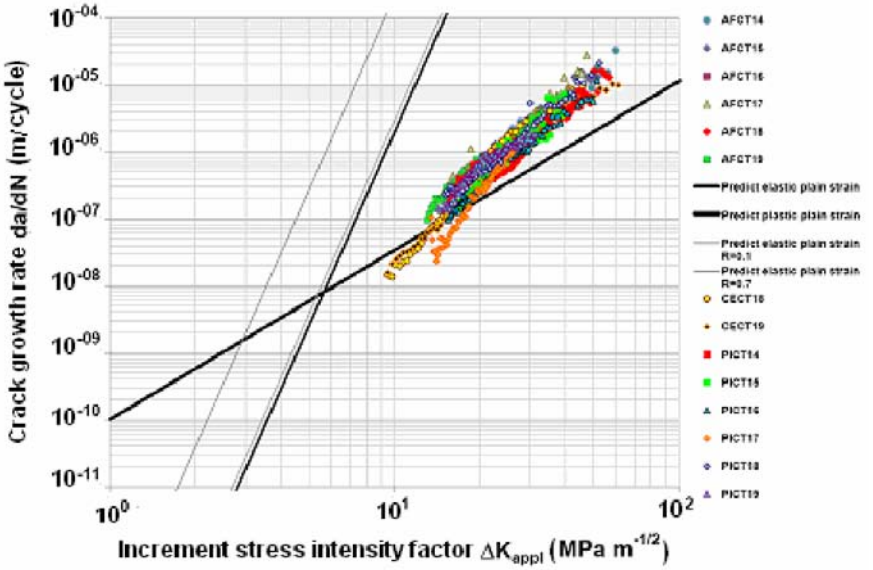

Fig. 8 Correlation obtained for FCGR's using two-parameter fatigue crack driving force for TURBISTAN loading sequences.

Figure 8 illustrates the predictions obtained using the predominantly elastic and plastic regimes for the TURBISTAN data. Good clustering of data can be noted in this figure, as well as in Figure 6, where the same results are plotted in a conventional way. However, the quality of predictions shown in Figure 8 for both predominantly elastic and plastic regimes requires further improvement.

4. Discussion

Consider the application of [0] methodology to a substantial set of experimental fatigue crack growth rate (FCGR) data in Ti-6Al-4V alloy. Most of the loading sequences considered in the experimental study were not constant amplitude sequences, but in fact contained combinations of major and minor cycles with different values of the R ratio, and also included complex TURBISTAN sequences with different levels of omission.

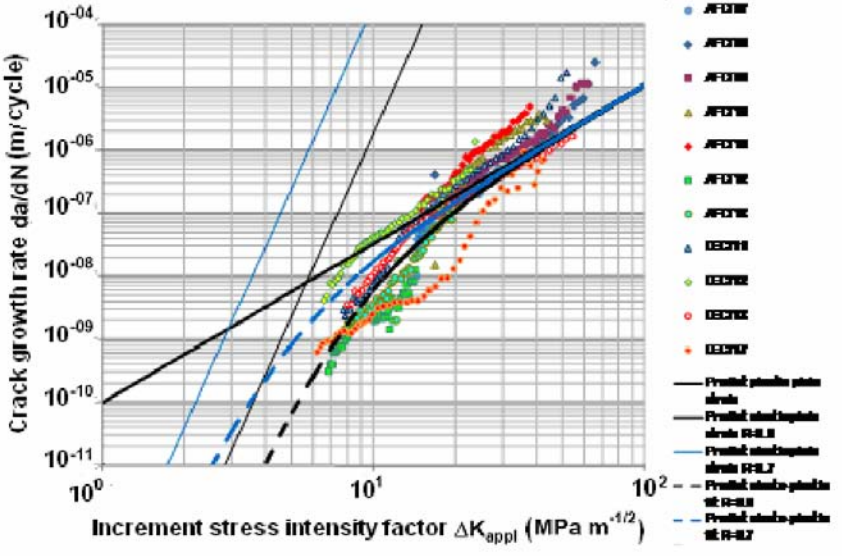

Fig. 9 Correlation obtained for FCGR's using two-parameter fatigue crack driving force for simple loading sequences.

Predictive description of fatigue crack growth rates is most importantly used for design calculations. It is therefore important to express the growth rate in the most compact form suitable for easy incorporation into numerical models. From this point of view, analytical expressions possess distinct advantages. It is therefore proposed here to identify a functional form for

the dependence of FCGR on the two-parameter fatigue driving force, as described below.

The fitting 'knee' function is sought in the form of a merging between two distinct power law functions that prevail in the predominantly elastic and plastic regimes, for the large and small values of $\Delta\kappa$ respectively. The form of this function is:

$$\frac{da}{dN} = C_{fit}\frac{\Delta\kappa^{\gamma_{el}}}{\left[1+\left(\frac{\Delta\kappa}{\Delta\kappa_0}\right)^{\frac{\gamma_{el}-\gamma_{pl}}{\chi}}\right]^{\chi}} \tag{12}$$

where

$$\Delta\kappa_0 = \left[\frac{\left[\frac{\left(\psi_{y,1}\right)^2}{4\pi\rho^*\sigma_f'^2}\right]^{-1/2b}\frac{1}{\left[(1-R)^{p_{el}-p_{pl}}\right]^{\gamma_{el}}}}{\left[\frac{\left(\psi_{y,1}\right)^2}{2^{\frac{n'+3}{n'+1}}\pi\rho^*\sigma_f'\varepsilon_f' E}\right]^{-\left(\frac{1}{b+c}\right)}}\right]^{\frac{1}{\gamma_{pl}-\gamma_{el}}} \tag{13}$$

$$C_{fit} = \frac{2\rho^*}{\left[(1-R)^{p_{el}-p_{pl}}\right]^{\gamma_{el}}}\left[\frac{\left(\psi_{y,1}\right)^2}{4\pi\rho^*\sigma_f'^2}\right]^{-1/2b} \quad \textit{in Plane Stress}$$

$$C_{fit} = \frac{2\rho^*}{\left[(1-R)^{p_{el}-p_{pl}}\right]^{\gamma_{el}}\left(1-\nu^2\right)^{1/2b}}\left[\frac{\left(\psi_{y,1}\right)^2}{4\pi\rho^*\sigma_f'^2}\right]^{-1/2b} \quad \textit{in Plane Strain}$$

and χ is a parameter representing the smoothness of the transition between the predominantly elastic and predominantly plastic behavior. This constant can be adjusted to provide the best match to experimental data. In the example shown in Figure 9 this parameter has been set to χ=4.5. It is apparent that the use of this function leads to a close agreement between prediction and the experimental data.

5. Conclusions

The original model of [0] for the correlation between fatigue crack growth rates and the two-parameter fatigue driving force has been applied directly to the data contained in the AGARD addendum report [0] with minimal

degree of adjustment. Material properties of alloy Ti-6Al-4V were taken from experimental cyclic dog-bone sample tests or from published literature [0]. Nevertheless, the quality of agreement achieved in this way was encouraging.

More reliable prediction of the effects of overloads and underloads present within loading sequences on the fatigue crack growth rates requires more careful analysis of the detailed interaction between local plastic deformation and damage at the crack tip. The process of crack advance leads to a gradual attenuation of the effects of overloads and underloads on further growth. The interaction of prior deformation history with subsequent plastic deformation is particularly intricate, and is probably most efficiently described by some phenomenological relationship [17].

A merging 'knee' function has been proposed for the description of transition between predominantly elastic and plastic regimes, respectively. The function provides a convenient means of incorporating the correlation in design calculations.

Table 1 Ti-6Al-4V specimen designations and loading sequences.

SPECIMEN	SEQUENCE
AF-CT-07	SS1, R=0.0
AF-CT-08	SSl, R=0.0
AF-CT-09	SS2, R=0.0
AF-CT-10	SS3, R=0.0
AF-CT-11	SS3, R=0.0
AF-CT-12	SS4, R=0.l
AF-CT-13	SS4, R=0.1
AF-CT-14	10% TURBISTAN
AF-CT-15	10%
AF-CT-16	30%
AF-CT-17	30%
AF-CT-18	50%
AF-CT-19	FULL TURBISTAN
CE-CC-07	CST AMP. R=0.7
CE-CC-08	SS1, R=0.0
CE-CC-09	SS2, R=0.0
CE-CC-10	CST AMP. R=0.1
CE-CT-11	CST AMP, R=0.1
CE-CT-12	CST AMP, R=0.7
CE-CT-13	SS1, R=0.0
CE-CC-14	SS3, R=0.0

CE-CC-15	SS3, R=0.0
CE-CC-16	SS4, R=0.1
CE-CT-17	SS4, R=0.1
CE-CT-18	10% TURBISTAN
CE-CT-19	FULL TURBISTAN
CE-CC-20	10%
CE-CC-21	10%
CE-CC-22	30%
CE-CC-23	30%
CE-CC-24	50%
PI-CC-07	10%
PI-CC-08	10%
PI-CC-09	30%
PI-CC-10	30%
PI-CC-11	50%
PI-CC-12	FULL TURBISTAN
PI-CC-13	FULL TURBISTAN
PI-CT-14	10%
PI-CT-15	30%
PI-CT-16	30%
PI-CT-17	50%
PI-CT-18	FULL TURBISTAN
PI-CT-19	FULL TURBISTAN
RR-CT-28	CST AMP, R=0.1

References

[1] Military Specification MIL-A-83444, Airplane Damage Tolerance equirements (U.S.) (1971).

[2] AGARD Conference proceedings 393, Damage tolerance concepts for critical engine components,(1985).

[3] Mom AJA. Working document for the AGARD cooperative test programme on titanium alloy engine disc material, NLR TR 84022L (1984).

[4] Elber W. The significance of fatigue crack closure. In: Damage tolerance in aircraft structures, STP 486, ASTM, Philadelphia, PA (1971) 230–42.

[5] Walker EK. The effect of stress ratio during crack propagation and fatigue for 2024-T3 and 7076-T6 aluminum. In: Effect of environment and complex load history on fatigue life. STP 462, ASTM, Philadelphia, PA (1970) 1–14.

[6] AGARD report R-766 (addendum), AGARD engine disc cooperative test programme, (1993).

[7] Pickard AC. Brown CW. and Hicks MA. The development of advanced specimen testing and analysis techniques applied to fracture mechanics lifing

of gas turbine components, ASME Intl Conf on Advances in Life Prediction Methods, Woodford DA. and Whitehead JR. eds., ASME (1983).
[8] A.A. ten Have, Cold TURBISTAN . Final definition of a standardized fatigue test loading sequence for tactical aircraft cold section engine discs, Combined report of the MTU, IABG, LBF, RWTH Aachen, Rolls-Royce, RAE, SNECMA, CEAT, ONERA, NLR, Univ. of Utah and NRC. National Aerospace Laboratory TR87054L, Holland (1987).
[9] Noroozi AH. G. Glinka G. and Lambert S. A two parameter driving force for fatigue crack growth analysis, International Journal of Fatigue, 27 (2005) 1277–1296.
[10] Noroozi AH. G. Glinka G. and Lambert S. A study of the stress ratio effects on fatigue crack growth using the unified two-parameter fatigue crack growth driving force, International Journal of Fatigue 29 (2007) 1616–1633.
[11] Creager M. and Paris PC. Elastic field equations for blunt cracks with reference to stress corrosion cracking. Int J Fract Mech 3 (1967) 247–252.
[12] Neuber H., *Kerbspannugslehre*. Berlin: Springer (1985).
[13] Kitagawa H.and Takahashi S. Applicability of fracture mechanics to very small cracks in the early stage. Second Intl Conf on Mechanical Behaviour of Materials, Metals Park, American Society for Metals (1976) 627–631.
[14] Neuber H. Theory of stress concentration for shear-strained prismatic bodies with arbitrary nonlinear stress–strain law, ASME J Appl Mech 28 (1961) 544–551.
[15] Pommier S. A study of the relationship between variable level fatigue crack growth and the cyclic constitutive behaviour of steel. Int J Fatigue 23 (2001) 111–118.
[16] Smith KN. Watson P. and Topper TH. A stress–strain function for the fatigue of metals, J Mater 5 (1970) 767–778.
[17] Glinka G. private communication, 2007.

Some Practical Implications of Exponential Crack Growth

L. Molent[1*], **S. Barter**[1] **and R. Jones**[2]
[1]Air Vehicles Division, Defence Science and Technology Organisation, 506 Lorimer Street, Fishermans Bend 3207, Australia
[2]Department of Mechanical Engineering, Monash University, P.O. Box 31, Victoria, 3800, Australia
**Email: Lorrie.Molent@defence.gov.au*

Abstract

A review of experimental data show that for many lead fatigue cracks in service components loaded with service spectra, exponential growth (i.e. log crack depth versus cycles or hours) applies for the majority of the life. This behaviour is shown to extend from the micro to macro range of crack sizes in a variety of metals. As a consequence of this, it will also be shown that the crack growth rate is directly proportional to the crack depth. By combining these observations with traditional fracture mechanics approaches to crack growth modelling, a model that is a function of the stress intensity factor (K) with a fixed crack depth influence (non-similitude for the K parameter alone) is proposed. It will then be shown that this model allows for Region I to be smoothly integrated with Region II of the constant amplitude da/dN data. Further, it will be shown that for variable amplitude crack growth data, crack growth ranging from microns to many millimetres can be modelled using this single model.

This modelling approach is of particular importance in structural integrity analysis where fatigue cracking cannot always be avoided and the majority of the fatigue life of highly stressed, nominally gross defect free structure is spent growing physically small cracks from initiating discontinuities (i.e. loads in Region I for constant amplitude loading growth rates) up to the point of loss in acceptable strength.

1. Introduction

Where fatigue cracking is inevitable, as is the case for many critical structures such as aircraft, trains and rails, oil rigs and bridges etc., it is generally accepted that the majority of the fatigue life of metallic components is governed by the growth of the fatigue cracks while they are small. It is also true that the cyclic loading leading to fatigue cracking is of variable amplitude (VA), whereas fatigue life predictions are usually based on con-

G.C. Sih (ed.), Multiscale Fatigue Crack Initiation and Propagation of Engineering Materials: Structural Integrity and Microstructural Worthiness, 65–84.

stant loading cycle data. Generally these cracks start from some form of discontinuity in the material and over time grow to a size where the component can no longer support the applied loading. There has been so much research into fatigue crack growth (CG) that it is virtually impossible to summarize. It therefore may seem surprising that a reliable and accurate means for characterizing the growth of cracks under variable loading (VA) is still unavailable [0]. One possible explanation for this may be that the characterisation of so-called small CG, that aligns with Region I on a Paris type constant amplitude (CA) CG rate d*a*/d*N* versus stress intensity (*K*) range (ΔK) plot (where *a* is the crack depth and *N* is a load cycle) and Region II (Paris Region) of the same type of plot, is yet to be fully unified. These Regions are indicated on a typical data set shown in Fig. 1.

Unification of the Region I and II' growth has not yet been fully achieved, despite numerous models that have been developed to achieve this goal. These models include the El Haddad model [2] in which a crack

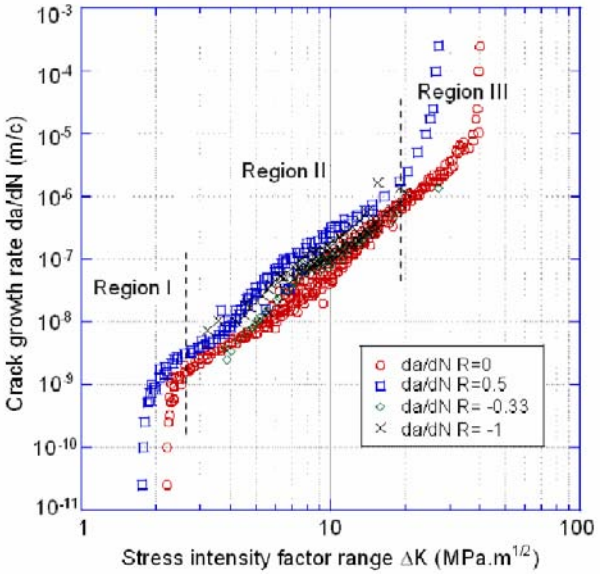

Fig. 1 Typical long crack CA d*a*/d*N* data for Al7050-T7451 for cracking in the L-T orientation taken from AFGROW [4]. In terms of long crack data the three Regions of growth are indicated approximately.

size dependency on the threshold stress intensity range, K_{thes} is added to the physical crack length, so that ΔK is proportional to $\sqrt{a + a_0}$ instead of $\sqrt{a}$; and the FASTRAN model which adds a fictitious plastic zone size dependent crack size to the physical crack [3].

A problem for prediction of the fatigue life of a structural component is that the data used for life calculation are inevitably based on cracking typically tens of millimetres long, which is used to produce the Paris-type CA plot as shown in Fig. 1. These data are known as long crack data. In contrast, most critical fatigue cracking initiates from small discontinuities in a material, and these cracks can spend a significant proportion of their lives at sizes below about 1mm in depth for small discontinuities and high stresses. These differences can lead to significant differences in the CG rate calculated using long crack Region 1 data and that measured experimentally for a given ΔK. This is the so called small or short crack inconsistency [5]. These inconsistencies occur at low ΔK values, and this behaviour is sometimes (incorrectly) referred to as anomalous CG [5]. This variation in the threshold values and CG rates in Region I is a serious problem when it comes to crack life prediction for cracks that grow from small initial discontinuity sizes. As stated by others (e.g. [6]), it will be shown here that it is the short crack or low crack tip ΔK regime that governs a large portion of the life of many fatigue critical components. In this chapter a simple model will be described and shown to be applicable to the prediction of CG for small cracks or low crack tip K levels for VA CG ranging from microns to many millimetres. The model is shown to bridge both Region I and II for CA loading, or small cracks through to many millimetres regime for VA loading. The model is explicitly dependant on crack length. The equivalent Region III CG where the crack is approaching failure under static modes of crack extension is also considered despite this period usually only representing a small portion of the total life in many components.

2. Crack Growth Model

The CG model described below is based on observations indicating that the Regions I and II (or equivalent for VA loading) produce consistent and regular CG in practical circumstances. An example of this is shown in Fig. 2, where the surface of a fatigue crack that was grown in an ex-service F/A-18 aircraft component with the mini-FALSTAFF VA loading spectrum [7] is presented. The component was made from aluminium alloy (Al)7050-T7451. Each of the repeating marks indicated is a block of the mini-FALSTAFF spectrum. The peak load in this spectrum generated a K_{max} of less than 1MPa$(m)^{0.5}$ at the initial crack size of 0.01mm shown, while this value was about 10 MPa$(m)^{0.5}$ by the end (upper edge) of the view in this Figure. These K values can be compared to those presented in Fig. 1 (for CA data) i.e. spanning the equivalent Region I and II.

From Fig. 2 it can be seen that the crack grows from a surface crack only a few microns deep (starting from a small crack that had grown during service) in a fashion that appears regular and systematic, being free of the inconsistencies suggested by short crack effects. This indicates that for such a spectrum of loads, the small to relatively large CG regimes should be easily predicted.

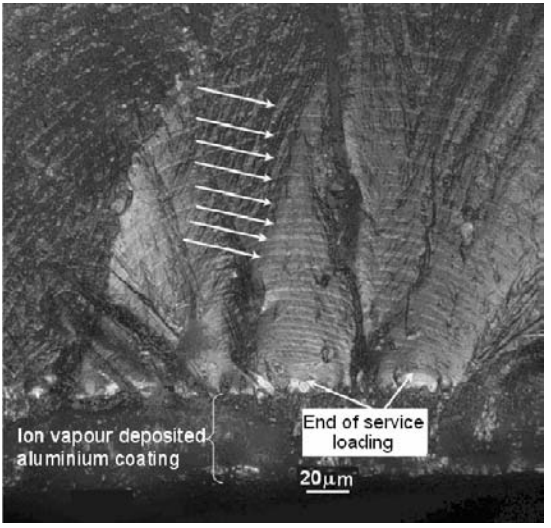

Fig. 2 An optical view of a fatigue crack surface in an Al7050-T7451 component after post service fatigue testing [8]. Between each of the repeating marks (arrows) is a block of growth due to the application of a single block of the mini-FALSTAFF load spectrum.

The simple model discussed in this chapter is based on four primary observations, namely:

1) The growth of naturally occurring surface cracks commences shortly after the introduction into service (i.e. the initiation phase is an insignificant portion of the total life). Thus CG can be assumed to occur from the first load cycle and the total life is represented by the CG from the initiating defect size to the point of loss in residual strength at the critical crack size;
2) The growth of critical (i.e. the fastest) surface initiating cracks in near ambient conditions loaded under VA loading will produce approximately exponential growth, which when presented on log crack depth versus linear life (in load cycles, or blocks of cycles) plot, gives straight line. This appears to consistently arise in the absence of fluctuating

stress fields (residual stress, stress gradients, load shedding etc.), significant changes in geometry (i.e. finite width effects are negligible) and/or significant changes in environment. This behaviour has been shown to apply for a wide range of problems [9];

3) If the CG history data are generated on a spectrum block-by-block basis, the rate of CG (i.e. d*a*/d*B, where B is one block of the loading spectrum*), is directly proportional to the crack depth [10], again implying exponential CG based on crack depth. Thus, when testing, it is important to generate data for many blocks of crack growth (≈ 10 or more blocks); and
4) The d*a*/d*N* or d*a*/d*B* for a given spectrum is approximately proportional to the applied stress cubed. This was first noted for CA loading [11] and later for VA loading [9].

Whilst a CG model could be developed based on the crack depth and applied stress (see [9], [11]), there is an advantage in using *K;* as it includes a geometry factor (β), for which many geometries have been analysed and the results of which are available in the open literature e.g. [12]. In addition, much CA CG data of the form of d*a*/d*N* versus *K* for many materials already exists. The Paris and related formulations rely on an exponent of *K* to describe the CG rate found from long crack growth experiments. However, as will be shown in this chapter, the VA growth is typically exponential based on the crack length. Therefore the power on crack length *a* needs to be fixed (with an exponent of unity) while the power on *K* should be allowed to vary along with the long crack data. This leads to a Paris-like related model of the form [9] for CA data:

$$\frac{\mathrm{d}a}{\mathrm{d}N} = C * a^{(1-m^*/2)} \, (\Delta K)^{m^*} \tag{1}$$

or for VA data:

$$\frac{\mathrm{d}a}{\mathrm{d}B} = C * a^{(1-m^*/2)} \, (K_{ref})^{m^*} \tag{2}$$

where, *C**, and *m** are constants for a given material, spectrum and applied stress. Here it should be noted that d*a*/d*N* is a function of both *a* and ΔK (which when combined give the CG a ΔK dependence with a correction that makes the CG exponentially dependent on crack depth).

While Equation (1) may be suitable for CA data, a further complication occurs in that ‘spectrum effects’ su ch as overloads and underloads, when applied as part of a group of loads may have a significant influence on the

overall damage created by the spectrum or block of loads. The damage may be greater or lesser than the sum of the damage created by the loads when applied constantly as occurs in CA loading. But if a block of loads, which includes the overloads and/or underloads is treated singularly in the same manner as a single cycle of CA loading (i.e. on a block-by-block basis) the same formulae (in the form of Equation (2)) will be shown to be applicable with the exception that a reference K value such as K_{max} (the peak K applied in the 'block' of loading) is used, as will be seen in this chapter.

This model was derived to predict exponential crack growth when m* was approximately equal to 3 (i.e. cubic stress dependency). Further Region III (or growth due to quasi-static modes of failure) can be accounted for by incorporating K_c in the formulation, where here blocks (B) of loads are considered instead of single loads:

$$da/dB = (\tilde{C}\, a^{1-m^*/2}\, K_{max}{}^{m^*})/(1.0 - K_{max}/K_c) \quad (3)$$

where $\tilde{C}$ is material, stress and spectrum dependent, K_c is the apparent mode I fracture toughness depending on the plane stress or plane strain or a mix of the values depending on the apparent fracture toughness of the component with the fatigue crack just prior to failure. K_c may simply be calculated using the K formulation, which for a block-by-block analysis can be based on the maximum stress in the block, σ_{max}:

$$K_c = \sigma_{max}\, \beta\, \sqrt{(\pi a)} \quad (4)$$

In the remainder of this chapter the model is shown to fit several examples of CG, where the cracks have grown in components with complex geometries and loading. The β were taken from standard handbook solutions.

3. Low Threshold Constant Amplitude Crack Growth

Much has been written on the so-called short crack effect [13] for CA data. To adequately reinvestigate this region of growth, data needs to be assessed which includes the a versus N along with the corresponding ΔK. Unfortunately, published data with the a explicitly included is rare, although one such data set (Fig. 3: crack depth versus cycles, and Fig. 4: crack growth rate versus ΔK) is available for Al2024-T351 [14], and is investigated here. These data were generated from standard middle through crack coupons of length = 152mm, thickness = 12.7mm, width = 76.2mm and initial notch width $2a$ = 12.7mm, tested at R=0.1. The crack lengths

reported were the average value of the extension from both sides of the notch.

From Fig. 4 it can be seen that the data appear to produce the classic sigmoidal shape that represents growth from Region I through to Region III. Now, if it is considered that the low CG rate data extends up to approximately 1 x 10^{-7} m/cycles as indicated on Fig. 4, and the rate data are expressed as a function of *a*, which is shown in Fig. 5, then it can be seen that this region represents crack lengths of up to 10mm. From Fig. 3 this may be seen as the majority of the life of these specimens.

When Equation 1 is applied to these data, it can be seen in Fig. 6 that a near linear relationship, regardless of the region, is produced suggesting a unification of Regions I to III.

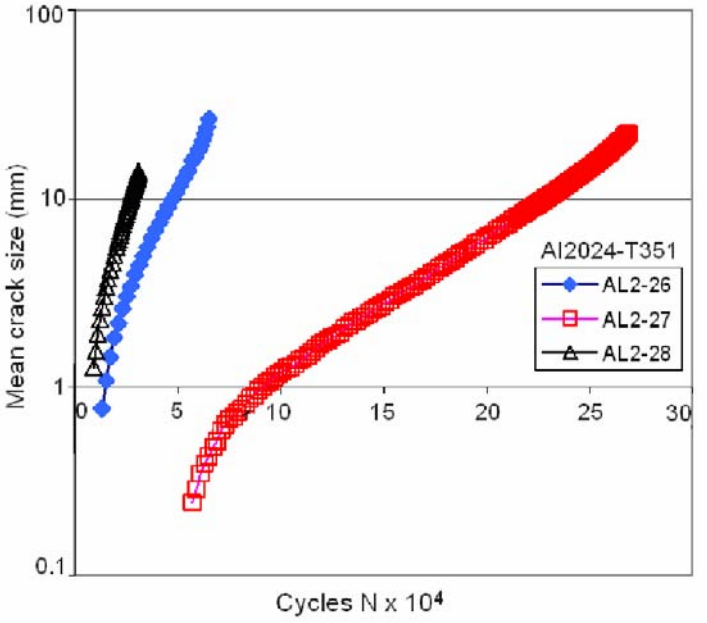

Fig. 3 Crack growth history data (measured from notch edge).

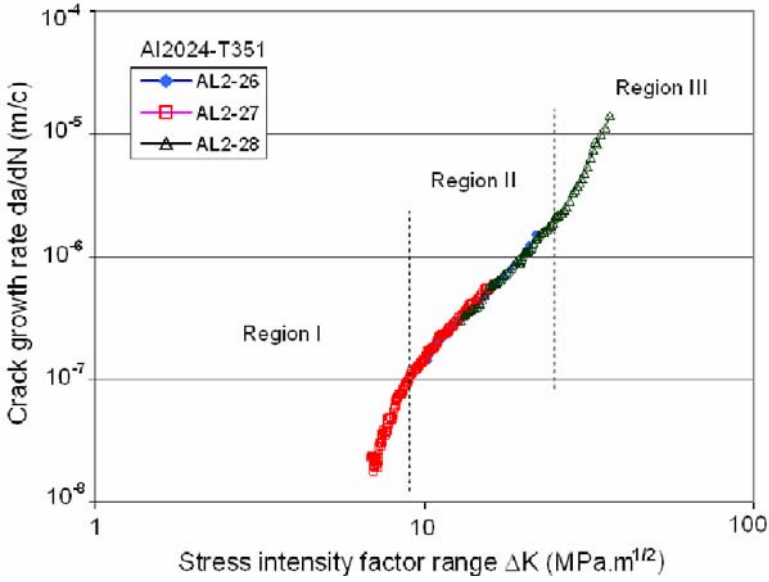

Fig. 4 Crack rate data for Al2024-T4 from [14]. Note log-log scale. Region Iappears to end at about the line indicated.

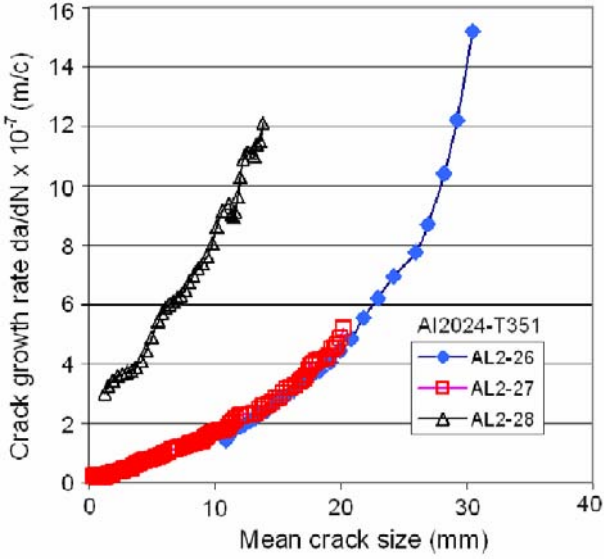

Fig. 5 Crack rate data versus crack depth.

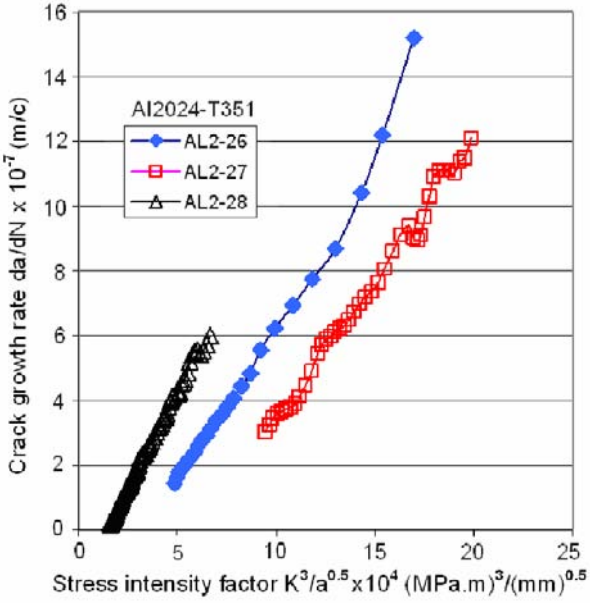

Fig. 6 Crack growth data as per Equation (1). Note the linear-linear scale.

4. Exponential Crack Growth for Describing Spectra Data

An examination of the CG of fatigue cracks grown with many spectra has found that the CG curves suggest exponential growth [6]. This has been found to be the case for most of the life of cracks grown in service or from full-scale fatigue tests [16], in addition to coupon tests carried out under service spectra [9]. The following formulations describe this growth:

$$\ln(a) = \psi N_L + \ln(a_0) \text{ or } a = a_0 e^{\psi N_L} \tag{5}$$

where ψ is a parameter that is geometry, material and load dependent, a is the crack depth at time N_L, and a_0 is the initial crack-like flaw size (depth of the crack at the start of loading, N=0), and N_L is the number of cycles to grow from a_0 to a.

By way of an example of this CG behaviour, some CG history data for Al7050 material tested under a VA service fighter aircraft spectrum and measured by quantitative fractography (QF), is shown in Fig.7. Equation 5

describes the growth depicted well and the extent of this agreement spans from approximately 0.01 to several millimetres. In this fatigue test program [15] up to five hour glass' (very low K_t) Al7050 specimen sets were tested at up to four stress levels each. The specimens were 6.35mm thick and 28mm wide at their thinnest width with material properties as listed in Table 1. The coupon is shown schematically in Fig. 8. Five complex service load sequences typical of fighter aircraft spectra, were applied (two sets of CG curves covering two of the spectra at one stress level are shown in the figure). The CG curves shown in Fig.7 demonstrate exponential growth.

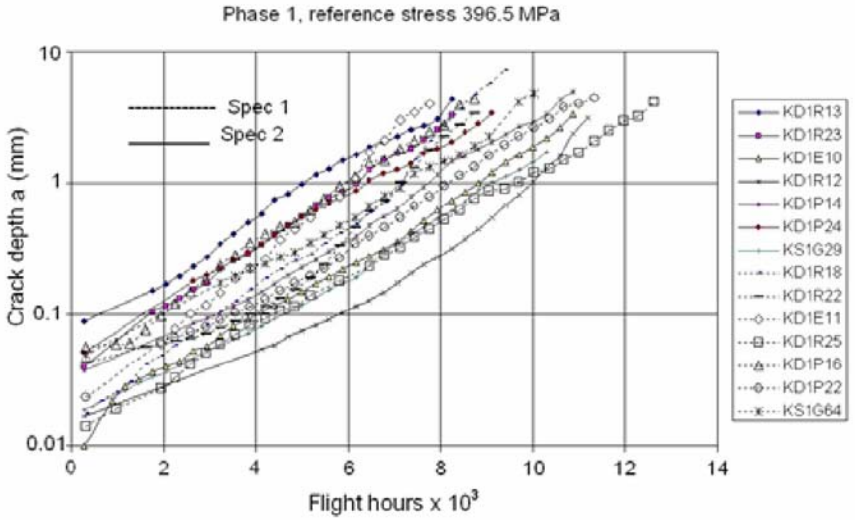

Fig.7 Graph of QF crack depth against flight hours for cracks in aluminium alloy 7050-T7451 test coupons loaded with two F/A-18 usage spectra, from [15].

Table 1 Material properties of the Al7050-T7451 coupons used to generate the crack growth shown in Fig.7.

Coupon properties	UTS L MPa	UTS LT MPa	UTS ST MPa	YS L MPa	YS LT MPa	YS ST MPa	Hardness HV10	Conductivity %IACS	Plate Thickness
	532	542	510	480	480	435	181	39	144mm

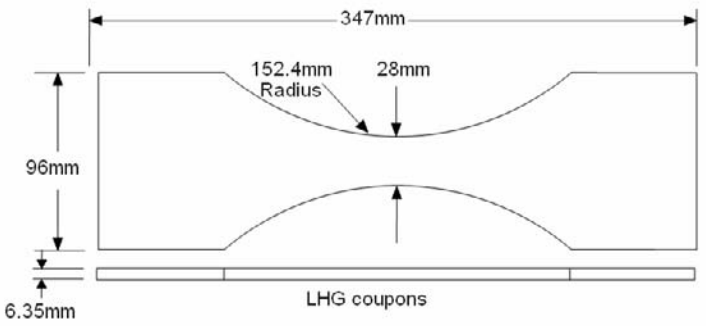

Fig. 8 Schematic of the coupons used to generate the crack growth shown in Fig.7.

In addition to the coupon results shown above, the same form of cracking (exponential) can be shown to exist in full scale structure. The crack surface shown in Fig. 2 was one of several cracks that occurred in a bulkhead from an F/A-18 aircraft that was tested to failure in the Flaw Identification through Application of Loads (FINAL) series of tests [8] after being withdrawn from service. The test article in the test rig, along with the locations of the cracks measured is shown in Fig. 9. Eight cracks were measured using QF; four from each side of the bulkhead. The CG curves are presented in Fig. 10 where exponential growth over a crack depth range from less than 0.01mm to several millimetres is evident.

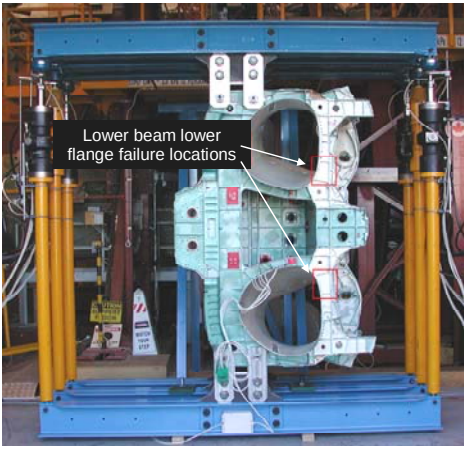

Fig. 9 An F/A-18 CB mounted in the FINAL rig. The locations where the measured cracks occurred have been highlighted in red.

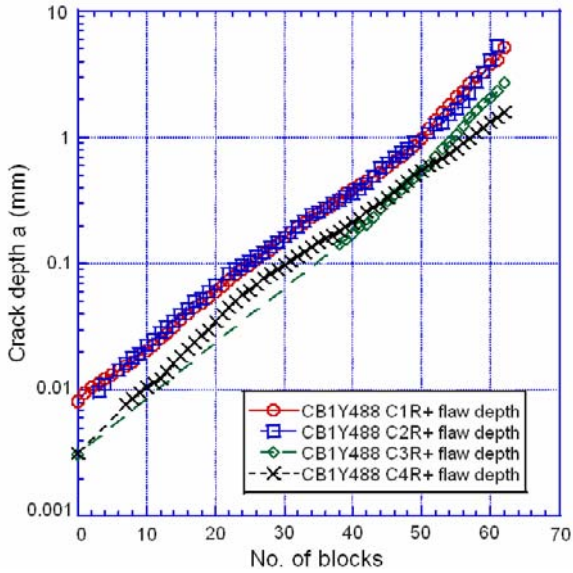

(a) First set

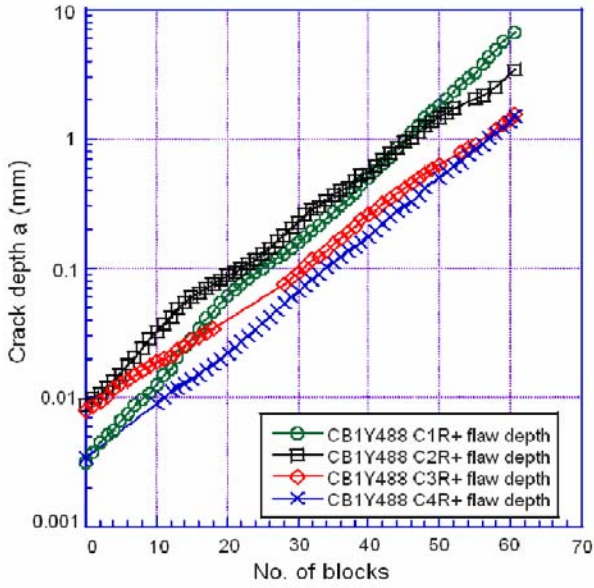

(b) Second set

Fig. 10 Crack growth curves for the four largest fatigue cracks from the failure on either side of the lower beam of an Y488 bulkhead from the F/A-18 aircraft tested in the FINAL' series of tests [8]. The curves were derived from measurement of the growth per block of mini-FALSTAFF on the fracture surface. The flaw depth includes the growth from service.

5. Crack Growth Rate for Spectra Data

Taking the CG data from the two spectra shown in Fig.7 [15], the CG rates were calculated and these are presented in Fig. 11 in the form of CG rate; d*a*/d*B* versus *a* data. Here the trend lines represent the average of all the CG rates in the tests at this single stress level. The units of d*a*/d*B* are mm's per block and the crack sizes cover the range shown in Fig.7. (For these cracks the β factor remained essentially constant.) These data show the advantage of analysing crack growth data on a block-by-block basis, since such an analysis inherently captures any spectrum sequence effects.

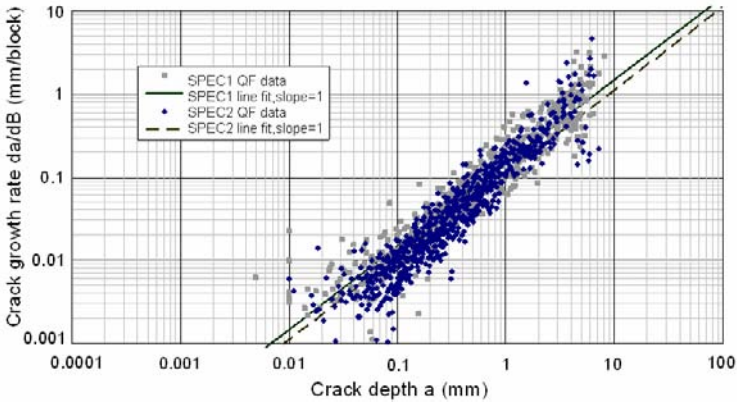

Fig. 11 Apparent growth rate versus the crack depth *a*, adapted from [15]. Some crack growth data shown in Fig.7.

Fig. 11 also shows the trend line for each spectrum and reveals a near linear relationship between d*a*/d*B* and the crack depth (a). The slope of this curve is the exponent of the power curves fitted by linear regression. This Paris-like exponent is approximately 2 for this alloy. This implies exponential growth as has been found to be the case for a wide range of other fatigue cracks [10].

Using Equation 5, Fig. 12 presents the slopes of the QF CG curves from [15] derived from the results of CG measurement of coupons tested at the four different maximum stress levels (including those presented in Fig.7), plotted against peak applied stress. It can be seen that by fitting power curves of the form $\lambda = C_1 \sigma_{max}$ where C_1 is a constant and ξ is the exponent, to these data the exponent was found to be about 3, thus suggesting that a cubic describes the crack growth variation with stress.

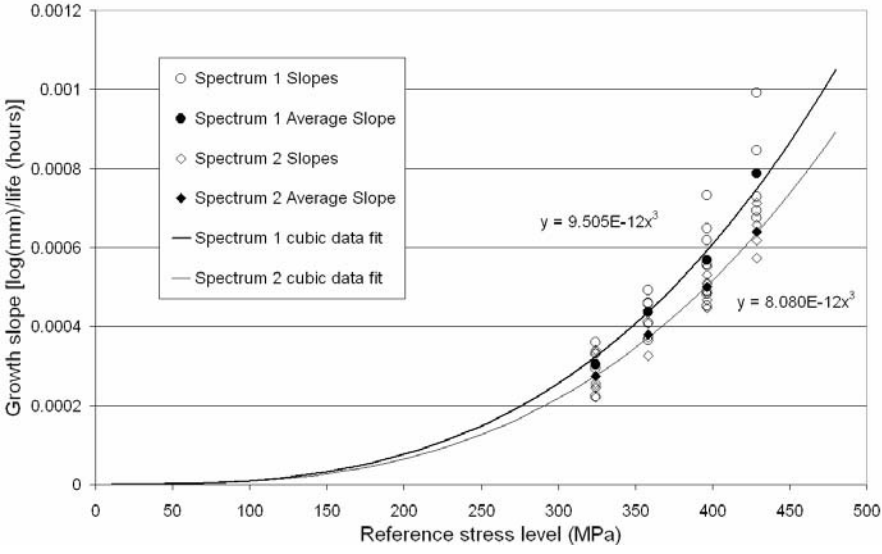

Fig. 12 Crack growth slopes versus notch stress for two spectra, from [15].

Using this cubic power relationship, as suggested by the fits of the data shown in Fig. 12, along with work presented in the literature [10],[11], it can be shown to allow prediction of growth rates at one stress level (σ_1) from those of another stress level (σ_2) given the a_0 for the new crack, the β for the original crack growth and that the loading sequence is the same:

$$a_2 = a_{2_0} e^{\left(\frac{\sigma_2}{\sigma_1}\right)^3 \psi_1 N} \tag{6}$$

To illustrate the predictive capabilities of this simple transfer function, CG data for two different stress levels taken from an F4 aircraft wing coupon test program presented in [17] is reproduced here in Crack growth curves for the 207 and 248 MPa peak loaded coupons are shown in this Figure. The growth of 248 MPa loaded crack is predicted using the data from the 207 MPa loaded crack, using Equation 5. An initial crack (a_o) size of 0.154mm was used. Other examples are given in [9]. Note that both crack growth curves are essentially exponential.

One practical outcome of this is that Equations 5 and 6 appear to provide a means for scaling the results of fatigue testing performed at one stress level to a different stress level (for the same spectrum).

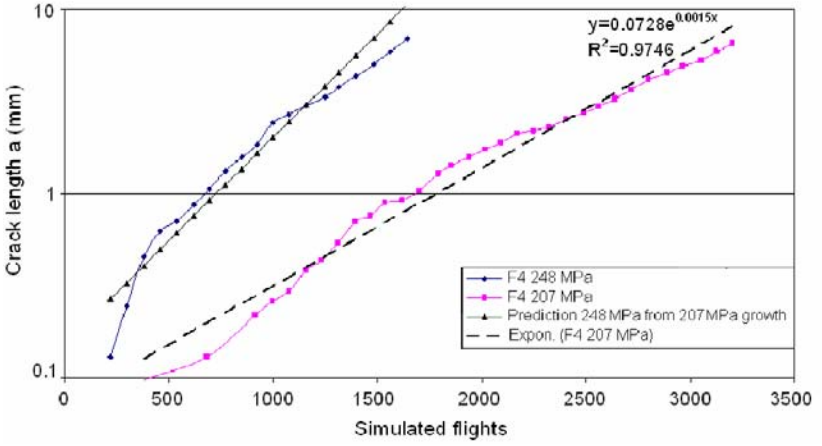

Fig. 13 Crack growth data for F4 wing, Figure 9.2.1a in [17]. A prediction of the 248 MPa crack has been made from the 207 MPa crack using 0.154mm as the a_o.

This section has demonstrated that assumption that m* in Equations 1, 2 and 3 is reasonable.

6. Modeling Crack Growth Histories

In order to demonstrate the validity and flexibility of Equation 2 a number of case studies are considered in this Section.

Case 1: Crack Growth in Centre Notched Panels

The fatigue performance of 110mm wide, 5mm thick centre notch Al7050-T736 panels under either a gust loading spectrum (MINITWIST) with an in-flight stress of 55 MPa; or manoeuvre spectrum loading (FALSTAFF) with a maximum stress of 171.3 MPa are considered. These data are drawn from Reference [18]. The measured and computed results, using Equation (3) (with d*a*/d*N* substituted by d*a*/d*Flights*) with the best fit estimates of $C^* = 1.4 \times 10^{-8}$ and $\gamma = 3$ and K_c of 40 MPa $\sqrt{m}$, for the MINITWIST spectrum are presented in Fig. 14, and the measured and computed results, using the best fit estimates of $C^* = 1.8 \times 10^{-8}$ and $m^* = 3$ and an apparent toughness K_c of 60 MPa$\sqrt{m}$ for the FALSTAFF spectrum are presented in Fig. 15. In both cases we see good agreement between the measured and the computed crack length histories.

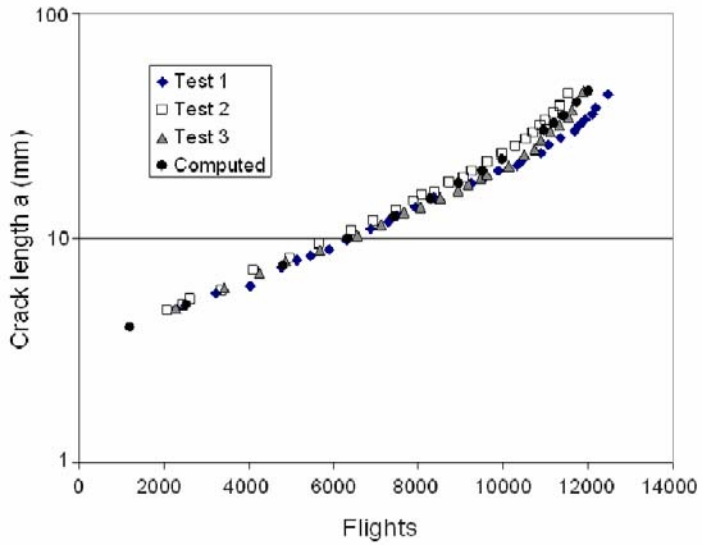

Fig. 14 Measured and computed crack growth histories under MINITWIST loading, adapted from [18].

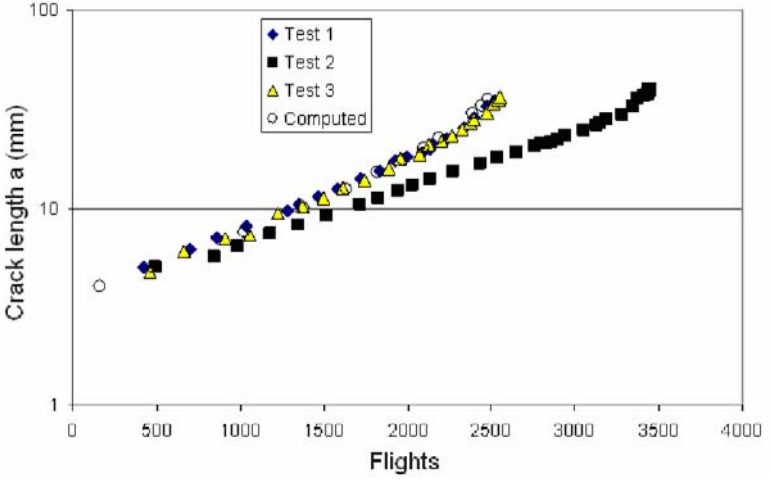

Fig. 15 Measured and computed crack growth histories under FALSTAFF loading, adapted from [18].

Case 2: Crack growth for a range of fighter aircraft spectra

The next set of data considered was chosen specifically because it had been generated for a modern aircraft design and included a full range of spectrum types likely to be experienced in the aircraft's lifetime [19]. The spectrum characteristic (from [19]) and estimated constants are presented in Table 2 and the experimental and computed (using Equation 2) data are presented in

Fig. 16(a) and (b). The material was an Al 7xxx series (not specified) and the geometry of the coupons was not specified [19]. However it can be inferred that the testing conformed to ASTM E 647 with spectrum loading applied. It can be seen that for all the spectra types considered the CG conforms reasonably well to that predicted by Equation 3 and the predictions are reasonable.

Table 2 Crack growth constants and spectrum characteristics.

Coupon (identifier)	Estimated $\tilde{C}$ x10^{13}	m*	K_c (ksi √in) (MPa √m	Estimated Max stress MPA (%DLS)	Mean R	No. of Cycles
Fuselage Bulkhead Wing Attach (FBWA)	2.9	3	103.5 (93)	293.3. (0.493)	0.014	26388
Fuselage Bulkhead Upper Cap (FBUC)	4.9	3	74.0 (68)	154.9 (0.934)	0.374	35529
Wing Spar Lower Cap (WSLC)	0.76	3	98. (90)	275.3 (0.557)	-2.431	29214
Vertical Tail Tip Rib Attach 1 (VTRA)	2.9	3	45.7 (43)	175.1 (0.54)	-2.266	28083
Vertical Tail Skin (VTS)	1.8	3	37.0 (34)	169.7 (0.876)	0.182	21896

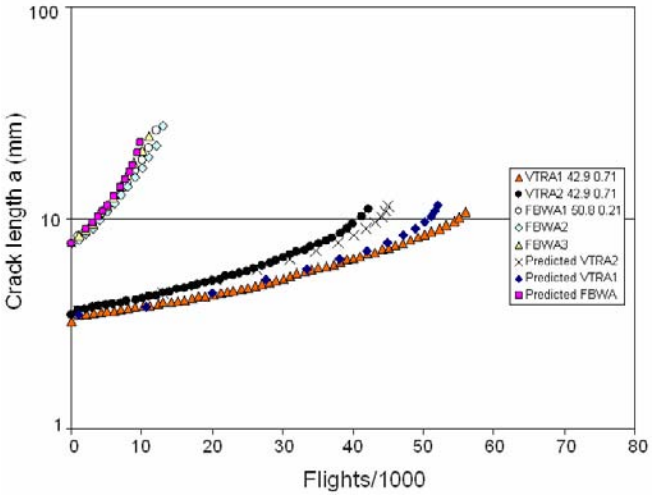

(a) Five sets measured and three sets predicted.

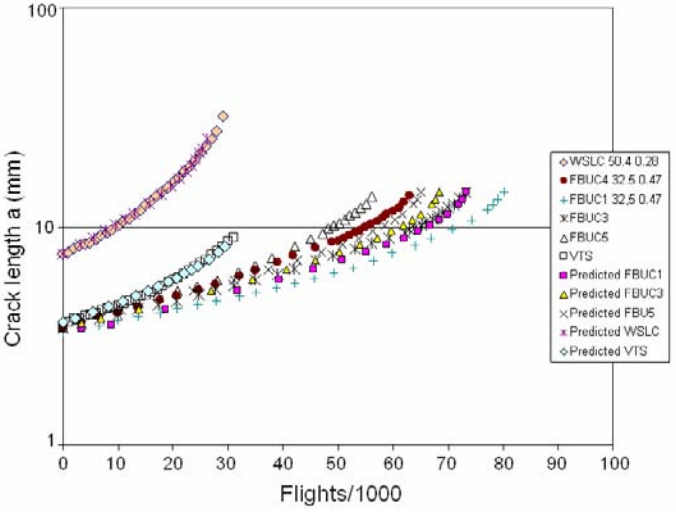

(b) Six sets measured and six sets predicted.

Fig. 16 Measured and computed crack growth for the control points

7. Discussion

It would appear that for practical applications when modelling CG histories using Equation 3 there are essentially only two constants that when determined allow simple predictions to be achieved for variable amplitude

loading cases. This can be seen from the examples presented in here. Further, the constant $m^* \approx 3$ was shown to be a good approximation for the examples given here and has been found to be applicable for a wide range of problems [9]. Consequently, since m^* may be approximated as 3 then for prediction a single parameter, $\tilde{C}$ needs to be derived from CG data or estimated by other methods. These methods, which may be used to derive $\tilde{C}$ for untested spectra are beyond the scope of this chapter and will be the subject of future work.

8. Conclusions

A three parameter crack growth model was shown to adequately model the growth of cracks under variable amplitude block loading from microns through to many millimetres in length i.e. bridging Region I through to Region III for constant amplitude data.

This is a particularly important development in structural integrity analysis where fatigue cracking cannot always be avoided and the majority of the fatigue life of nominally gross defect free structure is spent growing physically small cracks from initiating discontinuities (Region I for constant amplitude loading) up to the point of loss in acceptable strength. The model described in this chapter was based on the observation that for lead surface initiating cracks the majority of the life follows approximately exponential crack growth. The Region III, or the onset of static failure modes, was also accounted for by considering the fracture toughness of the material.

By assuming a crack growth rate that is an approximate function of the applied stress cubed then the model simplifies to only a single parameter ($\tilde{C}$) problem given that the fracture toughness of interest is known. However, methods of defining $\tilde{C}$ require further research. This model was shown to fit experimental crack growth data produced under a wide range of variable amplitude loading. By considering the crack growth data on a spectrum block-by-block approach sequence effects are inherently captured. This simple model involving only one parameter has significant advantages in the understanding and prediction of crack growth.

References

[1] Schijve J. Fatigue of structures and materials in the 20th century and the state of the art. International Journal of Fatigue 25 (2003) 679-702.

[2] El Haddad MH, Smith KN and Topper TH. Fatigue crack propagation of

short cracks. Engineering Materials and Technology, Trans. ASME, (1979) 42.
[3] Newman JC Jr. FASTRAN II - A fatigue crack growth structural analysis program, NASA TM-104159.
[4] AFGROW (2006) Version 4.11.14.0. http://www.siresearch.info/index.php
[5] Pearson S. Initiation of fatigue cracks in commercial aluminium alloys and the subsequent propagation of very short cracks. Eng. Fract. Mech., 1975: 235.
[6] Davidson DL and Lankford J. Fatigue crack growth in metals and alloys: mechanisms and mircomechanics, International Materials Reviews 37/2 (1992) 45-76.
[7] van Dijk GM and de Jonge LB. Introduction to a fighter aircraft loading standard for fatigue evaluation FALSTAFF', Proc. Eighth ICAF Symposium, Emmen, Switzerland, Swiss Federal Aircraft Establishment (FW), 3(61) (1975) 1-39.
[8] Molent L, Dixon B., Barter SA., Medved, J. & Nguyen, Q. (2005) The *FINAL* program of enhanced teardown for a fighter aircraft. proc. ICAF 2005 Hamburg, Jun 8-10, 2005.
[9] Barter S, Molent L, Goldsmith N and Jones R. An experimental evaluation of fatigue crack growth. Engng Fail Anal 12(1) (2005) 99-128.
[10] Molent L, Jones R, Barter S and Pitt S. Recent developments in crack growth assessment, J of Fatigue 28(12) (2006) 1759-1768.
[11] Frost NE and Dugdale DS. The propagation of fatigue cracks in test specimens. J Mechanics and Physics of Solids 6 (1958) 92-110.
[12] Sih GC. Handbook of Stress-Intensity Factors, Institute of Fracture and Solid Mechanics, Lehigh Univ. USA (1973).
[13] Suresh S and Ritchie RO. Propagation of short fatigue cracks. International Metals Reviews, 6 (1984) 445.
[14] Forth SC, Wright CW and Johnston WM Jr. 7075-T6 and 2024-T351 Aluminum Alloy Fatigue Crack Growth Rate Data," NASA/TM-2005-213907, 2005.
[15] Pell RA, Mazeika PJ and Molent L. The Comparison Of Complex Load Sequences Tested At Several Stress Levels By Fractographic Examination, Engineering Failure Analysis12(4) (2005)586-603.
[16] Molent L and Barter SA. A comparison of crack growth behaviour in several full-scale airframe fatigue tests, Int J Fatigue 29 (2007) 1090-1099.
[17] USAF Damage Tolerance Design Handbook. 1998. Wright Patterson AFB, USA.
[18] Wanhill RJH. Damage tolerance engineering property evaluations of aerospace aluminium alloys with emphasis on fatigue crack growth, NLR TP 94177, 1995.
[19] Ball DL and Norwood DS and TerMaath SC. Joint Strike Fighter Airframe Durability and Damage Tolerance Certification, Proceedings 47th AAIA/ASME/ASCEI Structures, Structural Dynamics, and Materials Conference, pp 1-17, 1 - 4 May 2006, Newport, Rhode Island, USA.

Fatigue Behaviour of FS, LB and MIG Welds of AA6061-T6 and AA6082-T6

P. M. G. P. Moreira*, **V. Richter-Trummer and P. M. S. T. de Castro**
Faculdade de Engenharia da Universidade do Porto
Rua Dr. Roberto Frias, 4200-465 Porto, Portugal
**Email: pmgpm@fe.up.pt*

Abstract

The increasing use of aluminium alloys in transportation industry, not only in aeronautics but also in automotive industry, creates the need for research on more efficient and reliable welding processes to be used. In order to allow the industry to use novel manufacturing techniques as Laser Beam Welding and Friction Stir Welding, which promise high efficiency, research work on S-N and crack growth fatigue data from the weld zone is required to provide tools to assess the damage tolerance. This chapter is a contribution to this effort, contrasting the fatigue behaviour of joints made using a traditional process, Metal Inert Gas welding, with those made with Friction Stir and Laser Beam Welding.

1. Introduction

Notwithstanding the widespread interest in the possibilities offered by friction stir and laser beam welding, data comparing the fatigue behavior of joints obtained using these processes is still needed. In this study the fatigue behavior of joints made using a traditional process (metal inert gas welding), was contrasted with the behavior of joints made using laser beam welding and friction stir welding.

Friction stir welding [1], a solid-state joining process developed and patented by The Welding Institute, emerged as a welding technique to be used in high strength alloys that were difficult to join with conventional techniques. The process was developed initially for aluminum alloys, but since then FSW was found suitable for joining a large number of materials. In aeronautics, for instance, riveting is the preferred manufacturing process for aircraft fuselage structures; nevertheless, FSW is emerging as an appropriate alternative technology due to low distortion, high strength of the joint and high processing speeds.

Conventional fusion welding of aluminum alloys produces a weld prone to defects such as porosity, consequence of entrapped hydrogen gas not being able to escape from the weld pool during solidification. An example of

G.C. Sih (ed.), Multiscale Fatigue Crack Initiation and Propagation of Engineering Materials: Structural Integrity and Microstructural Worthiness, 85–111.

a fusion process is the Gas Metal Arc Welding (GMAW) process, MIG (Metal Inert Gas) welding process [2]. In the MIG welding process the arc and the weld are protected from atmospheric contamination by a gas shield, and an electric potential is established between the electrode and the workpiece causing a current flow, which generates thermal energy in the partially ionized inert gas [3].

The Laser Beam Welding (LBW) process is also a thermal effecting melting process which causes metallurgical changes in the weld metal as well as in the heat affected area beside the weld seam. Effects such as oxidation reactions are comparable to other thermal treatments in the case of aluminum; but because of the short cycle time oxidation of the weld seam is very low [4].

Because of the large temperature interval between melting and solidification in the heat affected zone the material is partially molten in the solid aluminum matrix. In the transition area between the weld seam and heat effected zone small defects (solidification cracks and pores) occur during the solidification process. Because of their size there is no special negative influence on the mechanical properties. The thermal influence on the material structure beside the weld seam itself is very small. Welding an alloy which does not require additional wire because of metallurgical effects shows that there is no change in chemical composition compared to the base material. The main reasons for this feature are: the high welding speed; the short cycle time of the melting and solidification process; the deep penetration effect of the keyhole with a very large ratio of depth to width; and the turbulent melt pool dynamic.

In Friction Stir Welding (FSW) the interaction of a non consumable and rotating tool with the workpieces being welded creates a welded joint trough frictional heating and plastic deformation at temperatures below the melting temperature of the alloys being joined.

Studied is the fatigue behavior of friction stir and laser beam butt welds of two 3*mm* thickness age hardenable aluminum, 6082-T6 and 6061-T6 alloys, is presented. For the case of the laser beam welds the aluminum 6061-T6 was the only material tested. For comparison, MIG butt welds of the same alloys were also performed and tested. Tensile tests and microhardness measurements of weld joints and base materials were performed in order to determine the influence of each welding process in the mechanical properties. The fatigue behavior (S-N curves) of specimens of all welding process was analyzed. Microstructure was examined and correlated with the macroscopic mechanical behavior. Scanning electron microscopy was carried out and the fractographic features of friction stir welds and MIG welds compared.

2. Material and Welding Processes

The alloys 6082-T6 and 6061-T6 are high strength Al–Mg–Si alloys that contain manganese to increase ductility and toughness. The alloy was solution heat treated at ≈540°C, followed by quenching to room temperature which leads to a supersaturated solution. If the material is stored at room temperature natural ageing takes place (T4 condition). The T6 condition is obtained through artificial ageing at a temperature of approximately 180°C [5].

The MIG welding parameters used were: 128*A*, 17.1*V*, 700*mm/min* and Argon at a 20*l/min* flow rate. A filler wire AWS ER5356 (with the designation ESAB OK Autrod 18.15) with a diameter of 1*mm* [6] was used. Welds were performed using an automated welding robot, GMF ROBOTICS – Arc Mat Sr.

The laser beam welds were performed using a ABB IRB6600 robot in conjunction with a Nd:YAG laser, with a power source of 4*kW*. The following parameters were used in tests: welding speed 50*mm/seg*; focal distance 200*mm*; 40*l/min* He flow; gap between plates 0.2*mm*; filler wire of 1.2*mm* diameter with a feeding speed of 5.5*m/min* ER4043.

The friction stir welds were performed in a prototype machine with a capability of 6*m* weld length developed to be used in a Portuguese shipyard. For both aluminum alloys were used the same parameters: welding speed of 800*mm/min*; pitch angle of 2º; rotating speed of 1500*rpm*. The FSW process of the aluminum 6082-T6 was performed using a tool with a 6*mm* diameter threaded pin and the shoulder had 15*mm* diameter. For the aluminum 6061-T6 a tool with a 4*mm* diameter threaded pin and a shoulder of 10*mm* diameter were used. Since the optimal welding speed depends on several factors: alloy type, penetration depth and joint type being the most important these parameters were chosen by trial and error attempts until no visually detected defects could be identified. The penetration depth was adapted to fully penetrated butt joint in a material of 3*mm* thickness.

3. Tensile Tests

Tensile tests were performed to determine the mechanical properties of the welded and un-welded material (yield stress σ_{yield}, rupture stress σ_{upt} and Young modulus E). The average values of σ_{yield}, σ_{rupt} and E of tests performed in base material specimens of both aluminum 6082-T6 and aluminum 6061-T6 alloy are presented in Table 1. The aluminum 6061-T6 has an ultimate tensile stress about 6% higher than the aluminum 6082-T6. All base material (BM) specimens failed in the same manner, 45º shear plane.

The average values of σ_{yield}, σ_{rupt} and E of tests performed in base material specimens of both aluminum 6082-T6 and aluminum 6061-T6 alloy welded by MIG, LBW and FSW technique are also presented in Table 1. Since the rupture stress of the MIG welded specimens is lower than the yield stress of the parent material the elongation measured in the fractured surface will only reflect the measurement of the material affected by the welding process. This resulted in lower values of elongation when compared with the base material.

Table 1 Material properties obtained in tensile tests.

Specimen type	Material	σ_{yield} [MPa]	σ_{rupt} [MPa]	E [GPa]	Elongation [%]
Base material	6082-T6	276.2	322.9	67.1	17.5
	6061-T6	306.3	342.0	68.5	17.1
MIG	6082-T6	176.8	210.0	-	4.0
	6061-T6	156.3	221.2	-	4.2
FS welded	6082-T6	140.5	226.1	-	5.5
	6061-T6	158.7	241.5	-	4.0
LB welded	6061-T6	171.0	265.4	-	3.7

It was found that the friction stir welded specimens have lower yield stress values than MIG specimens but higher values of the rupture stress. Also the elongation of the friction stir welded specimens presented higher values.

For the case of MIG welded specimens rupture occurred outside the welding seam in the HAZ (heat affected zone) as presented in Figure 1. Similar observations are presented by Ericsson *et al.* [5] where a 45º fractured surface was also found. The aluminum 6082-T6 MIG welded specimens present a yield stress and a rupture stress of 65% of the base material. The yield stress obtained in this work is 20% higher than the results presented by [5]. The aluminum 6061-T6 MIG welded specimens has a yield stress of 51% of the base material and a rupture stress of 65% of the base material. Comparing MIG weldments of both alloys it was found that the yield stress of the 6082-T6 is higher but the rupture stress is higher for the 6061-T6 MIG welded specimens.

Fig. 1 Fracture surface of a MIG welded specimen of AA6061-T6.

In the case of the 6082-T6 friction stir welded specimens fracture occurred near the weld edge, Figure 2, where a decrease of hardness occurs [7]. The fracture surface presents a 45º angle, as presented by Svensson *et al.* [8]. In the case of the aluminum 6061-T6 the fracture started at the weld root indicating that a lack of penetration occurred during welding (root flaw). Since the fracture surface occurred at the weld middle line it is possible to identify the different layers of material that were formed by each rotation of the welding tool. Dickerson *et al.* [9] suggested that root flaws up to 0.35*mm* deep do not cause degradation in mechanical performance when compared to flaw-free welds. The elongation of all friction stir welded specimens (4% to 5%) is approximately 25% of the base material (17%).

Fig. 2 Crack path of AA6082-T6 FS welded specimen.

The aluminum 6082-T6 friction stir welded specimens present a yield stress of 51% and a rupture stress of 70% of the base material. Scialpi *et al.* [7] obtained also a relation of rupture stress of 76% between the base material and friction stir welded specimens. Values of the same magnitude are also reported by Ericsson [5], Harris [10], and Nicholas [11] in their literature reviews.

The aluminum 6061-T6 friction stir welded specimens have a yield stress of 52% and a rupture stress of 71% of the base material. Hong *et al.* [12] performed friction stir weld of 4*mm* thick aluminum 6061-T651 plates

and found lower values for the yield stress and rupture stress when compared with those obtained in this study.

From all type of welded specimens, laser beam welded specimens present the higher yield and rupture stress. The aluminum 6061-T6 laser beam welded specimens have a yield stress of 56% and a rupture stress of 78% of the base material. These results are higher than the ones presented in [4, 13]. Nevertheless, the elongation presents the lowest values. In the 6061-T6 laser beam welds fracture occurred near the weld bead edge with a 45º angle, Figure 3.

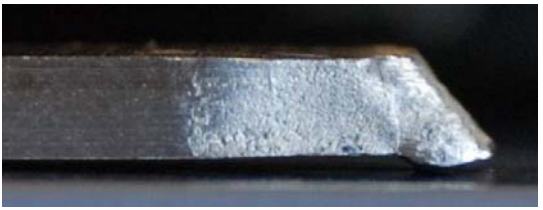

Fig. 3 LB weld crack orientation.

4. Microhardness Profiles

The hardness profiles can assist in the interpretation of the weld microstructure and mechanical properties. Microhardness tests were performed to characterize the Vickers hardness profile in the vicinity of the weld area. Measurements were performed at the specimens' middle thickness using a 100*gf* load. Figure 4 illustrates the hardness profiles of the MIG welded aluminum 6061-T6 and 6082-T6 specimens. The major softened areas are the weld centre line, and the two transitions zones just at the limit of the HAZ. In these areas the hardness reaches a minimum value near 50*HV* and the base material has values over 90*HV*. Minimum average values are found in the aluminum 6082-T6 specimen.

In the friction stir welded aluminum 6082-T6 and 6061-T6 a hardness decrease is identified in the TMAZ (thermo-mechanically affected zone). The average hardness of the nugget zone was found to be significantly lower than the hardness of the base alloy. There is a zone outside the nugget zone which has the lower hardness value. The welding process softened the material reducing the hardness to 33% of the parent material, as shown in [7]. The hardness minimum values are obtained in the welding retreating side, *e.g.* [8]. As it also suggested in [10] the variation of the microhardness values in the welded area and parent material is due to the difference between the microstructure of the base alloy and weld zone. A di-

rect comparison of measurements of both friction stir welded alloys is presented in Figure 5.

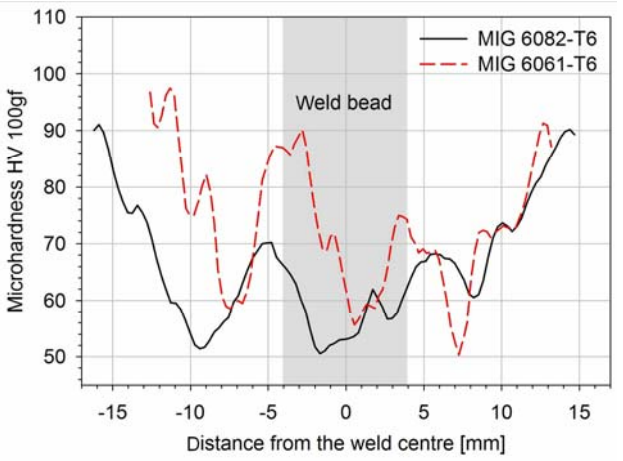

Fig. 4 Microhardness profiles of the MIG welded 6061-T6 and 6082-T6 specimens.

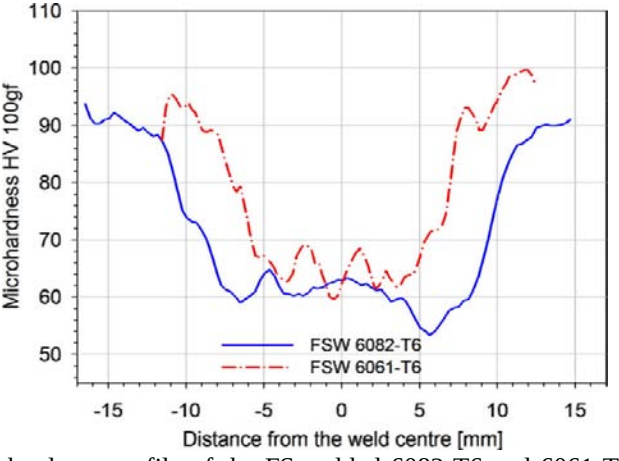

Fig. 5 Microhardness profile of the FS welded 6082-T6 and 6061-T6 (6082-T6: 6*mm* diameter pin, shoulder 15*mm*; 6061-T6: 4*mm* diameter pin, shoulder 10*mm*).

As described in the literature in alloys such as 6082 and 6061 the main strengthening precipitate is β″-Mg5Si6 which is stable at temperatures < 200°C [14]. This precipitate exists in the unaffected base material but is absent in the nugget and in the HAZ. In the friction stir weld temperatures are expected to be over 200-250°C, during heating, the β″ is easily dissolved [8]. This β″ precipitate is the mainly responsible for hardening. It

was reported [8] that no other fine scale precipitation was found in the nugget, while in the HAZ precipitation of β'-Mg1,7Si occurred on the Al–Mn–Si dispersoids. On cooling, precipitation of β′ is favorable to β″, and since the β′ precipitates have less of a strengthening effect compared to β″, a lower hardness is obtained. The β' will act as a nucleation sites for the precipitates. Following the diagram of continuous cooling precipitation (CCP) presented in 14], in the HAZ where temperatures are near or less than 300ºC the precipitation of β' is very high, it occurs the transition from β'' to β' by dissolution. In the weld nugget, where the temperature is expected to be higher and so the MgSi precipitates go into solution. On cooling, the time for precipitation is limited, and so only a small volume fraction of the β′ precipitates form in the weld nugget. The nugget hardness recovery is due to recrystallization of a very fine grain structure.

The microhardness profile, at mid thickness, of the aluminum 6061-T6 laser beam weld is presented in Figure 6. The minimum hardness value found was obtained inside the weld bead, near its limit, and has a value of approximately 60*HV*. The bead limit presented a width of 2.5*mm* and the HAZ, which corresponds to hardness values lower than the base material, has a width of approximately 4.5*mm* from each side of the bead limit.

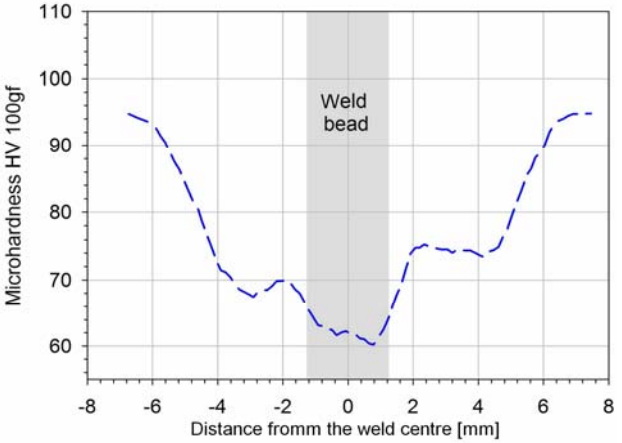

Fig. 6 Microhardness profile of the LB welded AA6061-T6.

As presented in Figure 7, when compared with the friction stir welds and MIG welds, the laser beam welds presented the smaller area (width) affected by the welding process, approximately 12*mm*. For the friction stir welds the width of the welding affected area was approximately 15*mm*, and in the MIG welding process 24*mm*.

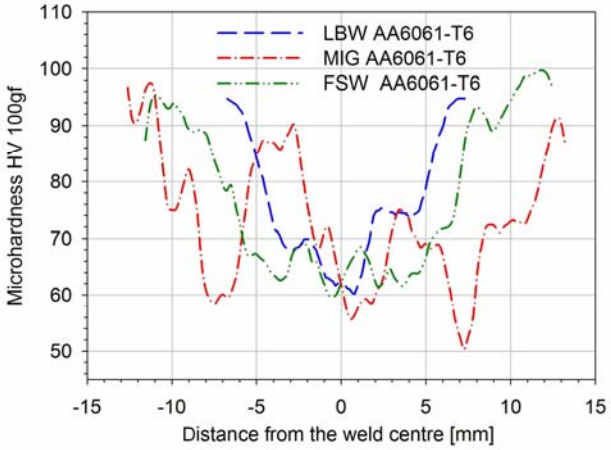

Fig. 7 Microhardness profile of the LB, MIG and FS welded AA6061-T6.

5. S-N Fatigue Data

Fatigue tests were carried out in a servo-hydraulic MTS testing machine and specimens' dimensions were chosen according to the ASTM standard E466 [15]. The weld was perpendicular to the load direction in the S-N tests and to the material rolling direction. The maximum stress levels used were selected as a function of the yield stress for each type of joint. Values of 120% to 40% of the yield stress were chosen. A stress ratio of R=0.1 was used and the frequency was in the interval of 7–26*Hz* depending upon the stress level. Life was defined as the number of cycles to failure and the number of cycles considered as a threshold for infinite life was 10^7 cycles. An extensive program was performed analyzing all type of specimens of aluminum 6082-T6 and 6061-T6: base material specimens, MIG specimens, friction stir welded specimens and laser beam welded specimens (of aluminum 6061-T6 only). All specimens were tested in the as-welded configuration.

For the MIG welding specimens the geometrical detail of the transition from the weld seam to the plate surface of the base material can be interpreted as a geometrical defect that enhances the initiation of a first crack. For the MIG weld specimens fracture occurred in the HAZ near the notch created during the deposition of filler material (Figure 8). Figure 9 presents examples of the fracture surface of MIG specimens.

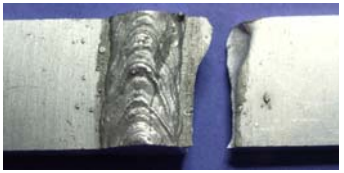

(a) Fracture weld after fatigue

(b) Side view

Fig. 8 Fracture location of MIG specimens AA6082.

(a) AA6082-T6 MIG specimen with fracture surface

(b) AA6061-T6 MIG specimen with fracture surface

Fig. 9 Fracture surface for the fatigue tested MIG specimens.

Some MIG welded specimens presented defects due to the welding process. Due to the fusion nature of this process, during the welding the materials entrapped pores appear which influences the specimen mechanical behavior. An example of this phenomenon is identified in the fractograph presented in Figure 10. This fractograph corresponds to a MIG welded 6061-T6 specimens tested at 75% of its yield stress and had a fatigue life of 16492 cycles (six times lower than the average fatigue life for this remote load). Results for the fatigue tests are presented in Figure 11.

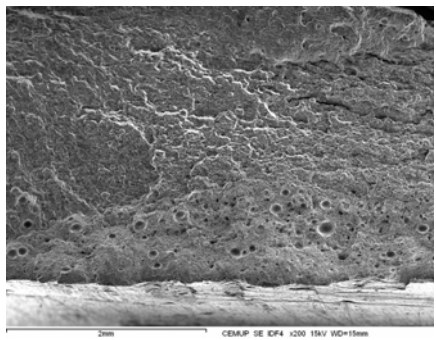

Fig. 10 Fractograph of a MIG welding specimen containing entrapped pores.

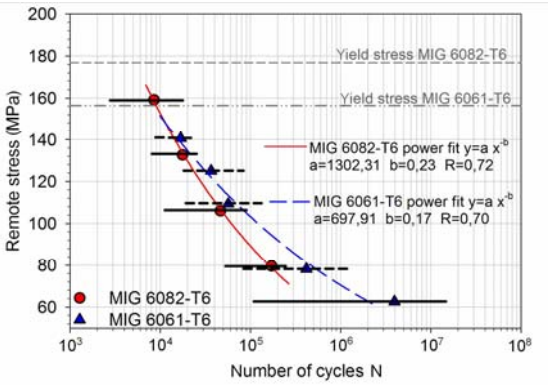

Fig. 11 S-N fatigue data of the MIG welded specimens.

Data was fitted using a power equation and some fatigue scatter was found in the as-welded MIG specimens. The 6061-T6 MIG welded specimens presented higher fatigue lives than the MIG 6082-T6 specimens.

Friction stir welded specimens of both base materials were fatigue tested. The fracture location of the frictions stir welded specimens is shown in Figure 12. In the friction stir welded aluminum 6082-T6 specimens fracture propagated at the centre of the weld and in the aluminum 6061-T6 near the shoulder limit. These fracture locations were also identified in the tensile tests. Figure 13 presents examples of the fracture surface for all types of friction stir welded specimens where a more irregular surface is identified in the aluminum 6082-T6.

(a) AA6082-T6 FS welded fatigue tested specimen, fracture location

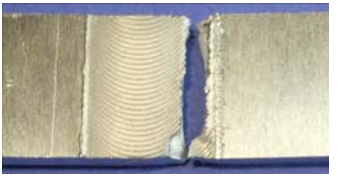

(b) AA6061-T6 FS welded fatigue tested specimen, fracture location

Fig. 12 Fracture location of FS welded specimens.

(a) AA6082-T6 FS welded specimen

(b)AA6061-T6FSwelded specimen

Fig. 13 Fracture surface for the fatigue tested FS welded specimens.

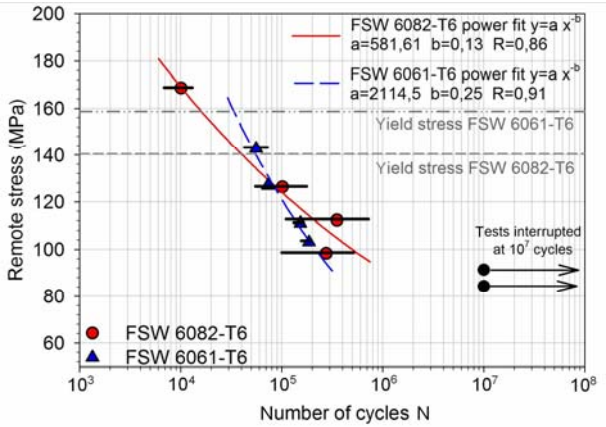

Fig. 14 S-N fatigue data of the FS welded specimens.

Results of fatigue life obtained for the friction stir welded specimens are presented in Figure 14.

In tests of friction stir welded specimens, data shows a narrow scatter and was fitted using a power equation. For the friction stir welded 6082-T6 it was found that for 65% and 60% of the yield stress the fatigue life is considered infinite. In friction stir welded specimens fatigue cracks have propagated at the centre of the weld, as verified in [8] when studying friction stir welded 5*mm* and 10*mm* thick 6082-T6 specimens. Also, Ericsson *et al.* [5] in their study on the fatigue life assessment of the same alloy obtained a fatigue life of 5×10^5 cycles to failure with a stress range of about 90*MPa*, at a stress ratio, R=0.5. In the present study, the fatigue life of 5×10^5 cycles is obtained at a stress range of 105*MPa*. The friction stir welded 6061-T6 specimens presented lower lives than the friction stir 6082-T6 specimens when tested at stresses lower than 130*MPa*. For the friction stir welded 6061-T6 specimens' cracks have propagated near the limit of the tool shoulder.

Laser beam welded specimens of aluminum 6061-T6 were fatigue tested. The laser beam welds were carried out using additional wire and there was a seam overfill of approximately 1*mm* at the top of the weld seam. The fracture location of the laser beam welded specimens occurred at the end of the overfill. Results of fatigue life obtained for the friction stir welded specimens are presented in Figure 15.

Results of fatigue tests obtained in this study are significantly higher than the ones presented on [4]. When compared to its base material, there is a decrease of approximately 60% of the fatigue strength. The reasons for this decrease in the properties are the reduced strength capabilities in the

weld metal and heat affected zone, and also a strong influence of geometrical discontinuities (especially in fatigue).

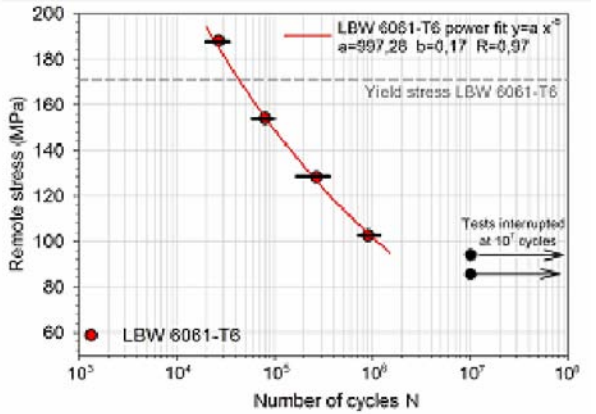

Fig. 15 S-N fatigue data of the LB welded AA6061-T6 specimens.

Base materials specimens were also fatigue tested at stresses between 90% and 65% of their yield stress. A comparison between the data from the base materials tests and all welded specimens is presented in Figure 16. The base materials specimens presented much higher fatigue live than any type of welded specimens, being the aluminum 6061-T6 the one that performed better.

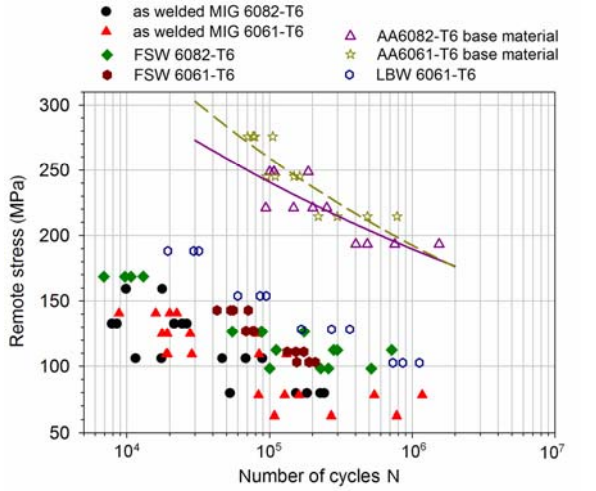

Fig. 16 S-N data of base material and welded specimens.

6.1 MIG welded specimens

6.1.1 MIG welded AA6082-T6

The macrostructure of the aluminum 6082-T6 MIG weld is presented in Figure 17. The identification of the two weld beads is straightforward, and the transition between the HAZ and base material is also identified. Examples of microstructures are shown in Figure 18.

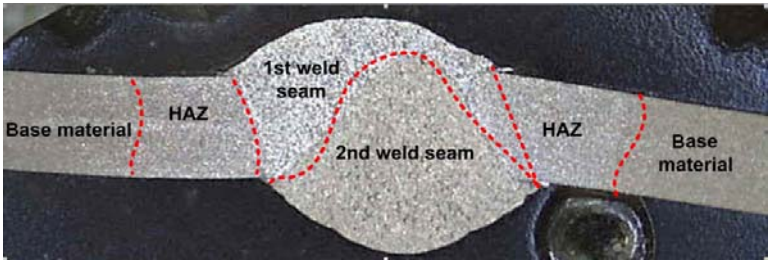

Fig. 17 Macrostructure of the MIG welded AA6082-T6.

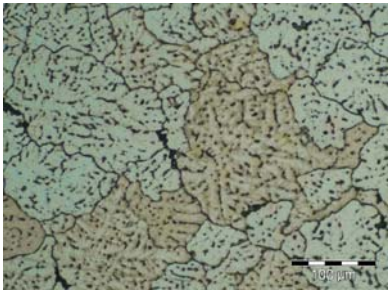

(a) Microstructure 1, weld

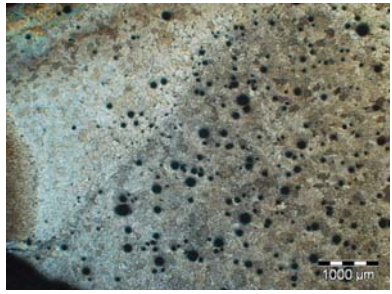

(b) Microstructure 2, weld

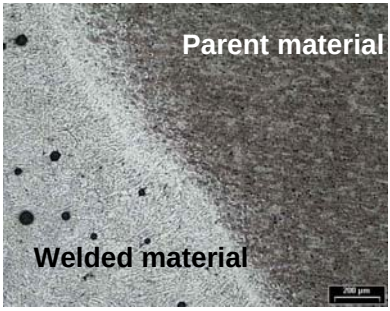

(c) Microstructure 3, weld

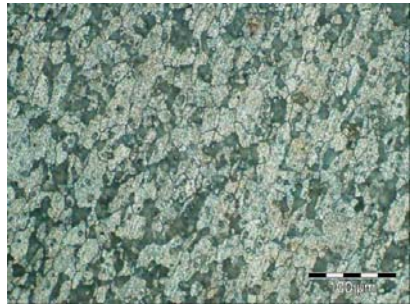

(d) Microstructure 4, base material

Fig. 18 MIG welded AA6082-T6 microstructures.

Microstructure 1 shows the structure in the centre of the weld. Micropores with a diameter no larger than 100μm, dispersed in the matrix are identified in microstructures 2 and 3. These pores are due to the fusion nature of the MIG welding technique. The transition between the material that suffered fusion to the material only affected by the heat generated during welding is shown in microstructure 2. A structure of larger grains is identified in the left side of microstructure 3 which corresponds to material that suffered fusion. The HAZ material has a structure similar to the base material, fine grains with dispersed precipitates. Microstructure 4 shows the base material.

6.1.2 MIG welded AA6061-T6

The macrostructure of the aluminum 6061-T6 MIG weld is presented in Figure 19. Also, the identification of the two weld beads is straightforward, and the transition between the HAZ and base material is also identified. Examples of microstructures are shown in Figure 20.

In microstructures 1 and 2, solidification structure, centre of the weld are identified micropores with approximately a maximum of 100μm of diameter disperse in the matrix. In microstructure 3 is identified the transition between the material that suffered fusion (right side) to the material only affected by the heat generated during welding (left side). In the virtual line that defines the transition between the HAZ material and the fused material it is possible to identify a structure containing grains formed due recrystallization. Microstructure 4 shows the base material matrix where grains of approximately 80μm and some precipitates are present.

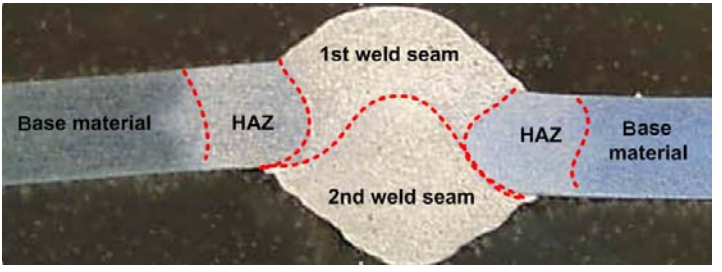

Fig. 19 Macrostructure of the MIG welded AA6061-T6.

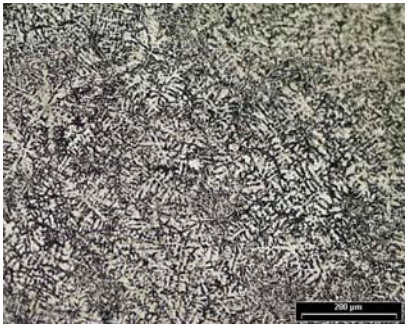

(a) Microstructure 1, weld

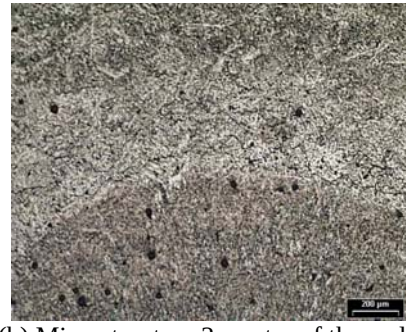

(b) Microstructure 2, centre of the weld

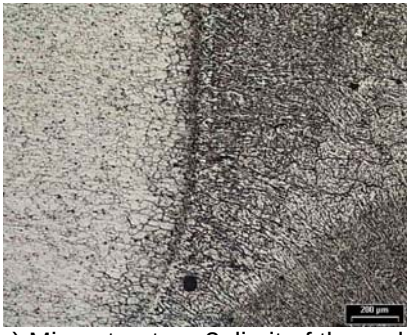

(c) Microstructure 3, limit of the weld bead

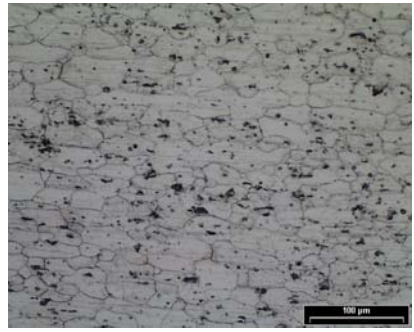

(d) Microstructure 4, base material

Fig. 20 MIG welded AA6061-T6 microstructures.

6.2 LBW welded specimens

The macrostructure of the aluminum 6061-T6 LB weld is presented in Figure 21. The identification of the weld bead is straightforward, and the transition between the HAZ and base material is also identified. Examples of microstructures are shown in Figure 22.

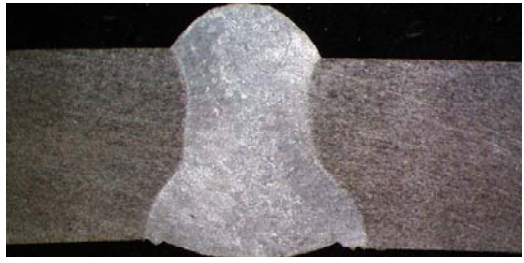

Fig. 21 Macrostructure of the LBW welded AA6061-T6.

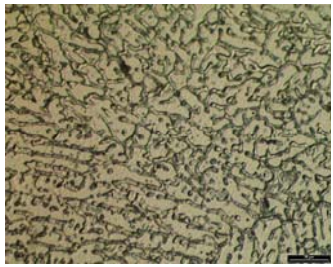

(a) Microstructure 2,centre of the weld detail

(b) Microstructure 3,limit of the weld bead

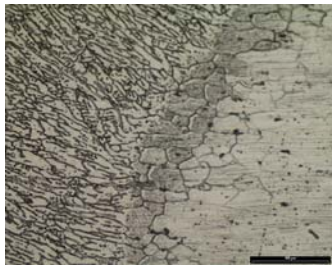

(c) Microstructure 4, limit of the weld bead detail

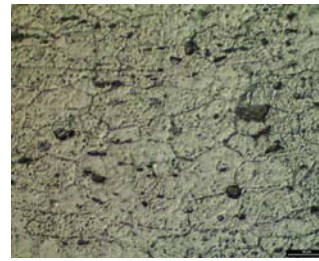

(d) Microstructure 5, HAZ

Fig. 22 LBW welded AA6061-T6 microstructures.

The microstructural analysis revealed a structure similar to the one found for MIG welding, but since the heat was very localized the area that experienced microstructural changes is much smaller in LBW. In microstructures 1 and 2, solidification structure, centre of the weld is almost absent of pores. In microstructure 3 is identified the transition between the material that suffered fusion to the material only affected by the heat generated during welding (HAZ). Microstructure 5 shows grain structure in the HAZ.

6.3 FSW specimens

6.3.1 FS welded AA6082-T6 specimens

In Figure 23 the macrostructure of the friction stir weld of the aluminum 6082-T6 alloy is presented. At the centre is possible to identify the weld nugget (NZ) with its typical shape of onion rings. The weld nugget experiences high strain and is prone to recrystallization. Immediately at its side is the TMAZ which ends at the tool shoulder delimited by the dashed lines. After the TMAZ appears a zone affected only by the heat generated during the welding process, *e.g.* [7, 17]. Friction stir welding gives rise to microstructure changes.

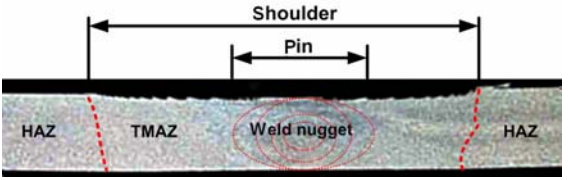

Fig. 23 Macrostructure of the FS welded AA6082-T6.

Microstructures obtained in the different locations are shown in Figure 24. Friction stir welding gives rise to microstructure changes. As observed in [8] the base material contains two sizes of grains owing to partial recrystallization. The recrystallized grains are approximately $20\mu m$ in size while the non-recrystallized grains can be larger than $100\,\mu m$. Microstructure 3, structure at the weld nugget, shows dynamic recrystallized grains much smaller and equiaxed when compared to the elongated base metal microstructure. The grain evolution between the base material and the welded affected material is evident comparing microstructures 3 and 4. The grains in the nugget zone are equiaxed [8]. In the HAZ the grain size is similar to the base metal. Second-phase particles in the workpiece are essentially stirred into the weld zone. Similar observations are presented in [7]. The dynamic continuous recrystallization microstructure which characterizes the friction stir welding process of this alloy is well documented in [18].

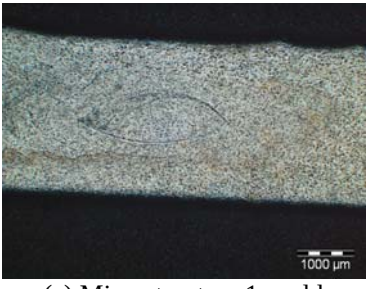

(a) Microstructure 1, weld

(b) Microstructure 2, weld

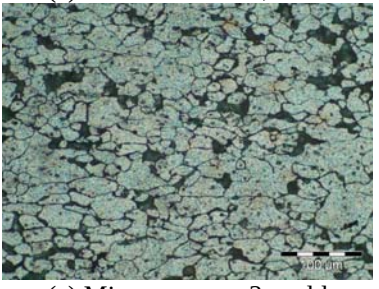

(c) Microstructure 3, weld

(d) Microstructure 4, BM

Fig. 24 FS welded AA6082-T6 microstructures.

6.3.2 FS welded AA6061-T6 specimens

In Figure 25 the macrostructure of the friction stir weld of the aluminum 6061-T6 alloy is presented. At the centre is possible to identify the weld nugget. The thermo-mechanically affected zone ends at the tool shoulder delimited by the dashed red lines. After the thermo-mechanically affected zone appears the heat affected zone. In this weld sample, particularly at the advancing side, a high penetration of the shoulder is identified creating a small notch effect that could affect mainly the fatigue lives.

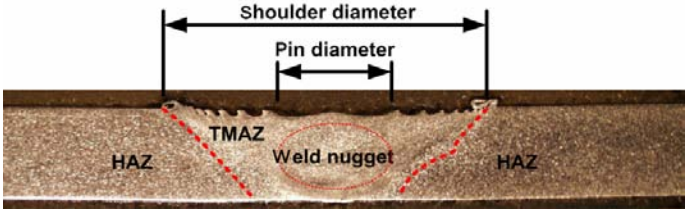

Fig. 25 Mcrostructure of the FS welded AA6061-T6.

For the case of the friction stir welded aluminum 6061-T6 the micro-structures obtained in the different locations are shown in Figure 26.

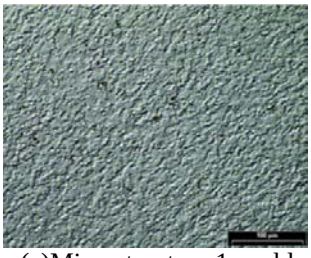

(a)Microstructure 1, weld nugget

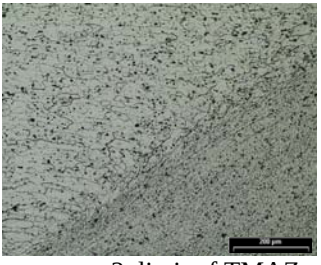

(b) Microstructe 2, limit of TMAZ to HAZ

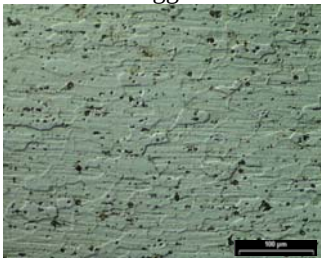

(c) Microstructure 3, base material

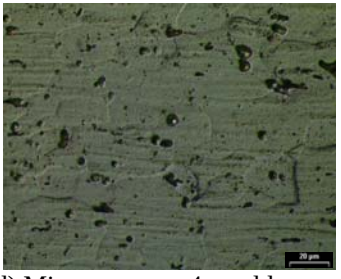

(d) Microstructure 4 , weld nugget

Fig. 26 FS welded AA6061-T6.

In the welded zone grain shape and dimensions evolution is quite evident. In the heat affected zone the grain size is similar to the base metal. Second-phase particles in the workpiece are essentially stirred into the weld zone. Similar observations are presented in [7]. The dynamic continuous recrystallization microstructure which characterizes the friction stir welding process of this alloy is well documented by Liu *et al.* [18]. As in the aluminum 6082-T6, the grains in the nugget zone have an approximate equiaxed shape and a large difference between the base material and the nugget zone is easily identified as already shown by Liu *et al.* [18].

7. SEM Analysis

Fractured fatigue test specimens were analyzed by SEM. Measurements were performed considering the crack initiation site as the origin and measurements were obtained through the crack length. The result in a coordinate is the average of four measurements of the number of striations in a perpendicular line to their orientation.

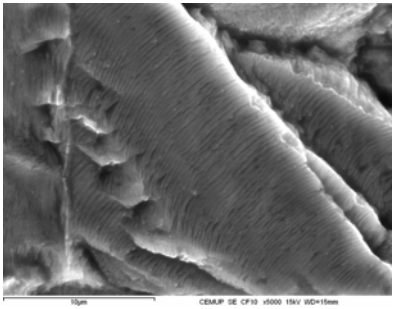

(a) AA6082-T6 fractograph 4, crack length of 0.503mm

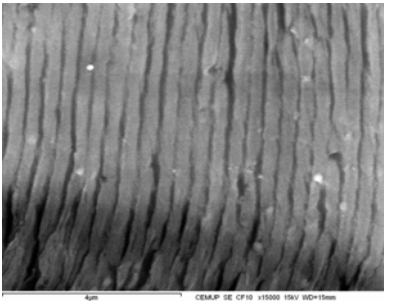

(b) AA6082-T6 fractograph 18 crack length of 3.763mm

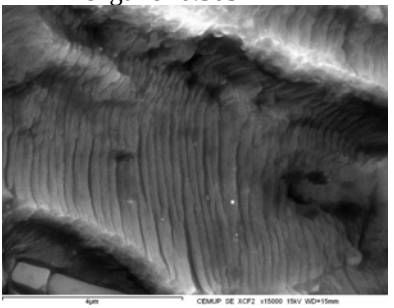

(c) AA6061-T6 fractograph 6, crack length of 0.377mm

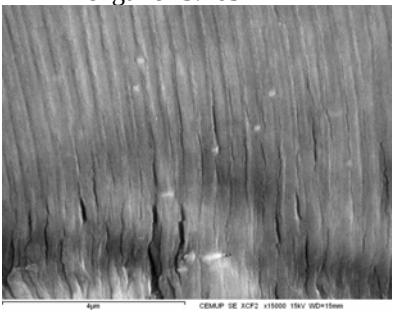

(d) AA6061-T6 fractograph 19, crack length of 3.401mm

Fig. 27 Fatigue striations for different crack lengths.

7.1 Base material striations spacing

A fatigue test specimen of aluminum 6082-T6 and another of aluminum 6061-T6 subjected to fatigue tests with a maximum stress of 70% of the yield stress (193.3*MPa* for the aluminum 6082-T6 and 214,4*MPa* for the aluminum 6061-T6) and R=0,1 were analyzed. The 6082-T6 base material specimen analyzed had a fatigue life of 485858 cycles and the 6061-T6 a fatigue life of 783586 cycles.

For the aluminum 6082-T6 the fatigue area has 12.6mm^2 and a crack length of 4.38*mm*. For the aluminum 6061-T6 the fatigue area has 13.4mm^2 and a crack length of 4.60*mm*. Figure 27 shows fatigue striations at different crack lengths. The striation spacing *vs.* crack length for such specimens is presented in [19], where some of the data concerning MIG and FSW joints is also presented.

7.2 MIG welded specimens, striations spacing

Two MIG butt welded specimens in the as-welded configuration were analyzed after fatigue testing (R=0.1). The specimen of aluminum 6082-T6 was fatigue tested at a maximum stress of 60% of the yield stress (106.1*MPa*), and the specimen of aluminum 6061-T6 was tested at a maximum stress of 70% of the yield stress (109.4*MPa*). The aluminum 6082-T6 specimen presented a fatigue life of 46645 cycles and the 6061-T6 specimen had a fatigue life of 28476 cycles. In the MIG welded specimens fatigue cracks appeared at the end of the weld seam, near the V notch effect due to the extra material deposited by the melted feed wire.

For the aluminum 6082-T6 the fatigue area has 24.8mm^2 and a crack length of 12.56*mm*. For the aluminum 6061-T6 the fatigue area has 22.4mm^2 and a crack length of 12.50*mm*.

In the aluminum 6082-T6 MIG welded specimen the striations identification process was very hard to carry out. The fatigue crack surface presented a heterogenic structure with different structures randomly dispersed. Figure 28 shows SEM images of fatigue striations at two crack lengths for the aluminum 6082-T6 MIG welded specimen. For example in fractograph 9, presented in Figure 28, besides the larger striations at the top of the fractograph a finer type of striations are identified. This leads induces that the coarser striations are of a second order that contain several finer striations.

Figure 29 shows SEM images of fatigue striations at two crack lengths for the aluminum 6061-T6 MIG welded specimen.

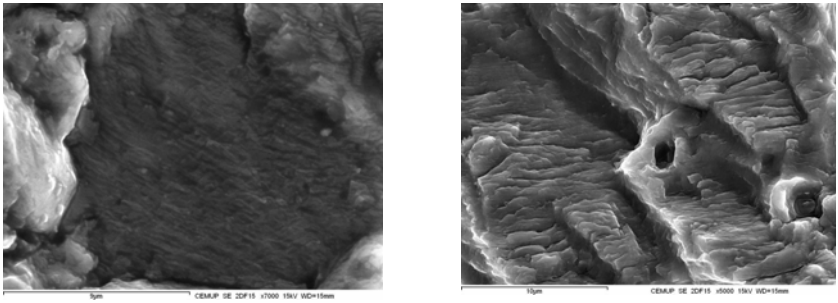

(a) Fractograph 4, crack length of 0.361mm

(b) Fractograph 9 crack length of 2.582mm

Fig. 28 Fatigue striations for two crack lengths, AA6082-T6 MIG welded specimen.

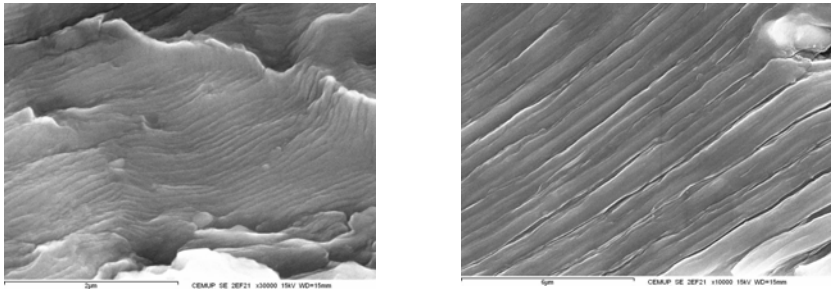

(a) Fractograph 8, crack length of 1.893mm

(b) Fractograph 17 crack length of 10.250mm

Fig. 29 Fatigue striations for two crack lengths, AA6061-T6 MIG welded specimen.

In this specimen the striations identification process was easier than in the aluminum 6082-T6 specimen. Nevertheless the fatigue crack surface was a heterogenic structure with several different structures dispersed randomly. For example, in fractograph 8 presented in Figure 29 fine striations are identified in an irregular structure. In fractograph 17, almost at the end of the fatigue crack are, coarse striations are found.

Figure 30 presents two examples of features identified in the SEM analysis of the aluminum 6061-T6 MIG welded specimen. In fractograph 6, besides some fatigue striations, some gaps in the material continuity are identified. These gaps were probably formed in the heating and cooling during welding leading to the appearance of internal cracks. These gaps are micro-cracks that can be signs of small hot cracks. Hot cracks can be formed in AlMgSi fusion welds when the low melting MgSi eutectic in the grain boundaries remains liquid during weld solidification and subsequent material shrinkage [5]. Heat treatable aluminum alloys are sensitive to hot short

cracking, which results form HAZ liquidation during welding [20]. This specimen presents no less micropores than the aluminum 6082-T6 MIG specimen. In fractograph 7 striations with a V shape orientation were found. The image shows the random distributions that can be found in striations if the fatigue crack is observed with high magnifications.

Figures 31 and 32 present the striation spacing versus crack length for the aluminum 6082-T6 and 6061-T6 MIG welded specimens.

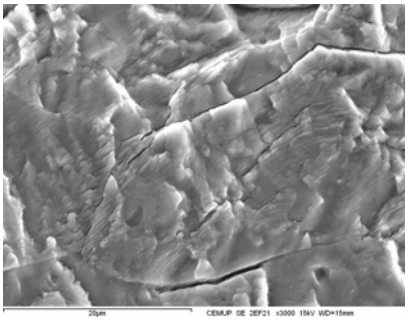

(a) Fractograph 6, crack length of 0.611mm

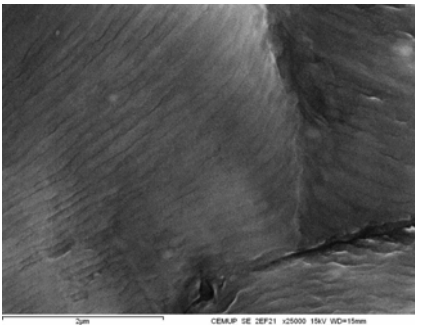

(b) Fractograph 7, crack length of 1.794mm

Fig. 30 SEM analysis of the AA6061-T6 MIG welded specimen.

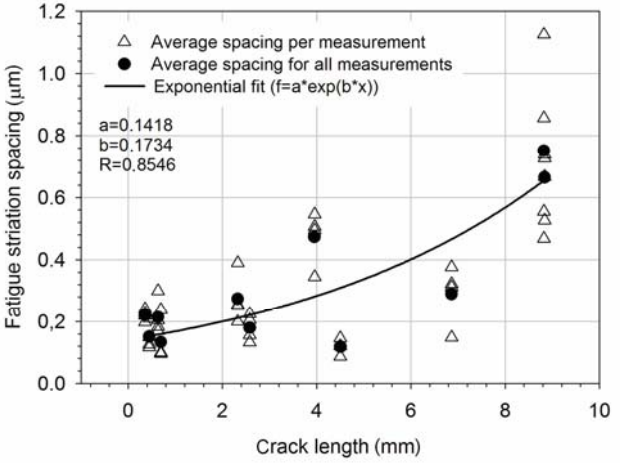

Fig. 31 Fatigue striation spacing *vs.* crack length AA6082-T6 MIG welded specimen.

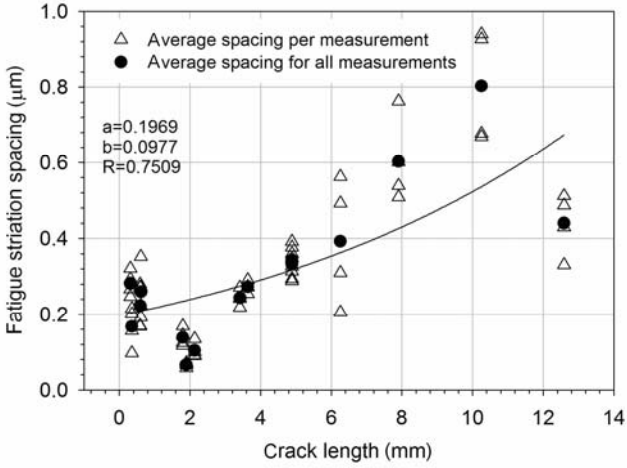

Fig. 32 Fatigue striation spacing *vs.* crack length AA6061-T6 MIG welded specimen.

7.3 FS welded specimens, striations spacing

The specimens were fatigue tested at a maximum stress of 70% of their yield stress (98.4*MPa* for the aluminum 6082-T6 and 111.1*MPa* for the aluminum 6061-T6). The 6082-T6 specimen presented a fatigue life of 258827 cycles and the 6061-T6 specimen had a fatigue life of 173499 cycles. For the aluminum 6082-T6 the fatigue area has 20.4mm^2 and a crack length of 10.29*mm*. For the aluminum 6061-T6 the fatigue area has 24.8mm^2 and a crack length of 12.50*mm*.

The friction stir welded aluminum 6082-T6 specimen has an irregular structure in its entire fracture surface preventing the identification of measurable striations.

For the aluminum 6061-T6 friction stir welded the fatigue crack propagated near the shoulder edge. Despite the heterogeneity found in the fractured surface the striations measurement process was feasible. In fractograph 5 presented in Figure 33 several striations sets with different orientations are identified. In fractograph 21, almost at the end of the fatigue crack, are found coarser striations.

Figure 34 presents the striation spacing versus crack length for the aluminum 6061-T6 friction stir welded specimen.

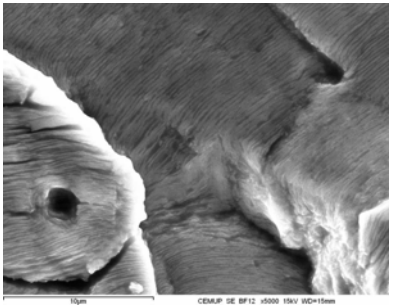

(a) Fractograph 5, crack length of 0.877mm

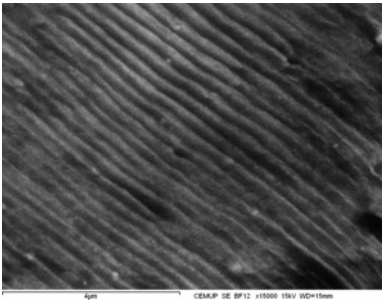

(b) Fractograph 21 crack length of 9.544mm

Fig. 33 Fatigue striations for two crack lengths, AA6061-T6 MIG welded specimen.

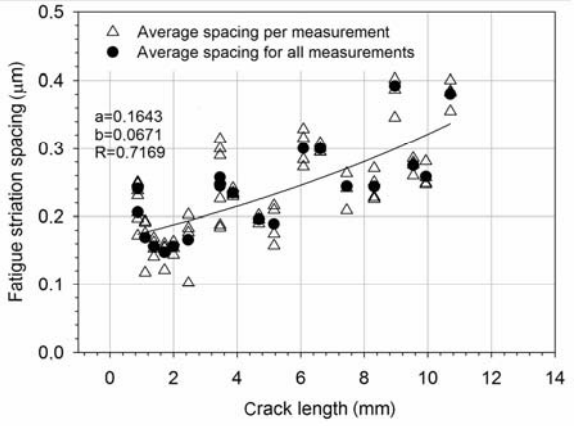

Fig. 34 Fatigue striation spacing *vs.* crack length AA6061- T6 FS welded specimen.

8. Conclusions

Sound welds have been obtained using MIG and FSW for 3*mm* plate thickness of two aluminum alloys 6082-T6 and 6061-T6. Tensile testing of the weld joints and base material produced adequate tensile strength values.

Yield and rupture stress of friction stir welded and MIG welded specimens are lower than for base material. All welding processes lead to a decrease of the material mechanical properties, more pronounced in the MIG specimens. Detailed hardness examination revealed lower hardness values in the MIG welded specimens.

When compared with the friction stir welds and MIG welds, the laser beam welds presented the smaller area (width) affected by the welding process.

The friction stir welded 6061-T6 specimens presented lower lives than the friction stir 6082-T6 specimens when tested at stresses lower than 130*MPa*. Fatigue scatter is somewhat higher in the MIG welded specimens. Its fatigue lives are lower than friction stir welded specimen. The MIG welded 6061-T6 specimens presented higher fatigue lives than the MIG 6082-T6 specimens.

The general microstructure was in good agreement with previous published researches. In friction stir welding the nugget has recrystallized grains smaller than the base material. A SEM analysis of fatigue striation measurements was performed for fatigue specimens of both welding processes and fatigue crack growth rate can be estimated from using these measurements.

Acknowledgments

The work was partially supported by PhD scholarship FCT SFRH/BD/19281/2004, FP6 project AST3-CT-2004–516053 and FCT PTDC/EME-TME/66362/2006. The collaboration of Rui Louro of ISQ, Miguel Figueiredo, Sérgio Tavares and Rui Silva of FEUP is gratefully acknowledged.

References

[1] Thomas W. Nicholas E. Needham J. Murch M. Templesmith P. and Dawes C. Improvements Relating to Friction Welding, TWI, Editor. 1992.

[2] PLC Air Products, Welder's Handbook, For Gas Shielded Arc Welding, Oxy Fuel Cutting & Plasma Cutting 3rd edn ed, ed. A.P. PLC. 1999.

[3] Wahab M. Painter M. and Davies M. The prediction of the temperature distribution and weld pool geometry in the gas metal arc welding process. Journal of Materials Processing Technology, 77(1-3) (1998) 233-239.

[4] Behler K. Berkmanns J. Ehrhardt A and Frohn W. Laser beam welding of low weight materials and structures. Materials & Design, 18(4-6) (199) 261-267.

[5] Ericsson M. and Sandstrom R. Influence of welding speed on the fatigue of friction stir welds, and comparison with MIG and TIG. International Journal of Fatigue, 25(12) (2003) 1379-1387.

[6] AB ESAB. ESAB Welding Handbook -Filler Materials for Manual and Automatic Welding. 2003. Goteborg Sweden.

[7] Scialpi A. de Filippis L and Cavaliere P. Influence of shoulder geometry on microstructure and mechanical properties of friction stir welded 6082 aluminium alloy. Materials & Design, 28(4) (2007) 1124-1129.
[8] Svensson L. Karlsson L. Larsson H. Karlsson B. Fazzini M. and Karlsson J. Microstructure and mechanical properties of friction stir welded aluminium alloys with special reference to AA 5083 and AA 6082. Science and Technology of Welding & Joining, 5(5) (2000) 285-296(12).
[9] Dickerson T and Przydatek J. Fatigue of friction stir welds in aluminium alloys that contain root flaws. International Journal of Fatigue, 25(12) (2003) 1399-1409.
[10] Harris D. and Norman A. Properties of Friction Stir Welded Joints: A Review of the Literature. in EUROSTIR. 2003. Progress report presented at the 6th PSG Meeting.
[11] Nicholas E and Kallee S. Friction Stir Welding - a decade on. in IIW Asian Pacific International Congress. 2000. Sydney.
[12] Hong S. Kim S. Lee C. and Kim S. Fatigue crack propagation behavior of friction stir welded Al-Mg-Si alloy. Scripta Materialia, 55(11) (2006) 1007-1010.
[13] Weston J. Jones I. and Wallach E. Laser welding of aluminium alloys using different laser sources, in CISFFEL 6 - International Conference on Laser and Power Beam Welding. 1998: Toulon, France.
[14] Grong Ø. Metallurgical Modelling of Welding. second edt ed. Materials Modelling Series, ed. T.I.o. Materials. 1997, London.
[15] ASTM, Constant Amplitude Axial Fatigue Tests of Metallic Materials. [16] ASM, ASM Handbook: Metallography and microstructures. Vol. 9. 1995, ASM, Materials, Park, OH.
[17] Woo W. Choo H. Brown D. Vogel S. Liaw P. and Feng Z. Texture analysis of a friction stir processed 6061-T6 aluminum alloy using neutron diffraction. Acta Materialia, 54(15) (2006) 3871-3882.
[18] Liu G. Murr L. Niou C. McClure J. and Vega F. Microstructural aspects of the friction-stir welding of 6061-T6 aluminum. Scripta Materialia, 37(3) (1997)355-361.
[19] Moreira P. de Figueiredo M and de Castro P. Fatigue behaviour of FSW and MIG weldments for two aluminium alloys, Theoretical and Applied Fracture Mechanics, 48(2) (2007) 169-177.
[20] Davis J. Aluminum and aluminum alloys. ASM Specialty Handbook. 1993, Materials Park, OH: ASM International. 784.

Fatigue Damage from Surface to Bulk

C. A. Rodopoulos
Laboratory of Technology and Strength of Materials, Department of Mechanical Engineering and Aeronautics, University of Patras, Panepistimioupolis, Patras 26500, Greece
Email: Rodopoul@mech.upatras.gr

Abstract

The work continuous with the Fatigue Damage Map Method (FDMM) that attempts to unify the propagation rates with the concept of the effective plastic strain. Reference is made to the local strain characterizing the crack tip modified to include the variation of flow resistance as a function of crack length. Comparison with experimental data of multiscale crack growth rates is provided.

1. Introduction

Two mechanical properties are strongly affiliated to fatigue damage (FD); these are the maximum tensile part of the fatigue or endurance limit of smooth specimens for fully reverse loading, $\sigma_{FL,MAX(R=-1)}$, and the cyclic yield stress, σ_y^c. The first defines the maximum permissible tensile stress below which, an inherited or newly formed fatigue crack constrained by the first major microstructural barrier, will never experience an incremental tendency of its growth rate and hence it will reach propagation rates equal or smaller than one Burger's vector (crack arrest), see Figure 1. Here, the size of this crack cannot be larger than the largest grain found on the surface. The condition stands for the natural tendency of the large grains to exhibit maximum deformation.

The cyclic yield stress on the other hand, quantifies as the bulk resistance of the material towards plastic flow. Plastic flow is a rather precise term because its rate can either increase or decrease for the same amount of energy per cycle depending on the nature of the material for hardening or softening. Inevitably, plastic flow saturation will be reached indicating that the majority of grains in the particular plane have achieved plastic deformation (Figure 2). The choice of fully reverse loading should not be ignored since it contains vital information regarding internal materials' plastic flow controllers (Bauschinger).

The fundamental difference between the fatigue limit and plastic flow resistance is scale. The first is related to the response of the surface and the

G.C. Sih (ed.), Multiscale Fatigue Crack Initiation and Propagation of Engineering Materials: Structural Integrity and Microstructural Worthiness, 113–131.

second to the response of the bulk to cyclic loading. In the text that follows characterisation of such a difference is attempted.

Fig. 1 Arrested fatigue crack by grain boundary in 2024-T351 aluminium alloy.

Fig. 2 Regular plastic deformation in Super Pure Aluminium after 800 cycles at 0.1% plastic strain.

2. An Experimental Fact

To facilitate the distinction between surfaces and bulk it is important to jog the memory of the reader to a rather well known experimental fact. In a specimen failed by natural initiation of fatigue cracks, striations are only found in the bulk of the specimen and never on the surface. Herein the surface defines the region near the crack nuclei. Figures 3a, b are showing such a case. The reader should refrain from associations with pre-cracked,

especially through-thickness specimens. An explanation is provided later in the text.

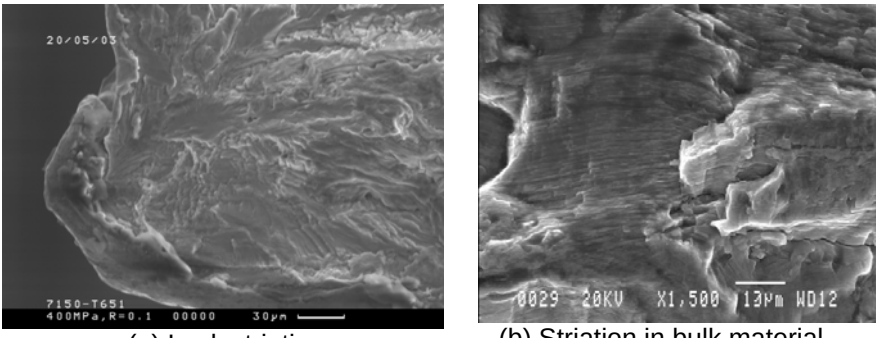

(a) Lack striation (b) Striation in bulk material

Fig. 3 Lack of striations at the region of crack nuclei in a 7150-T651 aluminum alloy and well defined striations inside the bulk of the material.

To appreciate the phenomenon it is imperative to conceptualize the mechanism of fatigue striations and identify those parameters controlling it. From the several models proposed over the years, to explain the mechanism of fatigue striations, those in [1, 2] are the most prominent. Both postulate that there is a continuous, following the loading waveform, blunting and re-sharpening of the crack front due to a symmetrical alternating shear on two dominant slip planes. Similarly the work in [3] used symmetrical shear stresses to explain crack propagation through dislocation generation and movement. In all the above cases, a symmetrical deformation field is needed to dictate for the steady-state development of fatigue damage. Despite the fact that the term steady-state is somehow loosely defined outside the strict boundaries of elasticity, it can be simplistically linked to the proportionality instituted between the monotonic and cyclic crack tip plasticity. Where the first, is the product of single sign dislocations, while the second, is the result of dislocation dipoles (two opposite signs). It is therefore important to associate the lack of fatigue striations found near the region of the crack with some sort of absence of symmetrical deformation.

3. Defining the Absence of Symmetry

Grain boundaries and other microstructural barriers (martensitic laths, eutectoid colony, ferrite-pearlite boundary, and so on) are known to constraint the spread of crack tip plasticity (the term tip is introduced because it is not known whether barriers can homogeneously constrain the volu-

metric crack plasticity) and hence the propagation of the crack [3, 4]. The term “spread” is rather precise since it reflects the tendency of the crack tip plasticity to expansively broaden if it was not for some internal resistance by the material. In the classical fracture mechanics this is expressed by the yield stress of the material. Herein the reader should question whether the macroscopic yield stress contains sufficient scale range to be portrayed as the internal material’s resistance. It is therefore rational to assume that the size of crack tip plasticity is more likely to be controlled by microstructural barriers rather than by a more wide-ranging interaction of surface and bulk displacements. The strength of these barriers and especially of the grain boundaries is encapsulated in the parameter *k* of the Petch-Hall equation [5]. Its value depends on the crystallographic system, solute additions (dislocation pinning) and work hardening (dislocation interaction) [5]. In a number of modelling works [6,7], it was reported that there is critical surface crack length or a critical surface crack tip plasticity size, considering that its end is bounded by the barriers, beyond which the near-tip strain field is strong enough to: a) underpin dislocations through the boundary; b) activate a new dislocation source in an adjacent grain and c) to produce an internal crack in an adjacent grain which will then coalescence with the main crack [8]. In either case, once the critical crack length is reached, the constrained crack tip plasticity expands and the crack is now partially free to propagate until the process repeats itself. Such rationale explains the ladder type propagation of short cracks, as seen from the surface, Figure.4.

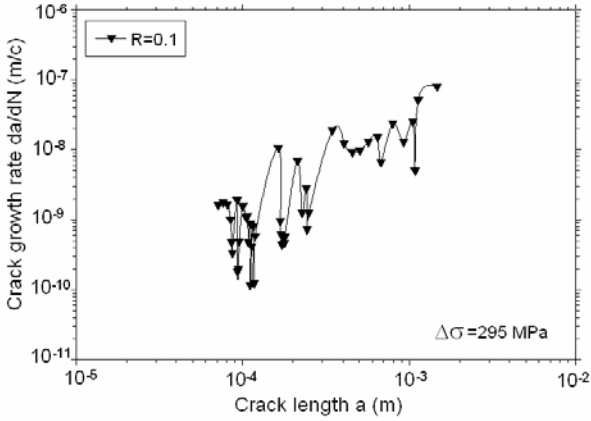

Fig. 4 Typical propagation behaviour of short crack in 2024-T351.

Yet, under the assumption of coherent crack growth, a homogeneous spread of crack tip plasticity in the adjacent grains along the crack front is

required. The above comes against differences in the crystal orientation, size and shape of the adjacent grains, angle distribution of the grain boundaries and creates an additional difficulty towards the homogeneous spread of crack tip plasticity [9]. Armstrong et al in 1962 [10], initially tackled the phenomenon also known as slip mismatch, in terms of the strength of the grain boundary to constraint plasticity and by Navarro and de los Rios in terms of crack arrest through the term “grain orientation factor” [11]. A typical depiction of the slip mismatch is shown in Figure 5.

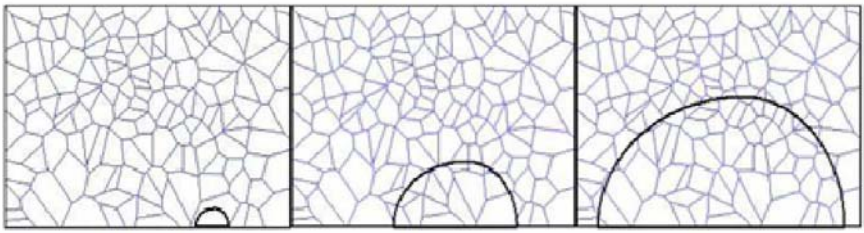

Fig. 5 In sequence crack in solid line occupies the largest surface grain, the region with tripling surface length with crack tip plasticity zone (more than 23 grains) and a crack length 6 times its initial size covering more than 60 grains.

As is easily understood, the rate, describing the dynamic probability of engulfing a “new/different” grain, will eventually become infinitesimal indicating conditions of fully polycrystalline behaviour (the bulk mechanical properties are in effect). Slip mismatch is known to follow a rectangular hyperbolic distribution function reflecting the rate of the number grains engaged by crack tip plasticity per unit crack length (slip mismatch rate). Of course it is easily understood that the number of cycles required to produce the unit crack length is inversely proportional to crack length. In simple terms attendance of fully polycrystalline behaviour signifies that the average value of the slip mismatch rate remains the same. In general, the grain orientation factor is expected to define saturated polycrystalline behaviour of the material when asymptotically reaching values of 3.07 for FCC (Taylor) and 2.0 for BCC (Sachs) structures. Without doubt, slip mismatch is a rather complex phenomenon to be modelled in terms of fatigue since additional parameters, like grain boundary orientation, microtexture, favourable slip planes, slip behaviour, grain size distribution, and so on, are actively present [12, 13]. Yet, their effect is somehow included into the Kitagawa-Takahashi or crack arrest diagram, see Figure 6.

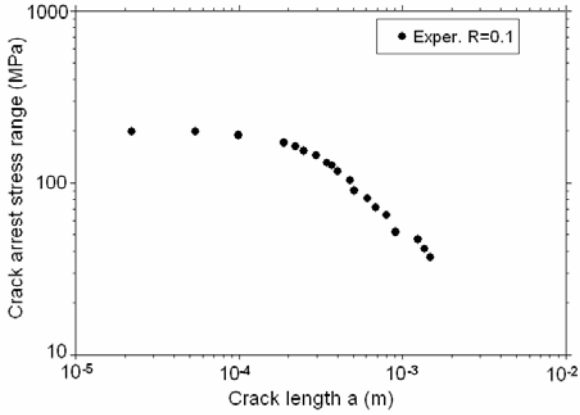

Fig. 6 Experimental crack arrest data from 2024-T351 at stress ratio 0.1.

Herein effects coming from the dynamic interaction between crack lengths, far-field stress, history of crack tip plasticity and crack shapes are integrated into a single response controlling crack growth. To demonstrate the difficulty in attaining the shear stress symmetry, postulated by elasticity, it is imperative to engage a graphical narrative. Let us consider a short 2D crack as appears in Figure 5. When the crack is microstructurally short (Figure 7a) coherent crack growth emanating from the symmetrical alternating shear is possible since both component of stress stretch within the same grain. The process can explain the plateau found in the crack arrest data for crack lengths smaller or equal to the largest grain. Herein the grain orientation factor is considered as unity. Expansion of the crack beyond the first grain (Figures 7b,c) defines conditions for unsymmetrical alternating shear since the dominant slip planes can be found in more than one different grains. This asymmetry tends to modify the crack shape and particularly its aspect ratio. The process its energy consuming and can cause changes in the crack path or bifurcation. If however the crack shape is to be maintained, the dislocation density, the parameter can be used to define the level of alternating shear, needs to be comparable. The process necessitates the deceleration of the crack tip as that approaches the grain boundary and the continuous increase in dislocation density. The process will continue until the dislocation density in the two slip planes is high enough as to be considered comparable. Once done, the crack will accelerate and the process repeats itself. The phenomenon manifests itself by the saw cut crack growth behaviour as seen in Figure 4. Of course it is easily understood that the difference in the dislocation density as this defines the unsymmetrical alternating shear, will end once the probability of the crack tip slip planes to enter a largely different grain diminishes, Figure 7.

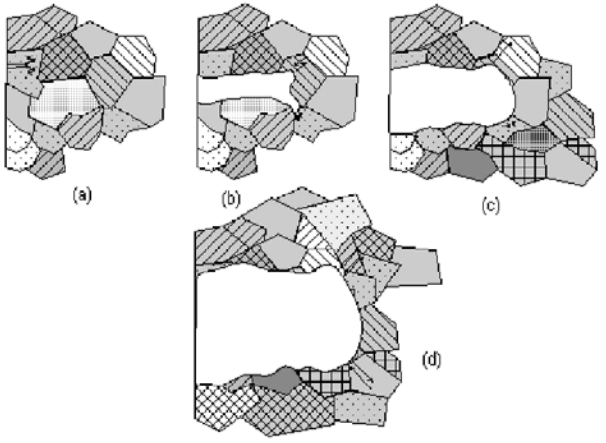

Fig. 7 Schematic representation of the unsymmetrical and symmetrical alternating shear.

To tackle the problem is imperative to consider that every polycrystal acts as an aggregate with grain boundaries providing internal strengthening. The notion immediately points towards the know Petch-Hall equation. Herein, the flow resistance of the material is known the increase inversely to the average grain size. The average grain size is a well-known material property and yet conceals a number of important elements.

4. Scaling Fatigue Damage – Microstructural Worthiness

In [14] it was suggested that in order to identify the relationship between the bulk yield stress of polycrystals and the Petch-Hall equation there is a minimum volume (number) of grains that should be used to express the grain size distribution. Considering what is already known in statistics, it was suggested that since a polycrystal behaves as an aggregate there is a critical number of grains necessary to accurately identify a selected grain size distribution and extract average values. If the number is smaller than the critical, the bulk yield stress will show large scatter. Expanding the above notion in the case of fatigue damage such number will depend on the size of the crack tip plasticity. Hence, it can be postulated “the plastic flow resistance depends on the number of grains sampled by the perimeter of the crack (in the case of crack arrest-including the history of plastic flow resistance when the crack was propagating as in threshold tests) or by the crack tip plasticity area (in the case of present crack growth)”. The above points towards the following rationale. The flow resistance of the material depends on the number of grains sampled by the crack tip plasticity and

has the tendency to increase to a saturated value (bulk yield stress), once the number is large enough as to qualify for average value. Herein, it is important to note that the crack will follow a particular route, laid by the largest possible grains within the spectrum of available paths defined by the maximum stress level. As a result the flow resistance as a function of crack length will appear below that given by its bulk value. It is also imperative to consider that high stress levels will endorse the crack with energy reserves, which associated with the low flow resistance, will allow the crack to propagate considerable faster compared to a value calculated via the symmetry of alternating stress. In addition, with the crack having to choose from a large spectrum of crack paths the potential scatter in the number of cycles to failure will be low. At low stress levels the mechanism is somehow different. First the number of available paths is small while they are not necessarily the easiest. Secondly the energy reserves are just sufficient (for stress levels slightly over the fatigue limit) and hence the crack can experience significant delays in its growth rate.

Based on the above, it is reasonable to ascertain that the crack arrest test represents the minimisation of crack tip plasticity starting from different values of flow resistance especially. Its profile is defined by the grain size distribution since the latter defines the available crack paths. To better understand the influence of grain size on crack paths it is necessary to keep in mind that fatigue damage will always start from the largest possible grain found on the surface. Progression will take place through a path, which allows growth of the crack with minimum energy needs. Therefore it is not difficult to understand that the crack will follow a path laid by the largest possible grain allowed by the material. For this reason it is imperative to examine some statistical distributions of grain size. Figure 8 shows the grain size distribution of 7150-T651 aluminium alloy and low carbon steel. The analysis reveals, for the aluminium alloy, a maximum grain size of 132μm, an average grain of 60.1μm and standard deviation of 26.4μm. Whether the 132μm grain will accommodate the crack origin is a question having to do with its probability and the size of the specimen/component. In a more broadly accepted case, it is statistically correct to consider that the spectrum of crack paths, bringing the range-average of the number of grains embedded inside the area of crack tip plasticity from its maximum value to its average, is controlled by the standard deviation. Here it is important to note that BCC structures are exhibiting smaller standard deviation in their grain size than FCC structures. A comparison between Figures 8a and 8b reveals the case. A theoretical analysis was published in [15].

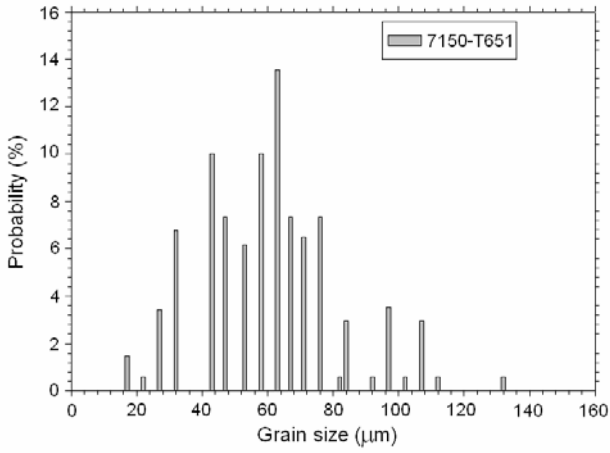

(a) 7150-T651

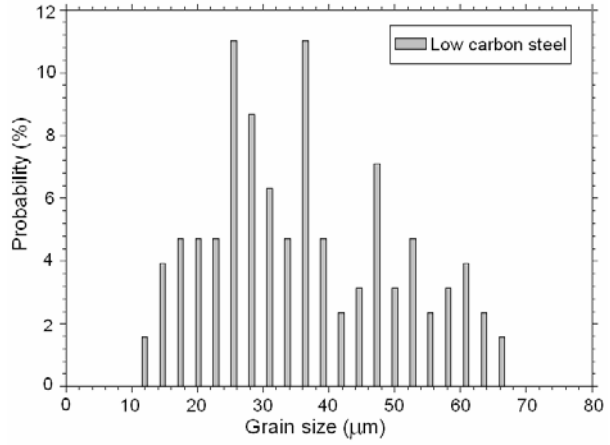

(b) Low carbon steel

Fig. 8 Grain size distribution.

The rationale mentioned earlier motivated the work in [16] which suggested a simplified solution based on three engineering boundary conditions for the case of surface crack arrest defined by the following equation,

$$\Delta\sigma_{arrest} \le \frac{1}{Y}\frac{m_i}{m_1}\frac{\left[\dfrac{2\sigma^{max}_{FL(R=-1)}\sigma_{UTS}}{2\sigma_{UTS}(1-R)+2(1+R)\sigma_{FL(R=-1)}}\right]-\sigma_1}{\sqrt{2a/D}}+\sigma_1 \text{ , } -\infty < R < 1 \tag{1}$$

where Y is the crack correction factor to be used only when the crack has LEFM conditions, $\sigma^{max}_{FL(R=-1)}$ is the maximum tensile part of the fatigue limit for fully reverse loading, σ_{UTS} is the ultimate tensile strength, R is the stress ratio (far-field stress ratio between the minimum and maximum stress in a predetermined loading cycle), $\sigma_1(a)$ is the crack closure stress as a function of the crack length a, $\bar{D}$ is the average grain size and m_i/m_1 is the grain orientation factor. The subscript i defines the number of half grain constituting the fatigue damage (crack length and crack tip plasticity, see [16]). The first engineering condition considers that the orientation factor of the first grain is always set at 1, to encapsulate the high probability of finding a favourably oriented grain for slip along the surface. This translates into,

$$\frac{m_i}{m_1} = 1 \text{ for } i = 1,\ \Delta\sigma_{\text{arrest}} = \sigma^{\max}_{FL(R=-1)} \tag{2}$$

The second condition considers that polycrystalline saturation behaviour should take place, at the latest, at the point where crack arrest is determined by small scale yielding conditions and hence the long crack threshold is in effect. The above is converted into,

$$\frac{m_i}{m_1} = 3.07 \text{ (FCC) or 2.0 (BCC)}, \Delta\sigma_{arrest} \le \frac{\sigma_Y}{3} \tag{3}$$

The third condition protects the physical tendency of the crack arrest capacity of the material to exhibit maxima in the region of microstructural short cracking (the fatigue limit is the highest permissible crack arrest stress). The conditions is written as,

$$i \ge 1,\ \Delta\sigma_{\text{arrest}} \le \sigma^{\max}_{FL(R=-1)} \tag{4}$$

In Eq. (3) the condition $\Delta\sigma_{\text{arrest}} \le \frac{\sigma_Y}{3}$, where σ_y stands for the monotonic yield stress, implies the truthful application of LEFM to describe the elastic stress field ahead of the crack tip with an error not exceeding 7% [17]. Incorporation of such boundary condition into Eq. (1) yields,

$$\frac{m_i}{m_1} = 3.07 \text{ (FCC) or } 2.0 \text{ (BCC)},$$
$$\text{i} \ge \frac{81\sigma^{\max}{}^{2}_{\text{FL(R=1)}}}{\sigma_Y{}^{2}} \text{ (FCC) or i} \ge \frac{36\sigma^{\max}{}^{2}_{\text{FL(R=-1)}}}{\sigma_Y{}^{2}} \text{ (BCC)} \tag{5}$$

where *i* in the case of crack arrest is the crack length, $\text{i}=2\text{a}/\overline{\text{D}}$.

Based on the above, the following equations have been determined [16],

$$\left(\frac{m_i}{m_1}\right)_{FCC} = 3.07 - \frac{2.31}{\left(1+0.05\frac{2a}{\overline{D}}\right)^{1/0.34}} \tag{6}$$

for Face-Centred Cubic (FCC) crystal structures, and

$$\left(\frac{m_i}{m_1}\right)_{BCC} = 2.0 - \frac{1.2}{\left(1+0.05\frac{2a}{\overline{D}}\right)^{1/0.34}} \tag{7}$$

for Body-Centred Cubic (BCC) metals.

5. The KT Diagram

The above passage points towards a realisation of the K-T diagram in terms of the grain size distribution, as shown in Figure 9. Herein, the first part denoted by the fatigue limit is controlled by the largest grain found on the surface. The transition towards the threshold condition is controlled by the distribution of the grain size which directly affects the probable number of grains sampled by the crack perimeter of a particular geometric shape. In other words, the number of grains sampled within this area is be-

low the critical one expressing the material's bulk flow resistance. Finally, threshold stress through the use of the bulk property, σ_y or σ^c_y, implies the use of the average grain size taken from a number of grains exceeding the critical value. The parameter σ^c_y stands for the cyclic yield stress.

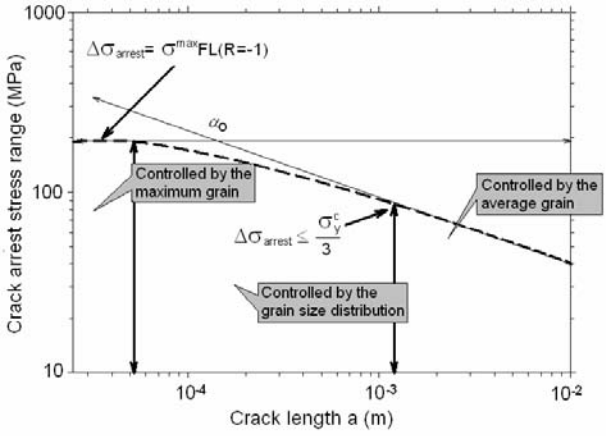

Fig. 9 Schematic showing the Kitagawa-Takahashi crack arrest diagram influenced by the grain size distribution incorporated into the crack length.

Modeling the effect of grain size on the crack arrest diagram requires extensive analysis of three critical features. It is known that different materials, not just those of a different crystallographic structure, exhibit a broad spectrum of grain size distributions types. The second feature emanates from the sampling assortment. In other words, should it be a particular direction for sampling probabilities? The third case comes from the definition of a condition to portray the critical number of grains, which directly incorporate crack geometry effects. Based on the above, the previous boundary conditions need to be redrawn,

CONDITION 1:

$$\frac{m_i}{m_1} = 1 \; for \; i = 1, \; i = \frac{2a}{D_{max}} \rightarrow \Delta\sigma_{arrest} = \sigma^{max}{}_{FL(R=-1)} \tag{8}$$

CONDITION 2:

$$\frac{m_i}{m_1} = 3.07(FCC) \text{ or } 2.0(BCC), i = \frac{2a}{\overline{D}} \rightarrow \Delta\sigma_{arrest} \le \frac{\sigma_y}{3} \tag{9}$$

or, to include the elasto-plastic behaviour of the material,

$$\frac{m_i}{m_1} = 3.07 \text{ (FCC) or } 2.0 \text{ (BCC)}, i = \frac{2a}{\bar{D}} \rightarrow \Delta\sigma_{arrest} \leq \frac{\sigma^c{}_Y}{3} \qquad (10)$$

The above yields,

$$\frac{2a}{\bar{D}} \geq \frac{81\sigma^{max}{}_{FL(R=1)}{}^2}{\sigma^c{}_Y{}^2} \text{ (FCC)} \quad or \quad \frac{2a}{\bar{D}} \geq \frac{36\sigma^{max}{}_{FL(R=-1)}{}^2}{\sigma^c{}_Y{}^2} \text{ (BCC)} \qquad (11)$$

and CONDITION 3:

$$\begin{aligned} &1 < i \leq \frac{81\sigma^{max}{}_{FL(R=1)}{}^2}{\sigma^c{}_Y{}^2},\ i = \frac{2a}{\overline{D_Z}},\ D_{max} > \overline{D_Z} \geq \bar{D} \\ &\rightarrow \sigma^{max}{}_{FL(R=-1)} > \Delta\sigma_{arrest} > \frac{\sigma^c{}_y}{3} \end{aligned} \qquad (12)$$

for FCC and

$$\begin{aligned} &1 < i \leq \frac{36\sigma^{max}{}_{FL(R=1)}{}^2}{\sigma^c{}_Y{}^2},\ i = \frac{2a}{\overline{D_Z}},\ D_{max} > \overline{D_Z} \geq \bar{D} \\ &\rightarrow \sigma^{max}{}_{FL(R=-1)} > \Delta\sigma_{arrest} > \frac{\sigma^c{}_y}{3} \end{aligned} \qquad (13)$$

for BCC. Note that $\overline{D_Z}$ is the average size of the number of grains sampled within a selected probability range and intercepted by the crack perimeter. Solution of the above boundary conditions in terms of constitute equations (no fitting exercises have been performed to identify their interaction and the system is solved in a singular manner) for a variety of crack lengths and mechanical properties, resulted into,

$$\left(\frac{m_i}{m_1}\right)_{FCC} = 3.07 - \frac{2.31}{\left(1+0.05\frac{2a}{\overline{D_z}}\right)^{1/0.34}} \tag{14}$$

$$\left(\frac{m_i}{m_1}\right)_{BCC} = 2.0 - \frac{1.2}{\left(1+0.05\frac{2a}{\overline{D_z}}\right)^{1/0.34}} \tag{15}$$

The parameter $\overline{D_z}$ can either be extracted through a generalised function to describe different types with some degree of error but maintaining its nature as to be hold under the same equation umbrella, or, via discrimination of materials into several types of probability density functions at the expense of a universal nature.

6. Crack Propagation Rate

In a number of works [17-20], it is known that the number of available dislocation defining plastic deformation is proportional to the grain size. Considering that the propagation rate of the crack can be described by the elasto-plastic crack tip opening displacement, δ_{tip} as,

$$\frac{da}{dN} = \phi\delta_{tup} \tag{16}$$

with ϕ a dimensionless parameter representing the fraction of dislocations in the slip band participating in the process of crack extension and takes values between 0 and 1, it is easily understood that a crack path engaging a number n of the largest possible grains, will endorse the crack with the highest possible propagation rates. In other words, the energy needs of the crack per unit new surface will be kept at minimum. The likelihood of such potential optimum condition is controlled by the grain size distribution itself and especially by the probability value of the largest grain. To incorporate the potential of the largest grain to self determine the number of grains sampled by the crack perimeter, the parameter *n* is written as,

$$n \geq \frac{P_c}{D_{max}} \tag{17}$$

and the proportion or right tail estimate of the size distribution is,

$$\frac{n}{N} \geq \frac{P_c}{ND_{max}} \tag{18}$$

The parameter P_c stands for the crack tip perimeter. Determination of the value that satisfies the proportion value, denoted by D_z, is achieved by,

$$\int_{D_z}^{D_{max}} f(D)dD \approx \frac{P_c}{ND_{max}} \tag{19}$$

Since D_z is now known, a range-average (or range mid-point) needs to be calculated. Such value, defined as $\overline{D_Z}$ is given as,

$$\overline{D}_z = \frac{D_{max} + \left(\frac{P_c}{D_{max}} - 1\right) D_z}{\frac{P_c}{D_{max}}} \tag{20}$$

It is worth noting that for values of (P_c, N, D_{max}) such as $\overline{D_z} < \overline{D}$, Eq. (20) reduces to $\overline{D_z} = \overline{D}$ by construction. Such boundary condition signifies the critical number of grains further which, the mid-point equals the average grain size related to N. In other words, Eq. (20) provides the distribution of the number of sampled grains towards their critical number (corresponding to the bulk properties) as a function of the crack shape. Solution for the case of the low carbon steel and the 7150-T651 aluminium alloy is depicted in Figures 10-11 for the grain orientation factor and crack arrest stress range.

From the above analysis assume that slip mismatch relates the cyclic yield stress and the fatigue limit, for conditions of crack arrest, through the relationship,

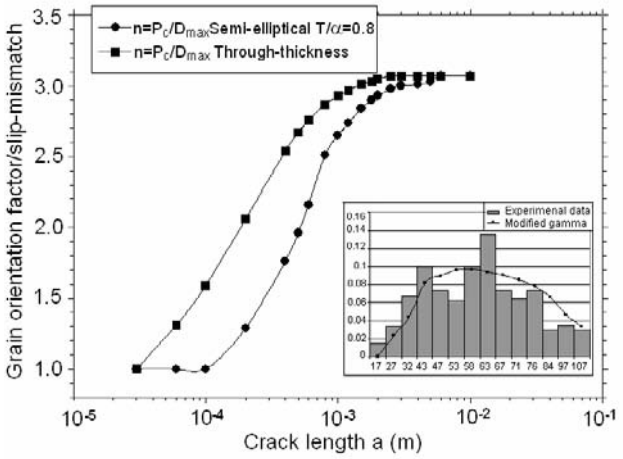

Fig. 10 Profile of grain orientation factor for 7150-T651 aluminium alloy considering a semi-elliptical surface crack and a through-thickness crack (thickness 5mm).

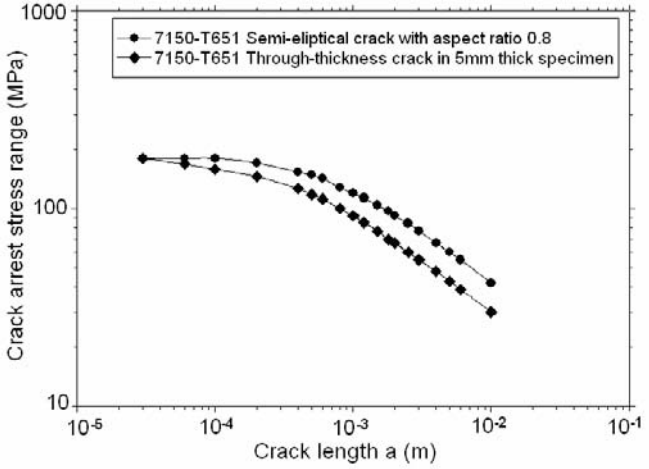

Fig. 11 Crack-arrest diagram for 7150-T651 according to Eq.(1) and R=-1.

$$\sigma_{arrest\ flow}^{FCC} = \left[3.07 - \frac{2.31}{\left(1 + 0.05 \frac{2a}{D_z} \right)^{1/0.34}} \right] \sigma_{FL(R=-1)} \tag{21}$$

$$\sigma_{arrest\ flow}^{BCC} = \left[2.0 - \frac{1.2}{\left(1 + 0.05 \frac{2a}{D_z} \right)^{1/0.34}} \right] \sigma_{FL(R=-1)} \tag{22}$$

Such case provides a rational explanation towards the transition from large to small scale yielding conditions as a function of crack length, geometry and material. It can also be easily seen that in the case of the fatigue limit (arrest of a crack with length no larger than the largest grain, the value of plastic flow resistance is equal to the far field stress (fatigue limit).

7. Conclusions

The work considers that the scale effects related to fatigue damage are encapsulated inside the crack arrest diagram. Herein, the initial stress plateau corresponds to the fatigue limit and extends to crack length related to the largest grain found in the material. From there on there is an irregular but continuous drop of the stress with crack length. The phenomenon will continue up to the point where the stress degradation and the size of the crack obtain some sort of equilibrium denoted by a constant gradient. The gradient is usually found at –0.5 signifying potential association with conditions of Linear Elastic Fracture Mechanics or symmetrical alternating shear. Between these two limiting cases, a lot of research has been denoted to the explanation of such a potentially complex situation. The concept of short crack behaviour has emerged and consumed a very large portion of research funding. Of particular interest is the fact that there was and possibly still is, a severe incision within the research community between those approaching the problem from the viewpoint of the material and those using traditional mechanics. The role of the devil's advocate was played by experimentalists who found particular cases where neither the case of short

cracking was always identified and neither solutions given by the mechanics was always applicable. This work represents a rather innovative way of attacking the problem and steams from the fact that the above discrepancies should be somehow explained and incorporated. Taking into account the role of the material and particularly of the grain size distribution, the corresponding crack paths simulating the effect of stress and the role of the crack shape and geometry tends to provide a platform for integration. The work concludes that the flow resistance of the material which controls the plastic deformation and hence the available energy which needs to be minimised in order for the crack to arrest, is not constant and tends to start from a value being the fatigue limit and saturate to a more macroscopic value that of the cyclic yield stress with crack length.

References

[1] Laird C. The influence of metallurgical structure on the mechanisms of fatigue crack propagation, In Fatigue Crack Propagation, STP, 415 (1967) 131-168, ASTM, Philadelphia.
[2] Newman P. Coarse slip model of fatigue, Acta Metall, 17 (1969) 1219-1225.
[3] Sadananda K and Glinka G. Dislocation process that affect kinetics of fatigue crack growth, Phil. Mag, 85(2-3) (2005) 189-203.
[4] Fang B, Hong Y and Bai Y. Experimental and theoretical study on numerical density evolution of short fatigue cracks, Acta Mech. Sinica, 11(2) (1995) 144-152.
[5] Miller K J. Metal Fatigue-Past, Current and Future, The John Player Lecture, Proc. IMECHE, London, 205(5) (1991) 291-304.
[6] Petch N J. The cleavage strength of polycrystals, J. Iron Steel Inst, 174 (1953) 25-28.
[7] de los Rios ER, Tang Z and Miller KJ. Short crack fatigue behaviour in a medium carbon steel, Fatig.Fract.Engng.Mater.Struct, 7(20) 1984) 97-108.
[8] Navarro A and de los Rios ER. Fatigue crack growth modelling by successive blocking of dislocations, Proc. R. Soc. London, A437 (1992) 375-390.
[9] Li GS. A three-dimensional finite element analysis for a crystallographic crack near the interface of an incompatible bicrystal, Fatig. Fract. Engng. Mater. Struct., 16(1) (1993) 21-35.
[10] Peralta P, Dickerson R, Dellan N, Komandur K and Jameel MA. Effects of local grain orientation on fatigue crack growth in multicrystalline FCC metallic materials, J Engng. Mater. Techn., 127 (2005) 23-32.
[11] Armstrong RW, Codd I, Douthwaite RM and Petch NJ. The plastic deformation of polycrystalline aggregates, Phil, Mag, 7 (1962) 45-58.
[12] de los Rios ER, Navarro A. Considerations of grain orientation and work hardening on short-fatigue crack modelling, Phil. Mag. A, 61(3) (1990) 435-449.

[13] Zhai T, Wilkinson AJ and Martin JW. A crystallographic mechanism for fatigue crack propagation through grain boundaries Acta Mater., 48 (2000) 4917-4927.
[14] Kurzydzsowski KJ. A model for the flow stress dependence on the distribution of grain size in polycrystals, Scr. Metall. Mat., 24 (1990) 879-883.
[15] Rodopoulos CA, de los Rios ER. Theoretical Analysis on short fatigue cracks, Inter. J. of Fatigue, 24 (2002) 719-724.
[16] Rodopoulos CA. Evolution of fatigue damage using the fatigue damage map method, Theo. Appl. Fract. Mech., 45 (2006) 252-265.
[17] Brown M.W Interfaces between short, long and non-propagating cracks, In: The Behaviour of Short Fatigue Cracks, K. J. Miller and E. R. de los Rios eds, (Mechanical Engineering Publications, London, (1986) 423-439.
[18] Pelloux RM. Crack extension by alternating shear, Engng. Fract. Mech., 1 (1970) 697-704.
[19] Eastbrook JN. A dislocation model for the rate of initial growth of Stage I fatigue cracks, Inter. J. of Fracture, 24 (1984) R43-R49.
[20] de los Rios ER, Tang Z and Miller KJ. Short crack fatigue behaviour in a medium carbon steel, Fatig. Fract. Engng. Mater. Struct., 7(2) (1984) 97-108.

Microcracking in High Temperature Low Cycle Fatigue

S. L. Mannan[1*] **and M. Valsan**[2]
[1]National Engineering College, Kovilpatti, TN, India
[2]Indira Gandhi Centre for Atomic Research, Kalpakkam, TN, India
**Email: Sadari_mannan@yahoo.com*

Abstract

At elevated temperatures, fatigue deformation and fracture are influenced by synergistic actions of several time dependent damage mechanisms. These include dynamic strain ageing, oxidation, creep and phase transformations. Studied are the influence of dislocation density, precipitates, strain rate, temperature and hold time on the high temperature low cycle fatigue behaviour of austenitic and ferritic steels and their weld joints and a Nimonic PE16 superalloy. Cycling hardening and softening response in various alloys would be discussed in terms of accompanying substructural changes.

1. Introduction

Low Cycle Fatigue (LCF) is an important consideration in the design of many high temperature operating equipments such as aircraft gas turbines, heat exchangers and power plant components like steam turbines, pipings and reactor vessel. In this context, many researchers have attempted the evaluation and characterization of LCF properties of alloys widely used in service at elevated temperatures [1-5]. LCF damage occurs in these components due to large plastic strains introduced during start-up/ shut-down operations or power transients. Further on-load periods introduce creep-fatigue interactions which is more deleterious than either creep or fatigue acting separately. At high temperatures the fatigue deformation and life are influenced by several time dependent mechanisms such as differences in slip mode, dynamic strain ageing (DSA), oxidation, creep and phase transformations. This has been reviewed in detail by several investigators [6-9]. These damage processes can lead to premature failure when compared with fatigue failure under time-independent conditions. The time-dependent mechanisms mentioned above may influence the fatigue life either synergetically or independently depending on test conditions.

G.C. Sih (ed.), Multiscale Fatigue Crack Initiation and Propagation of Engineering Materials: Structural Integrity and Microstructural Worthiness, 133–179.

Considered are the factors that influence the formation and growth of microcracks in high temperature fatigue would be examined by conducting tests on smooth samples. The role of initial microstructure and the microstructure that evolves during testing would be studied by tests on samples of different size and volume fractions of the γ' precipitates in Nimonic PE16 Superalloy. Further, the influence of various test conditions like temperature, strain rate, dwell-time on the formation and growth of microcracks is examined based on tests conducted on this material and on 316L(N) Stainless steel, 316 weld metal and a modified 9Cr-1Mo ferritic steel [10-20]. In certain situations cyclic deformation led to strain localization resulting in rapid crack initiation and propagation. The mechanisms affecting crack initiation and propagation are examined to understand variations in high temperature LCF life as a function of microstructure and test variables in smooth specimens. A fatigue crack generally initiates at the surface of the smooth specimen first, grows along crystallographic slip direction and then crack growth occurs at 90^o to the stress axis marked by fatigue striations. Fatigue failure towards last few cycles is reflected in a drastic reduction in load drop in the tension part of the hysteresis loop and cusp formation in the compression part. A 20% drop in the tensile load is taken as the failure life in the present study. Smooth specimens employed in this study have been considered to be part of the plastic zone around the notch in actual components and the fatigue life of the specimens has been taken as the crack initiation life in actual components [21].

1.1 Material and heat treatment

The materials used in this study are candidate materials for the primary and secondary sodium circuits of the fast breeder reactors. Nimonic PE-16 finds application as wrapper tubes and clad tubes in fast reactors apart from applications at high temperatures as a material for aircraft ducting systems, gas turbine flame tubes, missile hot components and superheater tubes. LCF studies on this relatively simple precipitation hardened system (with a low volume fraction, 11% maximum, of γ') would also facilitate fundamental understanding of the operative deformation and fracture mechanisms and correlation with fatigue life in this class of superalloys. The prior microstructure of the alloy is chosen with two different γ' sizes namely 18nm and 35nm such that the former favours precipitate shearing and the latter Orowan looping. Consequently the influence of these on strain localization and micro-cracking can be evaluated.

316L(N) stainless steel and 316 weldmetal find application in the primary sodium circuit of the fast reactor as reactor vessel, pipings and heat exchangers. The choice of this alloy is based on its excellent high-temperature tensile, creep, fatigue and creep-fatigue strengths in combination with good fracture toughness and fabricability. 316L(N) has lesser susceptibility to sensitization and associated intergranular corrosion.

Modified 9Cr-1Mo ferritic steel (with alloying additions of Niobium and Vanadium and controlled amount of nitrogen) is extensively used as a structural material at elevated temperatures up to 873 K in fossil-fired power plants, petrochemical industries and as a material for tubing in the reheater and superheater portions and as thick-section tube sheet material in the steam generators of Liquid Metal Cooled Fast Breeder Reactor [22]. High thermal conductivity and low thermal expansion coefficient coupled with enhanced resistance to stress corrosion cracking in steam-water systems are important considerations in the selection of this steel for these applications. The alloy also exhibits good weldability and microstructural stability over very long periods of exposure to high temperature service conditions.

These alloys were tested under different temperature and strain rate combinations including those which promote strain localization and enhanced transgranular and intergranular cracking. Further intergranular and transgranular cracking assisted by creep and oxidation are evaluated by conducting tests with hold times at tension and compression peaks in the strain cycle.

1.1.1 Nimonic PE-16 Superalloy

Nimonic PE-16 superalloy is a nickel-iron base superalloy that is strengthened by chromium and molybdenum in solid solution and also by ordered face centered cubic Ni_3 (Al,Ti) precipitates. The chemical composition of the alloy is given in Table 1. The alloy in the form of 20 mm diameter rods was solution treated at 1313 K for 4 hours. Solution annealing was found to dissolve majority of the preexisting carbides and all the γ' except some TiCN precipitates. This was designated as Microstructure A.

Table 1 Chemical composition of nimonic PE 16 superalloy (in wt%).

Ni	Cr	Ti	Al	C	Mo	Zr	S	B	Mn	Cu	Fe
43.2	16.5	1.2	1.2	0.07	3.3	0.03	0.004	0.0015	0.04	0.06	33.83

PE-16 alloy is generally subjected to two-step ageing treatments to achieve the specified mechanical properties. The rationale for the choice of different temperatures for the intermediate and final ageing treatments is as

follows: the solvus temperature of γ′ phase for the PE-16 alloy varies in the temperature range 1133-1148 K depending on the specific composition of the alloy [23]. Hence the two intermediate temperatures of ageing were chosen such that 1173 K is above the solvus temperature and 1073 K is below. Thus ageing at 1073K would lead to the precipitation of both γ′ and carbides whereas ageing at 1173 K would cause the precipitation of carbides alone. Intermediate ageing at 1173 K resulted in the precipitation of MC carbides primarily along the grain boundaries and occasionally within the matrix. A comparison of the effect of final ageing treatments namely 973 K and 1023 K, on the tensile properties of the alloy after intermediate ageing revealed that the maximum strength values are attainable at 973 K. This has been attributed to the maximum volume fraction of γ′ formed at 973 K compared to that obtained at 1023 K for the same duration [24]. Optimum tensile properties at room temperature have been obtained by heat treatment 1313 K/4h + 1073 K/2h + 973 K/16h (yield strength :556 MPa, UTS : 983 MPa, % elongation : 26).This was designated as Microstructure B which consisted of maximum volume fraction of γ' precipitate (0.11). γ' precipitate was uniformly distributed in the matrix with a size of 18nm. Aging at 1073 K for 2 hours had also led to the precipitation of $M_{23}C_6$ type carbides in both intra and intergranular locations. Another batch of the solution annealed samples was subjected to a double aging treatment of 1173K/1h followed by 1023 K/8 h. This was designated as Microstructure C which consisted of intra and intergranular MC and $M_{23}C_6$ type carbides and γ' of 35nm diameter, 0.08 volume fraction.

1.1.2 316L(N) Stainless steel and welds

The chemical composition of 316L(N) SS and 316 weld metal used in this investigation is given Table 2. 316L(N) material obtained in mill-annealed condition was given a solutionising treatment at 1373 K/1h followed by a water quench. This heat treatment yielded an average grain size of 85 μm. Evaluation of elevated temperature LCF behaviour of 316L(N) stainless steel has received much attention in the recent years [12,15,19,25-31]. Nitrogen addition has been reported to be beneficial, and the LCF life has been found to saturate around 0.12% N [28]**.**

Table 2 Chemical composition of 316L(N) base metal and 316 weld metal (in wt%).

Alloy	C	Mn	Ni	Cr	Mo	N	S	P
316L(N) Base	0.002	1.75	12.0	17.0	2.4	0.078	0.002	0.023
316 weld metal	0.06	1.42	11.9	18.8	2.0	0.05	0.01	0.009

Welds are the weak links in structures. Most of the service failures are found to occur either in the HAZ or in the weld metal, which are more frequently associated with the presence of defects or microstructural inhomogeneities compared to the base metal. In austenitic stainless steel welds, ferrite introduced to reduce their tendency to hot cracking and micro fissuring, transforms to a hard and brittle phase known as phase, when these materials are exposed to elevated temperatures (773-1173 K) for extended periods of time, leading to low ductility creep ruptures when sufficiently high stresses are applied at elevated temperatures. Weld metal specimens were machined from weld pads prepared by shielded metal arc welding process using 316 electrodes. X-ray radiography was used for assessing the soundness of the welds followed by δ-ferrite measurements using a magne-gauge. The average ferrite number in the weld metal was between 4 and 5.

1.1.3 Modified 9Cr-1Mo Steel

Modified 9Cr-1Mo steel was obtained in the form of hot-forged rods of 70 mm diameter and also in the form of extruded tube of 30 mm wall thickness. The chemical compositions of these two product forms are given in Table 3. The normalizing treatment of this steel was carried out at 1313 K for 1 hour plus air cooling and tempering was done at 1033 K for 1 hour plus air cooling which resulted in a tempered martensitic structure.

Table 3. Chemical composition of modified 9Cr-1Mo ferritic steel (in wt%).

Product	Cr	Mo	C	V	Nb	Mn	Si	S	P	N	Ni	Fe
Forged bar	8.72	0.90	0.096	0.22	0.08	0.46	0.32	0.006	0.012	0.051	0.1	Bal.
Extruded pipe	8.2	0.92	0.11	0.13	0.09	0.48	0.3	0.005	0.018	0.051	0.12	Bal

2. Experimental

2.1 Low cycle fatigue testing

Fully reversed total axial strain controlled LCF tests were conducted at 773, 823 and 873 K in air on the 316L(N) base metal, 316 weld metal and modified 9Cr-1Mo specimens using a servo hydraulic machine equipped with a radiant heating facility. Cylindrical smooth specimens of 25mm gauge length and 10mm diameter were used in these tests. Tests were carried out with total strain amplitudes in the range ±0.25% to ±1.0% with a strain rate of 3×10^{-3} s^{-1}. Temperature effect was evaluated on 316L(N)

stainless steel and Modified 9Cr-1Mo steel in the temperature range 300-923 K at a strain range of ±0.6%. In Nimoinic PE-16 superalloy LCF tests were conducted at 723, 823 and 923 K at various strain amplitudes. In all these materials strain rate effects were evaluated in the range 3×10^{-5} s^{-1} to 3×10^{-2} s^{-1} at a strain amplitude of ±0.6%. Creep-fatigue interaction experiments were conducted by introducing tension/compression holds and tension plus compression holds in the range varying from 1 min. to 90 min. at 873 K at strain amplitudes ±1.0% and ±0.6%.

2.2 Metallography

The tested samples were sectioned parallel to the loading direction, polished, etched and examined under an optical microscope. The 316L(N) base metal and Nimonic PE-16 superalloy were etched using 70% HNO_3 while the etching of weld metal was done using a modified Murakami's reagent (30g. of KOH, 30g. of $K_3Fe(CN)_6$ in 150 ml water) at 363 K for 30 seconds. Fractography of the failed specimens was carried out using a scanning electron microscope and substructural changes were studied by transmission electron microscope. Samples for transmission electron microscopy (TEM) for 316L(N) base metal and Nimonic PE-16 superalloy were obtained from thin slices cut at a distance of 3 mm away from the fracture surface. These samples were first mechanically polished down to 250μm, and then electropolished in a solution containing 20% perchloric acid and 80% methanol at 243 K with a d.c. voltage of 10 V. The slip-band spacing measurements were performed on the longitudinal sections of the fatigue-tested samples using an SEM or an optical microscope with a graduated eye-piece depending upon the resolution needed for measuring the slip band spacing.

3. Results and Discussion

The results of this investigation are discussed under the following sections:

- Influence of microstructure – role of precipitates
- Strain rate and temperature effects
- Creep – fatigue – environment interactions – hold time effects

3.1 Influence of microstructure –role of precipitates

The initial and evolving microstructural changes would be reflected in the cyclic stress response curves. These changes have a pronounced influence on the microcracking. In this section, the role of precipitates in influencing

deformation (planar slip versus uniform deformation) and cracking - resulting from slip localization due to shearing of small size γ' precipitates and grain boundary cracking due to slip band impingement on grain boundaries - would be illustrated by examining results of tests on three microstructural conditions of Nimonic PE-16 superalloy. The role of carbide precipitates would also be brought out. The prior microstructure after double ageing (Microstructure B) consisted of ordered γ' precipitate of average size 18nm (Fig. 1).

The cyclic stress response was characterized, generally by an initial hardening to a peak stress followed by a softening regime under all testing conditions at 923 K (Figs. 2(a) through (c)). The initial hardening during cycling has been attributed to dislocation-dislocation and dislocation-γ' precipitate interactions. The operative deformation mechanisms are found to depend on the size of the γ': namely, shearing for very fine precipitates and Orowan looping for coarse precipitates (for γ' with d= 35nm). In Microstructure A the contribution to hardening comes from dislocation – dislocation interaction. However, when shearing of γ' precipitates takes place, the contribution to hardening is derived also from dislocation accumulation on γ' precipitates initially and order hardening contribution from the precipitate once it is subjected to shearing. When precipitates are coarse, they are circumvented by Orowan looping process, as in the case of Microstructure C [4]. The dislocation-precipitate interaction displaces the dislocations from the primary slip planes. This process repeats, eventually resulting in homogenization of slip due to linkup in three dimensions.

Various mechanisms have been presented in the literature to explain the cyclic softening in precipitation hardened systems. The two mechanisms which are widely accepted are (1) disordering of γ' due to mechanical scrambling [32,33] and (2) reduction in the size of the precipitate due to repeated shearing [34]. The mechanism underlying the cyclic softening observed in fatigue testing of Nimonic PE-16 was examined earlier by the present authors [11]. Based on TEM studies on samples interrupted to various fractions of fatigue life, it has been established that the reduction in the size of γ' is responsible for cyclic softening. Figure 3 shows the cyclic stress response of Microstructure B fatigue tested at 823 K at strain amplitude of ±0.6%. TEM microstructure of samples fatigue tested to various fractions of fatigue life are superimposed in this diagram. These studies revealed that dislocations are accumulated in the first few cycles as shown in samples interrupted after 10 cycles representing the hardening stage in the cyclic stress response and partial slicing of the γ′ precipitates are observed after 80 cycles (representing the softening stage). However, after 300 cycles (representing the saturation stage) all the γ' precipitates are

completely sliced by the dislocations and spherical particles are no longer present in the sample. It is observed that the precipitates are completely offset and they cease to act as obstacles to the motion of dislocations. Thus cyclic softening is attributed to reduction in the size of γ'.

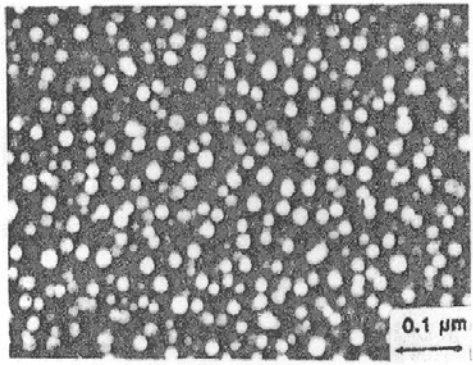

Fig. 1 Dark field micrograph showing γ' precipitate morphology before testing.

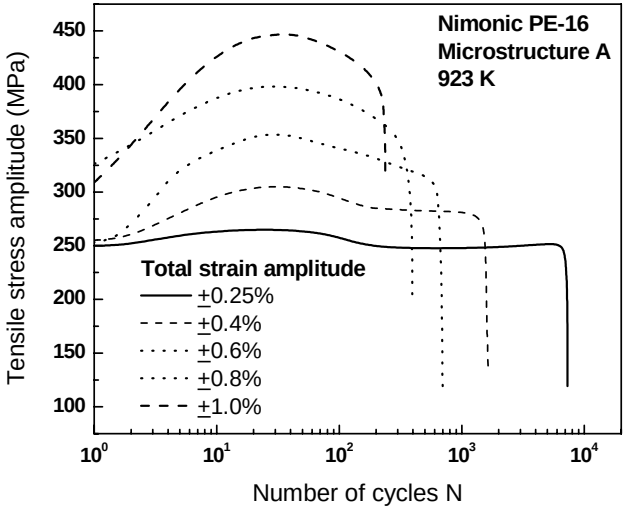

(a) Microstructure A at 923 K

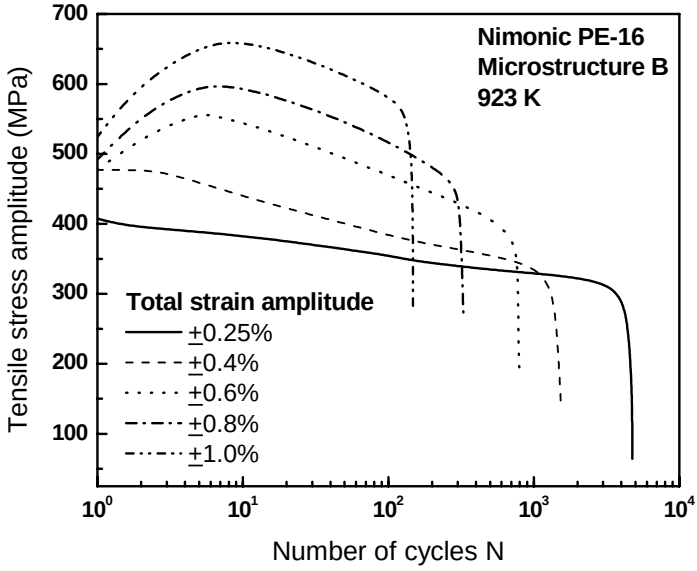

(b)Microstructure B at 923 K

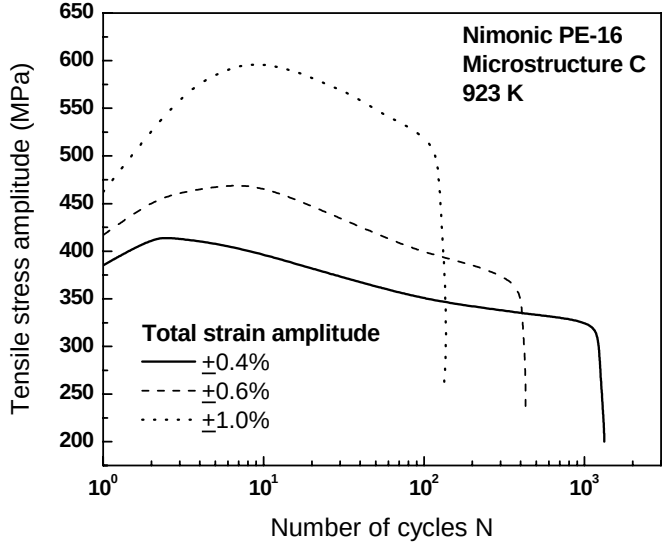

(c) Microstructure C at 923 K

Fig. 2 Cyclic Stress Response of Nimonic PE-16.

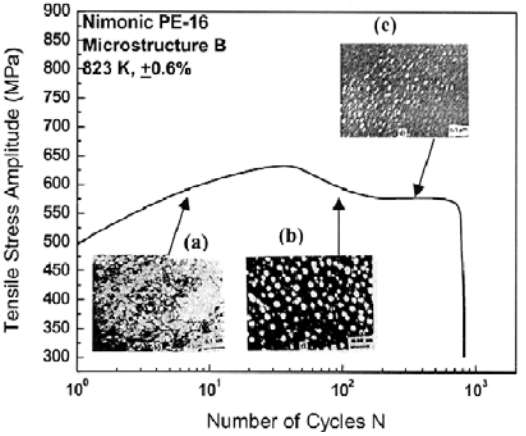

Fig. 3 Cyclic stress response of Nimonic PE-16, Microstructure B at 823 K (insert (a) Dislocation accumulation in slip bands after 10 cycles, (b) dark field micrograph of γ' after 80 cycles and (c) dark field of micrograph of γ' after 300 cycles).

In Microstructure A, softening has been attributed to shearing of fine γ' formed during testing at 923 K. In Microstructure C, the size of the γ' particles (35nm) is too large to permit shearing. Hence, Orowan looping is predominant. However, the evidences have been reported for the fresh precipitation of fine γ' at 923 K. The lower volume fraction of γ' in Microstructure C (0.08) has resulted in the fresh precipitation of γ' during testing. The occurrence of superdislocation pairs, Fig. 4, indicates that cyclic softening in this microstructure is due to shearing of fine γ' formed during testing.

Fatigue life and fracture behaviour depend on the deformation processes operating during cycling. Fatigue life of Nimonic PE-16 alloy was found to be influenced by the amount and size of the precipitates (as it determines the slip processes), Fig. 5. Material in solution annealed condition (A) showed the highest fatigue life followed by B and then C. The superior fatigue life of Microstructure A can be attributed to the planar slip mechanism, Fig. 6(a) which promotes increased reversibility in slip processes. Microstructure A exhibits transgranular fracture, Fig. 6(b) and the reversibility in slip increases the resistance of A to both transgranular crack initiation and propagation and leads to the highest fatigue life.

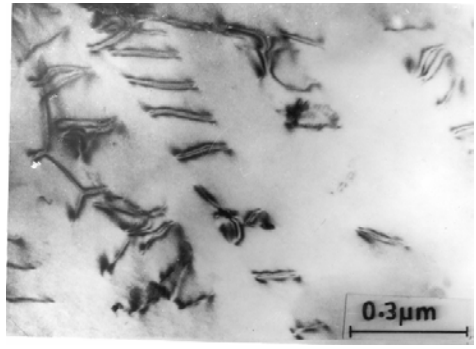

Fig. 4 Superdislocation pairs in Microstructure C, strain amplitude ±1.0% - indicating precipitate shearing and strain localization.

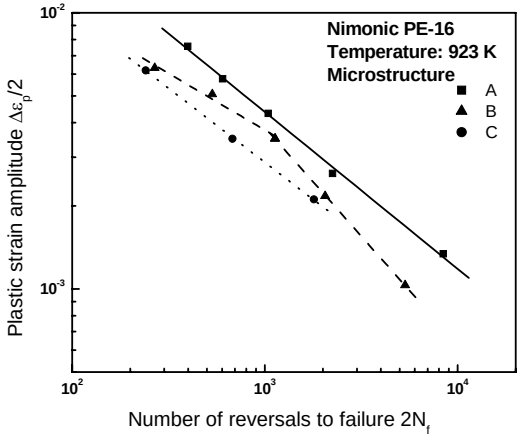

Fig. 5 Fatigue life plot for Nimonic PE-16 microstructure A, B and C, 923 K.

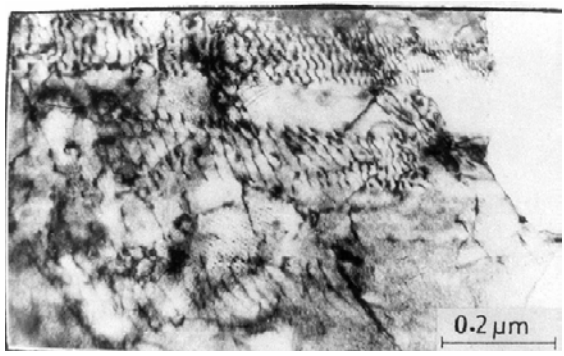

(a) Planar dislocation arrangement, microstructure A, strain ampl. ±0.4%

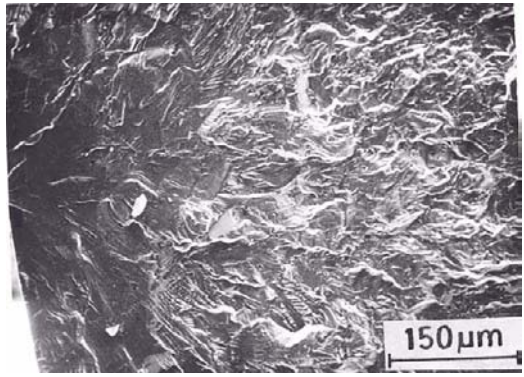

(b) Transgranular cracking, microstructure A, 923 K, strain ampl. ±0.4%

Fig. 6 Microstructure arrangement.

The beneficial effects of planar slip on fatigue life have been attributed to a high degree of slip reversibility at the propagating crack tip [35]. A lower crack propagation rate when γ′ particles are sheared during deformation has also been reported in an Fe-Ni-Al alloy [36].

However, the beneficial effect of planar slip may get eclipsed in situations where the microstructure is such that (1) stress concentrations associated with the dislocation pileups cause intergranular cracks and (2) localized deformation in widely spaced slipbands cause transgranular cleavage cracks. In such situations, homogeneity of the slip process will be beneficial to fatigue life. The two-slope behaviour observed in fatigue life plot, Fig. 5 and cyclic stress strain curve, Fig. 7 for Microstructure B has been rationalized on the above basis. In Microstructure B, precipitate shearing mechanism is found to be predominant in planar slipbands, since γ′ size is only 18nm. This enhances the reversibility of the slip processes. Nevertheless, over the strain amplitudes investigated, the variation of the slipband spacing with plastic strain amplitude for Microstructure B shows a deviation from the general trend, especially at low strain regimes, Fig. 8. At low strains, slip is rather concentrated in specific bands, producing inhomogeneous deformation, Fig. 9(a). These slipbands produce pile-ups at the grain boundaries, causing stress concentration and mixed mode fracture Fig. 9(b). Furthermore, in Microstructure B, the grain boundaries are decorated with $M_{23}C_6$ carbide precipitates with accompanying reduction in the ductility. Hence, the stress concentrations associated with the pileups cause carbide-matrix interface decohesion and intergranular cracking. At higher strains, the dislocation substructure becomes more homogeneous because of the operation of multiple slip. This results in lower stress concentrations

at the grain boundaries and a reduced susceptibility to intergranular failure, Fig. 9(c).

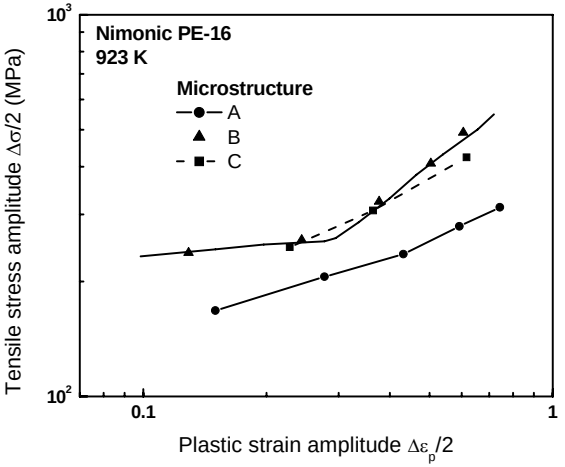

Fig. 7 Cyclic Stress-Strain Curves of Nimonic PE-16, Microstructures A, B & C at 923 K.

The two-slope behaviour has also been reported in Nimonic PE-16 at room temperature[37]. It has been found that at high strains, intersections of densely packed dislocations in three different slipbands led to a break-down of slip planarity, which reduced the stress concentration due to pile-ups. The two-slope behaviour in the Coffin-Manson life plot has also

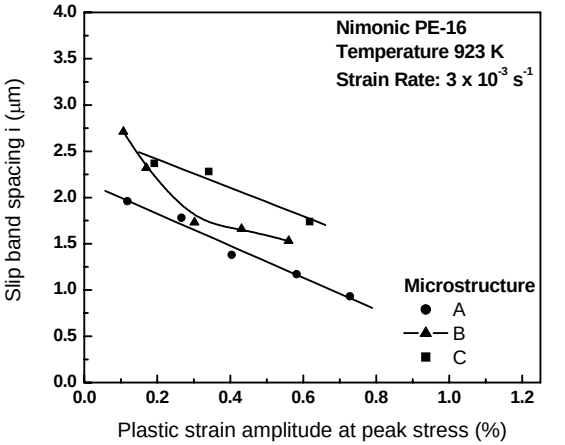

Fig. 8 Variation of slip band spacing (i) with plastic strain amplitude for Nimonic PE-16, microstructures A, B and C.

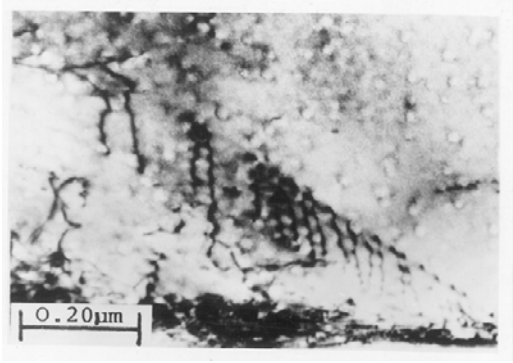

(a) Planar dislocation in microstructure B with, strain amplitude ±0.4%

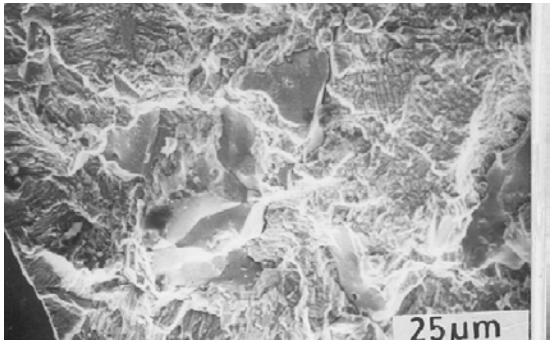

(b) Mixed mode cracking at low strain in microstructure B, ±0.4%

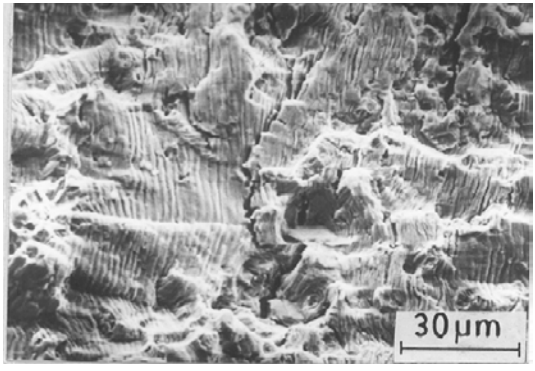

(c) Transgranular fracture at high strain for microstructure B, ±1.0%

Fig. 9 Microstructure in Nimonie PE-16.

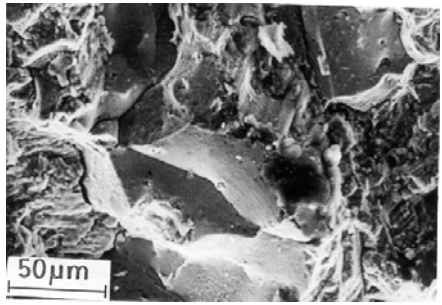

Fig. 10 Facetted Fracture in Microstructure C, 923 K, strain amplitude ±0.6%.

been reported in various other alloy systems, e.g. dual -phase steels [38], aluminium alloy[39] and Nimonic 80 A[34]. In these investigations, the change in the Coffin-Manson slope has been ascribed to a change in deformation mechanism from slipband formation at low strains to twinning and grain boundary rotation at high strains.

In double aged condition C precipitate shearing with superdislocation pair was observed (Fig. 4). Further, evidences for in-situ precipitation were found in several areas [4]. Deformation in Microstructure C is clearly demarcated by regions where Orowan looping mechanism (homogeneous deformation) is operating and places where strain localization due to precipitate shearing are predominant. Since overcoming of large γ' particles requires either cross slip or Orowan loop formation, slip is not reversible as in the cutting process. The Orowan looping process in Microstructure C is, therefore, consistent with a higher crack propagation rate. In addition, the microstructure deforms in a heterogeneous manner and exhibits large slipband spacings, Fig. 8. The wider slipband spacing in Microstructure C is considered to result from the strain localization effects in regions where fine γ' precipitates form during testing. Since shearing of the fine γ' is more favourable mechanism compared to looping of coarse γ' (originally present in the alloy), slip will be mainly restricted to these soft regions. Accordingly, in Microstructure C, due to the precipitation of fine γ' in widely spaced regions, it behaves like a heterogeneous matrix consisting of a soft region and a hard region, and strain will be unequally distributed among them. This localization is expected to have two consequences: (1) faceted fracture resulting from channelization of dislocations due to precipitate shearing, Fig. 10 and (2) de-cohesion of grain boundary carbides caused by dislocation pileups. Thus, in Microstructure C, secondary cracks are created in the matrix and on the grain boundaries, leading to an accelerated fatigue crack propagation. The reduced fatigue life of the Microstructure C, is therefore, attributed to the presence of a large number of internal

cracks and reduced slip reversibility associated with the Orowan looping process.

The effects of testing temperature and frequency/strain rate on the LCF behaviour of structural alloys used in high temperature applications have been studied using balanced loading waveforms(equal ramp rates in tensile-going and compressive-going directions) as these parameters influence cracking behaviour and hence life [10,15-18, 40,41]. With decrease in frequency/strain rate at high testing temperatures deformation mechanisms such as dynamic strain ageing (caused by solute dislocation interactions) and oxidation become predominant.

3.2 Strain rate and temperature effects on cyclic properties and fatigue life

3.2.1 Role of dynamic strain ageing

Cyclic stress response (CSR) as a function of strain rate on 316L(N) SS at 823 K is shown in Fig. 11(a). At 773 and 823 K the degree of hardening increased significantly with decreasing strain rate and maximum hardening is observed at the lowest strain rate of 3×10^{-5} s^{-1} , Fig.11(a) [15]. The negative strain rate stress response observed at these temperatures and strain rates is also reflected in a negative strain rate dependence of the half-life stress, Fig. 11(b). Further, negative temperature dependence of CSR in 316L(N) SS in the temperature range 573 K to 873 K is shown in Fig. 11(c). The negative strain rate stress response in cyclic stress response curves has also been noticed in Nimonic PE-16 Superalloy at various temperatures, (typically at 823 K, Fig. 11(d)). These are the various manifestations of DSA operating in these alloys.

Dynamic strain ageing was found to influence the deformation and fracture behaviour of the 316L(N) SS and Nimonic PE-16 under specific strain rate and temperature conditions. The increase in stress response in the DSA regime has been found to be related to an increase in the dislocation density in between the slip bands. Figures 12(a) and (b) give a comparison between dislocation densities observed at higher strain rates and lower strain rates respectively in between slip bands. Condition conducive to DSA results in higher dislocation densities, Fig. 12(b). In 316L(N) stainless steel planar slip bands are observed in the DSA operating range whereas cell structure is noticed in the non-DSA regime (Figs. 13(a) and (b) respectively). Enhancement of slip planarity (presence of planar slip) in the DSA range has also been reported in AISI 310 steel [42]. Further, DSA also results in increased degree of localization of slip which is reflected in an increase in slip band spacing. Typical slip band spacing values as a

function of strain rate and temperature as observed in Nimonic PE-16 superalloy for Microstructures A and B are shown in Figs. 14(a) and (b) respectively. It is found that slip band spacing is larger in the DSA regime (lower strain rates) indicating enhanced slip localization. The solute dislocation interaction during DSA restricted cross slip of dislocations and increased slip planarity. Impingement of planar slip bands on the grain boundary leads to intergranular cracking typically as shown in Fig. 15. Intergranular cracking associated with slip band impingement in the DSA range was also observed in 304 stainless steel [40]. Enhanced intergranular cracking associated with slip band impingement led to reduced fatigue life in the DSA regime for Nimonic PE-16 at low strain rates at 723 and 823 K, Fig. 16. At 923 K oxidation reduces the fatigue life at low strain rates in this alloy. The role of oxidation in reducing life at 923 K will be discussed in the subsequent sections.

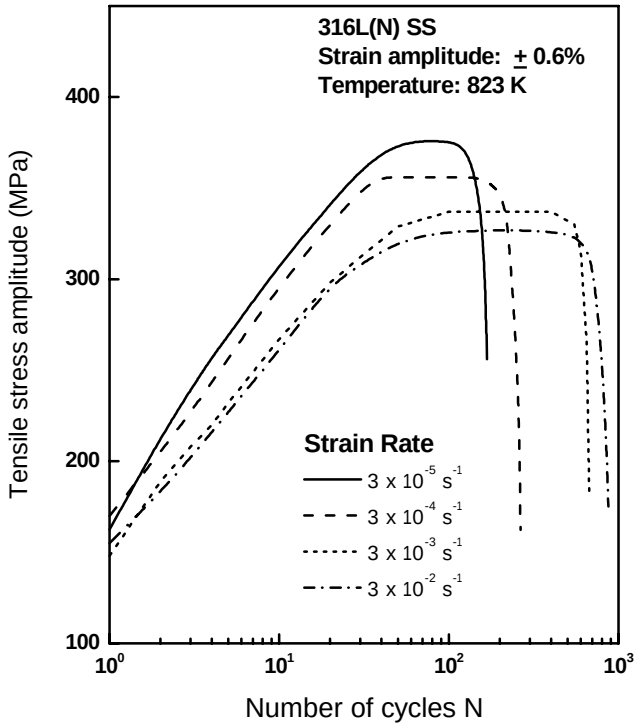

(a) Cyclic stress response at 823 K

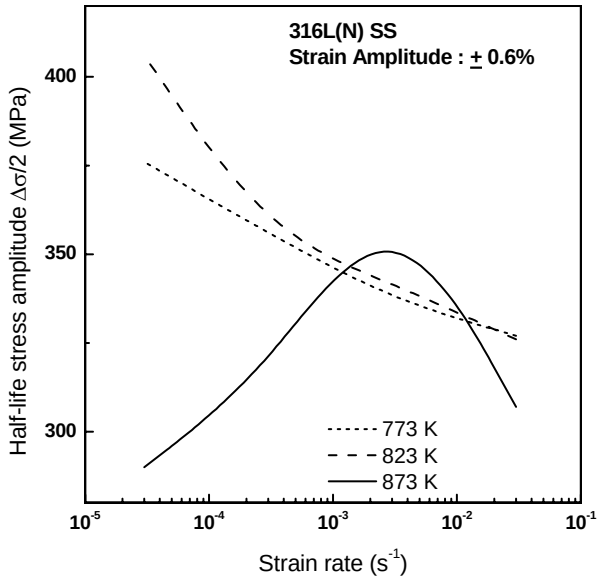

(b) Variation of half-life stress amplitude for 316L(N) SS

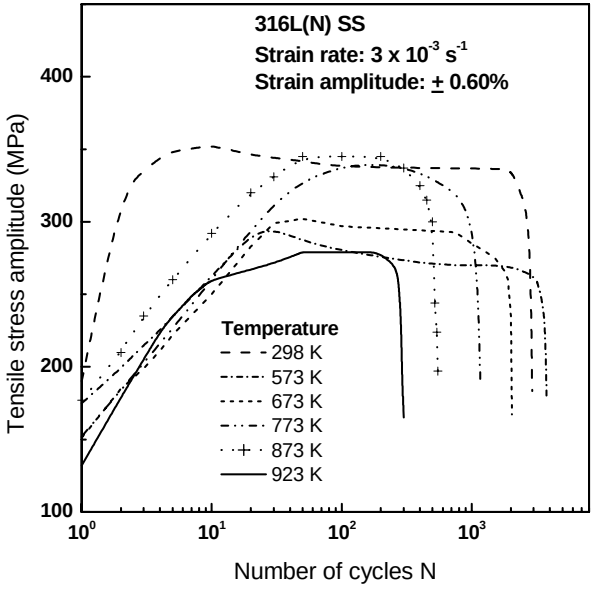

(c) Negative temperature dependence on cyclic stress response

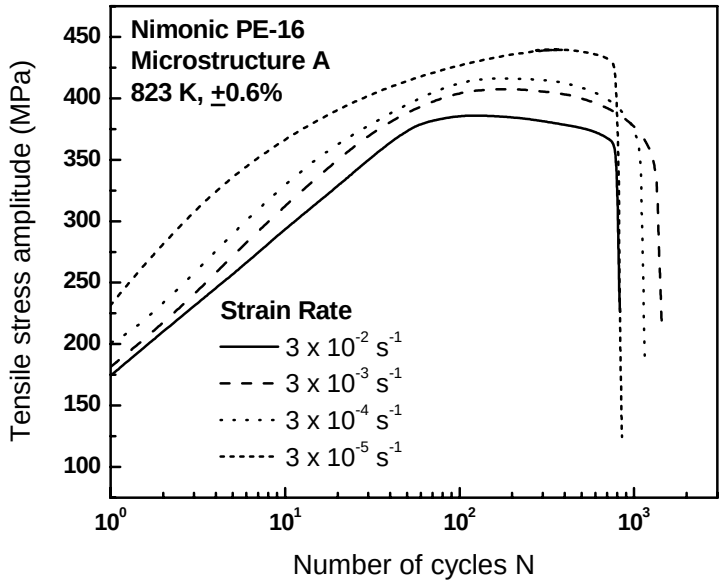

(d) Cyclic stress of Nimonic PE-16 with microstructure A at 823 K

Fig. 11 Strain rate effect.

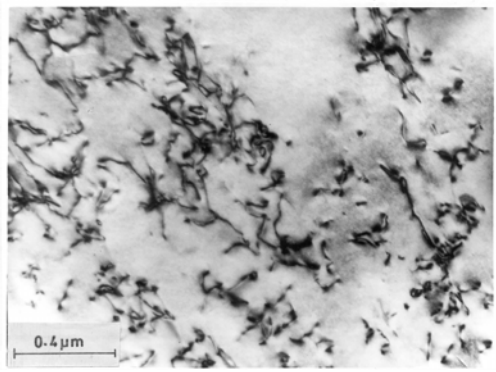

(a) Low dislocation density

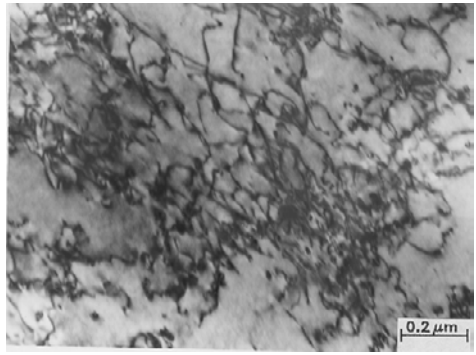

(b) High dislocation density

Fig. 12 Microstructure at 823 K, 3 x 10^{-3} s^{-1} and strain amplitude ±0.6%.

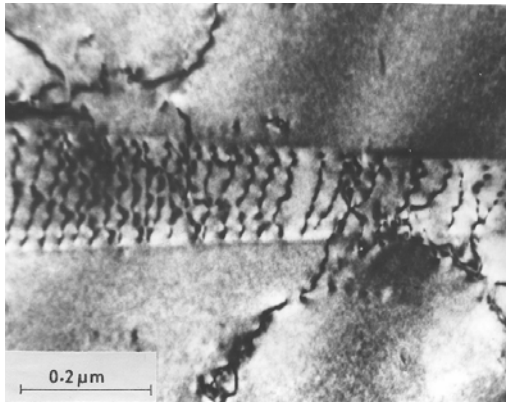

(a) 873 K

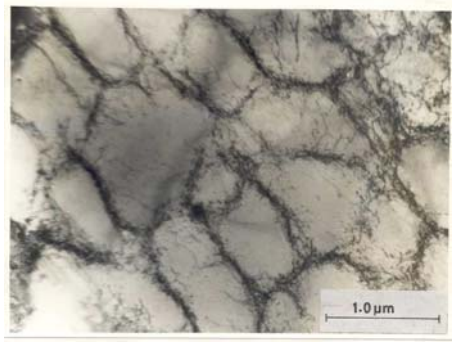

(b) 573 K

Fig. 13 Well developed cell microstructure at strain amplitude of ±0.6%.

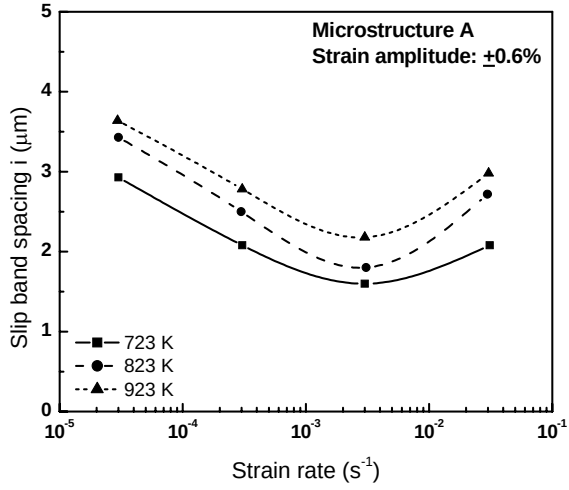

(a) Microstructure A

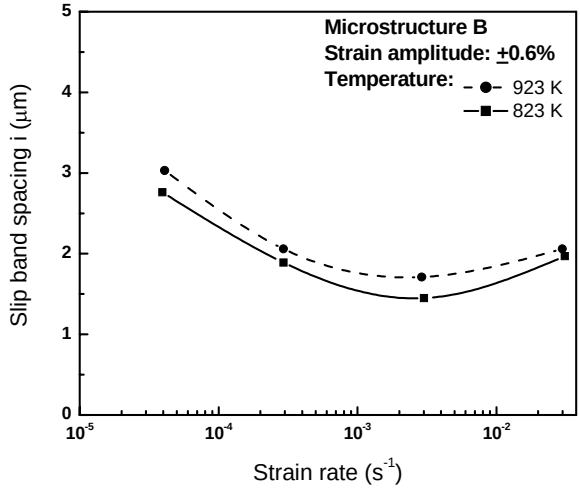

(b) Microstructure B

Fig. 14 Variation of average slip band spacing Nimonic PE-16 with strain amplitude ±0.6%.

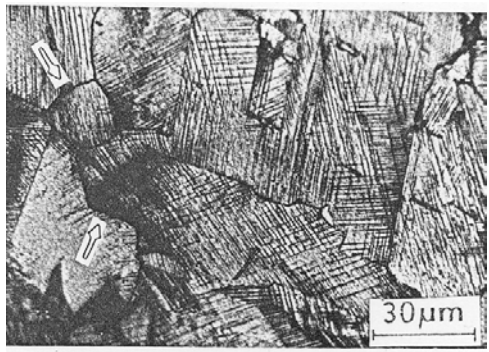

Fig. 15 Grain boundary cracks associated with impingement of slip bands in PE-16 Superalloy, Microstructure A, 3×10^{-5} s^{-1}, strain amplitude ±0.6%.

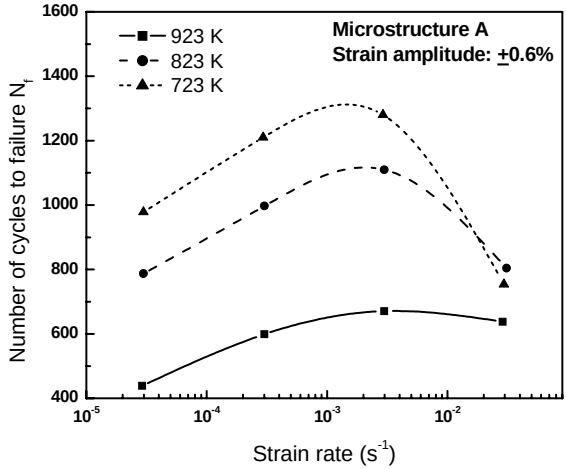

Fig. 16 Variation of fatigue life with strain rate in Nimonic PE-16, strain amplitude ±0.6%.

In 316L(N) SS a significant reduction in fatigue life is noticed when testing strain rate is reduced to 3×10^{-5} s^{-1} from 3×10^{-2} s^{-1} at temperatures 773, 823 and 873 K (Fig. 17). It is noticed from this figure that with increase in temperature, fatigue resistance generally decreases except for specific cross overs at strain rates < 3×10^{-3} s^{-1}. That is at strain rates below 3×10^{-3} s^{-1} , fatigue resistance is lower at 823 K compared to that at 873 K. These observations can be correlated with the influence of DSA on the deformation and fracture behaviour.

The influence of planar slip on cracking can be assessed by measuring the total length of intergranular and transgranular secondary crack density in the DSA regime. Crack density (crack length per unit area) as a function

of strain rate at 773 K (typically for 316L(N) SS) is shown in Fig. 18(a) and crack length distribution in Fig. 18(b). The secondary crack density was found to be maximum in the DSA regime (low strain rates) for this alloy. With decrease in strain rate both intergranular and transgranular crack density increased indicating accelerated crack initiation and propagation. Further, very long cracks (a consequence of crack coalescence) are seen at low strain rates. More number of longer cracks were observed at 823 K at lower strain rates compared to 873 K. (Figs. 18(c) and (d). The stress concentration associated with the intersection of planar slip bands with the grain boundaries has contributed to the enhanced internal grain boundary cracking and reduced lives at low strain rates in these alloys. Since crack coalescence can lead to faster crack propagation, a reduced fatigue life is observed at strain rate – temperature conditions where long cracks are observed.

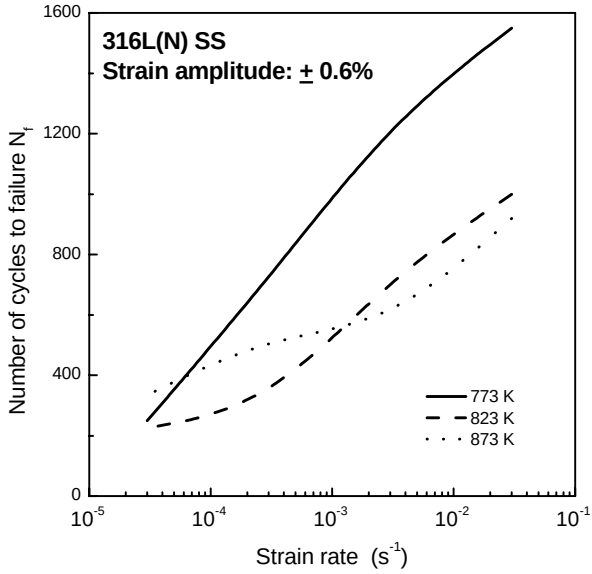

Fig. 17 Variation of fatigue life with strain rate in type 316L(N)SS, strain amplitude ±0.6%.

It must be pointed out that within the strain rate employed, DSA operates over the temperature range of approximately 573 to 873 K in 304 SS [40]. DSA enhances the degree of inhomogeneity of deformation during LCF by solute locking of slow moving dislocations between slip bands [9]. Presumably, the dislocation velocities inside the slip bands were too high for dynamic ageing of mobile dislocations to take place and consequently

DSA enhanced the partitioning of strains into separate regions characterized by high and low amplitudes of dislocation movement leading to enhanced inhomogenity of deformation [43]. Further slow moving dislocations become aged by the solute atmospheres and additional dislocations are generated to maintain the imposed deformation rate. This process caused an increase in total dislocation density. The negative strain rate dependence of cyclic stress response over the temperature and strain rate range where DSA operates results from an increase in total dislocation density during deformation. The matrix was hardened during DSA, causing an increase in flow stress needed to impose the same total strain during successive cycles.

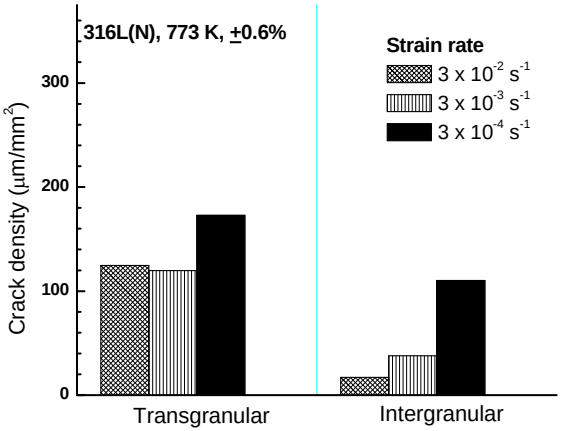

(a) Crack density as a function of strain rate at 773 K

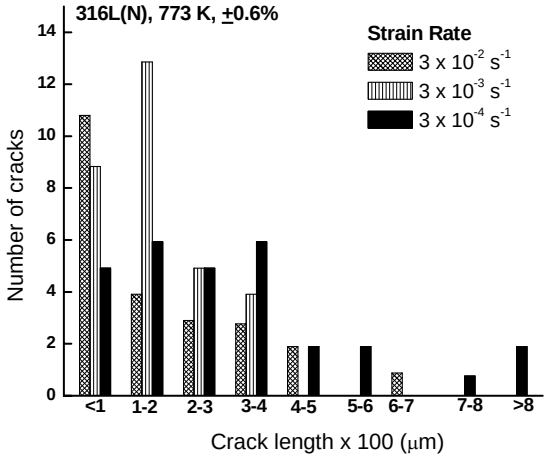

(b) Crack length distribution as a function of strain rate at 773 K

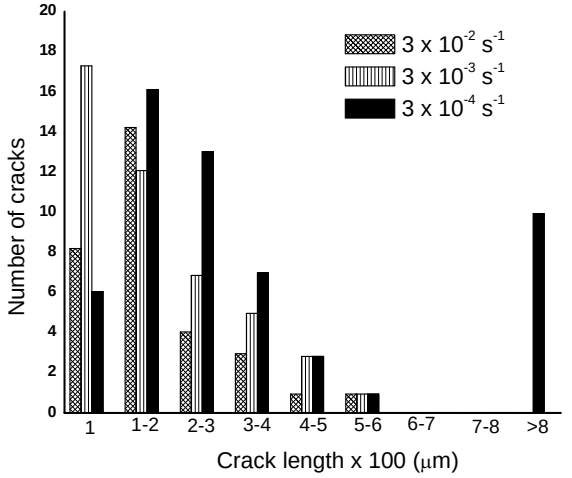

(c) Crack length distribution as a function of strain rate at 823 K

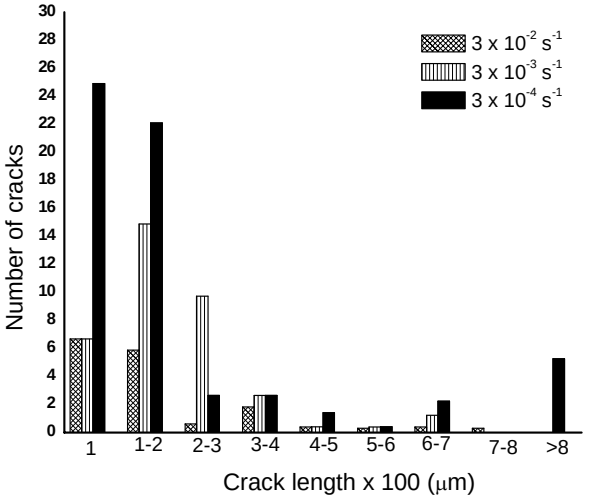

(d) Crack length distribution as a function of strain rate at 873 K

Fig. 18 Crack distribution for different temperation at strain amplitude ±0.6%.

The influence of DSA on number of cycles to transgranular crack initiation and evolution of the microcrack density with number of cycles have been investigated in Alloy 800H [44]. In this study, a comparison has been made with test results in vacuum to eliminate the effect of environment on crack initiation. It has been found that DSA leads to: (a) an overall decrease in the number of cycles to crack initiation, (b) an appreciably higher

crack density, and (c) reduction in fatigue life. The enhanced transgranular crack density observed under DSA conditions may be a consequence of the increased slip step height formed at the free surface. At medium to high strain levels, slip steps play an important role in planar slip alloys, in which fine homogeneous distribution of slip confers optimum resistance to crack initiation. The increased tendency for transgranular crack initiation in DSA regime could be due to the increased slip step height at the surface.

Dynamic strain ageing has also been reported to cause a faster reduction in life by way of rapid crack propagation where transgranular fracture is dominant. Higher response stresses developed during cyclic deformation can lead to a larger stress concentration at the crack tip, which would account for increased crack growth rates and hence a reduced number of cycles in the crack propagation stage [10,15].

3.2.2 Role of oxidation at high temperatures and low strain rates

In order to assess the influence of oxidation at high temperatures and low strain rates detailed studies have been conducted on Modified 9Cr-1Mo steel. The dependence of fatigue life on test temperature (300-873 K) at a constant strain amplitude of ±0.6% and strain rate of 3×10^{-3} s^{-1} is plotted in Fig. 19. The alloy exhibited a decrease in fatigue life with increasing temperature. The effect of temperature on life was more pronounced at lower strain amplitudes, as seen in Fig. 20. Further, the variation of fatigue life with strain rate showed a maximum at the intermediate strain rate of 3×10^{-3} s^{-1} at all the temperatures investigated (Fig. 21).

Extensive branching of transgranular cracks is noticed on the tested samples associated with second phase boundaries especially at high strain amplitudes of testing, Fig. 22(a). Further, microcracking perpendicular to the loading direction in the vicinity of the main crack is noticed at a strain rate of 3×10^{-2} s^{-1}, Fig. 22(b). However, at lower strain rate of 3×10^{-3} s^{-1}, secondary crack density was found to be much lower, Fig. 22(c). Hence the reduction of the fatigue life at high strain amplitudes and higher strain rates could be rationalized based on the accelerated crack initiation and accelerated crack propagation associated with crack linkage observed in this alloy.

With decrease in strain amplitude from ±1.0% to ±0.25%, crack branching was reduced.[16]. Ingress of oxygen and oxidation of surface-connected grain boundaries and slip bands were observed at lower strain amplitudes and lower strain rates of testing. Failure at 873 K was found to be strongly influenced by oxidation, particularly at lower strain amplitude of testing (±0.25%). Figure 23(a) shows a SEM fractograph depicting

crack initiation and propagation being assisted by oxidation at the strain amplitude of ±0.25%. The optical micrograph in Fig. 23(b) shows cracks filled with oxide debris obtained in low strain rate testing conditions. It may be mentioned that the lower strain rates at elevated temperature provide adequate time for the environmental interaction to take place, which accelerates both the crack initiation and propagation phases. In contrast, under conditions of low temperatures and high strain rates, oxidation effects were not significant.

The detrimental effect of oxidation was reflected in transgranular crack initiation and stage I and stage II crack propagation. The reduction in the LCF life under high temperature and low strain rate conditions could thus be ascribed to the enhanced environmental effects. Both crack initiation and propagation were seen to be transgranular under all the testing conditions investigated.

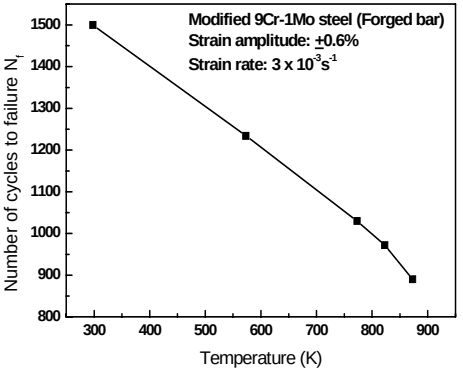

Fig. 19 Temperature effect on fatigue life of Modified 9Cr-1Mo steel (forged bar).

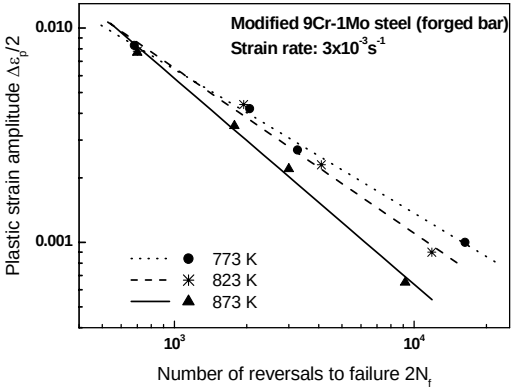

Fig. 20 Fatigue lives at various temperatures and strain amplitudes of Modified 9Cr-1Mo steel.

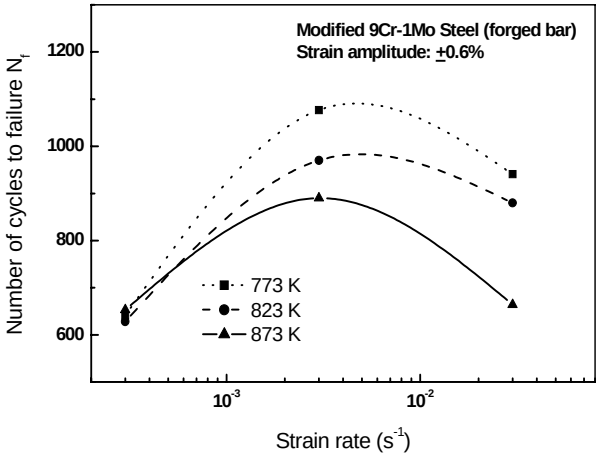

Fig. 21 Variation of LCF life with strain rate at different temperatures, Modified 9Cr-1Mo steel.

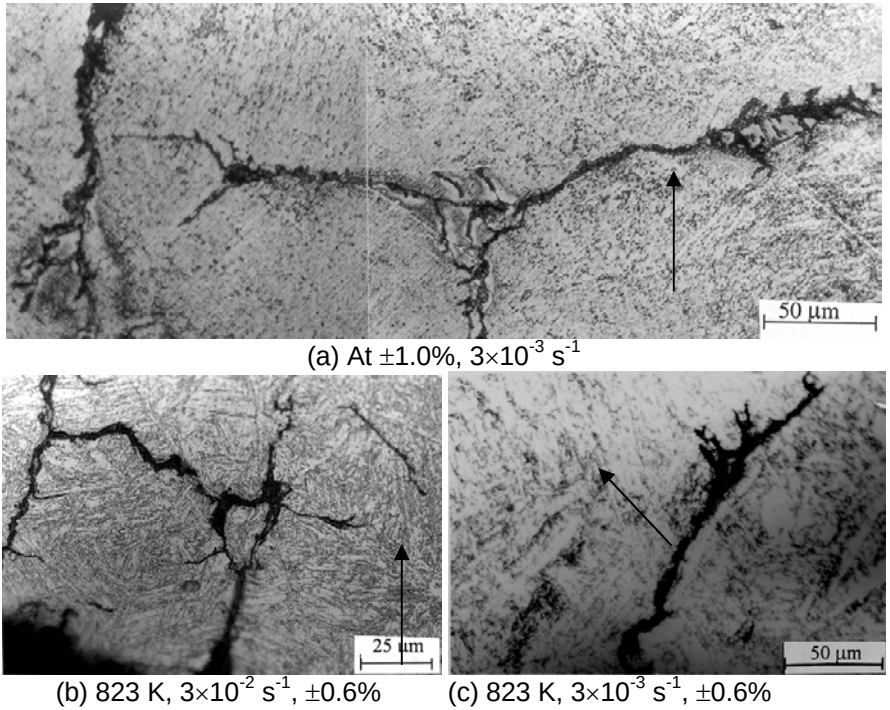

Fig. 22 Crack propagation at 873 K (arrows indicate the loading direction), Modified 9Cr-1Mo steel (forged bar).

Measurement of the distribution of the secondary crack number density versus crack length at strain amplitudes of ±0.6% and ±1.0% in the temperature range of 300-873 K is shown in Figs. 24(a) and (b), respectively. It is observed that the total number of secondary cracks was higher at higher strain amplitudes (±1.0%, Fig. 24(b)) of testing compared to ±0.6% (Fig. 24(a)). However, contrary to expectations, it was noticed that the number of long secondary cracks decreased with increase in the test temperature from 300 to 873 K, Fig. 24(a). This could be understood from the fact that these measurements were taken at failure. At 873 K, since the alloy was exposed to lesser number of cycles before failure (which is assisted by oxidation) and experienced lower stresses compared to that at 300 K, the secondary cracks at higher temperatures (773, 873 K) did not grow in length. However, at larger strain amplitudes (±1.0%) where oxidation effects were less apparent, significant differences in the crack density with temperature did not exist.

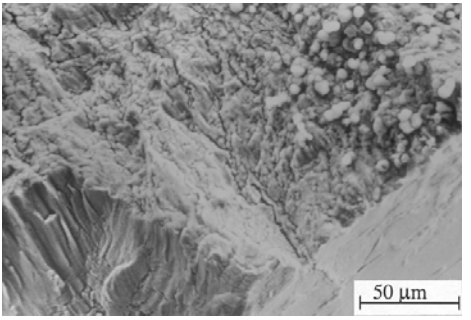

(a)Oxidation-assisted crack initiation and propagation at ±0.25%

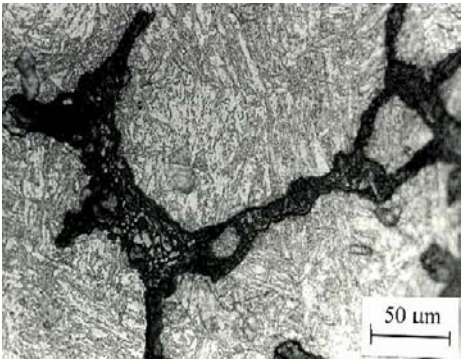

(b)Modified 9Cr-1Mo steel (forged bar) at ±0.6%.

Fig. 23 Cracking at 873 Kand 3×10^{-4} s^{-1}.

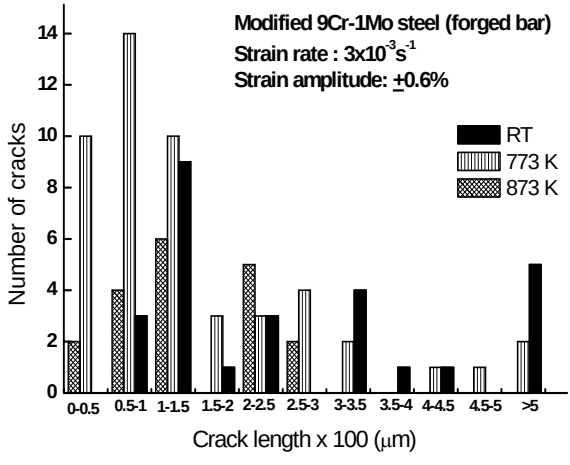

(a) At ±0.6%

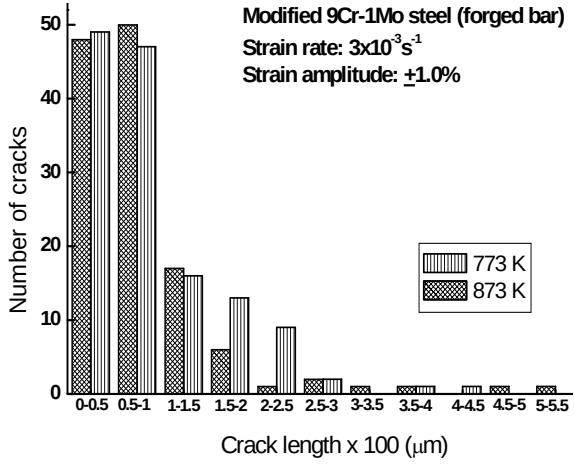

(b) At ±1.0%

Fig. 24 Frequency distribution of secondary cracks in Modified 9Cr-1Mo steel (forged bar) .

3.3 Creep-fatigue-environment interaction - Hold time effects

Hold times are introduced in a strain cycle either in tension, compression or tension plus compression peaks. This leads to creep-fatigue interaction. However, in air testing oxidation effects also play a role in degrading the

fatigue life of the material at high temperatures. Tension hold is found to be more damaging than compression hold in stainless steels namely SS 304[45], 304L[46], 316[47], 316L[48], 316L(N)[49] and Alloy D9 [50] whereas, the converse holds good for 2.25 Cr–1Mo[51, 52], IMI 829 [53], nickel base alloys [54,55] and Modified 9Cr-1Mo [18, 56-58]. In the following section studies conducted by the present authors to understand the hold time effects on 316L(N) SS and its welds are discussed first followed by the influence of hold time on Mod.9Cr-1Mo steel.

3.3.1 316L(N) Stainless steel base metal and weld metal

The introduction of strain hold at the peak strain in tension/compression in total strain controlled testing causes stress relaxation leading to creep-fatigue interaction. The creep-fatigue lives of the 316L(N) base metal and 316 weld metal as a function of the length of the hold time are shown in Fig. 25. It could be seen that, at 873 K, in both continuous cycling and hold time tests, 316 weld metal showed a higher fatigue endurance compared to the base metal. It was also evident that the hold time effect on fatigue life was dependent on the position as well as the duration of hold. Compared to continuous cycling conditions, imposition of hold at peak strain was found to decrease the fatigue life. Tensile hold was observed to be more damaging than the compression hold. Further, a significant reduction in fatigue life was observed by increasing the duration of tensile hold.

The greater creep fatigue life of the weld metal compared to the base metal at 873 K can be correlated to the crack propagation differences between the base metal (Fig.26(a)) and weld metal, Fig. 26(b). In base metal under 1 min. tension hold the crack initiation occurs in intergranular mode and crack propagation by mixed mode, Fig. 26(a). However in weld metal microstructural changes influences the microcrack growth (crack growth slowed down by crack deflection), Fig. 26(b). The fine duplex austenite-ferrite microstructure in 316 weld metal with its many transformed phase boundaries at these testing conditions, offered a greater resistance to the extension of the fatigue cracks by causing deflection of the crack paths compared to the base metal. δ ferrite got transformed to brittle σ phase during testing. Crack deflection at the transformed δ phase boundaries was found to increase the crack propagation resistance causing an enhanced fatigue life.

At a given strain amplitude, the relaxed stress during hold time at half life for the 316L(N) base metal is provided in Table 4. In all the hold time tests, rapid stress relaxation occurred in the first few seconds of the strain hold, followed by a slower rate of stress relaxation during the rest of the hold period. During stress relaxation, conversion of elastic to plastic strain

took place and the strain rates were typically of the order of 10^{-4} s^{-1} to 10^{-8} s^{-1} during the slow relaxation period. The build up of tensile inelastic strain led to the accumulation of grain boundary creep damage in the form of cavities. With increase in the duration of the hold time a significant amount of stress relaxation took place, leading to enhanced build up of intergranular creep damage. This conforms with the magnitude of σ_r developed during stress relaxation (Table 4) i.e. σ_r increases with increase in the length of the hold time and is greater in tension hold compared with the compression hold.

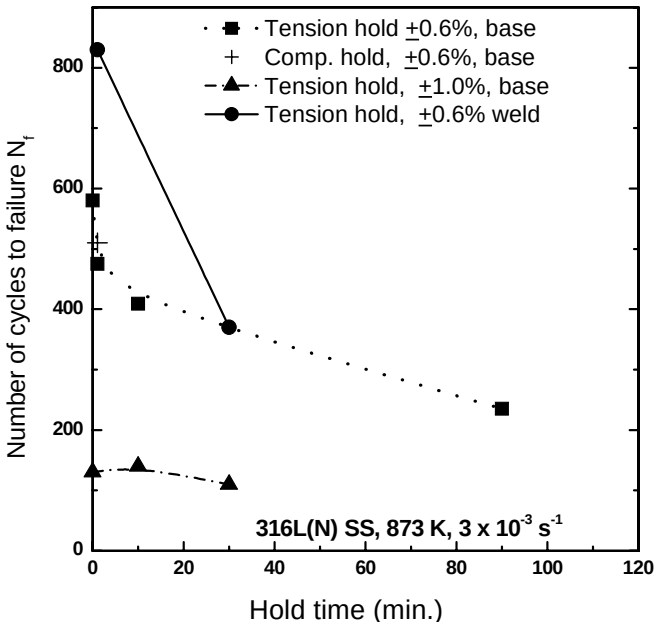

Fig. 25 Fatigue life as a function of hold time.

It must be pointed out that the absolute magnitude of the σ_r alone could not be associated with the damage that determines the creep-fatigue life. As a function of the strain amplitude, it was observed that σ_r was relatively large at high strain amplitudes. However, the degree of reduction in life during hold time tests, defined as N/N_f (N, the fatigue life during hold-time tests and N_f the corresponding fatigue life in continuous cycling) was found to be larger at lower strain amplitudes, compared to higher strain amplitudes of testing (Table 4). The strain rates during relaxation at higher strain amplitudes were generally higher than those observed at low strain amplitudes of testing. In general, the relaxation strain rates of magnitude >

10^{-4} s^{-1} observed at high strain amplitudes are typically expected to cause matrix deformation, while those observed at low strain amplitudes namely, $\leq 10^{-4}$ s^{-1}, corresponded to that of creep deformation. It has been suggested that relaxation strain rates $\leq 10^{-4}$ s^{-1} generally contribute to grain boundary damage and cause a greater reduction in life [59, 60].

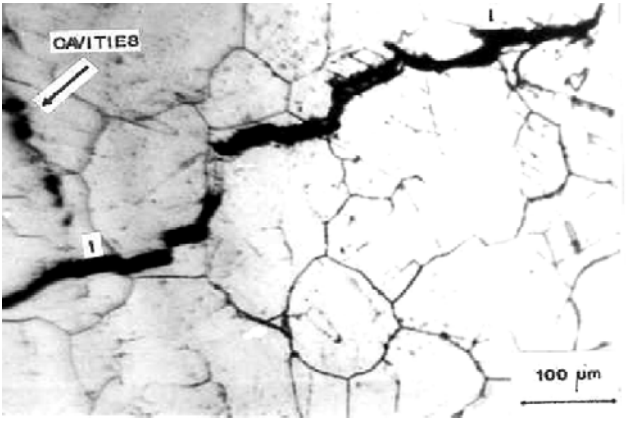

(a) Mixed mode crack growth in 1 min. tension hold, 316L(N) base metal

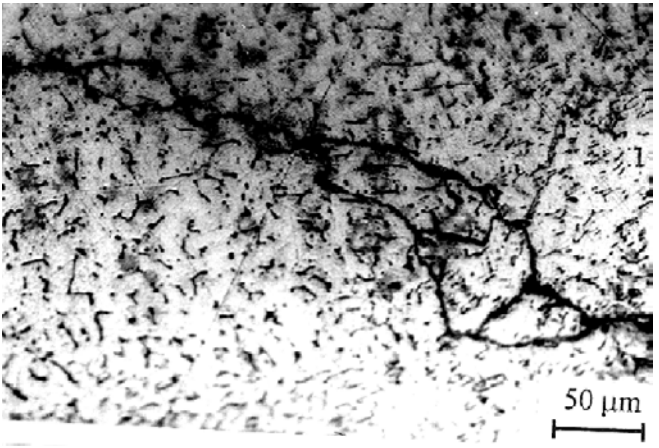

(b) Crack growth in 316 weld metal, 1 min. T hold and ±0.6%

Fig. 26 Crack morphology at 873 K.

Table 4 Effects of hold time on LCF properties at 873 K.

Hold (min)	$\Delta\varepsilon_t/2$ (%)	$\Delta\sigma/2$ (MPa)	σ_r (MPa)	N (Cycles)	N/N_f
0	±0.6	328	-	580(N_f)	1
1t	,,	307	51	475	0.819
1c	,,	323	45	510	0.879
10t	,,	291	57	409	0.705
30t	,,	288	74	330	0.635
90t	,,	274	94	235	0.405
0	±1.0	370	-	130(N_f)	1
10t	,,	342	68	140	1.08
30t	,,	322	96	110	0.846

where,
t : Tensile hold ; c : Compression hold;
$\Delta\varepsilon_t/2$: Total strain amplitude
$\Delta\sigma/2$: Half-Life stress amplitude
N : Number of cycles to failure (with hold)
N_f : Number of cycles to failure (without hold)
σ_r : Relaxed stress during hold

The grain boundary damage developed during relaxation changes the modes of crack initiation and propagation. In 1 min. compression hold, the crack initiation and propagation occurs by transgranular mode (Fig.27(a)) similar to continuous cycling conditions, Fig. 27(b). However, under tension hold conditions crack initiation becomes intergranular and propagation is mixed mode (trans- + intergranular), Fig. 26(a).

It is seen that the surface-connected slip bands are oxidized under 10 min. tension hold conditions, Fig. 28(a) and the fracture surface is marked periodically by fatigue striations and intergranular cracks , Fig. 28(b). Oxidation interaction is found to be more as the length of the hold time is increased to 90 minutes (Fig. 29(a)). Both crack initiation and propagation seem to be strongly assisted by oxidation and fracture surface is completely covered by a thick oxide layer, Fig. 29(b).

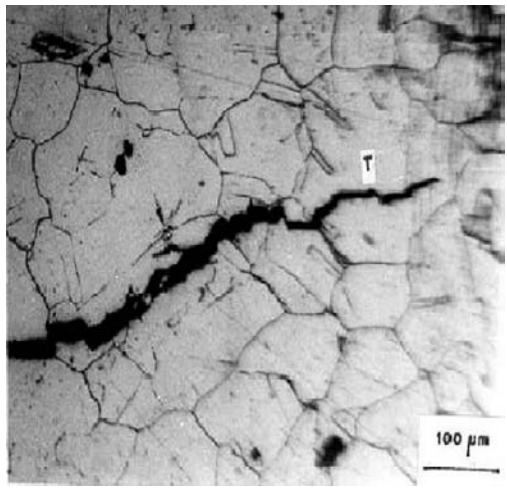

(a) Within 1 min. compression hold for 316L(N) base metal

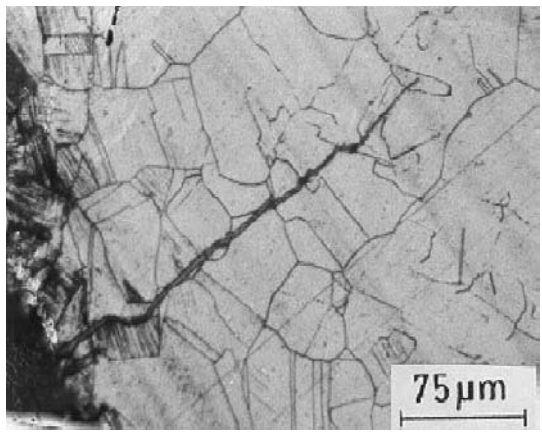

(b)Include crack initiation at 873 K:continuous cycling at strain amplitude ±0.6%

Fig. 27 Microstructure for transgranular crack propagation.

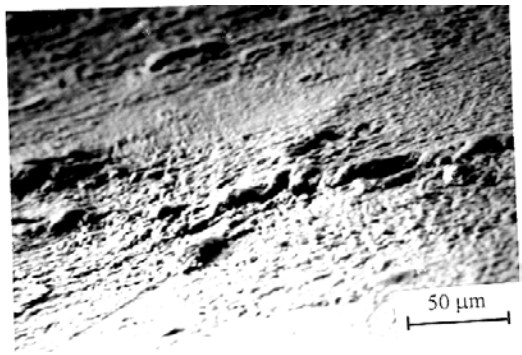

(a) Oxidation assisted crack initiation from slip bands

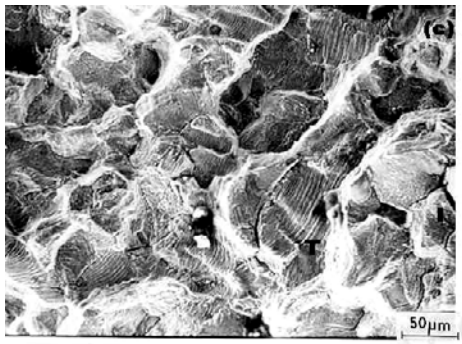

(b) Mixed mode crack propagation assisted by oxidation

Fig. 28 Microsdtructure for 316L(N) SS with 10 minutes tension hold at 873 K.

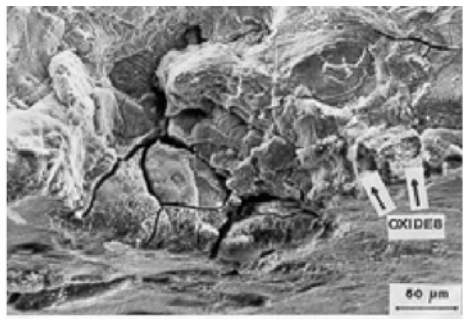

(a) Oxide location A

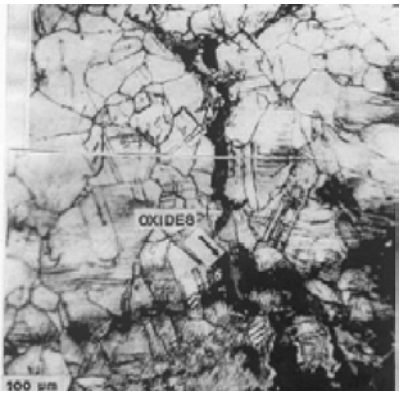

(b) Oxide location B

Fig. 29 Oxidation induced Intergranular Cracking in 90 min. Tension Dwell Tests, 316L(N) Base Metal, strain amplitude ±0.6%.

The influence of the predominant fracture mode on fatigue can be assessed from a quantitative measurement of crack density i.e. cumulative length of the trans- and intergranular secondary cracks on the longitudinal section per unit area, as shown in Fig. 30(a) along with the frequency distribution of the crack length, Fig. 30(b). It was seen that intergranular crack density was the lowest in compression hold test, and crack propagation was mainly transgranular. This behaviour could be attributed to the following reasons. During stress relaxation in compression hold, the growth of internal grain boundary cavities was very unlikely, since this needed both shear and normal tensile stresses across the grain boundary. Thus for cycles containing compression hold periods, failure was dominated by transgranular crack initiation and growth mechanisms and fatigue lives were longer, compared with tensile hold periods. However, bulk creep damage was favoured under tension hold conditions. Crack density measurements on this steel, Fig.30(a) indicated that the transgranular crack density decreased with an increase in the length of the hold-time in tension and crack propagation was mainly intergranular. Moreover, it was noted that crack linkage becomes extensive as the length of the hold time increased and long intergranular cracks were observed in 10 and 90 minutes tension-hold tests, Fig. 30(b). Thus the reduced fatigue life for longer hold-times could be ascribed to the occurrence of enhanced creep and oxidation damage at grain boundaries that facilitates accelerated intergranular crack initiation and propagation.

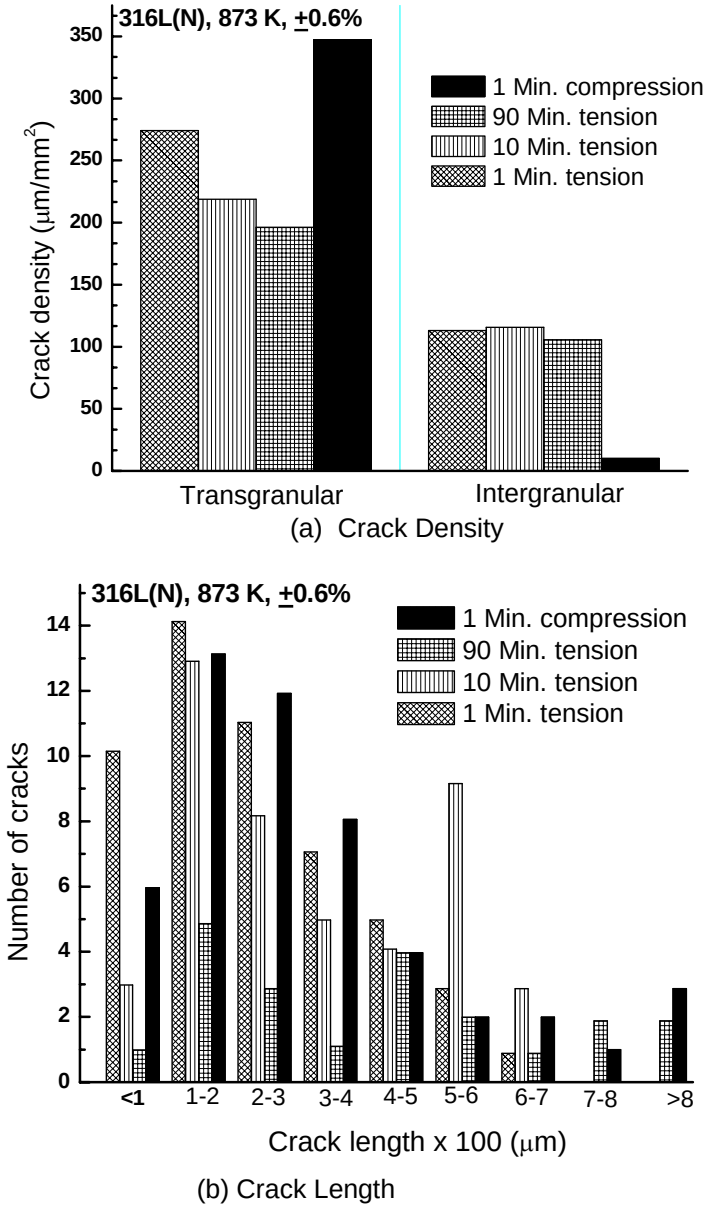

Fig. 30 Crack distribution as a function of hold time with 873 K at ±0.6%.

3.3.2 Modified 9Cr-1Mo steel

The influence of tensile and compressive hold times on LCF behaviour of modified 9Cr-1Mo steel was investigated at 873 K at a strain amplitude of ±0.6%. The variation of fatigue life with the duration of tensile hold time up to 30min on Mod.9Cr-1Mo steel (forged condition) at 873 K is shown in Fig. 31 and a comparison of the effect of tensile, compressive and tensile plus compressive hold time on fatigue life at 873 K of Modified 9Cr-1Mo material (extruded tube) is shown in Fig. 32. It was seen that the fatigue life decreased with increase in the length of hold time up to 30 min. Dwell in compression was found to be more deleterious than dwell in tension and tension-plus-compression dwell was found to be the most detrimental. Enhanced dwell sensitivity in compression has also been reported in this alloy by other investigators [56,57]. Further, it has been reported that tension hold is more damaging than compression hold in vacuum testing whereas the converse to be true for air testing [58]. Large tensile dwell sensitivity is essentially observed in materials exhibiting creep cavitation [45-50]. However, enhanced compressive dwell sensitivity, can be attributed to one of the following reasons, namely, development of tensile mean stress, shape and size of cavities and oxidation behaviour.

The greater vulnerability of 2.25Cr-1Mo steel to compression hold has been interpreted in terms of the behaviour of oxides [61]. It was shown that in compression after a tensile hold, the oxide spalls, thus revealing a

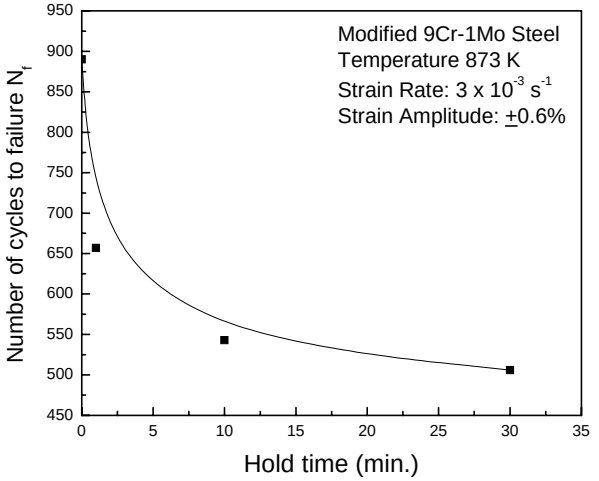

Fig. 31 Influence of hold time on fatigue life at 873 K.

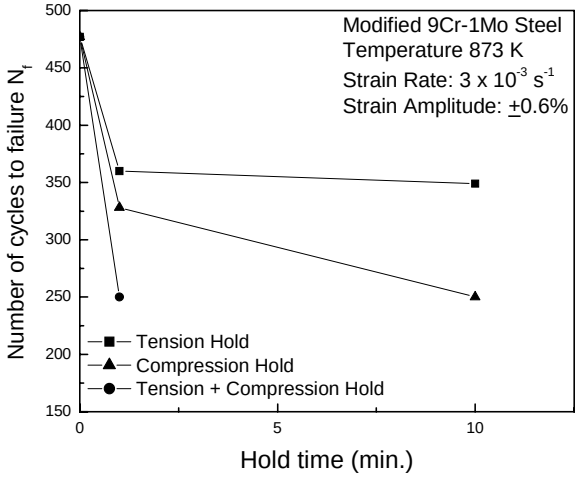

Fig. 32 Fatigue life as a function of hold time, Mod. 9Cr-1Mo steel (extruded tube), 873 K.

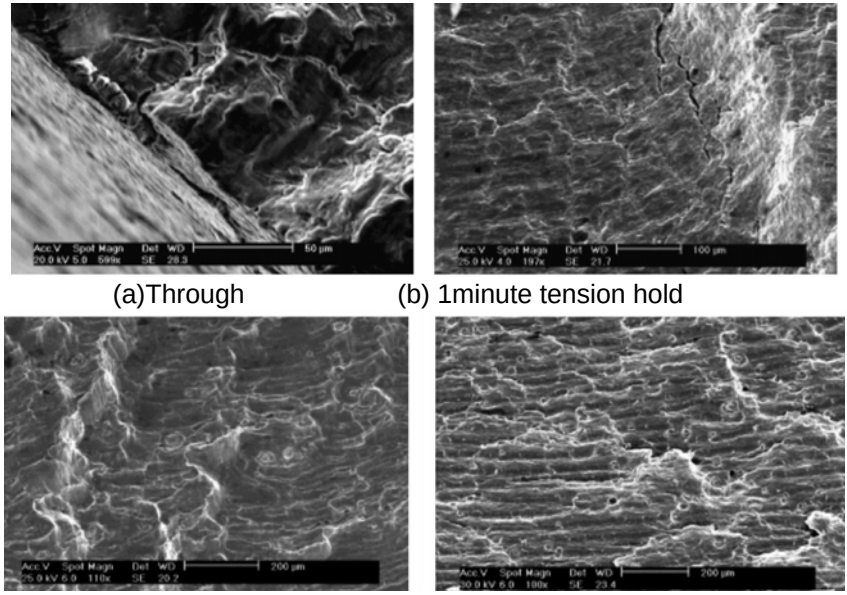

Fig. 33 Fractograph showing slip band cracking under continuous cycling.

fresh surface, enabling the removal of surface damage. Conversely, in tension after a compression hold, the oxide film cracks facilitating early crack nucleation in the underlying material. This behaviour was related to the tensile strain in the oxide [62].

In Modified 9Cr-1Mo steel no appreciable tensile mean stress in compression hold has been noticed. Further, creep cavitation was also not observed during hold time experiments. Fractographs of the fatigue tested samples under continuous cycling, 1 min tension, 10 min tension and 1 min compression shown in Fig. 33(a) through (d) respectively showed clearly transgranular crack initiation from surface connected slip bands and transgranular crack propagation marked by fatigue striations. This clearly negates the role of intergranular cavities in degrading the fatigue life of this material under hold time conditions.

Detailed metallography conducted on longitudinal sections of the fatigue tested samples (under 1 min tension, 10 min tension and 1 min compression depicted in Figs. 34 (a) through (c) respectively) showed multiple crack initiation sites and oxidation assisted crack initiation and propagation. Also the number density of secondary cracks was more in the case of compression hold compared to tension hold. This clearly indicated that the larger compression dwell sensitivity in Modified 9Cr-1Mo ferritic steel essentially arises from the oxidation effects. However, unlike 2.25Cr-1Mo steel no oxide spallation was noticed in this steel during tension hold. It is conceived that in modified 9Cr-1Mo steel an oxide layer formed on the surface of the specimen cracks which on further oxidation during tension hold leads to crack tip blunting, while during compression hold they stay sharp [56]. Moreover, it has also been proposed that the wedge effect of the exfoliated oxide cause oxidation-assisted cracking in Modified 9Cr-1Mo steel. Further, the oxide layer formed on the surface of the specimen was a weak barrier that could be easily overcome by slip and several crack initiation sites were observed in air-tested specimen compared to that in vacuum [63]. The reduced life in this steel, under creep-fatigue interaction conditions has thus been attributed to oxidation assisted crack initiation and propagation.

4. Concluding Remarks

Discussed are a few aspects of how microstructure, both initial and that developed subsequently during LCF deformation influence the formation and propagation of microcracks which eventually determine fatigue life, from examples of authors' work on materials of interest to fast breeder reactor technology. In Nimonic PE-16 shearing of γ' precipitates leads to cyclic softening. Shearing of precipitates under heterogeneous distribution

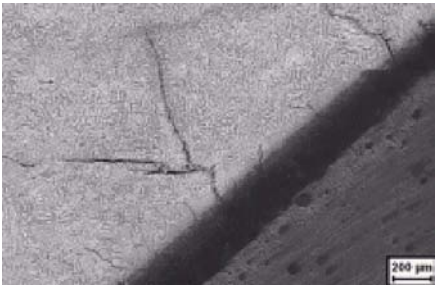

(a) 1 minute tension hold

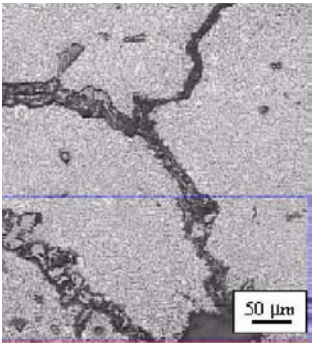

(b) 10 minutes tension hold

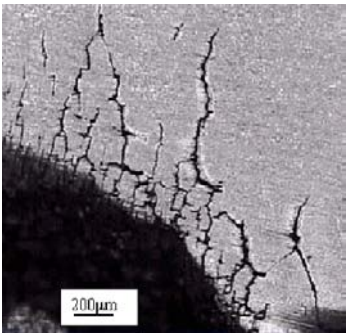

(c) 1 minute compression hold, modified 9Cr-1Mo steel (extruded tube), 873 K, ±0.6%.

Fig. 34 Optical Metallograph of longitudinal section of fatigue tested samples depicting secondary cracks.

can lead to localization of strain resulting in enhanced transgranular and intergranular cracking and a reduced fatigue life. Intergranular fracture is

accentuated by the presence of carbide precipitates on the grain boundaries. Dynamic strain ageing is found to influence fatigue deformation and fracture at high temperatures and low strain rates conducive to dislocation solute atom interaction. DSA leads to enhanced localization of slip leading to inhomogeneity of deformation and accelerated intergranular and transgranular cracking. This caused a reduction in life. In austenitic stainless steel base metal and weld metal fatigue life decreased with the introduction of hold. Tension hold was found to be more deleterious than compression hold. Further, fatigue life decreased with increase in the length of the hold time. Creep and oxidation contributed to reduction in fatigue life with hold time. In situations where crack deflection associated with the δ ferrite transformation occurred, 316 weld metal showed a higher fatigue life compared to the base metal. In Modified 9Cr-1Mo ferritic steel compression hold was found to be more deleterious than tension hold. It is suggested that the thin oxide layer formed on the surface is cracked by slip processes in this steel. Further, crack tip blunting by oxidation during tension hold reduces the crack propagation rate, whereas in compression hold the crack remains sharp leading to enhanced crack propagation rate. Understanding of mechanism of microcracking in different alloy systems under a variety of test conditions is important for the development of microstructures resistant to fatigue cracking under specific test conditions. Further considering the fact that many approaches are available for life prediction at elevated temperatures, understanding of the mechanisms of deformation and damage would lead to realistic life assessment and prediction techniques.

References

[1] Coffin LF. Effect of frequency and environment on fatigue crack growth of A286 at 1100 F. In: Carden AE, Mc Evily AJ, Wells CH (eds) Fatigue at elevated temperatures. STP 520, ASTM, Philadelphia, PA, (1973) 112-122.

[2] Gell M and Leverant GR. Mechanism of high temperature fatigue. In: Carden AE, Mc Evily AJ, Wells CH (eds) Fatigue at elevated temperatures. STP 520, ASTM, Philadelphia, PA, (1973,) 37-67.

[3] Antolovich SD, Liu S and Baur R. Low cycle fatigue behaviour of Rene 80 at elevated temperature. Metall Trans A, 12 (1981) 473-481.

[4] Valsan M, Parameswaran P, Bhanu Sankara Rao K, Vijayalakshmi M, Mannan SL and Sastry DH. High-temperature low cycle fatigue behaviour of a Nimonic PE-16 superalloy - correlation with deformation and fracture. Metall Trans A, 23 (1992) 1751-1761.

[5] Mannan SL, Valsan M High temperature low cycle fatigue, creep-fatigue and thermomechanical fatigue of steels and their welds. Int J Mechanical Sciences 48 (2006) 160-175.

[6] Sidey D and Coffin LF Jr. Low cycle fatigue damage mechanisms at high temperature. In: Fong JT (ed) Symp. on fatigue mechanisms. ASTM STP, 675 (1979) 528-570.
[7] Wells CH, Sullivan CP and Gell M. Mechanism of fatigue in creep range, In: Manson SS (ed) Metal fatigue damage: mechanism, detection, avoidance and repair. ASTM STP, 495 (1971) 61-122.
[8] Bhanu Sankara Rao K. Time dependent low cycle fatigue behaviour of high temperature alloys. Trans Indian Inst Met, 42 (1989) 61-82.
[9] Mannan SL. Role of dynamic strain ageing in low cycle fatigue. Bull of Mater Sci, 16(6) (1993) 561-582.
[10] Valsan M, Sastry DH, Bhanu Sankara Rao K and Mannan SL. Effect of strain rate on high-temperature low-cycle fatigue properties of a Nimonic PE-16 superalloy. Metall Trans A, 25 (1994) 159-171.
[11] Valsan M, Sundararaman D, Ray SK and Mannan SL. Low cycle fatigue deformation behaviour of a Nimonic PE-16 superalloy in a double-aged microstructural condition. Trans Indian Inst Met, 49(4) (1996) 471-477.
[12] Srinivasan VS, Sandhya R, Bhanu Sankara Rao K, Mannan SL and Raghavan KS. Effects of temperature on the low cycle fatigue behaviour of nitrogen alloyed type 316L stainless steel. Int J of Fatigue, 13(6) (1991) 471-478.
[13] Valsan M, Sundararaman D, Bhanu Sankara Rao K and Mannan SL. A comparative evaluation of low cycle fatigue behaviour of type 316L(N) base metal, 316 weld metal and 316L(N)/316 weld joint. Metall and Mater Transactions A, 26 (1995) 1207-1219.
[14] Nagesha A, Valsan M, Bhanu Sankara Rao K and Mannan SL. Strain controlled fatigue of type 316L(N) base metal and 316 SS weld metal at elevated temperatures. In: Xue-Ren Wu, Wang ZG (eds) Proceedings of the seventh International fatigue conference, FATIGUE '99,2. Beijing, China, (1999) 1303-1308.
[15] Srinivasan VS, Valsan M, Sandhya R, Bhanu Sankara Rao K, Mannan SL and Sastry DH. High temperature time-dependent low cycle fatigue behaviour of a type 316L(N) stainless steel. Int J of Fatigue, 21 (1999) 11-21.
[16] Nagesha A, Valsan M, Kannan R, Bhanu Sankara Rao K and Mannan SL. Influence of temperature on the low cycle fatigue behaviour of a modified 9Cr-1Mo ferritic steel. Int J of Fatigue, 24(12) (2002) 1285-1293.
[17] Mannan SL, Bhanu Sankara Rao K, Valsan M and Nagesha A. Strain controlled low cycle fatigue and creep-fatigue interaction behaviour of Modified 9Cr-1Mo ferritic steel. Trans Indian Inst Met, 58(2-3) (2005) 159-168.
[18] Vani Shankar, Valsan M, Kannan R, Bhanu Sankara Rao K, Mannan SL and Pathak SD. Low cycle fatigue behavior and microstructural evolution of 9Cr-1Mo-V-Nb ferritic steel. Mat Sci and Engg, 437(2) (2006) 413-422.
[19] Srinivasan VS, Valsan M, Bhanu Sankara Rao K, Mannan SL and Raj B. Low cycle fatigue and creep-fatigue interaction behaviour of 316L(N) stainless steel and life prediction by artificial neural network approach. Int J of Fatigue, 25 (2003) 1327-1338.
[20] Srinivasan VS, Sandhya R, Valsan M, Bhanu Sankara Rao K and Mannan SL. Comparative evaluation of strain controlled low cycle fatigue behaviour

of solution annealed and prior cold worked 316L(N) stainless steel. Int J of Fatigue, 26 (2004) 1295-1302.

[21] Coffin LF Jr. Fatigue at high temperature. In: Carden AE, Mc Evily AJ, Wells CH (eds) Fatigue at elevated temperatures. ASTM STP, 520 (1973) 1-34.

[22] Brinkman CR, Gieseke BG and Maziasz PJ. The influence of long term thermal ageing on the microstructure and mechanical properties of modified 9Cr-1Mo steel. In: Liaw PK, Viswanathan R, Murty KL, Simonen EP, Frear D (eds) Microstructure and mechanical properties of ageing material. The Minerals, Metals and Materials Society, (1993), 107-115.

[23] White RJ and Fisher SB. The precipitation and growth kinetics of γ' in Nimonic PE-16. Mat Sci and Engg, 33 (1978) 149-157.

[24] Seetharaman V, Bhanu Sankara Rao K, Mannan SL and Rodriguez P. Microstructure and mechanical properties of a Nimonic PE-16 superalloy subjected to double ageing treatment. Mat Sci and Engg, 63 (1984) 35-50.

[25] Taillard R, Degallaix S and Foct J. Effect of nitrogen upon the low cycle fatigue behaviour of 316L stainless steels. In: Rie KT (ed) Low cycle fatigue and elasto-plastic behaviour of materials. Elsevier, Munich, (1987) 83-88.

[26] Sandstrom R, Engstrom J, Nilsson JO and Nordgren A. Elevated temperature low cycle fatigue of the austenitic stainless steel type 316 and 253 MA – influence of microstructure and damage mechanisms. High Temp Technol, 7 (1989) 2-9.

[27] Nilsson JO. The influence of nitrogen on high temperature low cycle fatigue behaviour of austenitic stainless steel. Fat Fract Engg Mater Struct 7, (1984) 55-64.

[28] Vogt B, Degallaix S and Foct J. Low cycle fatigue life enhancement of 316L stainless steel by nitrogen alloying. Int J Fatigue, 6(4) (1984) 211-215.

[29] Nilsson JO. The effect of slip behaviour on the low cycle fatigue behaviour of two austenitic stainless steels. Scripta Metall, 17 (1983) 593-596.

[30] Taillard R and Foct J. Mechanisms of the action of nitrogen interstitials upon low cycle fatigue behaviour of 316 stainless steels. In: Foct J, Hendry A (eds) Proc Int conf on high nitrogen steels 88. The Institute of Metals and the Socitie francaise de Metallurgie , Lillie, France, (1988) 387-391.

[31] Nilsson JO and Thorvaldsson T. The influence of nitrogen on microstructure and strength of a high-alloy austenitic stainless steel. Scand J Metall, 15 (1985,) 83-89.

[32] Stoltz RE and Pineau AG. Dislocation-precipitate interaction and cyclic stress-strain behaviour of a γ' strengthened superalloy. Mater Sci Eng, 34 (1978) 275-284.

[33] Calabrese C and Laird C. Cyclic stress-strain response of two phase alloys part I. Microstructure containing particles penetrable by dislocations. Mater Sci Engg, 13 (1974) 141-157.

[34] Lerch A and Gerold V. Cyclic hardening mechanisms in Nimonic 80A. Metall Trans A, 18 (1987) 2135-2141.

[35] Kim WH and Laird C. Crack nucleation and stage I propagation in high strain fatigue – II mechanism. Acta Metall, 26 (1978) 789-799.

[36] Hornbogen E and Zum Gahr KH. Microstructure and fatigue crack growth in a γ Fe-Ni-Al alloy. Acta Metall, 24 (1976) 581-592.
[37] Arbuthnot CHD. The Micro-mechanisms of fatigue deformation in Nimonic PE-16. In: Maurer KL, Matzer FE (eds) Proc 4th european conf on fracture and role of microstructure 2. Leoben, Austria, The Chameleon press Ltd., London, United Kingdom, (1982) 407-413.
[38] Mediratta SR, Ramaswamy V and Rama Rao P. Two stage cyclic work hardening and two-slope Coffin-Manson relationship in dual phase steels. Scripta Metall, 20 (1986) 555-558.
[39] Sanders TH Jr and Starke EA Jr. The relationship of microstructure to monotonic and cyclic straining of two age hardening aluminum alloys. Metall Trans, 7A (1976) 1407-1418.
[40] Bhanu Sankara Rao K, Valsan M, Sandhya R, Mannan SL and Rodriguez P. Synergistic interactions during high temperature fatigue of type 304 stainless steel-grain size dependence. Trans Indian Institute of Metals, 44(3) (1991) 255-270.
[41] Bhanu Sankara Rao K, Valsan M, Sandhya R, Mannan SL and Rodriguez P. Grain size dependence of dynamic strain ageing during low cycle fatigue of type 304 stainless steel. In: Salama K, Ravi Chandar K, Taplin DMR, Rama Rao P (eds) ICF-7, Advances in fracture research 2, Pergamon, Oxford, (1989) 1323-1330.
[42] Kanazawa K, Yamaguchi K and Nishijima S. Mapping of low cycle fatigue mechanisms at elevated temperatures for an austenitic stainless steel. In: Solomon HD, Halford GR, Kaisand LR, Leis BN (eds) Low cycle fatigue. ASTM STP 942, Philadelphia, (1988) 519-530.
[43] Abdel-Raouf H, Plumtree A and Topper TH. Effect of temperature and deformation rate on cyclic strength and fracture of low carbon steel. In: Coffin LF, Krempl E (eds) Cyclic stress-strain behaviour- analysis, experimentation and failure prediction. ASTM STP, 519 (1971) 28-57.
[44] Bressers J. Fatigue and microstructure. In: Marriott JB, Merz M, Nihoul J, Ward J (eds) High temperature alloys, their exploitable potential. Elsevier Applied Science, Amsterdam, (1987) 385-410.
[45] Lee SB and Miller AK. A phenomenological model for intergranular fatigue by r-type and wedge type cavitation. J Engg Mater Tech, 117 (1995) 311-321.
[46] Halford GR, Johnson JR and Brown JA. In: Richmond RJ, Wu ST (eds) Advanced earth – to – orbit propulsion technology. NASA Conf publications, (1986) 2437-2450.
[47] Yamaguchi K and Kanazawa K. Effect of strain wave shape on high temperature fatigue of type 316 steel and application of strain range partitioning method. Metall Trans, 11A (1980) 2019-2027.
[48] Shi HJ and Pluvinage G. Cyclic stress strain response during isothermal and thermomechanical fatigue. Int J Fatigue, 16 (9) (1994) 549-557.
[49] Srinivasan VS, Nagesha A, Valsan M, Bhanu Sankara Rao K, Mannan SL and Sastry DH. Effect of hold time on low cycle fatigue behaviour of nitro-

gen bearing 316L stainless steel. Int J of Pressure Vessels and Piping, 76 (1999)863-870.

[50] Sandhya R, Bhanu Sankara Rao K and Mannan SL. Creep fatigue interaction behaviour of a 15Cr-15Ni Ti Modified austenitic stainless steel as a function of Ti/C ratio and microstructure. Mat Sci and Engg A, 392 (2005) 326-334.

[51] Brinkman CR, Strizak JP, Brooker MK and Jaske CEJ. Time dependant strain controlled fatigue behaviour of annealed 2.25Cr-1Mo steel for use in nuclear steam generator design. J Nucl Mater, 62 (2/3) (1976) 181-204.

[52] Goswami T. Creep-fatigue: Paper 1. Compilation of data and trends in the creep fatigue behaviour of low alloy steels. High Temp Mater Proc, 14(1) (1995) 1-19.

[53] Plumbridge WJ and Stanley M. Low cycle fatigue of a Titanium 829 alloy. Int J Fatigue, 8 (1986) 209-216.

[54] Plumbridge WJ and Ellison EG. Low cycle fatigue behaviour of superalloy blade materials at high temperatures. Mater Sci Tech, 3 (1987) 706-715.

[55] Nazmy MY. High temperature low cycle fatigue of Inconel 783 and application of strain range partitioning. Metall Trans, 14A (1983) 449-461.

[56] Aoto K, Komine R, Ueno F, Kawasaki H and Wada Y. Creep-fatigue evaluation of normalized and tempered modified 9Cr-1Mo. Nucl Engg Design, 153 (1994) 97-110.

[57] Van Den Avyle JA and Jones WB. Substructure and strengthening mechanisms in 2.25Cr-1Mo steel at elevated temperatures. Metall Trans, 11A (1980) 1275-1286.

[58] Kim S and Weertman JR. Investigations of microstructural changes in a ferritc steel caused by high temperature fatigue. Metall Trans A, 19 (1988) 999-1007.

[59] Bhanu Sankara Rao K, Meurer HP and Schuster H. Creep-fatigue interaction of Inconel 617 at 950 °C in simulated nuclear helium. Mat Sci and Engg, 104A (1988) 37-51.

[60] Rie KT, Schmidt RM, Ilschner B and Sam SW. A model for predicting low cycle fatigue life under creep-fatigue interaction. In: Solomon HD, Halford GR, Kaisand LR, Leis BN (eds) Low cycle fatigue. ASTM STP 942, Philadelphia, (1988) 313-328.

[61] Teranishi H and McEvily AJ. On the fatigue crack initiation and propagation at elevated temperatures. In: Francois O (ed) ICF 5, Advances in Fracture Research, Pergamon Press, Paris, (1980) 2439-2445.

[62] Challenger KD. Elevated temperature fatigue of 2.25Cr-1Mo steel. In: Valluri SR, Taplin DMR, Rama Rao P, Knott JF, Dubey R (eds) ICF6, New Delhi, India, (1984) 2239-2248.

[63] Ebe G and McEvily AJ. Effect of processing in high temperature low cycle fatigue properties of modified 9Cr-1Mo steel. Fatigue and Fracture Engg Mat Struct, 17 (1984) 299-314.

Invariant Form of Micro-/Macro-Cracking in Fatigue

G. C. Sih [1, 2 *]
[1] International Center for Sustainability, Accountability and Eco-Affordability of Large Structures (ICSAELS)
Advanced Technology for Large Structural Systems (ATLSS)
Lehigh University, Bethlehem, PA 18015, USA
[2] School of Mechanical and Power Engineering, East China University if Science and Technology, Shanghai 200237, China
**Email: gcs8866@yahoo.com, gcs1@lehigh.edu*

Abstract

The size/time transitory character of fatigue cracking can be hidden in the data or revealed explicitly depending on the manner of presentation. The former can correspond to the crack length while the latter to the crack growth rate variations, both referred to the number of fatigue cycles. Conventionally speaking, the sigmoidal curve for the plot of log da/dN against log ΔK consists of three regions known as I, II and III. They are referred to, respectively, as crack initiation, stable crack growth and fast fracture although the transition from one region to another involving scale shifting is seldom discussed. Even though damage by very small defects are recognized in fatigue but their representation may become dubious when the parameter "a" in the crack growth rate expression da/dN may have to adopt a different physical interpretation. Using the line crack configuration for describing crack growth in metals, reference will be made to three approximate crack size range of a ≈10-80 mm (macromechanical) for regions II and III, a ≈10^{-3} to 10^{-1}mm (micro- structural) for region I and presumably a ≈10^{-4} mm or smaller (nano- chemical) for the lower scale regions.

The objective of developing a multiscale fatigue crack growth model is to determine the increment of a stress intensity or energy density parameter such that the data in regions I, II and III can be related. One way is to have the crack growth rate da/dN to lie on a straight line such that linear interpolation can be applied to relate the nano, micro and macro fatigue data. This behavior is referred to as form-invariant. The proposed scheme accounts for two succeeding scales such as micro/macro and nano/micro. In this way. the scaling shifting capability can be extended, say from nano to macro. The dual scale micro/macro line crack model will be presented. It consists of three physical parameters d* (micro/macro length), μ*

G.C. Sih (ed.), Multiscale Fatigue Crack Initiation and Propagation of Engineering Materials: Structural Integrity and Microstructural Worthiness, 181–208.

(micro/macro material constants) and σ* (external/internal stresses). The model can also delve into the details of the material microstructure when needed. For structural applications many of the incidental material parameters can be absorbed by the macro empirical parameters which will be limited to two such that the present findings can be incorporated into the current fracture control methodology.

Using the available fatigue crack growth data for the 7075-T6 and 2024-T3 aluminum panels, the sigmoidally-curved regions I, II and III will be shown to become a straight line whose slope and y-intercept in a log-log plot will depend on the mean stress σ_m and stress amplitude σ_a that are accounted for simultaneously by the dual scale energy density expression. The slopes of lines line referred to the energy density plots ranged from 2.890 to 3.019 when σ_m varied from 9 to 12 kg/mm^2 and σ_a from 2.5 to 6.5 kg/mm^2. The slopes obtained a wider scatter of 3.532 to 4.224 when the energy density range was replaced by the stress intensity range. This was expected because the stress intensity approach leaves out the mean stress effect. The present work is offered as the first step to include scaling effects so that micro material behavior can enter into the macro fatigue crack growth process.

1. Introduction

The macro mechanical properties are known to be affected by the material microstructure which can be changed by heat treatment and/or high pressure. Various processing techniques have been developed and applied to alter the strength of uniaxial specimens. The results presumably can be extended to the design of structural members under multi-axial stress states. As the test data scatter increased with increasing material strength, it was found necessary to account for the effect of pre-existing defects. The classical notion of plane stress for thin bodies and plane strain for thick sections were realized to be inadequate as they entail only global scale dimensions. The size of failure initiation locality relative to global instability is fundamental. This has led to crack initiation and propagation as the two events considered in the facture mechanics discipline [1-3]. Scale segmentation was also necessary such that analyses can be divided into different ranges referred to as nanoscopic, microscopic and macroscopic. The inter-connecting gap has been known as the mesoscopic [4,5] region. These distinctions were necessary to avoid considering the process of non-equilibrium [6,7] where the material properties changed not only from location to location but also in elapsed time. By tradition, the open thermodynamic system has been simplified to a closed system where

the conditions on the boundary are assumed to be known and hence specified. The fluctuations or movements at the interface are assumed to be localized for large bodies and ignored. As the body size is decreased, the average and bulk properties are no longer representative of the physical behavior. At the nano scale, the physical laws can differ [8,9] and the description of matter can adopt an uncertain character as advocated in quantum mechanics where the origin of failure may initiate from the non-uniform distribution of the electrons [10].

Advancement in micro/macro crack interaction in fatigue has been crawling at the a snail's pace because not enough attention has been directed to understand the mechanism of crack opening followed by closing in the same cycle repeated many times. Most of the data are collected for metals undergoing low amplitude loads alternating at one-half of the yield strength according to the ASTM standard. This corresponds to the situation where the elements ahead of a macroscopic crack would undergo permanent deformation such that the local hyteresis loops would be measurable. The cracked material at the microscale has sufficient restraint to close upon unloading, A restraining force or stress is said to prevail that changes with the crack length. This mechanism is believed to be fundamental in describing the transitory character of micro-/macro-cracking that correspond to regions I and II of the conventional sigmoidal fatigue crack growth rate curve. The dual scale crack model [11,12] provided the impetus for developing a fatigue crack model that can switch from a microcrack to a macrocrack and vice versa. Such a crack prevails in a non-homogeneous medium where the top and bottom surface of the crack would subject to different constraint that can be modeled by the free-fixed boundary condition. That is the crack path would in general wonder about without symmetry. This led to the discovery of a crack with double stress singularity [13]. The weak singularity of order $1/r^{0.25}$ can model the microcrack behavior and the strong singularity of order $1/r^{0.75}$ can model the macrocrack. The solution was validated by satisfying the equations of continuum mechanics with finite displacements at the singular crack tip. In addition, the microstructure effects of the material were also shown to affect the angular distribution of the double singularity local stress field. Hence, two additional parameters φ_1 and φ_2 would affect the angular variations of the stresses where the coordinate angle θ is measured from the line extended from the original crack plane. The details can be found in [14]. They reveal the complexities of the analysis when the microstructural effects of the material are included.

The influence of material microstructure on fatigue crack growth has received much interest in recent years [15-20] although the approaches

varied from the empirical to the semi-analytical models. The results when presented in terms of the crack growth rate da/dN can be irratic if the spatial and temporal scale is not carefully observed. Variance in data presentation cannot be avoided if no agreement can be found in defining nano-, micro- and macro-crack size in relation to time. Consistency in data presentation appears to be needed before progress can be made to understand the underlying physical mechanisms that govern fatigue crack growth.

2. Statement of Fatigue Crack Growth Rate Models

The advent of linear elastic fracture mechanics was followed by the development of the two-parameter fatigue crack growth relation [21]

$$\frac{da}{dN} = A(\Delta K)^p \tag{1}$$

In Eq.(1), A and p were found empirically from a log-log plot of da/dN versus ΔK which is known as the macro-stress intensity factor such that it depends on the stress amplitude range and the square root of the half crack length *a* for a panel with a central crack of length 2*a*. To be more specific, reference can be to the plot in Fig.1 for aluminum alloys [22]. Region II refers to long cracks for *a* from 10 to 40mm. For short cracks with *a* in the range of 1 to 10mm, the curve acquires a different slope and has been referred to as the "threshold". Under alternating tension and compression loading, the crack mouth opens and closes for each cycle. It can change from invisible (microscopic) to visible (macroscopic). The corresponding data switches from region I to region II. For lower da/dN, the crack size is even smaller with dimensions of 10^{-2} to 10^{-1}mm. The recent concern is whether the classical ΔK correlation should be replaced by other quantities to account for the change of small to large cracks. This would no doubt alter the shape of the da/dN curve, in addition to a possible reinterpretation of the physical mechanism(s) that is causing this change.

Although countless empirical forms of ΔK in Eq.(1) has been proposed to offer a better fit of the data, few of the models revealed any significant progress. The exception is the work in [23,24] that gave an exponent of p=2 using a self-similitude argument in contrast to p=4 [21] arrived from a plot of a multitude of fatigue data for aluminum alloys. By in large; the form of Eq.(1) has been retained while the exponent p may vary in application. In what follows, the classical form of ΔK will be replace by ΔK_{micro}^{macro} such that

$$\frac{da}{dN} = C(\Delta K_{micro}^{macro})^{n} \tag{2}$$

The superscript "macro" and subscript "micro" are introduced to show that ΔK_{micro}^{macro} can represent the intensity factor for the microcrack or the macrocrack depending on the tightness ratio σ^* of the contacting crack surfaces in addition to the micro/macro shear modulus ratio μ^* and a relative length parameter d^* that defines the relative size of the local crack tip region as shown in Fig.2. The restraining stress σ_o that controls the tightness of the crack surfaces is normalized to the applied stress σ_∞ to define σ^*. In situations where the mean stress σ_m plays an important role in addition to the stress amplitude σ_a, Eq.(2) will be further replaced by the range of the micro/macro energy density factor ΔS_{micro}^{macro} offering another form of the fatigue crack growth relation:

$$\frac{da}{dN} = B(\Delta S_{micro}^{macro})^{m} \tag{3}$$

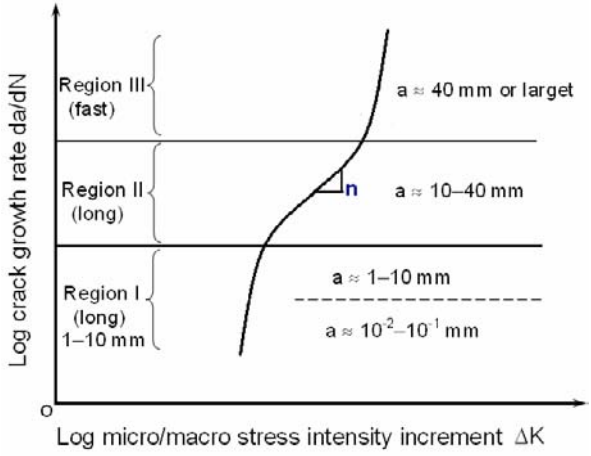

Fig. 1 Fatigue crack size increase with growth [22].

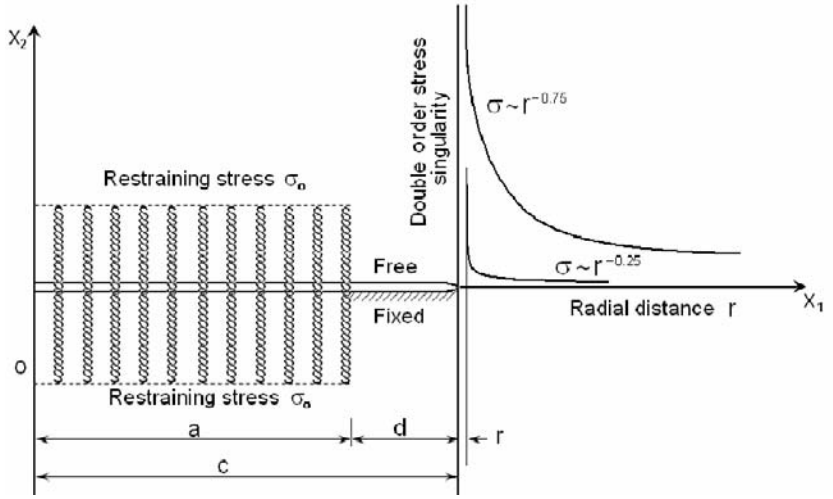

Fig. 2 Strong and weak stress singularity for the dual scale crack model.

3. Stress Intensification Approach

The strength of stress singularity near a crack tip played a fundamental role in the development of the linear elastic fracture mechanics model as it can be related to the energy released by a unit extension of a self-similar crack. Such a simple interpretation ceases to prevail for a microcrack where anti-symmetry becomes the rule rather than the exception. A brief description of the double singularity stress field will be made for the sake of continuity.

3.1 Double singularity stress field

The double singularity solution can be found in [13]. Adopted in this discussion is a crack with free-fixed surface condition. Two singularities of different order prevail at the same crack tip. There is the strong singularity with order $1/r^{0.75}$ and the weak singularity with order $1/r^{0.25}$ having the respective intensities of $(K^S)^{macro}_{micro}$ and $(K^W)^{macro}_{micro}$ as shown by

$$(\sigma_{ij})^{macro}_{micro} = \frac{(K^S)^{macro}_{micro}}{\sqrt{2\pi r^{0.75}}} f_{ij}(\varphi_1,\theta) + \frac{(K^W)^{macro}_{micro}}{\sqrt{2\pi r^{0.25}}} g_{ij}(\varphi_2,\theta) + \cdots \qquad (4)$$

The method of scale multiplier can be used [13] to give

$$(K^S)^{macro}_{micro} = \sqrt{d}\,(K^W)^{macro}_{micro} \tag{5}$$

Eq. (1) can thus be re-written only in terms of $(K^S)^{macro}_{micro}$ as

$$(\sigma_{ij})^{macro}_{micro} = \frac{(K^S)^{macro}_{micro}}{\sqrt{2\pi}\ r^{0.75}}[f_{ij}(\varphi_1,\theta)+\sqrt{\frac{r}{d}}\ g_{ij}(\varphi_2,\theta)]+\cdots \tag{6}$$

To be reminded is the notation $(\,)^{macro}_{micro}$ that applies to the dual scale model to denote that the crack can be micro or macro depending on the ratio d/r (or d^*) and the restraining stress σ_o to applied stress ratio σ_∞ ratio given by σ^* that is contained in $(K^S)^{macro}_{micro}$. Large σ^* would close the crack making it invisible and the opposite would result if the restraining stress is small. Refer to Fig.1. This effect is particularly important in fatigue where loading and unloading tend to open and close the crack continuously. As it can be seen from Eq. (6), the local crack tip stresses depend on the distance on the relative distance r/d. Such a character is also necessary for addressing micro/macro effects. Since both $(K^S)^{macro}_{micro}$ and $(K^W)^{macro}_{micro}$ are related by Eq.(5), it suffices to consider $(K^S)^{macro}_{micro}$ only and superscript s can be dropped to give

$$K^{macro}_{micro} = \frac{16\sqrt{\pi}(1-\nu_{macro})\mu_{micro}\sigma_\infty\sqrt{c^2-a^2}}{f(\varphi_1,\varphi_2)\mu_{macro}d^{0.25}}(1-\frac{2\sigma_o}{\pi\sigma_\infty}\sin^{-1}\frac{a}{c}) \tag{7}$$

provided that

$$f(\varphi_1, \varphi_2)=5\varphi_1+7\varphi_2+12 \tag{8}$$

The relation between c and a can be found in Fig.1. Eq. (4) can be found in [13] and will not be elaborated any further.

3.2 Crack growth relation based on stress intensity

Assuming that the maximum and minimum values of applied and crack tip stresses occur at the same time without phase change, then the increment change of the local stress intensification K^{macro}_{micro} can be denoted by

$$\Delta K_{micro}^{macro} = (K_{micro}^{macro})_{max} - (K_{micro}^{macro})_{min} \tag{9}$$

Making use of Eq.(7) and letting σ_∞ equal to σ_{max} at maximum stress and to σ_{min} at minimum stress, it is found that

$$(K_{micro}^{macro})_{max} = \frac{16\sqrt{\pi}(1-\nu_{macro})\mu_{micro}\sqrt{c^2-a^2}}{f(\varphi_1,\varphi_2)d^{0.25}\mu_{macro}}\left(1-\frac{2\sigma_o}{\pi\sigma_\infty}\sin^{-1}\frac{a}{c}\right)\sigma_{max} \tag{10}$$

$$(K_{micro}^{macro})_{min} = \frac{16\sqrt{\pi}(1-\nu_{macro})\mu_{micro}\sqrt{c^2-a^2}}{f(\varphi_1,\varphi_2)d^{0.25}\mu_{macro}}\left(1-\frac{2\sigma_o}{\pi\sigma_\infty}\sin^{-1}\frac{a}{c}\right)\sigma_{min} \tag{11}$$

Inserting Eqs. (10) and (11) into Eq. (9), there results

$$\Delta K_{micro}^{macro} = \frac{16\sqrt{\pi}(1-\nu_{macro})\mu_{micro}\sqrt{c^2-a^2}}{f(\varphi_1,\varphi_2)d^{0.25}\mu_{macro}}\left(1-\frac{2\sigma_o}{\pi\sigma_\infty}\sin^{-1}\frac{a}{c}\right)(\sigma_{max}-\sigma_{min}) \tag{12}$$

Recall that $\sigma^*=\sigma_o/\sigma_\infty$ and $\mu^*=\mu_{micro}/\mu_{macro}$. The length d=c–a is defined in Fig.1 and the quantities φ_1 and φ_2 can be identified with different microcrack branching patterns [14]. They may also be related to fissures and striations that are observed by micrographs in the fatigue of aluminum alloys. Although these microscopic effects involving the φs can be included in Eq. (12), it is more pertinent to focus attention on the invariant form of da/dN by first expressing Eq.(2) in the form

$$\frac{da}{dN} = C_1(\Delta K_{micro}^{macro})^n \tag{13}$$

At this stage, the incidental variables φ_1 and φ_2 or the function $f(\varphi_1,\varphi_2)$ can be absorbed into the macro-parameters. More specifically, the quantity $3f(\varphi_1,\varphi_2)/40$ may be factored out of Eq.(13) after eliminating ΔK_{micro}^{macro} by using Eq.(12). This renders a new ΔK_{micro}^{macro} without $f(\varphi_1,\varphi_2)$ that will be understood to be

$$\Delta K_{micro}^{macro} = \frac{6\sqrt{\pi}(1-\nu_{macro})\mu_{micro}\sqrt{c^2-a^2}}{5d^{0.25}\mu_{macro}}(1-\frac{2\sigma_o}{\pi\sigma_\infty}\sin^{-1}\frac{a}{c})(\sigma_{max}-\sigma_{min}) \quad (14)$$

A new parameter C can now be defined as

$$C = \left[\frac{40}{3f(\varphi_1,\varphi_2)}\right]^n C_1 \quad (15)$$

Application of Eqs.(14) and(15) can convert, Eq.(13) to the form of Eq.(2) which will be used for the calculation of numerical data. There should be no confusion between the use of ΔK_{micro}^{macro} in Eq.(12) with $f(\varphi_{1,}\varphi_2)$ and the use of ΔK_{micro}^{macro} in Eq.(14) without $f(\varphi_{1,}\varphi_2)$. Both form of da/dN involves only two empirical parameters C_1 and n or C and n. The foregoing exercise shows explicitly that microscopic effects can be hidden in the macroscopic empirical constants C, C_1 and n.

4. Energy Density Intensification Approach

The local energy density factor can be used to include the effect of mean stress. The form of dW/dV that can be applied to micro-/macro-cracking given by

$$\left(\frac{dW}{dV}\right)_{micro}^{macro} = \frac{[S(r,\theta)]_{micro}^{macro}}{r} \quad (16)$$

4.1 Strength of energy density singularity

The 1/r singularity for dW/dV applies also for the double stress singularity field of Eq.(4) or (6). Knowing that K is related to S [3], it can be shown that [13]

$$S_{micro}^{macro} = \frac{(1-\nu_{macro})^2(c^2-a^2)}{128f^2(\varphi_1,\varphi_2)\mu_{micro}d^{0.5}r^{0.5}}(\frac{\mu_{micro}}{\mu_{macro}}\sigma_\infty)^2(1-\frac{2\sigma_o}{\pi\sigma_\infty}\sin^{-1}\frac{a}{c})^2F(\theta) \quad (17)$$

Note that

$$F(\theta) = \frac{1}{2}[f_r(\theta) - f_\theta(\theta)]^2 + 2[f_{r\theta}(\theta)]^2 \tag{18}$$

in which $f_r(\theta)$, $f_\theta(\theta)$ and $f_{r\theta}(\theta)$ are complicated functions of θ and φ_j with j=1, 2. They can be found in [13] and will not be repeated here since they can be absorbed into the empirical parameters to be shown later. The energy density intensification is non-uniform around the crack and S_{micro}^{macro} in Eq.(17) can depend on the radial distance r from the crack tip and the microstructural details via $f(\varphi_1, \varphi_2)$.

4.2 Crack growth relation based on energy density intensification

While non-local effects are included in ΔK_{micro}^{macro} of Eq.(2), ΔK of Eq.(1) applies locally only in the limit that the distance r approaches zero. Scaling for crack growth has also been excluded in the classical ΔK. This limitation does not exist in the ΔS_{micro}^{macro} which can be regarded as the energy released when the crack extends by the amount $r=\Delta a$. Now let $(S_{micro}^{macro})_{max}$ be associated with σ_{max} and $(S_{micro}^{macro})_{min}$ associated with σ_{min} such that

$$\Delta S_{micro}^{macro} = (S_{micro}^{macro})_{max} - (S_{micro}^{macro})_{min} \tag{19}$$

and using Eq. (17), it can be shown that

$$\Delta S_{micro}^{macro} = \frac{(1-\nu_{macro})^2(c^2-a^2)}{128 f^2(\varphi_1,\varphi_2)\mu_{micro} d^{0.5} r^{0.5}} \left(\frac{\mu_{micro}}{\mu_{macro}}\right)^2 \left(1-\frac{2\sigma_o}{\pi\sigma_\infty}\sin^{-1}\frac{a}{c}\right)^2 F(\theta)(\sigma_{max}^2 - \sigma_{min}^2) \tag{20}$$

A two parameter fatigue crack growth rate relation can thus be obtained:

$$\frac{da}{dN} = B_1(\Delta S_{micro}^{macro})^m \tag{21}$$

This is reminiscence of the classical strain energy density approach to fatigue in [3] if ΔS_{micro}^{macro} in Eq. (21) is replaced by ΔS for macrocracking only. A simplified version of Eq. (20) or (21) may be used by leaving out

the details of the incidental parameters φ_1 and φ_2. This can be accomplished by letting

$$B = [\frac{F(\theta)}{32f^2(\varphi_1,\varphi_2)(1-2\nu_{micro})}]^m B_1 \tag{22}$$

and defining a new ΔS_{micro}^{macro} without f(φ_1, φ_2). Again, there should be no confusion between Eq.(20) with f(φ_1, φ_2).and Eq.(23) without f(φ_1, φ_2). In what follows, Eqs.(22) and (23) will be used such that da/dN can be computed from Eq.(3). This completes the derivation of the dual scale line crack model based on the energy density intensification approach. Calculation of numerical results will follow.

$$\Delta S_{micro}^{macro} = \frac{(1-2\nu_{micro})(1-\nu_{macro})^2(c^2-a^2)}{4\mu_{micro}d^{0.5}r^{0.5}}(\frac{\mu_{micro}}{\mu_{macro}})^2(1-\frac{2\sigma_o}{\pi\sigma_\infty}\sin^{-1}\frac{a}{c})^2(\sigma_{max}^2-\sigma_{min}^2) \tag{23}$$

5. Invariant Form of Two-Parameter Fatigue Crack Growth Rate Relation

The two parameter crack growth rate relation of Eq. (1) was first proposed in [21] and discussed in [23, 24] with reference to the value of the exponent p on ΔK. Although much work has been done in the ways that A and p in Eq.(1) are affected by microscopic effects, it is rather recent that da/dN were made reference to small cracks [25,26]. While crack sizes can be addressed with reference the three regions I, II and III in Fig.3, it is not clear how the crack size/time effects can be identified with the ΔK since the two parameter fit applies only to region II by the equation

$$\log\frac{da}{dN} = p\log(\Delta K)+\log A \tag{24}$$

With data fitted to a straight line, A can be determined from y-intercept and p from the slope of the line in Fig. 3. The three regions I, II and III are also referred to the micro, macro and fast crack growth in Fig.4(a). Use of ΔK_{micro}^{macro} or ΔS_{micro}^{macro} can make the fatigue data to lie on a straight line as shpwn in Fig. 4(b). In this way, linear interpolation can be used to connect the results of regions I, II amd III and Eqs.(2) nd (3) are said to be form invariant for microcracking and macrocracking in fatigue.

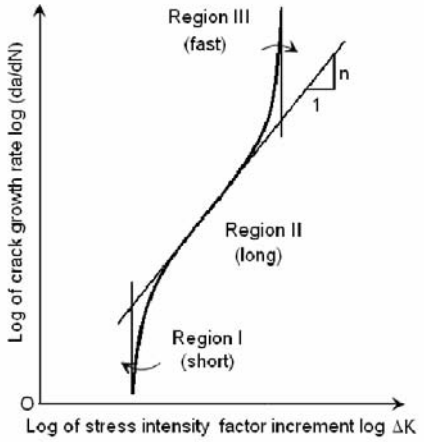

Fig. 3 Fatigue data representation of Eq.(1) for through cracks in two dimensions.

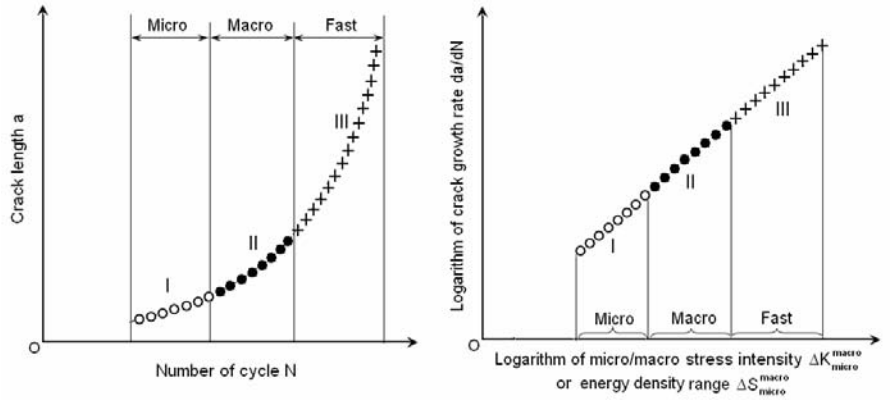

(a) Crack growth data (b) Invariant form of ΔK or ΔS

Fig. 4 Invariant form of crack growth rate in relation to region I, II and III: (a) Crack growth data; (b)Linear line plot of ΔK or ΔS.

5.1 Crack surface tightness stress ratio

As mentioned earlier, accommodation for the opening and closing of the crack surfaces is a major consideration for modeling the fatigue crack growth behavior. This implies that the restraining stress σ_o in relation to the applied stress σ_∞ or the ratio σ_o/σ_∞ should vary with the crack half length a. Assuming that

$$\frac{\sigma_o}{\sigma_\infty} = \begin{cases} 0.65, \text{ for } a = 3\text{mm} \\ 0.48421, \text{ for } a = 10\text{mm} \\ 0.01049, \text{ for } a = 65\text{mm} \end{cases} \tag{25}$$

the bilinear relationship between the stress ratio σ_o/σ_∞ and the crack half length a is adopted.

$$\frac{\sigma_o}{\sigma_\infty} = \begin{cases} -0.023684a + 0.72105, \text{ for } 1 \le a \le 10\text{mm} \\ -0.008613a + 0.57034, \text{ for } 10 \le a \le 65\text{mm} \end{cases} \tag{26}$$

The unit of length a is millimeter. The two stage bilinear relationship is displayed in Fig. 5. The corresponding numerical values of the curve in Fig. 5 are summarized in Table 1.

5.2 Microcrack tip open segment ratio

As the micro/macro crack extends, the tip opening segment length d can also have an effect. That is local intensification will depend on the relative distance r/d which will increase with a as the microcrack becomes macroscopic. This ratio is not sensitive for very small cracks. The behavior

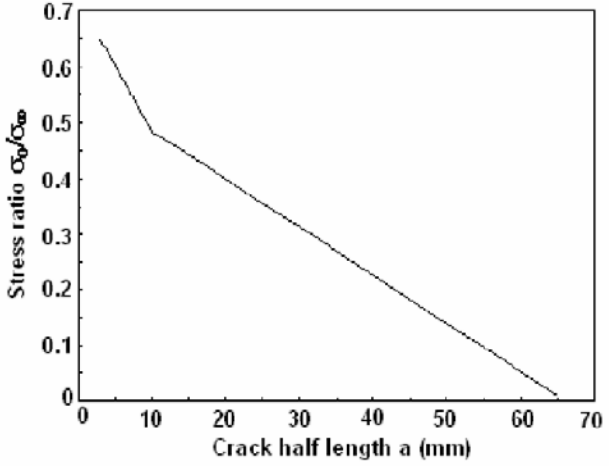

Fig. 5 Bilinear relationship for stress ratio σ_o/σ_∞ versus crack half length a.

Table 1 Values of stress ratio σ_0/σ_∞ with the crack half length a.

a(mm)	σ_0/σ_∞
3	0.65
5	0.60263
10	0.48421
15	0.44114
20	0.39808
25	0.35501
30	0.31195
35	0.26888
40	0.22582
45	0.18275
50	0.13969
55	0.09662
60	0.05356
65	0.01049

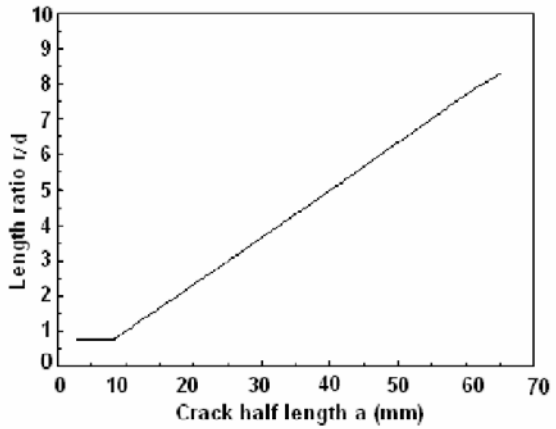

Fig. 6 Length ratio r/d versus crack half length a.

Table 2 Values of length ratio r/d with the crack half length a.

a(mm)	≤8	10	40	60	65
r/d	0.73	1	5	7.7	8.3

is shown in Fig. 6 and the numerical results can be found in Table 2. The ΔK_{micro}^{macro} model of Eq.(14) is independent of the radial distance r. A value of d=1mm will be used. The curve in Fig. 6 applies only to the ΔS_{micro}^{macro} of Eq. (23).

It suffices to know the trends of the curves in Figs. 5 and 6 for application of the dual scale model. Moreover, only Fig. 5 is needed to make the form

of the crack growth rate relation in Eq.(14) invariant. However, better correlation of fatigue data is obtained using Eq. (23) where Fig. 6 is also used. This because Eq.(23) corrects for the mean stress effects whereas Eq. (14) does not.

6. Linearization of Micro-/Macro-Data for Fatigue Crack Growth Rate

Referring to the data in [22] for the fatigue tests of 2024-T3 and 7075-T6 aluminum pre-cracked panels, the dual scale models based on ΔK_{micro}^{macro} in Eq. (14) and ΔS_{micro}^{macro} in Eq. (23) will be used such that data in regions I, II and III as shown in Fig.3 would lie on a straight line without any bends. The shear modulus ratio μ_{micro}/μ_{macro} will be set at two because its value is not known to change with the crack length. The parameters σ^* and d^* will account for the transition of microcracking to macrocracking and vice versa. Use will be made of the macroscopic properties of 2024-T3 and 7075-T6 given in Table 3. Data [22] for six different cases will be analyzed. They are referred to the means stress $\sigma_m = (\sigma_{max}+\sigma_{min})/2$ and the stress amplitude $\sigma_a = \sigma_{max}-\sigma_{min}$ as shown in Table 4 with R being the mean stress ratio $\sigma_{min}/\sigma_{max}$.

Table 3 Mechanical properties of 2024-T3 and 7075-T6 aluminum alloy.

Material type	Yield strength σ_{yd} (kg/mm^2)	Ultimate strength σ_{ult} (kg/mm^2)	Shear modulus μ_{macro}(kg/mm^2)	Poisson's ratio ν_{macro}
2024-T3	37.1	48.3	2812	0.33
7075-T6	47.3	53.0	2742	0.33

Table 4 Case classification of fatigue crack growth data.

Case	σ_m (kg/mm^2)	σ_a (kg/mm^2)	R
I	12	2.5	0.655
II	12	4.0	0.500
III	12	6.5	0.291
IV	9	2.5	0.565

V	9	4.0	0.385
VI	9	6.0	0.161

6.1 Discussion of results using Eq.(2)

Based on the numerical results provided earlier, the log of da/dN versus log of ΔK_{micro}^{macro} may be plotted. The curves for 2024-T3 and 7075-T6 aluminum alloy are displayed in Fig. 7. Note that the data in all three regions I, II and III can now be adequately represented by straight lines. The slope for 2024-T3 signified by n is 3.532 which is smaller than that of 7075-T6 with n=4.179. This means that the crack growth rate of 2024-T3 is slower than that of 7075-T6 which is to be expected. Not to be misled is that the x-coordinate in Fig. 7 has been shifted and did not start from zero. The full scale is exhibited in Fig. 8 such that the y-intercepts give log C=-6.967 for 7075-T6 and -6.710 for 2024-T3. When the stress amplitude σ_a is raised from 2.5 to 4.0 kg/mm^2 for the same mean stress σ_m= 12 kg/mm^2 although the stress ratio R is reduced from 0.655 to 0.500, a slight increase in the crack growth rate da/dN for both materials are seen. This is

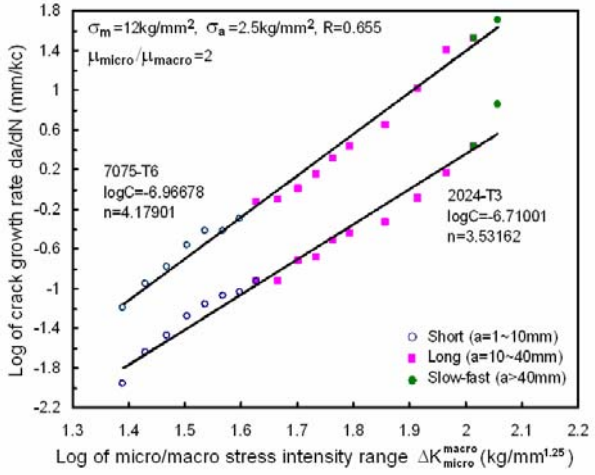

Fig.7 Log crack growth rate da/dN v.s. log micro/macro stress intensity range ΔK_{micro}^{macro} for Case I.

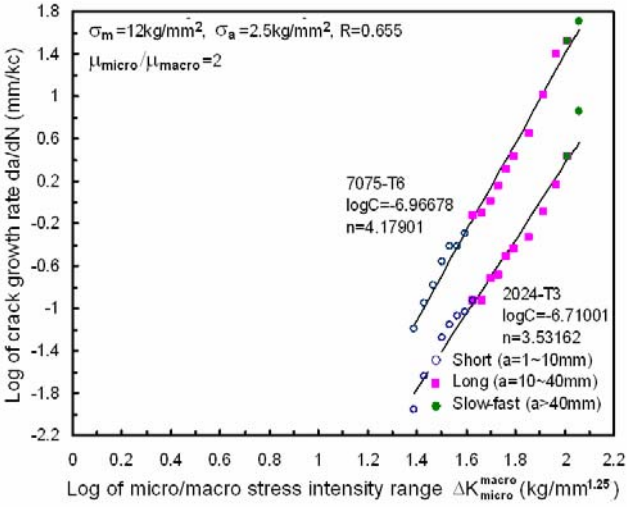

Fig.8 Coordinates redefined for log crack growth rate da/dN v.s. log micro/macro stress intensity range $\Delta K_{\text{micro}}^{\text{macro}}$ for Case I.

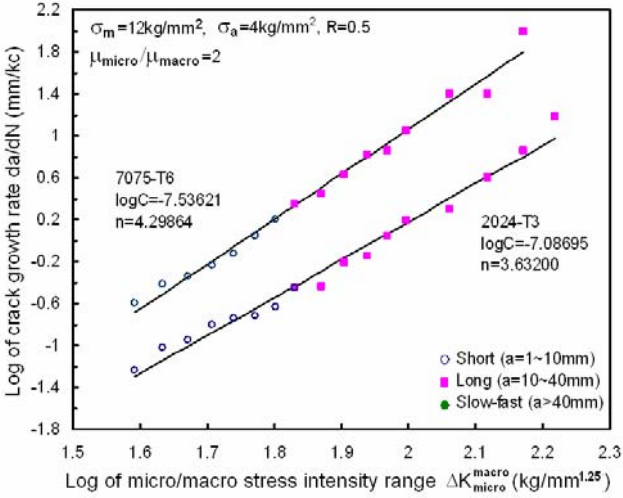

Fig.9 Log crack growth rate da/dN v.s. log micro/macro stress intensity range $\Delta K_{\text{micro}}^{\text{macro}}$ for Case II.

the results of increase in the slopes of the straight lines for 2024-T3 (n=3.632) and 7075-T6 (n=4.297). The straight line fit in Fig. 9 is good because most of the data points pertained to half crack length in the range 10 to 40 mm corresponded to region II.

A further increase of the stress amplitude to σ_a = 6.5 kg/mm^2 with σ_m= 12 kg/mm^2 leads to additional reduction in R to 0.297. This shows that the slopes of da/dN acquire further gain with n=4.224 for 2024-T3 and n=4.742 for 7075-T6 although the data gained more scatter as shown in Fig.10. The detrimental effect of increase stress amplitude on fatigue life is exemplified as in the use of the classical S-N curve where no consideration to crack growth was made. Reduction of the maximum stress also has a noticeable effect on the crack growth rate. Consider Case IV in Table 4 where σ_a = 2.5 kg/mm^2 with σ_m= 9 kg/mm^2 and R = 0.565 being similar to that in Case I. A complete set of data points for all three regions were obtained as exhibited in Fig. 11. Decrease in the slopes of the curves confirms a reduction of the crack growth rate when the stress amplitude is decreased. The effect of stress amplitude starts to take over in Case V when σ_a = 4.0 kg/mm^2 with σ_m= 9 kg/mm^2 and R = 0.385. Fig. 12 shows that the slopes of the curves are increased to n=3.725 for 2024-T3 and n=3.781 for 7075-T6. Further aggravation of the crack growth rate is seen by the curves in Fig. 13 when the stress amplitude is raised to σ_a = 6.0 kg/mm^2. Now the slopes attain even higher values of n=3.812 for 2024-T3 and n=4.511 for 7075-T6.

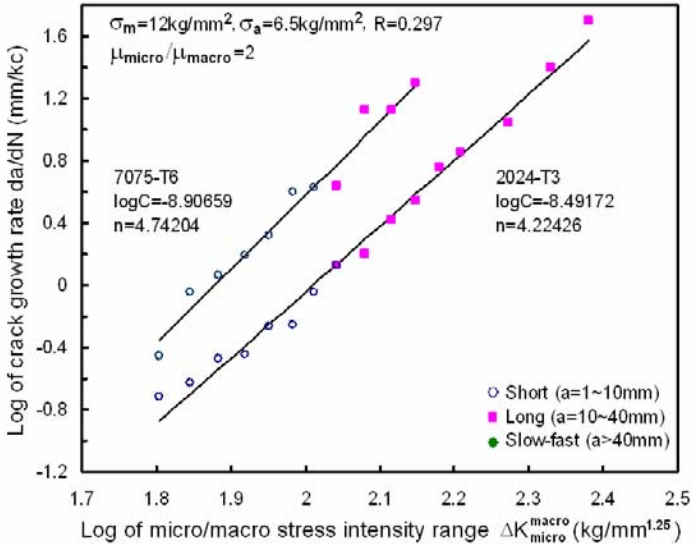

Fig.10 Log crack growth rate da/dN v.s. log micro/macro stress intensity range ΔK_{micro}^{macro} for Case III.

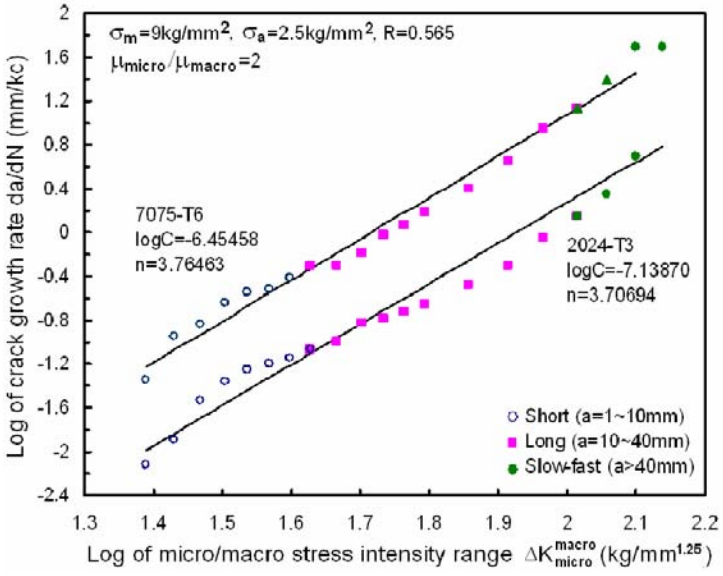

Fig.11 Log crack growth rate da/dN v.s. log micro/macro stress intensity range ΔK_{micro}^{macro} for Case IV.

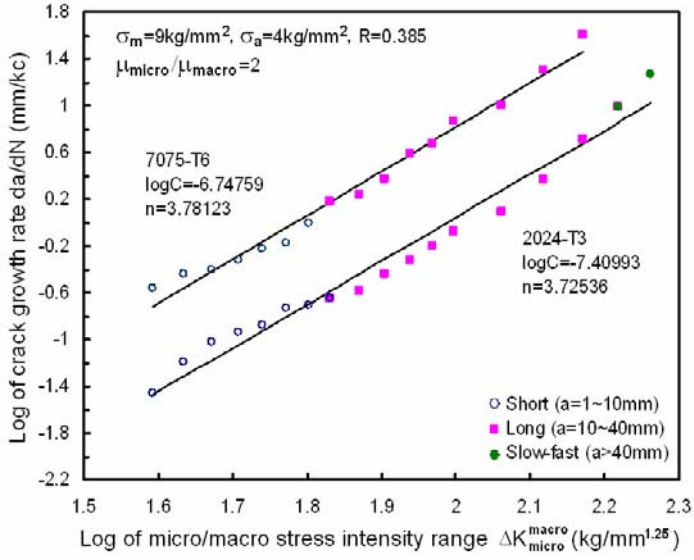

Fig.12 Log crack growth rate da/dN v.s. log micro/macro stress intensity range ΔK_{micro}^{macro} for Case V.

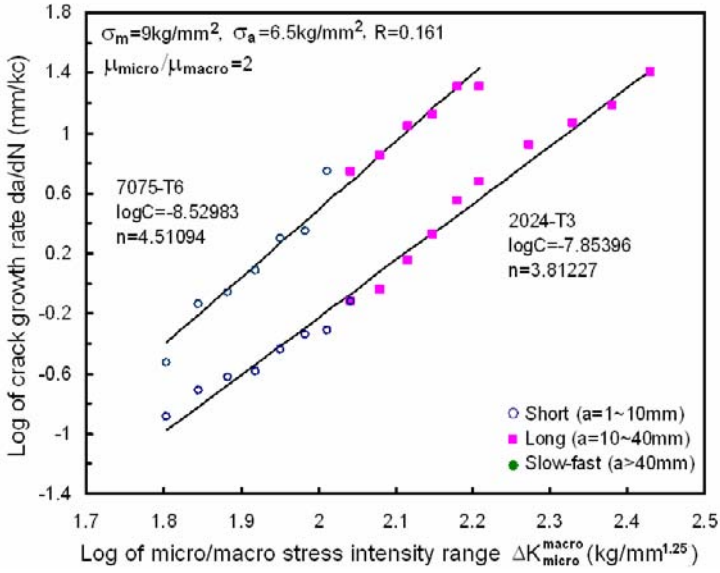

Fig.13 Log crack growth rate da/dN v.s.log micro/macro stress intensity range ΔK_{micro}^{macro} for Case VI.

The findings in Figs. 7 and 13 can be summarized in Table 5 for a comparison of the data for the 2024-T3 and 7075-T6 material, particularly with reference to the parameters C and n in Eq. (2) for the ΔK_{micro}^{macro} model. The stress amplitude is seen to play a dominant role by the fatigue data in Table 5. Cases I to III show that the increase in stress amplitude tends to increase the crack growth rate by raising both the y-intercept log C and the slope n. The reduction of maximum stress reflected by lowering the mean stress σ_m for Cases IV to VI did lower the da/dN as shown by Case IV but the further increase in the stress amplitude again raised the absolute log C and n values as summarized in Table 5.

Table 5 Stress amplitude and mean stress effects on C and n in Eq. (2).

Case	7075-T6		2024-T3	
	Log C	n	Log C	n
I	-6.961	4.179	-6.770	3.532
II	-7.336	4.297	-7.067	3.632
III	-8.907	4.742	-8.492	4.224
IV	-6.455	3.765	-7.139	3.707
V	-6.748	3.781	-7.410	3.725
VI	-8.530	4.511	-7.854	3.812

6.2 Discussion of results using Eq.(3)

The difference between ΔK_{micro}^{macro} in Eq. (14) and ΔS_{micro}^{macro} in Eq. (23) is not insignificant and will vary for different test conditions and materials. Based on the same crack growth data as those used for obtaining the curves in Figs. 7 to 13, Fig. 14 displays a plot of log(da/dN) versus log(ΔS_{micro}^{macro}). All data points fell on straight lines, one for 2024-T3 and one for 7075-T6 with the respective slopes of m=2.690 and 3.394. These values are smaller than those of n=3.532 and 4.179 in Table 5 for Case I of the ΔK_{micro}^{macro} model. The difference in slopes for the two materials using the two models is about the same. Fig. 15 shows similar trends for Case II where the data are more scattered as the stress amplitude was increased from 2.5 to 4.0 kg/mm^2. Much more scatter of the data resulted in Case III where σ_a is increased to 6.5 kg/mm^2 with σ_m kept at 12 kg/mm^2. This is also accompanied by an increase in the crack growth rates as illustrated in Fig. 16. The values of the slope m in Figs. 14 to 16, however, are much closer together when the same data are represented by the ΔK_{micro}^{macro} model shown by the curves in Figs. 7 to 10 inclusive. A good fit of the data is found in Fig. 17 for Case IV. The two straight lines for 2024-T3 and 7075-T6 are nearly parallel with slopes of m=3.036 and 3.055. The superiority of the fatigue crack growth resistance for 2024-T3 does not show up for the applied mean stress and stress amplitude. The 7075-T6 aluminum would have served equally well. This illustrates the location specificity when selecting the use of materials in non-uniform stress and/or energy density fields. The crack growth behavior of the two materials start to deviate from one another as the stress amplitude is raised to 4.0 kg/mm^2 with a mean stress of 9 kg/mm^2 as in Case V where the plot of ΔS_{micro}^{macro} is given in Fig. 18. Case VI for σ_a=6.0 kg/mm^2 corresponds to the results in Fig. 19. Data for large stress amplitudes tend to have more scatter. It is worthwhile to note the slopes m in Table 6 and compare them to the values n in Table5. An important conclusion is that the variations of the m values are much less than those for n as the mean stresses are change. This is to be expected because the ΔS_{micro}^{macro} model accounts for the mean stress effect whereas the ΔK_{micro}^{macro} model does not. This concludes the presentation of the numerical results for the fatigue crack growth rate where the data were transformed onto a straight line relationship. To be noted is that the position of the x-axis in Figs. 14 to 19 has been shifted and did not start from the origin. The difference in reference can be seen from the curves in Figs. 7 and 8. The

locations of the y-intercepts in Table 6 should now be clear. Moreover, the $\log \Delta S_{micro}^{macro}$ in Figs 14 to 19 are negative while ΔS_{micro}^{macro} in Eq. (23) is positive definite.

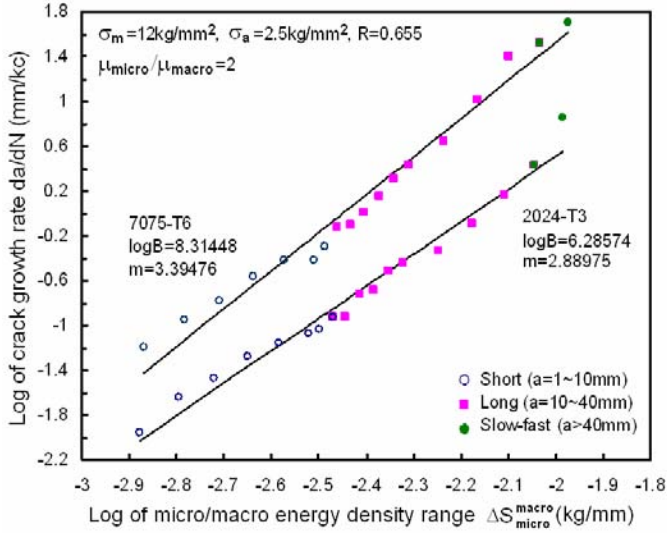

Fig. 14 Log crack growth rate da/dN vs. log micro/macro energy density range ΔS_{micro}^{macro} for Case I.

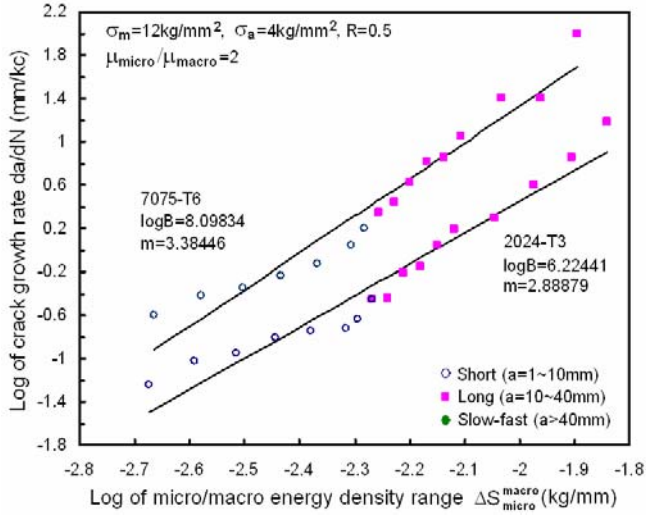

Fig. 15 Log crack growth rate da/dN vs. log micro/macro energy density range ΔS_{micro}^{macro} for Case II.

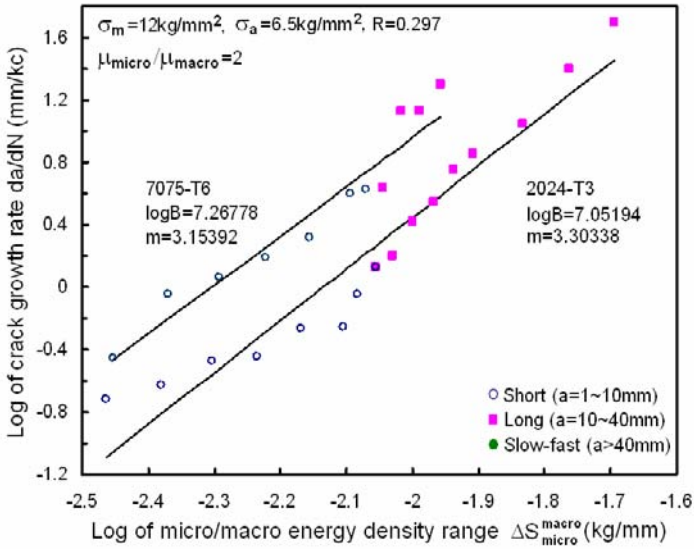

Fig. 16 Log crack growth rate da/dN vs. log micro/macro energy density range $\Delta S_{\text{micro}}^{\text{macro}}$ for Case III.

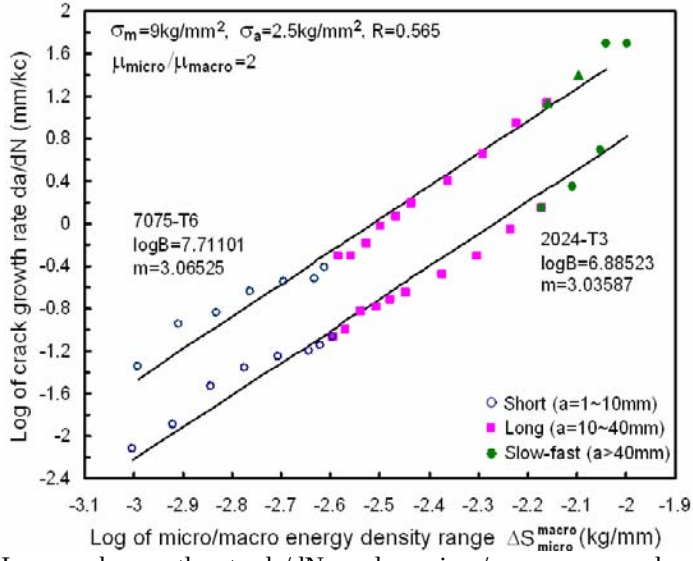

Fig. 17 Log crack growth rate da/dN vs. log micro/macro energy density range $\Delta S_{\text{micro}}^{\text{macro}}$ for Case IV.

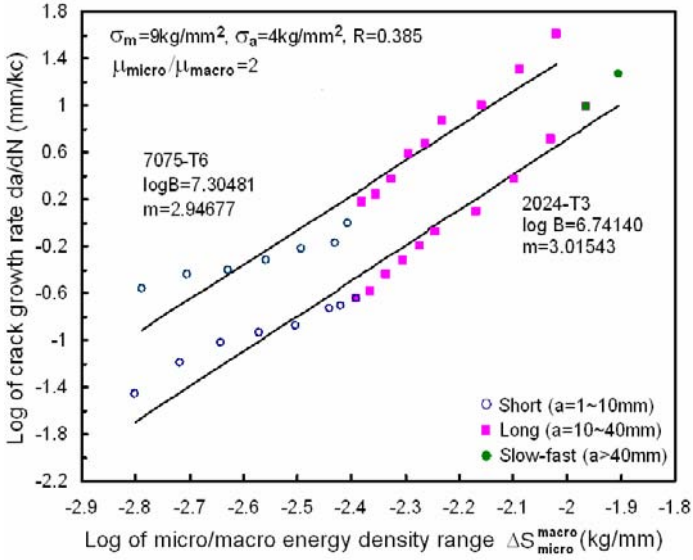

Fig. 18 Log crack growth rate da/dN vs. log micro/macro energy density range $\Delta S_{\text{micro}}^{\text{macro}}$ for Case V.

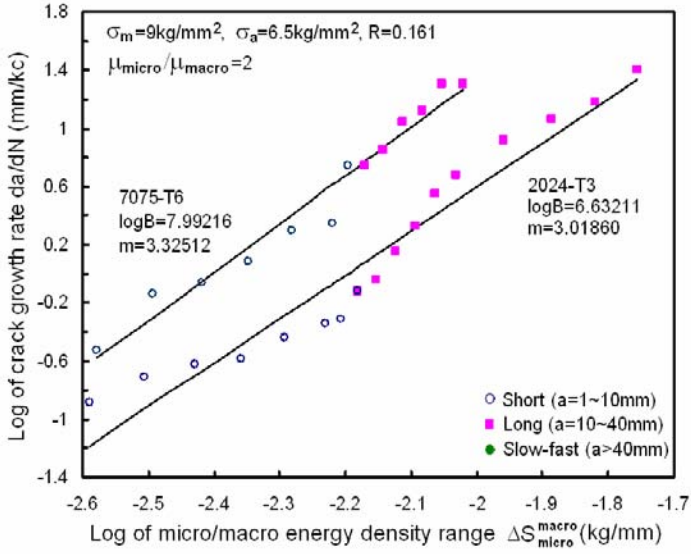

Fig. 19 Log crack growth rate da/dN vs. log micro/macro energy density range $\Delta S_{\text{micro}}^{\text{macro}}$ for Case VI.

Table 6 Stress amplitude and mean stress effects on B and m in Eq. (21).

Case	7075-T6		2024-T3	
	Log B	m	Log B	m
I	8.314	3.394	6.286	2.890
II	8.098	3.394	6.224	2.888
III	7.268	3.153	7.052	3.303
IV	7.711	3.055	6.885	3.036
V	7.035	2.947	6.741	3.015
VI	7.992	3.326	6.632	3.019

7. Concluding remarks

Even though metal fatigue has been researched for more than a century, full confidence is still lacking when prediction of fatigue life of structural components is at stake.. By in large, the effort has been concerned with relating the onset of rapid fracture to the initiation of cracks under low stress but repeated many times. In more recent times, attention has been focused on explaining the size and time scaling effects associated with the fatigue crack growth rate da/dN models with reference to the commonly known regions I, II and III. In particular, the use of the macroscopic stress intensity factor range ΔK for region I is questioned. The concerns are whether data for micron size and smaller cracks could still be adequately correlated by the two parameter relation. Hence, a fourth region for crack nucleation has been proposed [25.26]. This region is effectively concerned with nanometer size cracks with length $a \approx 10^{-4}$ mm or smaller. Crack nucleation may have to be identified with a fifth region. What this indicates is that the discovery of defect initiating at smaller and smaller time and size scales necessitates a more refined procedure for modeling the evolution of crack initiation to propagation. Several issues are in need of additional attention:

(1) Is it possible to retain the two parameter da/dN relation using $\Delta K^{\text{macro}}_{\text{micro}}$ or some other parameter and describe nano-scale cracks assuming that the line crack configuration can be retained?
(2) If the answer to (1) is positive, then will it be possible to establish an invariant form of da/dN using $\Delta K^{\text{macro}}_{\text{micro}}$ or $\Delta S^{\text{macro}}_{\text{micro}}$?

What has been learned from experience is that through crack specimens are more conducive to the aircraft structure engineers who entail crack length a ≈10-80 mm (macromechanical) that falls into region II. Material engineers are more concerned with surface cracks due material microstructure effects associated with region I where a $\approx 10^{-3}$ to10^{-1}mm (microstructural). The fourth region would presumably fall into the scale range most sensitive to chemical reactions. This corresponds to a $\approx 10^{-4}$ mm or smaller (nanochemical) [27]. Defects in this size range appear very early and are deeply trapped to the interior of the material. The inherent coupling of size and time scale possesses a hierarchy in the damage process that can be referred to as macromechanical, microstructural and nanochemical. Subatomic effects will no doubt be of interest to the biologists that may be further classified with the prefix pico or femto. The point to be made is that the creation of different imperfections, defects or cracks are intimately related to the dissipated energy density of a particular physical process. They are inherently paired in size and time.

It is clear that length alone is not adequate for distinguishing micro- and macro-cracks. In fatigue, the time variable is accounted for by dN/dt which is in fact the frequency of the fatigue cycles. Hence data can be represented in terms of da/dt just as well as da/dN. Tightness of the crack mouth, however, is regarded important because it can change microcracking to macrocracking or the other way around under alternating tension and compression loading. The clue that there prevails a very small segment of the microcrack tip that does not close because of micro-asymmetry prompted the discovery of double singularity stress field [13]. Two competing singularities prevail one being stronger with the order $1/r^{0.75}$ and the other weaker with the order $1/r^{0.25}$. The simultaneous consideration of the double singularity is responsible for explaining the transitory behavior of micro- and macro-cracking. In retrospect, any multiscale crack models should have the capability to alter the morphology of the defect during scale transition. At the same time, connection of the results at the different scales can be best achieved by linear interpolation if the da/dN data can be made to lie on a line. Such a possibility can also be realized in a transformed plane that is often used in space transformation. An immediate extension of the present approach would be the development of a triple scale model of macro/micro/nano cracks.

References

[1] Griffith A A. The phenomenon of rupture and flow in solids, Philosophical Transactions, Royal Society of London, Series A221 (1921) 163-198.

[2] Irwin GR. Fracture Mechanics, In: Structural Mechanics, Pergamon Press,

New York, (1960) 557-592.
[3] Sih GC. Mechanics of fracture initiation and propagation. The Netherlands: Kluwer Academic Publishers, 1991.
[4] Sih G.C. Crack front behavior of mesofracture in non-equilibrium mechanics, Journal of Physical Mesomechanics, 1(1) (1998) 77-87.
[5] Popov VL. and Kroner E. On the role of scaling in elastoplasticity, Journal of Physical Mesomechanics, 1(1) (1998) 103-112.
[6] Sih GC. Thermomechanics of solids: nonequilibrium and irreversibility, J. of Theoretical and Applied Fracture Mechanics, 9(3) (1988) 175-198.
[7] Sih GC. Some basic problems in nonequilibrium thermomechanics, eds. S. Sienietyez and P. Salamon, Taylor and Francis, New York, 1992, 218-247.
[8] Schwab K. Henrikson E. A., Worlock J. M. and Roukes M. L. Measurement of the quantum of thermal conductance, Nature, 404 (2000) 974-976.
[9] Roukes ML. Plenty of room indeed. In: The Edge of Physics, Scientific America (2001) 92-100.
[10] Sih GC. Signatures of rapid movement of electrons in valence band region: interdependence of position, time and temperature, J. of Theoretical and AppliedFracture Mechanics, 45(1) (2006) 1-12.
[11] Sih GC. and Tang X. S. Dual scaling damage model associated with weak singularity for macroscopic crack possessing a micro/mesoscopic notch tip, J. of Theoretical and Applied Fracture Mechanics, 42(1) (2004) 1-24.
[12] Tang X.S. and Sih G. C. Weak and strong singularities reflecting multiscale damage: micro-boundary conditions for free-free, fixed-fixed and free-fixed constraints, J. of Theoretical and Applied Fracture Mechanics, 43(1) (2005) 5-62.
[13] Sih G.C. and Tang X. S. Simultaneous occurrence of double micro/macro stress singularities for multiscale crack model, J. of Theoretical and Applied Fracture Mechanics, 46(2) (2006) 87-104.
[14] Tang XS. and Sih GC. Evaluation of microstructural parameters for micro-/ macro-line crack damage model, J. of Theoretical and Applied Fracture Mechanics,46(3) (2006) in press.
[15] Sih GC. and Tang XS. Simultaneous occurrence of double micro/macro stress singularities for multiscale crack model, J. of Theoretical and Applied Fracture Mechanics, 46(2) (2006) 87-104.
[16] Vasudevan AK. Sadananda K. and Louat N. A review of crack closure, fatigue crack threshold and related phenomena, Material Science and Engineering, A188 (1994) 1-22.
[17] Newman Jr. JC. Brot A. and Matias C. Crack-growth calculations in 7075-T7351 aluminum alloy under various load spectra using an improved crack-closure model, Engineering Fracture Mechanics 71 (2004) 2347–2363.
[18] Noroozi AH. Glinka G. and Lambert S. A two parameter driving force for fatigue crack growth analysis, International Journal of Fatigue, 27 (2005) 1277-1296.
[19] Jones R. Barter S. Molent L. and Pitt S. Crack growth at low K's and the Frost-Dugdale law, Journal of the Chinese Institute of Engineers, Special Issue inHonour of Professor G. C. Sih, 27(6) (2004) 869-875.

[20] Jones R. and Pitt S. On the Frost-dugdale law and the two parameter driving force for fatigue crack growth analysis, Sixth Int. Conf on Fatigue Damage of Structural Materials: Fatigue Damage VI, Hyannis, Massachusetts, Sept. 17-22, 2006.
[21] Paris PC. The growth of cracks due to variations in load, Ph. D. Dissertation, Department of Mechanics, Lehigh University (1962).
[22] Broek D. and Schijve J. The influence of the mean stress on the propagation of fatigue cracks in aluminum alloy sheets, National Aeronautics and Astronautics Research Institute NLR-TN M. 21111, Amsterdam (1963) 1-57.
[23] Liu HW. Fatigue crack propagation and applied stress range, ASME Trans., J. Basic Eng. 85D(1) (1963) 116-122.
[24] Liu HW. A review of fatigue crack growth analyses, J. of Theoretical and Applied Fracture Mechanics 16 (1991) 91-108.
[25] McDowell DL. Multiaxial small fatigue crack growth in metals, Int. J. Fracture, 19(1) (1997) S127-S135.
[26] Wang CH. Effect of stress ratio on short fatigue crack growth, ASME Journal of Engineering Materials and Technology, 118 (1996) 362-366.
[27] Sih GC. Crack tip system for environment assisted failure of nuclear reactor alloys: multiscaling from atomic to macro via mesos, J. of Pressure Equipment and Systems, 3(2005)1-25.

Fatigue Crack Growth Rate of Cable-Stayed Portion of Runyang Bridge: Part I–Cable Crack Growth Due to Disproportionate Cable Tightening/Loosening and Traffic Loading

G. C. Sih [1, 2 *] **and X. S. Tang** [3]

[1] International Center for Sustainability, Accountability and Eco-Affordability of Large Structures (ICSAELS)
Advanced Technology for Large Structural Systems (ATLSS)
Lehigh University, Bethlehem, PA 18015, USA

[2] School of Mechanical and Power Engineering, East China University of Science and Technology, Shanghai 200237, China

[3] School of Bridge and Structural Engineering, Changsha University of Science and Technology, Changsha, Hunan 410076, China

[*] *Email: gcs8866@yahoo.com, gcs1@lehigh.edu*

Abstract

Relatively little is known about the fatigue crack growth behavior of bridge cables. Such information can become increasingly more important in time for the cable-stayed bridges whose structural integrity can be greatly affected by the degradation of the individual cable material due to aging as well as defect growth. Moreover, crack initiation and propagation are intimately related such that they have to be treated as one of the same process. This requires a dual scale fatigue crack growth model involving both micro- and macro-cracking where the interaction of three micro/macro material, geometric and load parameters is considered. Based on the design data for the stresses in the 52 cables of the Runyang cable-stayed bridge, three typical cables referred to as #28, #38 and #50 are selected for analyzing fatigue crack growth under traffic and no traffic conditions. The initial tension in the cable can vary by using α=1 as the reference such that deviation from the design condition may be regarded as tightening and loosening. Under traffic, initial tightening and loosening of the cable can enhance and impede fatigue crack growth, respectively. When traffic is removed, initial tightening and loosening of the cable can impede and enhance fatigue crack growth. Opposing effects of fatigue crack growth are observed for cables with and without traffic. These results are discussed in terms of crack growth rate and crack length as a function of the fatigue cycles assuming that the cable has a life of two million cycles. Substantial variance in fatigue crack growth is found. Crack

G.C. Sih (ed.), Multiscale Fatigue Crack Initiation and Propagation of Engineering Materials: Structural Integrity and Microstructural Worthiness, 209–247.

length can vary from a few mm to 50 mm and more before reaching the onset of rapid fracture. The stiffness of the cable is also affects crack growth. Each cable is found to behave as a structure of its own. Replacement of cables appears to be eminent during the life span of cable-stayed bridge because of the wide variance of fatigue lives of the cables. This means that some cables will fail while others may still have ample remaining life.

1. Introduction

The critical components in a cable-stayed bridge are no doubt the cables each of them behaves differently and acts as a structure in itself. The effects of the main load carried by the bundles of high strength steel wires are susceptible to change in time because aging and degrading of the material property will occur in addition to corrosion caused by the environment conditions. The current construction of the cables inhibits and prevents the successful use of non-destructive testing despite extensive efforts are being made in health monitoring. For bridges that have been in service after a decade or more the situation becomes even more uncertain because damage accumulates at the different scales, say micro and macro. This fact was recognized from the earlier research on dual scaling [1,2]. Empirical models may not be adequate because they are unable to know the presence of tightly closed cracks even though the material may have separated locally. In this case, there is no signal to transmit for detection. To reiterate, this is especially true for situations where the faults can closed and remain dormant but they can open to inflict serious damage under overload or unexpected accidents such as earthquakes or vehicle impact. The undetected flaws can alter a situation of fail-safe to one that triggers disaster. On site health monitoring is only as effective as knowing the locations where gages should be placed. The critical sites are often hidden and inaccessible for inspection until damage becomes excessive. Not enough emphasizes can be placed on knowing the potential sites of damage for a given design and how damage would develop in service. An understanding of fail-safe in the design of large structures [3] is vital for the mitigation or prevention of potential injury/life and property. The period for the inspection of bridges is every two years. This is a mandatory requirement of the US National Bridge Inspection Standard (NBIS). The recent disaster of the I-35W bridge in Minnesota [4] is indicative of the ineffectiveness of implementing the standards.

Although the current state-of-the-art of bridge maintenance and inspection recognizes the importance of flaw detection caused by fatigue for steel structure bridges [5,6] but relatively little attention [7-9] has been devoted

to the long term fatigue of cables for suspension and cable-stayed bridges. Most of the cable fatigue works address the initial design requirement [10,11] which can cast false confidence on the interpretation of field data, particularly when uncertainties prevail with the assumed boundary conditions in design. This problem is particularly acute for the cable-stayed bridge that may possess more than one hundred cables and each of them can have widely different behavior. It means that some of them may be on verge of breaking while others may still have ample remaining life. The study in [9] has shown such effects to be prevalent by using the design data of the cable-stayed portion of the Runyang bridge [12]. The diversification of cables'behavior is typical as they can experience loosening and tightening every hours of the day where the traffic may vary from full to no load, not counting for wind that also causes variation in cable tension. This becomes increasingly problematic for aging cable-stayed bridges as the cables do not deteriorate at the same rate. Some may have ample remaining life while others are in need of replacement. The present monitored data are not capable of sorting out the degree of cable damage because no confidence can be placed on their association with the actual physical damage. *This problem cannot be alleviated by embedding sensors into the cables during fabrication.* There is not a direct correspondence between the sensor and the local damaged area. It is necessary to have a validated software that can address fatigue damage for interpreting the sensor data, preferably over an area that is large in comparison with the damage. Not enough emphasis can be placed on the latter, especially when microcracking and macrocracking are both mingled in the signal. It was demonstrated in [9] that the crack growth behavior in two of the Runyang bridge cables differed widely when fatigued under traffic and no traffic conditions. The discrepancy can be the difference of stable crack growth and the onset of rapid fracture. Additional work is carried out in this communication to offer a more complete discussion of the fatigue crack growth behavior of cables for the Runyang bridge. Considered in particular is the crack growth rates of some typical cables showing that the variance may be relevant for the future development of maintenance and inspection procedures.

2. Problem Statement

The Runyang bridge consists of two portions as shown in Fig. 1(a) for the cabled-stayed portion and Fig. 1(b) for the suspension portion. A close view of the cables for the cable-stayed portion can be found in Fig. 2. Note that the cables are mounted onto the two towers and anchored at the girders of the bridge. The distance between the two compressed towers is

406m. The structure is sufficiently flexible such that it can sway. Because of the load variations, tightening and loosening of the cables is expected. Considered are conditions for the bridge under traffic and no-traffic conditions. The large variations of fatigue lives for the cables are identified for several different scenarios of cable tightening and loosening that can be caused by climate changes, a particular concern in recent years. The results are needed for the development of inspection procedures for the health monitoring of the Runyang bridge. Similar analysis should be done for the suspension portion of the bridge.

(a) Cable-stayed portion

(b) Suspension portion

Fig. 1 Close view of the cable-stayed and suspension portions of Runyang bridge.

Fig. 2 The Runyang cable-stayed portion of the bridge with 406m span.

2.1 Cable forces with and without traffic

Assuming symmetry, only 52 of the total of 104 cables of the Runyang cable-stayed bridge need to be shown. The tension in the cable with no traffic and with traffic is as shown, respectively, in Figs. 3 and 4. The position

of each cable is shown and numbered from left to right. The largest forces prevail in cables #3 and #50. They are located, respectively, third from the left and right end position. The small differences in the forces in cables #1~#26 and #27~#52 can be ignored. To be examined are the fatigue crack growth characteristics in cables #28, #38 and #50 where cable #38 corresponds to the minimum tension.

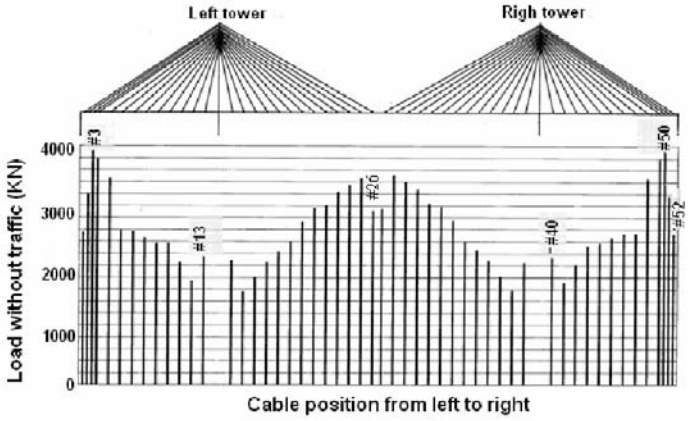

Fig. 3 Load in cables without traffic.

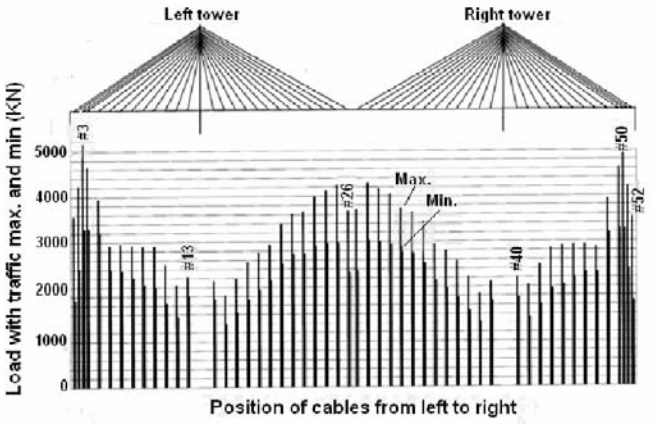

Fig. 4 Maximum and minimum load in cables with traffic.

2.2 Multiscale application of fracture mechanics

Modern bridge design takes into account the influence of material properties such as high to very high strength, high temperature and corrosive resistance. This implies that the microstructural effect of the material comes

into play. From the fracture mechanics view point, it is necessary to consider the behavior of small cracks that might be dormant under one condition and grow to large cracks under another condition. Microcracks and its transition to macrocracks must be accounted for. The traditional sigmoidal curve as illustrated in Fig. 5 can no longer be represented by the two-parameter crack growth rate relation [13] because it remains straight only for the portion Region II for macrocrack growth (or long cracks). Microcracks grow in Region I referred to as the threshold. Region III pertains to fast crack propagation heading towards the onset of global instability. Non-destructive testing should therefore be designed to detect the stable macrocrack growth in Region II.

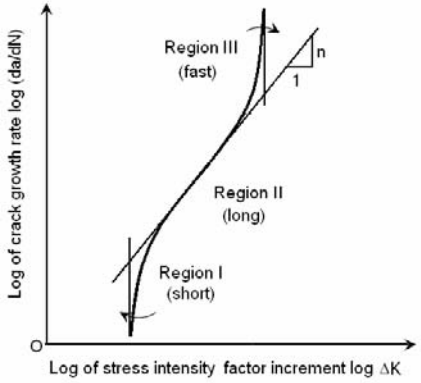

Fig. 5 Traditional two-parameter fatigue crack growth rate.

Fig. 6(a) shows the crack growth curves partitioned with reference to the crack size from nano to macro. In order to preserve the traditional framework of fracture control of using only two empirical parameters, a multiscale model of crack growth was advanced [14,15] by replacing the range of stress intensity factor ΔK [13] for macrocracks only with ΔK_{micro}^{macro} or ΔS_{micro}^{macro} that can account for the transition of microcracks to macrocracks or vice versa. The extension to triple scale involving nano, micro and macro is straightforward. In general the use of ΔS_{micro}^{macro} is preferred because it accounts for the effect of mean stress. Examples of using ΔK_{micro}^{macro} or ΔS_{micro}^{macro} can be found in [14,15]. In a log da/dN versus $\log \Delta K_{micro}^{macro}$ or $\log \Delta S_{micro}^{macro}$ domain, the three Regions I, II and III no longer appear as sigmoidal. Instead, a straight line is obtained. This is shown in Fig. 6(b). This enables the shifting of the results from nano to micro and from micro to macro or directly from nano to macro.

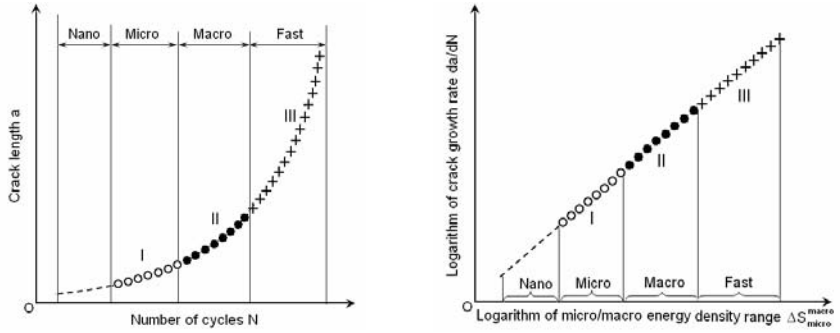

(a) Crack growth curve (b) Crack growth rate

Fig. 6 Form invariant property of multiscale crack growth rate relation.

2.3 Stress amplitude and mean stress

The simultaneous consideration of stress amplitude $\sigma_a=\sigma_{max}-\sigma_{min}$ and mean stress $\sigma_m=(\sigma_{max}+\sigma_{min})/2$ suggests the application of ΔS_{micro}^{macro} which will be made use of in the sequel. Here, σ_{max} and σ_{min} are the maximum and minimum cyclic applied stress, respectively. Further distinction must be made because they are different under traffic and no-traffic conditions. The superscripts α refers to traffic condition and o to traffic absent condition. The values of σ_{max}^{o} and σ_{max}^{α} for the 52 cables of the Runyang bridge can be found in Table A1 of Appendix I of [9]. Two Cases I and II will be considered; they are defined as

$$\textit{Case I}:\ \sigma_a=\alpha\sigma_{max}^{\alpha}-\sigma_{max}^{o},\ \sigma_m=\frac{\alpha\sigma_{max}^{\alpha}+\sigma_{max}^{o}}{2} \tag{1}$$

$$\textit{Case II}:\ \sigma_a=\sigma_{max}^{\alpha}-\alpha\sigma_{max}^{o},\ \sigma_m=\frac{\sigma_{max}^{\alpha}+\alpha\sigma_{max}^{o}}{2} \tag{2}$$

Case I in Eq. (1) refers to tightening of the cables that correspond to α=1.0, 1.2, 1.4 and 1.6 with α=1 (normal tension) as the reference. Numerical values of σ_a, σ_m and $\sigma_a\sigma_m$ for the 52 cables in Runyang bridge with α=1.0, 1.2 and 1.6 are given in Tables A2, A3 and A4, Appendix II of [9]. Case II in Eq. (2) refers to loosening of the cables that correspond to σ=0.91, 0.94, 0.97, 1.00 (normal tension). Henceforth, $\alpha\sigma_{max}^{\alpha}$ will be referred to as "max. stress with traffic" and $\alpha\sigma_{max}^{o}$ as "max. stress without traffic." Remember that α=1.0 stands for normal tension while $\alpha\geq$1 and $\alpha\leq$1refer, respectively to more and less cable tension. Cable tightening and loosening are defined in terms of σ_a and σ_m as given by Eqs.(1) and (2).

2.3.1 Case I: cable tightening and loosening with traffic

Fig. 7 displays a plot of the product $\sigma_a\sigma_m$ for the cables as a function of the cable position from left to right numbered as 1 to 52. Note that the product $\sigma_a\sigma_m$ fluctuates according to the variations of the tension in the cables due to varying traffic as indicated in Fig. 4. The end cables peak with a dip for the middle cable. The minima tension occur in cables #14 and #38. Symmetry about cable #26 is not quite preserved. The cable tightens with increasing α from 1.0 to 1.6 with the maximum $\sigma_a\sigma_m$ at α=1.6 which will tend to reduce fatigue life. The peaks of the curves corresponding to cable #3 and #50 rise very quickly with the parameter α.

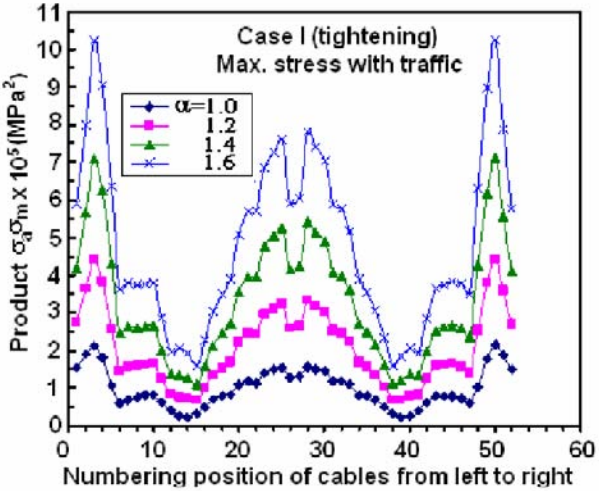

Fig. 7 Product $\sigma_a\sigma_m$ of cables versus position of cables for Case I (tightening) with α=1.0, 1.2, 1.4 and 1.6 under varying traffic.

Numerical values of σ_a, σ_m and $\sigma_a\sigma_m$ for the 52 cables of the Runyang bridge with α=0.97 and 0.91 can be found in [9] as mentioned earlier. Loosening of the cable under traffic has a beneficial effect to fatigue life. This can be seen from Fig. 8 where decreasing α from 1.00 (normal tension) to 0.91 (less tension) reduces the amplitude of $\sigma_a\sigma_m$ although the amount of reduction in Fig. 8 is not as pronounced as the rise in Fig. 7 for cable tightening. It can be said that *cable tightening under varying traffic tends to increase the product* $\sigma_a\sigma_m$ *while cable loosening under varying traffic decreases the product* $\sigma_a\sigma_m$ *that is beneficial.*

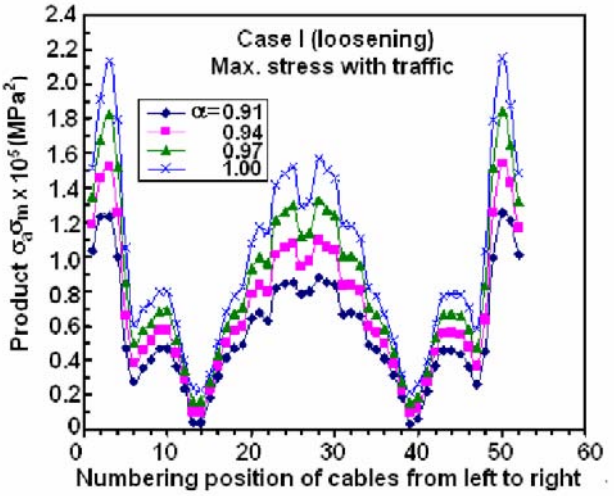

Fig. 8 Product $\sigma_a\sigma_m$ of cables versus position of cables for Case I (loosening)with α=0.91, 0.94, 0.97 and 1.00 under varying traffic.

2.3.2 Case II: cable tightening and loosening without traffic

Consider now Case II in Eq. (2) where the bridge is not under traffic while the tension in the cables can still vary that is accounted for by α as defined in Eq. (2). Numerical values of σ_a, σ_m and $\sigma_a\sigma_m$ for the 52 cables of the Runyang bridge with α=1.00, 1.04 and 1.12 are given in Tables A7, A8 and A9 of Appendix IV [9]. Case II refers to max. stress without traffic while $\alpha \geq 1$ corresponds to more tension in the cables. It can be concluded from the results in Fig. 9 that tightening of the cable will now have a beneficial effect as the product $\sigma_a\sigma_m$ will decrease when α is increased from 1.00 to 1.12 corresponding to "tightening". Fig. 10 provides the results for loosening of the cables without traffic. This increases $\sigma_a\sigma_m$ as α is decreased from 1.0 to 0.7. Therefore loosening of the cable is of no help in the absence of traffic. Numerical values of σ_a, σ_m and $\sigma_a\sigma_m$ for the 52 cables of the Runyang bridge with α=0.9 and 0.7 are given, respectively, in Appendix V of Tables A10 and A11 [9]. The results in Figs. 7 to 10 inclusive are summarized in Table 1.

Table 1. Effect of cable tightening and loosening on $\sigma_a\sigma_m$ with and without traffic.

Cases	$\sigma_a\sigma_m$	$\sigma_a\sigma_m$
Case I (traffic)	Decrease (loosening)	Increase (tightening)
Case II (no traffic)	Decrease (tightening)	Increase (loosening)

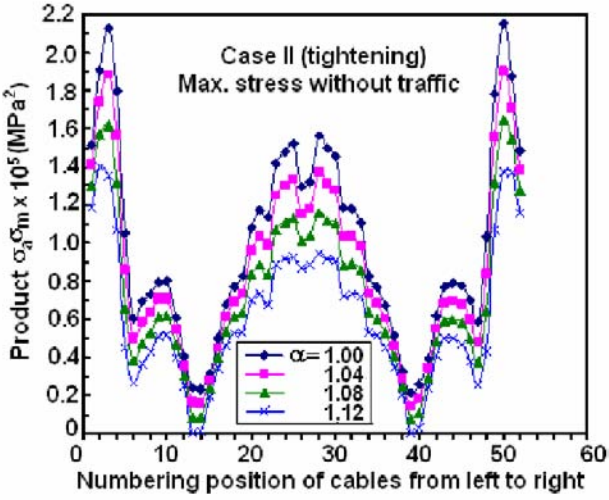

Fig. 9 Product $\sigma_a\sigma_m$ of cables versus position of cables for Case II (tightening) with α=1.00, 1.04, 1.08 and 1.12 in absence of traffic.

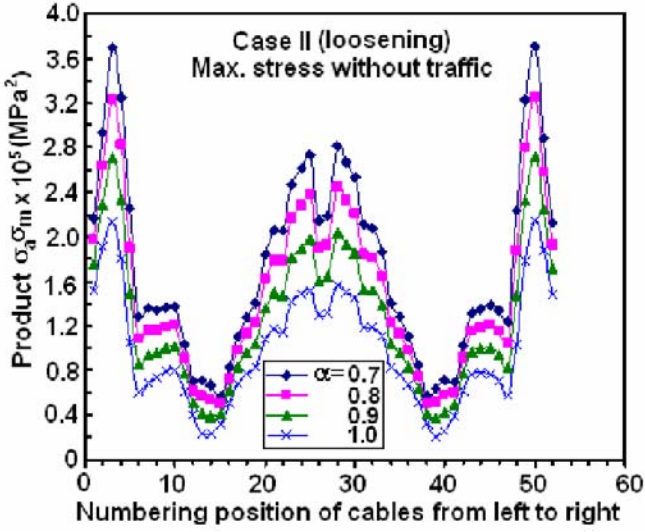

Fig. 10 Product $\sigma_a\sigma_m$ of cables versus position of cables for Case II (loosening) with α=0.7, 0.8, 0.9 and 1.0 in absence of traffic.

3. Multiscale Micro-/Macro-Crack Model

Multiscale crack growth models [7-9] must not only distinguish the size and time effects of small and large cracks but they must also be able to treat the transition region behavior of the cracks, say the transfer of micro- to macro-cracking if only two scales are involved. Hence both the micro- and macro-scale material properties must be considered in addition to micro- and macro-length that must be differentiated. A dual scale model must contain at least three parameters d^*, μ^* and σ^* such as

$$d^* = \frac{d}{d_o},\ \mu^* = \frac{\mu_{micro}}{\mu_{macro}},\ \sigma^* = \frac{\sigma_o}{\sigma_\infty} \tag{3}$$

in which d^* is the normalized characteristic dimension compared to the micro length d_o. A comparison between the micro- and macro-modulus is reflected by μ^* while σ^* accounts for the ratio of the material restraining stress σ_o to the applied stress σ_∞ such that σ_o/σ_∞ must always be less than one. This corresponds to the threshold for the onset of crack growth. Such a behavior manifests the closing of the microcrack in contrast to the macrocrack that is defined to possess a macro-distance crack opening. The transition of microcracking to macrocracking can be essential in fatigue where the applied load switches repeatedly from tension to compression or vice versa for each cycle.

3.1 Fatigue crack growth of cable

The bridge cable is a composite made of strands of steel wires wrapped in polymeric tubes with spacing filled by polymers. Although the properties of the cable will be obtained by approximation but they will be different from those for the wire. The details of which are discussed in [9]. It is more pertinent to consider the growth rate da/dN of a fatigue crack with length *a* (cm) in a cable as given by

$$\frac{da}{dN} = \Psi_o (\Delta S_{micro}^{macro})^{\psi} \tag{4}$$

where Ψ_o and ψ can be found by test data in a regular fatigue test. Here, Ψ_o is the y-intercept and ψ the slope of the curve for the straight line portion of the log-log plot of Eq. (4). The crack length can be computed by integrating Eq. (4). The results for ψ=1 is given by

$$a(N)=a_o e^{q(N-N_o)},\ \text{for } \psi=1 \tag{5}$$

In Eq. (5), N stands for the load cycle as specified by the traffic. By making the contractions

$$q = \Psi q_o,\ \text{for } \psi=1 \text{ and } q_o = (1-2\nu_{micro})\mu^*(1-\sigma^*)^2\sqrt{d^*} \tag{6}$$

and using the expression for ΔS_{micro}^{macro} given as [9]

$$\Delta S_{micro}^{macro} = \frac{2(1-\nu_{macro})^2 \sigma_a \sigma_m \sqrt{d_o}}{\mu_{macro}\sqrt{r}} q_o a \tag{7}$$

Under these considerations, there results

$$\Psi = \Psi_o \frac{2(1-\nu_{macro})^2 \sigma_a \sigma_m}{\mu_{macro}} \sqrt{\frac{d_o}{r}}, \text{ for } \psi=1 \tag{8}$$

Eq.(4) can thus be simplified to the form

$$\frac{da}{dN} = qa, \text{ for } \psi=1 \tag{9}$$

Keep in mind that the radial distance from the crack tip r in Eq. (7) and (8) can be micro or macro in size.

3.2 Fatigue properties of cable obtained from steel wire

Although fatigue tests of cable and steel wire have known to be made, but the data are not readily available except for the work in [16,17] that was made use of in [8,9] to study fatigue crack growth in a steel wire. For this material, the log-log plot of the da/dN versus ΔK data based on the classical stress intensity range can be found in Fig. 11. Again the conversion of the log-log da/dN versus ΔK to log-log da/dN versus ΔS_{micro}^{macro} has already been given in [9] and will not be repeated. Since Eq. (4) can be written as

$$\log\left(\frac{da}{dN}\right) = \log(\Psi_o) + \psi \log(\Delta S_{micro}^{macro}) \tag{10}$$

The y-intercept Ψ_o and the slope ψ of the line represented by Eq.(10) can be found as

$$\psi=1,\ \Psi_o=4.2\times10^{-8} \text{ for the cable.} \tag{11}$$

The relevant material and geometric parameters for the cable can be obtained from

$$E_c = \beta E_w, \text{ for } \beta \le 1 \tag{12}$$

where E_c and E_w denote the Youngs moludus for cable and wire, respectively.

The following numerical values are used:

$$\mu^* = \frac{\mu_{micro}}{\mu_{macro}} = 2,\ \sigma^* = \frac{\sigma_o}{\sigma_\infty} = 0.3,\ d^* = \frac{d}{d_o} = 1,\ d_o = 10^{-3}\text{mm},\ \mu_{micro} = 0.4,\ r/d_o = 1 \tag{13}$$

and $\mu_{macro}=\mu_w$, $E_{macro}=E_w$ and $\nu_{macro}=\nu_w$ while the initial values of a_o= 0.01mm, $N_o=0.1\times10^6$ apply to fatigue. For the wire with diameter D_w=5mm, it follows that

$$E_w=199.82\text{GPa},\ \nu_w=0.3,\ \mu_w=E_w/[2(1+\nu_w)]=76.85\text{GPa}. \quad (14)$$

The normalized quantities in Eqs.(13) together with d_o and ν_{micro} are assumed to be valid for both the cable and wire. Appropriate value of β in Eq. (12) such as β=1.0, 0.9, 0.8, 0.7, --- can be selected together with the data in Table 2 to study the crack growth rate relation for the cable. The subsequent results are generated for cables with an assumed life of two million cycles, i.e., $N_f=2\times10^6$ cycles.

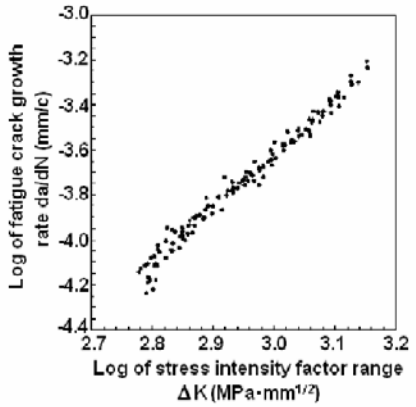

Fig. 11 Log-log plot of da/dN versus ΔK for high strength steel data from [16].

Table 2 Mechanical properties of bridge steel wire [16,17].

Elastic modulus E_w (GPa)	Ultimate stress σ_{ult}^w (MPa)	Ultimate strain ε_{ult}^w (%)
199.82	1722.55	5.5

3.3 Equivalent surface crack growth

Recall that Ψ_o and ψ in Eq. (11) were found empirically from a plate specimen and not that of the assumed shape of a round bar for the cable or the wire. This, however, would not affect the qualitative feature of the results since the shape factor can be absorbed into Ψ_o quantitatively. To this end, an equivalent crack length *a* can be used regardless of the specific crack shape. More precisely, the clam shaped fatigue surface crack in Fig. 12(a) can be replaced by a straight edge crack in Fig. 12(b). For a homogeneous cross section cable, the diameter D_c is approximated by a single

edge crack specimen of thickness D_c. This completes the determi-nation of the empirical parameters for the crack growth rate relation of the cable.

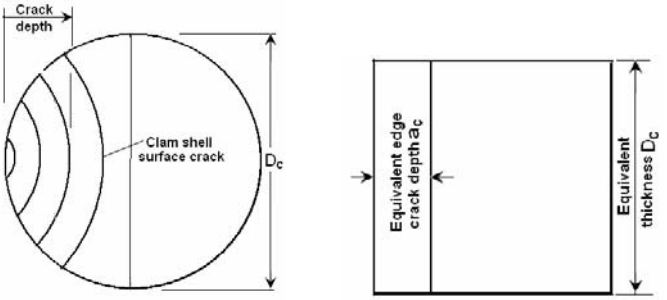

(a) Clam shell surface crack (b) Equivalent edge crack

Fig. 12 Surface crack simplified as through crack in cable and wire.

4. Crack Growth Rate of Bridge Cable

According to Eq. (12), the parameter β controls the difference between the stiffness of the cable as compared with that of the steel wire with its modulus E_w as given in Table 2. Since the cable stiffness is less than that of a single steel wire β as defined in Eq. (12) is always less than one since the cable is not completely filled by wires. For practical consideration, β=0.7 will be assumed for the discussion of numerical results. Making use of the numerical values of the relevant parameters as given by Eqs. (13) and (14). The crack growth rate da/dN can be computed directly from Eq. (4) with the help of Eq. (11). The quantity α can be made to vary depending on whether the cable is tight for $\alpha \geq 1$ or loose for $\alpha \leq 1$. These conditions are specified by Eqs. (1) and (2).

4.1 Case I: Cable tightening and loosening for β=0.7

The variations of the crack growth rate with the number of fatigue cycles N will be examined for three typical cables which are referred to as #28, #38 and #50 under traffic and no traffic conditions.

4.1.1 Cable #28

Fig. 13 displays the variations of da/dN with N for cable #28. Note that for α less than 1.2, the crack growth rate is negligibly small up to the two million cycles. As α is gradually increased, da/dN tends to increase with N. For $\alpha \geq 1.6$, the slopes of the curves in Fig. 13 tend to become vertical when

$N=1.4\times10^6$ cycles is approached. This implies that tightening of the cable would result in earlier unstable growth which is undesirable.

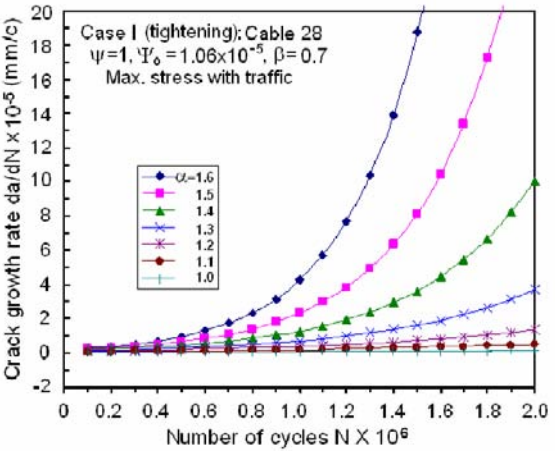

Fig. 13 Crack growth rate da/dN versus number of cycles N for cable #28 and Case I (tightening) with $\alpha\geq1$ and $\beta=0.7$ under traffic.

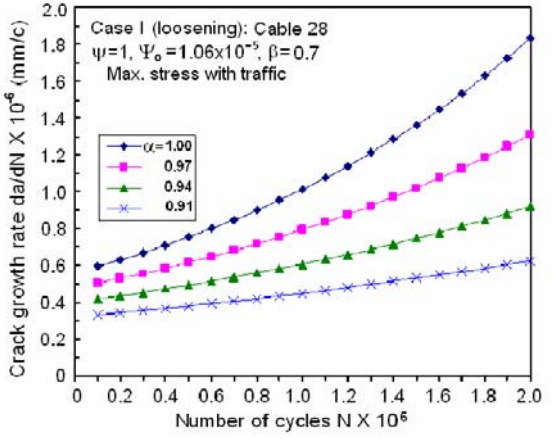

Fig. 14 Crack growth rate da/dN versus number of cycles N for cable #28 and Case I (loosening) with $\alpha\leq1$ and $\beta=0.7$ under traffic.

Loosening of the cable for $\alpha\leq1$ on the other hand leads to beneficial effects because it decreases the crack growth as illustrated in Fig. 14 for the same material and geometric parameters as those used to obtain the data in Fig. 13. With the same α of 1.6, it can be seen that the slope of the top curve in Fig. 14 still correspond to stable crack growth after $N=2\times10^6$ cycles while the same curve in Fig. 13 has nearly reached unstable crack growth at $N=1.4\times10^6$ cycles. This difference is significant and indicates that the ten-

sion of the cables for cable-stayed bridges should be monitored and hence can be adjusted when the need arises.

4.1.2 Cable #38

The situation in cable #38, however, is entirely different. Even for α=1.6, Fig. (15) shows that da/dN $\approx 1.9\times10^{-6}$mm/c at N$\approx 2\times10^{6}$ cycles as the fatigue crack is still propagating in a stable manner. This corresponds to the tightening condition of cable #38. Fig. 16 indicates that further slow down of the crack results when α is made to be less than one for loosening of the cables.

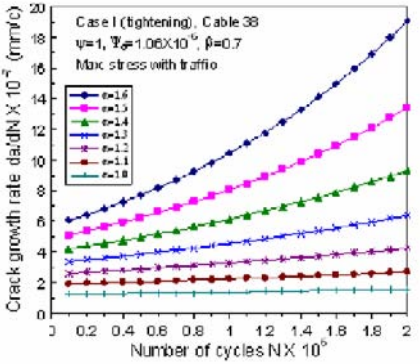

Fig. 15 Crack growth rate da/dN versus number of cycles N for cable #38 and Case I (tightening) with $\alpha\geq1$ and β=0.7 under traffic condition.

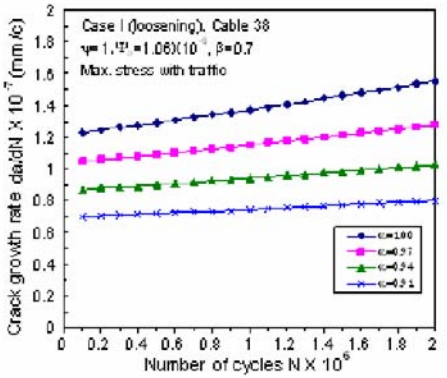

Fig. 16 Crack growth rate da/dN versus number of cycles N for cable #38 and Case I (loosening) with $\alpha\leq1$ and β=0.7 under traffic condition.

4.1.3 Cable #50

The crack growth behavior of cable #50 in Fig. 17 is more severe than that of cable #28 in Fig. 13. Comparing the curves for α=1.6 and N≈1.3×10^6 cycles, Fig. 17 gives an approximate crack growth rate of da/dN≈50×10^{-5} mm/c and Fig. 13 gives da/dN≈10×10^{-5}mm/c, a factor of 5 difference. That is the crack growth rate in cable #50 is five times greater than that in cable #28. The non-uniformity of the tension in cables #28, #38 and #50 are exhibited.

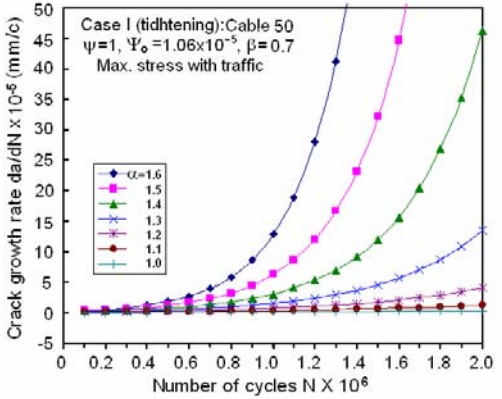

Fig. 17 Crack growth rate da/dN versus number of cycles N for cable #50 and Case I (tightening) with $\alpha \geq 1$, β=0.7 with traffic.

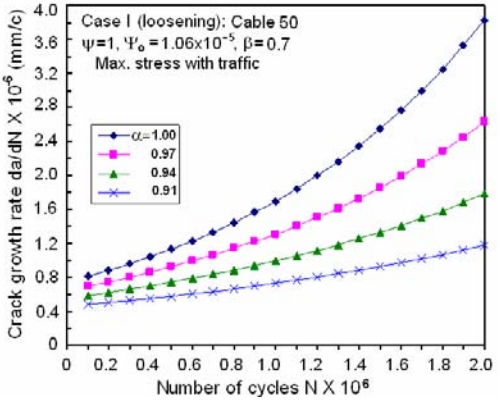

Fig. 18 Crack growth rate da/dN versus number of cycles N for cable #50 and Case I (loosening) with $\alpha \geq 1$, β=0.7 with traffic.

Loosening of the cables #28 and #50 under traffic can impede crack growth. The disparity between the results is similar and can be seen from Figs. 14 and 18.

4.2 Case II: Cable tightening & loosening for β=0.7

Instead of varying the cable tension under the traffic condition, the variation of cable tension without traffic can be different. Hence, the effects must be studied separately. Even though the same symbol α is used for $\alpha\,\sigma^{\alpha}_{max}$ and $\alpha\,\sigma^{o}_{max}$, the individual values of α are different. This will be shown for the results of cables #28, #38 and #50.

4.2.1 Cable #28

Plotted in Fig. 19 are the crack growth rate as a function of N for cable #28 where Eq. (2) has been implemented with α=1.04, 1.08 and 1.12 that correspond to increasing of initial cable tension. This increase is seen to be beneficial as the curves with α=1.08 and 1.12 give lower da/dN than those with curves with α=1.00 and 1.04 corresponding to less tension. For $N\approx 2\times10^6$ cycles, $da/dN\approx 1.8\times10^{-6}$mm/c for α=1.00 as compared to $da/dN\approx 0.6\times10^{-6}$mm/c for α=1.12. That is higher initial tension cable under no traffic can reduce the crack growth rate by three or 3.00 times after two million cycles. This effect is not significant for low fatigue cycles. Decrease of initial cable effects without traffic are shown in Fig. 20 for α=0.7, 0.8 0.9 and 1.00. Again the effects become more pronounced with increasing fatigue cycles. The maximum difference is about 5.3 times in da/dN at $N\approx 2\times10^6$ cycles.

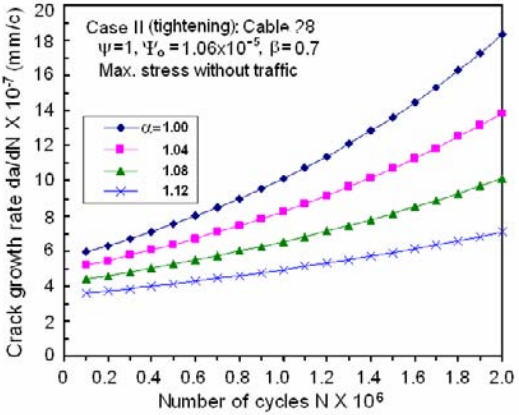

Fig. 19 Crack growth rate da/dN versus number of cycles N for cable #28and Case I (tightening) with $\alpha\geq1$, β=0.7 without traffic.

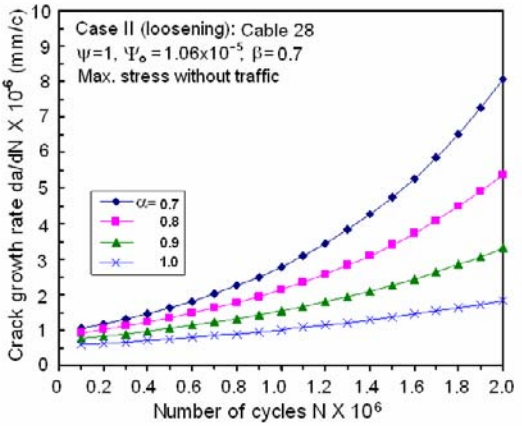

Fig. 20 Crack growth rate da/dN versus number of cycles N for cable #28 and Case I (loosening) with $\alpha \geq 1, \beta = 0.7$ without traffic.

4.2.2 Cable #38

The variations of da/dN with N in cable #38 is quite different. First of all, the crack growth rate as shown in Fig. 21 for each α from 1.00 to 1.12 is nearly constant for all fatigue cycles from 10^5 to 2×10^6 cycles. They differ from the range $(0.75\text{-}1.23)\times10^{-7}$ to $(0.85\text{-}1.51)\times10^{-7}$mm/c for $\alpha \geq 1$. That is when the initial cable tension is increased. The results for decreasing the cable tension with α=1.00, 1.04, 1.08 and 1.12 can be found in Fig. 22. The change of da/dN with N is similar to the trends of the curves in Fig. 21 except that the α values are now smaller than one and the curves tend to increase more as N is increased.

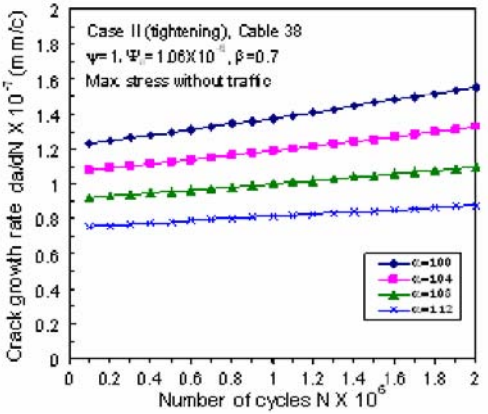

Fig. 21 Crack growth rate da/dN versus number of cycles N for cable #38 and Case II (tightening) with $\alpha \geq 1$ and $\beta = 0.7$ in absence of traffic.

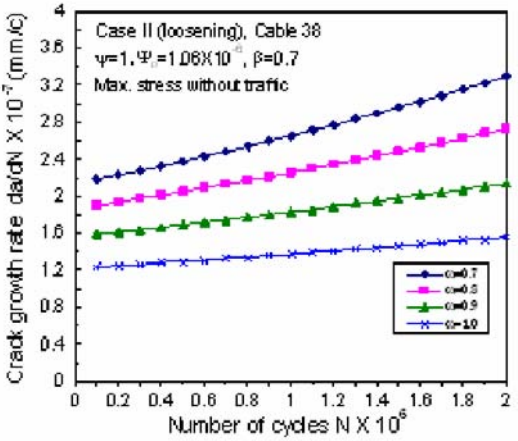

Fig. 22 Crack growth rate da/dN versus number of cycles N for cable #38 and Case II (loosening) with $\alpha \leq 1$ and $\beta=0.7$ in absence of traffic.

4.2.3 Cable #50

Cable #50 behaves more like cable #28 where the change in da/dN is small for small N and the difference increase with increasing N as shown in Fig. 23. For $N \approx 2\times10^6$ cycles, $da/dN \approx 3.8\times10^{-6}$mm/c for $\alpha=1.00$ in contrast to $da/dN \approx 1.3\times10^{-6}$mm/c for $\alpha=1.12$. That is higher initial tension cable under no traffic can reduce the crack growth rate by 2.93 times after two million cycles. This factor is slightly lower than 3.00 for cable #28 in Fig. 19. Fig. 24 shows the results for decreasing the initial tension of cable #50 which corresponds to $\alpha \leq 1$. The four curves with $\alpha=0.7$, 0.8, 0.9 and 1.00 indicate that there are hardly any differences in da/dN for small N but the curves start to spread out appreciably at $N=2\times10^6$ cycles, at which point the difference in the crack growth rate reaches a factor of 6.67. This is significant. It again reflects the non-uniformity of tension in the cable can lead to appreciable difference in the crack growth rate. This implies some cables may fail by fatigue much earlier than others.

5. Crack Length as a Function of Fatigue Cycle

The da/dN curves in Figs. 19 to 24 may be integrated to yield the results for crack length as a function of fatigue cycles. Such information can be used to check with test data and used in fracture control. The following discussions pertain to cables #28, #38 and #50.

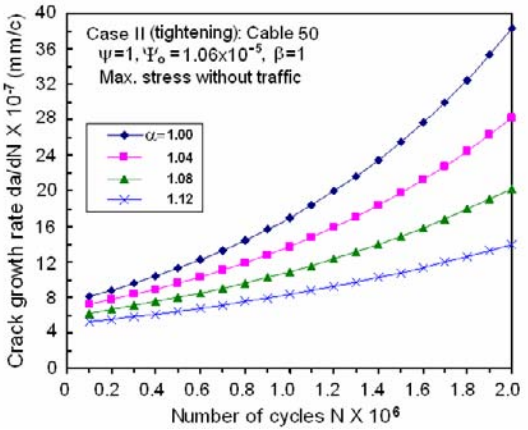

Fig. 23 Crack growth rate da/dN versus number of cycles N: for cable #50 and Case II tightening) with $\alpha \geq 1$, $\beta=0.7$ without traffic.

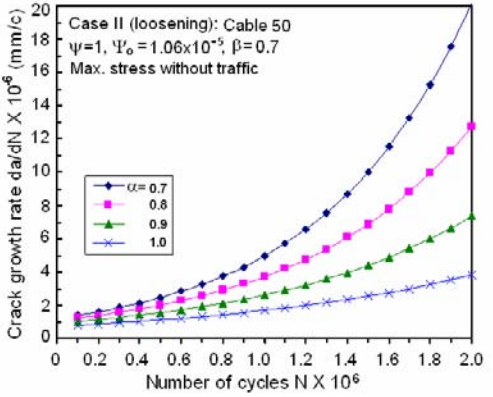

Fig. 24 Crack growth rate da/dN versus number of cycles N for cable #50 and Case II (loosening) with $\alpha \leq 1$ and $\beta=0.7$ in absence of traffic.

5.1 Case I: Tightening & loosening for β=0.7

In view of Eq. (9), the crack length a can also be obtained directly from da/dN without integration since q in Eq. (9) can be found from Eqs. (6) and (8). This procedure happens to apply for the present case of $\psi=1$ as stated in Eq. (11).

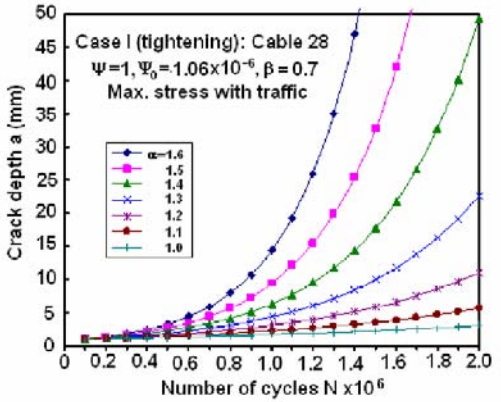

Fig. 25 Crack depth a versus number of cycles N for cable #28 and Case I (tightening) with $\alpha \geq 1$ and $\beta=0.7$ under traffic.

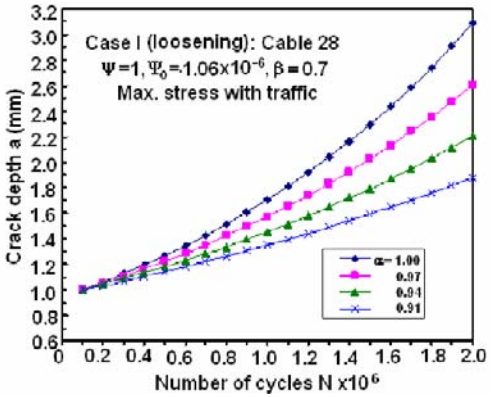

Fig. 26 Crack depth a versus number of cycles N for cable #28 and Case I (loosening) with $\alpha \leq 1$ and $\beta=0.7$ under traffic.

5.1.1 Cable #28

The reference crack growth curve is given by $\alpha=1.0$ as shown in Fig. 25. It remained nearly constant for the range of fatigue cycles N up to two million. As the cable is tightened gradually with $\alpha=1.1$, 1.2, ---, 1.6, the curves start to deviate from the reference with increasing crack length. At $N=1.4\times10^6$ cycles and $\alpha=1.5$, the crack depth is 25mm. This length is doubled to 50mm at the same fatigue cycles when the cable tension in raised with $\alpha=1.6$. In this case, increase cable tension tends to enhance crack growth. On the other hand, a decrease of the initial cable tension with $\alpha \leq 1$, crack growth can be impeded. Fig. 26 shows the four curves for $\alpha=1.00$, 0.97, 0.94 and 0.91. A crack depth of 3.1 mm at $N=2\times10^6$ cycles and

α=1.00 reduces to 1.8 mm when the initial cable tension is decreased with α=0.91. These effects are different for different cables.

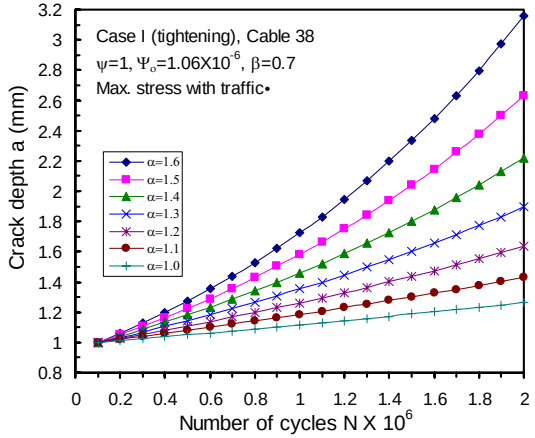

Fig. 27 Crack length a versus number of cycles N for cable #38 and Case I (tightening) with $\alpha \leq 1$ and β=0.7 under traffic.

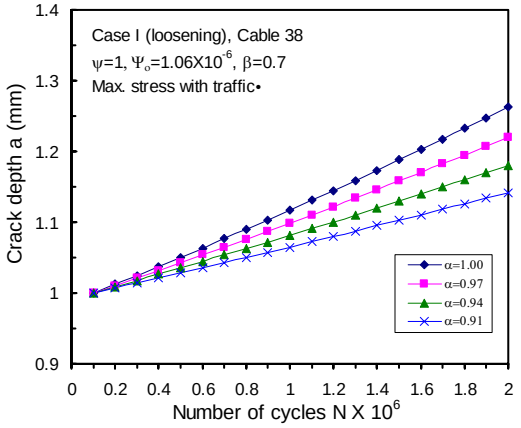

Fig. 28 Crack length a versus number of cycles N for cable #38 and Case I (loosening) with $\alpha \leq 1$ and β=0.7 under traffic.

5.1.2 Cable #38

The results for cable #38 are summarized in Fig. 27 for Case I where the initial cable tension is increased with α=1.0, 1.1, ---, 1.6. All the curves start with an initial crack length of 1 mm. They then increase in amplitude with increasing N. The magnitude of the reference curve α=1.00 increase

very slowly with N while the other curves increase faster as α is increased. A factor of 3.2 in crack depth is gained at $N=2\times10^6$ cycles for $\alpha=1.6$. Fig. 28 further shows the effects of decreasing the initial cable tension with $\alpha=1.00$, 0.97, 0.94 and 0.91. Not much change can be observed as all of the curves in Fig. 28 are bunched together.

5.1.3 Cable #50

Crack growth is most pronounced in cable #50 and the results are sensitive to the initial cable tension. For $\alpha=1.6$, it took 1.1×10^6 cycles to advance the crack from 1 mm to 50 mm whereas 1.5×10^6 cycles were required for the crack to growth the same depth if α is reduced from 1.6 to 1.4. An addition of 400,000 cycles are needed if the initial increase in cable tension were reduced by the equivalent amount of 0.2 in α. Again the change in crack growth by decreasing the initial tension is not significant. This can be seen from the curves in Fig. 30.

5.2 Case II: Tightening & loosening for β=0.7

Similar behavior can be demonstrated when the cable tension is altered under no traffic conditions although the effects are not as dramatic.

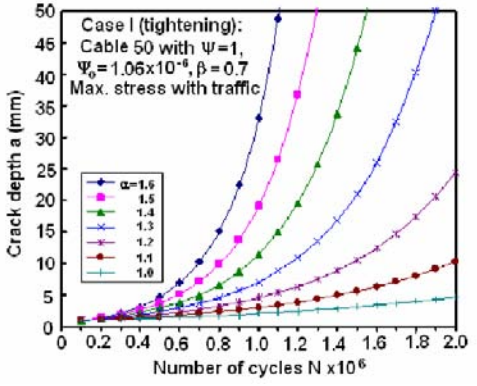

Fig. 29 Crack depth a versus number of cycles N for cable #50 and Case I (tightening) with $\alpha\geq1$ and $\beta=0.7$ under traffic.

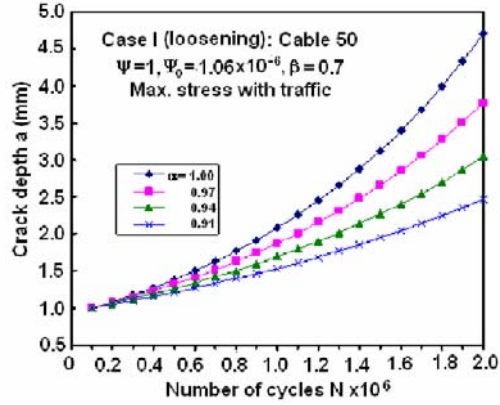

Fig. 30 Crack depth a versus number of cycles N for cable #50 and Case I (loosening) with $\alpha \leq 1$ and $\beta=0.7$ under traffic.

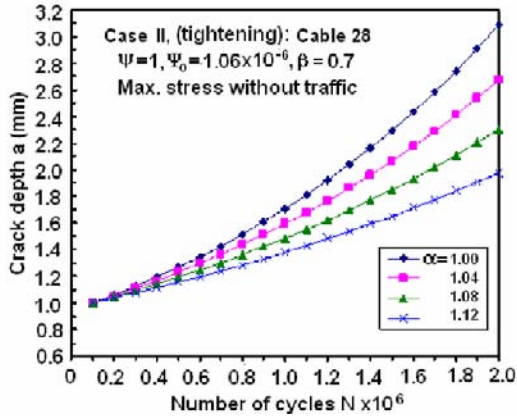

Fig. 31 Crack depth a versus number of cycles N for cable #28 and Case II (tightening) with $\alpha \geq 1$ and $\beta=0.7$ in absence of traffic.

5.2.1 Cable #28

Fig. 31 plots the crack depth a as a function of the cycle number N for α=1.00, 1.04, 1.08 and 1.12. First of all, the change in crack depth is relatively small even when N reached two million cycles. Moreover, the crack growth ranged from 1.9 to 3.1 mm which is small compared to 50 mm and beyond under traffic conditions. Refer to Fig. 25 for cable #28. The opposite effects are seen when comparing the results of Fig. 26 with traffic to those in Fig. 32 without traffic. For α=0.7, 0.8, 0.9 and 1.0, Fig. 32 shows that the crack growth range is from 2.8 to 7.5 mm at $N=2\times10^6$ cycles as

compared to the range of 1.8 to 3.1 mm in Fig. 26 for the same cable under traffic. Contrary to intuition, more crack growth occurred for cable tension that corresponds to no traffic conditions.

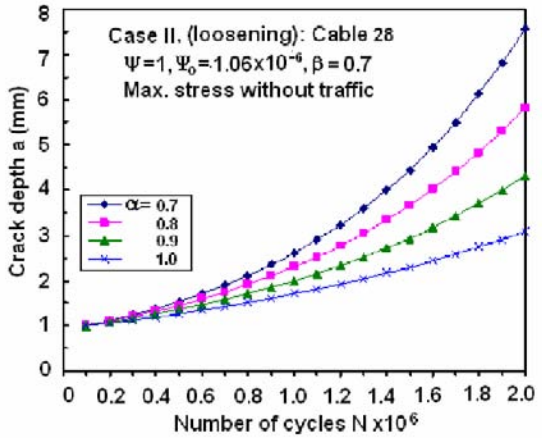

Fig. 32 Crack depth a versus number of cycles N for cable #28 and Case II (loosening) with $\alpha \leq 1$ and $\beta=0.7$ in absence of traffic.

5.2.2 Cable #38

Maximum crack growth in cable #38 ranged from 1.14 to 1.25 mm at $N \approx 2\times10^6$ cycles under no traffic conditions. With traffic, the crack growth range was found to be about 1.20 to 3.20 mm at $N \approx 2\times10^6$ cycles as shown by Fig. 27. This trend, however, is not always observed as it was seen for cable #28 and will also be different for the case when the initial cable tension is decreased, i.e, for $\alpha \leq 1$. Referring to Fig. 34, the crack growth range of 1.23 to 1.50 mm at $N \approx 2\times10^6$ cycles under no traffic turns out to be larger than that of 1.12 to 1.26 mm in Fig. 28 when the cable is under traffic. Up to now, it is seen that each cable behaves differently, a very typical feature of the cable-stayed bridge.

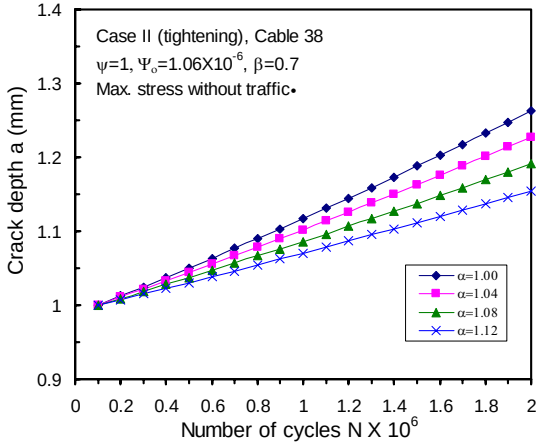

Fig. 33 Crack depth a versus number of cycles N for cable #38 and Case II (tightening) with $\alpha \geq 1$ and $\beta=0.7$ in absence of traffic.

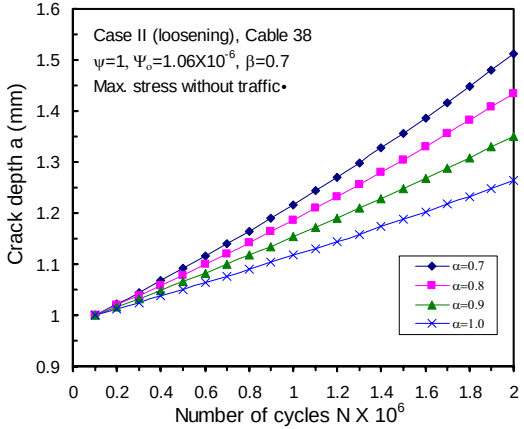

Fig. 34 Crack depth a versus number of cycles N for cable #38 and Case II (loosening) with $\alpha \leq 1$ and $\beta=0.7$ in absence of traffic.

5.2.3 Cable #50

The behavior of cable #50 without traffic differs significantly from that under traffic. For $\alpha \geq 1$ without traffic, crack growth is very limited as it can be seen from Fig. 35 where the range of crack growth after $N \approx 2 \times 10^6$ cycles is only 2.54 to 4.54 mm. This is significantly different from the corresponding results under traffic in Fig. 29 where crack growth extended into the range of 50 mm and beyond at $\alpha=1.3$ even though N has reached only 1.9 million cycles.

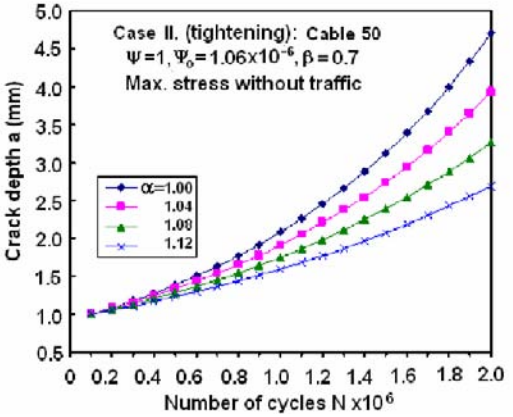

Fig. 35 Crack depth a versus number of cycles N for cable #50 and Case II (tightening) with $\alpha \geq 1$ and $\beta=0.7$ in absence of traffic.

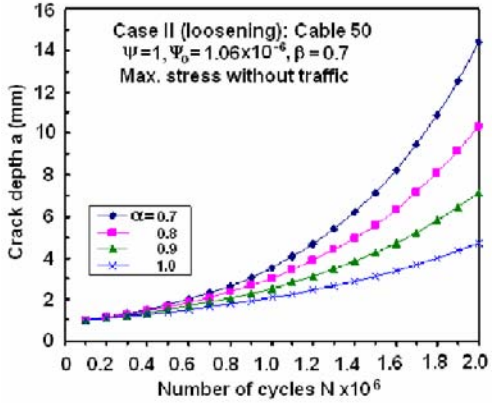

Fig. 36 Crack depth a versus number of cycles N for cable #50 and Case II (loosening) with $\alpha \leq 1$ and $\beta=0.7$ in absence of traffic.

For $\alpha \leq 1$ and $N \approx 2\times10^6$ cycles, the crack growth range of 4.50 to 14.1 mm in Fig. 36 without traffic is greater than the range of 2.35 to 4.55 mm in Fig. 30 with traffic.

6. Cable Stiffness Effects

With a knowledge that the fatigue life can be greatly influenced the cable tension, it goes without saying that cable stiffness can have similar effects, particularly when the mechanical properties of the bridge cables are fabrication specific. Using the stiffness E_w of the steel wire as the base, E_c for the cable will be regarded as certain percentage of E_w via a parameter β as

indicated by Eq. (12) such that $\beta \leq 1$ will always hold as the cable can only be partially filled with wires. The maximum cable stiffness corresponds to $\beta=1$. Crack growth will be studied for cables #28, #38 and #50 with $\beta=0.7$, 0.8, 0.9 and 1.0.

6.1 Case I: Tightening and loosening for varying β

Under traffic, two cases will be considered: increase of initial tension to $\alpha=1.6$ and decrease of initial tension to $\alpha=0.9$. In what follows, the numerical results will be presented.

6.1.1 Cable #28: $\alpha=1.6$ (tightening) and $\alpha=0.91$ (loosening)

With an initial starter line crack of depth 1 mm, the depth extends to 50 mm as N reaches 2 million cycles. This corresponds to $\beta=1$ in Fig. 37. For $\beta=0.9$, the crack depth has propagated way beyond the onset rapid fracture before $N=2\times10^6$ cycles. Even earlier crack instability applies to $\beta=0.7$ and 0.8. A decrease of the initial tension with $\alpha=0.9$, Fig. 38 shows that the crack depth is still sub-critical at $N=2\times10^6$ cycles. For $\beta=0.7$, 0.8, 0.9 and 1.0, the crack has extended to 1.85, 1.70, 1.60 and 1.53 respectively for the situation when the initial cable tension is decreased below the design value. It can thus be said that change in the cable stiffness does not seem to exert appreciable effect on crack growth.

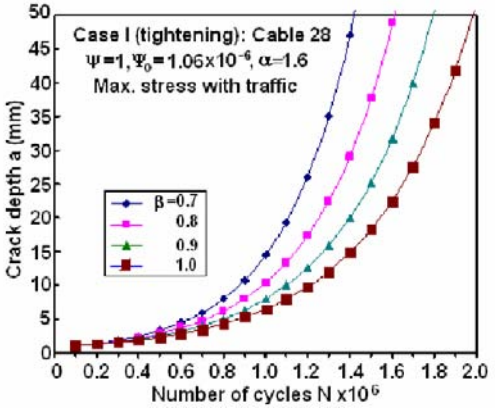

Fig. 37 Crack depth a versus number of cycles N for cable #28 and Case I (tightening) with $\alpha=1.6$ and $\beta=0.7$, 0.8, 0.9 and 1.0 under traffic.

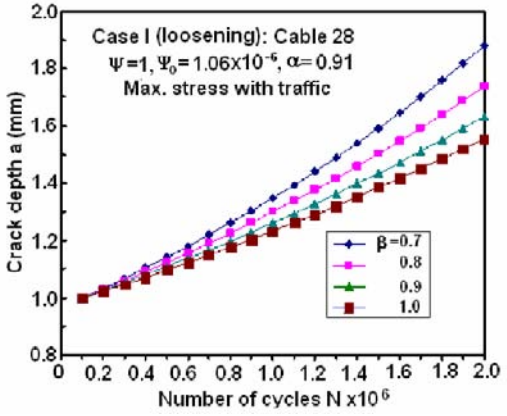

Fig. 38 Crack depth a versus number of cycles N for cable #28 and Case II (loosening) with α=1.6 and β=0.7, 0.8, 0.9 and 1.0 under traffic.

6.1.2 Cable #38: α=1.6 (tightening) and α=0.91 (loosening)

Crack growth behavior for Cable #38 is not significant. Fig. 39 shows that as β changes from to 0.7, the largest difference in crack depth is from 2.15 to 3.18 mm with α=1.6. That is when the initial tension was increased. Decreasing the initial tension with α=0.91, the change in the crack depth is even less as shown by the results in Fig. 40.

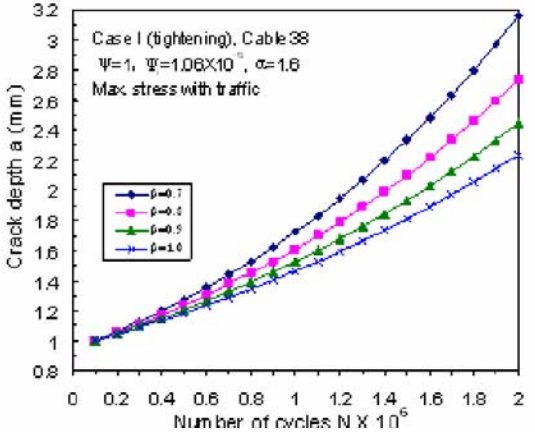

Fig. 39 Crack depth a versus number of cycles N for cable #38 and Case I (tightening) with α=1.6 and β=0.7, 0.8, 0.9 and 1.0 under traffic.

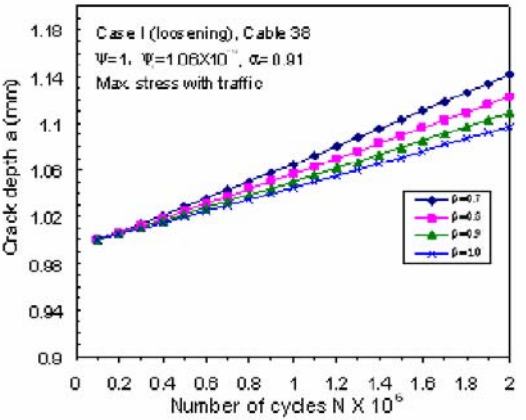

Fig. 40 Crack depth a versus number of cycles N for cable #38 and Case II (loosening) with α=1.6 and β=0.7, 0.8, 0.9 and 1.0 under traffic.

6.1.3 Cable #50: α=1.6 (tightening) and α=0.91 (loosening)

Appreciable crack growth occurred in cable #50 for α=1.6 and β=0.7. The crack depth reached 50 mm when the fatigue cycles are only 1.1×10^6 as illustrated in Fig. 41. Decrease of initial cable tension with α=0.91 does not exert appreciable influence on crack growth. This can be seen from the curves in Fig. 42 that undergo little changes as N is increased.

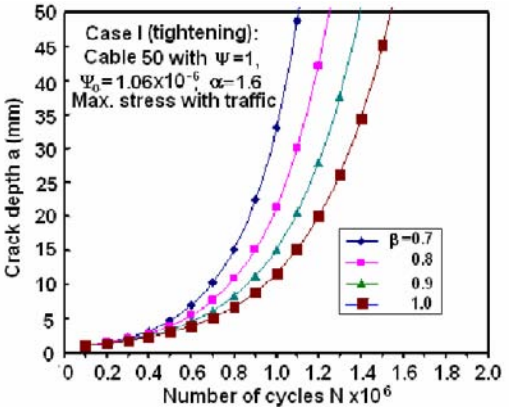

Fig. 41 Crack depth a versus number of cycles N for cable #50 and Case I (tightening) with α=1.6 and β=0.7, 0.8, 0.9 and 1.0 under traffic.

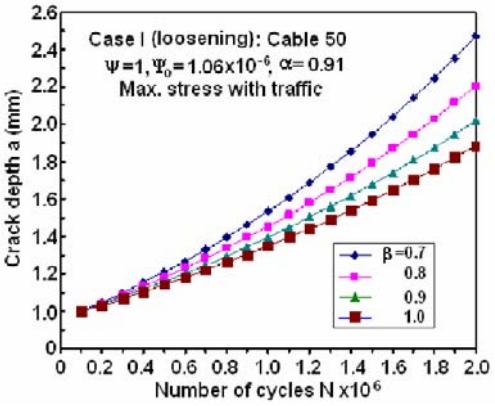

Fig. 42 Crack depth a versus number of cycles N for cable #50 and Case II (loosening) with α=1.6 and β=0.7, 0.8, 0.9 and 1.0 under traffic.

6.2 Case II: Tightening & loosening for varying β

Suppose that the traffic is now removed so that the tension in the cables will be reduced accordingly. However, the distribution will not be altered in proportion such that each cable will have to be analyzed individually. Moreover the amount of initial tension will be dictated by Eq. (2) which differs from that of Eq. (1) for the case when traffic is present.

6.2.1 Cable #28: α=1.12 (tightening) and α=0.70 (loosening)

Summarized in Figs. 43 and 44 are the crack growth characteristics of cable #28 in the absence of traffic load. Decrease in cable stiffness tends to enhance crack growth. For an increase of the initial cable tension with α=1.12, the crack depth increased from 1.60 to 1.99 mm after two million cycles as β is decreased from 1.00 to 0.7, respectively. The results correspond to those in Fig. 43.The trend of the curves in Fig. 44 is similar to that in Fig. 44 except that the crack depth now changes from 4.0 to 7.5 mm at $N=2\times10^6$ cycles with α=0.7 which is a measure of the initial decrease of cable tension.

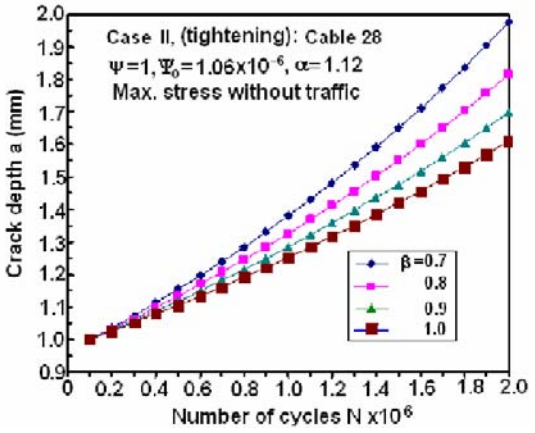

Fig. 43 Crack depth a versus number of cycles N for cable #28 and Case I (tightening) with α=1.12 and β=0.7, 0.8, 0.9 and 1.0 without traffic.

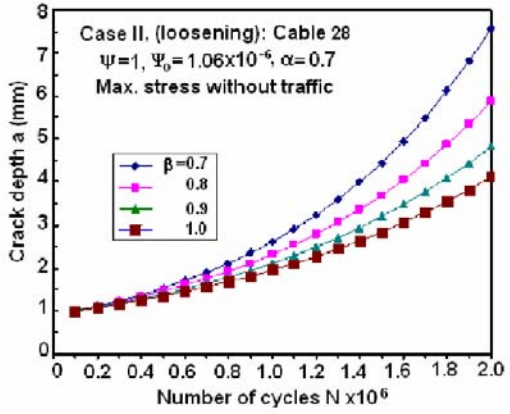

Fig. 44 Crack depth a versus number of cycles N for cable #28 and Case II (loosening) with α=0.7 and β=0.7, 0.8, 0.9 and 1.0 without traffic.

6.2.2 Cable #38: α=1.12 (tightening) and α=0.70 (loosening)

By the same token, Figs. 45 and 46 exhibit the crack growth results for cable #38 with α=1.12 and 0.7, respectively, when the traffic load is not present. No direct comparison can be made with the results in Figs. 39 and 40

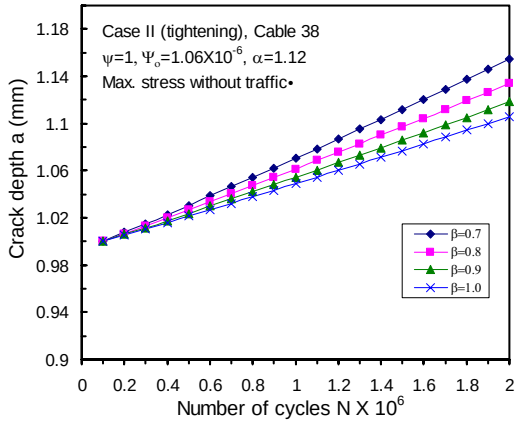

Fig. 45 Crack depth a versus number of cycles N for cable #38 and Case I (tightening) with α=1.12 and β=0.7, 0.8, 0.9 and 1.0 without traffic.

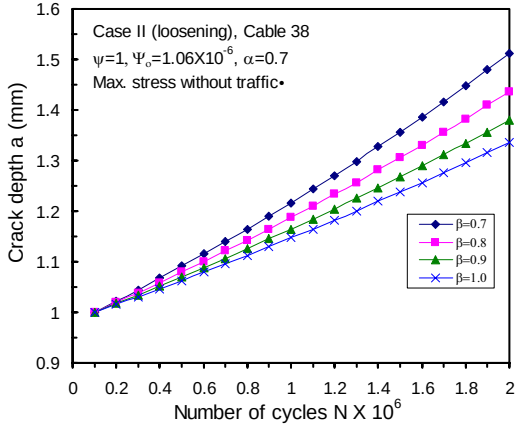

Fig. 46 Crack depth a versus number of cycles N for cable #38 and Case II (loosening) with α=0.7 and β=0.7, 0.8, 0.9 and 1.0 without traffic.

with the load present because the amount initial tension governed by α is not the same. They seem to have the opposite trend. That is the range of crack growth with 2.15 to 3.18 mm for α=1.6 in Fig. 39 and 1.09 to 1.14 mm for α=0.91 in Fig. 40 are contrasted with 1.10 to 1.15 mm for α=1.12 in Fig. 45 and 1.32 to 1.50 mm for α=0.70 in Fig. 46.

6.2.3 Cable #50: α=1.12 (tightening) and α=0.70 (loosening)

The influence of traffic load on cable #50 is most significant. With traffic, Fig. 41 for α=1.6 showed that crack grew up to a depth of 50 mm for β=0.7 after a million cycles. A stiffer cable with β=1.0 can sustain the same crack growth after 1.5×10^6 cycles. This is a substantial increase in fatigue cycles. Without traffic, Fig. 47 shows that crack growth is reduced considerably with α=1.12. A crack depth of 1.95 mm is found for β=1.0 and 2.65 mm for β=0.7. The results for a decrease of initial tension with α=0.7 are given in Fig. 48. The corresponding crack growth is 1.2 mm for β=1.0 and 1.44 mm for β=0.7. The effect of traffic loading in this case shown by Fig. 42 for α=0.91 is not significant since the increase in crack growth is only 1.85 mm for β=1.0 and 2.45 mm for β=0.7. This completes the discussion of crack growth in relation to the influence of initial cable tension.

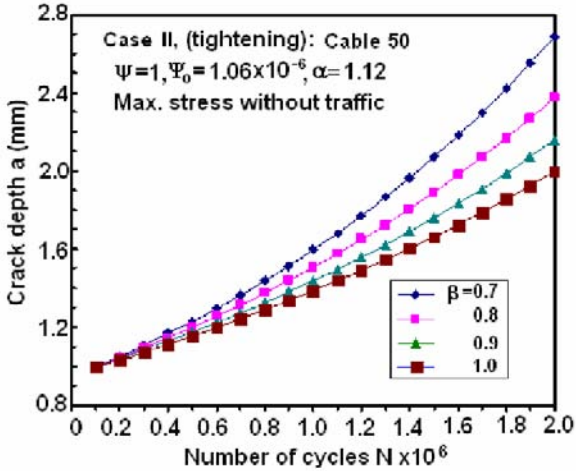

Fig. 47 Crack depth a versus number of cycles N for cable #50 and Case I (tightening) with α=1.12 and β=0.7, 0.8, 0.9 and 1.0 without traffic.

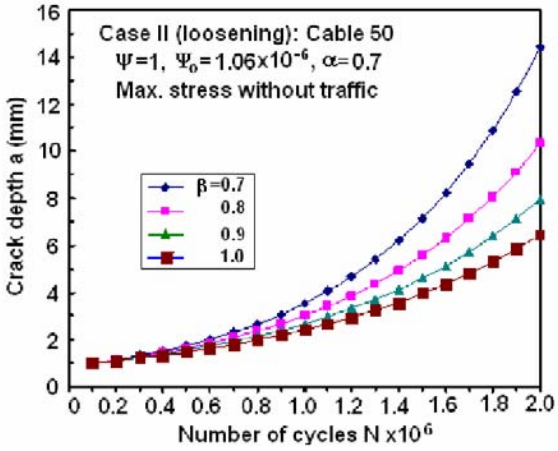

Fig. 48 Crack depth a versus number of cycles N for cable #50 and Case II (loosening) with α=0.7 and β=0.7, 0.8, 0.9 and 1.0 without traffic.

7. Concluding Remarks

Based on the design data supplied for the Runyang cable-portion of the bridge, the fatigue crack growth characteristics for the 52 cables are analyzed and the results are presented for three typical cable behavior referred to as cable #28, #38 and #50. Assessments are made for varying initial increase and decrease of the cable tension using the design condition as a reference under traffic and no traffic loading. Use is made of a dual scale fatigue crack growth model where microscopic and macroscopic effects can be distinguished. This includes the transitory behavior of micro- and macro-cracking, commonly referred to as Region I for fatigue crack initiation and II for fatigue crack propagation in a plot of log da/dN the crack growth rate against the log of the increment of the stress intensity factor ΔK that applies to linear elastic fracture mechanics (LEFM). The advent of modern materials with higher strength and toughness has delayed macroscopic crack growth by converting the available energy to extend the range of macrocracking. A description of fatigue cracking would thus entail damage at both the micro- and macro-scale, if not at an even lower scale. To this end, modern fatigue crack growth models must necessarily consider multiscale.

Under traffic, fatigue cracking in cable #3 or #50 (because of symmetry) is most severe as compared to those in #26 or #28 which are the next highest in crack growth rate. Examples are provided to show the effect of increase in the initial cable tension by using a parameter α to quantify the deviation from the design condition at α=1. For α=1.6 and N≈1.3×10^6 cy-

cles, the crack growth rate was found to be $da/dN \approx 50\times10^{-5}$ mm/c for cable #50 and $da/dN \approx 10\times10^{-5}$mm/c for cable #28 while all other conditions remain the same. This is difference of five times. Increase of initial cable tension under traffic condition enhances fatigue crack growth which is not beneficial. The opposite effect occurs when the initial cable tension is decreased. That is the fatigue crack growth can be impeded. The above results can also be expressed in terms of crack extension. Again for α=1.6, the crack advanced from 1 mm to 50 mm after 1.1×10^6 cycles. A reduction of α from 1.6 to 1.4 required an addition of 400,000 cycles to yield the same range of crack extension.

The behavior of cable #50 without traffic differs significantly from that under traffic. For an increase of initial cable tension with $\alpha \geq 1$ and no traffic, the crack grew only from 2.54 to 4.54 mm after $N \approx 2\times10^6$ cycles. For a decrease in initial cable tension with $\alpha \leq 1$, the crack growth range is 4.50 to 14.1 mm after $N \approx 2\times10^6$ cycles. The difference in fatigue crack growth with and without traffic can differ by at least one order of magnitude or more based on an upper limit of two million cycles for the cable life. It can thus be stated that

> Cable fatigue life can be enhanced and impeded, respectively, by decreasing and increasing the initial cable tension when the traffic is present.
>
> Cable fatigue life can be enhanced and impeded, respectively, by increasing and decreasing of the initial cable tension when the traffic is absent.

In contrast to earlier design of bridge cables, higher strength steel wires have been used to improve the cable strength. It is therefore useful to develop a relation between the fatigue life of the cable and that of the wires that are the basic elements of the cable. In this way, the test data for the cable and wire may correlated. It is not obvious that the same fatigue life of two million cycles should hold for both the cable and wire. It is also necessary to realize that the present tests are not representative of the actual situation of the bridge where the length of the cable and hence the wire comes into play. It is well known that the high strength material is sensitive to pre-existing surface defects that would be an inherent property of long wires. To this end, Part II of this investigation will be devoted to associating the fatigue behavior of the cable and the wire in the hope that the analytical work would encourage more extensive fatigue tests to which the analytical findings may be used as a guide.

References

[1] Sih GC and Tang XS (2004) Dual scaling damage model associated with weak singularity for macroscopic crack possessing a micro/mesoscopic notch tip. J. of Theoretical and Applied Fracture Mechanics, 42(1): 1-24.
[2] Sih GC and Tang XS (2006) Simultaneous occurrence of double micro/macro stress singularities for multiscale crack model. J. of Theoretical and Applied Fracture Mechanics, 46(2): 87-104.
[3] Sih GC (2007) Multiscaling aspects of fail-safe for material and structure. In: Sih GC. Tu SD. and Wang ZD. (eds.), Integrated Approaches for Materials and Structural Safety. East China University of Science and Technology Press, Shanghai, pp 1-13.
[4] Sih GC (2007) Collapse simulation of I-35W bridge: a dynamic finite element analysis. International Center for Sustainability, Accountability and Eco-Affordability of Large Structures (ICSAELS), College of Civil Engineering, Southeast University, Nanjing, 210096, China.
[5] Fisher JW (1980) Fatigue behavior of full-scale welded bridge attachments. Transportation Research Board, US National Research Council.
[6] Fisher JW (1984) Fatigue and Fracture of Steel Bridges. Wiley Interscience, New york.
[7] Mahmoud KM (2007) Fracture strength for a high strength steel bridge cable wire with a surface crack. J. of Theoretical and Applied Fracture Mechanics, 48(2): 152-160.
[8] Sih GC, Tang XS, Mahmoud KM and Kassir MK (2007) Effect of crack shape and size on estimating the fracture strength and crack growth fatigue life of bridge cable steel wires. J. of Bridge Structures, in press.
[9] Sih GC, Tang XS, Li AQ, Li ZX and Tang KK (2007) Fatigue crack growth behavior of cables and steel wires for the cable-stayed portion of Runyang bridge: disproportionate loosening and/or tightening of cables. J. of Theoretical and Applied Fracture Mechanics, in press.
[10] Cohen S, Bakst B, Borenstein S, Lohn M, Foley R and Krawczynski J (2007) Minnesota bridge problems uncovered in 1990, Associated Press, Aug. 3.
[11] Sih GC (2007) Lecture on "bridge design and construction: criteria for strength and efficiency". College of Civil Engineering. Southeast University, Nanjing, China, August.
[12] The Collection of Runyang Yangtze River Bridge. In: Wu Shengdong (ed.). Construction Volume 4, Cable Bridge, Peoples Communications Press, Bejing, China (2005), pp33-47.
[13] Paris PC (1962) The growth of cracks due to variations in load. Ph. D. Dissertation, Department of Mechanics, Lehigh University.
[14] Sih GC and Tang XS (2007) Form-invariant representation of fatigue crack growth rate enabling linearization of multiscale data. J. of Theoretical and Applied Fracture Mechanics, 47(1): 1-14.

[15] Sih GC (2007) Fatigue crack growth rate behavior of polyvinylchloride hidden by scaling: Reinterpreted by micro/macrocrack model. J. of Theoretical and Applied Fracture Mechanics, 47(2): 87-101.
[16] Wang SY and Dang ZJ (2002) Research on heavy load high fatigue stress amplitude cable and anchorage of cable-stayed bridge. J. of Bridge Construction, 3: 14-16 (Chinese).
[17] Practical Handbook of Engineering Materials. Chinese Standard Press, Beijing, Vol. 1 (1988) 375 (Chinese).

Fatigue Crack Growth Rate of Cable-Stayed Portion of Runyang Bridge: Part II – Steel Wire Crack Growth Due to Disproportionate Cable Tightening/Loosening and Traffic Loading

G. C. Sih [1, 2 *] **and X. S. Tang** [3]

[1] International Center for Sustainability, Accountability and Eco-Affordability of Large Structures (ICSAELS)
Advanced Technology for Large Structural Systems (ATLSS)
Lehigh University, Bethlehem, PA 18015, USA

[2] School of Mechanical and Power Engineering, East China University of Science and Technology, Shanghai 200237, China

[3] School of Bridge and Structural Engineering, Changsha University of Science and Technology, Changsha, Hunan 410076, China

[*] *Email: gcs8866@yahoo.com, gcs1@lehigh.edu*

Abstract

Having completed an investigation in Part I that deals with the fatigue crack growth in the cables of the Runyang cable-stayed bridge based the design data for the cables, Part II of this work is concerned with the fatigue crack growth of the steel wires being the constituents of the cables. The objective is not only to check the compatibility of the fatigue crack growth behavior of the cable and wire but also the independent design fatigue limits imposed on both the cable and wire. In particular, assumptions are made to relate the mechanical and fatigue properties of the cable in relation to those for the steel wire. The mean stress and stress amplitude are accounted for simultaneously such that the increase and decrease of the initial cable tension on the fatigue cracking of steel wires can be assessed. The increase use of higher strength wire materials calls for consideration of damage at both the micro- and macro-scale. That is more advanced material can absorbed more energy at the microscopic scale in contrast to energy dissipated by macrocracking. A dual scale fatigue crack model is therefore required to address the micro/macro interaction for the mechanical and fatigue properties of the material and their influence on crack growth.

Under traffic and an increase of the initial wire tension of α=1.6 with α=1 being the design reference for the cable, a defect of 0.1mm in the wire can extend more than 60% across a 5mm diameter wire after 9×10^5 cycles which is about 45% of the fatigue life of the wire. According to the cable

G.C. Sih (ed.), Multiscale Fatigue Crack Initiation and Propagation of Engineering Materials: Structural Integrity and Microstructural Worthiness, 249–274.

design specification, the defect should extend only 0.1mm after 2×10^6 cycles. This shows that the fatigue life of wires is sensitive to initial defects and to the initial wire tension. These conditions are not considered in the present design of the cable nor the wire. What this means is that inspection and maintenance procedures are not thought of at the design stage; they are established during the life span of the bridge. Even more of a disadvantage is that there are no basis for comparing the monitored data with wire and/or cable damage analyses in order to gain an understanding of the failure mechanisms of wire and cable.

1. Introduction

The risk of bridge failure has been the aging of material and increase in traffic. Both factors contribute to fatigue crack growth that cannot always be monitored because the locations of damage are not always obvious and they can and often escapes the attention of the inspector.

The collapse of the eight-lane steel-deck truss bridge in Minneapolis has called attention to deficiencies in many older spans around the nation. Although the feeling is that better material and design technologies should make bridges safer, relatively little efforts are being made to understand the basic mechanisms governing fatigue crack growth, particularly when the higher strength and tougher materials are now able to sustain microcracking in addition to macrocracking. This means that failure analysis would involve at least damage at both the microscopic and macroscopic scale, if not at an even lower scale. Such a need has not caught up to the attention of those who determine the rules of bridge design.

In recent times, the US Federal Highway Administration has started to enforce new rules for bridge design in order to make new structures more efficient, more reliable, safer and longer lasting. Among other improvements, the rules emphasize the ability of bridges to withstand peak traffic loads, brutal weather, in addition to events like ship collisions and earthquakes. The American Association of State Highway and Transportation also indicated that the new rules should encourage a more reliable way of designing a bridge. Relatively little is known with regard to the durability of cable-stayed structures which utilize steel cables as its primary load-carrying members. Traffic and wind loads induce wide stress variations in these cables that could make them vulnerable to failure by fatigue. Each cable consists of multiple high strength steel strands arranged in a bundle and encased in a polyethylene pipe filled with cement grout. The ends of each cable are anchored at the bridge deck level, while the center of the cable is draped over the top of the bridge tower or pylon, on a curved support called a "saddle." The cable is designed to withstand two million cy-

cles of axial load and fluctuating bending stress induced through vertical displacement of the saddle. Tests are usually performed at a minimum frequency of two Hz. The specification-required acceptance criteria limit the number of broken wires in fatigue testing to two percent, or five out of a total of some 250 and more wires. The combined capabilities of the axial and the saddle fixture tests are those commercially available in the U.S. for fatigue performance evaluation of bridge stay cables. The trend for the past few decades has been to increase the strength from approximately 1500 to 1700 MPa [1] which is known to have a trade-off effect with the fracture toughness. The design requirements for the limits set for the fatigue cycles of the cable and wire, however, appear to be arbitrary and their relationship is at best fortuitous. To begin with the length of the cable or wire tested does not coincide with the full structure. High strength wire is sensitive to pre-existing surface defects that are non-uniformly distributed over the full length of the wire. It is well known for high strength silicone glass fibers that the fiber strength is length dependent. Although no such information prevails for the high strength steel wire, it is likely that the test data for steel wire can have a large range of scatter and that the location failure is location dependent along the wire length. This would indicate the existence of surface defects in that would affect the tensile strength. It is believed that the results of cable breakage for long and short wires can be widely different, not to mention the difference in the stress states. Dissecting fatigue damaged cables should provide information on fracture initiation dependency on surface defects that would be scattered along the wire. The testing of single steel wire with different length should prove the point. Hence, long wires are susceptible to fatigue stress corrosion and hydrogen embrittlement that can result in a reduction of the fatigue life of wires [2-4] and hence the cable [5] in the long run.

2. Statement of Problem

The driving force for fatigue cracks has been attributed to the accumulation of energy density which is in fact the area inscribed by the hysteresis loops although the criteria may be expressed in different forms. Comparison of analytical models with test results, however, can vary, often due to insufficient information on the size and time scale of damage initiation and termination. A specimen can be regarded as globally reversible but locally irreversible on account of permanent deformation near the tip of a macrocrack. The local damage can still be macroscopic owing to the accumulation of energy density next to the crack tip. This corresponds to the ASTM recommendation of fatigue tests for pre-cracked metal specimens where the alternating stress amplitude should about 50% of the yield strength so

that the local macroscopic element would be deforming in the plastic range. This should be distinguished from damage done to a microscopic element where permanent microscopic deformation may have occurred for applied stress amplitude below 50% of the yield strength.

To be more specific, Fig. 1(a) shows a schematic of the cable that consists of multiple high strength steel strands arranged in a bundle and encased in a polyethylene pipe filled with cement grout. The ends of each cable are anchored at the bridge deck level, while the center of the cable is draped over the top of the bridge tower or pylon. The single steel wire considered in this work is 5mm in diameter as shown in Fig. 1(b).

Illustrated in Fig. 2 is the fracture surface appearance of a steel bolt that is formally similar to that of a steel wire tested under similar conditions. When the specimen is subjected to sufficiently low stress amplitude but repeated many

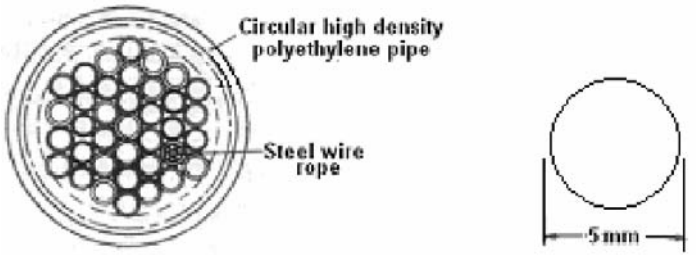

(a) Single cable (b) Single steel wire

Fig. 1 Bridge cable consisting of steel wires in polymer pipes and matrix.

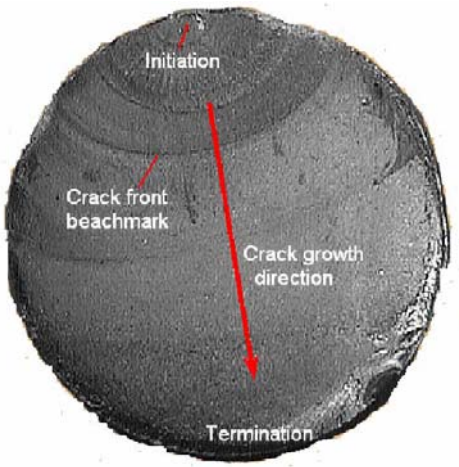

Fig. 2 Fatigue crack growth in steel bolt from initiation to termination.

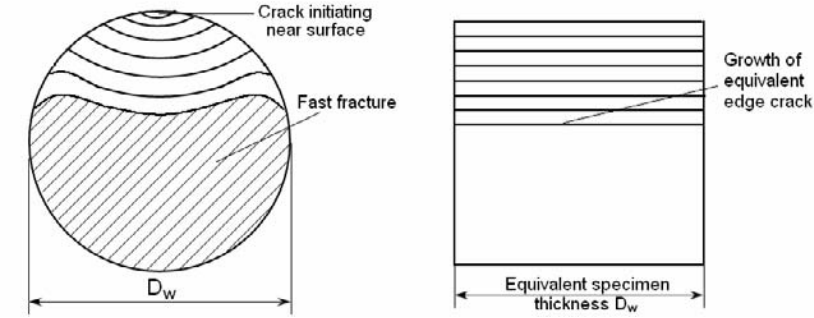

(a) Clam shell cracks (b) Equivalent edge cracks

Fig. 3 Clam shell cracks modeled as edge cracks.

times, a small crack next to the surface would initiate at the top and grow slowly and then rapidly towards to the bottom of the specimen until it terminates. The crack front beach marks are shown and they are sketched in Fig. 3(a) where the clam shell cracks would first grow in a stable manner until the crack front curvature starts to deviate from the clam shell pattern. The shaded portion of the specimen represents fast fracture. To simplify the analysis, an equivalent edge crack as indicated in Fig. 3(b) will be assumed where the crack would grow in segments until the onset of unstable fracture.

3. Dual Scale Fatigue Crack Model for Steel Wire

The discovery of double singularity [6,7] at the same crack tip had led to the development of a dual scale crack model. The strong and weak stress singularity can refer, respectively, to the macrocrack and microcrack which can be distinguished by the crack opening distance. That is a tightly closed crack that cannot be seen by the naked eye would be regarded as microscopic. This is particularly relevant in fatigue where the crack surface would open in tension and close in compression. Switching from micro to macro and vice versa occurs every full cycle. Such a behavior can be accounted for by the relation

$$\frac{da}{dN} = \Phi_o (\Delta S_{micro}^{macro})^{\phi} \tag{1}$$

with Φ_o and ϕ being the empirical constants assumed in the two-parameter model. The superscript “macro” and subscript “micro” are introduced to indicate that the increment of the energy density factor ΔS accounts for the microscopic and macroscopic effects. This can be best illustrated by considering the case of ϕ=1.

3.1 Equivalent fatigue crack growth relation for ϕ=1

Without loss in generality, it can be shown that

$$\frac{da}{dN} = pa \tag{2}$$

In Eq.(2), p stands for

$$p = \Phi p_o, \quad p_o = (1-2\nu_{micro})\mu^*(1-\sigma^*)^2\sqrt{d^*} \tag{3}$$

such that

$$\Delta S_{micro}^{macro} = \frac{2(1-\nu_{macro})^2\sigma_a\sigma_m\sqrt{d_o}}{\mu_{macro}\sqrt{r}}p_o a \tag{4}$$

can be replaced by having

$$\Phi = \Phi_o \frac{2(1-\nu_{macro})^2\sigma_a^w\sigma_m^w}{\mu_{macro}}\sqrt{\frac{d_o}{r}} \tag{5}$$

Note that $\sigma_a^w\sigma_m^w$ refers to the effect of the stress amplitude and mean stress felt by the wire which is not the same as that for the cable. All quantities in Eq. (5) refer to the wire. Defining Λ as the parameter relating $\sigma_a\sigma_m$ for the cable to $\sigma_a^w\sigma_m^w$ for the wire, there results

$$\sigma_a\sigma_m = \Lambda\sigma_a^w\sigma_m^w \tag{6}$$

Since p is independent of N, a(N) can be obtained from Eq. (2) by direct integration as

$$a(N) = a_o e^{p(N_o-N)}, \text{ for } \phi=1 \text{ for the wire} \tag{7}$$

3.2 Mechanical and fatigue properties of wire

The mechanical properties of the steel wire can be found in Table 1 [8] such that μ_{macro} and ν_{macro} in Eq. (4) or (5) can be replaced, respectively, by μ_w and ν_w as follows:

$$\Lambda=0.8,\ E_w=199.82\text{GPa},\ \mu_{macro}=\mu_w=E_w/[2(1+\nu_w)]=76.85\text{GPa}. \tag{8}$$

Table 1. Mechanical properties of bridge steel wire [8].

Elastic modulus E_w (GPa)	Ultimate stress σ_{ult}^w (MPa)	Ultimate strain ε_{ult}^w (%)
199.82	1722.55	5.5

Furthermore, the quantities in the second of Eqs. (3) are taken as

$$\mu^* = \frac{\mu_{micro}}{\mu_{macro}} = 2,\ \sigma^* = \frac{\sigma_o}{\sigma_\infty} = 0.3,\ d^* = \frac{d}{d_o} = 1,\ d_o = 10^{-3}\text{mm},\ \nu_{macro} = 0.3,\ \nu_{micro} = 0.4 \tag{9}$$

together with a_o=0.01mm, and $N_o=0.1\times10^6$ and r/d_o=1. The normalized quantities in Eqs. (9) together with d_o and ν_{micro} are assumed to be valid for both the cable and wire. The range of crack length is a=1~2.6mm with fatigue cycles in the range $N=0.1\sim2.0\times10^6$. The fatigue properties based on the classical stress intensity range ΔK are given in Fig. 4 [9]. The data can be substituted into

$$\log\left(\frac{da}{dN}\right) = \log(\Phi_o) + \phi\log\left(\Delta S_{micro}^{macro}\right) \tag{10}$$

while ΔS_{micro}^{macro} can be reduced to ΔK with ϕ=1. This gives

$$\phi = 1,\ \Phi_o = 2.15\times10^{-6} \text{ for the wire} \tag{11}$$

Numerical values of the crack growth rate and crack length can now be computed for studying fatigue cracking behavior of the steel wire in bridge cables.

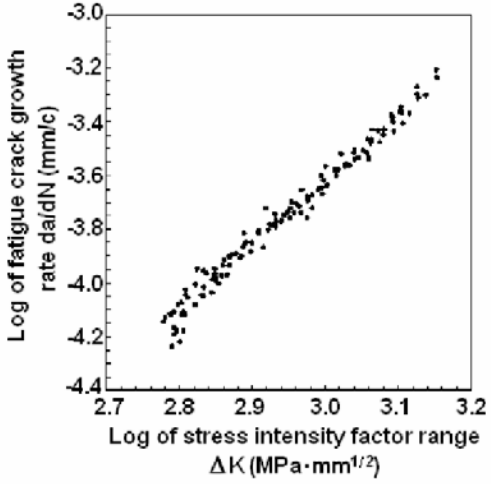

Fig. 4 Log-log plot of da/dN versus ΔK for high strength steel data from [9].

4. Crack Growth Rate versus Fatigue Cycles for Steel Wire

Examined will be the effects of initial tension of cables inflicted to the fatigue crack growth characteristics of the wire under traffic (Case I) and no traffic (Case II) which are defined as

$$\text{Case I: } \sigma_a = \alpha\sigma^{\alpha}_{max} - \sigma^{o}_{max},\ \sigma_m = \frac{\alpha\sigma^{\alpha}_{max} + \sigma^{o}_{max}}{2} \tag{12}$$

$$\text{Case II: } \sigma_a = \sigma^{\alpha}_{max} - \alpha\sigma^{o}_{max},\ \sigma_m = \frac{\sigma^{\alpha}_{max} + \alpha\sigma^{o}_{max}}{2} \tag{13}$$

The superscript parameter α is used to vary the tension in the cable in Eqs. (12) for the traffic condition and in Eqs. (13) for the no-traffic condition The quantity σ^{o}_{max} denotes the cable stress without traffic. Moreover, it is more expedient to use the stress amplitude σ_a and mean stress σ_m. Hence, σ^{o}_{max} and σ^{α}_{max} will be converted to the mean stress $\sigma_m=(\sigma_{max}+\sigma_{min})/2$ and the stress amplitude $\sigma_a= \sigma_{max}-\sigma_{min}$ with σ_{max} and σ_{min} being the maximum and minimum cyclic applied stress. This will be done for the cables and effects exerted on the wire can be found by using Eq. (6) for fixed values of Λ.

4.1 Case I: wire tightening & loosening under traffic

Numerical values of σ_a, σ_m and $\sigma_a\sigma_m$ for the 52 cables of the Runyang bridge with α=1.0, 1.2 and 1.6 are found from Eqs. (12). The values are tabulated only for cable #28, #38 and #50 as shown in Tables 2, 3 and 4, respectively. The conversion to $\sigma^{w}_{a}\sigma^{w}_{m}$ is then made by application of Eq. (6). The highest σ_a, σ_m and $\sigma_a\sigma_m$ occur in cable #50 followed by cable #28 while cable #38 attains the lowest stress amplitude and mean stress.

Similarly, the numerical values of σ_a, σ_m and $\sigma_a\sigma_m$ for cable #28, #38 and #50 with α=0.97 and 0.91 can be found in Tables 5 and 6, respectively. In what follows, the crack growth rate in the wires will be discussed.

Table 2 Values of σ_a, σ_m and $\sigma_a\sigma_m$ for Cable #28, #38 and #50 for Case I with α=1.0.

Cable No.	σ_a (MPa)	σ_m (MPa)	$\sigma_a\sigma_m \times 10^5$ (MPa^2)
28	196.46	797.03	1.56583
38	90.52	358.60	0.32461
50	238.73	900.23	2.14916

Table 3 Values of σ_a, σ_m and $\sigma_a\sigma_m$ for Cable #28, #38 and #50 for Case I with α=1.2.

Cable No.	σ_a (MPa)	σ_m (MPa)	$\sigma_a\sigma_m \times 10^5$ (MPa^2)
28	375.51	886.55	3.32909
38	171.29	398.99	0.68343
50	424.25	1002.19	4.43623

Table 4 Values of σ_a, σ_m and $\sigma_a\sigma_m$ for Cable #28, #38 and #50 for Case I with α=1.6.

Cable No.	σ_a (MPa)	σ_m (MPa)	$\sigma_a\sigma_m \times 10^5$ (MPa^2)
28	733.61	1065.60	7.81738
38	332.84	479.76	1.59680
50	850.49	1206.11	10.25785

Table 5 Values of σ_a, σ_m and $\sigma_a\sigma_m$ for Cable #28, #38 and #50 for Case I with α=0.97.

Cable No.	σ_a (MPa)	σ_m (MPa)	$\sigma_a\sigma_m \times 10^5$ (MPa^2)
28	169.60	783.60	1.32899
38	78.40	352.54	0.27641
50	208.15	884.93	1.84196

Table 6 Values of σ_a, σ_m and $\sigma_a\sigma_m$ for Cable #28, #38 and #50 for Case I with α=0.91.

Cable No.	σ_a (MPa)	σ_m (MPa)	$\sigma_a\sigma_m \times 10^5$ (MPa^2)
28	115.89	756.74	0.87695
38	54.17	340.43	0.18442
50	146.97	854.35	1.25564

4.1.1 Wire in cable #28 for $\alpha \geq 1$ and $\alpha \leq 1$

Plotted in Fig. 5 are the variations of the crack growth rate da/dN with the number of fatigue cycles N for the wire in cable #28 with α=1.0, 1.1, ---, 1.6 where the design condition α=1.0 serves as a reference. Note that da/dN remained negligibly small for α up to 1.3 over the design life of $N=2\times10^6$ cycles. One order of magnitude increase of da/dN is seen at $N=1.80\times10^6$ cycles for α=1.5 and $N=1.48\times10^6$ cycles for α=1.6. This is a difference of 320,000 cycles.

Shown in Fig. 6 are curves for α=0.91, 0.94 and 0.97. Compared to the reference curve α=1.0 for $da/dN \approx 75\times10^{-7}$ mm/c after two million cycles, they all decrease in the crack growth rate with lowest being 16×10^{-7} mm/c. This occurred at α=0.91 and $N=2\times10^6$ cycles.

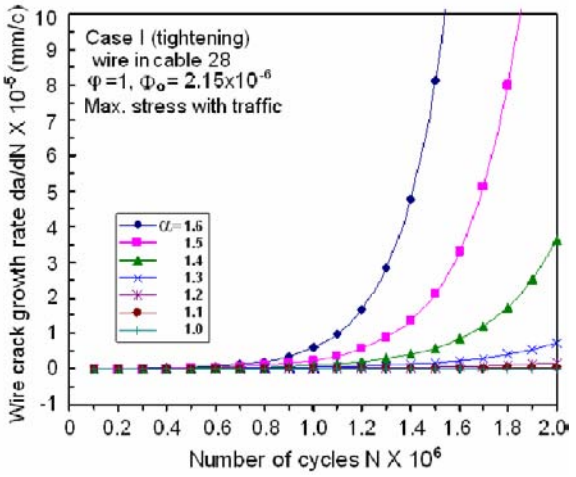

Fig. 5 Wire crack growth rate da/dN versus number of cycles N for wire in Cable #28 and Case I with $\alpha \geq 1$.

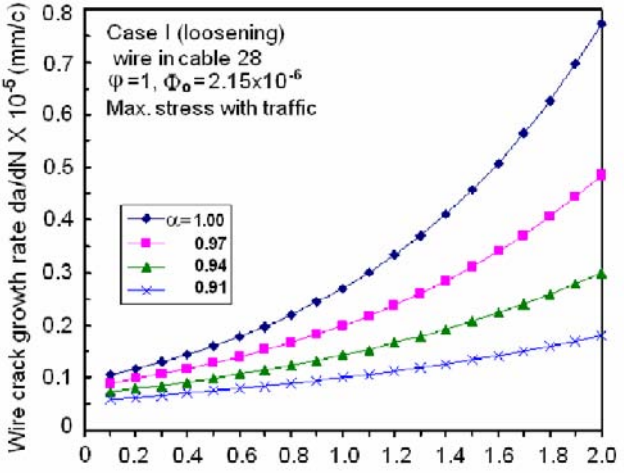

Fig. 6 Wire crack growth rate da/dN versus number of cycles N for wire in Cable #28 and Case I with $\alpha \leq 1$.

4.1.2 Wire in cable #38 for $\alpha \geq 1$ and $\alpha \leq 1$

The situation for the wire in cable #38 is not as severe. Fig. 7 shows that the crack growth rates for α=1.0, 1.1 and 1.2 are nearly constant as N increased up to two million cycles at which time da/dN remained within the range of 0.5 to 1.0×10^{-8} mm/c. This is several orders of magnitude smaller than the crack growth rate in Fig. 5 for the wire in cable #28.

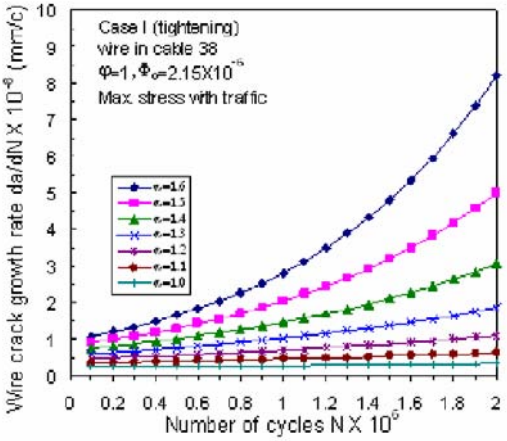

Fig. 7 Wire crack growth rate da/dN versus number of cycles N for wire in Cable #38 and Case I with $\alpha \geq 1$.

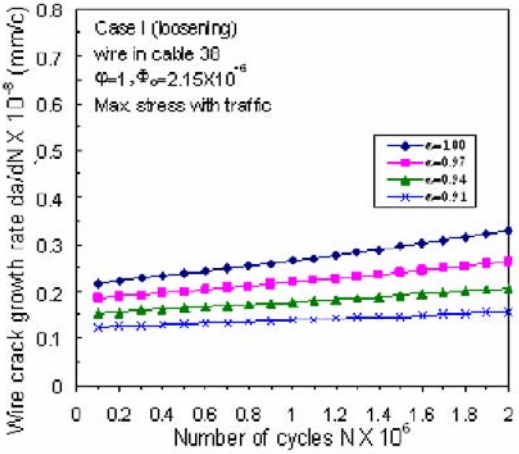

Fig. 8 Wire crack growth rate da/dN versus number of cycles N for wire in Cable #28 and Case I with $\alpha \leq 1$.

A significant reduction of da/dN can be seen from Fig. 8 for the wire in cable #38 when the initial cable tension is decreased with α=1.0, 0.97, 0.94 and 0.91. The corresponding crack growth rate ranged from 14 to 33×10^{-10} mm/c

4.1.3 Wire in cable #50 for $\alpha \geq 1$ and $\alpha \leq 1$

The outer most distanced cables of the bridge tend to be more stresses. This applies also to the wires in these cables such as #50. Fig. 9 indicates

that da/dN reached about 50×10^{-5} mm/c for $\alpha=1.5$ at $N\approx1.60\times10^{6}$ cycles and $\alpha=1.6$ at $N\approx1.33\times10^{6}$ cycles. At these high crack growth rates, there prevails the likelihood of fatigue crack growth failure. When the initial tension in cable #50 is decreased, the corresponding wires are les stressed since α in Eq. (13) would be less than unity. According to Fig. 10, da/dN at $N=2\times10^{6}$ cycles reduced to 4×10^{-7} mm/c at $\alpha=0.91$ and to 22×10^{-7} mm/c at $\alpha=1.0$.

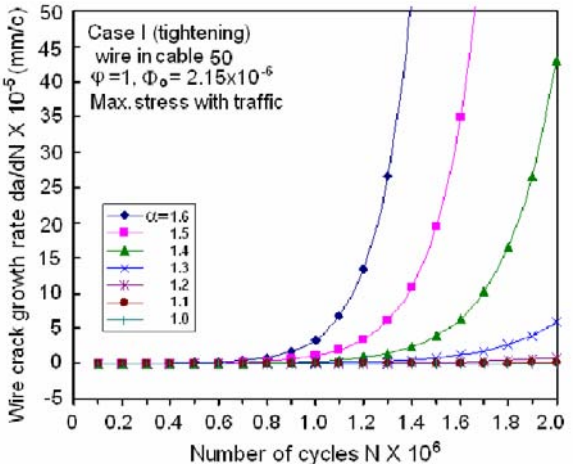

Fig. 9 Wire crack growth rate da/dN versus number of cycles N for wire in Cable #50 and Case I with $\alpha\geq1$.

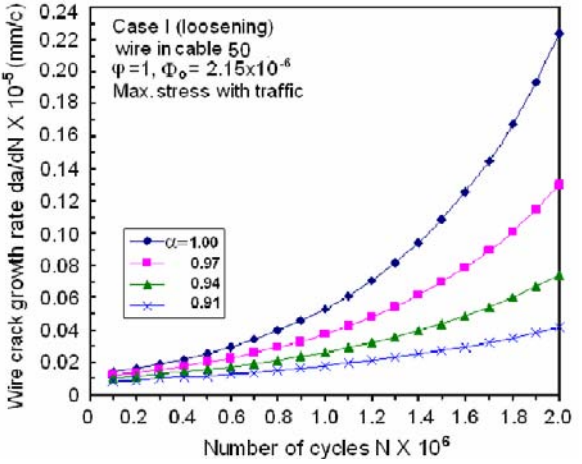

Fig. 10 Wire crack growth rate da/dN versus number of cycles N for wire in Cable #50 and Case I with $\alpha\leq1$.

4.2 Case II: wire tightening & loosening without traffic

Consider Eq. (13) where the traffic load is removed. The stress amplitude should be reduced accordingly. The maximum and minimum applied stresses determine the stress amplitude. The results of σ_a, σ_m and $\sigma_a\sigma_m$ for cable #28, #38 and #50 are given, respectively, in Tables 7, 8 and 9 for α=1.00, 1.04 and 1.12. Case II refers to max. stress without traffic while $\alpha \geq 1$ corresponding to increase of initial cable tension.

Tables 10 and 11 summarize the σ_a, σ_m and $\sigma_a\sigma_m$ for α=0.9 and 0.7 where the initial cable tension is decreased below the reference design level of α=1.0. Contrast to intuition, the values of σ_a, σ_m and $\sigma_a\sigma_m$ in Tables 10 and 11 are higher than those in Tables 5 and 6. Hence, decreasing the initial cable tension without traffic does not decrease the stress amplitude nor the mean stress.

Table 7 Values of σ_a, σ_m and $\sigma_a\sigma_m$ for Cable #28, #38 and #50 for Case II with α=1.0.

Cable No.	σ_a (MPa)	σ_m (MPa)	$\sigma_a\sigma_m \times 10^5$ (MPa^2)
28	196.46	797.03	1.56583
38	90.52	358.60	0.32461
50	238.73	900.23	2.14916

Table 8 Values of σ_a, σ_m and $\sigma_a\sigma_m$ for Cable #28, #38 and #50 for Case II with α=1.04.

Cable No.	σ_a (MPa)	σ_m (MPa)	$\sigma_a\sigma_m \times 10^5$ (MPa^2)
28	168.51	811.00	1.36659
38	77.99	364.87	0.28455
50	207.50	915.85	1.90038

Table 9 Values of σ_a, σ_m and $\sigma_a\sigma_m$ for Cable #28, #38 and #50 for Case II with α=1.12.

Cable No.	σ_a (MPa)	σ_m (MPa)	$\sigma_a\sigma_m \times 10^5$ (MPa^2)
28	112.60	838.95	0.94469
38	52.92	377.40	0.19972
50	145.03	947.08	1.37356

Table 10 Values of σ_a, σ_m and $\sigma_a\sigma_m$ for Cable #28, #38 and #50 for Case II with α=0.9.

Cable No.	σ_a (MPa)	σ_m (MPa)	$\sigma_a\sigma_m \times 10^5$ (MPa^2)
28	266.34	762.09	2.02973
38	121.85	342.93	0.41788
50	316.82	861.19	2.72842

Table 11 Values of σ_a, σ_m and $\sigma_a\sigma_m$ for Cable #28, #38 and #50 for Case II with α=0.7.

Cable No.	σ_a (MPa)	σ_m (MPa)	$\sigma_a\sigma_m \times 10^5$ (MPa^2)
28	406.10	692.21	2.81103
38	184.52	311.60	0.57497
50	472.99	783.10	3.70401

4.2.1 Wire in cable #28 for $\alpha \geq 1$ and $\alpha \leq 1$

The crack growth rates in Fig. 11 for the wire in cable #28 are found to decrease with increasing α from 1.00 to 1.12. After two million cycles da/dN

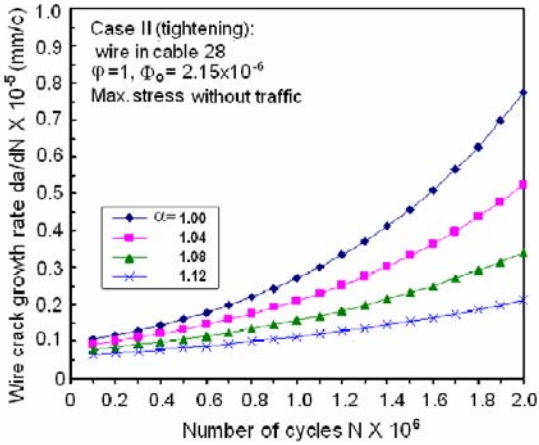

Fig. 11 Wire crack growth rate da/dN versus number of cycles N for wire in Cable #28 and Case II with $\alpha \geq 1$.

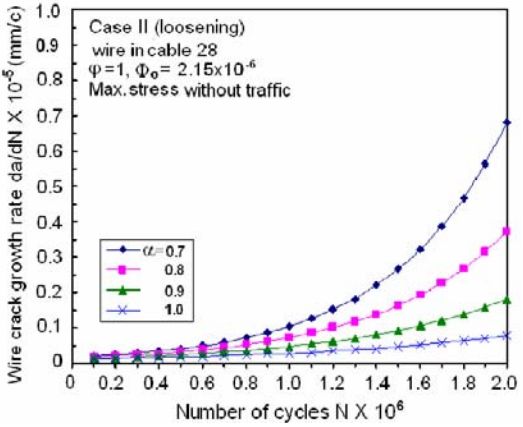

Fig. 12 Wire crack growth rate da/dN versus number of cycles N for wire in Cable #28 and Case II with $\alpha \leq 1$.

decreased from 75×10^{-7} mm/c at $\alpha=1.00$ to 17.5×10^{-7} mm/c at $\alpha=1.12$. If the initial cable tension is decreased by letting $\alpha=0.7$, 0.8, 0.9 and 1.0, then the da/dN in the wire becomes 66×10^{-7} mm/c at $\alpha=0.7$ and 5×10^{-7} mm/c at $\alpha=1.0$. These results can be found in Fig. 12.

4.2.2 Wire in cable #38 for $\alpha \geq 1$ and $\alpha \leq 1$

The wire crack growth rate in Fig. 13 refers to cable #38 with $\alpha \geq 1$ without the influence of traffic. The curves rise slowly with N and they are

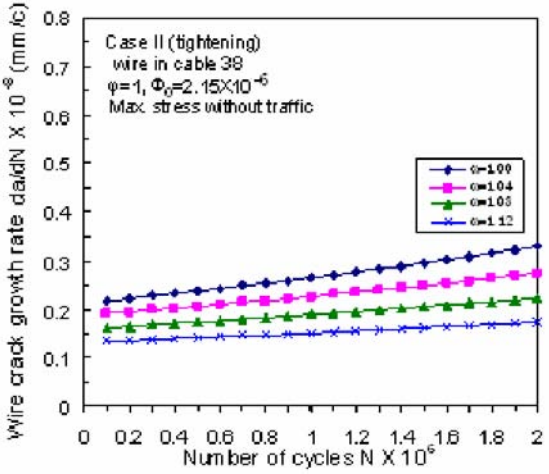

Fig. 13 Wire crack growth rate da/dN versus number of cycles N for wire in Cable #38 and Case II with $\alpha \geq 1$.

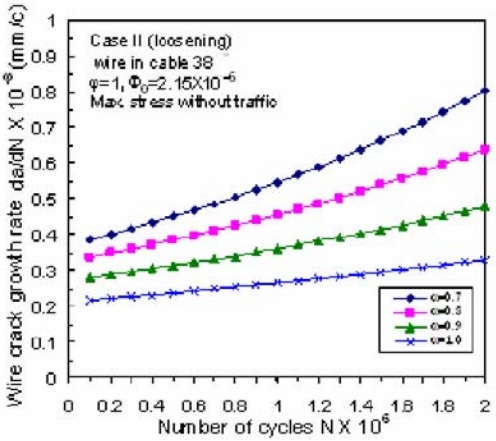

Fig. 14 Wire crack growth rate da/dN versus number of cycles N for wire in Cable #38 and Case II with $\alpha \leq 1$.

nearly parallel. The range of da/dN at $N=2\times10^6$ cycles is about 16×10^{-10} mm/c at $\alpha=1.12$ to 33×10^{-10} mm/c at $\alpha=1.00$. Fig. 14 plots the wire crack growth rate as a function of N for $\alpha=0.7$, 0.8, 0.9 and 1.0 when the initial tension in cable #38 is decreased. An increase in the wire da/dN is seen at $N=2\times10^6$ cycles. The range of wire da/dN for $\alpha=1.0$ to 0.7 is from 27.5×10^{-10} to 80×10^{-10} mm/c.

4.2.3 Wire in cable #50 for $\alpha \geq 1$ and $\alpha \leq 1$

The wire da/dN in cable #50 as shown in Fig. 15 increases by more than one order of magnitude for $\alpha=1.00$, 1.04, 1.08 and 1.12 without traffic.

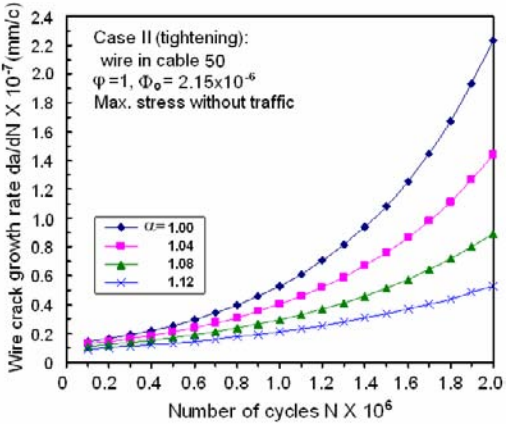

Fig. 15 Wire crack growth rate da/dN versus number of cycles N for wire in Cable #50 and Case II with $\alpha \geq 1$.

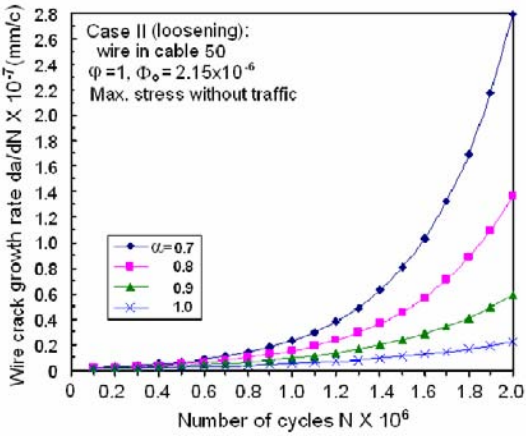

Fig. 16 Wire crack growth rate da/dN versus number of cycles N for wire in Cable #50 and Case II with $\alpha \leq 1$.

The curve rise slowly for low cycles and then increases more quickly as N approaches the limit of two million cycles. The beneficial effect is that the wire da/dN decreases as the initial cable tension is increased to α=1.12. The final drop in wire da/dN is from 22×10^{-8} at α=1.00 to 44×10^{-9} mm/c at α=1.12. The effect of decreasing cable tension in the absence of traffic is shown in Fig. 16. The curves are found to rise more quickly with decreasing α as N is increased. A wire da/dN of 15×10^{-9} mm/c at α=1.00 increases to 28×10^{-8} mm/c at α=0.7.

5. Crack Length as a Function of Fatigue Cycle for Steel Wire

The wire da/dN can be used to find the wire crack length as a function of the fatigue cycles. The will also be exhibited for the wire crack growth characteristics corresponding to cable #28, #38 and #50 with and without traffic.

5.1 Case I: wire tightening & loosening under traffic

Crack length serves as an indicator for the failure of structural components by cracking or fracture. Its variation with time or fatigue cycles consists of three stages: stable and slow growth, transition region and unstable and rapid propagation. Such information can be monitored and compared with the initial design condition to determine the current state of the structure system such that a decision could be made with reference to continuing service or interrupting service for repair. The intention of this study is to

determine the critical states of fatigue cracks in the wire by assuming that under service the cable tension can deviate from the design conditions.

5.1.1 Wire in cable #28 for $\alpha \geq 1$ and $\alpha \leq 1$

The wire crack depth corresponding to cable #28 is plotted as a function of the fatigue cycles N in Fig. 17 when traffic is present. No growth occurs

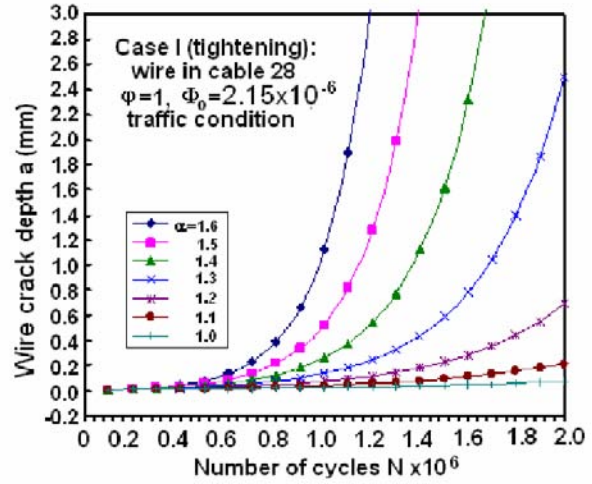

Fig. 17 Wire crack length a versus number of cycles N for Cable #28 and Case I with $\alpha \geq 1$.

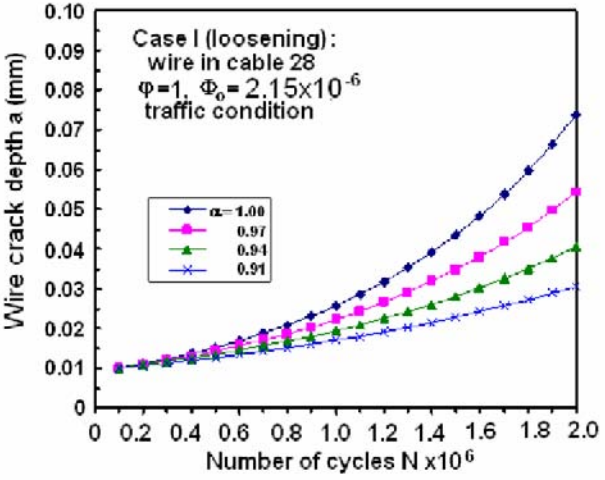

Fig. 18 Wire crack length a versus number of cycles N for Cable #28 and Case I with $\alpha \leq 1$.

for the reference state α=1. As α is increased in constant increment of 0.1 from 1.0 to 1.6, the wire crack depth starts to increase with increasing N. The curves for α=1.4 to 1.6 rise very quickly after one million cycles. All three curves reach a crack depth of 3 mm before the design life of $N=2\times10^6$ cycles although these results correspond to abnormal conditions where the initial cable tension were higher than the design value. For lower initial cable tension with $\alpha\leq1$, Fig. 18 shows that the wire crack depth is much smaller, they are .027 mm for α=0.91 and 0.071 mm for α=1.00.

5.1.2 Wire in cable #38 for $\alpha\geq1$ and $\alpha\leq1$

Wire crack depth for cable #38 is negligibly small. Fig. 19 shows that even after two million cycles for all $\alpha\geq1$, the crack depth a changes very little from its original size of $10x10^{-2}$ mm for α=1.0 and 1.1 although increase in the crack depth is seen as N increases. At $N=10^6$ cycles, $a \approx 75x10^{-2}$ mm for α=1.6. The variations in the crack depth in terms of α is much less for $\alpha\leq1$. The results are shown in Fig. 20. Note that the fatigue cracking behavior of the wires in cable #38 differed widely from those in cable #28. This illustrates the possibility for using different wire material in different cables such that the design in terms of wire fatigue life owing to crack growth could even out and would not undergo such wide variations.

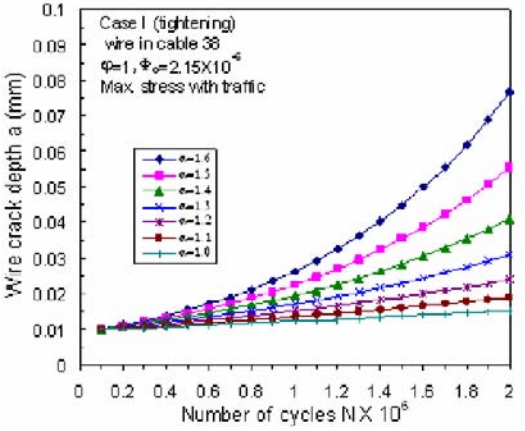

Fig. 19 Wire crack length a versus number of cycles N for Cable #38 and Case I with $\alpha\geq1$.

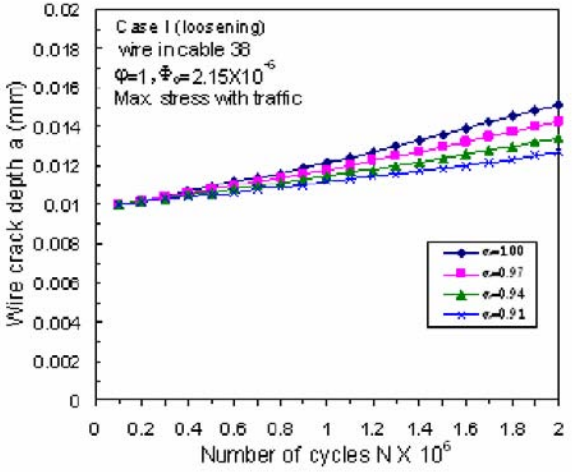

Fig. 20 Wire crack length a versus number of cycles N for Cable #38 and Case I with $\alpha \leq 1$.

5.1.3 Wire in cable #50 for $\alpha \geq 1$ and $\alpha \leq 1$

Crack depth for the wires in cable #50 is even more appreciable than those in cable #28 indicated by Fig. 17. Possible unstable wire crack instability may have occurred for α as small as 1.2 at or before the design

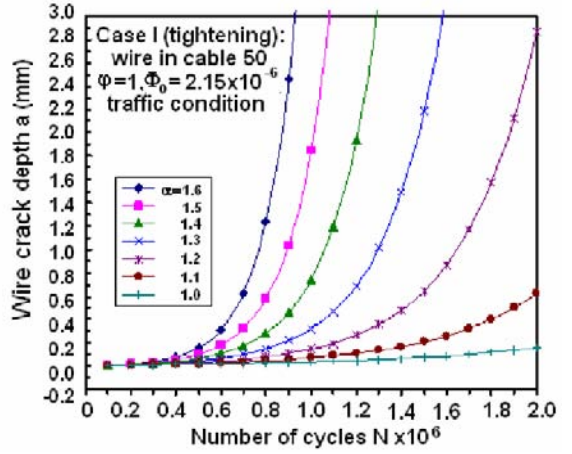

Fig. 21 Wire crack length a versus number of cycles N for Cable #50 and Case I with $\alpha \geq 1$.

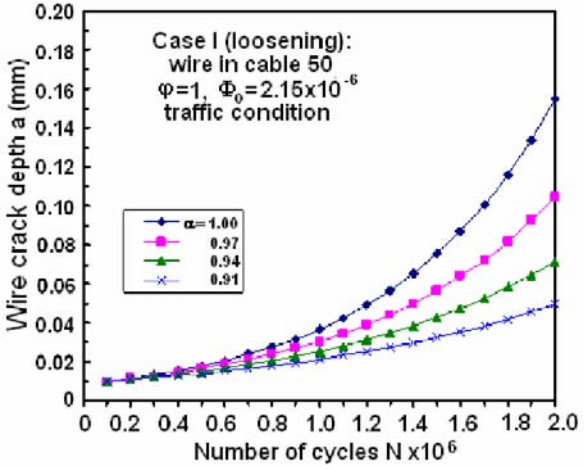

Fig. 22 Wire crack length a versus number of cycles N for Cable #50 and Case I with $\alpha \leq 1$.

fatigue life. For $\alpha=1.6$, the crack depth may nave reached a critical state after only 860,000 cycles. By decreasing the initial tension of the wires in cable #50 with $\alpha \leq 1$, a reduction in crack depth is seen in Fig. 22 where the largest crack depth at $\alpha=1.0$ is only 0.15 mm after two million cycles.

5.2 Case II: wire tightening & loosening without traffic

Removing the traffic leads to small crack growth. Summarized in Figs. 23 to 28 inclusive are the crack depth results for the wires in cable #28, #38 and #50.

5.2.1 Wire in cable #28 for $\alpha \geq 1$ and $\alpha \leq 1$

Figs. 23 and 24 show that the wire crack depth increase slowly with the fatigue cycles N for $\alpha \geq 1$ and $\alpha \leq 1$ as the initial tension of the wires are increased and decreased, respectively. Starting with the same initial crack length of $a_o = 10^{-2}$ mm, all the curves for N up to about 4×10^5 cycles are almost unchanged; they start to deviate with increasing N. Referring to Fig.23, the wire crack depth changed from 32×10^{-3} to 72×10^{-3} mm after $N=2 \times 10^6$ cycles as α changed from 1.12 to 1.00, respectively. Increasing α

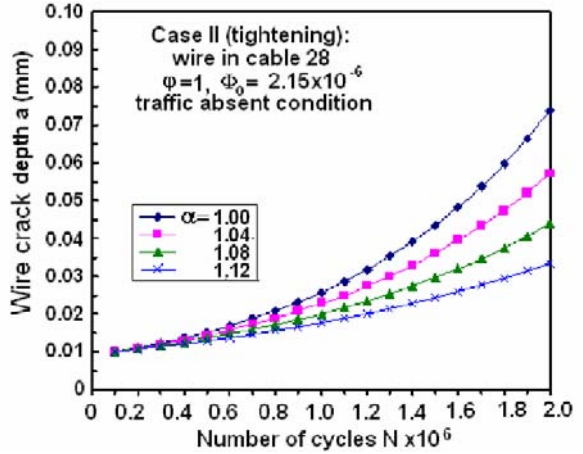

Fig. 23 Wire crack length a versus number of cycles N for Cable #28 and Case II with $\alpha \geq 1$.

decreased the crack depth. Fig.24 exhibits the results for $\alpha \leq 1$ in the same cable with the traffic absent. In this case, decreasing α resulted in greater crack depth. This trend can be found from the four curves in Fig.24 with reference curve with $\alpha=1$ giving the lowest crack depth. At $N=2\times10^6$ cycles, the crack depth is $60\text{x}10^{-3}$ mm for $\alpha=1$ and $36\text{x}10^{-2}$ mm for $\alpha=0.7$. Significant change in the crack depth is observed. The crack growth behavior is seen to depend sensitively on loosening and tightening of the wire.

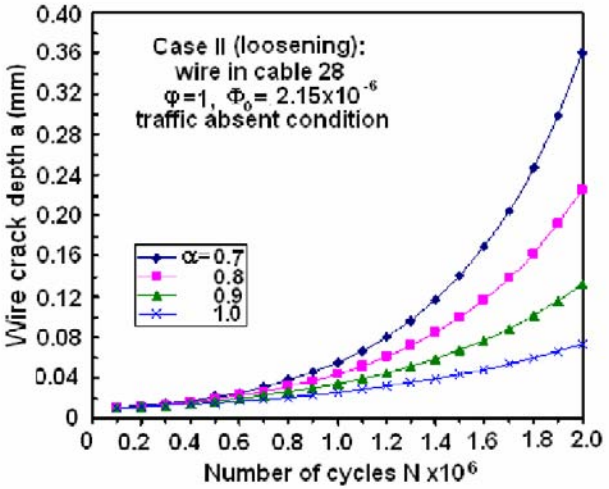

Fig. 24 Wire crack length a versus number of cycles N for Cable #28 and Case II with $\alpha \leq 1$.

5.2.2 Wire in cable #38 for $\alpha \geq 1$ and $\alpha \leq 1$

Even smaller crack depth occurs for the wire in cable #38. This can be seen from the results in Figs. 25 and 26. No further discussion is required for this case.

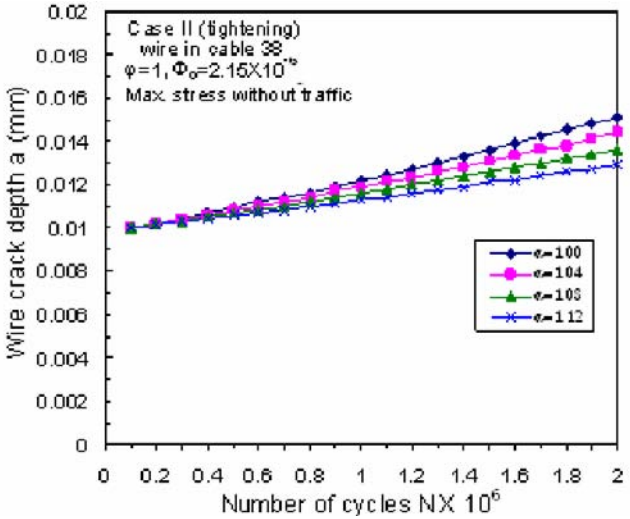

Fig. 25 Wire crack length a versus number of cycles N for Cable #38 and Case II with $\alpha \geq 1$.

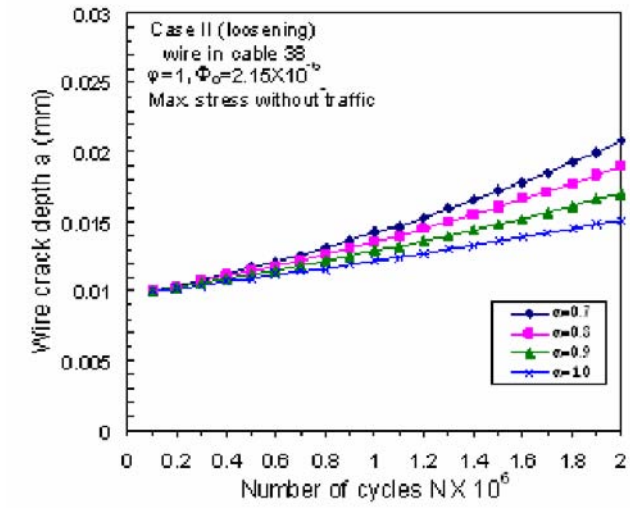

Fig. 26 Wire crack length a versus number of cycles N for Cable #38 and Case II with $\alpha \leq 1$.

5.2.3 Wire in cable #50 for $\alpha \geq 1$ and $\alpha \leq 1$

Finally, Figs. 27 and 28 show the crack depth for the wires in cable #50 for $\alpha \geq 1$ and $\alpha \leq 1$, respectively, in the absence of traffic. The wire crack increased about one order of magnitude as the fatigue cycles increased to two million cycles. The largest crack depth is 1.15 mm occurred at $\alpha=0.7$ in Fig. 28 when the initial wire tension is reduced below the design value. This completes the discussion of the wire crack growth characteristics.

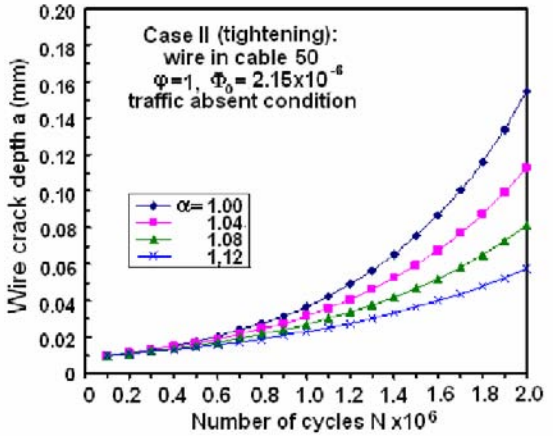

Fig. 27 Wire crack length a versus number of cycles N for Cable #50 and Case II with $\alpha \geq 1$.

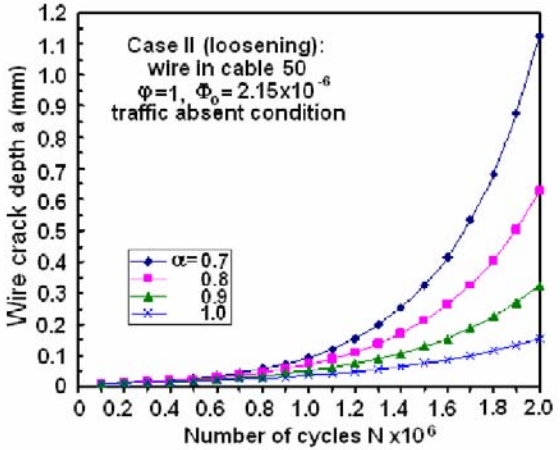

Fig. 28 Wire crack length a versus number of cycles N for Cable #50 and Case II with $\alpha \leq 1$.

6. Concluding Remarks

An attempt has been made to relate the fatigue crack growth characteristics of the steel wires that make up the bridge cables. This is analogous to that of relating the composite bundle strength from the properties of the fibers, a problem that is not only unresolved up to now but still lacks understanding. A possible attribute to the difficulties is incorporating the surface defects being related to the fiber or wire length because past tests have revealed the length dependency of the wire strength on its length. Since it is unpractical to test the full length of the bridge cables or wires, little is known on the validity of the present fatigue test data since they are based on specimens that are considerably shorter than the full structure. Despite the simplifying assumptions made in the present analytical model, the essential dual scale material and geometric parameters are considered such that their influence on fatigue crack growth is exhibited on a relative base. A wide variance of fatigue crack growth has been observed for the wires in the different cables. The results can vary by one order of magnitude or more according to the design cable data for the Runyang cable-stayed bridge. They show that the wires in the highly stresses cables can fracture by fatigue at only one-half of design fatigue life of two million cycles while others are still within the safe limits. The highly non-uniformly distributed cable tensions appear to a typical characteristic in the design of the present-day cable-stayed bridges. Not enough is known at present whether cable tension non-uniformity would over ride the beneficial aspects of cable-stayed bridge design when weighed in financial terms. Little efforts are made to this basic issue, rather the trend seems to rely on health monitoring to which some remarks are in order.

Recent works [10-12] have emphasized the necessity to correctly identify the monitored signals with the physical damage that is expected to be observed. Firstly, the scenarios selected for the design loads must be defined before deciding on the hardware (e.g. the type and accuracy of sensors) and software (model relating the signal to the type and size of damage) used for health monitoring. Keep in mind that software is needed to convert many of parameters such as stress, temperature, etc. from the change of displacement or electrical resistance. In addition, the non-equilibrium behavior of an open system introduces fundamental difficulties to the in-field measurements. More attention should be placed on the relative changes rather than the values of the specific parameters. Too much emphasis cannot be said with reference to the danger of placing false confidence on unqualified monitored data. Furthermore, it should also be said that analytical models are seldom devised to predict the physical out-

come but they are made available to guide tests and to minimize the number of tests by relating the results of two independent tests.

References

[1] Elices M. Llorca J. and Astiz MA. Fatigue of steels for concrete reinforcement and cables. In: Carpinteri, A. (Ed.), Handbook of Fatigue Crack Propagation in Metallic Structures. Elsevier, Amsterdam (1994) 191-220.
[2] Toribio J. and Lancha AM. Stress corrosion behavior of high-strength steel: design on the basis of the crack growth kinetics curve. Materials & Design, 16(5) (1995) 283-288.
[3] Mahmoud KM. Fracture strength for a high strength steel bridge cable wire with a surface crack. J. of Theoretical and Applied Fracture Mechanics, 48(2) (2007)152-160.
[4] Sih GC. Tang XS. Mahmoud KM and Kassir MK, Effect of crack shape and size on estimating the fracture strength and crack growth fatigue life of bridge cable steel wires. J. of Bridge Structures (2007) in press.
[5] Sih GC. and Tang XS. Fatigue crack growth rate of cable-stayed portion of Runyang bridge: Part I–cable crack growth due to disproportionate cable tightening/ loosening and traffic loading. In: G. C. Sih (Ed.), Multiscale Fatigue Crack Initiation and Propagation of Engineering Materials: Structural Integrity and Microstructural Worthiness, Springer (2008) 207-244.
[6] Sih GC. and Tang XS. Dual scaling damage model associated with weak Sin gularity for macroscopic crack possessing a micro/mesoscopic notch tip. J. of Theoretical and Applied Fracture Mechanics, 42(1) (2004) 1-24.
[7] Tang XS and Sih GC. Evaluation of microstructural parameters for micro-/ macro line crack damage model. J. of Theoretical and Applied Fracture Mechanics, 46(3) (2006)175-201.
[8] Practical Handbook of Engineering Materials. Chinese Standard Press, Bejing, Vol. 1 (1988) 375 (Chinese).
[9] Wang SY and Dang ZJ, Research on heavy load high fatigue stress amplitude cable and anchorage of cable-stayed bridge. J. of Bridge Construction, 3 (2002) 14-16 (Chinese).
[10] Sih GC, Signal recognition of fatigue crack growth in bridge structures connected to specimen behavior. J. of Bridge Struct. 2(3): (2006) 133-145.
[11] Sih GC, Dual scale monitoring of fatigue cracks based on time rate change of local compliance. In: Li AQ. Sih GC, Nied HF and Li ZX (eds.), Health Monitoring of Structure, Material and Environment, Southeast University Press, Nanjing, China, (2007) 17-36.
[12] Sih GC, Tang XS. Li ZX. Li AQ. and Tang KK. Fatigue crack growth behavior of cables and steel wires for the cable-stayed portion of Runyang bridge: disproportionate loosening and/or tightening of cables. J. of Theoretical and Applied Fracture Mechanics (2007) in press.

Fatigue of Small-Scale Metal Materials: From Micro- to Nano-Scale

G. P. Zhang* and Z. G. Wang
Shenyang National Laboratory for Materials Science, Institute of Metal Research, Chinese Academy of Sciences, 72 Wenhua Road, Shenyang 110016, P. R. China
**Email: gpzhang@imr.ac.cn*

Abstract

This work considers currently-developed fatigue testing techniques and evaluation methods for the small-scale metal materials. Then, a number of studies on fatigue damage behavior and fatigue properties are presented and highlighted as a function of the length scales. The relationship between length-scale-dependent microstructure evolution and fatigue behavior is addressed to understand fatigue damage mechanisms at small scales. Finally, the perspectives of studies on fatigue of the small-scale metal materials are proposed.

1. Introduction

Fatigue, as one of the most important failure modes in engineering structural materials, has been investigated for over one hundred years. In recent years, the transition from the traditional engineering to micro/nano technologies drives research interests in fatigue toward small-scale materials [1]. These small-scale materials are widely used in Micro-Electro- Mechanical Systems (MEMS)/microsystems, etc. high-tech fields [2]. For example, in microelectronics and communication thin metal films on a substrate are basic functional components. In automobile industry, MEMS accelerometers and rate gyroscopes are used in safety airbags and antilock braking systems to replace larger and more costly components. Small pressure sensors are used in engine fuel injection systems to monitor fuel and air pressure. In the biomedical field, some pressure and chemical sensors in pumps, respirators and dialysis machines are the most applicable MEMS-based devices.

In general, the small-scale materials can be classified into three categories according to their dimensions: (i) thin films whose dimension in one direction is close to micrometers or less; (ii) thin wires/fibers whose dimensions in two directions are very small; and (iii) small particles. On the other hand, these materials can also be roughly classified into two types

G.C. Sih (ed.), Multiscale Fatigue Crack Initiation and Propagation of Engineering Materials: Structural Integrity and Microstructural Worthiness, 275–326.

based on confinement: (i) free-standing thin films, small dimensional foils (Fig. 1(a)) and thin wires (Fig. 1(b)), and (ii) thin films confined by a substrate (Fig. 1(c)). No matter what kind of these materials are, at least one dimension of the material should be in the range from micrometers to nanometers.

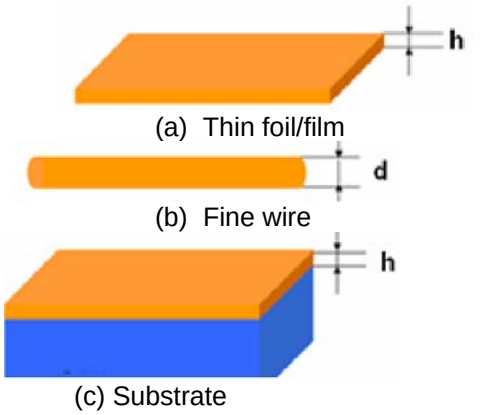

Fig.1 Schematic of the small-scale materials (top) free-standing thin foils/films, (middle) fine wires and (bottom) thin films confined by a substrate.

As metallization interconnects, thin metal films confined by a substrate are widely used in microelectronic devices and integrated circuits in semiconductor industry. The thin films are unavoidably subjected to thermal fatigue loading during temperature variation, which is caused by the difference in thermal expansion coefficients between film and underlying substrate. Temperature variation typically occurs during film preparation, micro-fabrication and also during device operation [3]. That leads to stress and strain cycles which can cause the onset of fatigue damage. For free-standing films or foils, they are usually microfabricated into small functional and/or structural components in MEMS/Microsystems. These small-dimensional components would be subjected to mechanical fatigue loading at different frequency in all kinds of environment. For example, micro radio frequency (RF) switches, etc., are constantly subjected to a cyclic load with high frequency during the period of their service. Fatigue usually causes a gradual change in the properties of the small-scale material [4, 5]. The formation of microcracks or damage in microcomponents due to fatigue would gradually change the resonant frequency and electrical resistance of microdevices, degrade the sensor output and, most seriously, lead to the failure of MEMS devices. Therefore, the failure induced by mechanical fatigue and thermal fatigue are the potential reliability threats to these systems. Understanding the underlying mechanisms of fatigue behavior and measuring fatigue strengths of these small-scale materials are

great challenges and may help us to improve the overall reliability of entire devices.

Today, the high integration density in micro/nano-systems is leading to material dimensions (geometrical and microstructural dimensions) shrinking toward the submicrometer and nanometer scale. To evaluate fatigue properties of such materials it is necessary to consider the following important questions corresponding to fundamental and experimental aspects.

1. Which fatigue testing method is suitable to evaluate the fatigue properties of small-scale materials like thin metal films with thickness of several micrometers or less?
2. Do the fatigue behavior and mechanism change with varying length scale? For example, what happens when the film thickness or grain size is smaller than the dimension of a typical fatigue-induced dislocation structure as observed in bulk materials?
3. How does a fatigue crack initiate and propagate in a small-scale material? What is the mechanism and size effect?

In this work, newly-developed experimental methods will be described for performing fatigue tests of the small-scale materials, and then fatigue failure process including crack initiation and growth will be introduced in sections 3 and 4, respectively. Furthermore, underlying physical mechanisms of fatigue damage of the small-scale materials will be discussed with consideration of size effects in section 5.

2. Fatigue Testing and Evaluation Methods of Small-Scale Materials

As the dimensions of the material decrease into the micrometer, submicrometer or even nanometer regime, new experimental methods have to be developed to measure fatigue properties accurately. It is suggested that the following factors are needed to be considered.

1. Ultra-low force load cell, closed-loop high resolution displacement actuator and PC-controlled data acquisition system.
2. Reliable clamping method that can overcome the difficulty in mounting thin films without damaging.
3. Application of a simple and homogenous stress state which makes extraction of fatigue data and comparison with bulk materials easier.
4. It is also anticipated to in-situ observe fatigue damage process, such as fatigue crack initiation and growth during fatigue loading.

5. Simple sample fabrication process that allows the fabrication of small-scale materials suitable for fatigue testing. Also the samples are easily prepared into transmission electron microscopy (TEM) samples.

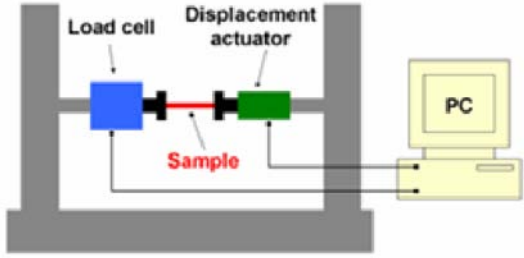

(a) Uniaxial cyclic loading

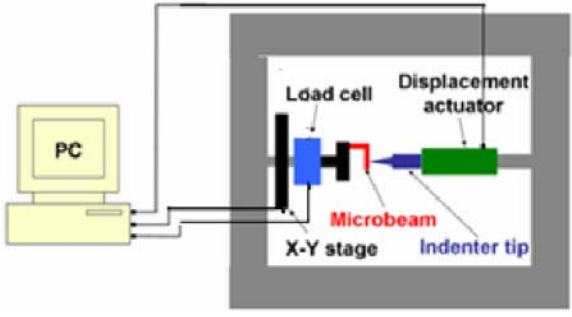

(b) Dynamic bending

Fig. 2 Schematic illustration of fatigue machine for small-scale materials through different testing methods.

Table 1 Summary of fatigue testing methods of small-scale materials.

Method	Materials	Sample shape	Reference
Uniaxial tension-tension	Cu	Free-standing thin wires, dog-bone shaped foils	[6-10]
Dynamic bending	Ni-P amorphous alloys Stainless steel Silver	Micro-sized cantilever beam	[11-13]
Resonant vibration	Cu/Nb	foils	[14]
Uniaxial tension-compression	Cu/Polyimide	Dog-bone shaped films confined by a substrate	[15]
Thermal-cyclic	Cu	Patterned metal lines	[16]

Concerning the points mentioned above, a couple of testing methods have been developed in recent years. Table 1 summaries the fatigue testing

methods and the corresponding materials conducted recently. In general, these methods are roughly classified into uniaxial cyclic loading and dynamic bending based on the loading mode. Like the conventional method used for bulk materials, the most common test method is uniaxial cyclic loading, which can directly measure the cyclic stress-strain behavior of the samples. Following this idea, a simple apparatus for fatigue of thin metal wires has been constructed in [6]. It applies a constant strain amplitude on the sample by means of an electromagnetic vibrator (a hard bass loudspeaker) being excited by a frequency generator. The force is measured by a load cell, and the strain is measured by an inductive strain gauge. A micrometer is used to apply the mean stress on the sample. After amplification, both signals are registered by a memory oscilloscope. Similarly, a new tension-tension fatigue apparatus was developed in [7], which could apply cyclic load by an electromagnetic actuator controlled by a frequency generator. High resolution piezoelectric sensors were used to measure the load. Fatigue tests were conducted successfully with free-standing Cu films in the thickness range of 20 μm-100 μm. After that, a couple of new methods are developed for uniaxial cyclic loading of free-standing metal foils [9, 10] through replacing the magnetic vibrator with piezoelectric actuator. The basic principle of a fatigue machine for small-scale materials is depicted in Fig. 2(a). A set-up in [10] is a piezoelectric-driven uniaxial stress-strain measurement system to evaluate fatigue properties of thin Ni films. The force calibration was linear over 0-1.50 N with a resolution of 0.2 mN. The displacement range of the closed-loop piezoelectric actuator in the test apparatus is 0-90 μm, with a displacement measurement resolution of 1.8 nm. The frequency response of the piezoelectric actuator is up to 10^3 Hz, which is sufficient for fatigue testing. To facilitate grip sample, three-axis micropositioning system and a CCD with remote microscope were used to locate the specially-designed glass grip appropriately. Furthermore, a MEMS-based apparatus was set up to conduct fatigue testing of very small samples.

Even though the fatigue properties of the metal foils have been measured, ideal tension-compression cyclic loading for very thin free-standing films (less than one micrometer) may not work using this method. Alternatively, the dynamic bending method was developed recently. A fatigue machine for small-scale materials was developed in [11] as schematically illustrated in Fig. 2(b). The machine has a displacement resolution of 5 nm and a load resolution of 10 μN. The various waveforms for cyclic loading and frequencies up to 100 Hz can be applied by using this machine. The cyclic loading of a free-standing Ni-P amorphous alloy and SUS304 stainless steel foils was conducted in [11,12] by using dynamic bending of

micro-cantilever beams, respectively. Before testing, the diamond tip of the indenter was precisely located at the loading point of the microbeam by the repeated calibrations using the CCD camera, and then the microcantilever beam was dynamically bent under constant load amplitude control. According to the elastic beam theory, when the beam was deflected dynamically, the top surface at the fixed end of the microbeam would be subjected to a pull–pull stress and the rear surface of the microbeam to a push–push stress. During dynamic bending tests, the microbeam stiffness was recorded automatically. Fatigue life of the free-standing small samples was determined based on the variation of the microbeam stiffness during dynamic bending because crack initiation would cause a decrease in the stiffness.

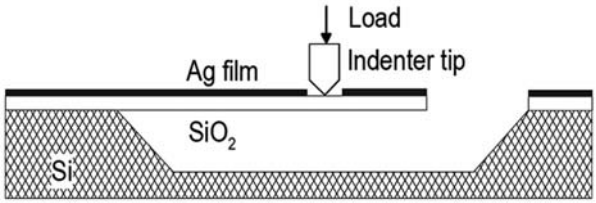

Fig. 3 Schematic of the bilayer Ag-SiO_2 beam deflection experiment. The indenter tip is used to deflect the beam [13].

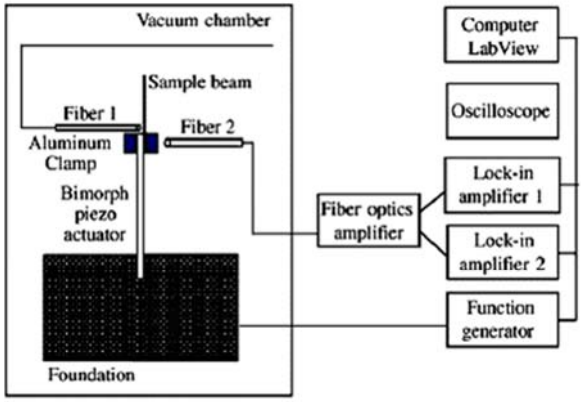

Fig.4 Schematic of the resonant frequency device to perform fatigue tests with fully reversed stress amplitudes on thin films [14].

A method to conduct cyclic tension-compression loading of thin Ag films deposited onto a SiO_2 substrate was proposed in [13] through a nanoindenter with a function of continuous stiffness measurement, as shown in Fig. 3. The dynamically elastic bending of the film/SiO_2 sub-

strate composite causes cyclic tension-compression loading to the thin Ag film at the top of the substrate. Fatigue failure of the Ag film was monitored by the variation of the stiffness of the microbeam. Recently, a device based on the resonant frequency method was constructed in [14], as shown schematically in Fig. 4. By this kind of dynamic bending method, fatigue properties of self-supported Cu/Nb multilayers with a total thickness of 40 μm and individual layer thickness of 40 nm were measured. Their results show that the resonant frequency method is efficient for fatigue testing of self-supported thin film materials. This method provides a new fatigue testing technique to investigate fatigue damage behaviors of metallic multilayers and/or thin films under a very high frequency and a relatively easy way to monitor fatigue failure lifetime compared with other methods.

Even though dynamic bending methods through repeated indentation or resonant vibration can obtain fatigue properties of the small-scale materials, the disadvantages of this method are the requirement for microfabrication of the samples and the nonuniform stress distribution at the cross-section of the microbeam does not facilitate extraction of fatigue data.

To overcome the disadvantages pointed out above, a new fatigue testing method was proposed in [15] through applying a uniaxial load to metal films deposited on a compliant substrate with a high elasticity and mechanical stability, as shown in Fig. 5(a). The film/substrate-composite is strained by tensile loading and unloading while the film is deformed elastically and plastically in tension and in compression on loading and unloading, respectively. In addition, to evaluate the applied plastic strain range, the cyclic stress-strain curves of the samples can also be measured in situ by X-ray diffraction goniometer, as shown in Fig. 5(b). The advantages of this method are:

1. A cyclic tension-compression load can be applied to the very thin metal films with thickness even down to tens of nanometers.
2. The bulk-like fatigue sample of metal film/substrate composite can be fabricated easily and fixed to the fatigue machine by relatively large clamps.
3. Fatigue tests can be controlled either by constant load range or total strain range.
4. Samples for Transmission Electron Microscopy (TEM) can be easily obtained from the fatigued specimens by conventional preparation methods.

Therefore, this method seems to be the most suitable one for fatigue investigations of thin films at room temperature. Following such a method, a

number of studies of fatigue behaviors of thin metal films and metallic multilayers are conducted.

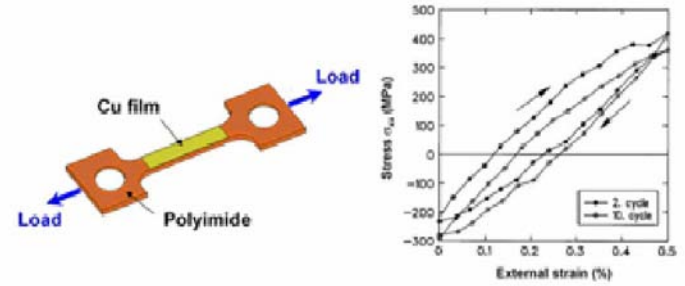

(a) Cu film/polyimide specimen (b)Film stress

Fig. 5 Cu film/polyimide substrate composite for fatigue testing and film stress σ_x as a function of substrate strain during the second and tenth cycle of the test on a 0.7 μm thick copper film. The arrows indicate the development of the film stresses during loading and unloading [15].

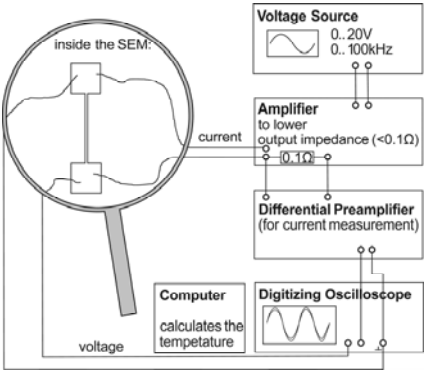

Fig. 6 Schematic illustration of the alternating current testing setup [16].

Thermal fatigue of the metal film/substrate system is a potential threat to the reliability of chip-level packaging. Since the film is bonded to a substrate that is much thicker than the film, the mismatch in coefficient of thermal expansion between the metal film and the substrate leads to changes in film strain upon changes in temperature. A direct method to generate thermal cyclic strain in the films is through repeated heating-cooling by a furnace. However, this slow process would not be suitable to generate a high enough number of thermal fatigue cycles for the evaluation of thermal fatigue damage of the films.

A method for thermal fatigue testing of thin metal films and lines was proposed in [16]. Fig. 6 schematically illustrates the setup of the in-situ alternating current (AC) testing system. The AC was generated by a signal

generator and applied to the Cu film by two metallic probes. The actual temperature in the Cu line was monitored by measuring the voltage and current in the lines by a four point measurement during the cycles. Knowing the resistance-temperature relationship of a line, the temperature can be determined by calculating the resistance changes from the measured current and voltage signals. Joule heating due to the AC causes temperature cycles, which result in cyclic strain and stress in the film bonded to a Si substrate. Different strain amplitudes could be adjusted by varying the amplitude of the electrical signal. This test system was installed in an SEM chamber and allowed in-situ observations of the fatigue damage evolution under different testing conditions. For example, cycling the temperature between 100 and 250 °C resulted in a total cyclic strain range of about 0.21% and caused damage in a 300 nm thin Cu lines after $3x10^7$ cycles at 200 Hz. Such a testing system can be of significance not only for the in-situ thermal-fatigue testing of thin metal films but also for the evaluation of the reliability of the actual metal interconnects by simulating the real working conditions of interconnect structures.

Even though several kinds of fatigue testing methods for small-scale materials have been developed, none of them has enough merits as mentioned previously. Thus, up till now there is a long way to find novel experimental methods and characterization ways special for the small-scale materials, especially for free-standing ultra-thin films and nano-scale wires. Nonetheless, a number of studies on fatigue properties and damage behavior have been carried out by these methods. Fatigue behavior different from that of bulk materials was found and will be reported in the following sections.

3. Fatigue Crack Initiation

It is well known that fatigue damage in a bulk metal usually originates from the surface of a material where there exists a locally-high stress concentration. These stress concentration sites on the material surface can be either surface flaws caused by mechanical machining or the places where fatigue extrusions/intrusions at the surface of the bulk materials are formed due to the development of cyclic strain localization. Beneath fatigue extrusions/intrusion, persistent slip bands (PSB) with typical dislocation structures can develop through the formation of dislocation walls. It is widely evidenced that the height of the fatigue extrusions/intrusions is about several micrometers and the spacing of the typical dislocation walls is about 1.3 μm. When the dimensions of the small-scale material is close to and even smaller than the characteristic dimensions of the fatigue extrusion, such as height, and the typical fatigue dislocation structures, such as dislo-

cation walls in PSBs, it is questionable whether fatigue extrusions /intrusions and typical dislocation structures similar to that observed in bulk materials can form in the small-scale materials and what the relationship between fatigue damage and the length scale of the material is?

Table 2 Fatigue tests of free-standing metal foils.

Material	Preparing method	h [μm]	d [μm]	Testing conditions	Contents	Reference
Cu	Rolling & HT	20-100	100	T-T R=0, f=70 Hz	S-N curve	[7]
Cu	ED & Wrought	25 35		LCF	FD	[8]
Cu	EBD	1.1	0.98			[9]
Cu	Rolling & HT	9-250	15-45	T-C; R=-1; f=20 kHz	FCGR FD	[17]
Cu	ED	35, 105	2-10	T-C; R=-1; f=20 kHz	FCGR FD	[17]
Al	Rolling and HT	50-250	140-218	T-C; R=-1; f=20 kHz	FCGR FD	[17]
Cu, Mo, Al	Rolling and HT	20-250		T-C; R=-1; f=20 kHz	FCGR	[18]
Cu	ED & Wrought	10-25	1-10	Flex fatigue	S-N curve	[19]
SUS304	Rolling and HT	25	2.89	DB R=0.2	S-N; FD FCGR	[12,20]
TiAl	Extruded	20		R=0.1, f=78-90 Hz	S-N; FD	[21]
Ni	LIGA	70, 270	2-5, 5-10	T-T R=0.1, f=10 Hz	S-N; FD	[22]
Ni	LIGA	200-400		T-T R=0.1, f=200 Hz	S-N	[23]
Ni	LIGA	10	1.1		S-N; FCGR	[24]
Ni	LIGA	70, 250	5, 0.015	T-C R=-1, f=20 Hz	FD	[25]
Ni-P	ED	12	-	R=0.1, 0.3, 0.5; f=10 Hz	FCGR; FD	[11,26]
Ni-P	ED	12	-	R=0.1, 0.3, 0.5; f=10 Hz	S-N curve	[27]
Cu/Nb	PVD	40	40	Resonance	S-N	[14]

T-C Tension-Compression; *T-T* Tension-tension; *DB* Dynamic bending; *HT* Heat-treatment; *ED* Electro-deposition; *EBE* Electron-beam evaporvated; *PVD* Physical Vapor Deposition; *LIGA* Lithographic, Galvanoformung, and Abformung; *FD* Fatigue damage; *LCF* Low-cycle fatigue; *FCGR* Fatigue crack growth rate

Table 3 Fatigue tests of thin metal films confined by a substrate.

Materials	Preparing method	h [μm]	d (μm)	Testing conditions	Contents*	Reference
Ag	Magnetron sputtering	1.5-0.3	1.0	Dynamic bending	FD	[13,29]
Cu	Magnetron sputtering	3.0-0.4	1.0	R=0, f=1 Hz	FD; Lifetime curve	[30-32]
Cu	Magnetron sputtering	0.2	1.0	R=0, f=1 Hz	FD	[32,33]
Cu	Magnetron sputtering	3.0-0.4	0.78-0.28	R=0, f=1 Hz	FD; Lifetime curve	[34,35]
Cu	Magnetron sputtering	0.128-0.05	0.02-0.03	R=0, f=10 Hz	FD; Lifetime curve	[36]
Cu/Ta	Magnetron sputtering	0.5	0.1	R=0, f=10 Hz	FD	[38,39]
Cu	Magnetron sputtering	0.2	1.0	Thermal fatigue	FD	[16]

Table 4 Fatigue tests of thin metal wires.

Materials	Preparing method	h [μm]	d [μm]	Testing conditions	Contents	Reference
Cu	Drawing and Annealing	30, 50, 90	15-45	R=0; f=20 Hz	S-N curve	[6]
Au	Drawing and Annealing	25, 100	140-218	R=0; f=20 Hz	S-N curve	[6]
Cu	Drawing and Annealing	10-125	10-125	T-C,	S-N curve	[28]

A number of studies of fatigue properties of free-standing thin metal foils [7-10, 11,12,14, 17-27], fine wires [6, 28], thin metal film [13,15,16,29-39] confined by a substrate have been carried out in recent years. These studies are summarized in Table 2 for the free-standing metal foils, Table 3 for thin metal films confined by a substrate and Table 4 for fine metal wires.

Fig. 7 summarizes some typical small-scale materials that have been studied based on their geometrical (foil/film thickness and wire diameter) and microstructural (grain size) dimensions. It is clear that some studies mainly concentrate on the foils/wires with geometric dimension being larger than grain size, while the others are the cases of the geometric dimen-

sion of the films/wires being smaller than grain size, especially the films confined by a substrate.

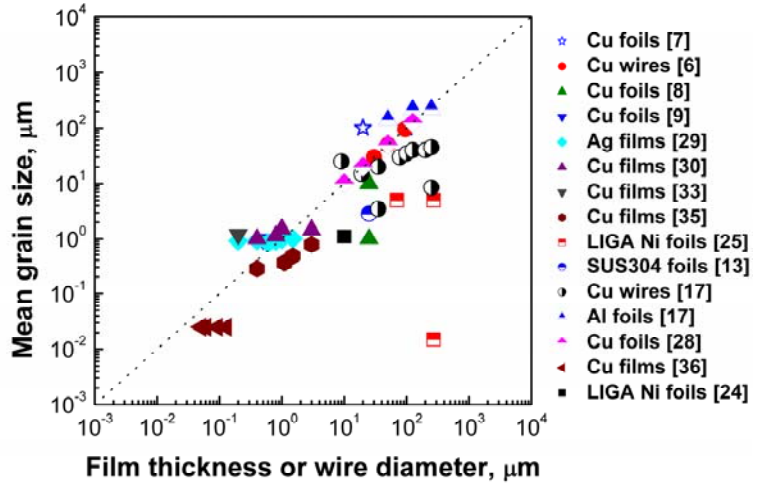

Fig. 7 A summary of the materials tested under cyclic loading based on the geometrical (foil/film thickness and wire diameter) and microstructural (grain size) dimensions.

For the free-standing thin foils/wires, a study in [7] showed that the 100 μm thick Cu foils contained a large number of well-defined and sharp slip bands with in some cases well-developed extrusions. However, for the 20 μm thick Cu foils they were almost free of extrusions and contained only a few grains with a low density of faint slip bands. These results indicated that the microstructural development toward failure is somehow delayed for the thinner foils. Especially, extrusions and microcracks in the thinner foils have been observed mainly at the end of fatigue life. Nevertheless, the microcrack observed is probably due to an extrusion. For the fine metal wires, it was found [6] that the absence of extrusion-like features on thin wire surfaces up to 10^5 cycles may be interpreted as the absence of PSBs of the type observed in marcoscopic specimens. It was reported [28] that slip bands corresponding to extrusions and intrusions formed on the surface of the bamboo-structured 20 μm and 50 μm wires shown in Fig. 8(a) and (b), respectively. Fatigue fracture in the wires occurred as a result of crack initiation at the slip bands in a deformed grain which propagated mostly in a transcrystalline mode, as shown in Fig. 8(c). The thinner wires failed in a transcrystalline manner with a pronounced crack path parallel to the slip bands, while the thicker wires showed cases of intercrystalline and transcrystalline failure.

The fatigue damage behavior of 25 μm thick 304 type stainless steel foils with fine grains of 2.89 μm was investigated in [12,20]. They found that the significant intrusion-like slip traces formed at the micrometer-sized foil surface due to the development of strain localization zone (SLZ), as shown in Fig. 9. The FIB examination of the SLZ indicates that the extrusions/intrusions-like damage formed in the fine grain, as indicated by an arrow in the upper right image of Fig. 9. Further characterization of the extrusion/intrusion-like damage by an atomic force microscopy (see the lower right image of Fig. 9) shows that severe strain localization has developed to form extrusions/intrusions with about several hundreds of nanometers dimensions (peaks/valleys), which may become the preferential site for crack initiation. Obviously, the strain localization by forming extrusion/intrusion-like damage in the 25 μm thick stainless steel foil is still preferred, and that is quite similar to that in the bulk materials.

Thus, the crack initiation was suggested to originate from the intrusion-like slip traces preferentially. Based on the microscopic observations, it is concluded that the fatigue damage process of the 25 μm thick foils experienced the following stages similar to the bulk 304 stainless steel: (1) cyclic strain localization and accumulation in the grains oriented preferentially; (2) extrusion/intrusion-induced crack nucleation and (3) crack growth from the nucleation site by the transgranular mode.

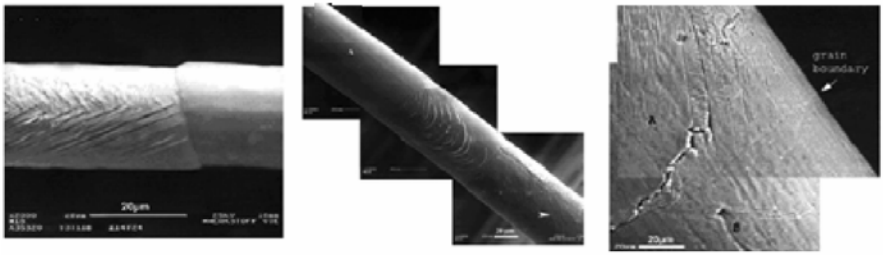

(a) Intrusions (b)Slip bands (c) Crack site

Fig. 8 SEM micrographs of fatigued Cu wires showing (left) inrusions on deformed grains of a microwire of 20 μm after $N=10^7$ cycles (middle) slip bands formation on the surface of a bamboo-structured 50 μm wire after $N=10^8$ cycles and (right) crack site in a bamboo-structured microwire of 125 μm after $N=6\times10^6$ cycles [28].

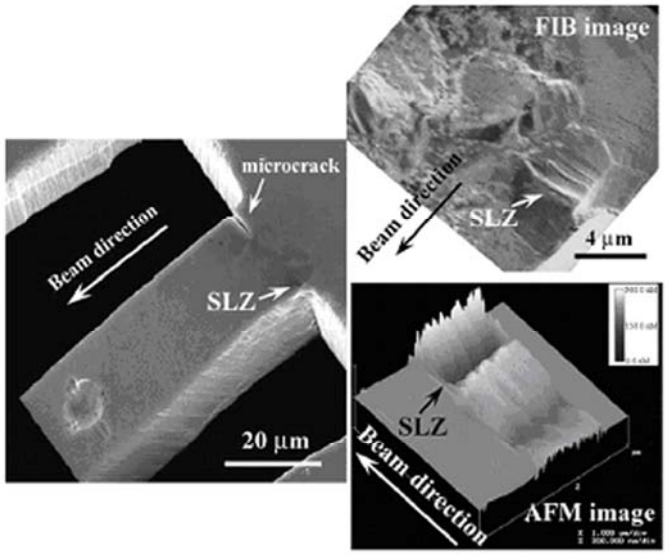

Fig. 9 Microscopic observations of the fatigue damage behavior of the microbeams: the left image is an overview of the fatigue sample at the stress amplitude of 234 MPa after 4.5×10^5 cycles, imaged by SEM, the upper right image is a close observation of the strain-localized zone (SLZ) imaged by FIB, the lower right image is an AFM characterization of the SLZ [20].

On the other hand, a few studies of high cycle fatigue properties of LIGA (Lithographic, Galvanoformung, and Abformung) Ni foils with thicknesses ranging from several tens of micrometers to hundreds of micrometers have been performed [10, 22-25]. Reported in [25] is the micrometer-thick Ni films with columnar grains, clear persistent slip bands (PSBs) occurred. Especially, it is found that crack nucleated from surface thickened oxides forming at slip bands. It was found in [40] that fatigue failure of 26 μm thick LIGA Ni foils initiated in zones of localized extrusions and intrusions associated with PSBs. Furthermore, the TEM examination of the deformation zone reveals that there existed an unexpected thick oxide on the surface of the PSBs. This PSB oxide thickening mechanism appears to be the source of crack initiation.

In general, the above studies of fatigue damage behavior of free-standing metal foils/wire with thickness/diameter larger than 10 μm clearly reveal that a fatigue crack can still originate from fatigue extrusions/intrusions, which act as a micro-notch with a high stress concentration. This process seems to be similar to that happening in the bulk materials.

However, for the much thinner films with a thickness less than 10 μm, it was [9] argued that the absence of clear slip steps on the sample surfaces and of dislocation cells in 1.1 μm thick Cu films indicated that dislocations moved individually or in small groups. A systematic investigation of fatigue damage behavior of metallic films and multilayers confined by a substrate has recently been conducted in [13,29,30-39]. In particular, the fatigue damage behavior of Ag films was conducted in [30] with a thickness ranging from 1.5 μm to 0.3 μm through dynamic microbeam deflection. The results show that fatigue failure of thin Ag films is related to the formation of voids, which were observed close to the film-substrate interface beneath extrusions. These extrusions were preferentially observed in (100)-oriented grains, whereas (111)-oriented grains were to a large extent undamaged after fatigue testing. This was suggested to be due to smaller flow stress in (100)-oriented grains. The extrusions appear as a narrow ribbon of squeezed-out material located in the interior of a single grain. The height of the extrusions was in the range of the film thickness with a regular surface structure. Beneath the extrusions voids were detected, as indicated by "C" in Fig. 10. The occurrence of voids beneath the extrusions was observed in all of the experiments performed, whereas closely spaced slip bands have only been observed one time. The void structure has been found to extend from the film-substrate interface towards the surface. These observations imply that the film-substrate interface may act as a blocking boundary to dislocations and to prevent them from leaving the film. The top surface is expected to act as a free surface, through which dislocations can leave the film and form surface steps. Therefore, fatigue damage still originates from small extrusions formed through dislocation glide.

Furthermore, low cycle fatigue tests of thin Cu films with a thickness ranging from 3.0 μm to 0.4 μm under an almost constant plastic strain range (0.83-0.91%) were carried out in [30]. Since the Cu film was deposited onto an elastic polyimide substrate, the film/polyimide-composite is strained by tensile loading and unloading while the film is deformed elastically and plastically in tension and in compression on loading and unloading, respectively. The Cu films were actually subjected to tension-compression load. The results show that surface extrusions and voids at the film/substrate interface dominate fatigue damage.

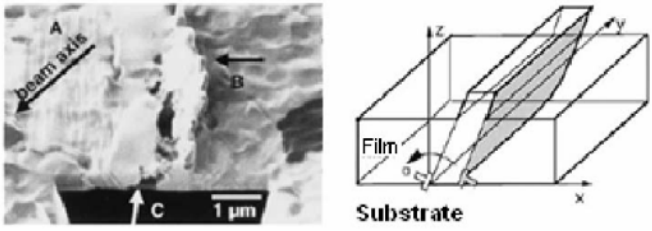

(a) Cross-section location (b) Dislocation motion

Fig. 10 FIB image of a cross-section that was cut into the extrusion (left) Schematic of dislocation motion and annihilation as possible mechanism resulting in the formation of voids and extrusions. Full and open dislocation symbols correspond to dislocations of opposite signs, produced during loading and unloading, respectively [13].

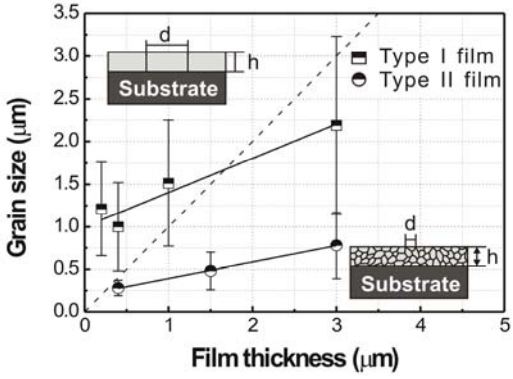

Fig. 11 Schematic of the relationship between geometric length scale (film thickness) and microstructural length scale (mean grain size) in the thin films studied [32].

The fatigue behavior of 0.2 μm thick Cu films under the same fatigue conditions (Plastic strain range, ~0.8%) as used in [30] was investigated [33]. All these Cu films have almost columnar grains with a size about 1 μm in diameter. It was found that fatigue crack initiation behavior of the 0.2 μm thick Cu films is quite different from that of the 3.0 μm thick Cu films. While the work in [35] conducted low cycle fatigue tests of thin Cu films with mean grain size ranging from 0.78 μm to 0.28 μm, which is smaller than the film thickness. A clear fatigue extrusion was found in the large grain of the 3.0 μm thick Cu films. To thoroughly understand fatigue damage behavior in these thin Cu films, systematic work of microscopic examination was conducted through focused-ion-beam microscopy (FIB) and TEM [32]. First of all, the metal films were classified into two categories, namely type I and type II films, as defined in Fig. 11. For the type I

films the grain size is about one micrometer scale, which is typically larger than the film thickness, and for the type II films, the grain size is normally submicrometer scale, which is smaller than the film thickness. The microstructure parameters and fatigue testing conditions of the above Cu films were summarized in Table 5.

For the type I films with a grain size about 1 μm, some clear size effects are found and summarized below based on FIB plan-view observations of the film surfaces after damage:

1. Fatigue extrusions/intrusions can still occur in the thin Cu films with a thickness ranging from 3.0 μm to 0.2 μm, as shown in Fig. 12;
2. However, with decreasing the film thickness the dimensions of the fatigue extrusions including height and width decrease (Figs. 12(a)-(c)). Especially, there are almost no fatigue extrusions/intrusions in the 0.2 μm thick films, as shown Fig. 12(d);
3. Fatigue damage in the 3.0 μm thick films was found to originate from the extrusions/intrusions, which is quite similar as of the bulk materials (Fig. 12(a)), while fatigue cracking in the 0.2 μm thick films (Fig. 12(d)) preferentially initiate along the grain boundaries and twin boundaries rather than fatigue extrusions/intrusions. As a result, a transition of fatigue damage behavior from the extrusion-induced mode to the boundary-induced mode occurs.

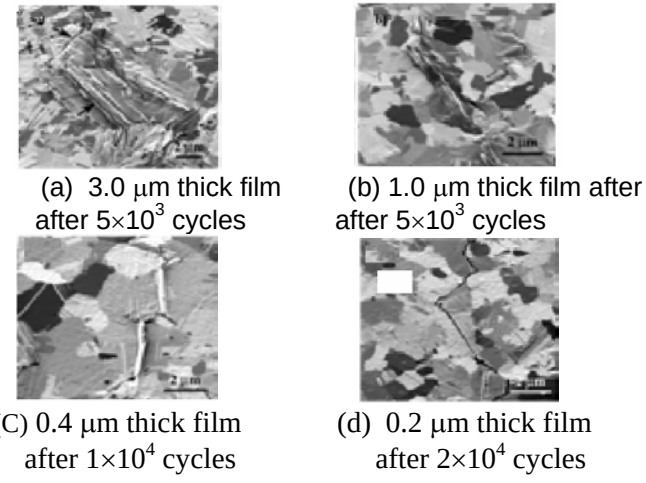

Fig. 12 Extrusions at the surfaces of the fatigued type I Cu thin films with micron-sized grains imaged by FIB at an angle of 45°. The tensile axis is the horizontal direction [32].

Table 5 Summary of microstructural parameters and fatigue testing conditions of the type I and II films reported in [32].

Thin Cu films	h (μm)	d (μm)	$\Delta\varepsilon_t$ (%)	$\Delta\varepsilon_{pl}$ (%)	N
Type I	3.0	2.19±1.04	1.0	0.91	5×10^3
	1.0	1.51±0.74	1.0	0.87	5×10^3
	0.4	1.00±0.52	1.0	0.86	1×10^4
	0.2	1.21±0.55	1.0	0.83	2×10^4
Type II	3.0	0.78±0.39	1.3	1.01	6×10^4
	1.5	0.48±0.22	1.3	0.92	6×10^4
	0.4	0.28±0.09	1.7	1.22	6×10^4

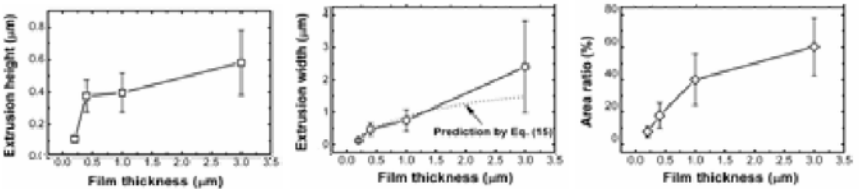

(a) Extrusion height (b)Extrusion width (c) Extrusion/grain area ratio

Fig. 13 Extrusion height, width and ratio of extrusion to grain area as a function of the film thickness in the type I Cu films. A best fit with Eq. (6.10) to the extrusion widths is included as a solid line. The extrusion height, width, and the extrusion area are the mean values of the measurements, while the error bars are the standard deviations [32].

Fatigue-extrusion features inside the grains gradually disappear with decreasing the film thickness even though the applied plastic strain ranges are almost the same for all films. Quantitative measurement of the height, width of the extrusions and the ratio of the extrusion area to the grain area clearly reveals a clear trend of the decrease in extrusion dimension with decreasing film thickness, as shown in Fig. 13. The variation of the morphology of fatigue extrusions indicates that localized accumulation of cyclic plastic strain within grains through the development of fatigue extrusions is restricted in the very thin films (0.2 μm).

For the type II films shown in Fig. 14, it was found that fatigue extrusions can not form in the submicrometer-sized grains, on the contrary the extensive cracking along grain boundaries and the surface roughening were found in the fatigue failured Cu films. A careful comparison of the film surface before and after fatigue loading (Fig. 14(b)) shows that the surface roughening in the 1.5 μm thick films with submicron grains may result from grain boundary grooving and the potential grain boundary slid-

ing. The findings in the type II films further demonstrates that interface-induced fatigue damage becomes more preferred in the films with small length scales either film thickness or grain size being about 200 nm.

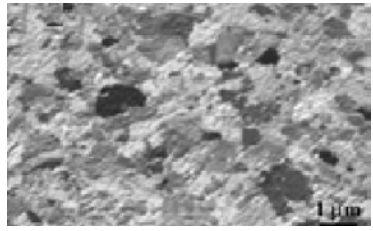

(a) Before fatigue

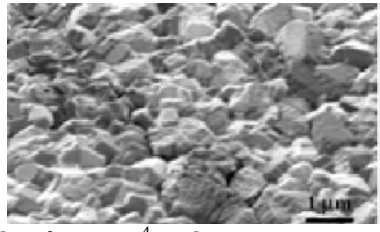

(b)After 6×10^4 cycles

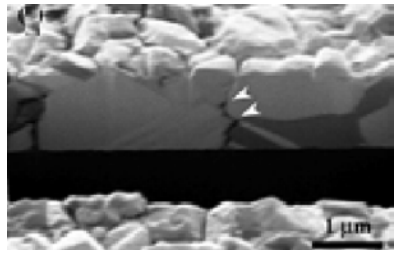

(c) Damage thin film

Fig. 14 FIB images of fatigue damage in the 1.5 μm thick type II films imaged by FIB at an angle of 45°. The tensile axis is the horizontal direction [32].

Summarizing observations of fatigue crack initiation behavior in the metal foils [7-10,13,17-20,22-25,40], wires [6,28] and thin films [29-39] confined by a substrate, it is noted that fatigue damage in the small-scale metal materials can still originate from the strain localization sites where fatigue extrusions/intrusions develop like that in the bulk materials when the length scales of the material (film thickness and grain size) are more than 1 μm, while as the length scale is less than 1 μm the suppression of the formation of fatigue extrusions/intrusions results in the interface-induced fatigue damage. It is suggested that the decrease in length scale inhibits the localized accumulation of plastic strain within grains, such as at extrusions/intrusions and in extended dislocation structures, and pro-

motes the formation of damage such as cracks at twin and grain boundaries during fatigue. Thus, it is predicted that the fatigue failure in the small-scale materials with length scale of only a few nanometers would be preferentially caused by interface-related damage.

4. Fatigue Crack Growth

Fatigue crack growth rate is an important factor to determine fatigue reliability and a necessary value to conduct damage-tolerance design of bulk materials. Conventionally, fatigue crack growth rate (da/dN) can be described by the Paris law as:

$$da / dN = C(\Delta K)^m \tag{1}$$

C and m are constants, which are related to microstructures, loading frequency and waveform, environment, temperature and load ratio. For a ductile alloy, m is about 2~4. ΔK is stress intensity factor range at the crack tip. Concerning fatigue crack growth of a small-scale material, up till now few studies have been conducted. The complexity of the fatigue crack growth behavior in small-scale materials may result from effects of the ratio of grain size (d) to film thickness (h) and the stress state (plane stress and plane strain) at the crack tip.

Studies [12, 20, 41] on fatigue crack propagation of 25 μm thick 304 type stainless steel foils with mean grain size of 2.89 μm indicate that fatigue crack growth of the material still exhibited the typical characteristics from the stage I (shear crack) to stage II (tensile crack), which is similar to that in bulk metals. Fatigue crack growth threshold from a notch was determined as 6.8 $MPm^{1/2}$ [41], which is quite close to that of the bulk counterpart [42]. The size effects on fatigue crack growth behavior of rolled Cu, Al and Mo foils about several tens of micrometers thick were examined [18]. For the foils with thickness up to about 150 μm intermittent crack arrest due to interaction with microstructural barriers and a negative curvature of the crack growth curve were observed, as shown in Fig. 15. It was explained the results in terms of LEFM based on the crack resistance and the ratio (r_p/h) of the prevalent radius (r_p) of plastic zone to the foil thickness (h) criteria resulting in a transition from plane stress to plane strain. The criteria are given as follows:

1. r_p /h<0.025 for cracking in plane strain
2. r_p /h>1 for cracking in plane stress

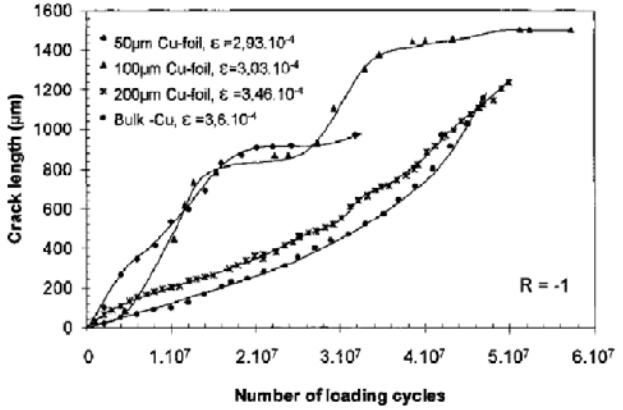

Fig. 15 Crack length as function of number of loading cycles of Cu foils (recrystallized) with varying thickness [18].

The radius of the plastic zone may be determined by

$$r_p = \frac{1}{2\pi}\left(\frac{K_{max}}{\sigma_y}\right) \tag{2}$$

where K_{max} is the maximum stress intensity factor during a loading cycle; σ_y is the yield stress after saturated cyclic hardening. The calculation of the r_p /h of the fatigued foils clearly indicates that the observed variation of crack growth curve in foils is well correlated with the transition from a state of plane stress to a state of plane strain with increasing foil thickness.
The fatigue testing of micron-scale Ni-P amorphous alloy thin foils was conducted through dynamic bending [26]. The small-scale cantilever beams of Ni-P amorphous alloy were fabricated by FIB. To examine fatigue crack growth behavior of the small-scale films, a micronotch with a depth of 3 μm was introduced into samples by FIB milling technique. SEM observation of the fracture surface of the fatigued Ni-P thin film shows that striation-like markings have appeared and were deduced to be fatigue striations. This may suggest that the fatigue crack has propagated by cyclic plastic deformation at the crack tip, i.e. blunting and resharpening mechanism like that of bulk materials. Furthermore, the fatigue crack growth rate under different stress ratios as a function of ΔK of the crack tip was estimated based on the measurement of the striation spacing, which was assumed to be equivalent to the fatigue crack propagating distance per cycle. A clear effect of stress ratio on fatigue crack growth rate was found

in Fig. 16 through the fact that the fatigue crack growth rates of the material under stress ratios of 0.3 and 0.5 are comparable although, in contrast, the fatigue crack growth rate at a stress ratio of 0.1 is lower at a given value of ΔK. The fact that the effect of stress ratio on the fatigue crack growth rate observed here is quite similar to the findings in bulk metals suggests that crack closure effects may still occur even in such micro-sized specimens, and thereby affect the fatigue crack growth behavior. It is worth noting that fatigue loading of micro-sized samples in their study has led to the extension of cracks by only 2-3 μm, which should be a short crack for a bulk metal, as schematically illustrated in Fig. 17(a). In the bulk metal with a short crack less than 100 μm, the crack closure effect is generally less pronounced. However, compared with the specimen size such a 2-3 μm crack in the present micro-sized sample should be sufficiently long and may actually not be a short crack, as schematically illustrated in Fig. 17(b). As a result, the crack closure effect is likely to be pronounced even for micro-sized specimens.

In general, a physically short crack in a bulk material would become a long crack in a small scale material, which potentially affects fatigue crack growth rate and behavior. On the other hand, the stress state at the crack tip such as plane stress and plane strain is also important factor controlling fatigue growth rate. However, more future work is needed to be conducted to understand microscopic process of the crack growth in small-scale materials.

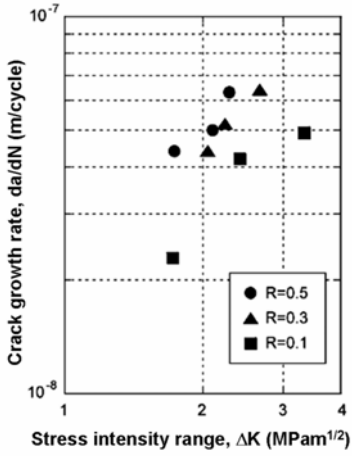

Fig. 16 Fatigue crack growth resistance curves for micro-sized specimens at different stress ratios [26].

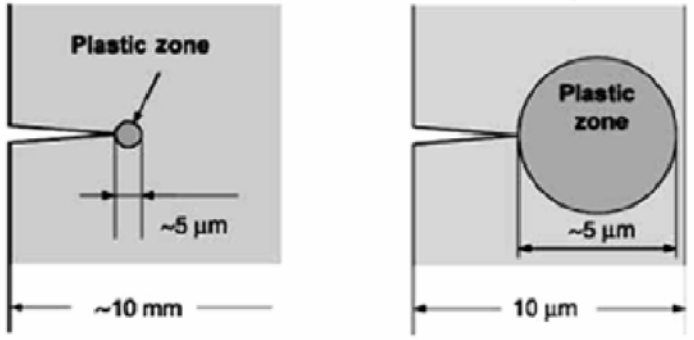

(a) Ordinary size specimen (b) Micro-size specimen

Fig. 17 Schematic drawing of plastic zone at crack tip for ordinary-sized and micro-sized specimens [26].

5. Fatigue Strength

Fatigue strength of all kinds of small-scale materials including metals and amorphous alloys has been given more attention and extensively investigated for recent years. To understand fatigue strength of the small-scale materials and their size effects, two categories of small-scale materials, i.e. free-standing thin foils/wires and thin films confined by a substrate, are presented as follows.

5.1 Fatigue strength of free-standing foils/wires

For metallic wires, tension-tension fatigue tests were conducted [6] (Table 4) for annealed Cu wires with a diameter of 30 μm, 50 μm and 95 μm, respectively. It was found that the number of cycles to failure of the Cu wires increases with decreasing diameter of the wires. The longer fatigue life of the 30 μm-diameter wire was consistent with the larger value for its yield strength. Systematic studies [28] of fatigue properties of Cu wires with four different diameters from 10 μm to 125 μm were carried out by using ultrasonic resonance fatigue testing system. The loading frequency is f=20 kHz and stress ratio R is -1. As shown in Fig. 18, for a certain number of loading cycles to failure the strain amplitude significantly increases for the 10 μm-diameter wires even though the strain amplitude of the 50

μm diameter wires is lower than that of the 125 μm-diameter wires. The improved fatigue properties of the 10 μm-diameter wire is suggested to be a result of the increase in the yield stress by a factor of two and the pronounced effect of the surface oxide layer of the thinnest wires, which results in dislocation pile-ups. Following the same assumptions described for the uniaxial testing the crack prohibiting effect of the surface oxide layer for the wires of 10 μm seems to be more effective. In addition, the improved fatigue performance of the thicker wires, that is the fatigue resistance of the 125 μm-diameter wires is larger than that of the 50 μm-diameter wires, could also be a result of higher tensile strength and fracture elongation values, dependence of crack propagation paths of the wire diameter as well as the more pronounced notch effects leading to fatal cracks of thinner wires. The tendency of the variation in fatigue strength with the wire diameter ranging from 20 μm to 125 μm found in [28] is just contrary to the findings reported in [6]. The differences may be attributed to purity and tensile properties of the wire, loading mode and number of loading cycles, thus the result of both studies may not be comparable.

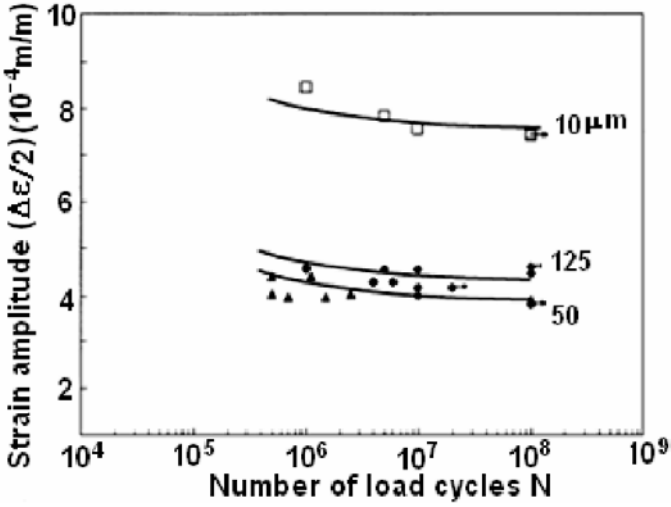

Fig. 18 Relationship between strain amplitude and the number of cycles to failure for Cu micro wires with different diameter [28].

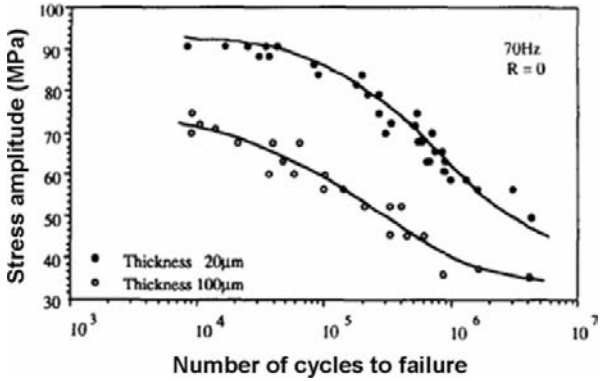

Fig. 19. S-N curves of specimens 100 μm and 20 μm thick foils. The frequency was 70 Hz [7].

Concerning the free-standing foil metallic materials, two kinds of materials are commonly produced. One is prepared by electro-deposition, which normally gets equiaxed grains, the other is produced through rolling, wrought, which mostly gives pancaked/elongated grains. It was reported in [7] that under R=0 and f=70 Hz and 700 Hz conditions the 100 μm thick Cu foils always failed after a number of cycles which was 10-30 times lower than that for the 20 μm thick samples, while at the same number of cycles, the fatigue resistance of the 20 μm thick foil is about 1.4 times higher than that of the 100 μm thick foil (Fig. 19). These results clearly reveal size effects on fatigue strength of free-standing metal films. Such size effects are attributed to the proximity of the surface for well-recrystallized samples, processing parameters and texture for as-rolled non-annealed samples.

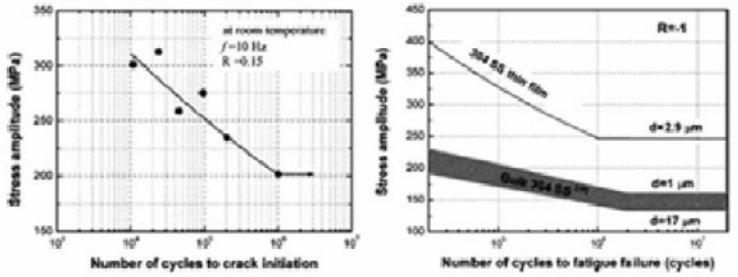

(a) Stress amplitude vs fatigue cycle (b) Fatigue strength

Fig. 20 Cycles to fatigue crack initiation for 304 stainless for R=0.15 and comparison of fatigue strength between micrometer-thick 304 stainless steel foil and bulk 304 stainless steel with different grain size under R= -1 [20].

The fatigue strength of 304 type stainless steel foils with thickness of 25 μm was examined through dynamic bending microbeams [20]. They obtained stress amplitude-fatigue life data of the material under the condition of f=10 Hz and R=0.15, as shown in Fig. 20(a). Considering the mean stress effect due to non-fully reversed loading here (stress ratio R=0.15), the Basquin relation modified in [43], which allows one to predict fatigue response for arbitrary values of various R, was used to fit the fatigue data. The Morrow relation is given as [43]

$$\sigma_a = (\sigma_f - \sigma_m)(2N_f)^b \tag{3}$$

$$\sigma_m = \frac{\sigma_a(1+R)}{1-R} \tag{4}$$

where N_f is fatigue life under a certain stress amplitude (σ_a) and σ_m is the mean stress. σ_f and b are parameters. The fitting of the stress amplitude-fatigue life under R=0.15 (see Fig. 20(a)) by using Eqs. (3) and (4) yields σ_f and b as 1471 MPa and -0.123, respectively. In order to compare the thin 304 stainless steel foil data with the values of bulk 304 stainless steel, which is obtained at the condition of σ_m = 0 and R = -1, the fatigue life of the 304 SS foils was predicted based on the Morrow relation, Eq. (3) for σ_m =0 and R =-1 and the obtained fatigue parameters (σ_f and b). Fig. 20(b) presents a comparison of the predicted fatigue life and the literature values for bulk 304 stainless steel with different grain sizes [44]. It can be seen that the fatigue strength of the 25 μm thick 304 stainless steel foil is much larger than that of the bulk 304 stainless steel with grain size from 1 μm to 17 μm. This comparison implies that the potential contribution of the geometrical dimensions to the enhanced fatigue strength should not be neglected in the micron scale material. The fatigue endurance limit of the thin films is 247 MPa, which is about 31% the ultimate tensile strength of the thin foils (σ_{UTS} = 802 MPa). The relation between the fatigue limit and the tensile strength is consistent with that of the bulk material, that is, the fatigue limit is generally about one-third of the tensile strength [45]. Even though fatigue damage behavior in the 25 μm thick 304 stainless steel foils still follows that of the bulk material as describe in section 3, but the fatigue strength has been enhanced due to the influences of both fine grain size and small geometrical dimensions.

The enhanced fatigue strength in the thin foils subjected to dynamic bending may be attributed to both microstructural and geometrical dimensions. Firstly, the 2.89 μm-sized grains of the thin 304 stainless steel foil promotes yield strength, and thus fatigue strength is improved. This trend

is similar to the finding in thin wires [6, 28] mentioned before. Secondly, the contribution of the geometrical dimensions may result from two aspects. (1) The increase in the ratio of surface to volume may change dislocations activity near the surface of the small scale sample. The increased fatigue strength in thinner Cu wires (30 μm in diameter) was attributed to the absence of the persistent slip bands (PSB) and walls structures [6]. The dislocations, which have a chance to contribute to the PSB walls by intersection processes and dipole formation, were presumably attracted by the image forces of the nearest surface and would escape more easily from the sample surface. That may affect the formation of dislocation structures in the small scale samples. This can be evidenced by the fact that the dislocation cell structures in the grains close to the beam surface disappeared [13]. Therefore, it is suggested that the enhanced fatigue strength should be associated with the small geometrical dimensions of the samples. (2) The deformation gradient induced by bending is expected to increase the dislocation interactions both between statistically stored dislocations (SSDs) and between geometrically necessary dislocations (GNDs) and SSDs [46]. That has been manifested by the fact that the bending yield strength (584 MPa) of the thin foil is higher than the tensile yield strength (454 MPa) of the thin foil [13]. Therefore, it is expected that the 25 μm thick 304 stainless steel foil would have a higher fatigue strength if they are cyclically deformed under a non-uniform loading condition. The dynamic bending-induced fatigue properties may be of importance for the fatigue reliability design of microbeam-type structural components in MEMS devices.

The low-cycle fatigue tests on 25 μm thick Cu foils electrodeposited in the additive-free solution (AF) and the additive-containing solution (AC) and 33 μm thick wrought foils were performed in [8] under stress-controlled conditions. Based on the Basquin equation [45], the relation between fatigue strength and number of cycles to failure can be described as

$$\sigma_{\mathrm{a}} = \sigma_{\mathrm{f}}^{'} (N_{\mathrm{f}})^{-b} \tag{5}$$

where σ_{a} is the applied stress amplitude, σ'_{f} is fatigue strength coefficient, N_{f} is the cycles to failure. b is a constant. σ'_{f} of the electrodeposited Cu foils with and without additives and wrought foils were obtained. It was found that σ'_{f} of the wrought thin foils is quite close to that of the bulk Cu, while that of the electrodeposited Cu foils (AF and AC foils) is higher than that of the bulk Cu. Again strong fatigue size effects can be evidenced here. Such a size effect was attributed to the difference in microstructures, such as grain size. Furthermore, the work in [8] also reported that the electrodeposited Cu foils exhibited cyclic hardening behavior.

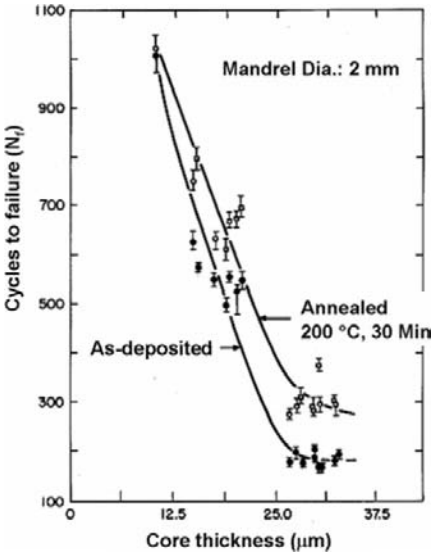

Fig. 21 Effect of core thickness and annealing on low cycle fatigue life (N_f) for the electro-deposition (DF8) foil [19].

The effects of grain structure, foil thickness and anneal softening on the flex fatigue of 12 to 35 μm thick rolled and electrodeposited copper foils were examined over a wide range of strain amplitude [19]. The results showed that at a fixed strain range the number of cycles to failure of the electrodeposited Cu foil with a grain size of about 1 μm in diameter increased with decreasing foil thickness, as shown in Fig. 21. Also the fatigue life was improved by annealing of the foils.

Furthermore, the fatigue testing of free-standing Cu film with a thickness of 1.1 μm prepared by electron beam evaporation was conducted in [9]. The surfaces of the film were covered by 50 nm thick Ti layers. The Cu film has hundreds of grains (about 0.98 μm) across the width but only one or a few through the thickness. A tension-tension fatigue testing with R=0.1 was performed. The results shows that fatigue resistance of the Cu films is superior to that previously reported for a set of Al thin films. The Cu data fall between the data for unnotched and notched stainless steel and Al sheet metal results reported in the literature. In fact, the Cu film system used in [9] is a Ti/Cu/Ti multilayered composite. It is believed that in addition to the decrease in Cu film thickness, the increase in fatigue strength of the 1.1 μm thick Cu film may result from the existence of the 50 nm thick Ti layers even though Read did not mention that. That was demonstrated by subsequent fatigue experiment of metallic multilayers.

Another kind of free-standing thin films is LIGA Ni film, which has been paid more attention due to its applications for MEMS structures, such as the case of accelerometers used for the deployment of airbags in cars. It was revealed in [22] that the thinner and the stronger 70 μm Ni films have a higher endurance limits than the 270 μm thick μm films. This difference was attributed partially to the effects of the columnar microstructures [23]. The improved stress-life behavior of the thinner (70 μm) structures is comparable to that of hardened bulk Ni. Furthermore, LIGA Ni thin films with nano-scale equiaxed grains have much greater strengths and fatigue resistance than LIGA Ni films with micro-scale columnar microstructures [25].

Above studies mainly concentrate on fatigue properties of metallic free-standing thin foils/wires with foil thickness/diameter of more than 10 μm. However, fatigue properties of free-standing thin films with a thickness of about several micrometers or less have not been investigated as extensively as that of thin foils/wires. The main cause should be attributed to difficulties in experimental technique for such a thin film, as mentioned in section 2.

5.2 Thin metal films confined by a substrate

For thin metal films confined by a substrate, a systematic work on fatigue resistance of thin Ag films with a SiO_2 substrate was conducted by using dynamic microbeam deflection method [29]. Fig. 22 presents a damage map, which shows the relationship between the stress amplitude and the film thickness of the fatigued Ag films at various mean stress levels ranging from 126 to 600 MPa. The upper right part of the graph indicates the formation of fatigue damage of the Ag films within 3.8×10^6 cycles, whereas no damage was found for conditions in the lower left corner. Damaged beams are denoted by open symbols, those that were not damaged by solid ones. It is clear that with decreasing film thickness the critical stress amplitude for damage increases.

Furthermore, systemic studies on fatigue strength of thin Cu films with columnar grains (Type I film defined in section 3) [30, 33] and equiaxed grains (Type II film) [35] were performed. Fig. 23 presents a comparison of fatigue strength of the thin Cu films with different grain size and film thickness. In Fig. 23, the solid symbols indicate type I Cu films with thicknesses ranging from 3.0 μm to 0.4 μm [30], 0.2 μm [33], while the half-solid symbols is type II Cu films [35]. Based on the comparison, three important results can be drawn:

1. Under almost constant plastic strain range (0.83-0.91%) the number of cycles to failure of the Cu films increases with decreasing film thickness of the type I films. This indicates that fatigue resistance is enhanced in very thin film. In this case, the enhanced fatigue strength of the thinner films was attributed to strong confinement of a film/substrate interface on threading dislocation motion due to the columnar grain structure of the type I film.
2. For the type II films under almost the same plastic strain range, the number of cycles to failure for the 3.1 μm thick films is larger than that of the 1.1 μm thick films, but both the 3.1 μm and 1.1 μm thick films have less fatigue resistance than 0.4 μm films.
3. A comparison of fatigue resistance between the type I Cu films and type II films shows that the number of cycles to failure for the type II films is larger than that of the type I films except the type I 0.2 μm thick films. This may be attributed to the fact that the type II films have submicrometer-sized grains, while the type I films have micrometer-sized grains. In addition to the confinement of the substrate, grain boundary strengthening mechanism is also expected to be involved in the improvement of fatigue resistance of the type II film.

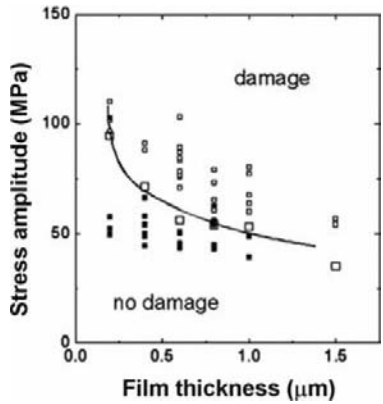

Fig. 22 A damage map of the Ag films showing the stress amplitude vs. the film thickness at various mean stress levels ranging from 126 to 600 MPa. Damaged beams are denoted by open symbols, those that were not damaged by solid ones [29].

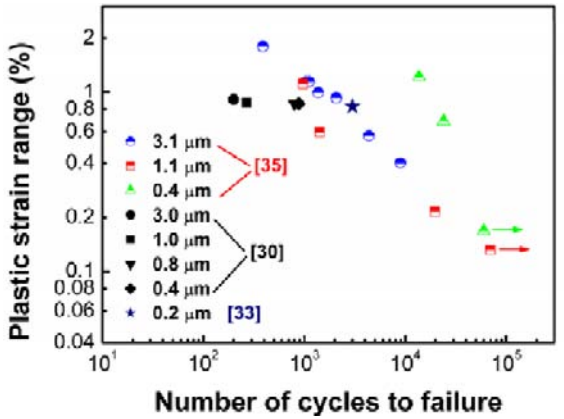

Fig. 23 Comparison of fatigue properties of thin Cu films with coarse- and fine-grains.

A further investigation of fatigue strength of thin Cu films with thicknesses ranging from 50 nm to 128 nm and nanometer-sized grains has recently been performed in [36]. The ultra-thin films were deposited onto a polyimide substrate. Measurement of fatigue lifetime of the ultrathin Cu films as a function of the film thickness under $\Delta\varepsilon_t$=1.1% shows that the fatigue lifetime still increases with decreasing film thickness even if the film thickness is in the range of several tens of nanometers. The comparison of the nanometer-grained Cu film [36] with the type II films [35] exhibits that the fatigue lifetimes of the present 50 nm, 60 nm and 90 nm thick Cu films are higher than those of the type II micron-thick films under $\Delta\varepsilon_t\approx$1.1%, but less than that of the 0.4 μm thick film. This implies that there may be a potential tendency of the decrease in the fatigue resistance of the nanometer-thick films as compared with that of the submicrometer-thick films. Of course, it should be noted that the nanometer-thick Cu films were not made in the same sputter system and conditions as that reported in [35], which may result in the difference in fatigue life due to the differences in some microstructural features, such as texture, grain size, purity etc.

Concerning fatigue strength of ultrathin film with nanometer scale thickness, it was reported [37] that a 5 μm thick Cu/Ni multilayer with equal individual layer thickness of 20 nm on a Cu substrate can effectively suppress fatigue crack initiation through decreasing surface roughening and enhance fatigue strength of the Cu substrate. This result reveals a tendency that the nanoscale multilayer may have a high fatigue resistance, which, as a coating material, can effectively improve fatigue strength of the substrate. Direct evaluation of fatigue strength of free-standing 40 μm thick Cu/Nb multilayers with individual layer thickness of 40 nm was per-

formed recently in [14], who used the resonant frequency method as introduced in section 2. Fig. 24 shows the normalized fatigue strength of the Cu/Nb multilayers. The results show that the ratio of the fatigue endurance limit to the ultimate tensile strength was about 0.35.

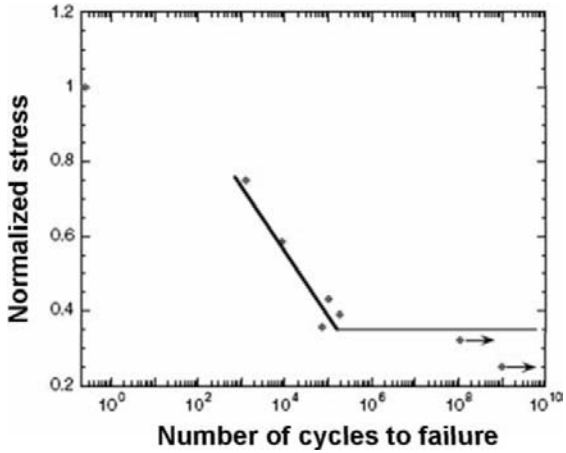

Fig. 24 Normalized S-N curve for the Cu/Nb multilayers with a total thickness 40 μm and individual layer thickness 40 nm. The normalization is defined as ratio of maximum stress to ultimate tensile stress [14].

Quite recently, the Cu/Ta multilayers with individual layer thicknesses ranging from 10 nm to 500 nm were deposited onto a polyimide substrate through radio-frequency magnetron sputtering method [38,39]. The multilayers have a grain size from about 60 nm to 120 nm. Following the same fatigue testing method adopted in [30,33] fatigue properties of the nanometer-scale multilayers were examined under f=10 Hz and R≈0 [39]. The Cu/Ta multilayers were actually subjected to tension-compression loading due to the stretch of the elastic polyimide substrate. Fatigue strength of the multilayer was defined as the critical stress range to cause fatigue cracking within 1×10^6 cycles. Fig. 25 presents the critical stress range as a function of individual layer thickness of the multilayer. It is found that fatigue strength gradually increases with decreasing individual layer thickness of the multilayer when the individual layer thickness is more than 20 nm, while it begins to drop when the individual layer thickness is less than 20 nm. Correspondingly, the applied strain range for the fatigue cracking also shows a similar trend with the individual layer thickness. The remarkable individual layer thickness dependent fatigue strength of the metallic multilayers found here is similar to that of yield strength of the multilayers.

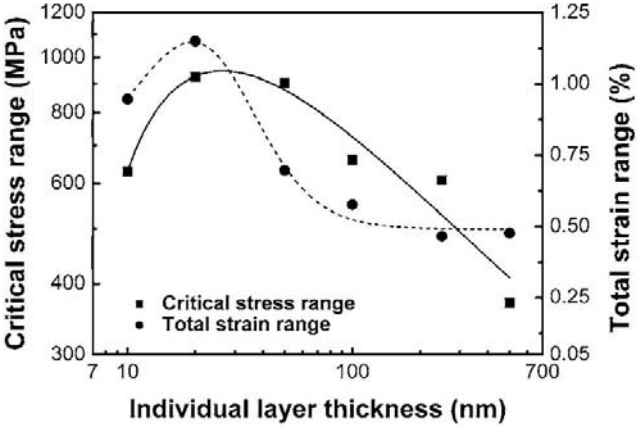

Fig. 25 Fatigue strength and the total strain range of Cu/Ta multilayer as function of individual layer thickness. The trend is similar to the relationship of yield stress and individual layer thickness in monotonic deformation [39].

6. Length-Scale Dependent Fatigue Mechanism

6.1 Dislocation activity at small scale

As mentioned in sections 3 and 4, extensive experimental results have clearly revealed the effects of film thickness and sample size on fatigue damage behavior and fatigue strength of the small-scale materials regardless of that the foils/films are confined by a substrate or not. However, the physical mechanism for the size effects of the small-scale materials confined and unconfined may not be the same. Furthermore, the minimum length scale between geometric and microstructural dimensions will be the dominant controlling factor.

It can be seen from sections 3-4 that the free-standing foils/wires with a length scale more than 10 μm exhibit the similar fatigue damage behavior as the bulk materials. This may be attributed to the fact that the minimum length scale of the material is still larger than the fatigue characteristic length scale, such as dimensions of fatigue extrusions/intrusions, the spacing of dislocation walls and the size of dislocation cells. Nevertheless, the fact that fatigue strength of the free-standing foils/wires is higher than that of the bulk counterpart and increases with decreasing the foil thickness/wire diameter still reveals clear size effects.

An explanation was proposed in [6] that the absence of extrusion-like features on thin wire surfaces up to 10^5 cycles may be interpreted as the absence of PSBs similar to that observed in macroscopic specimens. It is argued that because the space available for periodic slip motion is limited

by the small diameter, especially before sliding dislocation segments have a chance to contribute to the "knitting" of PSB walls by intersection processes and dipole formation, they are attracted by image forces of the nearest surface and annihilated or changed in configuration. Thus, the PSB wall structure will either not form at all or only after very high number of cycles. This could explain the longer lifetime of the 25 μm and 30 μm wire as compared to the thicker ones.

The study in [7] showed that the thicker specimens contained a large number of well-defined and sharp slip bands with in some cases well-developed extrusions, while the thinner specimens were almost free of extrusions and contained only occasionally a few grains with a low density of faint slip bands. This indicates that the microstructural development toward failure is somehow delayed for the thinner samples of 20 μm thick. TEM examination of the fatigued 25 μm thick 304 type stainless steel foils conduced in [12] shows that no PSB dislocation structures were observed in the micrometer-sized material with mean grain size of 2.89 μm.

The TEM observations of the fatigued 1.1 μm Cu films [9] concluded that the absence of clear steps on the specimen surfaces, combined with the absence of dislocation cells in the fatigued material, indicated that the dislocations move individually or in small groups and escape at the specimen surface. This is different from the behavior of bulk materials, where slip bands and dislocation cells are commonly reported. It was found in [28] that vein structure in one grain of a fatigued Cu wire of 50 μm diameter was formed. Depending on the amount of plastic strain in individual grains of the examined wire, a vein structure, elongated cells and regions of cellular structure near the crack site as well as regions of lower dislocation density can also appear.

In general, even though a significant size effect on fatigue strength was found in free-standing foils/wires, typical dislocation structures, such as vein structure, PSB walls and cell structure can still form in the micron-scale materials since their minimum dimensions are larger than the fatigue characteristic length scale. However, the finding in [9] presents an important indication that individual dislocations start to move instead of a group of dislocations to mediate cyclic plastic strain in the 1.1 μm thick film.

For the thin metal films confined by a substrate, fatigue mechanisms may not be the same as the bulk materials and the free-standing foils/wires. Physical reasons may originate from the constraint of a substrate, which strongly confines dislocation motion in the film channel. It is well known that dislocations in a thin film confined by a substrate can nucleate within a film, from grain boundary, film/substrate interface and a film surface. Whatever it is, the bowing-out dislocation loop will meet the film/substrate

interface and deposit a segment of dislocation line to the film/substrate interface. This will result in an additional work for the threading dislocations to move in the channel. In view of this, the flow stress to move a threading dislocation in the channel of an epitaxial film can be calculated in the model [3] as

$$\sigma_{Nix} = \frac{\sin\phi}{\cos\phi\cos\lambda}\frac{b}{4\pi(1-\nu)h}\left[\frac{2G_f G_s}{G_f + G_s}\ln\left(\frac{\beta_s}{b}h\right)\right] \tag{6}$$

ϕ is the angle between the film normal and the inclined {111} plane , λ the angle between the film normal and Burgers vector b. h is the film thickness. G_f and G_s are-the shear moduli of the film and substrate, respectively. β_s=1-2 is a numerical constant defining the cutoff radius of the stress field of the interfacial dislocation. Eq. (6) clearly indicates that the flow stress of the epitixial film increases with decreasing film thickness. Concerning a polycrystalline film, the yield stress for dislocation channeling can be expressed as [47]

$$\tau_y = \frac{Gb}{4\pi(1-\nu)}\ln\left(\frac{D}{b}\right)\left(\frac{2}{D} + \frac{\sin\phi}{h}\right) \tag{7}$$

where φ is the same meaning as Eq. (7). D is the grain size of the polycrystalline film. This equation results from comparing the mechanical work done in dislocation glide with the energy associated with depositing dislocations in the interfaces. From Eq. (7) one immediately finds an increase in yield stress of the film with the decrease in the grain size and film thickness.

For the confined metal films, as shown in section 3.1 fatigue damage behavior of the Cu films with different thicknesses and grain sizes is strongly controlled by the length-scale [32]. The main findings can be summarized by the fact that extensive extrusions/intrusions-induced damage occur in the large grains and micrometer-thick films, while boundary-induced damage dominates fatigue damage of the 0.2 μm thick Cu films.

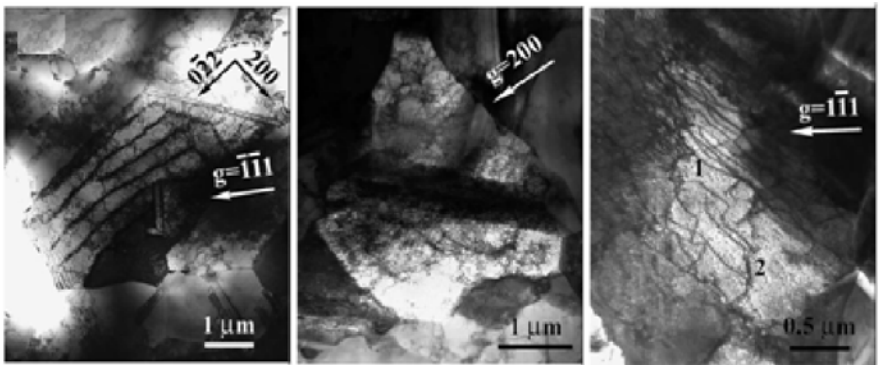

(a) 3.0 μm thick (b) 1.0 μm thick (c) 0.4 μm thick

Fig. 26 Plan-view TEM images of the dislocation structures in the fatigued type I Cu films [32].

The TEM cross-sectional sample of a fatigued 3.0 μm thick Cu films was prepared through FIB milling technique [30]. It was found that there exist less dislocation structures in the films. Subsequently, the TEM plan-view observations of the fatigued Cu films with different film thickness and grain size ranging from micrometers to submicrometers were performed [32]. As shown in Fig. 26, a clear effect of grain dimensions on dislocation structures that develop during fatigue has been observed. As the film thickness of the type I film is decreased from 3 μm to below 1 μm, the characteristic dislocation wall/cell structures (Fig. 26(a)) are replaced with loose tangles of dislocations (Fig. 26(b)) and then with individual dislocations (Fig. 26(c)). Furthermore, for the type I film with the same thickness, a similar transition of dislocation structure with film thickness was found in the type II film. Fatigue dislocation structures are generated by slip that takes place predominately on a single slip system, whereas the individual dislocations observed here are emitted from grain boundaries and are active on all three slip systems. Whether the grain dimensions are fixed by the film thickness or by the in-plane grain size makes no difference in the dislocation microstructure. Also, whether the grains are columnar or non-columnar is immaterial; in all cases the smallest grain dimension controls the type of dislocation structure.

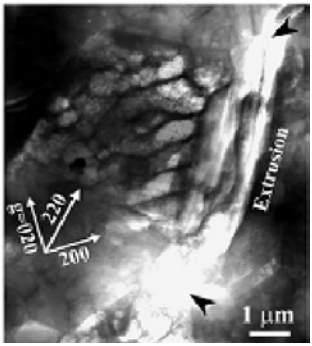

(a) Dislocation walls near larger extrusion in 3 μm film

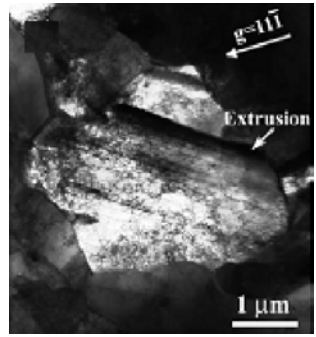

(b) Tangled dislocations near extrusion in 1.0 μm film

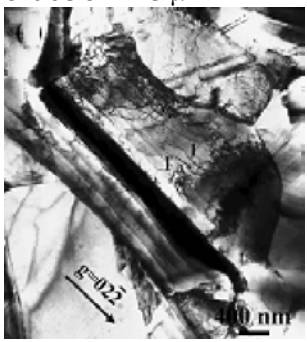

(c) Long dislocations near smaller extrusion in 0.4 μm film

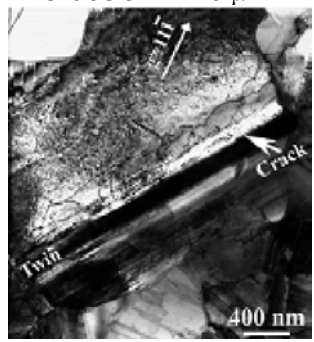

(d) Dislocations near crack close to twin in 0.2 μm film

Fig. 27 TEM observations of the dislocations near fatigue damage regions in the type I thin films [32].

In fatigued bulk metals, PSBs are typically found near extrusions and are believed to be the source of the dislocations that generate the extrusions [45]. In order to correlate the extrusions and other surface damage in the thin films with dislocations, the dislocation structures near fatigue damage regions were also examined [32]. The 3.0 μm thick type I film provided the only evidence of a correlation between extrusions and dislocation structures. For example, Fig. 27(a) shows {100} dislocation walls close to an extrusion in the 3.0 μm thick film. Cracks are also evident in the film at the intersection of the extrusion with the GBs (arrows in Fig. 27(a)). For thinner films, such as the 1.0 μm thick type I film, tangled dislocations with a cell-like structure are found near extrusions (Fig. 27(b)). When the film thickness is decreased to 0.4 μm, only individual dislocations are observed near extrusions. For example, in Fig. 27(c) many dislo-

cations (marked "**1")** with Burgers vector ½[110] lie on the $(\bar{1}11)$ slip plane parallel to the plane of the narrow extrusion and to a crack that has formed on this plane. Dislocations with Burgers vector ½ $[\bar{1}01]$ close to a crack along a TB were found in a 0.2 μm thick type I film as shown in Fig. 27(d). This is reminiscent of the dislocation pile-ups near GBs in the 0.2 μm thick films reported in [33]. For the type II films, intergranular cracking was frequently observed, for a 1.5 μm thick film. The bowed out dislocations reveal that dislocation emission has occurred from the triple junctions and from the crack at the GB. In the 0.4 μm thick film, the lighter regions along GBs and triple junctions indicate that extensive cracking, thinning, and possibly grain boundary sliding have occurred. No dislocations were found in the neighborhood of the GB grooves in the thinnest films.

In general, the careful TEM examination also reveals length-scale dependent dislocation structures. Well-defined dislocation walls and cells as observed in bulk material form when the minimum dimension of the crystal is at least 3 μm. With length scales ranging from 1 to 3 μm, rather diffuse, cell-like dislocation structures and small groups of tangled dislocations are observed. Only individual dislocations exist in crystals smaller than 1 μm. Possible reasons for this are considered below:

1. Proximity of free surface: In the thin films investigated here, both the film thickness and the grain size were varied between hundreds of nanometers and a few microns. No distinct dislocation structures were found in the thinner films and/or smaller grains, where the dislocations are closer to the film surface or grain boundaries. The dislocation image forces are very large close to the free surface and tend to draw dislocations toward the surface. Combined with the fact that the glide distance to the free surface is smaller, dislocations may rearrange and escape more easily in thin films. In fact, such an effect has been suggested to account for the absence of extrusion-like features in fatigued thin Cu wires [6]. However, it is unlikely to be the only explanation for the observed behavior since it is found that grain boundaries play a similar role to free surfaces in controlling fatigue dislocation microstructure.
2. Minimum length scale for dislocation self-organization: As we mentioned before, in bulk metals self-organized dislocation patterns with dimensions ranging from microns to sub-microns evolve during fatigue. The spacing between PSB walls in Cu is about 1.3 μm, while the spacing of dislocation walls in a labyrinth structure is about 0.75

μm [48,49]. The minimum size of dislocation cells is observed to be about 0.5 μm [50]. All of these imply that the formation of dislocation structures requires a minimum length l_{pat}, which is around 1 μm. An investigation of fatigued bulk fine-grained Ni showed that 1 μm is the critical grain size for the formation of dislocation structures [51]. In addition, a theoretical evaluation of the effect of grain size on dislocation patterning indicates that the repeat length of the dislocation structures approaches the grain size when the grain size is close to 1.0 μm [52].

For equiaxed grains, the available slip distance of dislocations along a {111} slip plane is equal to the grain size, and dislocation structures are expected to form if the grain size is larger than l_{pat}. For columnar grains in a film of thickness h, the dislocation slip distance L in the grain can be expressed as

$$L = \frac{h}{\sin\varphi} \tag{8}$$

where φ is the angle of the slip plane normal with the out-of-plane direction of the film (Fig. 11). Therefore, the minimum film thickness required for dislocation structure formation in columnar grains is $l_{pat}\sin\varphi$. Setting l_{pat} equal to 1.3 μm, which is the PSB wall spacing along the <110> direction in Cu, the minimum film thickness h required for the formation of a pair of PSB's walls can be estimated as 1.1 and 1.2 μm for <111> (φ =70.5°) and <100> (φ = 54.7°) out-of-plane oriented grains, respectively. As a result, either a film thickness or grain size of less than about 1 μm would not provide a large enough glide distance for the formation of PSB walls.

3. Constraints on dislocation nucleation and motion: In bulk Cu single crystals subjected to cyclic loading, dislocations accumulate on the primary slip plane, where mutual trapping of edge dislocations and annihilation of dislocations with opposite signs cause the formation of vein structures and eventually PSB wall structures [53]. A sufficiently high dislocation density is needed on the primary slip plane for dislocation interactions and the formation of structures. However, the availability and activation of dislocation sources, either within the grains, at GBs, or at the film/substrate interface, becomes more limited with decreasing length scale [54]. Furthermore, it has been observed that small grain size and film thickness constrain dislocation motion [15,55], which has been explained by a number of models in-

cluding “dislocation channeling” [3, 5, 54]. Supporting evidence for dislocation channeling has been found in fatigued 0.2 μm thick films [33]. Both the inhibition of dislocation sources and dislocation motion mean that at a given applied strain, there are fewer dislocations available on the primary slip system to interact and form dislocation structures. Instead, the TEM images support the idea that multiple slip systems are activated within the grains and GBs become more important either as barriers to dislocation motion or as dislocation sources.

6.2 Theoretical analysis

6.2.1 Length scale dependent strain localization

The findings of the decrease in extrusion width with decreasing film thickness and grain size mentioned in section 3 indicate that the localized accumulation of plastic strain in extrusions is hindered in small dimensions. Furthermore, as shown in section 5.1 the observation of dislocation walls near extrusions in the 3.0 μm thick film is in agreement with the behavior of bulk materials. However, the smaller extrusions in the 0.4 μm thick film are associated with individual dislocations that glide to the film surface. Presumably, dislocation structures are more effective at achieving plastic strain than individual dislocations, and the extrusions are smaller when the dislocation structures are not present. Even in grains where there are no dislocations structures, the extrusion dimensions decrease with film thickness and grain size, presumably due to the length scale constraints on dislocation nucleation and motion discussed in the previous section.

The trend in extrusion dimensions with the film thickness and grain size can be evaluated in terms of the extrusion widths shown in Fig. 13(b). Suppose the cyclic plastic strain applied to the thin film goes entirely to the formation of extrusions (i.e., it is assumed there are no other mechanisms for plastic strain accommodation). Each extrusion consists of a number of activated slip planes N_{slip} along which the dislocations glide. The applied plastic strain can be expressed as:

$$\varepsilon_{pl} = N_{slip}\varepsilon_{slip} \tag{9}$$

where ε_{slip} is the strain caused by dislocation motion in a given slip plane. Assuming that α dislocations sweep across the slip plane and are deposited

at the film/substrate interface and at the grain boundaries, as schematically illustrated in Fig. 11, the plastic strain from a given slip plane is given by

$$\varepsilon_{slip} = \alpha \frac{b \sin \lambda}{D} \tag{10}$$

where α is the number of dislocations that have traversed the slip plane, b is the Burgers vector, λ is the angle of the slip direction with the out-of-plane direction of the film, and D is the grain diameter. It has been proposed that the distance between active slip planes is equal to the trapping distance for dislocation dipoles S_d [57] so that

$$W_{ext} = (N_{slip} - 1) S_d \tag{11}$$

where W_{ext} is the extrusion width. The trapping distance of dislocation dipoles is given by [57]

$$S_d = \frac{Gb}{8\pi(1-\nu)\tau_s} \tag{12}$$

where G is the shear modulus, ν is Poisson's ratio, and τ_s is the saturation shear stress of the material. Therefore, the extrusion width can be obtained by combining Eqs. (9)-(12) as

$$W_{ext} = \left(\frac{\varepsilon_{pl} D}{\alpha b \sin \lambda} - 1 \right) \cdot \frac{Gb}{8\pi(1-\nu)\tau_s} \tag{13}$$

Thus, for a given plastic strain and saturation shear stress, the extrusion width should increase with the grain size.

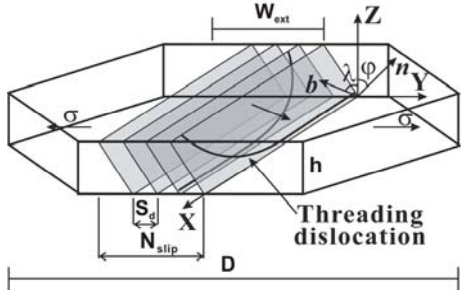

Fig. 28 A schematic of geometry for irreversible slip leading to extrusion formation in thin films.

The saturation shear stress in a thin film depends on film thickness and grain size, but has not been measured. For the sake of simplicity, we use the yield stress τ_y instead, which effectively ignores possible contributions from cyclic work hardening or softening. This is probably a reasonable assumption when no dislocation structures are formed, such as for the thinner and smaller grained films. It is not likely to be accurate for the thickest films, where dislocation structures form and change the flow stress. For a polycrystalline film, the yield stress for dislocation channeling as illustrated in Fig. 28 can be expressed as [47]

$$\tau_y = \frac{Gb}{4\pi(1-\nu)} \ln\left(\frac{D}{b}\right)\left(\frac{2}{D} + \frac{\sin\varphi}{h}\right) \tag{14}$$

where φ is the angle of the slip plane normal with the out-of-plane direction of the film. This equation results from comparing the mechanical work done in dislocation glide with the energy associated with depositing dislocations in the interfaces. Substituting Eq. (6.9) into Eq. (6.8), one can obtain for the extrusion width as

$$W_{ext} = \left(\frac{\varepsilon_{pl} D}{\alpha b \sin\lambda} - 1\right) \cdot \frac{1}{2\ln\left(\frac{D}{b}\right)\left(\frac{2}{D} + \frac{\sin\varphi}{h}\right)} \tag{15}$$

Based on Eq. (6.10), the extrusion width for the films with different thicknesses for a given plastic strain was estimated in [32]. Here the plastic strain ε_{pl} is set to be the mean of the plastic strains for all the films as measured by in-situ X-ray diffraction [30], $\varepsilon_{pl} \approx 0.85\%$. The grain size was set to be the mean grain size (D=3.58 μm) within which extrusions formed.

Other material parameters in Eq. (15) are set to be G=45 GPa, ν=0.324, and b=0.256 nm. λ and φ are 35.3° and 70.5°, respectively for an <111> out-of-plane oriented grain. Thus, the only fitting parameter is α, the number of dislocations active on a single slip plane in a single cycle. The best fit to the extrusion width data using Eq. (15) is shown by a solid line in Fig. 13(b), and is obtained with a value of 8 for α. This number is somewhat smaller than the 14 dislocations expected in a pileup of this size and at this stress. It can be seen that the model (Eq. (15)) proposed in [32] does qualitatively capture the experimentally observed variation of extrusion width with film thickness for film thicknesses less than 1.0 μm. However, for the 3.0 μm thick film the predicted value is less than the experimental average although it does fall within the standard deviation. This may be due to the fact that the actual grains containing extrusions in the 3.0 thick μm film are much larger than the assumed average of D=3.58 μm, or to the fact that dislocation structures have formed in these grains and the saturation shear stress is not equal to the yield stress.

In addition, the extrusion width was also predicted by Eq. (15) and is presented in Fig. 29 as a function of film thickness and grain size for a fixed plastic strain. A clear trend shows again that the fatigue extrusion width gets gradually smaller with decreasing film thickness or grain size. As the dimensions are decreased, the yield stress increases and the slip planes within a given extrusion become more closely spaced so that the plastic strain is localized in a narrower region. Eventually the extrusions will either be too small to be observed or the stresses required to generate them will become so large that other mechanisms, such as interface-induced damage, will take over.

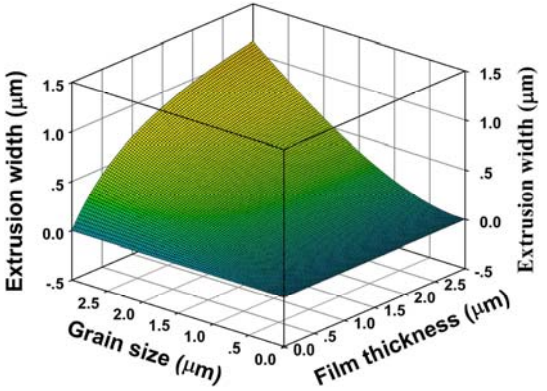

Fig. 29 Calculation of fatigue extrusion width as predicted by Eq. (6.10) as a function of film thickness and grain size for a fixed plastic strain of 0.85% [32].

6.2.2. On fatigue cracking

Fatigue cracking in bulk Cu polycrystals always occurs along extrusions/intrusions within grains [48, 58], or places where PSBs impinge GBs [58, 59], when the GB properties and geometry are suitable [60, 61]. In the larger grains of the films thicker than 3.0 μm, cracks were observed along extrusions and at the intersection of extrusions with GBs, just as in bulk materials. This means that the presence of the substrate and the columnar grain structure do not change the mechanisms for crack formation down to a length scale of roughly 3 μm. But when the film thickness or grain size is further decreased, the stress required to cause plastic strain increases. As a result, other stress relief mechanisms than extrusion formation may be activated, such as crack formation in the absence of extrusions along GBs and TBs [32, 33].

The previous TEM results [33] show that one stress relief mechanism in the thinnest films and the smaller grains is the activation of individual dislocations on multiple slip systems. Multiple slip will lead to relatively homogenous deformation within the grain and the dislocations will interact with the GBs and TBs rather than with each other. It is also frequently observed that the individual dislocations are piled up near GBs and/or TBs. These pile-ups generated large stresses which may initiate the formation of cracks at the GBs and TBs. Thus, as film thickness and grain size are decreased, the interaction of dislocations with boundaries is expected to increase and cracking along GBs or TBs will become more prevalent.

6.2.3. A mechanism map of length scale-controlled fatigue behavior

Based on the observation of the fatigue damage behavior in the previous publications [29-31, 33-35], a mechanism map is summarized in Fig. 30 as a function of film thickness and grain size [32]. The map presents the experimental observations of surface damage (extrusions as filled triangles versus interface cracking as open triangles) and dislocation microstructure (dislocation walls/cells as filled circles, diffuse cells as half-filled circles and individual dislocations as open circles). The data summarized in Fig. 30 were acquired using somewhat different strain ranges and different cycle numbers, but nonetheless are with each other. Based on the success of Eq. (6.10) in describing the dependence of the extrusion widths on film thickness, the same equation is used to divide the mechanism map into three regimes. The largest grains of the 3.0 μm thick film showed the largest extrusions in addition to well-defined dislocation structures. Therefore this extrusion width (2.41 μm) is used in Eq. (15) to predict the separation between Regime I for “bulk-like behavior”, characterized by dislocation

structures and surface extrusions, and Regime II for "transition behavior", characterized by dislocation tangles and small surface extrusions or intense slip bands. In the 0.2 μm thick film interface-mediated damage had begun to prevail and the extrusions were only just observable. Thus, this extrusion width (0.13 μm) is used in Eq. (15) to predict the separation between Regime II and Regime III for "small volume" behavior characterized by individual dislocations and interface-mediated damage behavior such as cracking along GBs and TBs, voiding at GBs, and grain boundary diffusion.

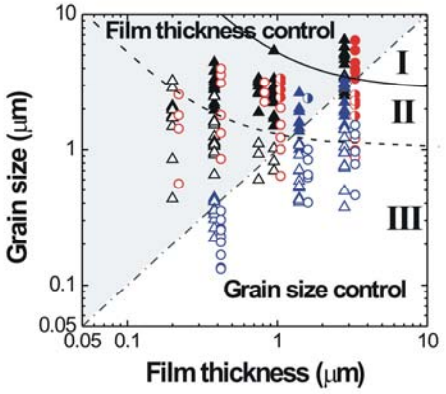

Fig. 30 Fatigue damage mechanism map for Cu thin films. Experimental observations are summarized with data symbols: presence of extrusions (▲) or absence of extrusions (△), dislocation structures (●), dislocation tangles (◑), or individual dislocations (○). The behavior is divided into three regimes described in the text. Regime I indicates bulk-like behavior, regime II is a transition region, regime III indicates "small volume" behavior. The lines separating the different regimes were obtained from Equation (6.10) for extrusion widths of 2.41 μm and 0.13 μm [32].

Fig. 30 can also be separated into two large regimes by a 45° line. The upper left corner regime corresponds to length scales for which fatigue behavior is predominately controlled by the film thickness, whereas the lower right corner regime corresponds to grain size controlled fatigue behavior. However it is important to remember that a wide distribution of grain sizes in a given film means that there will be competitive and/or coupled mechanisms. The different mechanism regimes as predicted by Eq. (15) are in reasonable agreement with both the experimentally observed surface morphology and the dislocation microstructure data. This success provides support for the idea that the change in surface damage morphol-

ogy and in dislocation microstructure are coupled effects and due to the same underlying change in mechanism: As it becomes more difficult to create and move dislocations to form dislocation structures and extrusions, individual dislocations begin to dominate and other stress relief mechanisms such as interface cracking and diffusion begin to take over.

7. Conclusion and Perspective

The main findings mentioned in previous sections are summarized below.

1. Current fatigue testing techniques to some extent can obtain fatigue properties of small-scale materials and reveal size effects of fatigue behavior of small-scale materials.
2. No matter whether small-scale materials are confined by substrates or not, the fatigue strength of the material is significantly enhanced with decreasing length scale of the material. This is generally attributed to the increase in yield strength with decreasing length scales including both microstructural and geometric dimensions.
3. For thin metal films confined by a substrate, convincible experimental evidence shows that when either the film thickness or the grain size is decreased below roughly 1 μm, the typical dislocation wall and cell structures found in fatigued coarse-grained bulk materials no longer develop and are replaced by individual dislocations. Similarly, the typical surface damage of fatigued bulk metals, such as extrusions and cracks near extrusions, is gradually suppressed and replaced by damage that is localized at interfaces, such as cracks, grooves, and voids along grain and twin boundaries. This gradual transition from damage characteristic of bulk metals to damage localized at interfaces is attributed to constraints on dislocation activity at submicron length scales.
4. Fatigue crack growth rate is strongly influenced by the geometric dimension of the material, and is well correlated with the transition from a state of plane stress to a state of plane strain with increasing foil thickness. It is worth noting that a physically-short crack in a bulk material would become a long crack in a small-scale material, which potentially affects fatigue crack growth rate and behavior.
5. Physical mechanism of fatigue damage of the small-scale materials confined and un-confined by substrates is different. For the free-standing small-scale materials, the short dislocation glide distance to the material surface and small grain size are suggested to be main reasons for the variation of fatigue damage behavior and the

enhanced strength, while for those confined by substrates the strong constraint of the film/substrate interface on dislocation nucleation and motion is a dominant mechanism.

6. A mechanism map of the dependence of fatigue behavior on length scale is proposed based on extensive experimental evidence and a theoretical analysis for extrusion formation. The suggested extrusion model not only successfully predicted the change in surface morphology but also the change in dislocation microstructure with length scale. It supports the idea that the two transitions are caused by a single mechanism change. This mechanism is proposed to be the inhibition of dislocation creation and motion in small volumes.

The strong length-scale dependent fatigue properties and damage mechanisms of the small-scale materials indicates that the design of small structures in micro- and nano-systems and the evaluation of their reliability under fatigue load should not simply follow conventional theories developed for bulk materials. Instead it is recommended that the input values for a reliability assessment should be determined by the standard experimental testing methods specially developed for small-scale materials, and that reliability should be estimated by taking the microstructural and interfacial effects into account. In view of these aspects, further systematic and in-depth studies on fatigue of small-scale materials with different length scales and interface structures are necessary to be conducted in the future.

1. Testing technigue. The development of a standard fatigue testing technique is still needed for small-scale materials with geometric dimension less than 1 μm.
2. Characterization methods. Through the standard testing technique the corresponding characterization methods for the determination of fatigue strength, crack growth rate, and S-N curves are expected to be proposed so that the experimental results are comparable.
3. Free-standing small-scale material. Systematic fundamental work on fatigue of free-standing single crystal metal foils/wires with thicknesses ranging from micrometers to nanometers should be a great challenge for one to get insight into length-scale-controlled fatigue mechanism of small-scale materials. For example, how do the strain localization and fatigue damage develop when the length scale of the free standing metal foils/wires is less than 1 μm?
4. Thin film on a substrate. Much fundamental work on the evolution of fatigue damage of the metal films with a thickness in a range of 1000 nm to 100 nm and less than 100 nm is required. In the case of the length scale between 1000 nm to 100 nm, what is the basic

mechanism for the formation of the small fatigue-induced extrusions/-intrusions in absence of typical fatigue dislocation wall/cell structures? For the thin films with a thickness less than 100 nm, how do the cyclic strain localization and fatigue damage develop?

5. Dislocation structure. It is necessary to understand the evolution of dislocation structures with decreasing length scale from micrometer to nanometer scales, establish the relation between fatigue properties and dislocation activity in the confined metal films.
6. Interface & surface. There is an indication that the decrease in the length scale down to submicron-scale or less makes the interfaces (including grain boundary, twin boundary, film/substrate interface as well as other heterogeneous interfaces) and surfaces of the materials more active to be involved in fatigue properties. How do the interfaces with different structures affect fatigue behavior and dislocation activities of the materials?
7. Multilayers with multi-physical scales and heterogenous interfaces. A mutilayer alternatively consists of two or more constituents with different crystal structure and layer thickness. In such a multilayered composite, heterogeneous interfaces including the constituent/ constituent interfaces and constituent/substrate interface and different individual layer thickness from micro- to nano-scales would strongly change fatigue properties of the materials.
8. Fatigue data base. For engineering design and theoretical modeling, data base of fatigue strength of all kinds of small-scale materials is needed to be obtained by the standard testing techniques.
9. Theoretical & simulation. A combination of fatigue experiments and multiphysics simulations would be helpful to understand and predict the reliability of the real small-scale structures used in micro/nano systems. Furthermore, unified understanding and more suitable theoretical models for fatigue behavior of the small-scale materials through extending conventional fatigue theories to the micro/nano-scale field are eventually needed.

References

[1] Ohring M. Reliability and Failure of Electronic Materials and Devices. Academic Press, San Diego, 1998.
[2] Menz W. and Paul O. Microsystem Technology. Wiley-VCH,Weinheim, 2001.
[3] Nix WD. Mechanical Properties of Thin Films. Metall Trans 20 (1989) 2217 2245.

[4] Spearing SM. Materials issues in microelectromechanical systems (MEMS) Acta Mater 48 (2000) 179-196.
[5] Arzt E. Size effects in materials due to microstructural and dimensional constraints: a comparative review. Acta Mater 46 (1998) 5611-5626.
[6] Hofbeck R. Hausmann K. Ilschner B. and Kunzi HU. Fatigue of Very Thin Copper and Gold Wires. Scripta Metall 20 (1986) 1601-1605.
[7] Judelewicz M., Kunzi HU., Merk N. and Ilschner B. Microstructural development during fatigue of copper foils 20-100 μm thick. Mater Sci Eng A 18(1996) 62-62.
[8] Hong S. and Weil R. Low cycle fatigue of thin copper foils. Thin Solid Films 283 (1996) 175-181.
[9] Read DT. Tension-tension fatigue of copper thin films. Int J Fatigue 20 (1998): 203-209.
[10] Son DKJ. Lim TW. and Kwon D. Evaluation of fatigue strength of LIGA nickel film by microtensile tests. Scripta Mater 50 (2004) 1265-1269.
[11] Takashima K. Higo Y. Sugiura S. and Shimojo M., Fatigue crack growth behavior of micro-sized specimens prepared from an electroless plated Ni-P amorphous alloy thin film. Mater Trans 42 (2001) 68-73.
[12] Zhang GP. Takashima K. Shimojo M. and Higo Y. Fatigue behavior of microsized austenitic stainless steel specimens. Mater Lett 57 (2003) 1555-1560.
[13] Schwaiger R. and Kraft O. High cycle fatigue of thin silver films investigated by dynamic microbeam deflection. Scripta Metall 41 (1999) 823-829.
[14] Wang YC. Misra A. and Hoagland RG. Fatigue properties of nanoscale Cu/Nb multilayers. Scripta Metall 54 (2006) 1593-1598.
[15] Hommel M. Kraft O. and Arzt E. A new method to study cyclic deformation of thin films in tension and compression. J Mater Res 14 (1999) 2373-2376.
[16] Mönig R. Keller RR. and Volkert CA. Thermal fatigue testing of thin metal films. Rev Sci Inst 75 (2004) 4997-5004.
[17] Klein M. Hadrboletz A. Weiss B. and Khatibi G. The 'size effect' on the stress–strain, fatigue and fracture properties of thin metallic foils. Mater Sci Eng A319 (2001) 924-928.
[18] Hadrboletz A. Weiss B. and Khatibi G. Fatigue and fracture properties of thin metallic foils. Int J Fract 109 (2001) 69-89.
[19] Merchant HD. Minor MG. and Liu YL. Mechanical fatigue of thin copper foil. J Electron Mater 28 (1999) :998-1007.
[20] Zhang GP. Takashima K. and Higo Y. Fatigue strength of small-scale type 304 stainless steel thin films. Mater Sci Eng A 426 (2006) 95-100.
[21] Halford TP. Takashima K. and Higo Y. Fatigue testing of microsized samples of γ-TiAl based material. Mater Res Soc Sym Proc 842 (2005) S6.9.1-S6.9.6.
[22] Allameh SM. Lou J. Kavishe F. Buchheit T. and Soboyejo WO. An investigation of fatigue in LIGA Ni MEMS thin films. Mater Sci Eng A 371 (2004) 256-266.

[23] Cho H.S. Hemker KJ. Lian K. Goettert J. and Dirras G. Measured mechanical properties of LIGA Ni structures. Sensors and Actuators A: Physical 103 (2003)59-63.
[24] Son D. Kim J. Kim J.Y. and Kwon D. Tensile properties and fatigue crack growth in LIGA nickel MEMS structures. Mater Sci Eng A 406 (2005) 274-278.
[25] Yang Y. Imasogie BI. Allameh SM. Boyce B. Lian K. Lou J and Soboyejo WO. Mechanisms of fatigue in LIGA Ni MEMS thin films. Mater Sci Eng A 444(2007) 39-50.
[26] Takashima K. and Higo Y. Fatigue and fracture of a Ni-P amorphous alloy thin film on the micrometer scale. Fatigue Fract Engng Mater Struct 28 (2005)703-710.
[27] Maekawa S. Takashima K. Shimojo M. Higo Y. Sugiura S. Pfister B. and Swain MV. Fatigue test of ni-p amorphous alloy microcantilever beams. Jpn J.Appl Phys 38 (1999) 7194-7198.
[28] Khatibi G. Betzwar-Kotas A. Gröger V. and Weiss B. A study of the mechanical and fatigue properties of metallic microwires. Fatigue Fract Engng. Mater Struct 28 (2005) 723-733.
[29] Schwaiger R. and Kraft O. Size effects in the fatigue behavior of thin Ag films. Acta Mater 51 (2003) 195-206.
[30] Schwaiger R. Dehm G. and Kraft O. Cyclic deformation of polycrystalline Cu films. Phil Mag 83 (2003) 693-710.
[31] Zhang GP. Schwaiger R. Volkert CA. and Kraft O. Effect of film thickness and grain size on fatigue-induced dislocation structures in Cu thin films. Phil Mag. Lett 83 (2003) 477-483.
[32] Zhang GP. Volkert C.A. Schwaiger R. Wellner P. Arzt E. and Kraft O. Length-scale-controlled fatigue mechanisms in thin copper films. Acta Mater 54(2006) 3127-3139.
[33] Zhang .P. and Volkert C. Damage behavior of 200-nm thin copper films under cyclic loading. J Mater Res 20 (2005) 201-207.
[34] Kraft O. Schwaiger R. and Wellner P. Fatigue in thin films: lifetime and damage formation. Mater Sci Eng A 319-321 (2001) 919-923.
[35] Kraft O. Wellner P. Hommel M. Schwaiger R. and Arzt E. Fatigue behavior of polycrystalline thin copper films. Z Metallkd 93 (2002) 392-400.
[36] Zhang GP. Sun K.H. Zhang B. Gong J. Sun C. and Wang ZG. Tensile and fatigue strength of ultrathin copper films. Mater Sci Eng A http://dx.doi.org/10.1016/j.msea.2007.02.132, (2007) Article in press.
[37] Stoudt MR. Cammarata RC. and Ricker RE. Suppression of fatigue cracking with nanometer-scale multilayered coatings. Scripta Metall 43 (2000) 491-496.
[38] Zhu XF, Zhang G.P. Tan J. and Zhu SJ., Cracking behavior of Cu/Ta bilayered films under cyclic loading. J Mater Res 22 (2007) 2478-2482.
[39] Zhu XF. and Zhang GP. Fatigue properties and damage mechanism of Cu/Ta multilayers. (2007) Unpublished research.

[40] Boyce BL., Michael JR. and Kotula PG. Fatigue of metallic microdevices and the role of fatigue-induced surface oxides. Acta Mater 52 (2004) 1609-1619.
[41] Zhang GP. Takashima K. and Higo Y. Size effects on deformation and fatigue behavior of a micron sized stainless steel. Acta Metall Sinica 41 (2005)337-341.
[42] Kelegtemur MH. and Chaki TK. The effect of various atmospheres on the threshold fatigue crack growth behavior of AISI 304 stainless steel. Int J. Fatigue 23 (2001) 169-174.
[43] Morrow JD. Fatigue Design Handbook-Advances in Engineering. Society of Automotive Engineers, Warrendale, PA. 1968.
[44] Di Schino A. and Kenny JM. Grain size dependence of the fatigue behaviour of a ultrafine-grained AISI 304 stainless steel. Mater Lett 57 (2003) 3182-3185.
[45] Suresh S. Fatigue of Materials. Cambridge University Press, Cambridge, 1998.
[46] Gao H. Huang Y. Nix WD. and Hutchinson JW. Mechanism-based strain gradient plasticity-I. Theory. J Mech Phys Solids 47 (1999) 1239-1263.
[47] Thompson AW. and Backofen WA. The effect of grain size on fatigue. Acta Metall 19 (1971) 597-606.
[48] Essmann U. Gosele U. and Mughrabi H. A model of extrusions and intrusions in fatigued metals I. Point-defect production and the growth of extrusions. Phil Mag A 44 (1981) 405-426.
[49] Ackermann F. Kubin L.P. Lepinoux J. and Mughrabi H. The Dependence of Dislocation Microstructure on Plastic Strain Amplitude in Cyclically Strained Copper Single Crystals. Acta Mater 32 (1984) 715-725.
[50] Mughrabi H. Lowe T.C. and Valiev RZ. Investigations and Applications of Severe Plastic Deformation. In: Lowe TC and Valiev RZ (eds) Nato science Series, Kluwer Academic Publishers, Norwell, (2000) 241.
[51] Thiele E. Holste C. and Klemm R. Influence of size effect on microstructural changes in cyclically deformed polycrystalline nickel. Z Metallkd 93 (2002) 730-736.
[52] Glazov MV. and Laird C. Size effects of dislocation patterning in fatigued metals. Acta Metall Mater 43: (1995) 2849-2857.
[53] Laird C. Charsley P. and Mughrabi H. Low energy dislocation structures produced by cyclic deformation. Mater Sci Eng 81 (1986) 433-450.
[54] Blanckenhagen B. Gumbsch P. and Arzt E. Dislocation sources and the flow stress of polycrystalline thin metal films. Phil Mag Lett 83 (2003) 1-8.
[55] Keller RM. Baker S.P. and Arzt E. Quantitative analysis of strengthening mechanisms in thin Cu films: effects of film thickness, grain size, and passivation.J Mater Res 13 (1998) 1307-1317.
[56] Nix WD. Yielding and strain hardening of thin metal films on substrates. Scripta Metall 39 (1998) 545-554.
[57] Neumann P. Fatigue. In: Cahn RW and Hasen P (eds) Physical Metallurgy, Elsevier science, Amsterdam, (1983) 1554–1593.

[58] Ma B.T. and Laird C. Overview of fatigue behavior in copper single crystals -I. Surface morphology and stage I crack initiation sites for tests at constant train amplitude. Acta Metall 37 (1989) 325-336.
[59] Mughrabi H. Wang R. Differt K. and Essmann U. Fatigue crack initiation by cyclic slip irreversibilites in high-cycle fatigue. In: Lankford J. Davidson DL. Morris WL and Wei RP (eds) Fatigue mechanisms: Advances in quantitative measurement of physical damage, ASTM STP, Philadelphia,PA, (1983) 5-45.
[60] Kim WH. and Laird C. Crack nucleation and stage I propagation in high strain fatigue--II. mechanism. Acta Metall 26 (1978) 789-799.
[61] Liu W. Bayerlein M. Mughrabi H. Day A and Quested P.N., Crystallographic features of intergranular crack initiation in fatigued copper polycrystals. Acta Metall Mater 40 (1992) 1763-1771.

Assessment of Fatigue Damage in Heterogeneous Materials by Application of a Novel Compliance Technique

H. Mughrabi* and H. W. Höppel
Department of Materials Science and Engineering
Universität Erlangen-Nürnberg
Martensstrasse 5, 91058 Erlangen, Germany
**Email: mughrabi@ww.uni-erlangen.de*

Abstract

It is well known that the reduction of the load-bearing cross section caused by fatigue damage gives rise to a characteristic extrinsic enhancement of the elastic compliance of the material. It is less well known that, in particular at higher strains, the elastic compliance effects stemming from fatigue damage are modified by the superposition of the intrinsic non-linear elastic compliance of the material. The latter can be assessed quantitatively and separated from the overall compliance effect, thus enabling the study of the extrinsic damage-induced compliance effects. The novel technique yields information on crack propagation, crack opening and crack closure and has the advantage of being applicable to plain unnotched specimens. It is particularly suited for the study of fatigued heterogeneous materials in which early fatigue damage occurs in the form of many statistically distributed microcracks some of which then coalesce into a larger main crack. Combined with a parallel replica study of surface microcracks and their coalescence, a deeper insight into the cracking process can be achieved. In the following, the potential of this new approach will be demonstrated by application to specific experimental situations. It will be shown that under favourable conditions the novel approach is a useful non-destructive tool to study the crack propagation process in fatigued plain unnotched specimens in its early and later stages.

1. Introduction & Background

There are many different ways in which fatigue cracks are initiated and propagate in different materials. The propagation of fatigue cracks has been studied by a variety of techniques, including compliance measurements [1,2]. However, compliance measurements are usually performed on notched specimens in which one single crack has been induced to propagate. This situation differs considerably from that encountered in

G.C. Sih (ed.), Multiscale Fatigue Crack Initiation and Propagation of Engineering Materials: Structural Integrity and Microstructural Worthiness, 327–343.

fatigued plain unnotched specimens. In this case, early fatigue damage frequently occurs in the form of a large number of microcracks which grow and one of which then propagates as the fatal life-determining crack. Gradual spreading of fatigue damage in the form of microcracks which then coalesce is very characteristic of fatigued heterogeneous materials in which pores, inclusions and other microstructural heterogeneities provide a large number of favourable crack initiation sites [3-9].

This work will focus on the experimental study of fatigue crack initiation and early propagation in unnotched specimens. Special cases considered will include subsurface fatigue crack initiation in heterogeneous materials and the development of concepts to define fatigue damage and to assess the characteristics of fatigue crack propagation in the case of heterogeneous materials containing internal defects. It will be shown that suitably conducted elastic compliance measurements which separate the intrinsic non-linear elastic behaviour of the material from the damage-induced elastic compliance effects can be applied advantageously in the case of fatigued plain (unnotched!) specimens.

2. Subsurface Fatigue Crack Initiation

In recent years, the fatigue failure mechanisms in materials fatigued in the ultrahigh-cycle fatigue (UHCF) regime, with fatigue lives in excess of 10^9 cycles to failure, have been studied in some detail [7-9], compare for example the Proceedings of the recent 4th International Conference on Very High Cycle Fatigue [10]. Many of these studies dealt with internal failures in high-strength materials containing inclusions. In these materials, when fatigued in the range of very low loading amplitudes and ultrahigh fatigue lives, fatigue cracks initiate at internal inclusions and lead to failure by so-called “fish-eye” fracture, compare [7-10]. Subsurface fatigue cracking can also occur at other internal heterogeneities such as pores or cavities, as found for example in cast materials. Examples of subsurface cracking at cast porosity are shown in metallographic sections from a study on the fatigued cast magnesium alloy AZ91 in Fig. 1(a). This mode of crack initiation leads to a large number of microcracks at the surface which then grow and coalesce. The subsequent propagation of the main crack then occurs along the interdendritic areas or through the dendrites, as shown in Fig. 1(b).

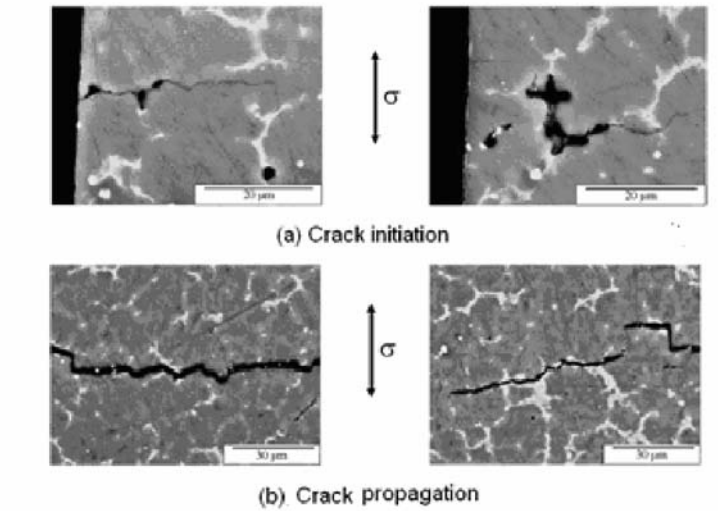

Fig. 1 Fatigue cracks in magnesium alloy AZ91: (a) Initiation at (subsurface) cast porosity. (b) Propagation along interdendritic areas or through the dendrites. After [6,11,12].

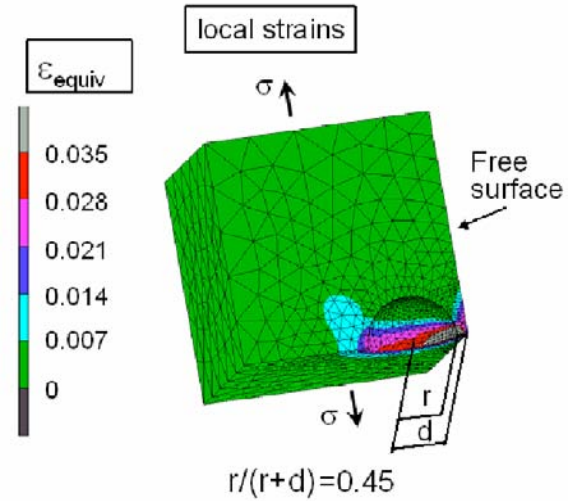

Fig. 2 Finite element calculation showing high local strains in the narrow bridge of material between a spherical pore and the surface of a stressed material. After [13].

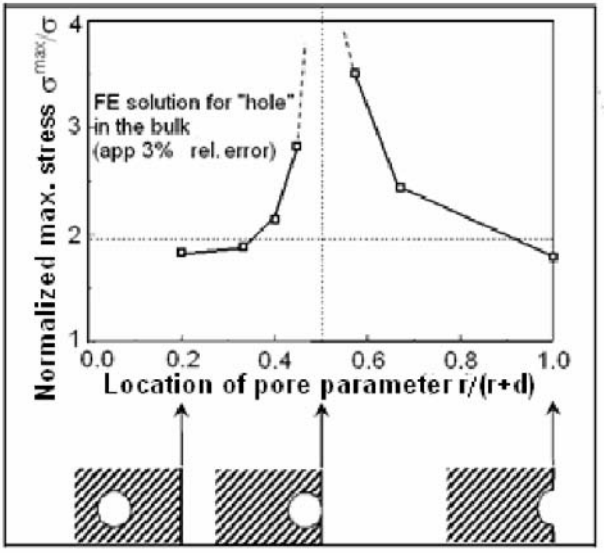

Fig. 3 Results of finite element calculation, showing maximum axial stress σ^{max} normalized with respect to applied stress σ for different locations of a pore. The stress concentration is largest, when the (spherical) pore just touches the free surface and is higher than that near an interior pore or an open pore at the surface. From [13].

In a finite element study [13], an attempt has been made to clarify why fatigue cracks seem to initiate more easily at a pore lying just beneath the surface than at an open pore lying at the surface. The computations were performed for a body under an axial stress σ, containing spherical pores of radius r with their centres lying at different distances d from the free surface. Figure 2 shows as an example the local equivalent strains ε_{equiv} for a pore located at a distance $d \approx 0.82\ r$ from the surface, corresponding to a value 0.45 of the "location parameter" $r/(r + d)$. There is a marked strain localization in the thin bridge of material separating the pore from the surface. This makes it plausible that, during cyclic deformation, this strain localization could lead to the initiation of a fatigue crack and ultimately to failure. It is interesting to consider the local stresses acting in the vicinity of pores located at different distances from the surface, as plotted in Fig. 3. Here, the maximum local axial stresses σ^{max}, normalized with respect to σ, are plotted for different locations of the pore, as shown schematically for three locations at the bottom. It should be noted that the local maximal stresses are indeed largest next to pores that just touch the surface ($r/(r + d)$

= 0.5) and smaller for pores lying deeper in the material (r/(r + d) < 0.5) and also for "open" pores at the surface (r/(r + d) = 1).

3. Intrinsic Non-Linear Elasticity and Elastic Compliance

3.1 Theoretical basis, stress dependence of Young's modulus

The differential Young's modulus of an undamaged material is defined as

$$E_D(\sigma) = \frac{d\sigma}{d\varepsilon_{el}} \tag{1}$$

where σ is the stress and ε_{el} the elastic strain. In the limit of vanishing stress, E_D approaches the constant value E_0 asymptotically. In that case, Hooke's law is valid in its linear form:

$$\sigma = E_0 \cdot \varepsilon_{el} \tag{2}$$

and E_0 then is the constant Young's modulus that is commonly used. However, at higher stresses, E_D becomes noticeably stress-dependent in the sense that E_D decreases (increases) with increasing tensile (compressive) stresses, as has been demonstrated experimentally [14,15]. This stress-dependence of the elastic modulus originates from the anharmonicity of the atomic potential. As the material is strained to larger and larger elastic strains, the anharmonicity of the potential is probed increasingly, giving rise to a non-linear elastic behaviour. The latter can be taken into account through an extension of the linear Hooke's law by adding a second-order term (corresponding to a third-order term in the potential energy). One then obtains [14]:

$$\sigma = E_0 \cdot \varepsilon_{el} + k \cdot \varepsilon_{el}^2 \tag{3}$$

The constant k describes the deviation from linear elastic behaviour. It is always negative. According to the work in [16], the constant k can be expressed in terms of the third order elastic constants. From Eqs. (1) and (3) the differential Young's modulus can be expressed as

$$E_D = \sqrt{E_0^2 + 4k\sigma} \tag{4}$$

The parameters E_o and k are real material constants which are closely related to the atomic potential curve of the material considered. In alloys or in more complex multiphase materials, the constants E_0 and k should be viewed as effective material constants averaged over the constituents of the material. The constants E_0 and k can be obtained experimentally in a cyclic deformation test on an undamaged specimen from the slopes of the elastic unloadings after the stress reversals in tension and compression and/or by intermittent elastic unloadings within a closed cycle, as will be shown in Section 4.2.

3.2 Combined representation of damage-induced compliance effects and intrinsic non-linear elastic behaviour

The non-linear elastic behaviour observed after damage has developed can still be described by eq. (3). However, the differential tangent modulus E_D and the parameters E_0 and k can now no longer be considered as real material constants and begin to deviate from their original values, reflecting an increasingly non-linear behaviour. The latter is characterized by reduced values of E_D as long as the cracks (cavities) are open. At the same time, a decrease of E_o and an increase in the magnitude of the negative parameter k are noted [6,11,17,18-20]. With the difference ΔE_D between the intrinsic value E_0 of E_D of the undamaged specimen and the corresponding modified value of the damaged specimen with opened cracks, $\Delta E_D/E_0$ can be defined as a suitable damage parameter [6,11,15,17,18] which corresponds approximately to the relative loss of load-bearing cross section. This approach is related to earlier work by Lloyd [21] on damaged material. As can be shown easily, the quantity ΔE_D can be expressed as

$$\Delta E_D = \sqrt{E_0^2 + 4k\sigma_T} - E_D(\sigma_T) \tag{5}$$

Here, σ_T is the stress at the tensile reversal point, and $E_D(\sigma_T)$ is the stiffness of the damaged specimen at that point. As stated before, ΔE_D can also be obtained from a series of elastic unloadings within a closed cycle, as will be shown in Section 3.3 and 4.2.

3.3 Identification of intrinsic material parameters

In order to apply the concepts described above, it is essential to first determine the intrinsic material parameters $E_D(\sigma)$, E_0 and k. This is done in a straightforward manner by analysis of the hysteresis loop of an

undamaged specimen. In order to achieve maximum accuracy and as explained elsewhere [11,14,15,19], it is expedient to plot the stress not against the total strain ε_t but against the plastic strain $\varepsilon_{pl} = \varepsilon_t - \sigma/E$. In this expression, the elastic strain has been taken into account in the linear Hooke approximation. In the σ vs. ε_{pl}-plot, the elastic line becomes vertical in the limit of vanishing stresses for $E_D(\sigma) = E_0$. At larger positive or negative stresses, deviations from the vertical slope occur which indicate lower and higher values of $E_D(\sigma)$, respectively. From the slopes which can be evaluated accurately, the differential Young's moduli can be obtained as described in the Appendix. An example of measurements, showing a series of elastic unloadings and reloadings in a closed cycle, is shown in Fig. 4. The material investigated was the metal matrix composite (MMC) AA6061-Al_2O_3-15p-T6 which is reinforced with a volume fraction f_p = 15% of Al_2O_3 particles. The unloading-reloading plots exhibit easily recognizable deviations from the vertical slope, indicating that $E_D(\sigma) < E_0$ for $\sigma > 0$ and $E_D(\sigma) > E_0$ for $\sigma < 0$, as expected. In a first approximation, the differential Young's moduli at the tensile and compressive peak stresses σ_T and σ_C can be evaluated from the slopes of the elastic curves immediately after stress reversal. With these two values, an optimal fit to eq. (3) yields E_0 and k. Alternatively, the elastic unloading-reloading data can be evaluated to yield values of E_D for the stresses from which the unloadings were performed. An optimal fit of these data to eq. (3) yields accurate values of E_0 and k. For the example shown in Fig. 4, the following values were obtained: $E_0 = 88.6 \pm 0.3$ GPa and $k = -318 \pm 20$ GPa [20]. Fig. 5 shows an example of the fit of the actually measured stress dependent values $E_D(\sigma)$ to eq. (3) for the case of a bainitic variant of the roller bearing steel SAE 52100 [14].

Once the elastic data of the undamaged material are known, the development of fatigue damage can be followed continuously during the fatigue test by repeating the procedures described and noting the changes in $E_D(\sigma)$, E_0 and k compared with the values of the undamaged specimen. This will be explained in more detail in the examples to be discussed subsequently.

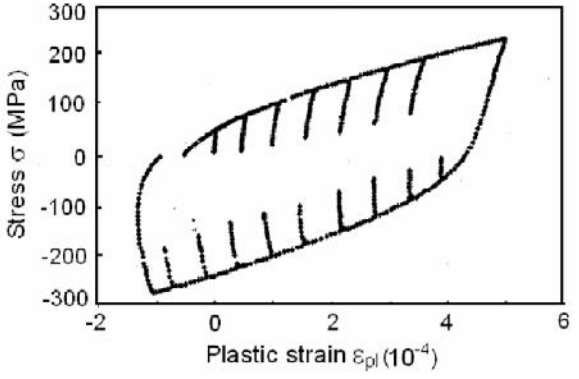

Fig. 4 Hysteresis curve of undamaged fatigued MMC AA6061-Al_2O_3-15p-T6, with elastic unloadings and reloadings. Note that the stress σ is plotted against the plastic strain ε_{pl} (obtained in the linear Hooke approximation), providing higher resolution. After [20].

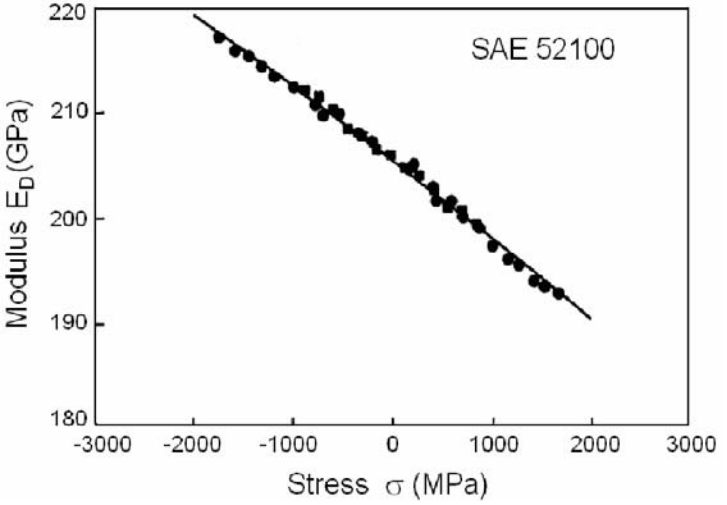

Fig. 5 Stress dependence of differential Young's modulus E_D of a bainitic variant of the roller bearing steel SAE 52100, as a consequence of non-linear elasticity effects. From [14].

4. Examples of Assessment of Fatigue Damage Based on Changes of Non-Linear Elastic Compliance

4.1 Fatigue damage in a particulate-reinforced metal-matrix composite

The study of fatigued particulate-reinforced metal matrix composites is suitable to demonstrate the usefulness of compliance measurements and the assessment of the variation of the parameters E_0 and k as a measure of the developing fatigue damage [17,18,20]. Figure 6 shows an example of such a study on the fatigued MMC AA6061-Al_2O_3-20p-T6 which contains a volume fraction f_p = 20% of Al_2O_3 particles. The data refer to different values of the total strain amplitude $\Delta\varepsilon_t/2$ in strain-controlled fatigue tests at half the fatigue life ($N = N_f/2$, where N is the number of cycles and N_f the number of cycles to failure). In the fatigued MMC studied, fatigue damage has been identified metallographically as the fracture of the particles, compare also [21], which occurs when the total strain amplitude $\Delta\varepsilon_t/2$ exceeds a value of ca. 0.004. It is evident that, with increasing damage, E_0 which is initially constant (97.9 GPa) loses its meaning as a material constant and starts to decrease as a result of the decreasing effective load-bearing cross section. In parallel, the elastic behaviour becomes increasingly more non-linear. This is reflected in the fact that the magnitude of the parameter k which is initially constant (-502 GPa) increases as the damage develops.

In the case of MMCs, it is difficult to relate the changes in the non-linear compliance quantitatively to the loss of the load-bearing cross section. One reason is that the Young's moduli of the matrix (≈ 68 GPa) and the particles (≈ 380 GPa) differ very strongly. Another reason is that the damage is internal and distributed more or less homogeneously throughout the volume and not in the form of discrete cracks. As will be shown in the next section, the approach described can be applied more specifically and with better accuracy to materials in which the damage prevails in the form of cracks that are initially confined to the surface region and then propagate into the interior.

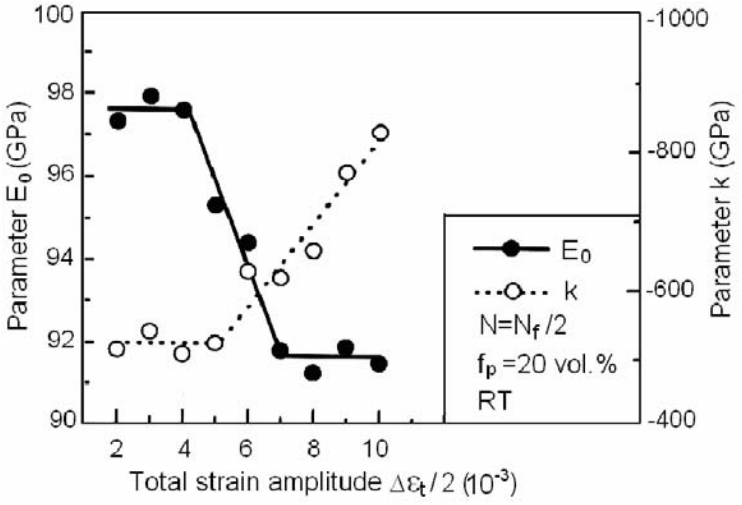

Fig. 6 Evolution of fatigue damage in particulate-reinforced metal-matrix composite AA6061-Al_2O_3-20p-T6, shown the variation of the parameters E_o and k with increasing damage (particle fracture) as a function of total strain amplitude $\Delta\varepsilon_t/2$ at half fatigue life, $N = N_f/2$. An increasingly non-linear elastic behaviour (with increasing |k|) is found as the particles fracture at $\Delta\varepsilon_t/2 > 0.004$. From [17].

4.2 Combined study of propagation of surface cracks in fatigued magnesium alloy AZ91 by replica techniques and compliance measurements

In Section 2, the initiation and propagation of fatigue cracks in the cast magnesium alloy AZ91 had been discussed qualitatively. Here, it will be shown that the compliance technique introduced before lends itself to study in detail specific features of the crack propagation process in the alloy AZ91. This approach can be combined advantageously with the study of crack evolution at the surface by a suitable replica technique, as introduced in [22]. In that case, the fatigue test is interrupted repeatedly in order to take acetate replicas of the surface of the gauge length. Before viewing these replicas at fairly high magnification in a scanning electron microscope, a thin layer of gold is evaporated onto them in order to enhance the contrast and to provide electrical conductivity. By inspection of the sequences of replicas taken, one can then trace back from the fatal crack to the origin of microcrack nucleation and follow the process of crack coalescence and propagation as seen on the surface. Fig. 7 is an example showing the same location of the surface of a fatigued specimen of the alloy AZ91 with the main crack, as seen in two (composite) replicas taken after different

numbers of cycles. From series of traces of the crack distribution in fatigued specimens of the alloy AZ91 it can be concluded how the main crack originated by a coalescence of a larger number of microcracks., as seen in the example shown in Fig. 8.

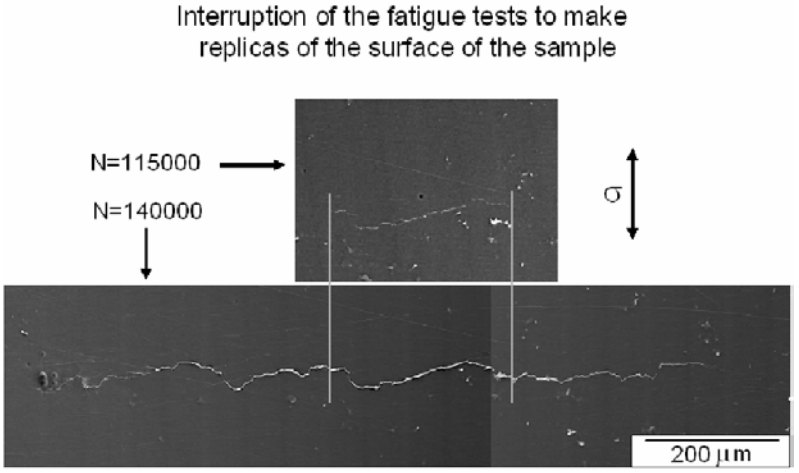

Fig. 7 Example of surface replicas taken from same location of fatigued magnesium alloy AZ91after different numbers of cycles. Plastic strain amplitude $\Delta\varepsilon_{pl}/2 = 9\times 10^{-5}$, room temperature. After [6,11].

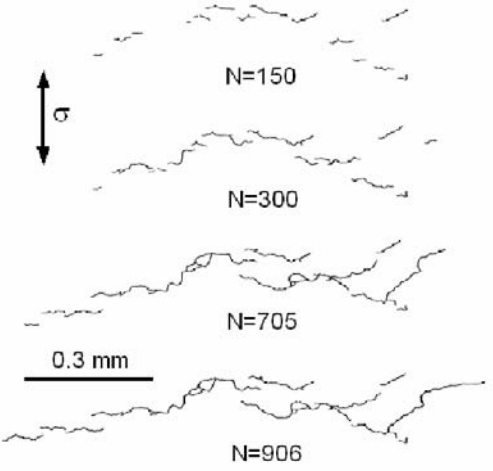

Fig. 8 Evolution of surface crack growth and coalescence in fatigued magnesium alloy AZ91, as obtained from successive replicas. Total strain amplitude $\Delta\varepsilon_t/2 = 5\times 10^{-3}$, room temperature. From [6,11].

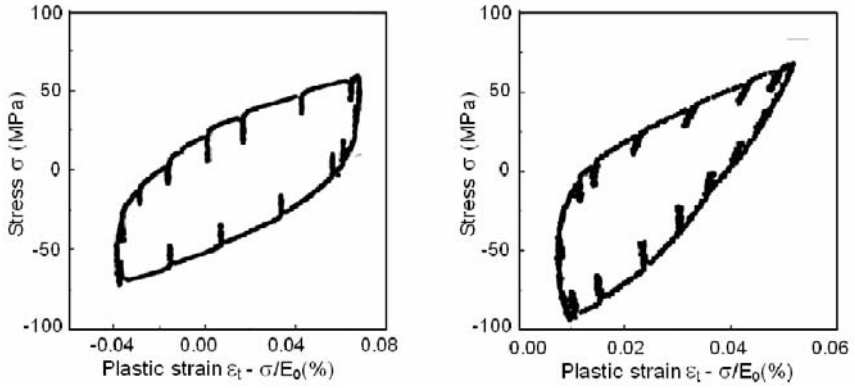

(a)Early in fatigue life; $N/N_f \approx 10\%$ (b)Later in fatigue life; $N/N_f \approx 80\%$

Fig. 9 Hysteresis loops of fatigued magnesium alloy AZ91. These are plots of stress σ as a function of plastic strain in linear Hooke approximation. $\Delta\varepsilon_t/2 = 2.25 \times 10^{-3}$, room temperature. After [6,11,12,15].

Complementary compliance measurements made during intermittent elastic unloadings and reloadings during a closed cycle reveal the loss of the load-bearing cross section and provide valuable additional information. This becomes evident when one compares the hysteresis loops with the unloadings/reloadings, as recorded early in fatigue life, see Fig. 9 (a), and near the end of fatigue life, shown in Fig. 9 (b). Early in the fatigue test, there is no influence from cracks. The slopes of the unloading/reloading paths are vertical in the limit of vanishing stresses and deviate marginally (to a large positive value) at higher tensile stresses and in the opposite sense at higher compressive stresses, as is typical of the intrinsic non-linear elastic behaviour. Once cracks have developed and grown over a larger portion of the cross section, a completely different situation is observed which reflects the superposition of an appreciable additional non-linear component due to the fatigue damage (Fig. 9 (b)). Now the slopes of the unloading/reloading paths deviate strongly and in opposite sense in the tensile and compressive phases of the cycle, respectively, from the initially vertical slope. The variation of the differential elastic modulus E_D during the cycle can be evaluated (with appropriate values of the constants E_0 and k) and plotted against the stress as shown in Fig. 10. In this figure, two important features can be recognized, namely the intrinsic stress dependence of E_D when the cracks are closed (upper inclined line and dashed extension) and the stress dependence due to damage, when the (main) crack has opened in tension (lower inclined line). Moreover, there is a jump ΔE_D between the two lines which allows to recognize the transition

from crack opening to crack closure (at ca. -25 MPa) and vice versa. Crack opening can be seen to occur at a tensile stress of about +12.5 MPa. This behaviour is appropriately described by the damage parameter $\Delta E_D/E_0$, as will be discussed next.

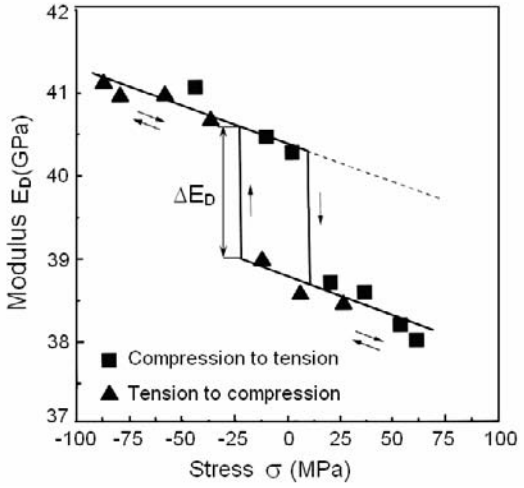

Fig. 10 Differential elastic modulus E_D (stiffness), determined by intermittent elastic unloadings, see Fig. 9 (b), showing crack opening at ca. +12.5 MPa and crack closure at ca. -25 MPa. $\Delta\varepsilon_t/2 = 2.25 \times 10^{-3}$, $N/N_f \approx 80\%$. After [6,11,12,15].

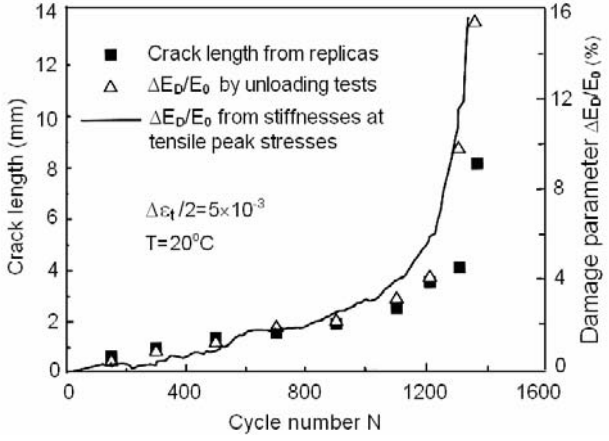

Fig. 11 Evolution of crack length (main crack) of fatigued magnesium alloy AZ91 at the surface (replicas) and in the bulk (see text), as derived from damage parameter $\Delta E_D/E_o$. in different ways. After [6,11,12,15].

Based on the assumption that, after the initial stage of microcrack initiation, there is one main fatal crack, crack growth can be evaluated in different ways by assessing the length of the main crack as a function of the number of cycles. Data thus obtained are plotted in Fig. 11. The damage parameter $\Delta E_D/E_0$ is in good approximation proportional to the length of the surface crack, as determined from the replicas, up to about 80% of fatigue life, whereupon it deviates to higher values, as the crack propagates deeper into the material [6,11]. The continuous curve represents an automatic calculation of the damage parameter $\Delta E_D/E_0$ from the stiffness values at the tensile reversal points of the hysteresis loops (with ΔE_D computed according to eq. (5)). There is a remarkably good agreement between these values and those determined by the elastic unloadings/reloadings. In summary, it can be said that the compliance measurements, evaluated with appropriate consideration of the intrinsic non-linear elastic properties, can yield detailed information on the crack propagation, including crack opening and crack closure stresses, in fatigued plain unnotched specimens of materials such as the cast magnesium alloy AZ91. Further complementary information can be obtained by combining the compliance technique with a replica study of the evolution of fatigue cracks at the surface. In closing, it is mentioned that a mesomechanical model has been developed which describes fatigue crack propagation and fatigue life of the alloy AZ91 very satisfactorily [23].

5. Summary and Conclusions

The studies discussed above lead to the following conclusions:

- The non-linear compliance of a fatigued plain unnotched specimen includes contributions from the intrinsically non-linear elastic material properties and from the damage-induced effects on the compliance.
- The intrinsic non-linear elastic behaviour reflects the anharmonicity of the atomic potential. It can be assessed experimentally in cyclic deformation tests and evaluated in terms of the Young's modulus in the limit of vanishing stresses and a parameter that characterizes the deviations from linearity at higher stresses.
- Compliance measurements, conducted on fatigued plain unnotched specimens and evaluated with appropriate consideration of the intrinsic non-linear elastic properties, are a useful tool to monitor the evolution of fatigue damage. Thus, detailed information on crack propagation in fatigued plain unnotched specimens,

including crack opening and crack closure stresses, can be obtained.

- The technique is particularly suitable to study fatigued materials in which one main fatal crack develops out of the initially large number of microcracks.
- The compliance technique can be combined advantageously with a replica study of the evolution of fatigue cracks at the surface to yield complementary information.
- The experimental approach described is novel and has the merit of providing crack growth data in a non-destructive manner during a standard strain-controlled fatigue test on a plain unnotched specimen without the need to use a standardized fracture mechanics specimen.

Appendix: Determination of differential Young's modulus E_D from slopes of elastic unloading curves in stress vs. plastic strain plots

If the elastic unloading curve in the σ vs. ε_{pl}-plot (with plastic strain defined as previously, i.e. $\varepsilon_{pl} = \varepsilon_t - \sigma/\varepsilon_{el}$) has a stress-dependent slope $S(\sigma)$ at a stress level σ, then this slope is related to the differential elastic modulus $E_D(\sigma)$ in the σ vs. ε_t-plot and the Young's modulus E_0 in the limit of vanishing stress as

$$\frac{1}{S(\sigma)} = \frac{1}{E_D(\sigma)} - \frac{1}{E_0} \tag{A1}$$

Resolving for $E_D(\sigma)$, it follows that the stress-dependent differential Young's modulus can be derived from the slope $S(\sigma)$ by the relation

$$E_D(\sigma) = \frac{E_0 \cdot S(\sigma)}{E_0 + S(\sigma)} \tag{A2}$$

References

[1] Saxena A. and Muhlstein CL. Fatigue crack growth testing.In: ASM Handbook,Vol. 19, Fatigue and Fracture, ASM International (1996) 168-184.

[2] Rroek D. Elementary Engineering Fracture Mechanics, Sijthoff & Noordhoff, Alphen aan den Rijn (1978) 316-321.

[3] Mayer HR. Lipowsky H. Papakyriacou M. Rösch R. Stich A. Zettl B. and Tanzl-Tschegg S. Application of ultrasound for fatigue testing of lightweight alloys, Fatigue Fract Eng Mater Struct 22, (1999) 591-599.
[4] Ting JC. and Lawrence FV. Modeling the long-life fatigue behavior of a cast aluminum alloy, Fatigue Fract Eng Mater Struct 16, (1993) 631-647.
[5] Couper MJ. Neeson AE. and Griffiths JR. Casting defects and the fatigue behaviour of an aluminium casting alloy, Fatigue Fract Eng Mater Struct 13, (1990) 213-227.
[6] Eisenmeier G. Holzwarth. Höppel HW. and Mughrabi H. Mater Sci Eng 319-321 A, (2001) 578-582.
[7] Murakami Y. Nomoto T. and Ueda T. Factors influencing the superlong fatigue failure in steels, Fatigue Fract Eng Mater Struct 22, (1999) 581-590.
[8] Bathias C. There is no infinite fatigue life in metals, Fatigue Fract Eng Mater Struct 22, (1999) 559-565.
[9] Mughrabi H. Specific features and mechanisms of fatigue in the ultrahigh cycle regime, Int J Fatigue 28, (2006) 1501-1508.
[10] Allison JE. Jones JW. Larsen JM. and Ritchie RO. Eds: Proceedings of 4th International Conference on Very High Cycle Fatigue (VHCF 4), TMS (The Minerals, Metals & Materials Society) (2007).
[11] Eisenmeier G. Ermüdungsverhalten der Magnesiumlegierung AZ91: Experimentelle Untersuchungen und Lebensdauervorhersage, Doctoral Thesis, Universität Erlangen-Nürnberg (2001).
[12] Eisenmeier G. Höppel HW. Ding HZ. and Mughrabi H. Ermüdungslebensdauer der Magnesiumlegierung AZ91: Experiment und Modellierung. In: DFG 2. Kolloquium Lebensdauervorhersage, Berlin, Deutscher Verband für Materialforschung und –prüfung e.V., (2002) 169-178.
[13] Borbély A. Mughrabi H. Eisenmeier G. and Höppel HW. A finite element modelling study of strain localization in the vicinity of near-surface cavities as a cause of subsurface fatigue crack initiation, Int. J. Fracture 115, (2002) 227-232.
[14] Sommer C. Christ HJ. and Mughrabi H. Non-linear elastic behaviour of the roller bearing steel SAE 52100 during cyclic loading, Acta Metall Mater 39, (1991) 1177-1187.
[15] Mughrabi H. Assessment of fatigue damage on the basis of nonlinear compliance effects. In: Handbook of Materials Behavior Models, Ed J. Lemaitre, Academic Press, (2001) 622-632.
[16] Wasserbäch W. Non-linear elastic behaviour and third-order elastic constants of a roller-bearing steel and some standard steels, Phys. Stat. Sol. (b) 164, (1991) 121-125.
[17] Hartmann O. Biermann H. and Mughrabi H. Cyclic stress-strain and fatigue behaviour of particulate-reinforced Al-matrix composites. In: Low Cycle Fatigue and Elasto-Plastic Behaviour of Materials, Eds K. T. Rie & P. D. Portella, Elsevier Science Ltd., (1998) 431-436.

[18] Biermann H. Kemnitzer M. and Hartmann O. On the temperature dependence of the fatigue and damage behaviour of a particulate-reinforced metal-matrix composite, Mater. Sci. Eng A 319-312, (2001)671-674.

[19] Mughrabi H. Some aspects of fatigue of engineering materials. In: Fracture Mechanics: Applications and Challenges, Invited Papers presented at the 13th European Conference on Fracture, ESIS Publication 26, M. Fuentes, M. Elices, A. Martin-Meizoso, J. M. Martinez-Esnaola, Eds, Elsevier, (2000) 13-28.

[20] Biermann H. Beyer G. and Mughrabi H. Spannungs-Dehnungs-Hyterese-kurven wechselverformter Proben eines etall-Matrix-Verbundwerkstoffes. In: Verbundwerkstoffe und Werkstoffverbunde, Ed. G. Ziegler, DGM I nformationsgesellschaft, Oberursel, (1996) 197-200.

[21] Lloyd DJ. Aspects of fracture in particulate reinforced metal matrix composites, Acta Metall Mater 39, (1991) 59-71.

[22] Ebi G. Ausbreitung von Mikrorissen in duktilen Stählen, Doctoral Thesis, Rheinisch Westfälische Technische Hochschule Aachen (1987).

[23] Ding HZ. Eisenmeier G. and Mughrabi H. A mesomechanical model of fatigue crack initiation and growth with application to the low-cycle fatigue life prediction of the cast magnesium alloy AZ91. In: Proceedings of Fourth International Conference FATIGUE 2000: Fatigue and Ductility Assessment of Materials, Components and Structures, Eds. M. R. Bache et al, EMAS Ltd, (2000) 209-217.

Fatigue Crack Growth of Aircraft Aluminum Alloys

Sp. G. Pantelakis[1]* and Al Th. Kermanidis[2]

[1]Laboratory of Technology and Strength of Materials (LTSM) Department of Mechanical Engineering & Aeronautics University of Patras, 26500 Patras, Greece
[2]Department of Mechanical and Industrial Engineering, University of Thessaly, 38334 Volos, Greece
**Email: pantelak@mech.upatras.gr*

Abstract

The microstructural characteristics and the influence of existing corrosion on fatigue crack growth in 2024 T351 aircraft aluminium alloy are investigated. Examined is the elongated grain morphology due to the rolling process that exhibited higher crack growth resistance than the microstructure of the sheet material with smaller equiaxed grains. Moreover, plate microstructure with high purity composition offered better damage tolerance characteristics in contrast to the conventional sheet microstructure.Shown is the need to account for the influence of pre-existing corrosion on the aluminum alloys in order to obtain more reliable results from fatigue and damage tolerance analyses of components with corroded areas.

1. Introduction

Damage tolerance analyses and reliable prediction of crack growth under fatigue loading rely heavily on experimental data and the comprehensive understanding of the underlying crack growth mechanisms. Fatigue damage in the material can be divided into a number of subsequent phases characterized by cyclic slip, crack nucleation, micro-crack growth and macro-crack growth up to the final material failure. The different physical processes, which prevail in the gradual fatigue damage accumulation during the fatigue life of a metallic component, are complex and interrelated. They develop with increasing number of fatigue cycles from atomic to macro-scale damage mechanisms and also entail a host of material, geometric and loading parameters [1]. Their interaction cannot be easily assessed in quantitative terms. Mechanistically, the fatigue damage phases mentioned above may be summarized in the crack initiation and crack growth stage, with the latter starting once cracks become visible. Different quantities are essential to assess crack initiation or crack growth respec-

G.C. Sih (ed.), Multiscale Fatigue Crack Initiation and Propagation of Engineering Materials: Structural Integrity and Microstructural Worthiness, 345–366.

tively. For crack initiation relevant is the severity of stress concentration. Material properties and loading conditions control principally the behaviour of long cracks. Crack growth is dominated by the intensity of the crack-tip stress distribution. The volume energy density criterion, [2-4], which first has been used to predict failure initiation under monotonic loading, can also be applied to predict crack initiation and crack growth under cyclic loading. It assumes that failure occurs in a critical element when the volume energy density reaches a certain threshold. The crack initiation model in [2] applies also to crack propagation [3,4], because attention is focused on a material element in a specimen without initial crack or in a local region ahead of a pre-existing crack. According to the crack closure theory [5], crack growth is dependent to crack closure, which is correlated to several features, such as fracture surface roughness, residual plasticity in the wake or ahead of the crack tip, oxide debris etc. Herein, the role of microstructure and material properties ahead of the crack tip is important. For instance, fracture surface roughness is correlated to the grain morphology of the alloy; the amount of residual plasticity in the wake of the crack is dependent on the material's yield stress. The same property influences crack growth retardation induced by the occurrence of an overload.

While these aspects are important in the development of damage tolerance analysis tools, the availability of sufficient experimental data is a prerequisite.

In the present chapter experimental fatigue crack growth data for selected aircraft aluminum alloys are presented and discussed with the support of metallographic analyses. The work presented, resulted from two extensive studies. In the first study the effect of variation in microstructure of the 2024 T351 alloy due to the aluminum product form (sheet or plate) as well as the purity content (Fe-Si content) of the alloy on the fatigue crack growth were investigated [6]. In the second study the fatigue crack growth behaviour of pre-corroded 2024 T351 alloy was investigated and discussed under the view of a synergetic effect of corrosion and corrosion-induced hydrogen embrittlement [7].

1.1 Aircraft aluminum alloys

Aluminum alloys are the primary material for aircraft structures since 1930. Despite the increasing use of advanced polymer matrix composites in aircraft structures, aluminum alloys remain the main choice for fuselage, wings and supporting structure of commercial airliners. High specific properties, superior damage tolerance behaviour and good corrosion resistance along with well known performance characteristics, design experi-

ence and established manufacturing methods represent the main reasons for the continued wide use of aluminum alloys in modern aircrafts. The 2xxx, 6xxx and 7xxx aluminum series as well as some Al-Li alloys enjoy the widest use in aircraft structural applications.

The 2xxx series alloys contain copper as the primary alloying element, which produces high strength but reduced corrosion resistance. The 2024 alloy is probably the most widely used alloy in aircraft applications. The lower yield stress of the 2xxx series alloys compared to the 7xxx series is compensated by improved damage tolerance, thus making this alloy series the first choice for damage tolerant primary structure applications. The 2xxx series alloys are not easily weldable but new alloy types along with advanced welding technologies make welding of these alloys manageable.

The 6xxx series contains magnesium and silicon, which form the magnesium silicide (Mg_2Si). The alloys of this series offer a good balance between corrosion resistance and strength along with a good weldability. The most popular alloy of the 6xxx series for use in aircraft applications is the 6061.

In the 7xxx group the primary alloying element is zinc. In this group two types of alloys exist: the aluminum –zinc –magnesium alloys and the aluminum – zinc-magnesium-copper alloys, with the second type being less corrosion resistant. This series includes some of the most high strength aluminum alloys such as 7075 and 7178, which are exploited for aircraft frames and structural components. All above mentioned aluminum alloy series are heat treatable.

Aluminum –Lithium alloys are attractive for lightweight aircraft applications due to the element Lithium, which is the lightest metallic element. They are often alloyed with copper, magnesium, zirconium and other elements to improve properties. They have been used in limited applications so far (2090 and 8090 are typical alloys used) mainly due to low corrosion resistance and anisotropic behaviour. New weldable Al-Li alloys of the 2xxx-series (copper being the greatest alloying element) seem to be attractive for further applications.

2. Microstructural Effects on Fatigue Crack Growth

It is known that microstructural features influence fatigue crack growth in the near threshold (low ΔK) regime where the slip characteristics are significant [8]. In the low ΔK regime crack growth has been found to be sensitive to crack closure, namely plasticity induced crack closure, corrosion oxide closure and surface roughness crack closure [5, 9-13]. In [14] the effect of sheet/plate microstructure on the 2090 aluminum–lithium

alloy on fatigue crack growth in the near threshold region has been demonstrated. At low ΔK values in the order of 10^{-10} m/cycle the sheet material exhibits significantly higher crack growth rates compared to the plate material.

In the crack growth region corresponding to medium ΔK values, the crack plane becomes normal to the applied nominal stress and crack growth sensitivity on microstructure is considered to be less significant. Nevertheless, a correlation between microstructural features and closure mechanisms in long crack growth behaviour of aluminum alloys seems to exist. Specifically, surface roughness induced closure (RICC) mechanisms have been found to influence Stage II fatigue crack growth rates [10-11, 14-15]. The closure mechanisms have been attributed to grain morphology characteristics. Additionally, crack deflection and consequent crack closure from wedging of fracture-surface asperities, which are related to variations in the degree of recrystallization, grain morphology and texture (evident between sheet and plate product forms) may increase the crack growth resistance of the material [14].

When fatigue load interaction effects are present the complex damage accumulation phenomena make a correlation between fatigue crack growth mechanisms and microstructure even more difficult. Suresh argued in [16] that the post-overload crack propagation behavior is influenced by microstructure as well as crack tip/grain boundary interactions. In the same work it is reported that surface roughness may lead to sustained crack growth retardation following the application of overloads by reducing the effective stress intensity range. However limited data can be found in the open literature on the post-overload fatigue crack response of the same alloy with variation in microstructure.

This work will first discussed the influence of variations in microstructure resulting from sheet and plate product form, as well as from variations in purity composition (Fe-Si content), on the long crack growth behaviour of the conventional 2024 T351 aluminum alloy is presented. The experimental results provide evidence that the effect of microstructural features (e.g. grain size and morphology) can influence the medium ΔK fatigue crack propagation, which is of high technological interest for damage tolerant wrought aluminium alloys design.

2.1 Material

The material used in the experimental investigation was aluminum alloy 2024 T351 in plate and sheet product configuration with a thickness of 15 and 3.2 mm respectively. Both plate and sheet materials were tested in

conventional and high purity (HP) composition, which refers to the 2024 material with reduced Fe-rich and Mg_2Si phases. The volume fractions of the respective phases are given in Table 1 for HP and reference material. In Figure 1 micrographs of the grain structure of the materials used in the present investigation are shown [6]. The grain morphology obtained for the plate and sheet product is the result of the different degree of rolling process in order to achieve the required thickness (15mm and 3.2 mm respectively). As a result a different grain microstructure was obtained which corresponds to larger, elongated grains for the plate materials compared to the fine equiaxed grains in the sheet microstructure.

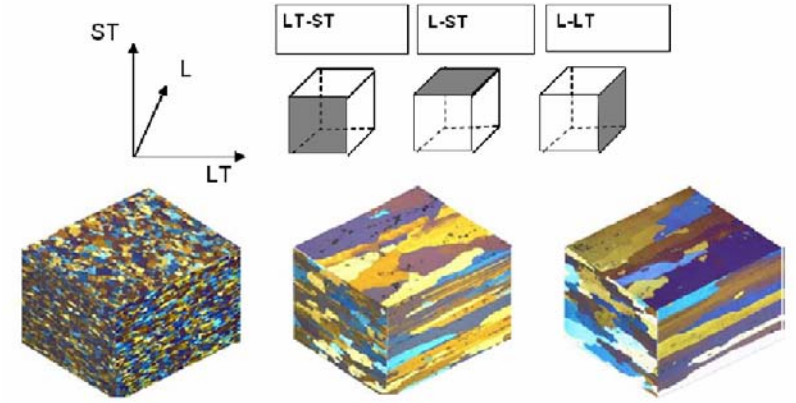

(a) AA2024 (b) AA2024 (c) 2024HP

Fig. 1 Micrographs showing grain morphology in the materials investigated [6].

Grain size measurements in terms of equivalent circle diameter in planes L-ST, LT-ST and L-LT are displayed in Table 2. The average grain size in the plate material was noticeably larger in all-3 planar dimensions measured exhibiting a coarse and elongated microstructure compared to the finer equiaxed grain structure in the sheet material. The largest grain sizes were measured in the plate with high purity composition, which for the case of the L-LT planar dimension reaches 700μm. The respective value for the sheet high purity alloy was 30 μm.

Table 1 Calculated volume fractions of Fe-rich and Mg_2Si phases in reference and HP material [6]

Phase	2024 plate	HP plate	2024 sheet	HP sheet
Fe-rich	1	0.5	1.26	0.65
$M_{g2}Si$	0.16	0.06	0.22	0.13
balance	1.16	0.56	1.48	0.78

Table 2 Average planar grain size measured in the four alloys [6].

	Plane direction and circle equivalent diameter (μm)			
	L-ST	LT-ST	L-LT	average
2024HP sheet	18,3	18,2	28,5	21,2
2024 plate	49,4	48,3	101,1	62,3
2024 HP plate	175,0	96,0	349,0	180,3
2024 sheet	97,0	62,0	707,0	162,0

2.2 Fatigue testing, results and fractographic observations

The fatigue tests carried out were constant amplitude fatigue crack growth tests as well as constant amplitude fatigue crack growth experiments including single and periodic tensile overloads. For the fatigue crack propagation experiments center cracked specimens of 3.2 mm thickness were machined according to ASTM E647 standard [17]. To avoid thickness effects in the investigation specimens were cut from the mid-plane of the plate product and were machined to the required thickness of 3.2 mm. The fatigue crack growth experiments performed are summarized in Table 3.

Table 3 Summary of fatigue crack growth tests.

Constant Amplitude Tests				
Material	Maximum stress σ_{max} (MPa)	Frequency (Hz)	Stress Ratio $R=\sigma_{min}/\sigma_{max}$	Overl.ratio σ_{ov}/σ_{max}
2024HP sheet	130	25	0.1	1.6
2024 plate	130	25	0.1	1.6
2024 HP plate	130	25	0.1	1.6
2024 sheet	130	25	0.1	1.6
Tests with single overload				
Material	Stress Ratio $R=\sigma_{min}/\sigma_{max}$	Overl.ratio σ_{ov}/σ_{max}	Crack length at overload (mm)	
2024HP sheet	0.1	1.6	8.5,11(2 tests)	
2024 plate	0.1	1.6	9,11(2 tests)	
2024 HP plate	0.1	1.6	10,12(2 tests)	
2024 sheet	0.1	1.6	7.5	
Tests with periodic overloads				
Material	Stress Ratio $R=\sigma_{min}/\sigma_{max}$	Overl.ratio σ_{ov}/σ_{max}	Crack length at overload (mm)	
2024HP sheet	0.1	1.6	6.5, 8, 10	
2024 sheet	0.1	1.6	6.5, 7.5, 10	

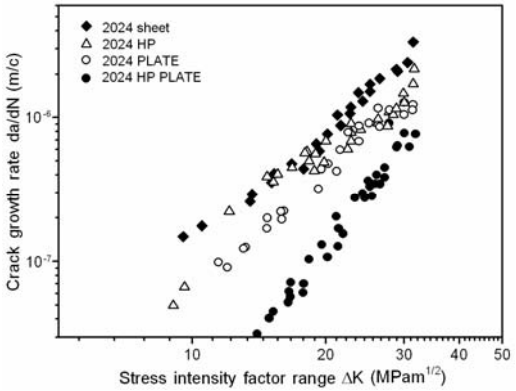

Fig. 2 Constant amplitude fatigue crack growth results.

In Fig. 2 constant amplitude fatigue crack propagation curves of the materials tested are displayed in terms of half crack length versus stress intensity factor range. The higher crack growth resistance for specimens taken from plate product is reflected through the lower crack growth rates compared to the sheet material in the medium ΔK region (10-30 MPam$^{1/2}$). For both rolling products the material with high purity composition exhibited superior crack growth behaviour in the mentioned ΔK region.

Optical micrographs of the fractured specimen surfaces with plate microstructure revealed increased roughness and discontinuities along the crack path direction (Fig.3). The surface roughness was evaluated by means of the surface profile parameter R_L according to the ASM guidelines [18]. R_L values measured for plate specimens were higher compared to the sheet material. The R_L values measured at specific segments taken at the same crack path location for plate and sheet 2024 material were R_{LPLATE} =1.18 and R_{LSHEET} =1.07 respectively (Fig. 4).

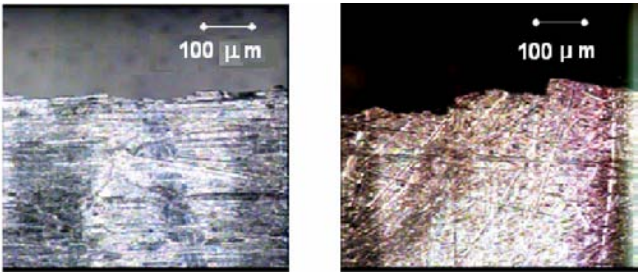

(a) Sheet (b) Plate material

Fig. 3 Micrographs showing segments of the free edge of fractured surfaces at the same location of crack propagation with different degree of surface roughness.

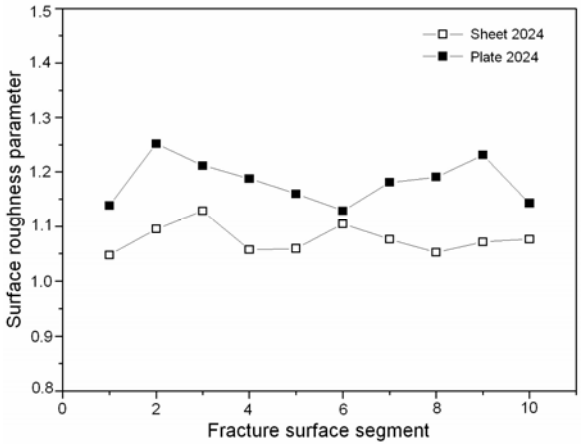

Fig. 4 Profile roughness parameter for sheet and plate material.

The obtained response under constant stress amplitude may be correlated to pronounced crack closure effects of specimens with plate microstructure due to increased surface roughness, which produces pronounced crack surface contact. The above observation is in agreement with results reported in [14-15,19]. The increased surface roughness along the crack path direction is promoted by the coarse and elongated grain morphology, as a result of the different rolling process involved. Macroscopic fractographic examination revealed a fractured surface region perpendicular to the load followed by shear fracture (Fig. 5). For all materials tested double shear lips are evident along the fracture path.

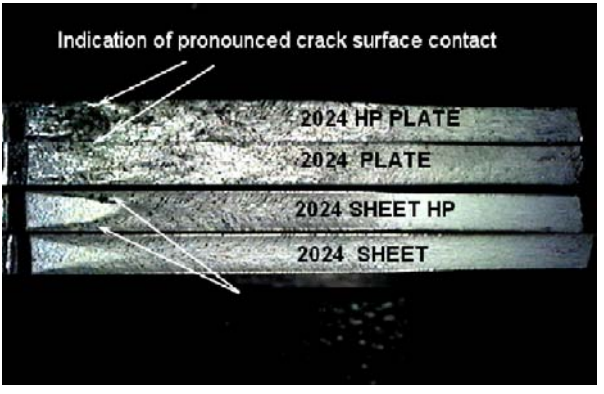

Fig. 5 Fractured surfaces macrographs of different materials subjected to constant amplitude fatigue tests.

As shown in Fig. 6 in the case of the plate product the fractured surface region which is perpendicular to the load is smaller and the developed shear lips are wider in comparison to the sheet material. On the fracture surfaces of the plate materials pronounced black debris could be observed, which according to [20] could be evidence of increased lower and upper crack surfaces contact during fatigue crack growth. By careful examination of fractured surfaces in Fig. 6 it can be observed that crack surface contact marks are more pronounced on the shear lips of plate material specimens. The described mechanism can lead to increased crack closure.

In order to assess the fatigue crack retardation response following application of overloads, constant stress amplitude fatigue crack growth experiments including single and periodic tensile overloads were carried out. The testing parameters were the same as in the previous tests. The applied overload ratio was σ_{ov}/σ_{max}= 1.6, while application of overload was performed at similar ΔK levels (at approximately 20 MPam$^{1/2}$). From the experimental crack growth curves obtained (Figs. 6-7) it was observed that crack growth rates measured at comparable ΔK levels in the post – overload stage were lower in the specimens with plate microstructure. The post overload crack growth behaviour observed is consistent with the results obtained in the constant amplitude crack propagation curves showing an increased crack growth resistance for the plate microstructures both in the prior and post overload stage. Figures 8, 9 and 10 are showing a sustained retardation of the alloy with high purity composition for the case of single and periodic overloads. Micrographs of fracture surfaces of the specimens subjected to tensile overloads revealed similar characteristics to the constant amplitude tests in terms of shear lip development and surface

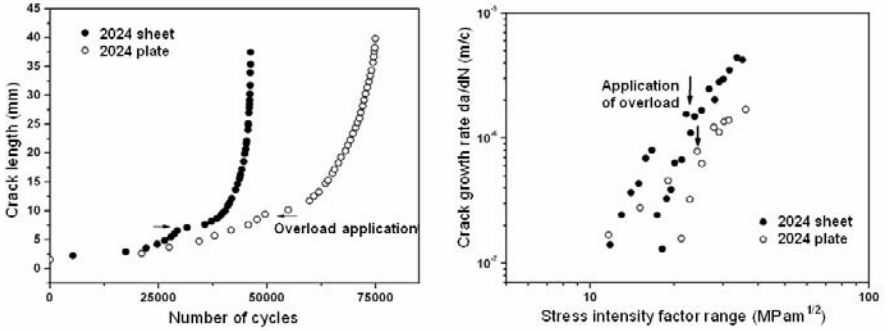

(a) Crack length (b) Crack growth rate

Fig. 6 Crack length and fatigue crack growth rates after tensile overload for sheet and plate material.

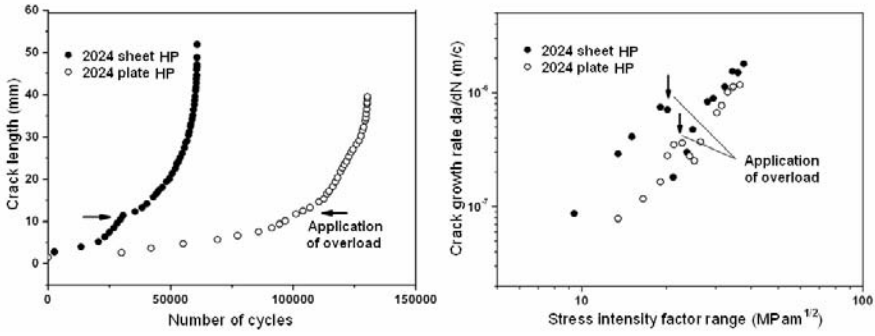

(a) Crack length (b) Crack growth rate

Fig. 7 Crack length and fatigue crack growth rates after tensile overload for sheet and plate material.

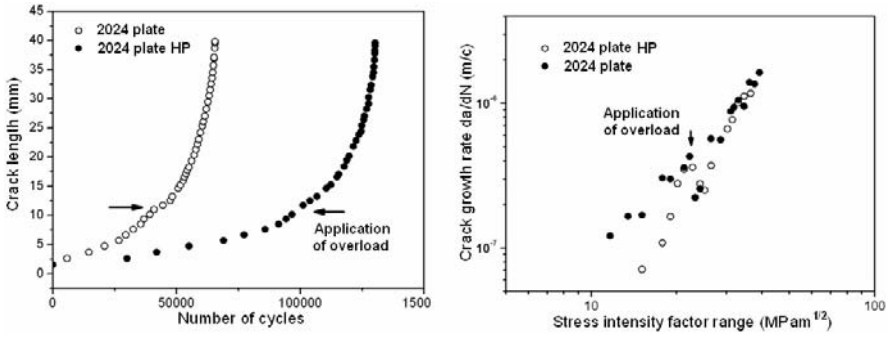

(a) Crack length (b) Crack growth rate

Fig. 8 Crack length and fatigue crack growth rates after tensile overload for sheet and plate material.

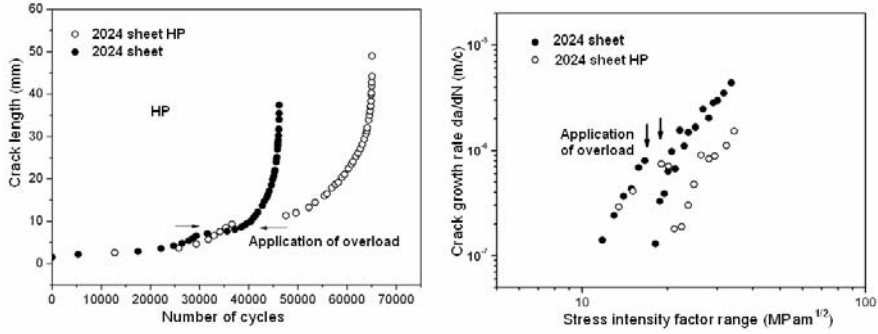

(a) Crack length (b) Crack growth rate

Fig. 9 Crack length and fatigue crack growth rates after tensile overload for conventional and HP sheet material.

roughness. In the case of single and multiple overloads the load interaction phenomena present lead to significant plasticity effects. Thus, crack growth mechanisms become more complex and the results obtained cannot be discussed solely under the viewpoint of pronounced crack closure effects due to fracture surface characteristics.

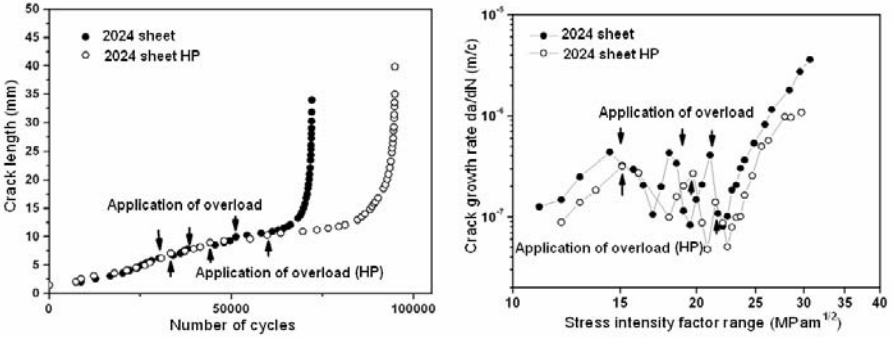

(a) Crack length (b) Crack growth rate

Fig. 10 Crack length and fatigue crack growth rates after periodic tensile overload for conventional and HP sheet material

3. Effect of existing corrosion damage on Fatigue Crack Growth

It is without doubt that the Aloha Airlines accident in 1988 showed the global aviation industry the dangers of the structural degradation of aging components. In the years that followed intensive investigations have shown that the occurrence of corrosion appreciably degrades the mechanical performance of aluminum alloys [e.g.21].

Corrosion damage of aluminum alloys has been classically attributed to the complex process of oxidation. In recent years experimental efforts on a series of aircraft alloys have provided evidence that corrosion is also the cause for diffusion controlled material hydrogen embrittlement [21-29]. This hydrogen embrittlement phenomenon is reflected into an appreciable reduction of tensile ductility of the corroded material areas [21-22,28–29]. The hydrogen embrittlement process is explained in [30] through a hydrogen induced local microplasticity. Both processes, corrosion and hydrogen embrittlement, are diffusion-controlled, hence the degradation of the material's mechanical performance is expected to occur in local scale. However at present there are neither experimental data nor an established methodology for assessing the values of the local material properties of the corroded areas of the material. Notice that experimental investigations on the interaction of corrosion and fatigue usually refer to fatigue and fatigue crack growth tests which are performed in a certain corrosive environment [31-

32] and not to tests performed on pre-corroded material whereby, the latter represents a different and, for a series of practical cases in older airplanes, more relevant situation.

Structural degradation due to existing corrosion has been considered as a load capacity decrease of the structural component [33]. Furthermore, it has been recognized that the occurrence of corrosion facilitates the onset of fatigue cracks [34-35] and, hence causes the decrease in fatigue life due to corrosion-pitting damage [34], as well as multi-site damage scenarios from corrosion pits [35]. In Figure 11 the S-N curves of uncorroded and pre-corroded 2024 T351 aluminum alloy specimens are displayed [36]. The results reveal the essential degradation of fatigue life in the corroded coupons as a result of premature onset of crack initiation due to corrosion pits. The degradation is reflected in a significant decrease in the material's fatigue limit of the order of 28.5 % compared to the uncorroded material.

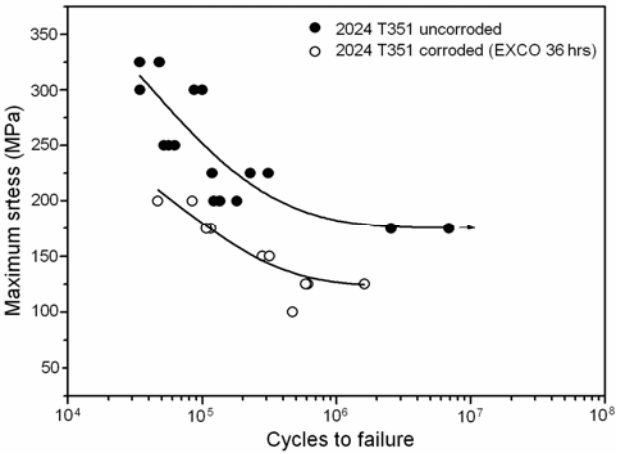

Fig.11 S-N curves of uncorroded and pre-corroded 2024 T351 aluminum alloy specimens

On the other hand, the effect of prior corrosion damage on the fatigue crack growth behaviour of aircraft structures is presently disregarded and a few experimental data exist correlating the effect of prior corrosion on the fatigue crack growth rate [37].

The fatigue and damage tolerance behaviour of pre-corroded 2024 T351 aluminum alloy specimens is presented and discussed under the viewpoint of a synergetic effect of corrosion and corrosion-induced hydrogen embrittlement. The results demonstrate the essential effect of existing corrosion on the fatigue and damage tolerance behaviour of the 2024 alloy, as well as the need to account for the effect of corrosion on the mechanical proper-

ties in fatigue and damage tolerance analyses of the corroded areas of a structure.

3.1 Experimental procedure, testing and results

The experiments were conducted on bare 2024 T351 aluminium alloy of 1.6 mm thickness. The performed experiments included fatigue crack growth tests for different stress ratio R on corroded and uncorroded material. An overview of the performed tests is given in Table 4. The selected fatigue stress ratios were $R=\sigma_{min}/\sigma_{max}$ 0.01, 0.1, 0.5 και 0.7 and the test frequency 20 Hz. In order to evaluate the R-effect the stress range $\Delta\sigma$ was kept constant at a σ_{max} between 101 and 180 MPa. Machining of the specimens was made according to ASTM E 647-93 specification. All specimens were cut in longitudinal (L) orientation relative to the rolling direction. The experimental investigation included uncorroded and pre-corroded specimens in exfoliation corrosion environment for 36 hours according to ASTM standard G34-90 [38]. Exfoliation corrosion environment has been selected as the environment that satisfactory simulates the effect of long duration outdoor corrosion exposure on the material's mechanical properties [34]. After exposure, the specimens were cleaned according to ASTM G34-90. During all fatigue crack growth tests crack growth was recorded via a DC Potential Drop measurement method.

Table 4 Summary of fatigue crack growth tests.

Corrosion exposure	Stress Ratio $R=\sigma_{min}/\sigma_{max}$	Frequency (Hz)	Max. stress σ_{max} (MPa)	No. tests
none	0.01	20	109	2
EXCO 36 hrs	0.01	20	109	2
none	0.1	20	101	2
EXCO 36 hrs	0.1	20	101	2
none	0.5	20	180.4	2
EXCO 36 hrs	0.5	20	180.4	1
none	0.7	20	176.1	2
EXCO 36 hrs	0.7	20	176.1	2

The fatigue crack growth results are summarized in Tables 5-7 and Figs. 12-16. In Table 5 the values of ΔK and K_{max} referring to the critical crack length are given. Calculation of ΔK and K_{max} was made with implementation of the equation [17]:

$$K = \beta\sigma\sqrt{\pi\alpha} \qquad (1)$$

In the interpretation of results the effect of corrosion on the correction factor β in Eqn. (1) was not taken into account. In Table 6 the number of cycles corresponding to specimen failure are displayed together with the critical crack length α_{cr} defined at a time step that corresponds to 3 seconds prior to specimen failure. The critical crack length was defined in this manner because of the unfeasibility due to the data recording frequency of measuring the actual value at fracture. The critical crack length corresponds to the last data point of the curves in Figs. 12a-15a.

Table 5 ΔK και K_{max} values at critical crack length.

Corrosion exposure	Stress ratio $R=\sigma_{min}/\sigma_{max}$	Stress int. factor range ΔK (at α_{cr}) [$MPa\cdot\sqrt{m}$]	Max. stress int. factor K_{max} (at α_{cr}) [$MPa\cdot\sqrt{m}$]
none	0.01	29.74	30.04
EXCO	0.01	22.87	23.09
none	0.1	32.54	36.16
EXCO	0.1	25.28	28.09
none	0.5	38.74	77.48
EXCO	0.5	16.94	33.88
none	0.7	11.70	40.32
EXCO	0.7	11.25	37.54

Table 6 Fatigue crack growth data of corroded and uncorroded specimens.

Corrosion exposure	Stress ratio $R=\sigma_{min}/\sigma_{max}$	Max. stress (MPa)	Fatigue life N_f (cycles-(mean values)	Critical crack length α_{cr} (mm-(mean values)
None	0.01	109	46640/47460 (47050)	20.02/16.46 (18.24)
EXCO 36 hrs	0.01	109	42700 (42700)	12.59 (12.59)
None	0.1	101	81620/69100 (75360)	24.8/23.2 (24.0)
EXCO 36 hrs	0.1	101	58640/51960 (55300)	15.59/21.31 (18.45)
None	0.5	180.4	43960/49820 (46890)	19.4/35.73 (27.56)

EXCO 36 hrs	0.5	180.4	30560/29560 (30060)	9.72/10.92 (10.32)
None	0.7	176.1	213540 (213540)	14.17 (14.17)
EXCO 36 hrs	0.7	176.1	139880/121260 (130570)	11.75/13.67 (12.71)

Table 7 Paris coefficients of corroded and uncorroded material.

Corrosion exposure	Stress ratio $R=\sigma_{min}/\sigma_{max}$	n	Mean value	C	Mean value
none	0.01	3.09	3.13	$7.38*10^{-11}$	$4.69*10^{-11}$
		3.16		$2.0*10^{-11}$	
	0.1	3.35	3.21	$5.56*10^{-11}$	$9.38*10^{-11}$
		3.07		$1.32*10^{-10}$	
	0.5	3.0	3.12	$1.94*10^{-10}$	$1.60*10^{-10}$
		3.23		$1.26*10^{-10}$	
	0.7	3.6	3.6	$9.25*10^{-11}$	$9.25*10^{-11}$
		-			
EXCO 36 hrs	0.01	-	2.85	-	$4.88*10^{-11}$
		2.85		$4.88*10^{-11}$	
	0.1	3.16	3.11	$1.62*10^{-10}$	$1.5*10^{-10}$
		3.05		$1.38*10^{-10}$	
	0.5	3.04	3.21	$2.38*10^{-10}$	$4.37*10^{-10}$
		3.38		$1.99*10^{-10}$	
	0.7	3.16	3.47	$5.03*10^{-10}$	$2.9*10^{-10}$
		3.78		$7.61*10^{-10}$	

In Figs. 12-16 the fatigue crack growth curves together with the crack growth rate measurements versus stress intensity factor range ΔK are displayed for the corroded and un-corroded specimens at different stress ratios.

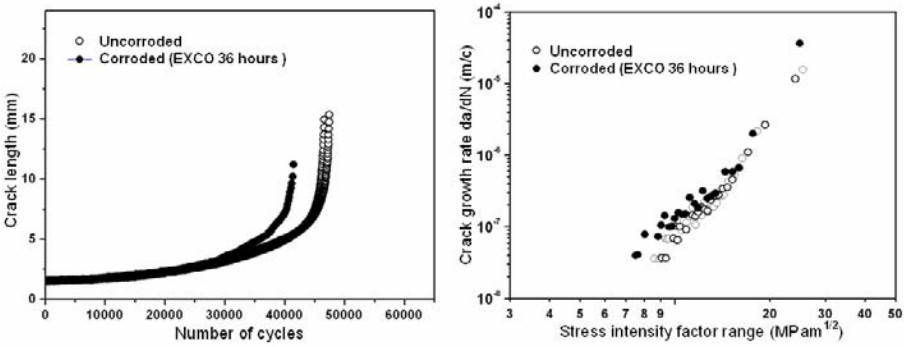

(a) Crack length (b) Crack growth rate

Fig. 12 Crack length and fatigue crack growth rates of corroded and un-corroded specimens at R=0.01.

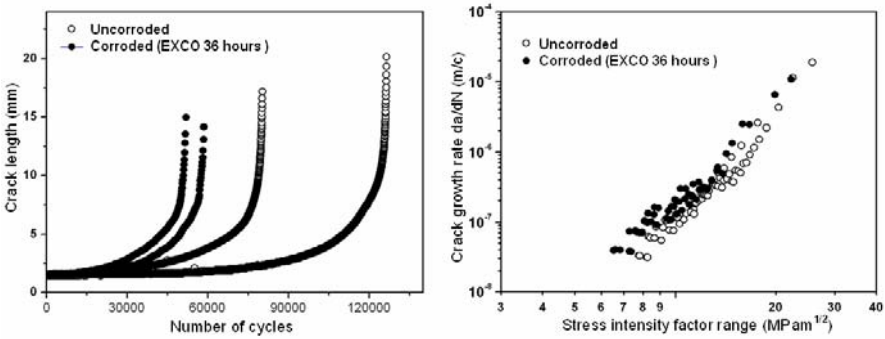

(a) Crack length (b) Crack growth rate

Fig. 13 Crack length and fatigue crack growth rates of corroded and uncorroded specimens at R=0.1.

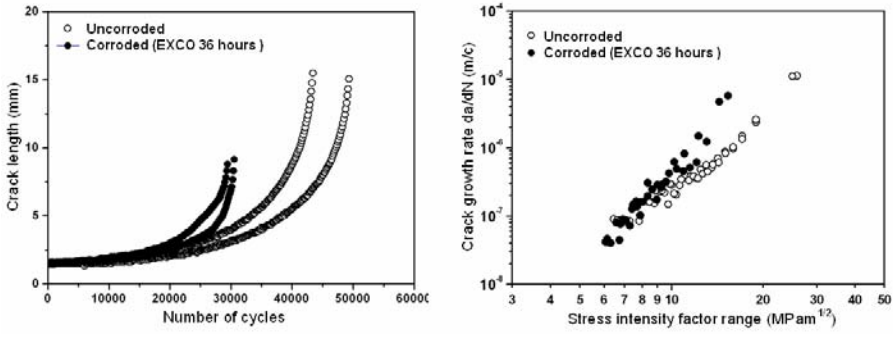

(a) Crack length (b) Crack growth rate

Fig. 14 Crack length and fatigue crack growth rates of corroded and uncorroded specimens at R=0. 5.

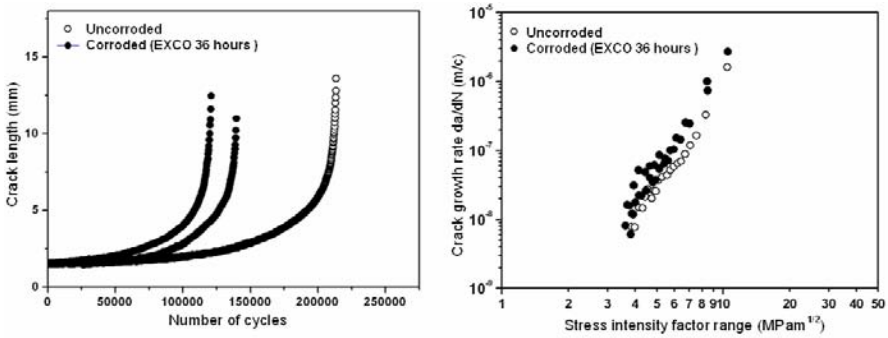

(a) Crack length (b) Crack growth rate

Fig. 15 Crack length and fatigue crack growth rates of corroded and uncorroded specimens at R=0.7.

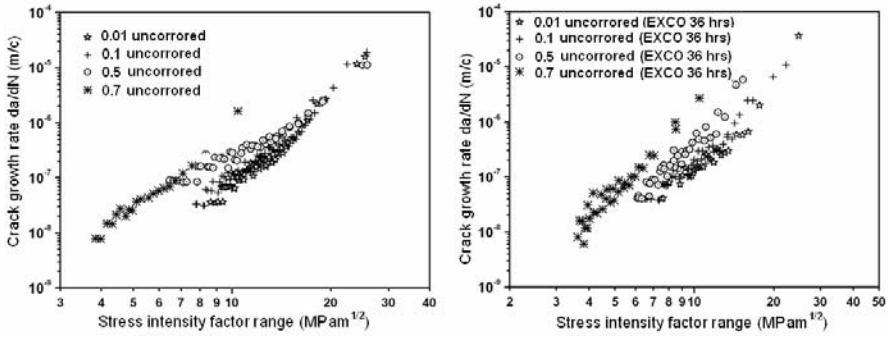

(a) Uncorroded (b) Corroded

Fig. 16 Fatigue crack growth rates of specimens at R=0.01, 0.1, 0.5, 0.7.

From the obtained results the deteriorating effect of corrosion on fatigue life of pre-corroded specimens is revealed for all stress ratios examined. Fatigue life reduction, corresponding to fatigue crack propagation cycles, which as expected is promoted by the existence of localized corrosion sites acting as stress concentration locations, is ranging from 12% (R=0.01) to 38.8% (R=0.7). The effect of corrosion on fatigue crack propagation is more pronounced for small values of R. The observed behaviour can be explained by considering the mechanisms of partial embrittlement of the specimens as a result of corrosion exposure. For small values of ΔK damage accumulation mechanisms seem not to be influenced to the same degree by the partially embrittled material. At higher tensile stresses (higher ΔK values) embrittlement may have a more pronounced effect in the ability of the material to deform plastically ahead of the crack tip.

By examining Table 6 the effect of corrosion damage on the critical crack length to failure is illustrated. The critical crack length of the corroded specimens is reduced by a magnitude of 45% compared to the respective value of the uncorroded specimens, while the stress intensity factor values corresponding to α_{cr} is reduced by 34% with regard to the uncorroded material. The stress intensity factor reduction is attributed to the reduction of the critical crack length due to fracture toughness degradation of the corroded alloy.

From the experimental findings obtained in Figs. 12-16 it can be concluded that the crack propagation resistance at high ΔK values suffers a significant degradation compared to the medium ΔK region where corrosion attack does not have the same impact. The latter observation is supported by the calculated differences in the coefficients of the Paris equation. The differences in the coefficients for the corroded and uncorroded specimens, derived from the da/dN–ΔK plots for stress intensity ranging from 10– 18 MPa $m^{1/2}$ are compared in Table 7. The coefficients do not differ appreciably. This is consistent with the results in [35]. At stage III crack growth (high ΔK), the calculated crack growth rates are high and cannot be described by the Paris law. At this stage Paris equation cannot assess the influence of corrosion on fatigue crack growth.

The obtained decrease in fatigue life of corroded specimens is attributed to the reduction of the critical crack length at failure. The latter is dependent on the material's fracture toughness. These parameters are influenced by the partially embrittled material due to corrosion. The fatigue crack growth behaviour described above is not easy to explain by means of the classical interpretation of corrosion. Fractographic analyses performed in [29] on 1.6 mm thick specimen subjected to exfoliation corrosion exposure for 24 h confirm the embrittlement of the material during the corrosion exposure. The fracture surface appearance varies from the specimen surface to the specimen interior. At the specimen surface the fracture is intergranular as shown in Fig. 17. Immediately below there is a zone of quasi-cleavage fracture and further below the fracture turns to entirely ductile (dimples) as shown in Fig. 17. The results underline the need to consider the fatigue crack growth behaviour of corroded 2024 as the result of the synergetic effect of corrosion and corrosion induced hydrogen embrittlement.

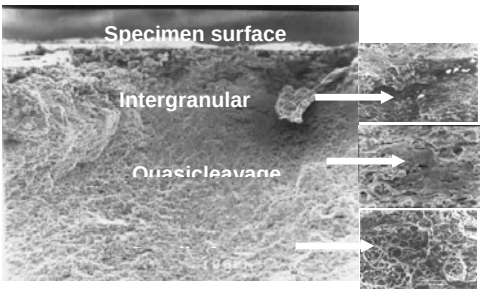

Fig. 17 Local embrittled areas in corroded 2024 specimens.

4. Concluding Remarks

The fatigue crack growth behaviour of 2024 T351 aircraft aluminium alloy (i) with variation in microstructural characteristics and (ii) under the influence of existing corrosion damage has been investigated.

The experimental findings concerning the microstructural effects on fatigue crack growth revealed the following:

(1) The effect of microstructural features (e.g. grain size and morphology), as well as variations in purity composition can influence fatigue crack propagation in the medium ΔK region, which is of high technological interest for damage tolerance design.

(2) Plate microstructure with elongated grain morphology induced by the rolling process exhibited higher crack growth resistance than the microstructure of the sheet material with smaller equiaxed grains. This behaviour could be attributed to pronounced roughness induced crack closure effects in the plate microstructure.

(3) The experimental results showed that the plate microstructure with high purity composition provides better damage tolerance characteristics compared to the conventional sheet microstructure. With regard to the effect of existing corrosion on the fatigue crack growth the following conclusions can be made:

(4) The synergetic effect of corrosion and corrosion-induced hydrogen embrittlement resulted in an appreciable decrease in fatigue resistance and damage tolerance of the corroded material.

(5) The experimental results have demonstrated the need to account for the influence of pre-existing corrosion on the material's properties for the reliable fatigue and damage tolerance analyses of components involving corroded areas.

References

[1] Suresh S. Fatigue of Materials, second ed., Cambridge University Press, 1998, ISBN 0521578477, 700 pages
[2] Sih GC. and Chao CK. Failure initiation of unnotched specimens subjected to monotonic and cyclic loading, Theor. Appl. Fract. Mech. 2(1), (1984) 67-73
[3] Sih GC. and Moyer ET. Jr., Path dependent nature of fatigue crack growth, Inter. J. Eng. Fract. Mech. 7, (1983), 269-280
[4] Sih GC.and Chao CK. Influence of load amplitude and uniaxial tensile preties on fatigue crack frowth, Theor. Appl. Fract. Mech. 2(3), (1984) 247-257
[5] Elber W. Damage Tolerance in Aircraft Structures, ASTM Spec. Tech.Publ.486, (1981) 230
[6] Investigation on Damage Tolerance Behaviour of Aluminum Alloys, IDA,European Project, Project No: GRD2001-40120, Final Report (2005)
[7] Kermanidis AlTh. Effect of Corrosion on the Structural Integrity of Lightweight Aircraft Structures, PhD Thesis, University of Patras, Department of Mechanical and Aeronautical Engineering, Patras, Greece, (2003)
[8] Garrett GG. and Knott JF. Crystallographic Fatigue Crack Growth in Aluminum Alloys, *Acta Metallurgica*, 25, (1975) 841-849
[9] Suresh S. and Ritchie RO. *Metall. Trans. A, 13,* (1982) 1627
[10] Zaiken E. and Ritchie RO. Effects of Microstructure on Fatigue Crack Propagation and Crack Closure Behavior in Aluminum Alloy 7150 *Materials Science and Engineering*, 70 (1985) 151-160.
[11] E. Zaiken E. and Ritchie RO. On the Location of Crack Closure and the Threshold Condition for Fatigue Crack Growth, *Scripta Metallurgica*, 18 (1984) 847-850
[12] Tzou JL.Suresh S. Ritchie RO. Fatigue Crack Propagation in Oil Environments-. 1 Crack Growth Behaviour in Silicone and Parafin Oils, *Acta Metall.* 33 (1) (1985) 105-116
[13] Minakawa K. and McEvily AJ. On Crack Closure in the near Threshold Region, *Scripta Metallurgica*, 15 (1981) 633-636
[14] Venkateswara KT. Rao RJ. Bucci KV. Jata. and Ritchie RO. A comparison of fatigue crack propagation behavior in sheet and plate aluminum-lithium alloys, *Materials Science and Engineering*, A141 (1991) 39-48
[15] Henk F. and Jong De. Thickness Direction Inhomogeneity of Mechanical Properties and Fracture Toughness as observed in Aluminum 7075 T651 Plate Material, *Enginneering Fracture Mechnanics* 13 (1980) 175-192
[16] Suresh S. Micromechanisms of fatigue Crack Growth Retardation Following Overloads, *Engineering Fracture Mechanics* 18. (3) (1983) 577-593,
[17] ASTM E647-93, Standard Test Method for Measurement of Fatigue Crack Growth Tests, *Annual Book of ASTM Standards, Metals –Test Methods and Analytical Procedures*, Section 3, Vol. 03.01, Metals-Mechanical Testing; Elevated Low-Temperature Tests; Metallography, (1994)

[18] ASM Handbook, Volume1 2, *Fractography*, The Materials Information Society, (2000)
[19] Pao PS. Cooley LA. Imam MA. And Yoder GR. Fatigue Crack Growth in 2090 Al-Li Alloy, *Scripta Metallurgica*, 23, (1989) 1455-1460
[20] Schijve J. Fatigue Cracks, Plasticity Effects and Crack Closure, Four Lectures on Fracture Mechanics, 1l. No. 1-L, (1978)
[21] Pantelakis SpG. Vassilas NI. and Daglaras PG. Effects of corrosive environment on the mechanical behaviour of the advanced Al–Li alloys 2091 and 8090 and the conventional aerospace alloy 2024, *Metall*, 47 (1993) 135–141.
[22] Pantelakis SpG. DaglarasPG. and Apostolopoulos ChAlk. Tensile and energy density properties of 2024, 6013, 8090 and 2091 aircraft aluminum alloy after corrosion exposure, J. Theor. Appl. Fract. Mech. 33 (2000) 117–134
[23] Papanikos P. and Kermanidis AlTh. Effect of corrosioninduced hydrogen embrittlement on the fracture toughness of 2024-T3 aluminum alloy, in: Proceedings of the 4th International Conference on New Challenges in Mesomechanics, Aalborg University, Denmark, (2002)
[24] Smiyan OD. Coval MV. and Melekhov RK. Local corrosion damage of aluminum alloys, Soviet Mater. Sci. 19 (1983) 422
[25] Tuck CDS. Evidence for the formation of magnesium hydride on the gra boundaries of Al–Zn–Mg alloys during their exposure to water vapour, in: Proceedings of the Third International Conference of Hydrogen on the Behavior of Materials, Jackson, Wyoming, (1980) 503– 511
[26] Scamans GM. R. Alani R. and Swann PR. Pre-exposure embrittlement andstress corrosion failure in Al–Zn–Mg alloys, Corros. Sci. 16 (1976) 443
[13] E. Charitidou E. Papapolymerou G, Haidemenopoulos GN. Hassiotis N. and Bontozoglou HV. Characterization of trapped hydrogen in exfoliation corroded aluminium alloy 2024, Script. Mater. 41 (1999) 1327
[27] Haidemenopoulos GN, Hassiotis N, Papapolymerou G. and Bontozoglou HV. Hydrogen absorption into aluminum alloy 2024-T3 during exfoliation and alternate immersion testing, Corrosion 54 (1998) 73
[28] Petroyiannis PV. Kermanidis AlTh. Papanikos P. and Pantelakis SpG, Corrosion-induced hydrogen embrittlement of 2024 and 6013 aluminium alloys, Special issue: Al.Th. Kermanidis et al. / Theoretical and Applied Fracture Mechanics 43 (2005) 121–132 131 mesofracture mechanics: current approaches to material damage at different size and time scales, Theor. Appl. Fract. Mech. 41 (1–3) (2004) 173
[29] P.V. Petroyiannis PV. Kermanidis AlTh. E. Kamoutsi E. Pantelakis SpG. Bontozoglou HV. and Haidemenopoulos GN. Evidence on the corrosion-induced hydrogen embrittlement of the 2024 aluminum alloy, Fatigue Fract. Eng. Mater. Struct., 28 (2005) 565-574
[30] Birnbaum HK. and Sofronis P. Hydrogen-enhanced localized plasticity-a mechanism for hydrogen-related fracture, Mat. Sci. Eng. A 176 (1994) 191
[31] Ruiz J. and Elices M. The role of environmental exposure in the fatigue behaviour of an aluminium alloy, *Corros. Sci*. 39 (12) (1997) 2117

[32] Lin CK. and Yang ST.Corrosion fatigue behavior of 7050 aluminum alloys in different tempers, *Eng. Fract. Mech*. 59 (6) (1998) 779
[33] Inman ME. Kelly RG. S.A. Willard SA. and Piascik RS. in: Proceedings of the FAA-NASA Symposium on the Continued Airworthiness of Aircraft Structures, Virginia, USA, (1997) 129
[34] Zamber JE. and Hillberry BM. Probabilistic approach to predicting fatigue lives of corroded 2024-T3, AIAA J. 37 (10) (1999) 1311.
[35] Bray GH. Bucci RJ. Colvin EL. and Kulak M. Effects of prior corrosion on the S/N fatigue performance of aluminium sheet alloys 2024-T3 and 2524-T3, in: W.A. Van der Sluys, R.S. Piascik, R. Zawierucha (Eds.), Effects of the Environment on the Initiation of Crack Growth, ASTM STP 1298, American Society for Testing and Materials, (1997) 89
[36] Kermanidis AlTh. Petroyiannis PV. and Pantelakis SpG. Fatigue and damage tolerance behaviour of corroded 2024 T351 aircraft aluminum alloy, Theoretical and Applied Fracture Mechanics 43 (2005) 121–132
[37] Chubb JP. Morad TA. Hockenhull BS. and Bristow JW. The effect of exfoliation corrosion on the fatigue behaviour of structural aluminium alloys, Structural Integrity of Ageing Airplanes, Springer-Verlag, Berlin, (1991) 87
[38] ASTM G34-90, Standard Test Method for Exfoliation Corrosion Susceptbility in 2xxx and 7xxx Series Aluminum Alloys, (EXCO Test), *Annual Book of ASTM Standards, Metals –Test Methods and Analytical Procedures*, Section 3, Vol. 03.02, Wear and Erosion; Metal Corrosion, (1995)

Author Index

Subject Index

Mechanics

SOLID MECHANICS AND ITS APPLICATIONS

Series Editor: G.M.L. Gladwell

Aims and Scope of the Series

The fundamental questions arising in mechanics are: *Why?*, *How?*, and *How much?* The aim of this series is to provide lucid accounts written by authoritative researchers giving vision and insight in answering these questions on the subject of mechanics as it relates to solids. The scope of the series covers the entire spectrum of solid mechanics. Thus it includes the foundation of mechanics; variational formulations; computational mechanics; statics, kinematics and dynamics of rigid and elastic bodies; vibrations of solids and structures; dynamical systems and chaos; the theories of elasticity, plasticity and viscoelasticity; composite materials; rods, beams, shells and membranes; structural control and stability; soils, rocks and geomechanics; fracture; tribology; experimental mechanics; biomechanics and machine design.

1. R.T. Haftka, Z. Gürdal and M.P. Kamat: *Elements of Structural Optimization*. 2nd rev.ed., 1990 ISBN 0-7923-0608-2
2. J.J. Kalker: *Three-Dimensional Elastic Bodies in Rolling Contact.* 1990 ISBN 0-7923-0712-7
3. P. Karasudhi: *Foundations of Solid Mechanics.* 1991 ISBN 0-7923-0772-0
4. *Not published*
5. *Not published.*
6. J.F. Doyle: *Static and Dynamic Analysis of Structures.* With an Emphasis on Mechanics and Computer Matrix Methods. 1991 ISBN 0-7923-1124-8; Pb 0-7923-1208-2
7. O.O. Ochoa and J.N. Reddy: *Finite Element Analysis of Composite Laminates.* ISBN 0-7923-1125-6
8. M.H. Aliabadi and D.P. Rooke: *Numerical Fracture Mechanics.* ISBN 0-7923-1175-2
9. J. Angeles and C.S. López-Cajún: *Optimization of Cam Mechanisms.* 1991 ISBN 0-7923-1355-0
10. D.E. Grierson, A. Franchi and P. Riva (eds.): *Progress in Structural Engineering.* 1991 ISBN 0-7923-1396-8
11. R.T. Haftka and Z. Gürdal: *Elements of Structural Optimization.* 3rd rev. and exp. ed. 1992 ISBN 0-7923-1504-9; Pb 0-7923-1505-7
12. J.R. Barber: *Elasticity*. 1992 ISBN 0-7923-1609-6; Pb 0-7923-1610-X
13. H.S. Tzou and G.L. Anderson (eds.): *Intelligent Structural Systems.* 1992 ISBN 0-7923-1920-6
14. E.E. Gdoutos: *Fracture Mechanics.* An Introduction. 1993 ISBN 0-7923-1932-X
15. J.P. Ward: *Solid Mechanics*. An Introduction. 1992 ISBN 0-7923-1949-4
16. M. Farshad: *Design and Analysis of Shell Structures*. 1992 ISBN 0-7923-1950-8
17. H.S. Tzou and T. Fukuda (eds.): *Precision Sensors, Actuators and Systems*. 1992 ISBN 0-7923-2015-8
18. J.R. Vinson: *The Behavior of Shells Composed of Isotropic and Composite Materials*. 1993 ISBN 0-7923-2113-8
19. H.S. Tzou: *Piezoelectric Shells*. Distributed Sensing and Control of Continua. 1993 ISBN 0-7923-2186-3
20. W. Schiehlen (ed.): *Advanced Multibody System Dynamics*. Simulation and Software Tools. 1993 ISBN 0-7923-2192-8
21. C.-W. Lee: *Vibration Analysis of Rotors.* 1993 ISBN 0-7923-2300-9
22. D.R. Smith: *An Introduction to Continuum Mechanics.* 1993 ISBN 0-7923-2454-4
23. G.M.L. Gladwell: *Inverse Problems in Scattering*. An Introduction. 1993 ISBN 0-7923-2478-1

Mechanics

SOLID MECHANICS AND ITS APPLICATIONS

Series Editor: G.M.L. Gladwell

24. G. Prathap: *The Finite Element Method in Structural Mechanics*. 1993 ISBN 0-7923-2492-7
25. J. Herskovits (ed.): *Advances in Structural Optimization.* 1995 ISBN 0-7923-2510-9
26. M.A. González-Palacios and J. Angeles: *Cam Synthesis.* 1993 ISBN 0-7923-2536-2
27. W.S. Hall: *The Boundary Element Method.* 1993 ISBN 0-7923-2580-X
28. J. Angeles, G. Hommel and P. Kovács (eds.): *Computational Kinematics.* 1993 ISBN 0-7923-2585-0
29. A. Curnier: *Computational Methods in Solid Mechanics*. 1994 ISBN 0-7923-2761-6
30. D.A. Hills and D. Nowell: *Mechanics of Fretting Fatigue*. 1994 ISBN 0-7923-2866-3
31. B. Tabarrok and F.P.J. Rimrott: *Variational Methods and Complementary Formulations in Dynamics.* 1994 ISBN 0-7923-2923-6
32. E.H. Dowell (ed.), E.F. Crawley, H.C. Curtiss Jr., D.A. Peters, R. H. Scanlan and F. Sisto: *A Modern Course in Aeroelasticity*. Third Revised and Enlarged Edition. 1995 ISBN 0-7923-2788-8; Pb: 0-7923-2789-6
33. A. Preumont: *Random Vibration and Spectral Analysis.* 1994 ISBN 0-7923-3036-6
34. J.N. Reddy (ed.): *Mechanics of Composite Materials*. Selected works of Nicholas J. Pagano. 1994 ISBN 0-7923-3041-2
35. A.P.S. Selvadurai (ed.): *Mechanics of Poroelastic Media*. 1996 ISBN 0-7923-3329-2
36. Z. Mróz, D. Weichert, S. Dorosz (eds.): *Inelastic Behaviour of Structures under Variable Loads*. 1995 ISBN 0-7923-3397-7
37. R. Pyrz (ed.): *IUTAM Symposium on Microstructure-Property Interactions in Composite Materials.* Proceedings of the IUTAM Symposium held in Aalborg, Denmark. 1995 ISBN 0-7923-3427-2
38. M.I. Friswell and J.E. Mottershead: *Finite Element Model Updating in Structural Dynamics*. 1995 ISBN 0-7923-3431-0
39. D.F. Parker and A.H. England (eds.): *IUTAM Symposium on Anisotropy, Inhomogeneity and Nonlinearity in Solid Mechanics.* Proceedings of the IUTAM Symposium held in Nottingham, U.K. 1995 ISBN 0-7923-3594-5
40. J.-P. Merlet and B. Ravani (eds.): *Computational Kinematics '95*. 1995 ISBN 0-7923-3673-9
41. L.P. Lebedev, I.I. Vorovich and G.M.L. Gladwell: *Functional Analysis.* Applications in Mechanics and Inverse Problems. 1996 ISBN 0-7923-3849-9
42. J. Menčik: *Mechanics of Components with Treated or Coated Surfaces.* 1996 ISBN 0-7923-3700-X
43. D. Bestle and W. Schiehlen (eds.): *IUTAM Symposium on Optimization of Mechanical Systems.* Proceedings of the IUTAM Symposium held in Stuttgart, Germany. 1996 ISBN 0-7923-3830-8
44. D.A. Hills, P.A. Kelly, D.N. Dai and A.M. Korsunsky: *Solution of Crack Problems*. The Distributed Dislocation Technique. 1996 ISBN 0-7923-3848-0
45. V.A. Squire, R.J. Hosking, A.D. Kerr and P.J. Langhorne: *Moving Loads on Ice Plates*. 1996 ISBN 0-7923-3953-3
46. A. Pineau and A. Zaoui (eds.): *IUTAM Symposium on Micromechanics of Plasticity and Damage of Multiphase Materials*. Proceedings of the IUTAM Symposium held in Sèvres, Paris, France. 1996 ISBN 0-7923-4188-0
47. A. Naess and S. Krenk (eds.): *IUTAM Symposium on Advances in Nonlinear Stochastic Mechanics*. Proceedings of the IUTAM Symposium held in Trondheim, Norway. 1996 ISBN 0-7923-4193-7
48. D. Ieşan and A. Scalia: *Thermoelastic Deformations.* 1996 ISBN 0-7923-4230-5

Mechanics

SOLID MECHANICS AND ITS APPLICATIONS

Series Editor: G.M.L. Gladwell

49. J.R. Willis (ed.): *IUTAM Symposium on Nonlinear Analysis of Fracture*. Proceedings of the IUTAM Symposium held in Cambridge, U.K. 1997 ISBN 0-7923-4378-6
50. A. Preumont: *Vibration Control of Active Structures*. An Introduction. 1997 ISBN 0-7923-4392-1
51. G.P. Cherepanov: *Methods of Fracture Mechanics: Solid Matter Physics*. 1997 ISBN 0-7923-4408-1
52. D.H. van Campen (ed.): *IUTAM Symposium on Interaction between Dynamics and Control in Advanced Mechanical Systems.* Proceedings of the IUTAM Symposium held in Eindhoven, The Netherlands. 1997 ISBN 0-7923-4429-4
53. N.A. Fleck and A.C.F. Cocks (eds.): *IUTAM Symposium on Mechanics of Granular and Porous Materials.* Proceedings of the IUTAM Symposium held in Cambridge, U.K. 1997 ISBN 0-7923-4553-3
54. J. Roorda and N.K. Srivastava (eds.): *Trends in Structural Mechanics*. Theory, Practice, Education. 1997 ISBN 0-7923-4603-3
55. Yu.A. Mitropolskii and N. Van Dao: *Applied Asymptotic Methods in Nonlinear Oscillations*. 1997 ISBN 0-7923-4605-X
56. C. Guedes Soares (ed.): *Probabilistic Methods for Structural Design.* 1997 ISBN 0-7923-4670-X
57. D. François, A. Pineau and A. Zaoui: *Mechanical Behaviour of Materials.* Volume I: Elasticity and Plasticity. 1998 ISBN 0-7923-4894-X
58. D. François, A. Pineau and A. Zaoui: *Mechanical Behaviour of Materials.* Volume II: Viscoplasticity, Damage, Fracture and Contact Mechanics. 1998 ISBN 0-7923-4895-8
59. L.T. Tenek and J. Argyris: *Finite Element Analysis for Composite Structures.* 1998 ISBN 0-7923-4899-0
60. Y.A. Bahei-El-Din and G.J. Dvorak (eds.): *IUTAM Symposium on Transformation Problems in Composite and Active Materials*. Proceedings of the IUTAM Symposium held in Cairo, Egypt. 1998 ISBN 0-7923-5122-3
61. I.G. Goryacheva: *Contact Mechanics in Tribology*. 1998 ISBN 0-7923-5257-2
62. O.T. Bruhns and E. Stein (eds.): *IUTAM Symposium on Micro- and Macrostructural Aspects of Thermoplasticity*. Proceedings of the IUTAM Symposium held in Bochum, Germany. 1999 ISBN 0-7923-5265-3
63. F.C. Moon: *IUTAM Symposium on New Applications of Nonlinear and Chaotic Dynamics in Mechanics*. Proceedings of the IUTAM Symposium held in Ithaca, NY, USA. 1998 ISBN 0-7923-5276-9
64. R. Wang: *IUTAM Symposium on Rheology of Bodies with Defects*. Proceedings of the IUTAM Symposium held in Beijing, China. 1999 ISBN 0-7923-5297-1
65. Yu.I. Dimitrienko: *Thermomechanics of Composites under High Temperatures*. 1999 ISBN 0-7923-4899-0
66. P. Argoul, M. Frémond and Q.S. Nguyen (eds.): *IUTAM Symposium on Variations of Domains and Free-Boundary Problems in Solid Mechanics*. Proceedings of the IUTAM Symposium held in Paris, France. 1999 ISBN 0-7923-5450-8
67. F.J. Fahy and W.G. Price (eds.): *IUTAM Symposium on Statistical Energy Analysis*. Proceedings of the IUTAM Symposium held in Southampton, U.K. 1999 ISBN 0-7923-5457-5
68. H.A. Mang and F.G. Rammerstorfer (eds.): *IUTAM Symposium on Discretization Methods in Structural Mechanics.* Proceedings of the IUTAM Symposium held in Vienna, Austria. 1999 ISBN 0-7923-5591-1

Mechanics

SOLID MECHANICS AND ITS APPLICATIONS

Series Editor: G.M.L. Gladwell

69. P. Pedersen and M.P. Bendsøe (eds.): *IUTAM Symposium on Synthesis in Bio Solid Mechanics*. Proceedings of the IUTAM Symposium held in Copenhagen, Denmark. 1999 ISBN 0-7923-5615-2
70. S.K. Agrawal and B.C. Fabien: *Optimization of Dynamic Systems*. 1999 ISBN 0-7923-5681-0
71. A. Carpinteri: *Nonlinear Crack Models for Nonmetallic Materials*. 1999 ISBN 0-7923-5750-7
72. F. Pfeifer (ed.): *IUTAM Symposium on Unilateral Multibody Contacts*. Proceedings of the IUTAM Symposium held in Munich, Germany. 1999 ISBN 0-7923-6030-3
73. E. Lavendelis and M. Zakrzhevsky (eds.): *IUTAM/IFToMM Symposium on Synthesis of Nonlinear Dynamical Systems*. Proceedings of the IUTAM/IFToMM Symposium held in Riga, Latvia. 2000 ISBN 0-7923-6106-7
74. J.-P. Merlet: *Parallel Robots*. 2000 ISBN 0-7923-6308-6
75. J.T. Pindera: *Techniques of Tomographic Isodyne Stress Analysis.* 2000 ISBN 0-7923-6388-4
76. G.A. Maugin, R. Drouot and F. Sidoroff (eds.): *Continuum Thermomechanics.* The Art and Science of Modelling Material Behaviour. 2000 ISBN 0-7923-6407-4
77. N. Van Dao and E.J. Kreuzer (eds.): *IUTAM Symposium on Recent Developments in Non-linear Oscillations of Mechanical Systems*. 2000 ISBN 0-7923-6470-8
78. S.D. Akbarov and A.N. Guz: *Mechanics of Curved Composites*. 2000 ISBN 0-7923-6477-5
79. M.B. Rubin: *Cosserat Theories: Shells, Rods and Points*. 2000 ISBN 0-7923-6489-9
80. S. Pellegrino and S.D. Guest (eds.): *IUTAM-IASS Symposium on Deployable Structures: Theory and Applications.* Proceedings of the IUTAM-IASS Symposium held in Cambridge, U.K., 6–9 September 1998. 2000 ISBN 0-7923-6516-X
81. A.D. Rosato and D.L. Blackmore (eds.): *IUTAM Symposium on Segregation in Granular Flows.* Proceedings of the IUTAM Symposium held in Cape May, NJ, U.S.A., June 5–10, 1999. 2000 ISBN 0-7923-6547-X
82. A. Lagarde (ed.): *IUTAM Symposium on Advanced Optical Methods and Applications in Solid Mechanics*. Proceedings of the IUTAM Symposium held in Futuroscope, Poitiers, France, August 31–September 4, 1998. 2000 ISBN 0-7923-6604-2
83. D. Weichert and G. Maier (eds.): *Inelastic Analysis of Structures under Variable Loads*. Theory and Engineering Applications. 2000 ISBN 0-7923-6645-X
84. T.-J. Chuang and J.W. Rudnicki (eds.): *Multiscale Deformation and Fracture in Materials and Structures*. The James R. Rice 60th Anniversary Volume. 2001 ISBN 0-7923-6718-9
85. S. Narayanan and R.N. Iyengar (eds.): *IUTAM Symposium on Nonlinearity and Stochastic Structural Dynamics.* Proceedings of the IUTAM Symposium held in Madras, Chennai, India, 4–8 January 1999 ISBN 0-7923-6733-2
86. S. Murakami and N. Ohno (eds.): *IUTAM Symposium on Creep in Structures*. Proceedings of the IUTAM Symposium held in Nagoya, Japan, 3-7 April 2000. 2001 ISBN 0-7923-6737-5
87. W. Ehlers (ed.): *IUTAM Symposium on Theoretical and Numerical Methods in Continuum Mechanics of Porous Materials.* Proceedings of the IUTAM Symposium held at the University of Stuttgart, Germany, September 5-10, 1999. 2001 ISBN 0-7923-6766-9
88. D. Durban, D. Givoli and J.G. Simmonds (eds.): *Advances in the Mechanis of Plates and Shells The Avinoam Libai Anniversary Volume*. 2001 ISBN 0-7923-6785-5
89. U. Gabbert and H.-S. Tzou (eds.): *IUTAM Symposium on Smart Structures and Structonic Systems*. Proceedings of the IUTAM Symposium held in Magdeburg, Germany, 26–29 September 2000. 2001 ISBN 0-7923-6968-8

Mechanics

SOLID MECHANICS AND ITS APPLICATIONS

Series Editor: G.M.L. Gladwell

90. Y. Ivanov, V. Cheshkov and M. Natova: *Polymer Composite Materials – Interface Phenomena & Processes*. 2001 ISBN 0-7923-7008-2
91. R.C. McPhedran, L.C. Botten and N.A. Nicorovici (eds.): *IUTAM Symposium on Mechanical and Electromagnetic Waves in Structured Media*. Proceedings of the IUTAM Symposium held in Sydney, NSW, Australia, 18-22 Januari 1999. 2001 ISBN 0-7923-7038-4
92. D.A. Sotiropoulos (ed.): *IUTAM Symposium on Mechanical Waves for Composite Structures Characterization*. Proceedings of the IUTAM Symposium held in Chania, Crete, Greece, June 14-17, 2000. 2001 ISBN 0-7923-7164-X
93. V.M. Alexandrov and D.A. Pozharskii: *Three-Dimensional Contact Problems*. 2001 ISBN 0-7923-7165-8
94. J.P. Dempsey and H.H. Shen (eds.): *IUTAM Symposium on Scaling Laws in Ice Mechanics and Ice Dynamics*. Proceedings of the IUTAM Symposium held in Fairbanks, Alaska, U.S.A., 13-16 June 2000. 2001 ISBN 1-4020-0171-1
95. U. Kirsch: *Design-Oriented Analysis of Structures*. A Unified Approach. 2002 ISBN 1-4020-0443-5
96. A. Preumont: *Vibration Control of Active Structures*. An Introduction (2^{nd} Edition). 2002 ISBN 1-4020-0496-6
97. B.L. Karihaloo (ed.): *IUTAM Symposium on Analytical and Computational Fracture Mechanics of Non-Homogeneous Materials.* Proceedings of the IUTAM Symposium held in Cardiff, U.K., 18-22 June 2001. 2002 ISBN 1-4020-0510-5
98. S.M. Han and H. Benaroya: *Nonlinear and Stochastic Dynamics of Compliant Offshore Structures*. 2002 ISBN 1-4020-0573-3
99. A.M. Linkov: *Boundary Integral Equations in Elasticity Theory*. 2002 ISBN 1-4020-0574-1
100. L.P. Lebedev, I.I. Vorovich and G.M.L. Gladwell: *Functional Analysis.* Applications in Mechanics and Inverse Problems (2^{nd} Edition). 2002 ISBN 1-4020-0667-5; Pb: 1-4020-0756-6
101. Q.P. Sun (ed.): *IUTAM Symposium on Mechanics of Martensitic Phase Transformation in Solids*. Proceedings of the IUTAM Symposium held in Hong Kong, China, 11-15 June 2001. 2002 ISBN 1-4020-0741-8
102. M.L. Munjal (ed.): *IUTAM Symposium on Designing for Quietness*. Proceedings of the IUTAM Symposium held in Bangkok, India, 12-14 December 2000. 2002 ISBN 1-4020-0765-5
103. J.A.C. Martins and M.D.P. Monteiro Marques (eds.): *Contact Mechanics*. Proceedings of the 3^{rd} Contact Mechanics International Symposium, Praia da Consolação, Peniche, Portugal, 17-21 June 2001. 2002 ISBN 1-4020-0811-2
104. H.R. Drew and S. Pellegrino (eds.): *New Approaches to Structural Mechanics, Shells and Biological Structures*. 2002 ISBN 1-4020-0862-7
105. J.R. Vinson and R.L. Sierakowski: *The Behavior of Structures Composed of Composite Materials*. Second Edition. 2002 ISBN 1-4020-0904-6
106. Not yet published.
107. J.R. Barber: *Elasticity*. Second Edition. 2002 ISBN Hb 1-4020-0964-X; Pb 1-4020-0966-6
108. C. Miehe (ed.): *IUTAM Symposium on Computational Mechanics of Solid Materials at Large Strains*. Proceedings of the IUTAM Symposium held in Stuttgart, Germany, 20-24 August 2001. 2003 ISBN 1-4020-1170-9

Mechanics

SOLID MECHANICS AND ITS APPLICATIONS

Series Editor: G.M.L. Gladwell

109. P. Ståhle and K.G. Sundin (eds.): *IUTAM Symposium on Field Analyses for Determination of Material Parameters – Experimental and Numerical Aspects.* Proceedings of the IUTAM Symposium held in Abisko National Park, Kiruna, Sweden, July 31 – August 4, 2000. 2003 ISBN 1-4020-1283-7
110. N. Sri Namachchivaya and Y.K. Lin (eds.): *IUTAM Symposium on Nonlnear Stochastic Dynamics.* Proceedings of the IUTAM Symposium held in Monticello, IL, USA, 26 – 30 August, 2000. 2003 ISBN 1-4020-1471-6
111. H. Sobieckzky (ed.): *IUTAM Symposium Transsonicum IV*. Proceedings of the IUTAM Symposium held in Göttingen, Germany, 2–6 September 2002, 2003 ISBN 1-4020-1608-5
112. J.-C. Samin and P. Fisette: *Symbolic Modeling of Multibody Systems*. 2003 ISBN 1-4020-1629-8
113. A.B. Movchan (ed.): *IUTAM Symposium on Asymptotics, Singularities and Homogenisation in Problems of Mechanics.* Proceedings of the IUTAM Symposium held in Liverpool, United Kingdom, 8-11 July 2002. 2003 ISBN 1-4020-1780-4
114. S. Ahzi, M. Cherkaoui, M.A. Khaleel, H.M. Zbib, M.A. Zikry and B. LaMatina (eds.): *IUTAM Symposium on Multiscale Modeling and Characterization of Elastic-Inelastic Behavior of Engineering Materials.* Proceedings of the IUTAM Symposium held in Marrakech, Morocco, 20-25 October 2002. 2004 ISBN 1-4020-1861-4
115. H. Kitagawa and Y. Shibutani (eds.): *IUTAM Symposium on Mesoscopic Dynamics of Fracture Process and Materials Strength.* Proceedings of the IUTAM Symposium held in Osaka, Japan, 6-11 July 2003. Volume in celebration of Professor Kitagawa's retirement. 2004 ISBN 1-4020-2037-6
116. E.H. Dowell, R.L. Clark, D. Cox, H.C. Curtiss, Jr., K.C. Hall, D.A. Peters, R.H. Scanlan, E. Simiu, F. Sisto and D. Tang: *A Modern Course in Aeroelasticity*. 4th Edition, 2004 ISBN 1-4020-2039-2
117. T. Burczyński and A. Osyczka (eds.): *IUTAM Symposium on Evolutionary Methods in Mechanics.* Proceedings of the IUTAM Symposium held in Cracow, Poland, 24-27 September 2002. 2004 ISBN 1-4020-2266-2
118. D. Ieşan: *Thermoelastic Models of Continua*. 2004 ISBN 1-4020-2309-X
119. G.M.L. Gladwell: *Inverse Problems in Vibration*. Second Edition 2004 ISBN 1-4020-2670-6
120. J.R. Vinson: *Plate and Panel Structures of Isotropic, Composite and Piezoelectric Materials, Including Sandwich Construction*. 2005 ISBN 1-4020-3110-6
121. *Forthcoming*.
122. G. Rega and F. Vestroni (eds.): *IUTAM Symposium on Chaotic Dynamics and Control of Systems and Processes in Mechanics*. Proceedings of the IUTAM Symposium held in Rome, Italy, 8–13 June 2003. 2005 ISBN 1-4020-3267-6
123. E.E. Gdoutos: *Fracture Mechanics. An Introduction*. 2nd edition. 2005 ISBN 1-4020-2863-2
124. M.D. Gilchrist (ed.): *IUTAM Symposium on Impact Biomechanics from Fundamental Insights to Applications*. 2005 ISBN 1-4020-3795-3
125. J.M. Huyghe, P.A.C. Raats and S.C. Cowin (eds.): *IUTAM Symposium on Physicochemical and Electromechanical Interactions in Porous Media*. 2005 ISBN 1-4020-3864-X
126. H. Ding, W. Chen and L. Zhang: *Elasticity of Transversely Isotropic Materials*. 2005 ISBN 1-4020-4033-4
127. W. Yang (ed.): *IUTAM Symposium on Mechanics and Reliability of Actuating Materials*. Proceedings of the IUTAM Symposium held in Beijing, China, 1–3 September 2004. 2005 ISBN 1-4020-4131-6

Mechanics

SOLID MECHANICS AND ITS APPLICATIONS

Series Editor: G.M.L. Gladwell

128. J.-P. Merlet: *Parallel Robots*. 2006 ISBN 1-4020-4132-2
129. G.E.A. Meier and K.R. Sreenivasan (eds.): *IUTAM Symposium on One Hundred Years of Boundary Layer Research*. Proceedings of the IUTAM Symposium held at DLR-Göttingen, Germany, August 12–14, 2004. 2006 ISBN 1-4020-4149-7
130. H. Ulbrich and W. Günthner (eds.): *IUTAM Symposium on Vibration Control of Nonlinear Mechanisms and Structures*. 2006 ISBN 1-4020-4160-8
131. L. Librescu and O. Song: *Thin-Walled Composite Beams. Theory and Application*. 2006 ISBN 1-4020-3457-1
132. G. Ben-Dor, A. Dubinsky and T. Elperin: *Applied High-Speed Plate Penetration Dynamics*. 2006 ISBN 1-4020-3452-0
133. X. Markenscoff and A. Gupta (eds.): *Collected Works of J. D. Eshelby*. Mechanics of Defects and Inhomogeneities. 2006 ISBN 1-4020-4416-X
134. R.W. Snidle and H.P. Evans (eds.): *IUTAM Symposium on Elastohydrodynamics and Microelastohydrodynamics*. Proceedings of the IUTAM Symposium held in Cardiff, UK, 1–3 September, 2004. 2006 ISBN 1-4020-4532-8
135. T. Sadowski (ed.): *IUTAM Symposium on Multiscale Modelling of Damage and Fracture Processes in Composite Materials*. Proceedings of the IUTAM Symposium held in Kazimierz Dolny, Poland, 23–27 May 2005. 2006 ISBN 1-4020-4565-4
136. A. Preumont: *Mechatronics. Dynamics of Electromechanical and Piezoelectric Systems*. 2006 ISBN 1-4020-4695-2
137. M.P. Bendsøe, N. Olhoff and O. Sigmund (eds.): *IUTAM Symposium on Topological Design Optimization of Structures, Machines and Materials*. Status and Perspectives. 2006 ISBN 1-4020-4729-0
138. A. Klarbring: *Models of Mechanics*. 2006 ISBN 1-4020-4834-3
139. H.D. Bui: *Fracture Mechanics*. Inverse Problems and Solutions. 2006 ISBN 1-4020-4836-X
140. M. Pandey, W.-C. Xie and L. Xu (eds.): *Advances in Engineering Structures, Mechanics and Construction*. Proceedings of an International Conference on Advances in Engineering Structures, Mechanics & Construction, held in Waterloo, Ontario, Canada, May 14–17, 2006. 2006 ISBN 1-4020-4890-4
141. G.Q. Zhang, W.D. van Driel and X. J. Fan: *Mechanics of Microelectronics*. 2006 ISBN 1-4020-4934-X
142. Q.P. Sun and P. Tong (eds.): *IUTAM Symposium on Size Effects on Material and Structural Behavior at Micron- and Nano-Scales*. Proceedings of the IUTAM Symposium held in Hong Kong, China, 31 May–4 June, 2004. 2006 ISBN 1-4020-4945-5
143. A.P. Mouritz and A.G. Gibson: *Fire Properties of Polymer Composite Materials*. 2006 ISBN 1-4020-5355-X
144. Y.L. Bai, Q.S. Zheng and Y.G. Wei (eds.): *IUTAM Symposium on Mechanical Behavior and Micro-Mechanics of Nanostructured Materials*. Proceedings of the IUTAM Symposium held in Beijing, China, 27–30 June 2005. 2007 ISBN 1-4020-5623-0
145. L.P. Pook: *Metal Fatigue*. What It Is, Why It Matters. 2007 ISBN 1-4020-5596-6
146. H.I. Ling, L. Callisto, D. Leshchinsky and J. Koseki (eds.): *Soil Stress-Strain Behavior: Measurement, Modeling and Analysis*. A Collection of Papers of the Geotechnical Symposium in Rome, March 16–17, 2006. 2007 ISBN 978-1-4020-6145-5
147. A.S. Kravchuk and P.J. Neittaanmäki: *Variational and Quasi-Variational Inequalities in Mechanics*. 2007 ISBN 978-1-4020-6376-3

Mechanics

SOLID MECHANICS AND ITS APPLICATIONS

Series Editor: G.M.L. Gladwell

148. S.K. Kanaun and V. Levin: *Self-Consistent Methods for Composites*. Vol. 1: Static Problems. 2008 ISBN 978-1-4020-6663-4
149. G. Gogu: *Structural Synthesis of Parallel Robots*. Part 1: Methodology. 2008 ISBN 978-1-4020-5102-9
150. S.K. Kanaun and V. Levin: *Self-Consistent Methods for Composites*. Vol. 2: Wave Propagation in Heterogeneous Materials. 2008 ISBN 978-1-4020-6967-3
151. U. Kirsch: *Reanalysis of Structures*. A Unified Approach for Linear, Nonlinear, Static and Dynamic Systems. 2008 ISBN 978-1-4020-8197-2
152. G.C. Sih (ed.): *Multiscale Fatigue Crack Initiation and Propagation of Engineering Materials: Structural Integrity and Microstructural Worthiness*. Fatigue Crack Growth Behaviour of Small and Large Bodies. 2008 ISBN 978-1-4020-8519-2